



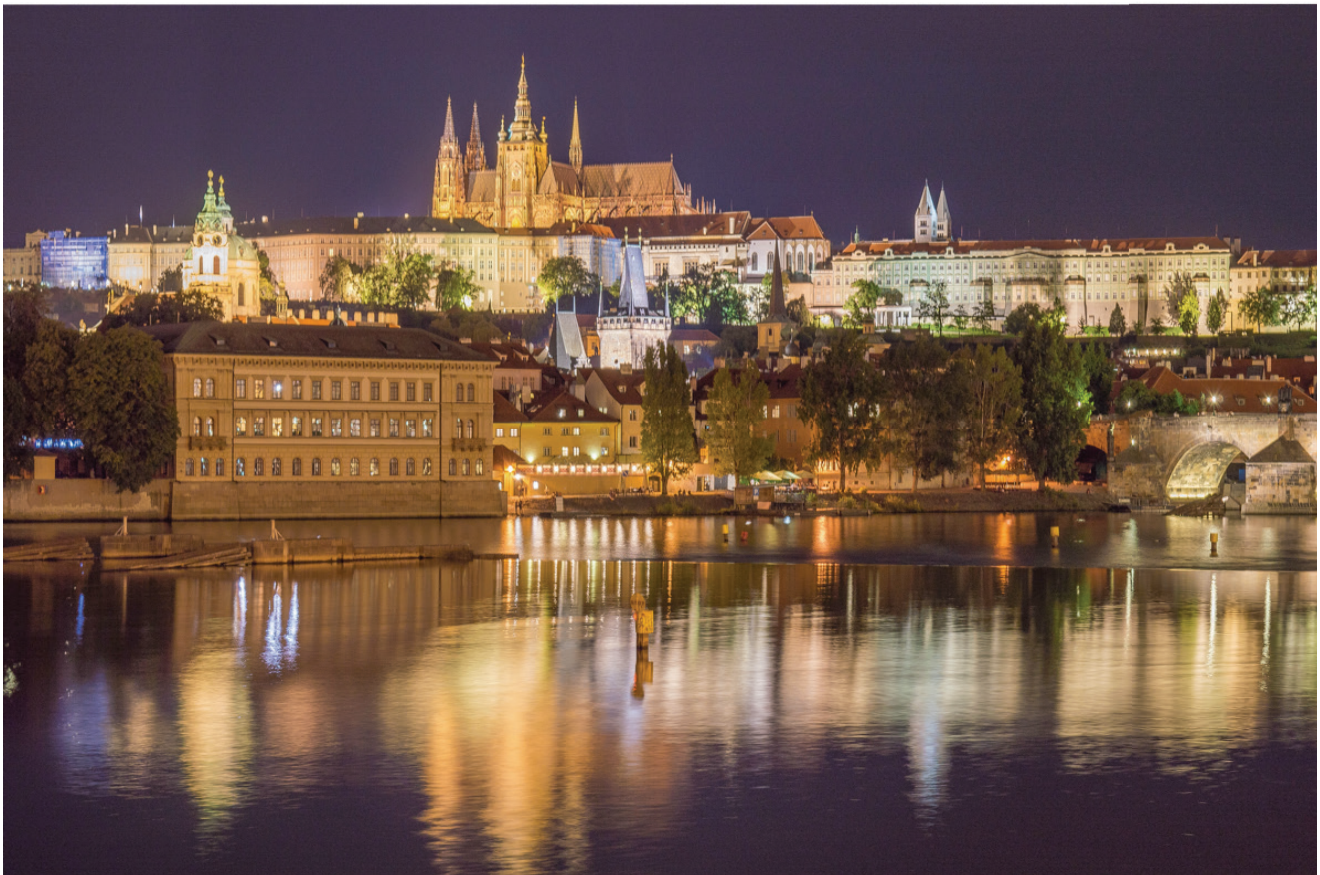
Czech Physical Society



Slovak Physical Society

20th CONFERENCE OF CZECH AND SLOVAK PHYSICISTS

7. 9. - 10. 9. 2020
Prague, Czech Republic



PROCEEDINGS

EDITORS

Andrea Džubinská & Marián Reiffers

20th CONFERENCE OF CZECH AND SLOVAK PHYSICISTS
PROCEEDINGS

Editors: Ing. RNDr. Andrea Džubinská, PhD., prof. RNDr. Marián Reiffers, DrSc.

All papers were anonymously reviewed

Published: Slovak Physical Society, Czech Physical Society
Printed: EQUILIBRIA, s.r.o., Košice
Košice 2020

ISBN 978-80-89855-13-1
EAN 9788089855131

OPENING ADDRESS

Dear colleagues,

20th conference of Czech and Slovak Physicists organized in Prague at the Faculty of Mathematics and Physics of the Charles University was a continuation of series of traditional meetings taking part alternately in both countries every three years. The conference was held under the auspices of the Mayor of Prague and the Ambassador of Slovakia in the Czech Republic. The conference contributed to preserve exceptional contacts and awareness about events in both national communities of scientists and teachers of physics, and to strengthen communication in physics across different fields of interests as well as across generations.

The conference addressed not only leading physicists in both countries but some parts of the program were freely accessible to teachers of physics and even a general public in order to provide a platform, where people can meet physicists doing supreme research and physicists can present their result and demonstrate indispensable role of physics in a daily life of a society.

However, this year the conference was negatively influenced by a running coronavirus pandemic. Although the border between the two countries was not closed, a risk of a necessary quarantine after a return back home did not allow a majority of attendants from Slovakia to arrive to Prague and present their results personally. Also the features of the infection evoked a fear among some Czech participants and therefore finally the conference was organized partially as on-site and partially as on-line one. A modern communication system built in a newly opened building of the Faculty of Mathematics and Physics called KOMPAKT enabled to present not only lectures of all on-line and on-site participants but also a series of experiments and discussions. Even a poster session was organized in parallel with all posters printed and displayed in the presentation hall and simultaneously also on web pages related to the conference.

In conclusion, we would like to thank all colleagues from the Czech Physical Society and the Slovak Physical Society, the members of the Organizing and Program Committees, as well as other colleagues, who contributed to the organization of this conference. We would like to thank all the participants of this Conference, mainly for their active attendance, valuable contributions, patience and generosity when not everything was running according to plans. We hope that the 20th Conference of the Czech and Slovak Physicists had despite of unfavorable conditions a high scientific level, was successful and useful for the further development of physics in our region. Finally we hope, that the next conference will take part in a more easy time and physicists from both countries would have the opportunity to meet again face-to-face in Slovakia.

Jan Mlynář, Miroslav Cieslar
Chairmen of conference

CONTENT

THE EXPERIMENT KATRIN LIMITED THE NEUTRINO MASS TO LESS THAN 1 eV	
O. Dragoun for the KATRIN Collaboration	1
ELECTROMAGNETIC STRUCTURE OF MESONS AND BARYONS	
C. Adamuščin, E. Bartoš, S. Dubnička, A. Liptaj, Z. Dubničková	7
SELECTED RESULTS OF THE ATLAS EXPERIMENT WITH SIGNIFICANT CONTRIBUTION OF CZECH AND SLOVAK PHYSICISTS	
T. Davidek	13
LASER – WORKING TOOL OF THE 21ST CENTURY	
M. Smrž	19
CZECH PARTICIPATION AT FACILITY FOR ANTIPROTON AND ION RESEARCH	
A. Kugler	25
TRENDS IN PHYSICS EDUCATION, EXPECTATIONS AND REALISATION	
M. Kireš, Z. Ješková	27
NITRIDE SEMICONDUCTORS – PROPERTIES AND APPLICATIONS	
A. Hospodková, F. Hájek, T. Hubáček, J. Oswald, F. Dominec, K. Kuldová	32
NUCLEAR METHODS FOR ASTROPHYSICAL PURPOSES	
G. D'Agata, J. Mrazek, V. Burjan, A. Cassisa	37
THE PROTON AND DEUTERON ACTIVATION AT NPI AND SPIRAL2/NFS FRANCE	
E. Šimečková, R. Běhal, V. Glagolev, J. Mrázek, J. Novák, M. Štefánik	39
DEVICES FOR NUCLEAR DATA MEASUREMENTS WITH COLLIMATED FAST NEUTRON BEAMS GENERATED ON U-120M CYCLOTRON	
M. Ansorge, J. Novák, M. Majerle, D. Koliadko	41
EFFECTS OF HIGH PRESSURE ON THE RADIOACTIVE DECAY	
A. Cassisa	43
MEASUREMENT OF OPEN-CHARM HADRONS IN Au+Au COLLISIONS AT $\sqrt{s_{NN}} = 200$ GeV BY THE STAR EXPERIMENT	
J. Vanek	45
RECENT RESULTS OF INCLUSIVE JET PRODUCTION IN Au+Au COLLISIONS AT $\sqrt{s_{NN}} = 200$ GeV BY THE STAR EXPERIMENT	
R. Licenik	47
SEARCH FOR JET QUENCHING EFFECTS IN HIGH-MULTIPLICITY PROTON-PROTON COLLISIONS AT $\sqrt{s} = 13$ TeV	
F. Krizek	49
IDENTIFYING HEAVY-FLAVOR JETS USING VECTORS OF LOCALLY AGGREGATED DESCRIPTORS	
G. Ponomatkin	51
RECENT RESULTS OF UPSILON PRODUCTION MEASURED WITH THE STAR EXPERIMENT	
L. Kosarzewski	53
NOVEL HIGH-LUMINOSITY FIXED-TARGET EXPERIMENT AT THE LHC	
B. Trzeciak	55
ALICE - ITS UPGRADE	
A. Isakov	57
OPEN-CHARM AND CHARM-TAGGED-JET PRODUCTION WITH ALICE AT LHC	
J. Kvapil	59
ANALYSING MYSTERIOUS TURBULENCE	
D. Duda, V. Yanovych, V. Uruba	61
EXPERIMENTAL STUDY OF EMERGENT GROUND STATE BEHAVIOUR IN RENi₅ (RE = Ce, Yb, Gd) SYSTEM	

A. Dzubinska, M. Reiffers, M. Giovannini, J. Rodríguez Fernández, R. Varga, J. I. Espeso, J. C. Gómez Sal	63
MICROSTRUCTURE OF STEELS STUDIED BY MÖSSBAUER SPECTROMETRY	
D. Košovský, M. Miglierini, T. Kmječ	65
STUDY OF MAGNETICALLY INDUCED CRYSTAL REORIENTATION OF Ni-Mn-Ga FERROMAGNETIC SHAPE MEMORY ALLOY	
Š. Sukup, S. Heczko, O. Heczko	67
NITRIDE MULTIPLE QUANTUM WELL CHALLENGE	
J. Oswald, A. Hospodková, T. Hubáček, K. Kuldová, J. Pangrác, F. Hájek	69
DIELECTRIC SPECTROSCOPY OF FUNCTIONALIZED CARBON NANOTUBES	
J. Kúdelčík	71
QUANTUM DOTS GROWN BY METALORGANIC VAPOR PHASE EPITAXY	
E. Hulicius, A. Hospodková, M. Slavická Zíková	73
THE MOMENTUM SPECTRUM VERSUS THE PROBABILITY FLUX DIRECTION IN QUANTUM MECHANICS	
J. Dittrich	75
PHYSICS AT FUTURE EIC EXPERIMENT	
M. Krelina, J. Nemchik	77
COMPARATIVE ELECTROCHEMICAL, OPTICAL AND X-RAY STUDIES OF POLYFLUORENE AND FLUORENE-BASED ALTERNATING COPOLYMER	
K. Gmucová, K. Végső, T. Váry, V. Nádaždy	79
MAGNETIC, MAGNETOCALORIC, THERMAL AND TRANSPORT PROPERTIES OF Gd₃Ni₂In₄	
K. Arun, T.P. Rashid, M. Reiffers, A. Dzubinska, R. Nagalakshmi	81
WIDE TEMPERATURE RANGE MAGNETOCALORIC EFFECT IN Dy_{6.5}Co₂Si_{2.5}	
K. Arun, T. P. Rashid, I. Curlík, S. Ilkovic, M. Reiffers, A. Dzubinska, R. Nagalakshmi	83
NIHILNOVI – A NOT SO NEW APPROACH TO DATA VISUALISATION PROMOTING PORTABLE AND SIMPLE TEXT FORMATS	
F. Dominec	85
APPLICATION OF MACHINE LEARNING IN SINGLE CRYSTAL GROWTH	
F. Hájek, F. Dominec, A. Hospodková, J. Oswald	87
IMPACT OF MACROSCOPIC PARTICLE COMPOSITION ON GAN EPITAXIAL GROWTH MORPHOLOGY AND LUMINESCENCE	
K. Kuldová, F. Dominec, R. Novotný, F. Hájek, T. Košutová, A. Hospodková	89
SCHOOL MEASURING SYSTEM USING A MICROCONTROLLER	
M. Choma, S. Il'kovič	91
MODELLING CHANGE IN GRAVITATIONAL ACCELERATION AND ITS EFFECT ON PRESSURE IN LIQUID	
M. Kováč	93
DEVELOPING THE CATEGORICAL SYSTEM OF BEHAVIOUR FOR STUDENT-LECTURER INTERACTION DURING PHYSICS DEMONSTRATIONS	
A. Nikitin, P. Káčovský, M. Snětinová	95
PHYSICS FOR THE YOUNGEST AND THEIR TEACHERS	
J. Houfková	97
THE SMÍCHOV INDUSTRIAL SCHOOL OF THE THIRD AGE	
V. Krajčová	99
STUDENTS' SOLVING OF MULTIPLE-CHOICE TASKS FOCUSED ON GRAPH SLOPE INTERPRETATION OBSERVED BY THE EYE-TRACKING METHOD	
M. Kekule	101
BRIDGING COURSES FOR MATHEMATICS AND SCIENCE TEACHER STUDENTS	
R. Holubová, J. Slezáková	103
STUDENTS' STRATEGIES FOR CREATING COMMENTS ON SILENT VIDEOS	

S. Gorčáková, K. Velmovská	105
CONCEPTUAL PROBLEMS AND GRAPHICAL REPRESENTATION IN INTRODUCTORY COURSE OF QUANTUM PHYSICS	
Z. Koupilová, P. Káčovský	107
SMART BIOMETRIC RECORDING SYSTEM	
A. Enikeev, J. Skopalík, T. Parák, K. Švík, J. Kolářová, V. Čmiel, J. Mašek	109
IT ACADEMY PROJECT IN THE LIGHT OF CHANGES IN PHYSICS EDUCATION	
Z. Ješková, M. Kireš	111
RESEARCH ON LEVEL OF STUDENTS' EDUCATIONAL INTEREST IN PHYSICS	
A. Klučarová, V. Šebeň	113
WAYS TO EVALUATE STUDENTS' ARGUMENTS IN TEACHING PHYSICS IN PRIMARY SCHOOL	
T. Kiss, K. Velmovská	115
PROBLEMS OF EVALUATION OF STUDENTS' SCORE IN NON-STANDARDIZED ACHIEVEMENT TEST	
J. Čevajka, K. Velmovská	117
SOLID-STATE ¹H NMR STUDY OF CORNSTARCH PLASTICIZED WITH UREA AND GLYCEROL DURING AGEING	
N. Šmídová, M. Kovařáková, V. Hronský	119
VIDEO ANALYSIS IN STEM EDUCATION	
P. Hockicko, G. Tarjányiová, J. Kúdelčík	121
COLLECTION OF SOLVED PHYSICS PROBLEMS AND COLLECTION OF PHYSICS EXPERIMENTS	
M. Snětinová, P. Káčovský, Z. Koupilová, D. Mandíková	123
PARTICIPATION OF CZECHOSLOVAKIA IN THE ESTABLISHMENT OF THE JOINT INSTITUTE OF NUCLEAR RESEARCH (DUBNA, RUSSIA)	
E. Těšínská	125
CALDEIRA-LEGGET MODEL FOR PARTICLE-BATH SYSTEMS IN THE PRESENCE OF A MAGNETIC FIELD	
V. Lisý, J. Tóthová	127
BROWNIAN MOTION IN A BATH AFFECTED BY AN EXTERNAL HARMONIC POTENTIAL	
J. Tóthová, V. Lisý	129
THERMAL TREND OF THE BIPARTITE ENTANGLEMENT IN THE SPIN-1/2 ISING-HEISENBERG PLANAR LATTICE OF INTER-CONNECTED TRIGONAL BIPYRAMIDS	
L. Gálisová	131
PHASE BIREFRINGENCE DISPERSION FUNCTION AS A COMPLEMENTARY TOOL FOR INVESTIGATION OF NEMATIC LC STRUCTURE	
N. Tarjányi, M. Veverčík, D. Káčik	133
COMPLEX VOLUME CHANGES INDUCED BY HIGH PRESSURE AND EXTERNAL MAGNETIC FIELD IN Ni₂MnSn-BASED HEUSLER ALLOY	
J. Kamarád, J. Kaštil, Z. Arnold, M. Míšek, O. Isnard	135
NEW VIEW ON THE ORIGIN OF HIGH CONDUCTIVITY OF POLYANILINE FILMS PROTONATED BY HYDROCHLORIC ACID	
R. Rutsch, J. Toušek, J. Toušková	137
MÖSSBAUER SPECTROMETRY IN THE STUDY OF METALLIC GLASSES	
M. Miglierini, M. Cesnek	139
PHASE TRANSFORMATIONS IN Al-Li-BASED ALLOY STUDIED BY IN-SITU TEM	
M. Cieslar, R. Králík, S. Belejová, B. Krivská, M. Šlapáková, L. Bajtošová, J. Švrčková	141
MONTE CARLO SIMULATIONS OF UPSILON MESON PRODUCTION	
J. Bielčík, J. Češka, L. Kosarzewski, M. Myška	143

SPECIFIC HEAT STUDY OF [Ni(2aepy)₂Cl(H₂O)]Cl·H₂O – A SPIN-1 QUASI-ONE-DIMENSIONAL ANTIFERROMAGNET	
M. Holub, E. Čížmár, S. Šterbinská, J. Kuchár, J. Černák	145
SHORT-RANGE CORRELATION INVESTIGATION IN DEUTERON INDUCED REACTIONS	
M. Janek, V. P. Ladygin, A.V. Averyanov, E.V. Chernykh, D. Enache, Yu.V. Gurchin, A.Yu. Isupov, J-T. Karachuk, A.N. Khrenov, D.O. Krivenkov, P.K. Kurilkin, N.D. Ladygina, A. N. Livanov, O. Mezhenka, S. M. Piyadin, S. G. Reznikov, Ya. T. Skhomenko, G. Tarjanyiova, A. A. Terekhin, A.V. Tishevsky	147
PROPERTIES OF YELLOW BAND IN GaN LAYERS	
T. Hubáček, V. Jarý, K. Kuldová, A. Hospodková, J. Pangrác, E. Hulicius	149
THE STUDY OF LATTICE DYNAMICS IN LOW-DIMENSIONAL QUANTUM MAGNETS WITH CHAIN-LIKE CRYSTAL STRUCTURE	
O. Vinnik, L. Lederová, R. Tarasenko, L. Kotvytska, K. Zakuťanská, N. Tomašovičová, A. Orendáčová	151
INTERDIFFUSION IN ALUMINUM-STEEL CLAD STRIP	
B. Křivská, M. Šlapáková, M. Kihoulou, R. Králík, L. Bajtošová, M. Cieslar, O. Grydin, M. Stolbchenko, M. Schaper	153
CHARACTERIZATION OF THIN FREE-STANDING AL-MG FILMS	
L. Bajtošová, R. Králík, B. Křivská, H. Libenská, J. Veselý, M. Cieslar	155
RECRYSTALLIZATION OF A TWIN-ROLL CAST AA8079 ALUMINUM ALLOY AFTER HOMOGENIZATION	
R. Králík, L. Bajtošová, B. Křivská, M. Cieslar	157
NANOFLUID BASED ON A NEW GENERATION OIL	
K. Paulovičová, J. Tóthová, M. Rajňák, M. Timko, P. Kopčanský, V. Lisý	159
STUDY OF RING-LIKE STRUCTURES IN PARTICLE EMISSION IN RELATIVISTIC NUCLEAR INTERACTIONS	
A. Kravčáková, M. Vařa, S. Vokál, J. Vrláková	161
COR SYSTEM FOR COSMIC RAYS TRAJECTORIES IN MAGNETOSPHERE SIMULATION	
D. Gecášek, J. Genči, P. Bobík	163
SEARCH FOR PSEUDORAPIDITY FLUCTUATIONS IN HIGH ENERGY NUCLEAR COLLISIONS	
J. Vrláková, S. Vokál, M. Vařa	165
STATISTICAL ERROR OF FP EQUATION	
V. Mykhailenko, P. Bobik	167
STUDY OF P3HT THIN FILM PHOTOLUMINESCENCE SPECTRA USING H- AND J-AGGREGATE THEORY	
S. Kotorová, J. Chlpík, T. Váry, J. Círák, V. Nádaždy	169
H-FUNCTION CALCULATION FOR SELECTED SPECTRAL BANDS OF OXYGEN	
J. Pokorný	171
A SETUP FOR MEASUREMENT OF THE TOTAL REACTION CROSS SECTION	
I. Siváček, Yu. E. Penionzhkevich, Yu. G. Sobolev, V. V. Samarin, M. A. Naumenko, S. S. Stukalov	173
PRESSURE INDUCED SUPERCONDUCTIVITY IN A CeRhSi₃ SINGLE CRYSTAL – THE HIGH PRESSURE STUDY	
D. Staško, J. Valenta, M. Kratochvílová, J. Prchal, P. Proschek, M. Klicpera	175
PHASE DIAGRAMS OF Ce₂Pd₂In INTERMETALLIC COMPOUND	
P. Král, J. Prchal, M. Klicpera, P. Doležal, J. Kaštil	177
OPEN DATA OF THE LHC EXPERIMENT ATLAS	
J. Chudoba	179

**UHECR ACCELERATION CAPABILITIES OF THE NEARBY SUPERMASSIVE
BLACK HOLES**

A. Tursunov, M. Kološ, Z. Stuchlík

181

PLASMALAB@CTU - NEW FACILITIES IN SUPPORT OF FUSION EDUCATION

J. Brotánková, J. Mlynář, M. Pfeifer, V. Svoboda

186

THE EXPERIMENT KATRIN LIMITED THE NEUTRINO MASS TO LESS THAN 1 eV

O. Dragoun for the KATRIN Collaboration, dragoun@ujf.cas.cz, Nuclear Physics Institute of the Czech. Acad. Sci., Řež, Czech republic

THE PROBLEM OF ENERGY CONSERVATION IN NUCLEAR BETA-DECAY

On 4th December of this year, physicists will celebrate a milestone birthday of the neutrino. On that day 90 years ago, Wolfgang Pauli wrote his famous letter that suggested a possible solution of the mystery of the continuous energy spectrum of electrons emitted in nuclear β -decay. Pauli assumed that in this process the mother nucleus decays into *three parts* – the daughter nucleus, electron and a new, then unknown neutral particle, later called the neutrino. In the decay into three or more parts, all products have continuous energy spectra.

Enrico Fermi developed the first successful theory of β -decay, incorporating the Pauli's neutrino already in 1934 [1]. The predicted β -spectra were found to agree with the measured ones which enabled Fermi to estimate the neutrino mass “to be smaller than the electron mass, most probably zero” [1].

THE MOST ABUNDANT MASSIVE PARTICLES

According our present knowledge, the neutrinos are together with photons the most abundant particles in the Universe. Most of them are the relic neutrinos created in the Big Bang with an average number density of about 340 cm^{-3} and kinetic energy of about 0.25 meV today. Neutrinos produced in the chain of thermonuclear reactions within the Sun core fall on the Earth surface with a density of $6 \times 10^{10} \text{ cm}^{-2} \text{ s}^{-1}$. A huge amount of 10^{58} neutrinos is created within a few seconds during a supernova explosion. The neutrinos are also produced in the interaction of high-energy cosmic rays with atoms in the Earth atmosphere, as well as in nuclear reactors and at some particle accelerators. Since our bodies contain a small amount of potassium with 0.01% of naturally radioactive ^{40}K , each of us emits about 4000 neutrinos per second. Neutrinos from all these sources can travel within the Universe thousands of years without any interaction.

The neutrinos appear in three kinds named according their charged partners (accompanying them in the weak interactions) as the electron ν_e , muon ν_μ and ν_τ neutrinos. They are among the twelve elementary particles of matter that constitute the Standard Model of particle physics.

Originally, the neutrinos were assumed to have zero rest mass. The neutrino oscillation experiments proved that ν_e , ν_μ and ν_τ are not states with a definite mass. They are *the quantum superposition* of the neutrino mass states m_i . At least two of these states have a mass greater than 0.01 eV and for at least one $m_i > 0.05 \text{ eV}$. Since the oscillation experiments examine the quantity $(m_i^2 - m_j^2)$, the values of m_i themselves cannot be determined in this way.

ELECTRON SPECTROSCOPY OF RADIOACTIVE NUCLEI

Magnetic spectrometers were the first precision instruments of the experimental nuclear physics. They enabled measurements of the energy spectra of electrons emitted in the decay of radioactive nuclei. First of all, these were the internal conversion electrons resulting from the electromagnetic interaction of excited nuclei with electrons of their own atomic shells. Systematic investigation of these monoenergetic electrons (see e.g. review [2]) enabled the determination of the energy and multipolarity of electromagnetic transitions in hundreds of nuclei. This was important information for the construction of the decay schemes of their excited levels including their spins and parities. Using a magnetic spectrometer, James Chadwick proved a continuous character of β -ray spectra already in 1914.

In the simplest case of only one neutrino mass state with the mass eigenvalue m_{ν_e} and no excitation of the daughter ion, the Fermi's β -spectrum of an allowed β -transition ($\Delta I_{\text{nucl}} = 0, 1$ and $\Delta \pi_{\text{nucl}} = 0$) has the form

$$\frac{dN}{dE} = A \cdot F \cdot p \cdot (E + m_e) \cdot \varepsilon \cdot \sqrt{\varepsilon^2 - m_{\nu_e}^2} \quad (1)$$

Here, A is the spectrum amplitude. E , p , m_e are the kinetic energy, momentum and the rest mass of the electron, respectively. $\varepsilon = E_0 - E$, where E_0 is the maximum electron energy for $m_{\nu_e} = 0$. The Fermi function $F(E, Z + 1)$ takes into account the Coulomb interaction of the emitted β -decay electron with the daughter nucleus of the charge $Z + 1$ and its surrounding atomic electrons. The Eq. (1) holds for $E < E_0 - m_{\nu_e}$.

Precision β -ray spectroscopy thus offers a unique possibility to determine the neutrino mass (or at least its upper limit) directly in a model independent way. The necessary conditions are:

- (i) Excellent instrumental resolution to distinguish between the cases $m_{\nu_e} = 0$ and $m_{\nu_e} \neq 0$,
- (ii) high spectrometer luminosity to record the uppermost part of the β -spectrum with sufficient statistics,
- (iii) low background to enable the search of small effect in the spectrum caused by $m_{\nu_e} \neq 0$,
- (iv) high-quality radioactive source in which the energy losses of β -decay electrons do not deteriorate the true spectrum shape. The same holds for an inelastic scattering of electrons on the spectrometer slits, etc.

In order to extract information about m_{ν_e} from the β -spectrum (measured always in the presence of a background B_{bg}), a usual approach is to compare it with the theoretical predictions for various values of m_{ν_e} . Typically, the method of least squares is applied and the fitting parameters are A , E_0 , $m_{\nu_e}^2$ and B_{bg} .

The fit requires the knowledge of the resolution function of the whole experimental setup $R(E)$ which

incorporates the transmission properties of the spectrometer with relevant properties of the radioactive source (electron energy losses and scattering, etc.). Electron guns with a small energy spread as well as monoenergetic conversion electrons with a small natural width proved useful in the $R(E)$ determination. Also computer programs for tracking charged particles in electromagnetic fields can yield $R(E)$, assuming that the dimensions of a real apparatus and the applied fields are described with sufficient precision, and the required electron cross sections are available.

PREVIOUS β -SPECTROSCOPIC SEARCHES FOR THE NEUTRINO MASS

The first targeted search for a signature of the neutrino in a β -spectrum was accomplished by Cook *et al.* [3] in 1948 when the neutrino was still a hypothetical particle. Using a magnetic spectrometer, the authors measured an upper part of the β -spectrum of ^{35}S , which has the decay energy $Q_\beta = 167$ keV and half-life $T_{1/2} = 87.5$ d. From the analysis of the uppermost part of their β -spectrum, the authors derived the limit $m_{\nu_e} < 5$ keV.

Practically all the following searches concentrated on the β -decay of tritium, $^3_1\text{H} \rightarrow ^3_2\text{He}^+ + e^- + \bar{\nu}_e$ with $Q_\beta = 18.57$ keV and $T_{1/2} = 12.3$ y, see Fig. 1. The reason is that the relative intensity of the β -spectrum part sensitive to m_{ν_e} is proportional to $1/Q_\beta^3$.

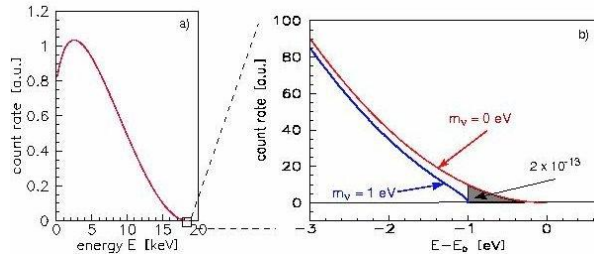


Fig. 1. The complete energy spectrum of the tritium β -decay electrons (a), and its uppermost part for two assumed values of the neutrino rest mass (b). E_0 is the β -spectrum endpoint for $m_\nu = 0$. Note the extremely small relative intensity on the grey area.

The energy resolution of electron spectrometers gradually improved. In 1972, it became clear [4] that the spectrum analysis has to take into account that a part of the decay energy Q_β can be spent for an excitation of the daughter ion $^3\text{He}^+$. The observed β -spectrum thus becomes a superposition of many partial β -spectra with endpoint energies $E_{0j} = E_0 - m_{\nu_e} - V_j$, where V_j is the energy of the j -th excitation state populated with the probability P_j :

$$\frac{dN}{dE} = A \cdot F(E, Z + 1) \cdot p \cdot (E + m_e) \cdot \sum_j P_j (\varepsilon - V_j) \cdot \sqrt{(\varepsilon - V_j)^2 - m_{\nu_e}^2} \cdot \Theta(\varepsilon - V_j - m_{\nu_e}). \quad (2)$$

Here, Θ is the Heaviside step function. Other very small or negligible correction terms are described in ref. [5].

For an isolated tritium atom, the quantities V_j and P_j can be precisely calculated, but all attempts to prepare a sufficiently strong β -spectroscopic source of atomic tritium are not yet successful. The β -spectrum of molecular tritium is more complicated since numerous electronic and rotational-vibrational states of the $(\text{HeT})^+$ ion can be excited (see Fig. 2). Although reliable calculations are available for this case, they are not yet experimentally verified. Thus, strictly speaking, the investigation of the β -spectrum of molecular tritium is not a direct kinematic method of determining m_ν completely free of any further assumption. Nevertheless, it is the least model dependent approach since the calculation of V_j and P_j for the isolated $(\text{HeT})^+$ ion is based on the well-known theory of electromagnetic interactions. Calculations for complex tritiated molecules or the tritium atoms imbedded in thin solid layers are much less reliable. This drawback sometimes caused a wrong interpretation of the measured β -spectra and led to erroneous values of derived m_{ν_e} .

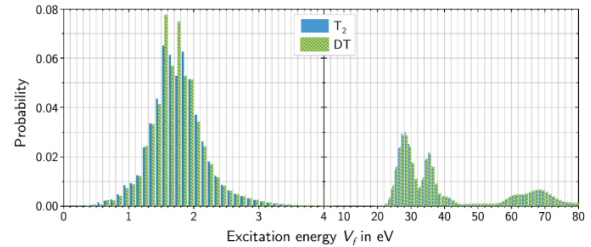


Fig. 2 Distribution of the final states of the molecular ions $(\text{HeT})^+$ and $(\text{HeD})^+$ after the β -decay of T_2 and TD [5].

Another promising candidate is the β -decay $^{187}\text{Re} \rightarrow ^{187}\text{Os} + e^- + \bar{\nu}_e$ which has the lowest known decay energy of $Q_\beta = 2.44$ keV. Due to the ^{187}Re half-life of 4.3×10^{10} y, its β -spectrum had to be measured with low temperature microcalorimeters. Despite several decades of efforts in developing this technique, the best achieved limit is $m_{\nu_e} < 15$ eV [6].

One could consider a simpler two-body decay, where the outgoing particles have discrete energy (no continuous spectra); for example, in the decay of pion at rest, $\pi^+ \rightarrow \mu^+ + \nu_\mu$ or $\pi^- \rightarrow \mu^- + \bar{\nu}_\mu$. The participating particles have no excited states and their rest masses are known to high precision. Although the muon momentum was measured with a remarkable precision of one ppm [7], the resulting upper limit of the m_{ν_μ} is only 190 keV. It is a consequence of the relation among a relativistic particle's total energy, momentum, and the rest mass, $E_{tot}^2 = p^2 + m^2$. Thus one can hope for a high sensitivity for the ν mass determination only when the neutrino is almost nonrelativistic. Otherwise, all the experimental precision is lost in the $(E_{tot}^2 - p^2)$ difference.

The phenomenon of neutrino oscillations offers a principal possibility to derive the values of the individual neutrino masses m_i as well as the squares of the elements of the neutrino mixing matrix $|U_{ei}|^2$ from carefully measured β -spectrum shape using the formula

$$\frac{dN}{dE} = A \cdot F \cdot p \cdot (E + m_e) \cdot \sum_j P_j (\varepsilon - V_j - m_i) \cdot \sum_i |U_{ei}|^2 \sqrt{(\varepsilon - V_j)^2 - m_i^2} \cdot \theta(\varepsilon - V_j - m_i). \quad (3)$$

In order to achieve this goal, the energy resolution of the best present β -spectrometers would have to be improved at least by one order of magnitude.

It follows from the neutrino oscillation experiments that the splitting of the individual neutrino mass states m_i is far too small to be resolved by current β -spectrometers. Therefore, all previous and current experiments investigate **the effective electron neutrino mass**

$$m_{\nu_e}^{eff} = \sqrt{\sum_i |U_{ei}|^2 \cdot m_i^2}, \quad (4)$$

where the sum is over the mass states m_i that are too close together to be resolved experimentally. For simplicity, we will still denote the quantity $m_{\nu_e}^{eff}$ as m_{ν_e} , keeping in mind that even the best current β -spectra can be analyzed with simpler formula (2). If the future β -experiments determine the value of m_{ν_e} , and all neutrino mass-squared differences ($m_i^2 - m_j^2$) together with the mixing parameters $|U_{ei}|^2$ are available from oscillation studies, the individual neutrino masses m_i can be calculated from the formula [8]

$$m_j^2 = m_{\nu_e}^2 - \sum_i |U_{ei}|^2 \cdot (m_i^2 - m_j^2). \quad (5)$$

Until recently, the best β -spectroscopic limits of the effective neutrino mass were determined as $m_{\nu_e} < 2.3$ eV in 2005 [9] and $m_{\nu_e} < 2.05$ eV in 2011 [10], both at 95% CL. These were the results of many years of measurements with a new type of β -ray spectrometers, so called the MAC-E filters, combining magnetic adiabatic collimation of electrons with their energy analysis by a retarding electrostatic field. These instruments exhibit the combination of excellent resolution and large angle acceptance. However, contrary to their predecessors, they do not measure differential spectra but integral ones as stepwise changes to the retarding potential are applied.

The seventy years effort of experimentalists for direct kinematic determination of the neutrino rest mass is described e.g. in the reviews [11–13].

THE KATRIN EXPERIMENT

The Karlsruhe Tritium Neutrino KATRIN [14] Collaboration was founded in 2001. Its aim is to explore the effective mass of the electron neutrino m_{ν_e} by improving the β -spectroscopic technique of the MAC-E-filter and the gaseous molecular tritium source. At present KATRIN has 150 collaborators from 20 institutions in six countries. The NPI at Řež is one of the founding members.

The KATRIN Design Report [15] calls for an improvement of the previous neutrino mass sensitivities [9, 10] by one order of magnitude to 0.2 eV at 90% CL. This means an increase in statistics and a reduction in

systematic uncertainties by two orders of magnitude, as the experimental observable is $m_{\nu_e}^2$.

The 70 m long KATRIN setup, the scheme of which is shown in Fig. 3, is located at the Karlsruhe Institute of Technology (KIT). The tritiated subsystems are placed in the Tritium Laboratory Karlsruhe, TLK (Fig. 4), the only one in Europe capable of supplying sufficiently large amount of tritium with extremely high chemical and isotopic purity. The extensive infrastructure of this unique laboratory enables the operation of the KATRIN tritium source in a closed cycle with the nominal column density in its beam tube of 5×10^{17} molecules per cm^2 , providing 10^{11} β -decay electrons per second.

The tritium source operates at the temperature of 30 K with remarkable stability of $\pm 0.1\%$ per hour achieved by two-phase neon cooling of the beam tube. The source was constructed as windowless in order to avoid a deterioration of the β -spectrum shape through additional electron energy losses. With its dimensions (10 m length, 9 cm diameter), more than 500 sensors and six cryogenic liquids (N_2 , He, Ne, Ar; radioactive T_2 , $^{83\text{m}}\text{Kr}$) the KATRIN tritium source presents evidently one of the most complex cryostats ever built.

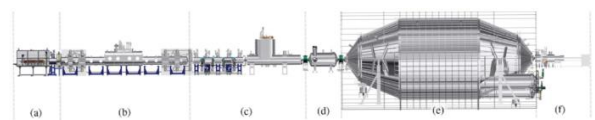


Fig. 3. The main components of the KATRIN setup consisting of a) the rear section for the electron beam diagnostics and monitoring of the tritium activity, b) the windowless gaseous source of molecular tritium, c) the differential and cryogenic sections protecting the penetration of tritium into the main spectrometer, d) the pre-spectrometer that cuts the dominant part of the β -spectrum bearing no information about the neutrino mass, e) the main spectrometer analyzing the uppermost part of the β -spectrum with an unprecedented combination of excellent energy resolution and extremely large input solid angle, f) the solid-state detector consisting of 148 independent pixels that count electrons from various parts of the magnetic flux tube.

The re-purified tritium is continuously injected into the middle of the source tube at a pressure of 3.4×10^{-3} mbar and pumped at both ends through a closed loop system operating continuously with 26 turbomolecular pumps. In order to eliminate source-related backgrounds, the residual tritium that flows into the spectrometer needs to be decreased by 14 orders of magnitude by means of the differential and cryogenic pumping. The large-capacity cryotrap uses an argon frost held at temperature of 3–4 K. The composition of six hydrogen isotopologues (radioactive T_2 , HT, DT and traces of H_2 , D_2 , HD) is continuously monitored by laser Raman spectroscopy with a precision of 0.1%. The $(\text{HeT})^+$ and other ions produced in the tritium source are removed from the beam tube by means of ring dipole electrodes.

The field of about 30 superconducting solenoids adiabatically guides the electrons in a magnetic flux tube of 190 Tcm^2 into the main KATRIN spectrometer – the MAC-E-filter, the principle of which is

demonstrated in Fig. 5. The relative energy resolution $\Delta E/E$ of the instrument is determined by the ratio B_{\min}/B_{\max} of applied magnetic fields. To achieve the energy resolution of 0.9 eV (full width) at the tritium endpoint of 18.6 keV, the main spectrometer has to have a diameter of 10 m. The maximum pitch angle of incoming electrons was set to 50.8° that corresponds to 19 % of the full solid angle 4π . The main KATRIN spectrometer with its volume of 1240 m^3 (see Fig. 6) is probably the largest vessel operating at an ultra-high vacuum below 10^{-11} mbar. It is achieved by means of turbomolecular pumps and non-evaporable getters.



Fig. 4. The windowless tritium gaseous source and electron transport system of the KATRIN setup inside the TLK.

The electrons that overcame the electrostatic barrier in the analyzing plane are guided to the detector placed at the spectrometer focal plane. The detector of 90 mm diameter is a radially and azimuthally segmented monolithic silicon p-i-n diode, composed of 148 individual pixels of the same area.

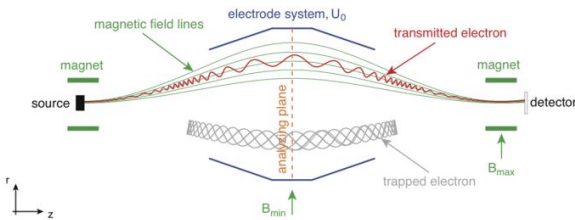


Fig. 5. The principle of the MAC-E-filter. The electron emitted in a broad entrance angle from the source moves around its magnetic field line and is adiabatically collimated in direction perpendicular to the analyzing plane. There, depending on its energy, it is either reflected by the retarding electrostatic field or reaccelerated to its original energy downstream of the spectrometer and hits the detector. The electron born inside the spectrometer volume may be trapped in this magnetic bottle. The trapped electrons become backgrounds when they escape from the trap.

The β -spectrum is recorded point-by-point via stepwise changes of the retarding potential that is stabilized and measured with ppm accuracy. The same retarding voltage is applied to the monitor spectrometer measuring continuously the position of the 17.8 keV calibration conversion electron line of $^{83\text{m}}\text{Kr}$. A shift of this line would indicate instabilities in the high voltage

system. The implanted sources of $^{83}\text{Rb}/^{83\text{m}}\text{Kr}$, developed in the Nuclear Physics Institute at Řež in collaboration with the University of Bonn, exhibit a stability of the line energy to within 0.3 ppm per month.



Fig. 6. A challenging transport of the main spectrometer vessel from the factory to KIT. The last 7 km of the journey on the ground after 8800 km journey on rivers and seas around Europe.

In addition, the Řež sources of gaseous $^{83\text{m}}\text{Kr}$ with activity up to 1.5 GBq (see Fig. 7 and ref. [16]) proved to be invaluable in the investigation of homogeneity and time stability of the KATRIN gaseous tritium source.



Fig. 7. The $^{83\text{m}}\text{Kr}$ generator inside the secondary containment installed at the TLK together with container for the transport of the $^{83}\text{Rb}/^{83\text{m}}\text{Kr}$ source from the NPI at Řež.

Extensive tests of the KATRIN parts were performed in 2016–2017. For this purpose a photoelectron gun with narrow beam of adjustable energy and entrance angle as well as monoenergetic conversion electrons from the $^{83\text{m}}\text{Kr}$ decay were applied. The first operation of KATRIN with tritium was accomplished in 2018 using 1 % admixture of DT in 99 % of D_2 carrier gas at nominal column density. The test verified the stable operating conditions of the whole setup (see ref. [17] and Fig. 8). In most cases the design parameters were achieved or even surpassed, but background exceeded the intended rate of 0.01 counts per second [15]. Two background sources, not observed in previous less sensitive experiments, were identified:

a) Electrons from the decay of ^{219}Rn ($T_{1/2} = 4 \text{ s}$) emanating in trace amounts from non-evaporable getters. The penetration of ^{219}Rn into the active flux-

tube volume is now mitigated by liquid-nitrogen traps in front of the getter.

b) Rydberg atoms sputtered off the inner spectrometer surfaces by ^{206}Pb recoil ions following the α -decay of ^{210}Po . These neutral atoms are in highly excited states and may be ionized by black-body radiation. The resulting electrons, accelerated by the MAC-E-filter, contribute to the detected background. The methods to suppress this effect are still being searched for.

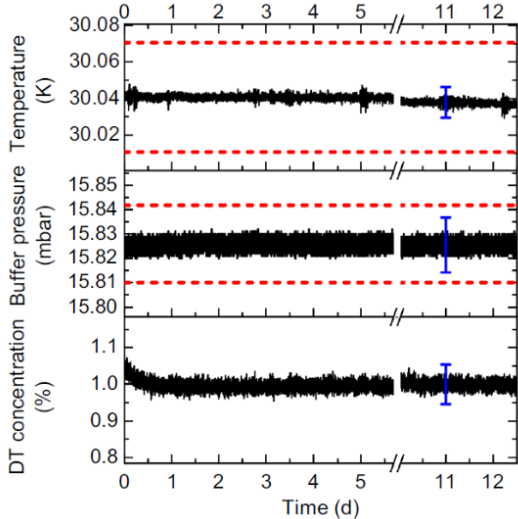


Fig. 8. Examples of the temporal stability during the first tests of the KATRIN setup with tritium: temperature of the source tube (top), pressure in the tritium buffer tank (middle) and DT concentration in front of the beam tube (bottom). The dashed red lines denote the range of the KATRIN specifications. The blue error bars indicate the systematic uncertainty on the absolute value of the respective parameters [17].

THE FIRST SCIENTIFIC RUN OF KATRIN

In spring 2019, the first scientific run lasting 22 days was accomplished. As expected, radiochemical reactions of tritium (e.g. generation of tritiated methane) with previously unexposed stainless steel parts of the apparatus did not allow the utilization of the full tritium column density. In order to secure the stable running conditions it had to be limited to 22 % of its nominal value. The gaseous source was operated at the average isotopic tritium purity of 97.7 %. The laser Raman spectroscopy revealed that 95.3 % of molecular tritium was in the form of T_2 , while HT and DT molecules contributed by 3.5 and 1.1 %, respectively. This is important information since tritium isotopologues differ in their spectra of final states after β -decay, see Fig. 2. The inactive species D_2 , HD and H_2 (that could serve as disturbing targets for inelastic electron scattering) were present only in trace amounts.

The uppermost part of the β -spectrum was repeatedly measured at 27 different retarding voltages. These non-equidistant voltage settings as well as the non-uniform measuring time distribution, shown in bottom of Fig. 9, were chosen to maximize sensitivity for m_{ν_e} . Most of the time was spent in the narrow region below the endpoint energy E_0 . One β -spectrum scan took about two hours. Inspection of the slow-control parameters proved that 274 scans were taken at

stable run conditions. Also 117 out of 148 detector pixels operated reliably. Thus, at this level of dominating statistical uncertainty, all the 32 058 single spectra could be merged into one spectrum for further analysis. This approach is supported by the fact that 274 values of E_0 from individual fits did not show any time dependence and had a Gaussian distribution with the standard deviation $\sigma = 0.25$ eV around the mean value. The retarding high voltage was continuously monitored with ppm precision and exhibited high reproducibility ($\sigma = 34$ mV). This was an important condition for assigning the individual counting rates of a particular β -spectrum point to the same high-voltage value.

THE ANALYSIS OF MEASURED β -SPECTRUM

The applied β -spectrum shape including various corrections, in particular the molecular final states and thermal Doppler broadening are specified in ref. [17]. There is also a detailed description of the KATRIN response function including electron scattering in the tritium source and energy losses in the flux tube due to the synchrotron radiation of electrons spiraling around the magnetic field lines. Ten possible sources of systematic uncertainties were specified, (e.g. fluctuations of tritium activity, high voltage and magnetic fields intensity) and their magnitudes were estimated by two independent methods. The results of the fit are displayed in Fig. 9. The goodness-of-fit of $\chi^2 = 21.4$ for 23 degrees of freedom (data from 27 spectrum points and four fitted parameters) corresponds to very satisfactory probability $p = 0.56$.

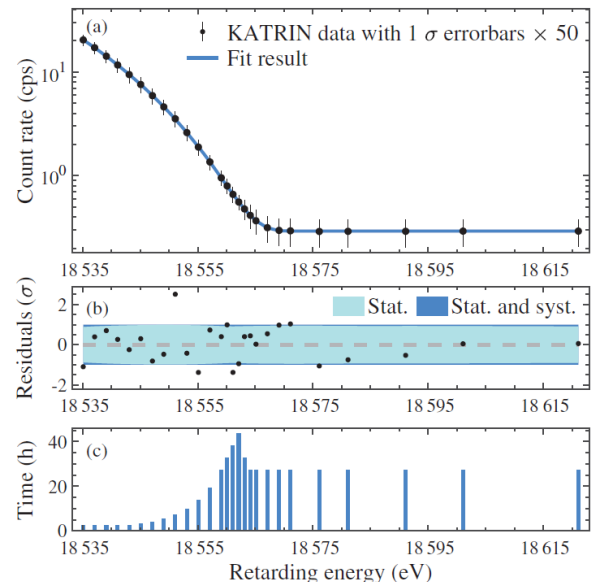


Fig. 9. (a) The uppermost part of the tritium β -spectrum obtained by stacking the data of 274 two-hour scans and recorded by 117 correctly operating detector pixels. The displayed 1σ statistical uncertainties were enlarged by a factor of 50 for better visibility. The full line shows the result of the best fit. (b) The spectrum of the fit residuals does not reveal any irregularities. The 1σ band demonstrates the dominant role of statistical uncertainties in the initial state of the long-term KATRIN measurements. (c) The measurement time and energy distribution of 27 spectrum points optimized for the highest sensitivity to $m_{\nu_e}^2$.

Following the procedure outlined in ref. [11], the fitted endpoint energy E_0 was recalculated to the decay energy of molecular tritium $Q_\beta = 18575.2 \pm 0.5$ eV. This value can be compared with $Q_\beta = 18575.72 \pm 0.07$ eV, derived from the atomic mass difference (${}^3\text{H} - {}^3\text{He}$) [18] adjusted for different electron binding energies and kinematic variables of atomic and molecular tritium [11]. The perfect agreement of both Q_β values manifests the reliability of the KATRIN energy scale.

IMPROVED UPPER LIMIT OF THE NEUTRINO MASS

The analysis of the measured β -spectrum, carried out by three independent KATRIN groups, led to the best fit value of $m_{\nu_e}^2 = (-1.0^{+0.9}_{-1.1})$ eV². Its small negative value (even in the case $m_{\nu_e} = 0$) may be a statistical fluctuation since the spectrum was taken in the presence of background. However, it also could indicate that the prediction and the real experiment did not meet perfectly with each other, as happened more than once in previous experiments (see e.g. reviews [11, 13]). From several recipes for assigning an upper limit in the case of a statistical fluctuation into the non-physical region, the most conservative method [19] was chosen. The first KATRIN limit **$m_{\nu_e} < 1.1$ eV at 90 % CL** [20] means that a half million of neutrinos has a smaller mass than one electron, the second lightest elementary particle. There is a realistic hope that KATRIN, after a reduction of background and 1000 days of data taking, will reach its design sensitivity of 0.2 eV (90 % CL) on m_{ν_e} [15].

An application of the time-of-flight method might improve the KATRIN neutrino mass sensitivity up to 0.1 eV if there were a technique that allows a precise determination of the start time of each analyzed electron that would not deteriorate its original energy without substantial shortening of the overall exposure time.

PROSPECTS FOR NEUTRINO MASS DETERMINATION

There are several new ideas for the exploration of the neutrino mass, see e.g. review [13]. The most advanced is The Project 8 [21], based on a precision spectroscopy of cyclotron radiation emitted by tritium β -decay electrons in magnetic field. The feasibility of this approach has been demonstrated. If the effort to prepare the gaseous source of *atomic* tritium (with the relative T_2/T purity better than 10^{-6}), held at temperature of about 150 mK in a volume of roughly 10 m^3 succeeds, the m_{ν_e} sensitivity can reach 0.04 eV.

The Particle Data Group [8], considers β -spectroscopy as a primary method for the neutrino mass determination. There are two other, at present more sensitive, but strongly model dependent ways to assess the neutrino mass.

The first one is the search for the neutrinoless double beta decay, $0\nu\beta\beta$. This process violates lepton-number conservation; thus it is not allowed in the Standard model of elementary particles. The experimental

observable is the half life $T_{1/2}^{0\nu\beta\beta}$ that depends of the effective neutrino mass $m_{\beta\beta} = \left| \sum_j |U_{ej}|^2 \cdot m_j \cdot e^{i\alpha_j} \right|$. Contrary to the effective mass m_{ν_e} given by Eq. (4), $m_{\beta\beta}$ depends on unknown Majorana CP-phases α_j . The nuclear matrix elements $M^{0\nu\beta\beta}$, needed for calculation of $m_{\beta\beta}$ from $T_{1/2}^{0\nu\beta\beta}$, have an uncertainty to within a factor 2–3. The current upper limit of $m_{\beta\beta}$ is about 0.2 eV [22].

The second method employs data from cosmological observations, in particular those on temperature fluctuations of the cosmic microwave background and the distribution of large scale structures of the universe. The interpretation is based on the minimal Λ CDM cosmological model extended by massive neutrinos, parameterized by the sum of the neutrino mass $\sum m_i$. The results depend on the choice of examined phenomena as well as on the particular data sets. For example, an upper limit of $\sum m_i < 0.16$ eV at 95 % CL was recently obtained [23].

The three ways to assess the absolute neutrino mass scale (the direct kinematic measurements, searches for $0\nu\beta\beta$ decay and precision cosmological observations) are complementary and, together with detailed examination of neutrino oscillations, are needed to explore the neutrino masses and their ordering.

REFERENCES

1. E. Fermi, Z. Phys. **88**, 161 (1934).
2. O. Dragoun, Advances in Electronics and Electron Phys. **60**, 1 (1983).
3. C. S. Cook *et al.*, Phys. Rev. **73**, 1394 (1948).
4. K-E. Bergkvist, Nucl. Phys. B **39**, 317 (1972).
5. M. Kleesiek *et al.*, Eur. J. Phys. C **79**, 204 (2019).
6. M. Sisty *et al.*, Nucl. Inst. Meth. A **520** (2004) 125.
7. K. Assamagan *et al.*, Phys. Lett. B **434**, 158 (1998).
8. P. A. Zyla *et al.*, (Particle Data Group), Progr. Theor. Exp. Phys. **2020**, 083C01 (2020).
9. C. Kraus *et al.*, Eur. Phys. J. C **4**, 447 (2005).
10. V. N. Aseev *et al.*, Phys. Rev. D **84**, 1 (2011).
11. E. W. Otten, C. Weinheimer, Rep. Prog. Phys. **71**, 1 (2008).
12. G. Drexlin *et al.*, Adv. High Ener. Phys. **2013**, 293986 (2013).
13. O. Dragoun, D. Vénos, Open Phys. J. **3**, 73 (2016).
14. <http://www.katrin.kit.edu>.
15. J. Angrik *et al.*, KATRIN design report 2004. <https://publikationen.bibliothek.kit.edu/270060419>
16. J. Sentkerestiová *et al.*, J. Inst. **13**, P04018 (2018).
17. M. Aker *et al.*, Eur. Phys. J. C **80**, 264 (2020).
18. E. G. Myers *et al.*, Phys. Rev. Lett. **114**, 013003 (2015).
19. A. V. Lokhov, F. V. Tkachov, Phys. Part. Nucl. **46**, 347 (2015).
20. M. Aker *et al.*, Phys. Rev. Lett. **123**, 221802 (2019).
21. A. Ashtari Esfahani *et al.*, J. Phys. G **44**, 054004 (2017).
22. M. J. Dolinski *et al.*, Annu. Rev. Nucl. Part. Sci. **69**, 219 (2019).
23. M. M. Ivanov *et al.*, Phys. Rev. D **101**, 083504 (2020).

ELECTROMAGNETIC STRUCTURE OF MESONS AND BARYONS

C. Adamuščin, E. Bartoš, **S. Dubnička**, stanislav.dubnicka@savba.sk, A.Liptaj, Institute of Physics SAS, Bratislava, Slovakia and A.-Z. Dubníčková, Department of Theoretical Physics, Comenius University, Bratislava, Slovakia

INTRODUCTION

As it is known, the building components of atoms, protons, neutrons and electrons, are called elementary particles. Stable charged particles, like electrons and protons, can be accelerated and in collisions with other protons or electrons can disappear and instead of them a lot of other new elementary particles and antiparticles is created. All of them are specified by various quantum numbers, like mass m_h , decay width Γ_h , parity P (+ or -), spin S , isospin I , electric charge Q etc. . There are known in nature four types of interactions between elementary particles - gravitational, weak, electromagnetic and strong and not all elementary particles are able of all four interactions. Particles with spin 1/2, electron, muon, τ -particle and associated neutrinos, ν_e, ν_μ, ν_τ , and their antiparticles are unable of strong interactios and they are called leptons. All elementary particles able of strong interactios are called hadrons and they are compound of quarks. Hadrons composed of quark-antiquark ($q\bar{q}$) are called mesons and ones composed of three quarks (qqq) are called baryons.

Mesons are classified according to the SU(3) symmetry into nonets, the most known are

nonet of pseudoscalar mesons

$\pi^+, \pi^-, \pi^0, K^+, K^-, K^0, \bar{K}^0, \eta, \eta'$

and **nonet of vector mesons**

$\rho^+, \rho^-, \rho^0, K^{*+}, K^{*-}, K^{*0}, \bar{K}^{*0}, \omega(782), \phi(1020)$, etc.

Baryons are commonly classified into octets, decuplets, etc. , the most known is **octet of $1/2^+$ baryons**

$p, n, \Lambda, \Sigma^+, \Sigma^0, \Sigma^-, \Xi^0, \Xi^-$.

ELECTROMAGNETIC STRUCTURE OF HADRONS

Hadrons in the interaction with charged leptons, like electrons and muons, manifest observable space structure to be called electromagnetic (EM) structure of hadrons, first time revealed for the proton in elastic scattering $e^-p \rightarrow e^-p$ in the middle of 50's of the last century, before the quark model of hadrons has been established (1964). At present days, the EM structure is automatically generalized also to all other existing hadrons.

The EM structure of any hadron is completely described by scalar functions (EM form factors (FFs)) of one variable. In a spacelike region - momentum transfer squared $t = -Q^2$ and in a timelike region - total c.m. energy squared $s = w^2$. The number of EM FFs depends on the spin of the hadron under consideration. If spin of a hadron $S=0$ e.g. $\pi^+, \pi^-, \pi^0, K^+, K^-, K^0, \bar{K}^0, \eta, \eta', He^4, C^{12}, O^{16}$, etc., there is only one EM FF $F_C(t)$ completely describing the hadron EM structure and it is defined by the matrix element of EM current

$$\langle h | J_\mu^{EM} | h \rangle = (p + p')_\mu F_C(t). \quad (1)$$

The EM structure of hadrons with spin $S = 1/2$ e.g. $p, n, \Lambda, \Sigma^+, \Sigma^0, \Sigma^-, \Xi^0, \Xi^-, He^3, H^3$, etc. is completely described by two FFs - electric $G_E(t)$ and magnetic $G_M(t)$. The EM structure of hadrons with spin $S = 1$ e.g. $\rho^+, \rho^-, \rho^0, K^{*+}, K^{*-}, K^{*0}, \bar{K}^{*0}, \omega(782), \phi(1020), D$, etc. is completely described by three FFs - electric $G_C(t)$, magnetic $G_M(t)$ and quadrupole $G_Q(t)$.

What does it mean to know the EM structure of some hadron? It means to know behaviors of all EM FFs of the hadron under consideration in the whole region of their definition, i.e. from $-\infty$ to $+\infty$. There is no theory up to now able to predict the behavior of hadron EM FFs from $-\infty$ to $+\infty$.

Therefore various phenomenological models are constructed for description of the EM structure of hadrons. Next we present our Unitary and Analytic ($U\&A$) model [1].

UNITARY AND ANALYTIC APPROACH

Our $U\&A$ model is essentially based on the hypothetical analytic properties of hadron EM FFs in complex plane of their variable and on the experimental fact of a creation of vector meson resonances with photon quantum numbers.

Model depends on some coupling constant ratios (f_{Vhh}/f_V) as free parameters and it is applicable only to hadrons for which some experimental data exist. So only the electromagnetic structure of

- the nonet of pseudoscalar mesons
 $\pi^+, \pi^-, \pi^0, K^+, K^-, K^0, \bar{K}^0, \eta, \eta'$ [2, 3, 4]
- the ground state $1/2^+$ octet baryons
 $p, n, \Lambda, \Sigma^+, \Sigma^0, \Sigma^-, \Xi^0, \Xi^-$ [5]

can be completely described in the framework of our $U\&A$ approach up to now.

MESON UNITARY AND ANALYTIC MODEL

We start with the nonet of pseudoscalar mesons $\pi^+, \pi^-, \pi^0, K^+, K^-, K^0, \bar{K}^0, \eta, \eta'$. A theoretical description of FFs can be improved by exploiting mixed transformation properties of the hadronic EM current $J_\mu^{EM}(0)$ under the rotation in the isospin space:

- part of $J_\mu^{EM}(0)$ transforms as an isoscalar
- its another part as the third component of isovector.

The latter leads to a splitting of the pseudoscalar meson EM FFs to flavourless isoscalar and isovector com-

ponents as follows

$$\begin{aligned}
F_{\pi^\pm}(s) &= F_\pi^{I=1}[W(s)] \\
F_{K^\pm}(s) &= F_K^{I=0}[V(s)] + F_K^{I=1}[W(s)] \\
F_{K^0}(s) &= F_K^{I=0}[V(s)] - F_K^{I=1}[W(s)] \\
F_{\pi^0\gamma}(s) &= F_{\pi^0\gamma}^{I=0}[V(s)] + F_{\pi^0\gamma}^{I=1}[W(s)] \\
F_{\eta\gamma}(s) &= F_{\eta\gamma}^{I=0}[V(s)] + F_{\eta\gamma}^{I=1}[W(s)] \\
F_{\eta'\gamma}(s) &= F_{\eta'\gamma}^{I=0}[V(s)] + F_{\eta'\gamma}^{I=1}[W(s)]. \quad (2)
\end{aligned}$$

The model takes into account all known properties of FFs:

- normalization of FFs
- asymptotic behaviour as predicted by the quark model
- analytic properties of FFs in complex plane of their definition
- unitarity conditions of FFs
- reality conditions of FFs $F^*(s) = F(s^*)$
- experimental fact of a creation of vector mesons in $e^+e^- \rightarrow$ hadrons processes
- then $F^{I=1}(s)$ are saturated by $\rho, \rho', \rho'',$ etc and $F^{I=0}(s)$ by $\omega, \phi, \omega', \phi',$ etc.

Experimental fact of a creation of very unstable $\rho, \omega, \phi, \rho', \omega', \phi',$ etc. in $e^+e^- \rightarrow$ hadrons has been historically taken into account by the so-called naive *VMD* model, considering vector mesons to be stable

$$F_M(s) = \sum_V \frac{m_V^2}{m_V^2 - s} (f_{VMM}/f_V) \quad (3)$$

$$F_{M\gamma}(s) = \sum_V \frac{m_V^2}{m_V^2 - s} (f_{VM\gamma}/f_V) \quad (4)$$

which, though automatically respects the asymptotic behaviors

$$F_M(s)|_{|s| \rightarrow \infty} \equiv F_{M\gamma}(s)|_{|s| \rightarrow \infty} \sim s^{-1} \quad (5)$$

of pseudoscalar meson and transition EM FFs, it is in contradiction with the unitarity condition as this condition forbids an existence of any pole on the real axis of the complex s -plane and creates the nonzero imaginary parts of FFs above the lowest threshold s_0 of $e^+e^- \rightarrow$ hadrons processes.

Moreover the naive *VMD* model leads to infinities of $e^+e^- \rightarrow$ hadrons cross sections at the position of vector meson poles under consideration. In order to remove these shortcomings, the *VMD* models are unitarized by an incorporation of two-cut approximation of the analytic properties by an introduction of two square root branch points s_0 and s_{in} leading to four sheeted Riemann surface on which meson and transition EM FFs are defined.

An unitarization of the naive *VMD* models is carried out by the non-linear transformations

$$s = s_0^v + \frac{4(s_{in}^v - s_0^v)}{[1/W(s) - V(s)]^2}, \quad (6)$$

and

$$s = s_0^s + \frac{4(s_{in}^s - s_0^s)}{[1/V(s) - V(s)]^2}, \quad (7)$$

where $s_0^v = m_{\pi_0}^2$ and $s_0^s = 9m_\pi^2$ are corresponding to the lowest possible physical thresholds in $e^+e^- \rightarrow$ hadrons processes and s_{in}^v and s_{in}^s are effective square-root branch points, approximating contributions of all higher relevant inelastic thresholds, given by the unitarity conditions of FFs. They are seen explicitly in the inverse transformations to (6) and (7)

$$W(s) = i \frac{\sqrt{\sqrt{\frac{s_{in}^v - s_0^v}{s_0^v}} + \sqrt{\frac{s - s_0^v}{s_0^v}} - \sqrt{\sqrt{\frac{s_{in}^v - s_0^v}{s_0^v}} - \sqrt{\frac{s - s_0^v}{s_0^v}}}}{\sqrt{\sqrt{\frac{s_{in}^v - s_0^v}{s_0^v}} + \sqrt{\frac{s - s_0^v}{s_0^v}} + \sqrt{\sqrt{\frac{s_{in}^v - s_0^v}{s_0^v}} - \sqrt{\frac{s - s_0^v}{s_0^v}}}}}, \quad (8)$$

$$V(s) = i \frac{\sqrt{\sqrt{\frac{s_{in}^s - s_0^s}{s_0^s}} + \sqrt{\frac{s - s_0^s}{s_0^s}} - \sqrt{\sqrt{\frac{s_{in}^s - s_0^s}{s_0^s}} - \sqrt{\frac{s - s_0^s}{s_0^s}}}}{\sqrt{\sqrt{\frac{s_{in}^s - s_0^s}{s_0^s}} + \sqrt{\frac{s - s_0^s}{s_0^s}} + \sqrt{\sqrt{\frac{s_{in}^s - s_0^s}{s_0^s}} - \sqrt{\frac{s - s_0^s}{s_0^s}}}}, \quad (9)$$

which are mapping the corresponding four sheeted Riemann surfaces always into one W and V plane, respectively. As a result, terms $\frac{m_W^2}{m_W^2 - s}$ and $\frac{m_V^2}{m_V^2 - s}$ in *VMD* representations are factorized into asymptotic terms $\left(\frac{1-W^2}{1-W_N^2}\right)^2$ and $\left(\frac{1-V^2}{1-V_N^2}\right)^2$ completely determining the asymptotic behavior $\sim s^{-1}$ of EM FFs and into resonant terms

$$\frac{(W_N - W_{r0})(W_N + W_{r0})(W_N - 1/W_{r0})(W_N + 1/W_{r0})}{(W - W_{r0})(W + W_{r0})(W - 1/W_{r0})(W + 1/W_{r0})} \quad (10)$$

and

$$\frac{(V_N - V_{r0})(V_N + V_{r0})(V_N - 1/V_{r0})(V_N + 1/V_{r0})}{(V - V_{r0})(V + V_{r0})(V - 1/V_{r0})(V + 1/V_{r0})} \quad (11)$$

giving a resonant behavior around $s = m_r^2$ and for $|s| \rightarrow \infty$ turning out to finite real constants. One can prove

1. if $m_r^2 - \Gamma_r^2/4 < s_{in} \Rightarrow W_{r0} = -W_{r0}^*, V_{r0} = -V_{r0}^*$
2. if $m_r^2 - \Gamma_r^2/4 > s_{in} \Rightarrow W_{r0} = 1/W_{r0}^*, V_{r0} = 1/V_{r0}^*$

which lead in the case 1. to the expressions

$$\frac{m_r^2}{m_r^2 - s} = \left(\frac{1 - W^2}{1 - W_N^2}\right)^2 \times \frac{(W_N - W_{r0})(W_N - W_{r0}^*)(W_N - 1/W_{r0})(W_N - 1/W_{r0}^*)}{(W - W_{r0})(W - W_{r0}^*)(W - 1/W_{r0})(W - 1/W_{r0}^*)} \quad (12)$$

$$\frac{m_r^2}{m_r^2 - s} = \left(\frac{1 - V^2}{1 - V_N^2}\right)^2 \times \frac{(V_N - V_{r0})(V_N - V_{r0}^*)(V_N - 1/V_{r0})(V_N - 1/V_{r0}^*)}{(V - V_{r0})(V - V_{r0}^*)(V - 1/V_{r0})(V - 1/V_{r0}^*)} \quad (13)$$

and in the case 2. to the following expressions

$$\frac{m_r^2}{m_r^2 - s} = \left(\frac{1 - W^2}{1 - W_N^2}\right)^2 \times \frac{(W_N - W_{r0})(W_N - W_{r0}^*)(W_N + W_{r0})(W_N + W_{r0}^*)}{(W - W_{r0})(W - W_{r0}^*)(W + W_{r0})(W + W_{r0}^*)} \quad (14)$$

$$\frac{m_r^2}{m_r^2 - s} = \left(\frac{1 - V^2}{1 - V_N^2} \right)^2 \times \frac{(V_N - V_{r0})(V_N - V_{r0}^*)(V_N + V_{r0})(V_N + V_{r0}^*)}{(V - V_{r0})(V - V_{r0}^*)(V + V_{r0})(V + V_{r0}^*)}. \quad (15)$$

Introducing the non-zero width of the resonances by a substitution

$$m_r^2 \rightarrow (m_r - i\Gamma_r/2)^2 \quad (16)$$

i.e. simply one has to rid of "0" in sub-indices of the previous two types of expressions. Finally one gets in the 1. case

$$\frac{m_r^2}{m_r^2 - s} \rightarrow \left(\frac{1 - W^2}{1 - W_N^2} \right)^2 \times \frac{(W_N - W_r)(W_N - W_r^*)(W_N - 1/W_r)(W_N - 1/W_r^*)}{(W - W_r)(W - W_r^*)(W - 1/W_r)(W - 1/W_r^*)} = \left(\frac{1 - W^2}{1 - W_N^2} \right)^2 L_r(W) \quad (17)$$

$$\frac{m_r^2}{m_r^2 - s} \rightarrow \left(\frac{1 - V^2}{1 - V_N^2} \right)^2 \times \frac{(V_N - V_r)(V_N - V_r^*)(V_N - 1/V_r)(V_N - 1/V_r^*)}{(V - V_r)(V - V_r^*)(V - 1/V_r)(V - 1/V_r^*)} = \left(\frac{1 - V^2}{1 - V_N^2} \right)^2 L_r(V) \quad (18)$$

and in the 2. case

$$\frac{m_r^2}{m_r^2 - s} \rightarrow \left(\frac{1 - W^2}{1 - W_N^2} \right)^2 \times \frac{(W_N - W_r)(W_N - W_r^*)(W_N + W_r)(W_N + W_r^*)}{(W - W_r)(W - W_r^*)(W + W_r)(W + W_r^*)} = \left(\frac{1 - W^2}{1 - W_N^2} \right)^2 H_r(W). \quad (19)$$

$$\frac{m_r^2}{m_r^2 - s} \rightarrow \left(\frac{1 - V^2}{1 - V_N^2} \right)^2 \times \frac{(V_N - V_r)(V_N - V_r^*)(V_N + V_r)(V_N + V_r^*)}{(V - V_r)(V - V_r^*)(V + V_r)(V + V_r^*)} = \left(\frac{1 - V^2}{1 - V_N^2} \right)^2 H_r(V). \quad (20)$$

So, every $F^{I=1}[W(s)]$ and $F^{I=0}[V(s)]$ in $F_{\pi^\pm}(s), F_{K^\pm}(s), F_{K^0}(s), F_{\pi^0\gamma}(s), F_{\eta\gamma}(s), F_{\eta'\gamma}(s)$ EM FFs represents one analytic function in the whole complex s -plane, besides two cuts on the positive real axis, with a series of pairs of complex conjugate poles on un-physical sheets and depends on only physically interpretable parameters $(f_{Whh}/f_W), (f_{Vhh}/f_V), s_{in}$.

Their predictions for the complete nonet of pseudoscalar mesons are presented in the following Figs. 1 and 2.

U&A MODEL OF $1/2^+$ OCTET BARYONS

According to SU(3) group classification of hadrons, $1/2^+$ baryon octet consists of

$$p, n, \Lambda, \Sigma^+, \Sigma^0, \Sigma^-, \Xi^0, \Xi^-.$$

The EM structure of every baryon from $1/2^+$ -octet is completely described by two independent functions $F_1^B(t)$ and $F_2^B(t)$, the Dirac and Pauli FFs, which are naturally obtained in a decomposition of the baryon matrix element of the EM current $J_\mu^{EM}(0)$ into a maximal number of linearly independent covariants to be constructed from four-momenta, γ -matrices and Dirac bispinors of baryons

$$\begin{aligned} < B | J_\mu^{EM}(0) | B > = \\ = e\bar{u}(p') \{ \gamma_\mu F_1^B(t) + \frac{i}{2m_B} \sigma_{\mu\nu} (p' - p)_\nu F_2^B(t) \} u(p). \end{aligned} \quad (21)$$

While Dirac and Pauli FFs are suitable for a theoretical description of the baryon EM structure, for an extraction of experimental information on it from the measured quantities, like cross sections and polarizations, the Sachs electric $G_E^B(t)$ and magnetic $G_M^B(t)$ FFs are more suitable.

PREDICTIONS FOR NUCLEON EM FFs

Then the relations between baryon Sachs FFs and isoscalar and isovector parts of the baryon Dirac and Pauli FFs are for "nucleons"

$$\begin{aligned} G_E^p(t) &= [F_{1s}^N(t) + F_{1v}^N(t)] + \frac{t}{4m_p^2} [F_{2s}^N(t) + F_{2v}^N(t)] \\ G_M^p(t) &= [F_{1s}^N(t) + F_{1v}^N(t)] + [F_{2s}^N(t) + F_{2v}^N(t)] \\ G_E^n(t) &= [F_{1s}^N(t) - F_{1v}^N(t)] + \frac{t}{4m_n^2} [F_{2s}^N(t) - F_{2v}^N(t)] \\ G_M^n(t) &= [F_{1s}^N(t) - F_{1v}^N(t)] + [F_{2s}^N(t) - F_{2v}^N(t)] \end{aligned} \quad (22)$$

with normalizations

$$\begin{aligned} G_E^p(0) &= 1; \quad G_M^p(0) = \mu_p \\ G_E^n(0) &= 0; \quad G_M^n(0) = \mu_n \\ F_{1s}^N(0) &= F_{1v}^N(0) = \frac{1}{2} \\ F_{2s}^N(0) &= \frac{1}{2}(\mu_p + \mu_n - 1); \quad F_{2v}^N(0) = \frac{1}{2}(\mu_p - \mu_n - 1) \end{aligned} \quad (24)$$

where μ_N $N = p, n$ are magnetic moments of the proton and neutron, respectively. For every isoscalar and isovector component of the nucleon Dirac and Pauli FFs, similarly to meson FFs, analytic expressions of

$$\begin{aligned} F_{1s}^N[V(s)] &= f[s; \frac{f_{\omega'NN}^{(1)}}{f_{\omega'}}, \frac{f_{\phi'NN}^{(1)}}{f_{\phi'}}, \frac{f_{\omega NN}^{(1)}}{f_{\omega}}, \frac{f_{\phi NN}^{(1)}}{f_{\phi}}, s_{in}^{1s}] \\ F_{1v}^N[W(s)] &= f[s; \frac{f_{\rho NN}^{(1)}}{f_{\rho}}, s_{in}^{1v}] \\ F_{2s}^N[U(s)] &= f[s; \frac{f_{\phi'NN}^{(2)}}{f_{\phi'}}, \frac{f_{\omega NN}^{(2)}}{f_{\omega}}, \frac{f_{\phi NN}^{(2)}}{f_{\phi}}, s_{in}^{2s}] \\ F_{2v}^N[X(s)] &= f[s; s_{in}^{2v}] \end{aligned} \quad (25)$$

can be derived as functions of s and dependent on some number of unknown vector-meson coupling constant ratios (f_{VNN}/f_V) and effective inelastic thresholds s_{in}^r $r = 1s, 1v, 2s, 2v$. They are numerically evaluated in a simultaneous analysis of reliable 582 experimental

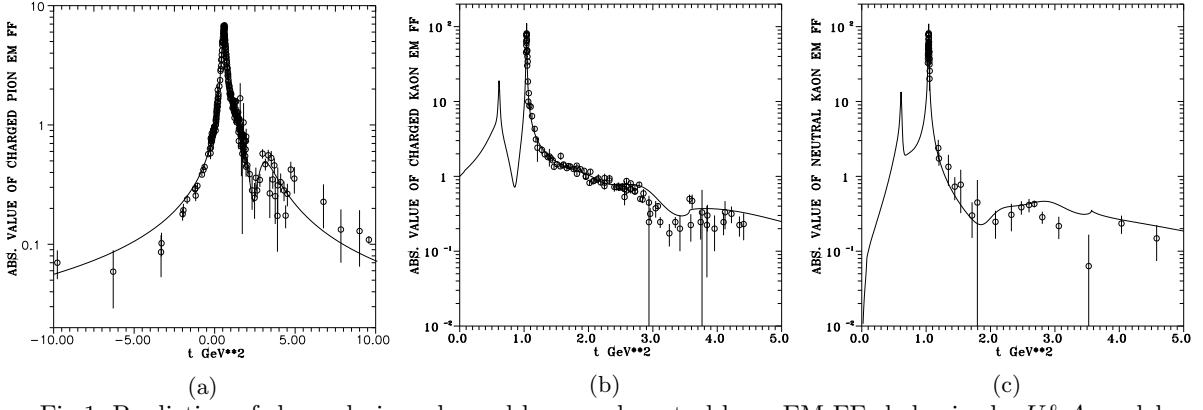


Fig.1: Prediction of charged pion, charged kaon and neutral kaon EM FFs behavior by $U\&A$ model.

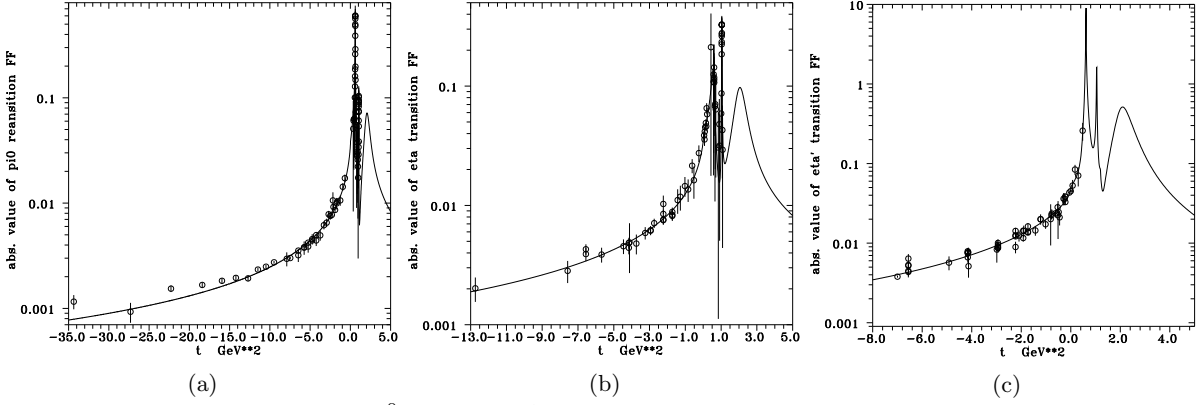


Fig.2: Prediction of $\pi^0\gamma$, $\eta\gamma$ and $\eta'\gamma$ transition EM FFs behavior by $U\&A$ model.

points on $G_E^N(s)$, $G_M^N(s)$ $N = p, n$ through the relations (22) and (23) with $\chi^2/ndf = 1.76$ while

$$\begin{aligned}
 s_{in}^{1s} &= 1.4653 \pm 0.0542 \text{GeV}^2; & s_{in}^{1v} &= 2.9631 \pm 0.3649 \text{GeV}^2 \\
 s_{in}^{2s} &= 1.8513 \pm 0.2519 \text{GeV}^2; & s_{in}^{2v} &= 2.3927 \pm 1.9928 \text{GeV}^2 \\
 \frac{f_{\omega'NN}^{(1)}}{f_{\omega'}} &= -0.2780 \pm 0.0056; & \frac{f_{\phi'NN}^{(1)}}{f_{\phi'}} &= -0.5214 \pm 0.0030 \\
 \frac{f_{\omega NN}^{(1)}}{f_{\omega}} &= 0.5988 \pm 0.0014; & \frac{f_{\phi NN}^{(1)}}{f_{\phi}} &= -0.0287 \pm 0.0009 \\
 \frac{f_{\phi'NN}^{(2)}}{f_{\phi'}} &= 0.0422 \pm 0.0156; & \frac{f_{\omega NN}^{(2)}}{f_{\omega}} &= -0.4872 \pm 0.0828 \\
 \frac{f_{\phi NN}^{(2)}}{f_{\phi}} &= 0.1216 \pm 0.0032; & \frac{f_{\rho NN}^{(1)}}{f_{\rho}} &= -0.6019 \pm 0.0026
 \end{aligned}$$

which give predictions as presented in Figs. 3(a)-(c) and 4.

PREDICTIONS FOR HYPERON EM FFs

Similar expressions to nucleons (25) as functions of s to be dependent on some number of unknown vector-meson-hyperon coupling constant ratios (f_{VYY}/f_V) can be found also for $\Lambda, \Sigma^+, \Sigma^0, \Sigma^-, \Xi^0, \Xi^-$ hyperons from $1/2^+$ baryon octet.

However, there are no data on EM FFs of $1/2^+$ octet hyperons, only some total cross section experimental points of e^+e^- -annihilation into hyperon-antihyperon exist and one can not repeat a similar to nucleons procedure in determination of these unknown

coupling constant ratios in the Unitary&Analytic hyperon EM structure model, in order to predict hyperon EM FFs behaviors.

Despite of this fact, we have found a method for numerical evaluation of unknown free hyperon coupling constant ratios (f_{VYY}/f_V) utilizing the known nucleon coupling constant ratios (f_{VNN}/f_V) and the SU(3) invariant Lagrangians of vector-meson interaction with octet baryons

$$\begin{aligned}
 L_{VB\bar{B}} &= \frac{i}{\sqrt{2}} f^F [\bar{B}_\beta^\alpha \gamma_\mu B_\gamma^\beta - \bar{B}_\gamma^\beta \gamma_\mu B_\beta^\alpha] (V_\mu)_\alpha^\gamma & (26) \\
 &+ \frac{i}{\sqrt{2}} f^D [\bar{B}_\gamma^\beta \gamma_\mu B_\beta^\alpha + \bar{B}_\alpha^\gamma \gamma_\mu B_\gamma^\beta] (V_\mu)_\alpha^\gamma + \\
 &+ \frac{i}{\sqrt{2}} f^S \bar{B}_\beta^\alpha \gamma_\mu B_\alpha^\beta \omega_\mu^0
 \end{aligned}$$

where baryons are represented here by the octet matrices

$$B = \begin{pmatrix} \frac{\Sigma^0}{\sqrt{2}} + \frac{\Lambda^0}{\sqrt{6}} & \Sigma^+ & p \\ \Sigma^- & -\frac{\Sigma^0}{\sqrt{2}} + \frac{\Lambda^0}{\sqrt{6}} & n \\ \Xi^- & \Xi^0 & -\frac{2\Lambda^0}{\sqrt{6}} \end{pmatrix}, \quad (27)$$

$$\bar{B} = \begin{pmatrix} \frac{\bar{\Sigma}^0}{\sqrt{2}} + \frac{\bar{\Lambda}^0}{\sqrt{6}} & \bar{\Sigma}^- & \bar{\Xi}^- \\ \bar{\Sigma}^+ & -\frac{\bar{\Sigma}^0}{\sqrt{2}} + \frac{\bar{\Lambda}^0}{\sqrt{6}} & \bar{\Xi}^0 \\ \bar{p} & \bar{n} & -\frac{2\bar{\Lambda}^0}{\sqrt{6}} \end{pmatrix}, \quad (28)$$

and the 1^{--} vector-meson nonet is classified into an

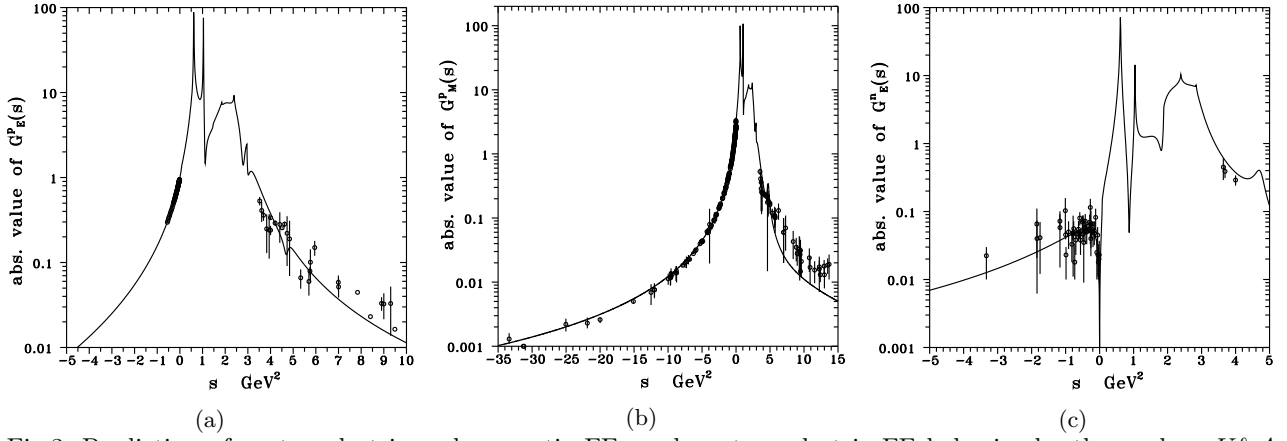


Fig.3: Prediction of proton electric and magnetic FFs and neutron electric FF behavior by the nucleon $U\&A$ model and its comparison with existing data.

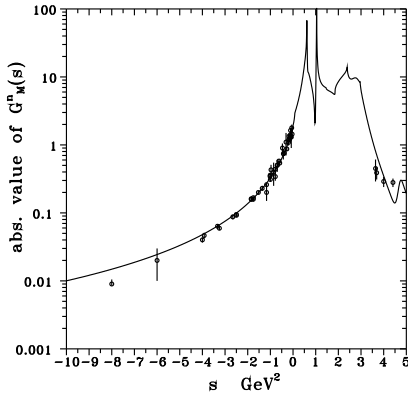


Fig.4: Prediction of neutron magnetic FF behavior by the nucleon $U\&A$ model and its comparison with existing data.

octet matrix and a singlet like

$$V = \begin{pmatrix} \frac{\omega_8}{\sqrt{6}} + \frac{\rho^0}{\sqrt{2}} & \rho^+ & K^{*+} \\ \rho^- & \frac{\omega_8}{\sqrt{6}} - \frac{\rho^0}{\sqrt{2}} & K^{*0} \\ K^{*-} & \bar{K}^{*0} & -\frac{2\omega_8}{\sqrt{6}} \end{pmatrix}, \quad \omega_0. \quad (29)$$

Decomposing SU(3) invariant Lagrangian into a sum of products of single matrix elements one can derive relations between f_{VBB} of all members of $1/2^+$ octet baryons and the coupling constants f^F, f^D, f^S of SU(3) invariant Lagrangian.

However, the ω_8, ω_0 in Lagrangian (26) do not represent experimentally observed particles and therefore one has to use the so-called $\omega - \phi$ mixing form through the real $\omega(782)$ and $\phi(1020)$ vector-mesons.

We have proved [6] that there are generally 8 different mixing forms, but only four of them

$$\begin{aligned} 1. \quad & \omega_0 = \omega \cos \theta + \phi \sin \theta \\ & \omega_8 = \omega \sin \theta - \phi \cos \theta \\ 4. \quad & \omega_0 = -\omega \cos \theta - \phi \sin \theta \\ & \omega_8 = -\omega \sin \theta + \phi \cos \theta \\ 5. \quad & \omega_0 = \omega \cos \theta - \phi \sin \theta \\ & \omega_8 = \omega \sin \theta + \phi \cos \theta \\ 8. \quad & \omega_0 = -\omega \cos \theta + \phi \sin \theta \\ & \omega_8 = -\omega \sin \theta - \phi \cos \theta. \end{aligned} \quad (30)$$

are physically acceptable.

Then the relations between f_{VBB} and the coupling constants f^F, f^D, f^S of SU(3) invariant Lagrangian, to be dependent on the previous mixings, take for nucleons the following four different forms

$$1. \quad f_{\rho NN} = +\frac{1}{2}(f^F + f^D) \quad (31)$$

$$f_{\omega NN} = +\frac{1}{\sqrt{2}}f^S \cos \theta + \frac{1}{2\sqrt{3}}(3f^F - f^D) \sin \theta$$

$$f_{\phi NN} = +\frac{1}{\sqrt{2}}f^S \sin \theta - \frac{1}{2\sqrt{3}}(3f^F - f^D) \cos \theta$$

$$4. \quad f_{\rho NN} = +\frac{1}{2}(f^F + f^D)$$

$$f_{\omega NN} = -\frac{1}{\sqrt{2}}f^S \cos \theta - \frac{1}{2\sqrt{3}}(3f^F - f^D) \sin \theta$$

$$f_{\phi NN} = -\frac{1}{\sqrt{2}}f^S \sin \theta + \frac{1}{2\sqrt{3}}(3f^F - f^D) \cos \theta$$

$$5. \quad f_{\rho NN} = +\frac{1}{2}(f^F + f^D) \quad (32)$$

$$f_{\omega NN} = +\frac{1}{\sqrt{2}}f^S \cos \theta + \frac{1}{2\sqrt{3}}(3f^F - f^D) \sin \theta$$

$$f_{\phi NN} = -\frac{1}{\sqrt{2}}f^S \sin \theta + \frac{1}{2\sqrt{3}}(3f^F - f^D) \cos \theta$$

$$8. \quad f_{\rho NN} = +\frac{1}{2}(f^F + f^D)$$

$$f_{\omega NN} = -\frac{1}{\sqrt{2}}f^S \cos \theta - \frac{1}{2\sqrt{3}}(3f^F - f^D) \sin \theta$$

$$f_{\phi NN} = +\frac{1}{\sqrt{2}}f^S \sin \theta - \frac{1}{2\sqrt{3}}(3f^F - f^D) \cos \theta.$$

and similarly for all hyperons. From such relations it is immediately seen that if one knows numerical values of f^F, f^D, f^S , then one can evaluate all coupling constants f_{VBB} of $1/2^+$ octet baryons with 1^{--} vector mesons.

How to find numerical values of f^F, f^D, f^S ?

For this aim it is very useful, that we know numerical values of nucleon coupling constant ratios (f_{VNN}/f_V) in our earlier investigations, from which by using universal vector-meson coupling constants f_ρ, f_ω, f_ϕ to be calculated from the corresponding lepton widths one could find all f_{VNN} .

However, signs of the universal vector-meson coupling constants f_ρ, f_ω, f_ϕ

$$\begin{aligned}
1. \quad & \frac{1}{f_\rho} : \frac{1}{f_\omega} : \frac{1}{f_\phi} = -\sqrt{3} : -\sin\theta : +\cos\theta \\
4. \quad & \frac{1}{f_\rho} : \frac{1}{f_\omega} : \frac{1}{f_\phi} = -\sqrt{3} : +\sin\theta : -\cos\theta \\
5. \quad & \frac{1}{f_\rho} : \frac{1}{f_\omega} : \frac{1}{f_\phi} = -\sqrt{3} : -\sin\theta : -\cos\theta \\
8. \quad & \frac{1}{f_\rho} : \frac{1}{f_\omega} : \frac{1}{f_\phi} = -\sqrt{3} : +\sin\theta : +\cos\theta
\end{aligned} \quad (33)$$

are also strongly dependent on the four physically acceptable different mixing forms [7]. As a result one finds four sets of vector-meson-nucleon coupling constants differing in the signs. However, substituting them into the nucleon inverse relations

$$\begin{aligned}
1. \quad & f^F = \frac{\sqrt{3}}{2}(f_{\omega NN} \sin\theta - f_{\phi NN} \cos\theta) + \frac{1}{2}f_{\rho NN} \\
& f^D = -\frac{\sqrt{3}}{2}(f_{\omega NN} \sin\theta - f_{\phi NN} \cos\theta) + \frac{3}{2}f_{\rho NN} \\
& f^S = \sqrt{2}(f_{\omega NN} \cos\theta + f_{\phi NN} \sin\theta) \\
4. \quad & f^F = \frac{\sqrt{3}}{2}(-f_{\omega NN} \sin\theta + f_{\phi NN} \cos\theta) + \frac{1}{2}f_{\rho NN} \\
& f^D = -\frac{\sqrt{3}}{2}(-f_{\omega NN} \sin\theta + f_{\phi NN} \cos\theta) + \frac{3}{2}f_{\rho NN} \\
& f^S = \sqrt{2}(-f_{\omega NN} \cos\theta - f_{\phi NN} \sin\theta)
\end{aligned} \quad (34)$$

and

$$\begin{aligned}
5. \quad & f^F = \frac{\sqrt{3}}{2}(f_{\omega NN} \sin\theta + f_{\phi NN} \cos\theta) + \frac{1}{2}f_{\rho NN} \\
& f^D = -\frac{\sqrt{3}}{2}(f_{\omega NN} \sin\theta + f_{\phi NN} \cos\theta) + \frac{3}{2}f_{\rho NN} \\
& f^S = \sqrt{2}(f_{\omega NN} \cos\theta - f_{\phi NN} \sin\theta) \\
8. \quad & f^F = \frac{\sqrt{3}}{2}(-f_{\omega NN} \sin\theta - f_{\phi NN} \cos\theta) + \frac{1}{2}f_{\rho NN} \\
& f^D = -\frac{\sqrt{3}}{2}(-f_{\omega NN} \sin\theta - f_{\phi NN} \cos\theta) + \frac{3}{2}f_{\rho NN} \\
& f^S = \sqrt{2}(-f_{\omega NN} \cos\theta + f_{\phi NN} \sin\theta)
\end{aligned} \quad (35)$$

correctly, together with mixing angle $\theta = 38.35^\circ$ to be evaluated by Gell-Mann-Okubo quadratic mass formula, from all four expressions for f^F, f^D, f^S identical numerical values of SU(3) f^F, f^D, f^S coupling constants are found.

Substitution of them into relations for $f_{VYY}, Y = \Lambda, \Sigma, \Xi$, for every hyperon again four different set values in signs are obtained, from which by division them with numerical values of SU(3) f^F, f^D, f^S coupling constants with correct signs, unambiguous values of $(f_{VYY}/f_V), Y = \Lambda, \Sigma, \Xi$, are evaluated to be completely independent on the $\omega - \phi$ mixing forms.

Substituting them into the corresponding $U\&A$ hyperon EM structure models one can predict also hyperon EM FFs behaviors in the whole region of their definition. A realization of this program is in progress.

CONCLUSIONS

The Λ, Σ, Ξ hyperons EM structure has been investigated as generalization of the nucleon $U\&A$ EM structure model.

Based on the fact that analytic properties of the hyperon EM FFs, up to the position of effective inelastic thresholds are equal with analytic properties of the nucleon EM FFs.

Models depend on some coupling constant ratios (f_{VBB}/f_V) as free parameters, they have been found from known nucleon coupling constant ratios and SU(3) invariant Lagrangians of vector-meson-baryon interaction.

In their specification a principal role played the $\omega - \phi$ mixing forms with universal vector-meson coupling constants f_V .

All coupling constant ratios as free parameters of the Λ, Σ, Ξ hyperon EM structure models have been evaluated numerically.

ACKNOWLEDGEMENT: This work was supported by the Slovak Grant Agency for Sciences VEGA, grant No. 2/0153/17.

REFERENCES

1. S. Dubnička, A. Z. Dubničková, Acta Phys. Slovaca **60**, 153 (2010).
2. E. Bartoš, S. Dubnička, A. Z. Dubničková, M. Fujikawa, H. Hayashii, Nucl. Phys. B (Proc. Suppl.) **198**, 186 (2010).
3. S. Dubnička, A. Z. Dubničková, A. Liptaj, Prog. Part. Nucl. Phys. **67**, 418 (2012).
4. A. Z. Dubničková, S. Dubnička, A. Liptaj, Acta Phys. Polonica B (Proc. Suppl.) **9**, 407 (2016).
5. C. Adamuščín, E. Bartoš, S. Dubnička, A. Z. Dubničková, Phys. Rev. **C93**, 055208 (2016).
6. C. Adamuščín, E. Bartoš, S. Dubnička, A. Z. Dubničková, Acta Phys. Polonica B (Proc. Suppl.) **11**, 519 (2018).
7. C. Adamuščín, S. Dubnička, A. Z. Dubničková, Acta Phys. Polonica (Proc. Suppl.) **13**, 25 (2020).

SELECTED RESULTS OF THE ATLAS EXPERIMENT WITH SIGNIFICANT CONTRIBUTION OF CZECH AND SLOVAK PHYSICISTS

T. Davidek, Tomas.Davidek@mff.cuni.cz, MFF UK, Praha, Czech republic

INTRODUCTION

ATLAS is one of the two general-purpose particle physics experiments installed at the Large Hadron Collider (LHC) at the European laboratory for particle physics (CERN) near Geneva, Switzerland. The LHC is the world's largest accelerator, which provides proton-proton (pp) and lead-lead collisions at unprecedented energies and intensities. ATLAS started regular data-taking with full swing in 2010, measuring the pp collisions at the centre-of-mass energy of 7 TeV. The beam energies and intensities were gradually increased, reaching the centre-of-mass energy of 13 TeV with the bunch-crossing frequency of 40 MHz already in 2015 and an average number of interactions per bunch-crossing of 36.1 in 2018 [1]. The goal of the experiment is to deepen our knowledge of elementary particles and their interactions, currently described by the theoretical framework called Standard Model (SM).

The ATLAS physics programme addresses precision measurements and tests of processes within the scope of the Standard Model (e.g. in the Higgs-boson sector, top-quark and electroweak processes, flavour physics, QCD and jet physics, diffractive processes) as well as searches for new particles and phenomena beyond the SM, including Supersymmetry, dark matter, excited quarks and leptons and processes with lepton flavour violation. The broad research activities are completed with heavy-ion programme, which focuses on collective effects in the quark-gluon plasma created in the central lead-lead collisions.

Czech and Slovak physicists are actively involved in the ATLAS experiment. Researchers and students from Charles University, Czech Technical University, Institute of Physics of the Czech Academy of Sciences, Nuclear Physics Institute of the Czech Academy of Sciences, Palacky University, Comenius University and Institute of Experimental Physics of the Slovak Academy of Sciences contribute to detector construction, operations, upgrade and successful physics data analyses.

The ATLAS collaboration obtained a large amount of first-class physics results and published almost 1000 papers to this date, which is not possible to summarise in a single document. Therefore, this contribution aims to highlight some recent ATLAS results with significant contributions from Czech and Slovak physicists. The main upgrade-related activities are also briefly described.

THE ATLAS DETECTOR

ATLAS is a multi-purpose particle detector with a forward-backward symmetry and nearly 4π coverage in the solid angle [2, 3, 4]. It consists of several sub-detectors that play different roles. Closest to the beam pipe is the inner tracking detector covering the pseudorapidity¹ range $|\eta| < 2.5$. It is surrounded by the super-

¹The angle with respect to the beam axis is usually expressed

conducting solenoid that provides a 2 T axial magnetic field. High-granularity electromagnetic ($|\eta| < 3.2$) and hadronic ($|\eta| < 4.9$) sampling calorimeters provide precision energy and direction measurement of electrons, photons, isolated hadrons and jets. The outer part of the whole detector contains the muon spectrometer ($|\eta| < 2.7$), with a toroidal magnetic field generated by three sets of large superconducting magnets. The spectrometer also includes fast trigger chambers used for the event selection in the first trigger level.

A schematic view of the ATLAS detector is displayed in Fig. 1.

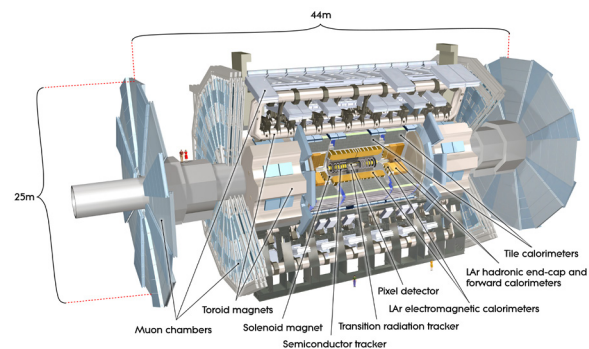


Fig. 1. The ATLAS detector. Czech and Slovak physicists participate in construction and operations of the Pixel detector, Semiconductor tracker, Liquid-argon electromagnetic calorimeter and Tile calorimeter as well as the detector of forward protons (AFP). The latter sub-detector is located 220 m from the detector centre and thus not shown in the figure.

SELECTED PHYSICS RESULTS

Higgs boson decay $H \rightarrow \tau\tau$

After the discovery of the Higgs boson in 2012 by ATLAS [5] and CMS [6] collaborations in the decays $H \rightarrow \gamma\gamma$, $H \rightarrow ZZ$ and $H \rightarrow WW$, the focus was moved to precise determination of its properties. The measurement of the Higgs-boson decay to a pair of τ -leptons represents its first decay to fermions ever observed and thus it provides an important scrutiny of the Yukawa coupling.

Since τ -leptons further decay either to light leptons ($\tau \rightarrow \ell\nu_\ell\nu_\tau$, denoted as τ_ℓ) or hadrons ($\tau \rightarrow \text{hadrons} + \nu_\tau$, referred to as τ_h), the measurement is performed in three channels reflecting the τ decay modes: $H \rightarrow \tau_\ell\tau_\ell$, $H \rightarrow \tau_\ell\tau_h$ and $H \rightarrow \tau_h\tau_h$. The event selection in each channel is further split into two main categories, targeting the Higgs production mode through gluon-gluon fusion (ggF) and vector boson fu-

in terms of the rapidity y or pseudorapidity η . They are defined as $y \equiv \frac{1}{2} \ln \left(\frac{E+p_z}{E-p_z} \right)$ and $\eta \equiv -\ln \tan(\theta/2)$, where E and p_z are the particle's energy and momentum along the beam axis and θ represents the polar angle measured from that axis.

sion (VBF), respectively. The main challenges of this analysis include:

- reconstruction of the Higgs-boson mass due to two or more neutrinos in the final state, an approximate technique called MMC [7] is applied;
- reliable description of the dominant background components, originating from $Z \rightarrow \tau\tau$ production and processes where an electron or jet are misidentified as τ_h or a jet is misidentified as electron (in case of τ_ℓ).

The reconstructed Higgs-boson mass is shown in Fig. 2, after the global likelihood fit combining all signal categories and control regions to constrain the main background components. The cross-sections for the two main production mechanisms are determined $\sigma(\text{ggF}) = 3.1 \pm 1.0(\text{stat})_{-1.3}^{+1.6}(\text{syst}) \text{ pb}$ and $\sigma(\text{VBF}) = 0.28 \pm 0.09(\text{stat})_{-0.09}^{+0.11}(\text{syst}) \text{ pb}$, respectively. When combining the results with earlier Run 1 data (2010–2012), the existence of the decay $H \rightarrow \tau\tau$ is confirmed with a significance of 6.4σ [8].

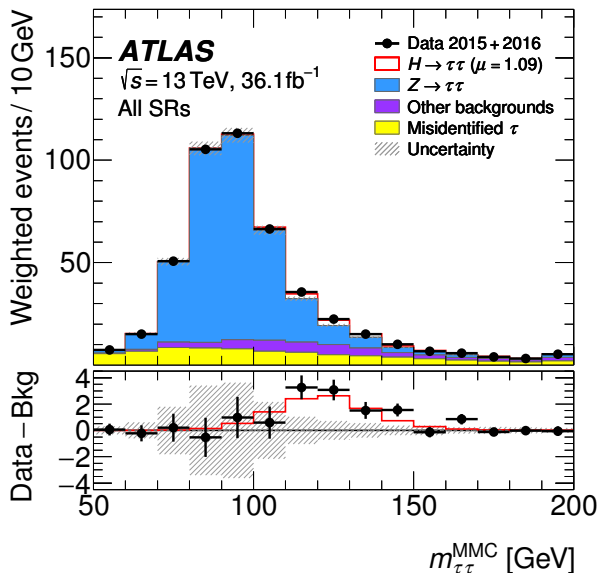


Fig. 2. The distribution of the reconstructed $\tau\tau$ invariant mass for the sum of all signal regions. The contributions of the different signal regions are weighted by a factor of $\ln(1 + S/B)$, where S and B are the expected numbers of signal and background events in that region, respectively. The bottom panel shows the differences between observed data events and expected background events after applying the same weights (black points). The observed Higgs-boson signal with the fitted signal strength $\mu = 1.09$ relative to the SM prediction is shown with the solid red line. The size of the combined statistical, experimental and theoretical uncertainties in the background is indicated by the hatched bands.

Charge asymmetry in $t\bar{t}$ events

The top-quark pair-production in pp collisions is dominated by the fully symmetric process $gg \rightarrow t\bar{t}$. Smaller contributions come from $q\bar{q}$ or qg processes, which are sources of small charge asymmetry. This

measurement provides a stringent test of the SM, possible contributions from beyond-SM processes would lead to different asymmetry.

Measured parton distribution functions suggest that top-quarks tend to be produced in the forward direction, while \bar{t} tends to be more central ($|y_t| > |y_{\bar{t}}|$). The charge asymmetry A_C is defined as the relative difference in number of events with the more- and less-probable kinematic configuration

$$A_C \equiv \frac{N(\Delta|y| > 0) - N(\Delta|y| < 0)}{N(\Delta|y| > 0) + N(\Delta|y| < 0)}, \quad (1)$$

where

$$\Delta|y| \equiv |y_t| - |y_{\bar{t}}|. \quad (2)$$

Semi-leptonic $t\bar{t}$ events ($t\bar{t} \rightarrow WbW\bar{b} \rightarrow \ell\nu b q\bar{q}\bar{b}$) appear in two different kinematic configurations: the resolved topology is characterised by the presence of four small-radius jets, while the hadronically decaying top-quark is reconstructed as one large-radius jet in the so-called boosted topology. This analysis exploits both these topologies.

An example of the differential measurement as a function of the invariant mass of the $t\bar{t}$ system is shown in Fig. 3. The charge asymmetry appears to be at the level of 1% and is in agreement with the state-of-the-art SM predictions [9].

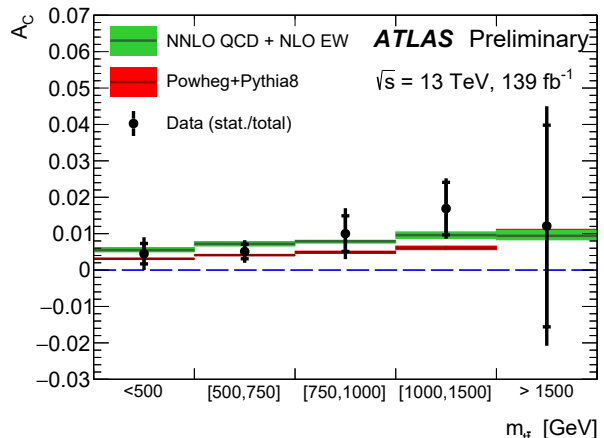


Fig. 3. The unfolded differential charge asymmetry as a function of the invariant mass of the $t\bar{t}$ system, resolved and boosted topologies are combined. Green hatched regions show SM theory predictions calculated at NNLO in QCD and NLO in electroweak theory [10]. Red hatched regions show parton-level truth asymmetry with its uncertainty extracted from the full phase space using nominal $t\bar{t}$ signal sample. Vertical bars correspond to the total uncertainties.

Differential cross-sections of $t\bar{t}$ production

Single- and double-differential cross-section measurements are performed for the production of top-quark pairs. Owing to the large $t\bar{t}$ cross-section at the LHC, such measurements allow a detailed study of the properties of the top-quark production and decay, enabling precision tests of several Monte Carlo generators and fixed-order SM predictions.

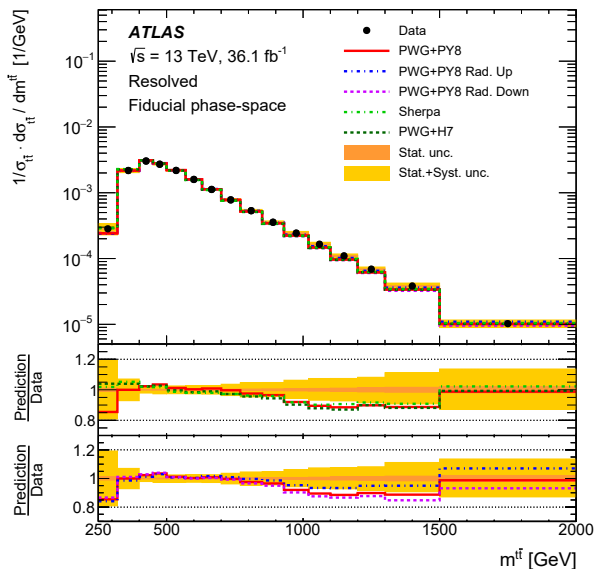


Fig. 4. The particle-level normalised differential cross-sections as a function of the mass of the $t\bar{t}$ system in the resolved topology, compared with different Monte Carlo predictions. The bands represent the statistical and total uncertainty in the data. Data points are placed at the centre of each bin. The lower panel shows the ratios of the simulations to data.

Similarly to the previous analysis, these studies also deal with semi-leptonic $t\bar{t}$ events, exploiting both resolved and boosted final state topologies.

The particle-level measurements are compared with next-to-leading-order (NLO) plus parton shower (PS) predictions as implemented in state-of-the-art MC generators. In general, predictions agree well with the single-differential measurements for both resolved and boosted topologies. An example is shown in Fig. 4. Somewhat poorer modelling is observed in specific regions of the probed phase-space. Overall, the NLO+PS MC generators show poorer modelling of the double-differential distributions, especially in combination that includes transverse momentum of the $t\bar{t}$ system as a probed variable in the resolved topology. Two best generators providing a good description of the largest fraction of variables are POWHEG+PYTHIA8 and POWHEG+HERWIG7 for the resolved and boosted topologies, respectively.

The measured parton-level differential cross-sections are compared with state-of-the-art fixed-order next-to-next-to-leading-order (NNLO) QCD predictions. A general improvement relative to the NLO+PS MC generators is observed [11].

Cross-section of $t\bar{t}Z$ process

This measurement provides important information about the $t\bar{t}Z$ coupling, possible deviations from the SM predictions might indicate new effects in the electroweak symmetry breaking mechanism.

This measurement deals with events where Z boson decays to a pair of electrons or muons and one or both W bosons from the $t\bar{t} \rightarrow WbW\bar{b}$ interaction also decay

to either electron or muon. The final state thus contains 3 or 4 light charged leptons. The analysis is split into several categories depending on number of leptons, one or two b -tagged jets and the same/different flavour leptons in case of 4ℓ final states. In order to constrain the main background components WZ +jets and ZZ +jets, two control regions are defined in addition. The inclusive cross-section is then derived from the profile likelihood fit to all six signal and two control regions. The results are shown in Fig. 5, the measured cross-section $\sigma(t\bar{t}Z) = 1.05 \pm 0.05(\text{stat}) \pm 0.09(\text{syst})$ pb is found to be in agreement with the most precise theoretical prediction.

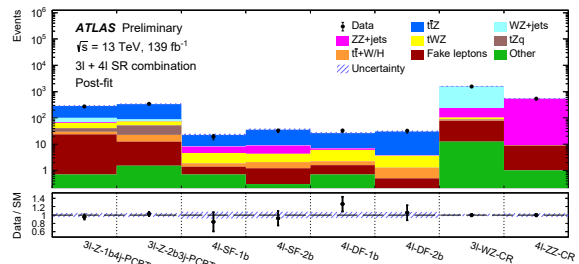


Fig. 5. The observed and expected event yields in the 3ℓ and 4ℓ signal regions as well as the WZ/ZZ + jets control regions after the combined fit. The bottom panel shows the ratio between data and the total SM prediction. The shaded band includes all sources of statistical and systematic uncertainty.

The differential cross-section measurements are performed at the detector, particle and parton level, an iterative Bayesian unfolding procedure is used. All measurements are limited by available statistics, differences between data and theory predictions are smaller than the corresponding uncertainties [12].

CP violation in $B_s^0 \rightarrow J/\psi\phi$ decay

The CP violation in b -hadron decays arises from the interference of the direct decay and the decay with $B - \bar{B}$ mixing. In case of the $B_s^0 \rightarrow J/\psi\phi$ decay, the SM predicts a small CP -violating phase ϕ_s , related to the Cabibbo-Kobayashi-Maskawa quark mixing matrix elements. Since the beyond-SM physics phenomena can significantly enhance this phase, its measurement provides another stringent test of the SM.

The analysis selects events $B_s^0 \rightarrow J/\psi\phi \rightarrow \mu^+\mu^-K^+K^-$ that are fully reconstructed in the tracking detector. An important issue is the flavour tagging of the opposite-side b -hadron. If the decay products of this b -hadron contain an electron or a muon, the flavour can be inferred from the lepton charge. Otherwise, the flavour is determined using the discriminant based on transverse-momentum-weighted electric charges of all tracks associated to that b -hadron decay. Another crucial ingredient to this analysis is the proper decay time measurement, which is important to assess the probability of the $B_s^0 - \bar{B}_s^0$ oscillation in each event. The proper decay time is determined in the transverse de-

tector plane as

$$t = \frac{L_{xy}m}{p_T}, \quad (3)$$

where L_{xy} represents the displacement of the B_s^0 decay vertex with respect to the primary vertex and m , p_T stand for the mass and transverse momentum of the B_s^0 meson.

The main physics parameters of interest, namely the CP -violating phase, the average decay width Γ_s and the decay width difference $\Delta\Gamma_s$, are extracted from an unbinned maximum likelihood fit performed on the events selected for the analysis. The results of partial Run 2 dataset (2015–2017) are combined with earlier Run 1 measurements and are shown in Fig. 6 along with recent results from other experiments. The measured CP -violating phase is consistent with the SM prediction [13].

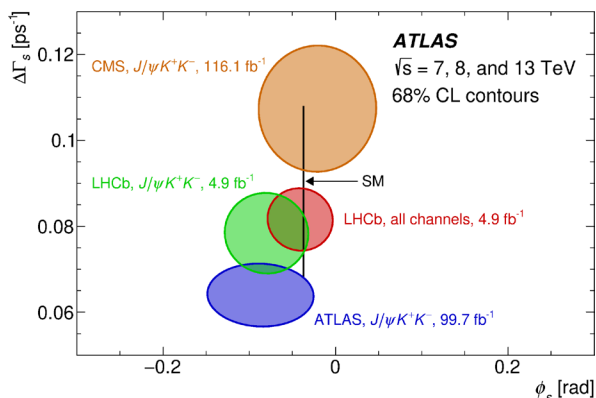


Fig. 6. Contours of 68% confidence level in the $\phi_s - \Delta\Gamma_s$ plane, including results from CMS (orange) and LHCb (green) using the $B_s^0 \rightarrow J/\psi K^+ K^-$ decay only and LHCb (red) for all the channels. The SM prediction [14, 15] is shown as a very thin black rectangle. In all contours the statistical and systematic uncertainties are combined in quadrature.

Observation of $\gamma\gamma \rightarrow W^+W^-$

The first observation of photon collisions producing pairs of W bosons demonstrates a new way of using the LHC, namely as a high-energy photon collider. As this process is governed by diagrams with only gauge bosons (γ , W , Z) at the tree level, it directly probes their trilinear and quartic coupling and it is also sensitive to anomalous gauge-boson interactions.

The analysis targets events where photons are radiated off the whole proton or off a parton. Consequently, three event categories exist – elastic, single-dissociative and double-dissociative events. The measurement is performed in the final state with different-flavour leptons, i.e. the whole interaction process is

$$pp(\gamma\gamma) \rightarrow p^{(*)}W^+W^-p^{(*)} \rightarrow e^\pm\nu_e\mu^\mp\nu_\mu. \quad (4)$$

In order to suppress the background originating from Drell-Yann production, $q\bar{q} \rightarrow WW$ and $\gamma\gamma \rightarrow \tau\tau$, events are required to pass thresholds on the transverse momentum ($p_T^{e\mu} > 30$ GeV) and the invariant mass

($m_{e\mu} > 20$ GeV) of the lepton pair. Leptons are required to originate from the same primary interaction vertex and no further tracks are allowed to be associated with it ($n_{\text{trk}} = 0$). The impact of these criteria on the event selection is demonstrated in Figures 7 and 8.

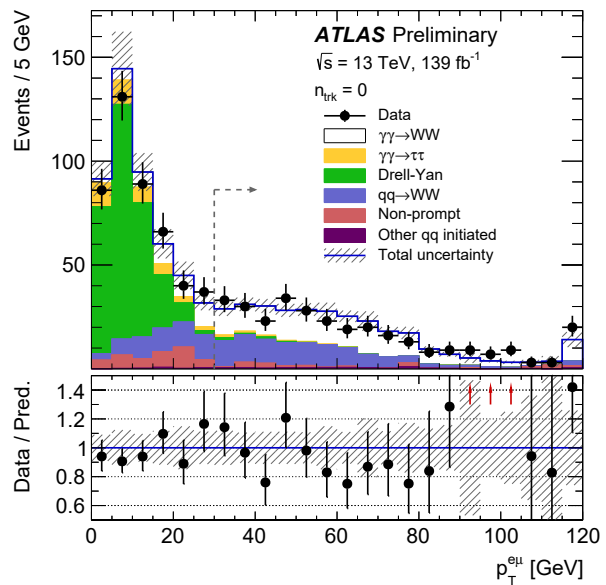


Fig. 7. The distribution of $p_T^{e\mu}$ for $n_{\text{trk}} = 0$. The fitted normalisation factors and nuisance parameters have been used. The total uncertainties are shown as hatched bands.

The lower panels show the ratio of the data to the prediction with the total uncertainty displayed as hatched band. The last bin in both distributions includes the overflow.

The signal is extracted using the profile likelihood fit to one signal and three control regions, defined by inverting the $p_T^{e\mu}$ and n_{trk} criteria. The interaction $\gamma\gamma \rightarrow W^+W^-$ is observed with a significance of 8.4σ and the cross-section of the full process (4) in a fiducial phase space close to the experimental selection is measured to be 3.13 ± 0.31 (stat) ± 0.28 (syst) fb [16].

Heavy-ion collisions

Hard-scattering processes in hadronic interactions generate partons (quarks and gluons) at high transverse momenta that subsequently fragment into hadrons, producing jets. In ultra-relativistic nuclear collisions, parton showers evolve in a hot and dense quark-gluon plasma (QGP) created by the collision. The interaction of partons with QGP leads to reduced parton and jet energies. This phenomenon, known as jet quenching, was observed by ATLAS in the first lead-lead collisions in 2010 [17].

ATLAS has recently investigated the effect of the splitting scale $\sqrt{d_{12}}$ – the transverse momentum scale for the hardest splitting in the jet defined as

$$d_{12} \equiv \min(p_{T,1}^2, p_{T,2}^2) \cdot (\Delta\eta_{12}^2 + \Delta\phi_{12}^2), \quad (5)$$

on the jet quenching. This analysis deals with large-radius jets containing sub-jets and uses the nuclear modification factor R_{AA} to express the suppression

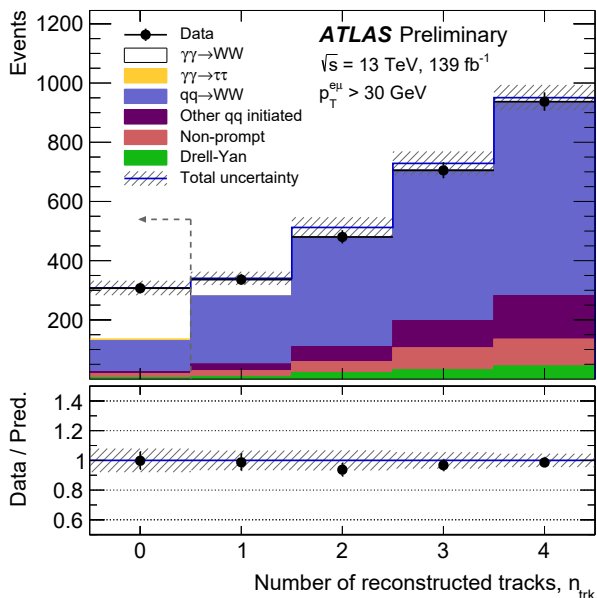


Fig. 8. The distribution of the number of tracks associated with the interaction vertex is shown. The fitted normalisation factors and nuisance parameters have been used. The total uncertainties are shown as hatched bands.

The lower panel shows the ratio of the data to the prediction with the total uncertainty displayed as hatched band.

in the QGP:

$$R_{AA} = \frac{1}{\langle N_{AA} \rangle} \cdot \frac{\text{yield in } AA}{\text{yield in } pp}, \quad (6)$$

where $\langle N_{AA} \rangle$ denotes the average number of binary collisions. Figure 9 displays R_{AA} for large radius jets as a function of the average number of participating nucleons, which is proportional to the centrality of the collision. As expected, jets are increasingly suppressed for more central collisions. Moreover, jets consisting of several sub-jets are more suppressed than those consisting of a single small-radius jet. This observation indicates that jets with hard internal splittings lose more energy in the QGP [18].

ATLAS UPGRADE

After the successful completion of Run 2 in 2018, the ATLAS detector entered the so-called Phase 1 upgrade. Small parts of the detectors that suffered from radiation damage are being replaced (e.g. the muon spectrometer small wheel) and new on-detector electronics prototypes are being installed. The data-taking should resume in 2022.

The major Phase 2 upgrade is planned for the high-luminosity (HL) phase. The LHC will undergo major improvement which will allow to reach the design centre-of-mass energy of 14 TeV and, more importantly, significant increase in the instantaneous luminosity. This implies important challenges for the experiments:

- Higher granularity in several sub-detectors is required to cope with more events in the same

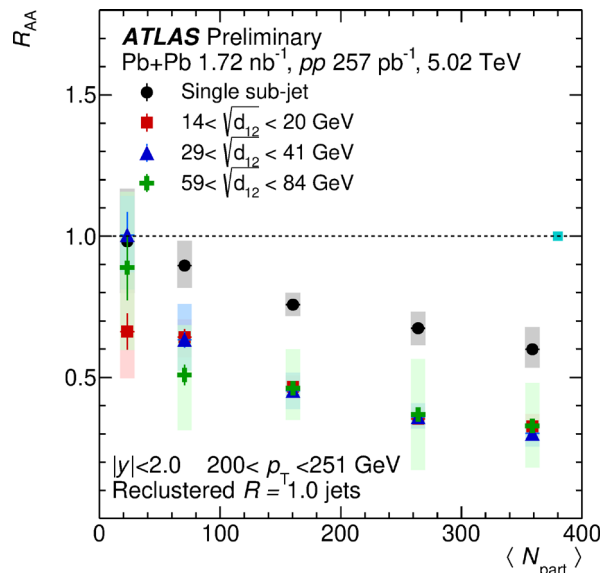


Fig. 9. The nuclear modification factor evaluated as a function of the average number of nucleons participating in the collision, for different intervals of $\sqrt{d_{12}}$. The vertical bars on the data points indicate statistical uncertainties, while the shaded boxes indicate systematic uncertainties.

bunch-crossing.

- More data has to be read-out, processed and stored, implying changes in the on-detector electronics as well as the whole trigger and data acquisition (TDAQ) system.
- High instantaneous luminosity will cause high radiation doses especially in the inner tracking detector, which will be completely replaced with higher granularity radiation-resistant silicon sensors.

Czech institutions invest a lot of effort in the inner detector upgrade, concentrating on the construction, production and quality assurance of the microstrip sensors and module production. Later they will also collaborate in the installation of the new detector in the ATLAS experimental hall. Czech institutions are also involved in the pixel detector upgrade.

Tile calorimeter has to replace its on-detector electronics in order to improve the reliability and redundancy of the system as well as to meet the requirements driven by the new TDAQ system. Czech and Slovak teams involved in this sub-detector participate in this activity by testing new prototypes in the laboratory as well as in dedicated beam tests.

The HL-LHC is expected to start its operation in 2027.

CONCLUSIONS

The discovery of the Higgs boson opened new possibilities in particle physics. Precise determination of the Higgs-boson properties is one of the key issues, since Higgs might be a portal to new physics beyond the SM. At the same time, precision measurements of other SM

parameters and processes are ongoing. Direct searches for new particles and physics phenomena complement the precision measurements, where possible deviations from the current theory should also provide hints on new physics.

The Czech and Slovak physicists actively participate in the ATLAS experiment, being involved in detector construction, operations and upgrade. They are also actively involved in many physics analyses as demonstrated in this short overview.

ACKNOWLEDGEMENT: The author is indebted to many ATLAS colleagues for providing important details and feedback on various analyses mentioned in this overview. The work was partly supported by two projects of the Ministry of Education, Youth and Sports of the Czech Republic: the research infrastructure CERN-CZ (project LM2018104) acting as gateway to CERN and its experiments as well as the Inter-Excellence/Inter-Transfer project LTT17018 supporting the physics analyses at CERN experiments.

REFERENCES

1. ATLAS Collaboration, *JINST* **15**, P04003 (2020).
2. ATLAS Collaboration, *JINST* **3**, S08003 (2008).
3. ATLAS Collaboration, <https://cds.cern.ch/record/1291633> (2010).
4. B. Abbott et al., *JINST* **13**, T05008 (2018).
5. ATLAS Collaboration, *Phys. Lett.* **B 716**, 1 (2012).
6. CMS Collaboration, *Phys. Lett.* **B 716**, 30 (2012).
7. A. Elagin, P. Murat, A. Pranko, A. Safonov, *Nucl. Instrum. Meth.* **A 654**, 481 (2011).
8. ATLAS Collaboration, *Phys. Rev. D* **99**, 072001 (2019).
9. ATLAS Collaboration, ATLAS-CONF-2019-026, <https://cds.cern.ch/record/2682109> (2019).
10. <http://www.precision.hep.phy.cam.ac.uk/results/>
11. ATLAS Collaboration, *Eur. Phys. J.* **C 79**, 1028 (2019).
12. ATLAS Collaboration, ATLAS-CONF-2020-028, <http://cdsweb.cern.ch/record/2725734> (2020).
13. ATLAS Collaboration, arXiv:2001.07115 [hep-ex] (2020).
14. J. Charles et al., *Phys. Rev. D* **91** 073007 (2015).
15. A. Lenz and U. Nierste, arXiv:1102.4274 [hep-ph] (2011).
16. ATLAS Collaboration, ATLAS-CONF-2020-038, <http://cdsweb.cern.ch/record/2727859> (2020).
17. ATLAS Collaboration, *Phys. Rev. Lett.* **105**, 252303 (2010).
18. ATLAS Collaboration, ATLAS-CONF-2020-056, <http://cdsweb.cern.ch/record/2701506> (2020).

LASER – WORKING TOOL OF THE 21ST CENTURY

M. Smrz, martin.smrz@hilase.cz, Hilase centre, Institute of Physics AS CR, Za radnici 828, Dolní Břežany, CZ

INTRODUCTION

Laser systems have undergone a long way since the laser invention by Theodore Maiman in 1960. From a laboratory curiosity they changed to a frequently used highly accurate real working tool in many application fields. Importance of lasers illustrate well several Nobel prizes awarded for contributions related directly to laser development since 1960, the very last one 2 years ago.

HiLASE centre [3-5] of the Institute of Physics of the Academy of Sciences of the Czech republic focuses since is establishing on development of diode-pumped pulsed solid state lasers for hi-tech industrial applications. Such lasers with high average power ranging from Watts up to 1 kW and pulse duration from nanoseconds to picoseconds are applicable under industrial conditions to highly precise micro- and nano-machining, 3D printing of complex plastic or metallic parts, production of high power UV radiation for manufacturing of high-frequency chips for computers and smart phones, increase of fatigue life of components for aerospace industry, production of combustion and electric car engines, functionalization of material surfaces for medicine and industry (friction and wettability engineering, antibacterial surfaces), or high-resolution imaging, etc.

HiLASE centre is developing and operating in-house developed sub-picosecond laser technology using so called thin-disk laser architecture benefiting from efficient cooling of ultra thin active laser media, and technology of liquid nitrogen-cooled multi-slab lasers enabling to generate high-energy nanosecond pulses. The lasers are based on Yb:YAG active material so they are emitting fundamentally close to wavelength of 1030 nm, however, emission spectrum broadening application potential can be extended by methods of nonlinear optics to UV, visible, and mid-infrared spectral range. This paper reports on technical details and the most important applications of this technology.

LASER FUNDAMENTALS

Laser [6-8] typically consists of following modules: 1) gain medium storing energy and converting it to energy of coherent radiation by stimulating emission. The gain medium defines laser wavelength; 2) pump source delivering the energy to the gain medium (optical, electrical, chemical pumping, etc.); 3) cooling system extracting waste heat coming from quantum defect and losses; 4) positive feedback, which is typically created by a mirror-based resonator. Such a system can emit coherent light in a form of continuous wave or pulses, however, average output power of a single gain medium is limited. To increase laser average output power, lasers are followed by amplifiers using the same principle of stimulated emission of light.

Most of the high power pulsed lasers work in MOPA scheme (Master Oscillator – Power Amplifier),

where high quality seed beam is amplified in one or more power amplifiers. Those power amplifiers can be regenerative or multi-pass, or both of them. They can be combined with so called CPA technique (Chirped pulse amplification) to amplify ultra-short pulses. To extract significant amount of stored energy in amplifiers and reach high efficiency of the system is important to select a suitable kind of laser amplifier. There are two basic types of laser amplifiers, regenerative amplifiers and multipass amplifiers.

REGENERATIVE AMPLIFIERS

Regenerative amplifiers [1], [6-8], offer solution for amplification of weak pulses with low energy. Trapping of the pulse in an optical cavity allows for realization of tens of round trips through the gain medium leading to efficient energy extraction. Amplification undergone in optical resonator (Fig. 1) does not degrade laser beam quality. Injected seed pulses to the amplifier are trapped in the cavity, usually by an acousto-optic switch, or more often by a Pockels cell and changing polarization state. Polarization locking by applying high voltage to a Pockels cell requires fast high voltage electronics and polarization optics in the cavity. Amplification of the trapped pulse – realization of tens or even hundreds of cavity round trips. Releasing of the amplified pulse from the cavity by switching of high voltage on the Pockels cell. Regenerative amplifiers are often used like first stage amplifiers for short pulse amplification. They are very efficient in power amplifiers of thin disk lasers, where they help to solve their main drawback – very low single pass gain.

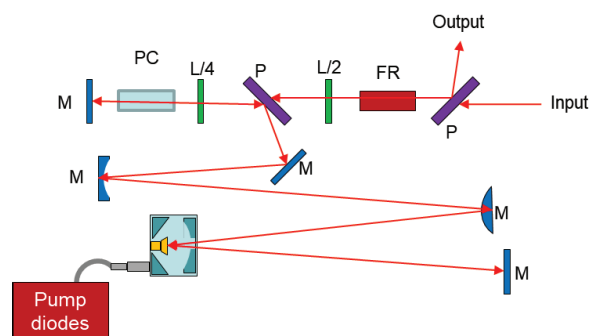


Fig. 1. Regenerative amplifier with a standing-wave cavity (M – mirrors, PC – Pockels cell, FR – Faraday rotator, P – polarizer, L/2 – half waveplate, L/4 – quarter waveplate) [1]

MULTI-PASS AMPLIFIERS

Unlike regenerative amplifiers, number of pulse round-trips in multipass amplifiers [1], [7-8] is fixed and given by spatial multiplexing, i.e. laser beam is folded by mirrors to multiple the number of roundtrips (Fig. 2). The geometrical constraints are therefore the main limiting factor of roundtrip number. Thus, multipass

amplifiers have to be able to extract all stored energy in few pulse roundtrips, and are normally used for power amplification in very last stages of a complex laser system, where net-gain lower than one order is sufficient. Frequently, the regenerative amplifier is followed by one or a series of multipass amplifiers in complex, high energy laser systems. Absence of resonator does not preserve excellent beam quality, however, diffraction is often compensated by image relaying between the subsequent passes of the pulse through the gain medium. Multipass amplifiers enable simple set-up without a need for complicated electro- or acousto- optic switches and high contrast polarizing optics, however, allow efficient operation only for pre-amplified laser pulses.

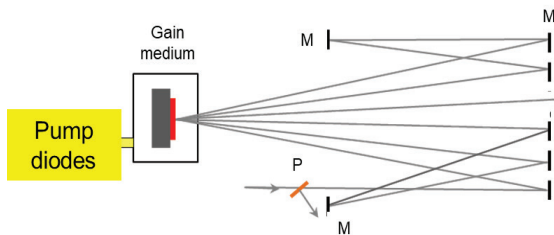


Fig. 2. Multipass amplifier with a thin-disk gain medium (M – mirrors, P – polarizer, L/4 – quarter waveplate) [1].

CHIRPED PULSE AMPLIFICATION

Amplification of ultrashort pulses brings complications with high intensity accumulating nonlinear phase and laser beam deformation described by high B-integral as the pulse energy increases during the amplification process. Additionally, laser induced damage threshold (LIDT) of optical materials drops with decreasing pulse length [9]. Crossing the damage threshold barrier of laser components and consequent damage on gain medium or dielectric coatings prevents direct amplification of femtosecond and picosecond pulses to high energy. Solution for such a drawback is amplification of broadband pulses stretched to nanosecond pulse duration, i.e. Chirped Pulse Amplification technique (CPA) [10] (Fig. 3).

Handling the pulse duration is possible due to dispersion effects. De-phasing of spectral components of bandwidth-limited pulses generated by an oscillator stretches the pulses and generates frequency chirp. After amplification, the pulses are compressed again to original pulse duration by opposite dispersion compensating the actual chirp. Chromatic dispersion $n(\omega)$ in materials in near infrared spectral range generates so called normal (material) dispersion when higher frequency components propagate slower. Material dispersion is often insufficient or impractical for a CPA stretcher or compressor because chromatic dispersion doesn't have opposite counterpart that can fully compensate it. Therefore, optical path difference between spectral components is generated during propagation of the pulse in media exhibiting angular dispersion. Typically, a pair of dispersive prisms or diffraction gratings showing anomalous dispersion is

used. Spatial separation of spectral components of the pulse generated after passing the second prism or grating can be compensated by a back-reflective mirror and double-pass configuration. Amount of generated frequency chirp is proportional to distance of prisms or gratings in the pair. Normal dispersion in near infrared range can be generated by grating pair with negative distance of the gratings, i.e. when the first grating is image relayed behind the second one by an imaging system between the gratings. Such pair of Martinez stretcher and Treacy compressor generate opposite dispersions that compensate each other very well [7].

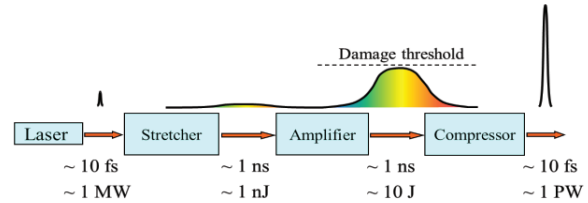


Fig. 3. Scheme of ultrashort pulse amplification by Chirped Pulse Amplification technique [1].

THIN-DISK LASER PERLA

Thin-disk lasers (Fig. 4) [1-2], [4-5], [8], [11] have several advantages over rod-type solid state lasers which face serious problems with thermal lensing and material expansion due to huge thermal gradients generated in a volume gain media. When operated in a pulsed regime, pulse propagation in the bulk induces nonlinear response described by an accumulated B-integral [7], [12] resulting, besides other effects, in self-focusing of laser beams inside the rod. Both phenomena can consequence in significant changes in laser behaviour and damage on optical components of the laser itself. The thin-disk geometry like a limiting case of a laser diode end-pumped rod with a gain medium diameter of >10 mm and length (thickness) typically of a fraction of mm prevents that behaviour. The gain medium is used like a thin, highly-active-ions-doped active mirror with an antireflective (AR) coating on a front side, a highly reflective (HR) one on a back side (Fig. 4, inset), and a water-cooled heat-spreader extracting waste heat in an axial direction of the optical setup bonded to the HR side, unlike a rod-type laser extracting waste heat radially. Thanks to the low thickness of the gain medium is also the accumulated B-integral negligible, even in a multi-pass geometry of the gain medium. On a contrary, low thickness of the gain medium is the most significant drawback of thin-disks because of low single-pass absorption of pump radiation, and low single-pass signal gain, even in highly doped crystals. To overcome this disadvantage, a compact optical image-relaying system consisting of a large parabolic mirror and a set of roof reflectors folding the pump beam path, and allowing to multiply the number of pump beam passes through the gain medium and absorption efficiency was proposed (Fig. 4). Nowadays, optical systems allowing up to 72

pump beam passes are commercially available. Achievable size of a pumped area and pump power density on a thin-disk depends on brightness of a pump source, and a focal length of an image-relaying optics, which is usually 50 – 150 mm. Whereas pump radiation reaches the disk surface under an angle, signal is propagating axially and reaches the gain medium through an opened central part of the parabolic mirror. In high power lasers where pump power reaches several kW, all optical components must be water cooled [2].

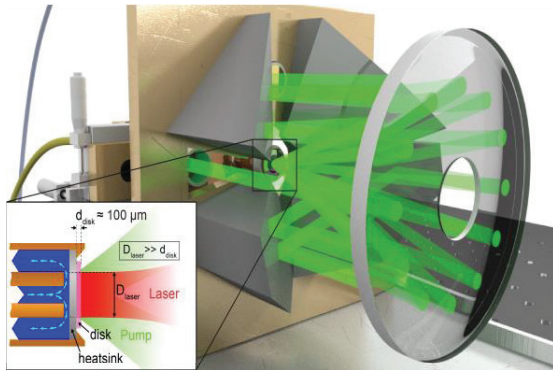


Fig. 4. Optical scheme of an optical system for efficient pumping of a thin-disk laser. Cross-section of a diamond-bonded thin-disk gain medium is in the inset. Courtesy of Martin Saraceno; ulp.ethz.ch [2].

Properties of a gain medium acting a role of the active mirror are critical for efficient operation of a thin disk laser. Enormous amount of waste heat approaching in some cases kW level, which is generated in a volume of few cubic millimeters, can be efficiently extracted thanks to the excellent ratio of a disk surface area to a disk volume through the large, highly reflective coated back side of the active mirror. However, front surface temperature of a pumped thin-disk area reaches often $>100^{\circ}\text{C}$, which generates step-like temperature change and, consequently, high mechanical stress and disk deformation caused by different thermal expansion of a material between the pumped and the unpumped disk regions. A bonding layer fixing the gain medium to a heat spreader must be extremely thin in order not to create high thermal resistance at the interface, and flexible but strong to absorb a different thermal response of both counterparts. Role of the heat spreader is fast and homogeneous heat extraction from the gain medium, heat transfer to cooling water, and thin-disk mechanical support because the thin-disk itself is extremely fragile. kW lasers use solely synthetic diamond substrates epoxy glued to the disk. Recently, new approaches using an epoxy-free diffusion bonding have been demonstrated [13]. Similar approaches frequently used for a direct bonding of two bulk optical materials cannot be straightforward applied to the thin-disk bonding since two different materials being connected here contain additional amorphous interlayer of a highly reflective optical coatings. Despite this issue we successfully demonstrated the Atomic Diffusion Bonding process based on recrystallization of thin atomic gold layers sputtered on both components being connected [13], [2].

Many materials with different spectral properties have been tested like a gain medium, however, Yb:YAG is the most frequently used one. It shows several advantages over the other ones. First, Yb:YAG has a broad absorption line centred around 940 nm, and long upper laser level lifetime approaching 1 ms, which makes it ideal for efficient pumping by cheap, high brightness, commercially available AlGaAs-based laser diodes. Second, Yb:YAG is a quasi-three-level gain medium, i.e. it shows a very low quantum defect and waste heat production only around 8 % when pumped at 940 nm. On the other hand, this choice brings a non-zero population at the lower laser level at elevated temperatures, which requires small amount of pumping for bleaching of the gain medium only. Finally, Yb:YAG has relatively high thermal conductivity, excellent mechanical properties, chemical stability, can be grown in large volumes with excellent quality, and technology of its polishing is well developed. A broad emission line centred at a wavelength of 1030 nm also allows for direct amplification of picosecond and sub-picosecond pulses. The Perla platform developed at the Hilase centre is therefore primarily based on Yb:YAG gain medium as well [2].

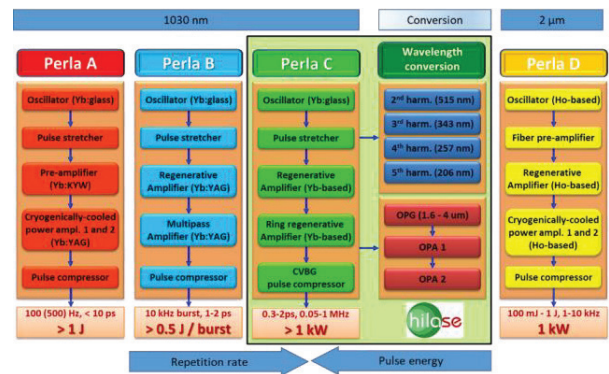


Fig. 5. Structure and target parameters of Yb:YAG Perla beamlines at the Hilase centre. The Perla C includes frequency conversion systems [2].

Yb:YAG lasers, are usually pumped to a broad absorption line around 940 nm, however, there exists a narrow absorption line close to 969 nm allowing more efficient pumping directly to the upper laser level, so called zero-phonon line pumping. Longer wavelength reduces a quantum defect, which prevents generation excessive waste heat [14-15], however, efficient zero-phonon line pumping requires narrow-band pump diodes stabilized by volume Bragg gratings to provide a stable flux of desired pump photons.

HiLASE centre operates several thin disk laser beamlines (Fig. 5). The most advanced one is a 0.5 kW picosecond regenerative amplifier Perla C (Fig. 6) operated at pulse repetition rate of 100 kHz. [4-5][16] It is a typical example of high average power thin-disk regenerative amplifier, one of the most powerful ones, with a single active medium in the main amplifier. The laser system is based on the CPA technology. For amplification from picojoule level is advantageous to

combine several amplifier geometries, in this case fiber-based front-end and thin-disk-based power amplifiers.

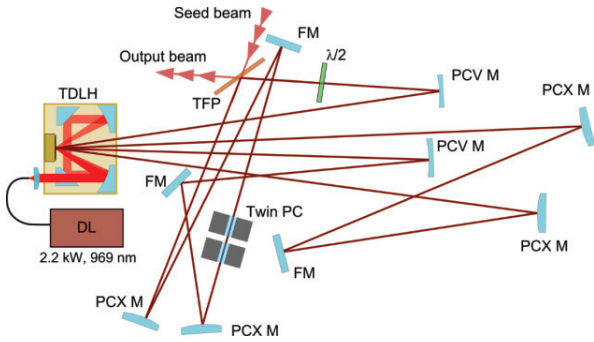


Fig. 6. Optical scheme of the 500 W Perla C thin-disk laser system (TFP – thin film polarizer, $\lambda/2$ – half waveplate, PC – Pockels cell, TDLH – thin-disk laser head, DL – pump diodes, HWP – half waveplate).

Yb-doped, single-mode fibre oscillator and preamplifiers with enormous single pass gain and excellent beam quality ($M^2 = 1.1$) shift pulse energy level in the front-end from picjoules to a fraction of microjoule. The front-end also contains pulse stretcher. The stretcher is based on chirped fibre Bragg grating. The repetition rate is finally reduced to 100 kHz in the first regenerative amplifier. To compensate insertion losses of the stretcher and the pulse picker, the front-end contains two Yb-doped fiber preamplifiers for boosting the output pulse energy up to 1 μ J.

The second-stage amplifier was seeded from the fibre preamplifier. This regenerative amplifier is a small footprint (900 x 1200 mm) single Yb:YAG thin disk amplifier with a standing wave cavity. More than 2 m long cavity is designed for a 2.7 mm pump spot on the Yb:YAG thin disk. The amplification is switched on and off by a double BBO (beta barium borate) Pockels cell with 8 x 8 mm aperture. High repetition rate high voltage switching of the Pockels cell can cause piezo ringing in the crystal and damage it if the crystal holder is wrongly designed. We developed two kinds of water cooled Pockels cell holders with spring loaded vibration absorbers that compensate these effects. The amplifier is pumped by continuous-wave fibre-coupled laser diodes at zero-phonon line wavelength (968.8 nm) as mentioned above. Amplified pulses from the amplifier reach 1.1 mJ of pulse energy in a nearly diffraction limited beam with M^2 parameter 1.1 at full power. Spectral bandwidth was 1.6 nm and bandwidth limit for sech² pulse shape is therefore 0.7 ps [1].

Fraction of the uncompressed output from the first stage (approximately 20 W, 200 μ J) is seeded into the main regenerative amplifier (Fig. 6). Thin-disk was located in a 6 m ring cavity with two V-passes through the disk per one roundtrip and footprint area of only 100x60 cm². Such a configuration compensates a main drawback of ring cavities comparing to standing wave cavities – only a single V-pass through an active medium per cavity roundtrip. On the other hand, scaling of the mode size is easier since ring cavities are shorter for given mode size than standing-wave cavities. The

thin disk was pumped by a CW, 968.8 nm fibre-coupled diode laser on a pump spot with diameter of 5.2 mm. Dual Pockels cell with two BBO crystals in in-house developed holders was operated at 10-kV half-wave voltage and repetition rate of 50 or 100 kHz. Maximum CW output power of 565 W was obtained at 1.21 kW of pump power, and the optical-to-optical efficiency was 47 % (Fig. 7). In seeded operation with the input pulse energy of 0.2 mJ, obtained pulses had up to 5-mJ at 100 kHz (500 W average output power) with extraction efficiency of 43 %. Pulses with 1.4 nm bandwidth (full width at half maximum, FWHM) had pulse duration of 1.8 ps (FWHM). In 50 kHz regime were generated 9 mJ pulses (450 W, uncompressed) with 1130 W of pump power, i.e. opt.-opt. efficiency reached an excellent value of almost 40 %. In the 50-kHz regime, a several-hours-long stable operation was demonstrated with average output power of 320 W (pulse energy of 6.4 mJ) in a nearly diffraction-limited beam with M^2 parameter equal to 1.4 before compression (Fig. 7 in inset). The laser was operated with power fluctuation (rms) as low as 1.2% in a laboratory. Output pulse is compressed by a dielectric diffraction grating-based pulse compressor down to pulse duration of 1.1 ps [1].

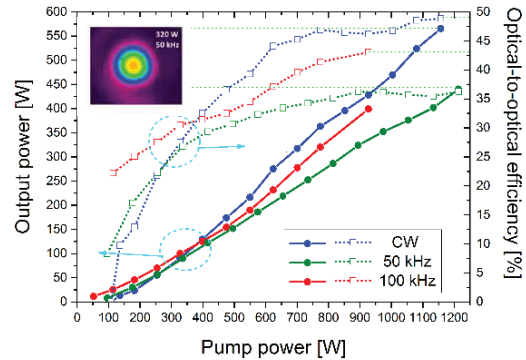


Fig. 7. Output power and optical to optical efficiency of the Perla C ring cavity amplifier in CW operation, and pulsed operation at repetition rates of 50 and 100 kHz [1-2]; Inset: near field beam profile of the Perla C at 320 W and 50 kHz pulse repetition rate.

The Perla C system can be extended by a harmonic frequency conversion set-up consisting of a LBO crystal for second harmonic frequency generation (515 nm, conversion efficiency approx. 60 %), third harmonic generation in a BBO crystal (343 nm, conversion efficiency approx. 25 % from a fundamental one), fourth harmonic frequency generation in a BBO or a CLBO crystal (257.5 nm, conversion efficiency approx. 10 % from a fundamental one when generated like a cascaded conversion via a second harmonic frequency) [5], [12],[17], and fifth harmonic frequency generation in a CLBO crystal (206 nm, sum frequency of a fourth harmonic frequency and a fundamental one) [2], [17-18].

Alternatively, the Perla platform can be equipped by a tunable mid-infrared source based on an optical parametric generator (OPG) followed by an optical parametric amplifier (OPA). The OPG system is based on a periodically-poled lithium niobate crystal, the OPA

on a KTA or KTP crystal pair. A signal beam from the OPA can be tuned from 1.6 to 1.95 μm in case of the KTP crystal, an idler beam from 2.15 to 2.65 μm in case of the KTP [19], or to 3.2 μm in case of the KTA crystal [2].

A thin disk high power laser is an ideal system for micromachining (Fig. 8).

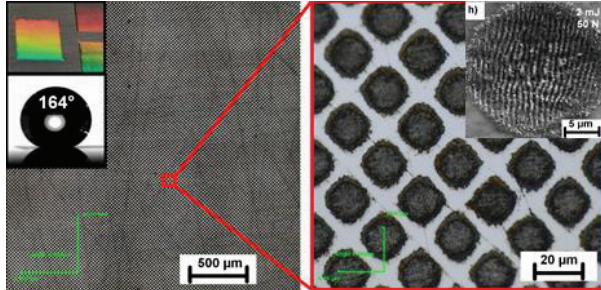


Fig. 8. Multibeam pattern in invar (1520 holes). Beams were generated by diffractive optical element (inset) [20].

HIGH-ENERGY MULTI-SLAB LASER BIVOJ

Other breakthrough laser system operated at Hilase is a cryogenically cooled Yb:YAG multislab laser Bivoj. Instead of thin disk gain medium it uses a set of slabs made of transparent ceramics, which are cooled down to 150 K. Bivoj laser holds a world record like the diode pumped laser with the highest average power.

The system DiPOLE/Bivoj [1], [3-5], [21-22] developed by STFC with participation of HiLASE incorporates a low-energy, fibre-based front end oscillator ($\sim \text{nJ}$), followed by a regenerative Yb $^{3+}$:CaF $_2$ amplifier that increases the output energy to the mJ level and a rod Yb $^{3+}$:YAG multi-pass booster amplifier to raise the output to 50 mJ. Two diode pumped, helium gas cooled large aperture power amplifiers then increase the output energy to 7 J (Main pre-Amplifier) and finally to 100 J (Main power Amplifier). The schematic of the system is in Fig. 9 [1].

The front end starts with a temperature stabilized wavelength tuneable CW fibre oscillator. The CW

output is then temporarily shaped in an A-O (acousto-optic) modulator to 200 ns long pulses with repetition rate of 10 kHz. The pulses are further amplified in a fibre amplifier and subsequently shaped by an E-O (electro-optic) modulator to produce 2-14 ns pulses with arbitrary shape. The pulses are then sent to regenerative rod amplifier based on Yb $^{3+}$:CaF $_2$ that boosts the energy to $\sim 4 \text{ mJ}$. A Pockels cell used to trap the pulses in the cavity also decreases repetition rate to 10 Hz. The Gaussian beam coming from the regenerative amplifier is then spatially shaped to a square super Gaussian profile in a beam shaper consisting of Pi-shaper and serrated aperture with spatial filter. The pulse is further amplified to $\sim 50 \text{ mJ}$ in a multi-pass booster amplifier (Lastronics GmbH) based on Yb:YAG. The beam is spatially expanded after the booster amplifier and is injected into the 10 J main pre-amplifier [1].

The 10 J main pre-amplifier is based on a multi-slab design. It consists of four circular Yb:YAG slabs. Each pair is with different doping levels of Yb $^{3+}$ (1.1, 2.0 at. %). The different doping levels are needed to uniformly divide the heat load among slabs. Each circular slab has diameter of 45 mm and thickness of 5 mm and the pumped area is square of 23 mm \times 23 mm. The pump beam is homogenized light from two diode pump modules operating at 939 nm and each producing 29 kW of peak power in 600 μs long laser pulses at a repetition rate of 10 Hz. The Yb:YAG is clad with 5 mm Cr $^{4+}$:YAG absorber (absorption coefficient of 6 cm $^{-1}$) that prevents ASE and parasitic oscillations. The amplifier is cooled at temperature of 150 K. After 7 passes, the beam is ejected from the amplifier with pulse energy of 7 J in the beam with a size of 22 mm \times 22 mm. The beam is then sent to application areas for experiments or expanded and sent to 100 J amplifier [1]. The 100 J power amplifier is also based on the multi-slab design. It consists of 6 square Yb:YAG slabs with three doping levels of Yb $^{3+}$ (0.4, 0.6, 1.0 at. %). The volume of each slab is 100 mm \times 100 mm \times 8.5 mm and the pumped area is square with dimensions of 78 mm \times 78 mm. The parameters of the pump light are similar to the 10 J amplifier, but the peak power is higher and

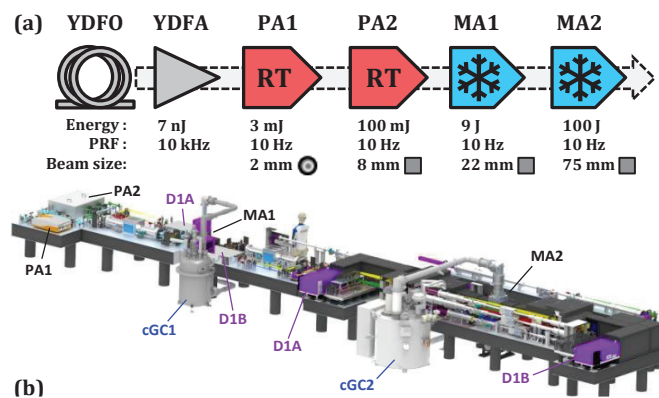


Fig. 1. (a) Schematic of DiPOLE100/Bivoj amplifier chain showing maximum output performance after each amplifier stage, including free-space beam size and shape: YDFO = Yb-silica fibre oscillator; YDFA = Yb-silica fibre amplifier (inc. temporal pulse shaping); PA = room-temperature pre-amplifier (1=Yb:CaF $_2$ regenerative, 2=Yb:YAG multi-pass); MA = main cryogenic amplifier (ceramic Yb:YAG multi-slab). (b) 3D model of DiPOLE100 system: D = Diode pumps; cGC = cryogenic gas coolers [1].

reaches 250 kW from each module and the pulse duration is longer, around 800 μ s. The Yb:YAG is clad with a 10 mm wide Cr⁴⁺:YAG absorber (absorption coefficient of 3 cm⁻¹) that prevents ASE and parasitic oscillations [1].

After the 1st pass, a deformable mirror is implemented to prevent degradation of the wavefront on subsequent passes. After 4 passes, the beam is ejected from the amplifier with pulse energy of up to 105 J with beam size around 75 mm \times 75 mm. The average fluence of the amplified beam is 2 J/cm². The amplifier is cooled by forced Helium gas flow with pressure around 10 bar and at temperature of 150 K.

The Bivoj system is a unique tool for so-called laser shock peening, hardening of material surface by a shock wave in order to increase fatigue life. Other application is measurement of laser-induced damage threshold of optical materials [3].

CONCLUSIONS

Nanosecond and picosecond high power laser systems became a versatile tool in many scientific experiments and industrial processes. Many hi-tech products from electronics to cars and medical implants could not exist without laser machining. HiLASE centre of the Academy of Sciences contributes to development of laser technology with breakthrough parameters pushing laser applications to new dimensions. The centre currently operates sub-1-kW in-house developed picosecond laser platform Perla, and 1 kW/100 J nanosecond platform Bivoj.

ACKNOWLEDGMENT: The European Regional Development Fund and the state budget of the Czech Republic (project HiLASE CoE: Grant No. CZ.02.1.010.0/0.0/15_006/0000674); The European Union's Horizon 2020 research and innovation programme (No. 739573); the Ministry of Education, Youth and Sports of the Czech Republic (Programmes NPU I Project No. LO1602).

REFERENCES

1. I. Divlianski: *Advances in High-Power Fiber and Diode Laser Engineering* (Institution of Engineering and Technology – 2019).
2. M. Smrž, M. Chyla, J. Mužík, S. S. Nagisetty, O. Novák, *MM Science Journal* **5**, 3620 (2019).
3. M. Divoky, M. Smrž, M. Chyla, P. Sikocinski, P. Severova, O. Novak et al., *High Power Laser Science and Engineering* **2**, 1 (2014)
4. O. Novak, T. Miura, M. Smrž, M. Chyla, S. S. Nagisetty, J. Mužík et al., *Applied Sciences* **5**, 637 (2015).
5. M. Smrž, O. Novák, J. Mužík, H. Turčičová, M. Chyla, S. S. Nagisetty et al., *Applied Sciences* **7**, 1016 (2017).
6. W. Koechner: *Solid-state laser engineering* (6th ed. - New York: Springer-Verlag – 2006).
7. J.-C. Diels, W. Rudolph: *Ultrashort laser pulse*

phenomena (2nd edn., Elsevier – 2006).

8. H. Injeyan, G. D. Goodno: *High-Power Laser Handbook* (McGraw Hill – 2011).
9. D. Ristau: *Laser-induced damage in optical materials* (CRC Press – 2015).
10. D. Strickland, G. Mourou, *Optics Communications* **56**, 219 (1985).
11. A. Giesen et al., *Applied Physics B* **58**, 365 (1994).
12. R. Boyd: *Nonlinear optics* (3rd edn., Academic Press – 2008).
13. S. S. Nagisetty et al., *Laser Physics Letters* **14**, 015001-6 (2016).
14. B. Weichelt et al., *Optics Letters* **37**, 3045 (2012).
15. M. Smrž et al., *Optics Letters* **39**, 4919 (2014).
16. M. Smrž et al., *Proc. of SPIE* **9513**, 951304 (2015).
17. O. Novák et al., *Optics Letters* **41**, 5210 (2016).
18. H. Turcicova et al., *Optics Express* **27**, 24286 (2019).
19. M. Vyvlečka et al., *Applied Optics* **57**, 8412 (2018).
20. P. Hauschwitz et al., *Optics&Laser Technology* **133**, 106532 (2021).
21. M. Sawicka, M. Divoky, A. Lucianetti, T. Mocek, *Laser and Particle Beams* **31**, 553 (2013).
22. P. Mason et al., *Optica* **4**, 438 (2017).

CZECH PARTICIPATION AT FACILITY FOR ANTIPROTON AND ION RESEARCH

A.Kugler, kugler@ujf.cas.cz, Nuclear Physics Institute CAS, 25068 Rez, Czech Republic

INTRODUCTION

Facility for Antiproton and Ion Research (FAIR) is a new European research infrastructure for nuclear and hadron physics included in ESFRI roadmap since 2006. FAIR is currently under construction at Darmstadt in Germany as a part of the capacity of *GSI Helmholtzzentrum für Schwerionenforschung*. FAIR-CZ, Czech Research Infrastructure (RI) (included in the Roadmap of Large Infrastructures for Research, Experimental Development and Innovation of the Czech Republic for the years 2016 - 2022) addresses the approach of the Czech Republic to FAIR in general, and access of the Czech communities to the research activities in hadron physics, nuclear physics and nuclear astrophysics in CBM (*Compressed Baryonic Matter*), PANDA (*Anti-Proton Annihilation at Darmstadt*) and NuSTAR (*Nuclear Structure, Astrophysics and Reactions*) research pillars of FAIR, but also to activities in other fields of science such as radiobiology and biophysics developed in APPA (*Atomic, Plasma Physics and Applications*) research pillar of FAIR. After its completion, FAIR will be leading worldwide facility for hadron and nuclear physics for several decades. FAIR will be unique in areas such as production of highly-compressed plasma exploiting intense heavy-ion beams, with unparalleled research program with cooled antiproton beam and internal-target storage-ring capabilities for Quantum Chromodynamics studies. The FAIR is expected, for example, to verify model of compressed matter, which is used to describe fusion of neutron stars assumed to be the source of recently detected gravitational waves (Nobel prize in 2017).

CZECH CONTRIBUTION TO FAIR SCIENCE

Currently the situation in Czech Republic is as follows:

- Teams from Nuclear Physics Institute in Rez (NPI) and Czech Technical University in Prague (CTU) are involved in CBM research pillar with aim to investigate baryonic matter under extremely high densities. Particularly, team from NPI, which is founding member of HADES collaboration, which is part of CBM research pillar, very actively participates in all HADES related research having three PhD students involved as well as senior scientists, see [1]. The deputy spokesperson of HADES is from NPI team, members of team are responsible for build up and operation of two large HADES subdetectors, i.e. TOF and ECAL etc. Last, team from Silesian University in Opava (SUO) is involved in theoretical studies related to HADES and CBM physics, see [2].
- Teams from Charles University (CUNI) and CTU are participating in PANDA with the aim to study structure of hadrons.

- Scientists from SUO working in Nuclear Astrophysics are participating in NuSTAR. They are concentrating on the experimental studies of rare decay of nuclei far from the stability, particularly (few-) proton decay of isotopes located in the vicinity of waiting points in rp-process of nucleosynthesis, which is occurring inside stars.
- Scientists from NPI working in radiobiology and dosimetry are aiming to participate in APPA activities. They are contributing to innovation in the oncology by developing microdosimetry and by study of modification in absorbed radiation dose due to implants.

CZECH IN KIND CONTRIBUTIONS TO FAIR

Within the FAIR-CZ following instruments are build or the Czech teams will significantly contribute to their construction:

- The Electromagnetic Calorimeter (ECAL) for HADES, see Fig.1. Currently four sectors of ECAL out of six planned are finished and were successfully operated during recent experiment in March 2019 by NPI team.
- The Projectile Spectator Detector (PSD) for CBM. Currently support frame of PSD is finished and it is transported to FAIR by CTU team, see Fig.2.
- Carbon beam pipe for PSD is currently designed by CTU team and prototypes are tested at NPI cyclotron.
- Avalanche Photo Diodes for readout of PSD are tested at NPI cyclotron as well as at CERN test beam facility.
- Electromagnetic PbWO₄ calorimetry system for PANDA. Currently 71 unique PbWO₄ scintillators are tested and delivered to FAIR by CUNI team. Testing of further scintillators are carried out at microtron of NPI and next bunch of them will be transferred to FAIR soon by CUNI team.
- The SUO team will provide substantial part of GADAST detector for EXPERT@NuSTAR.
- Vacuum stations for BIOMAT beam line located in APPA cave will be tendered by NPI.

This instrumental infrastructure will be then used not only by the Czech teams and their members, but by all collaborations, in which the devices will be included. Successful development, construction and operation of the mentioned infrastructure will positively present the Czech Republic as a country able to educate and retain top scientists, support the science infrastructure and participate in the cutting-edge research.

CZECH SCIENTIFIC COMMUNITY IS MEMBER OF FAIR

Due to significant contributions of Czech scientific community both to FAIR science and to FAIR experiment infrastructure, see above, “Aspirant Partner”,

a new type of participation in FAIR, was offered to Czech Republic recently. FAIR Council, the shareholders meeting of FAIR, created it in 2017 and decided in December 2018 to recognize the Czech Republic as the first FAIR “Aspirant Partner”. The contract has been signed by the managing directors of GSI and FAIR, Professor Paolo Giubellino, Ursula Weyrich and Jörg Blaurock, as well as by Dr. Petr Lukáš, Director of the NPI. Czech partners in FAIR-CZ consortium – represented by Prof. Vojtěch Petráček, Rector of the Czech Technical University in Prague, Prof. Gabriel Török, Vice-Rector of the Silesian University in Opava, Prof. Jan Kratochvíl, Dean of the Faculty of Mathematics and Physics, Charles University (FMP CU), Prof. Vladimír Baumruk, Vice-Dean of the FMP CU, and Dr. Andrej Kugler, FAIR-CZ coordinator – took part at the signing as well.

Czech Republic has thus been an aspirant member of the FAIR Large European Infrastructure since 27.3.2019 and it has the corresponding representation in the FAIR institutions including the FAIR Council (A.Kugler and M.Vyšinka).

CONCLUSION

During 2016-2019 period we successfully carried out R@D activities related to FAIR. HADES experiment with significant Czech contribution was successfully carried out in 2019, another experiment was carried out in 2020 as a part of the NuSTAR physics. Both experiments are part of FAIR Phase 0 activities. Two new institutions (UWB Pilsen and IPP Prague) became involved in FAIR related activities. The Technical University in Brno plans to join EXPERT (NuSTAR) activity since 2021. The CTU partner included into FAIR related activities colleagues from new faculty (FMP). Czech Republic became aspirant member of the FAIR in 2019.

For the future, it is planned to continue to develop and manufacture the cutting-edge scientific equipment necessary to complete the FAIR infrastructure. This will include, in particular, the completion of the remaining two sectors of the ECAL detector for the HADES experiment, the completion of the PSD detector (support structures, read-out diode tests and beampipe made of composite materials). For the PANDA detector, silicon tracking detectors will be completed and made ready for mass production. In addition, mass production in the Czech company CRYTUR and testing of PbWO_4 crystals at the NPI CAS microtron for electromagnetic calorimeter of the PANDA experiment will take place. Additional scintillation detector modules will be acquired and installed for the GADAST detector from EXPERT (NUSTAR) and the BIOMAT (APPA) experiment will be supported by the supply of vacuum components. FAIR-CZ will contribute to innovation in the oncology by R&D of technologies and detectors used in medicine (PET camera, diagnostic), energy industry (new materials for fusion) and machinery. FAIR-CZ will also provide basis for education of students. Czech companies will benefit from the

involvement of the Czech research community in FAIR by delivering sophisticated research instruments for FAIR and thus improve their technological expertise. Specific examples are massive production of unique PbWO_4 scintillators for FAIR in an order of about 20 MEuro, development for FAIR of new silicon sensors with high densities of pads and with high tolerance to radiation, which can be used for PET cameras in future.

ACKNOWLEDGMENT: FAIR-CZ activities are supported by MEYS:

2016-2019 OP VVV+LM2015049;

2020-2022 OP VVV+LM2018112;

2017-2021 LTT17003 (research activities of NPI + SUO).

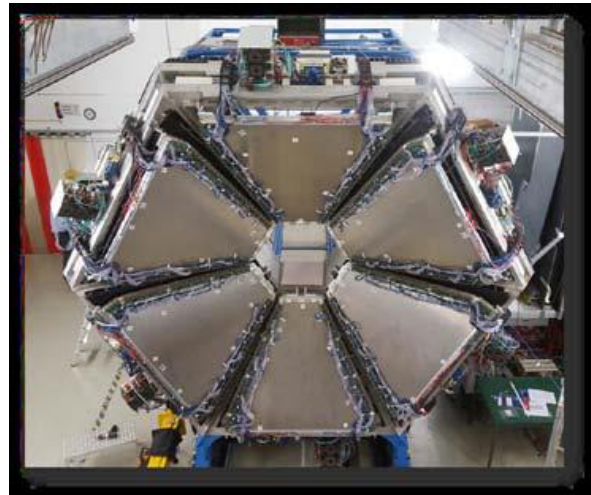


Fig. 1. ECAL installed in HADES cave



Fig. 2. PSD support frame

REFERENCES

1. Adamczewski-Musch et al., Nat. Phys. **15**, 1040 (2019). <https://doi.org/10.1038/s41567-019-0583-8A>.
2. T. Ablyazimov, A. Abuhoza, R. P. Adak et al., Eur. Phys. J. A **53**, 60 (2017). <https://doi.org/10.1140/epja/i2017-12248-y>.

TRENDS IN PHYSICS EDUCATION, EXPECTATIONS AND REALISATION

M. Kireš, marian.kires@upjs.sk, Z. Ješková, zuzana.jeskova@upjs.sk, Faculty of Science, Pavol Jozef Šafárik University in Košice, Šrobárova 1, 040 01 Košice

INTRODUCTION

Physics, as a school subject, is a unique space for active learning, inquiry teaching, formative assessment, collaborative learning, development of skills and competencies, higher cognitive processes. The complexity of making educational content available in physics, requires the cooperation of scientists, didactics and teachers in the areas of curriculum development, application of teaching methods, popularization and non-formal education. Ambitious expectations from the point of view of the graduate's profile place demands on education that will make a strong basements for constant adaptation, innovation, creativity, or solving global challenges, which we are only considering today. Thanks to national and international projects, educational concepts are already being implemented today that we believe will meet our expectations.

EXPECTATIONS AND TRENDS IN PHYSICS EDUCATION

We look at education as a process of making available the acquired knowledge and proven procedures from a selected area of human activity. It offers the use and continuity of the existing level of science, technology or social customs. Education is strongly influenced by the pace of scientific and technological innovations, social changes and therefore one of its tasks is not only to inform about the past, but especially to initiate the direction of society in the future. From the point of view of the individual, education is initiated by personal cognitive and subsequently educational needs. By observing the environment, asking questions and searching for one's own answers and explanations, gaining personal experience through one's own repetitive activity and observing good experiences, the individual's partial satisfaction of his cognitive needs occurs. Striving for deeper knowledge leads us to acquire knowledge and experience created by a wider group of people. Satisfying our individual educational needs is linked to a feeling of success, personal development, striving to apply, helping others and is strongly supported by internal motivation. From a social point of view, education is initiated by a social need, a community interest. In an organized society, roles are redistributed, defined professions and the required competencies are assigned to them. A sufficient number of people with targeted education is in the public interest. To achieve this, the society always defines an adequate educational system. The progress of society depends on the level of knowledge and the ability to use scientific knowledge for innovation. We will increase the level of knowledge through quality science and research; we will achieve the use of scientific knowledge through quality technology. Top experts for science, research and technology should produce a quality education system.

In the short term, from the point of view of expectations, we can evaluate the success of education, which topics or activities we would adjust, replace, which methods and forms we will give more space to. We can build partial decisions on existing educational goals and defined content. However, defining longer-term educational goals is a complex and strategic task. What knowledge, skills, attitudes and values will be required in 10 years? What methods can be used to achieve quality education? How to prepare teachers and create conditions for them to successfully guide the educational process?

The trend in education is the acquisition and development of literacy in many current contexts, such as digital, scientific, technical, reader, financial, media, linguistic, social. From the point of view of physics, we focus mainly on the basic components of scientific literacy [1], which are: scientific ideas (understanding), scientific attitude to reality, the competences of scientific work. A scientifically literate person is manifested by his approach to everyday reality and competences: observe, ask questions, understand the meaning of concepts, look for arguments, formulate predictions, obtain and create relevant information, compare the expected and real course and outcome of processes.

The OECD study Education to 2030 [2], [3] presents an illustrative learning compass. Emphasis is placed on three basic components: knowledge, skills, attitudes, and values. These contribute to the development of individual literacy of the student through transformational skills (creating new value, reconciling tension and dilemmas and taking responsibility). The student is influenced by parents, teachers, peers and the community, with whom he fulfils expectations, realizes actions and constantly reflects on reality. The ambition is to fulfil personal and social prosperity by 2030.

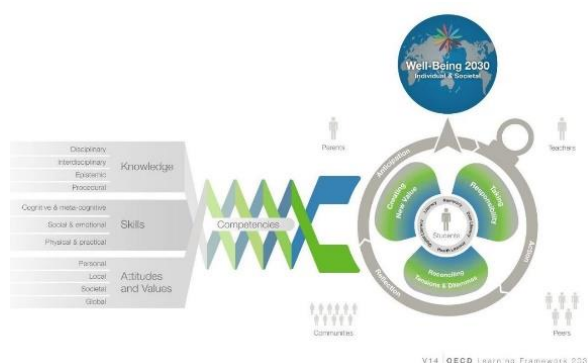


Fig.1. The OECD Learning Framework 2030 – learning compass

Similarly, the Center for Curriculum Redesign staff [4] view trends in education, defining four dimensions of education: knowledge (what to know and what to

understand), skills (how to use what we know), character (how to behave and engage in the world), and meta-learning (how to reflect and adapt).

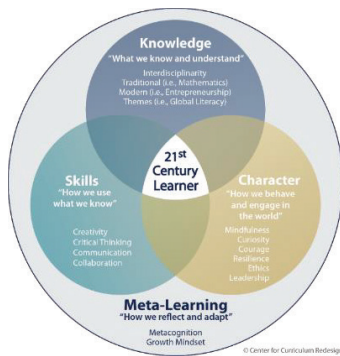


Fig.2. The foundational framework of the Center for Curriculum Redesign [4]

We see the dimension of knowledge [5] from the point of view of physics education in the constant innovation of educational content with regard to new knowledge in science, strengthening interdisciplinarity and creating space for the development of skills and competences. The definition of educational content is represented by a study [1] called Big Ideas in Science Education. Defining ten key areas of knowledge, together with guidance on how to make them accessible to students, is a significant navigation for curriculum development.

The dimension of a student's skills and competencies is growing in importance in terms of learning outcomes. The term skill means being able to perform simple activities quickly, well and reliably (manually as well as intellectually). Competence is the ability to use in a coordinated manner several skills and knowledge in a given area, necessary for the performance of more complex activities. Competence means the right to use professional competence in solving new tasks. We consider the classification of key competencies developed within the OECD DeSeCo project [6] as well as the defined 21st century skills [7] and 4C skills (creativity, critical thinking, communication, cooperation) as “learning skills” [8] to be overlapping studies showing a trend towards a stronger focus on skills development. We are currently committed to a defined European framework of personal (self-regulation, flexibility, well-being), social (empathy, communication, collaboration) and learning to learn (positive thinking, critical thinking, learning management) Life Competences [9].

From the point of view of education, it is necessary to point out that skills and competencies can be developed only by active learning activity of the student.

The increasing emphasis is on the size of the student's character. How he will behave and engage in the world. What will be his self-awareness, curiosity, courage, resilience, ethics and leadership.

On the background of three dimensions of education, the fourth is classified, namely the meta-learning dimension. It is about the student's ability to

plan, monitor, evaluate the procedures he uses when learning and learning. Learning to learn is about creating habits for lifelong learning [10]. It is a conscious activity that leads a person to knowledge, how he progresses when he knows the world [11].

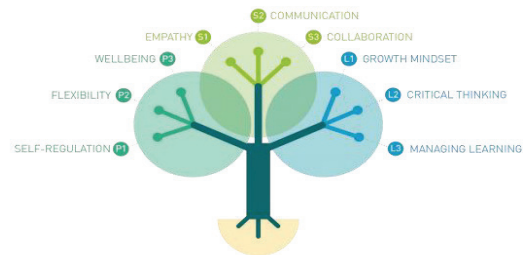


Fig.3. Life Competences tree [9]

Another strong factor is the digitisation of all spheres of human activity and the related educational requirements. In 2020, the European Commission published an update of the Strategic Education Paper entitled Digital Education Action Plan 2021-27: Renewing Education and Training for the Digital Age [12]. It brings a vision for quality, inclusive and affordable digital education in Europe. The action plan has two strategic priorities. Support the development of an efficient digital learning ecosystem and the enhancement of digital skills and competences for digital transformation. In particular, it is about effective planning of digital capacities, including infrastructure, connectivity and digital equipment, including the ability to use hybrid education. Emphasis is placed on stronger support for teachers in increasing digital competences and readiness to use digital technologies in education.

The digital ecosystem also requires quality educational content, user-friendly tools and secure platforms that respect social aspects, privacy and ethics. Education with the support of digital technologies requires a fundamental change in teaching methods, a strong focus on active cognition, immediate feedback and targeted development of skills and competences.

We transfer these general trends to physics education, emphasizing the innovation of educational content, the use of digital technologies and innovative teaching methods, active student learning, orientation to the targeted development of skills and competencies and the formation of attitudes and literacy.

REALISATION

In order to achieve a real impact on education at the national level, we obtained the national project IT Academy - Education for the 21st Century with the solution period 09/2016 - 10/2021 with its extension until 08/2021 [13]. Universities, the Ministry of Education through its directly managed SCSTI organization and representatives of the IT sector are involved in the project. The central goal of the project is to develop science literacy, form attitudes and increase interest in studying STEM disciplines. There are several tools to achieve your goals. Inquiry based innovative education activities for teaching informatics,

mathematics, sciences [14]. The concept of classes with extended teaching of natural sciences, mathematics and informatics and classes with a focus on informatics (30 informatics classes). Implementation of 10 new subjects into school educational programs at secondary schools, where physics is represented in the subject: Informatics in natural sciences and mathematics. Implementation of 28 new accredited courses of continuous teacher education. Establishment of 99 IT Science laboratories in schools. Offer non-formal education activities for teachers - popularization lectures, excursions, internships in IT companies. Offer and involvement of students with popularization activities. Creating local partnerships between primary schools, high schools, universities and IT companies, the so-called networking.

INNOVATIVE METHODOLOGIES FOR TEACHING PHYSICS

The innovation of physics teaching at primary and secondary schools is supported by the availability of 120 research-oriented methodologies, including a title page, a worksheet for students, methodological material for teachers and support files. Innovative methodologies have been pilot-tested in school practice and have been innovated on the basis of suggestions from verifiers (experienced physics teachers). The methodologies emphasize the use of digital technologies, research approach and the development of selected skills. Full-time education is provided by trained teachers, who offer open lessons, online webinars and participation in conferences dedicated to educational innovation.

An example of guided inquiry is activity, Shadows known and unknown. The students' task is to reveal the cause of the double shadow, as presented in Figure 1. The object placed on the mirror is illuminated by observing its shadow on the shade. The instructions in the worksheet guide students to a sequence of steps to help reveal the physical cause of the double shadow. Emphasis is placed on the systematic research work of the student, the investigation of the phenomenon at the boundary conditions and the interpretation of their own findings. The didactic problem of formal acquisition of the concept of shadow and its change to conceptual understanding is solved. With the 5E method, students work in small groups to expand in the form of a new problem: If we used an object that is not symmetrical instead of a snowman, what would its double shadow look like? Finding an answer to this problem will verify the achievement of conceptual understanding in students.

NEW SUBJECT INFORMATICS IN NATURAL SCIENCES AND MATHEMATICS - PART OF PHYSICS

We try to compensate for the insufficient time range of physics teaching by introducing a new subject at secondary schools, Informatics in Natural Sciences and Mathematics, with a time allowance of 2 hours/week and teaching in a divided class. The introduced subject has a compulsory thematic unit Informatics in the first quarter and in the following three quarters; it is possible

to choose from 5 optional thematic units. The teacher can choose 8 out of 10 teaching units in each thematic unit, the focus of which is uniformly devoted to modelling, imaging methods and working with databases.

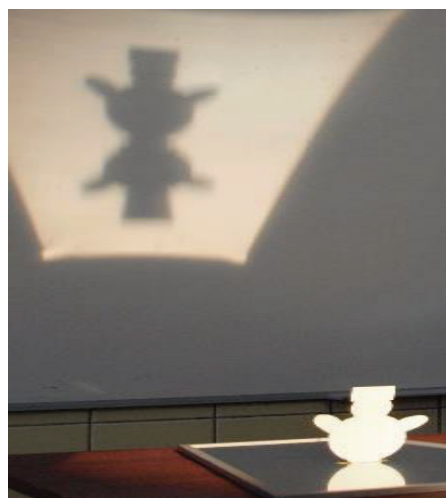


Fig.4. Double image

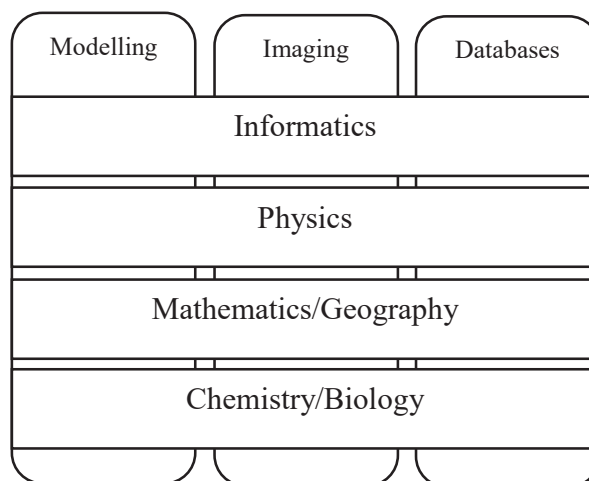


Fig.5. Schematic arrangement of the subject Informatics in natural sciences and mathematics

Our goal in the part of physics is to make available to students how science works and how scientists work, problems based on real situations, create models of simple situations up to models of more complex phenomena, program models in a suitable programming environment (iconographic modelling, Python), test the finished model by comparison with the results of the experiment, video measurements, and if the model does not correspond to the results of the experiment, adjust it to match.

In the section on working with databases, we use the less commonly used format of Fermi's problems by physics teachers. Students go through a series of instructions: 1: Search for Fermi's assignments on the Internet. Choose three tasks in the group and then in the class, which are the most interesting for you. 2: Get acquainted with the solution of one of the well-known Fermi problems. Study its annotated solution. 3:

Formulate your own Fermi assignments and present them to classmates. 4: Suggest a breakdown of your Fermi problem into basic problems. For each of them, write down what data you need to search for. Present your solution proposal to classmates and discuss its reliability. 5: Work out a solution to your Fermi problem. Check the obtained result by comparison with the relevant data. We try to argue to teachers that even a non-physical topic, such as: How many lessons will be missed at our school during the year? by solving the fermi problem, we develop many necessary skills in the student.

TAB.1. Contents of the part of physics in the subject Informatics in natural sciences and mathematics

Modelling in physics	
1.	Introduction to modelling
	Basics of modelling in iconographic mode and working with variables that enter the model. Models of tank filling, even movement of the train and a running cyclist. Compare motion models with results from video measurements of real movements.
2.	How does force affect movement?
	Creation of a model of a parachutist's jump from an airplane and elucidation of physical phenomena influencing the course of movement. Gradual addition and extension of the model. Comparison of the results of the model with a real jump of a parachutist, recorded on video.
3.	How did Felix reach supersonic speed?
	Motivational video recording of Felix Baumgartner's record jump and examination of the factors in exceeding the speed of sound during the jump. Creating a Felix motion model with a similar result to the recorder's crash.
4.	How does the rocket start?
	Creation of a model of rocket launch and extension by other parameters that affect the movement of the rocket. Students gradually modify the simple finished model of the rocket's motion by adding other relevant parameters to the model, thus refining the model and bringing it closer to reality.
5.	How to maintain the optimal temperature in the house
	Analysis of parameters that affect the temperature in the building. Creating a simple cooling model and comparing it with the result of a real experiment of cooling a cup of tea. Modifying the model by adding other relevant parameters to the model, which makes the model more precise and closer to reality.
Imaging methods	
1.	How we turn the sound into a picture
	Echolocation. Determining the distance of an obstacle from a sound source. Investigation of the intensity of signals reflected from the surface of various materials. Computer animation of creating A - mode and B

	- mode display objects.
2.	Non-contact temperature measurement
	Physical principles of absolute black body radiation. Introduction of the concept of grey body. Factors influencing thermographic measurements. Own measurements of surface temperatures of materials with different emissivity. Calibration of non-contact thermometer.
3.	How to take pictures of moving objects
	Basic parameters of digital photography and the process of digital image processing. Manually adjust exposure and ISO when shooting moving subjects. Create a sharp photo of a fast-moving subject.
Database systems	
1.	Solving Fermi's problems
	Formulation of research questions with interesting content as a motivation for independent cognitive activity. Assignments of selected Fermi problems with physical content. Analysis of sample solutions. Solving a series of tasks solved in groups, searching in recommended information sources on the Internet. Formulation of one's own research question, the solution of which requires obtaining data from databases of scientific information.
2.	Can we formulate a prediction, confirm / refute the hypothesis?
	Classification and examples of concepts: research question, prediction and hypothesis. Confirmation or rebuttal of the hypothesis based on relevant data from available records in databases. We know the hypotheses and examples of their verification. Formulation of predictions and hypotheses, solution of group work. Presentation and peer review.

PROPOSAL OF THE STUDY PROGRAMME GRAMMAR SCHOOL WITH A FOCUS ON INFORMATICS (STEM)

We are aware of the insufficient time range of teaching STEM subjects and insufficient conditions for the development of science literacy of students. Therefore, we come up with the concept of the study programme Grammar School with a focus on informatics (STEM). The main goals are:

- orientation of grammar school students to university studies in study fields and programs focused on informatics and DT and for employment in the IT sector,
- improving preparation for university studies in STEM disciplines and other programs that take advantage of high levels of digital literacy and computer thinking,
- development of digital literacy and computer thinking in the context of mathematical, computer

and science education of pupils through the systematic and coordinated use of innovative teaching methods based on the application of research approaches.

The main attributes of the new field of study in relation to the current state are:

- Increasing the number of hours of science subjects Mathematics - 18 hours, Informatics - 10 hours, Physics - 8 hours and introduction of a new subject Informatics in Natural Sciences and Mathematics - 2 hours.
- Increase the number of compulsory and available hours to 128 (113 and 15).
- All lessons of Informatics and Informatics in natural sciences and mathematics are taught in groups with max. 15 students in computer classrooms.
- The class is divided into groups in the subjects of physics, chemistry, biology, geography and mathematics at one hour of the week in each year.
- They set changes in educational areas in terms of content and scope.
- To support practical training in laboratories, it is recommended to establish the position of laboratory assistant.
- In order to ensure the equipment of the school and cooperation with the practice and primary schools in the field of digital technologies, it is recommended to establish the position of "digital coordinator".
- The norm for one pupil is increased to 1.5 for the norm of the study field grammar school with Slovak as the language of instruction.

The proposal of the study department of the Grammar School with a Focus on Informatics (STEM) received the support of the State Pedagogical Institute. A more detailed elaboration of content and performance standards is on the work of individual subject commissions.

CONCLUSION

Thanks to the national project IT Academy - Education for the 21st Century, we have set up IT Science laboratories in 90 schools. For teaching physics, we prepared and pilot-tested 60 innovative lessons for primary and 60 hours for high school. We provide education in each of the subjects with education [15] and supporting webinars focused on research-oriented teaching. We communicate in a targeted manner with school principals and support the cooperation of teachers in schools. We believe that the created support system will succeed in improving the quality of education in STEM disciplines.

ACKNOWLEDGMENT

This paper was made in the framework of the national project IT Academy – Education for the 21st century that is supported by European social fund and European regional development fund under the Operational program Human resources. This paper was supported by the Scientific Grant Agency of the Ministry of Education of the Slovak Republic and the Slovak Academy of Sciences – grant VEGA 1/0265/17

“Formative Evaluation in Teaching Sciences, Mathematics and Informatics”.

REFERENCES

1. W. Harlen: Working with Big Ideas of Science Education [online]. (Science Education Programme of IAP: Trieste – 2015) ISBN 9788894078404. <https://www.ase.org.uk/bigideas>.
2. [https://www.oecd.org/education/2030-project/about/documents/E2030%20Position%20Paper%20\(05.04.2018\).pdf](https://www.oecd.org/education/2030-project/about/documents/E2030%20Position%20Paper%20(05.04.2018).pdf) – The future of education and skills – Education 2030 (OECD – 2018).
3. OECD Future of Education and Skills 2030, OECD Learning Compass 2030, A series of concept notes (OECD Publishing - 2019).
4. Fadel & Groff, J. W. Cook (ed.), Sustainability, Human Well-Being, and the Future of Education, https://doi.org/10.1007/978-3-319-78580-6_8, (2019).
5. A. Schleicher: World Class: How to build a 21st-century school system, Strong Performers and Successful Reformers in Education (OECD Publishing, Paris – 2018). <http://dx.doi.org/10.1787/4789264300002-en>
6. D. S. Rychen & L. H. Salganik (Eds.): Key competencies for a successful life and a well-functioning society (Hogrefe & Huber Publishers – 2003).
7. J. R. Shavelson, L. Huang, The Magazine of Higher Learning **35**, 10 (2003) DOI: 10.1080/00091380309604739.
8. http://www3.weforum.org/docs/WEF_New_Vision_for_Education.pdf
9. A. Sala, Y. Punie, V. Garkov, M. Cabrera Giraldez, LifeComp: The European Framework for Personal, Social and Learning to Learn Key Competence, EUR 30246 EN (Publications Office of the European Union, Luxembourg – 2020) ISBN 978-92-76-19418-7, doi:10.2760/302967, JRC120911.
10. G. Schraw, D. Moshman, Educ. Psychol. Rev. **7**, 351 (1995). <https://doi.org/10.1007/BF02212307>
11. J. Prucha, E. Walterová, J. Mareš: Pedagogický slovník (Praha: Portál – 2009) ISBN 978-80-7367-647-6.
12. https://ec.europa.eu/education/education-in-the-eu/digital-education-action-plan_en - Digital Education Action Plan (2021-2027), Resetting education and training for the digital age
13. IT Academy project, <http://itakademia.sk/>
14. M. Ganajová, R. Orosová, I. Sotáková: Formative evaluation in the Slovak republic, INTED2020 Proceedings (2020) pp. 4730-4737. doi: 10.21125/inted.2020.1302.
15. M. Ganajová, I. Sotáková, R. Orosová: Training of future chemistry teachers in the inquiry based teaching, ICERI2019 Proceedings (2019) pp. 6973-6982. doi: 10.21125/iceri.2019.1657.

NITRIDE SEMICONDUCTORS – PROPERTIES AND APPLICATIONS

A. Hospodková, hospodko@fzu.cz, F. Hájek, hajek@fzu.cz, T. Hubáček, hubacekt@fzu.cz, J. Oswald, oswald@fzu.cz, F. Dominec, dominecf@fzu.cz, K. Kuldova, kuldova@fzu.cz, Institute of Physics CAS, v.v.i., Cukrovarnická 10, CZ-16200 Prague 6, Czech Republic

INTRODUCTION

Nitrogen is one of the elements about which we can say that it surrounds us everywhere. Nitrogen represents a dominant part of atmosphere, it is macro biogenic element present in all amino acids and proteins, we can find it in RNA, DNA, chlorophyll, haemoglobin etc. When industrial usage of nitrogen is mentioned, production of fertilizers and explosives is usually evoked. However, nitrogen became also very important for semiconductor industry in last thirty years and many new light emitting or electronic applications are based on nitride semiconductors, such as blue or UV light emitting diodes (LEDs), laser diodes (LDs) or high electron mobility transistors (HEMTs) used for high power and high frequency applications [1]. The basic nitride semiconductor is GaN which has wurzite crystal structure with lattice constants $a = 3.186 \text{ \AA}$, $c = 5.186 \text{ \AA}$, see Fig.1. The chemical bond between Ga and N is strong which has consequences in small lattice constant and high GaN band gap energy of 3.4 eV at room temperature.

COMPOUND SEMICONDUCTORS

GaN belongs to the wide family of compound semiconductors. Their intensive research and application started at 60-ties in the last century. Band gap energy and lattice parameters of different types of compound semiconductors is shown in the Fig. 1.

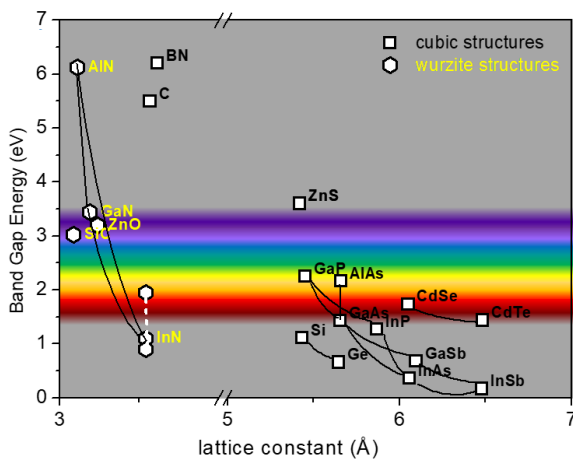


Fig. 1. Band gap energy versus lattice parameters for different compound semiconductors. Symbol suggests type of crystal lattice (square – cubic, hexagonal – wurzite structure).

In a very simplified way the band gap energy can be conceived as an energy required to extract the valence electron from bond in the semiconductor lattice and it represents the energy difference between the valence and the conduction band. The same energy is also

released when thermalized electron is captured by empty bond in semiconductor lattice or in other words when it recombines with hole. In case of some semiconductors this energy released by electron-hole recombination can be used for photon generation. Semiconductors which can effectively emit photons are called “direct”, those without effective light emission are called “indirect” semiconductors. For example Si, the most widely used semiconductor, as well as Ge or AlAs are indirect semiconductors and cannot be used as active light emitting layers in LEDs. On the other hand examples of direct semiconductors can be GaAs, InAs, GaSb, InP, ZnO and many others. Also all nitride semiconductors GaN, AlN, InN and their ternary (InGaN, AlInN or AlGaIn) as well as quaternary (AlInGaIn) alloys are direct semiconductors.

Probably the most important advantage of compound semiconductors is possibility to form heterostructures – quasi monocrystalline structures consisting of thin layers with different composition and properties. A similar lattice constant with lattice mismatch below 7% and the same crystal type are required to achieve good crystal quality of final heterostructure. By proper design of layer sequence and their composition devices with advanced functionality can be achieved such as high efficient LEDs, lasers or transistors with high electron mobility. Majority of applications using compound semiconductors is based on heterostructures.

The band gap energy and lattice parameter of nitrides can be tuned by replacing of some Ga atoms in GaN crystal structure by other group III elements such as In or Al atoms (see Fig. 4). Nitride based devices use heterostructures combining GaN, InGaN, AlInN or AlGaIn layers. The first application of nitrides was blue LED [2]. Development of technology of blue LED preparation was so difficult that it was awarded by Nobel Prize 2014 in Physics.

DEVELOPMENT OF NITRIDE TECHNOLOGY

The technology which enabled first epitaxy of nitrides was Metal Organic Vapor Phase Epitaxy (MOVPE). The main obstacle was absence of GaN substrate, which is necessary for homoepitaxial growth. Even nowadays the GaN substrates are very expensive, but at the time when the nitride technology was developed no GaN substrates were available. First, some suitable alternative substrate had to be found. Sapphire was supposed to be most promising candidate. The way how the wurzite GaN structure is bonded to sapphire hexagonal lattice is shown in Fig. 2. The GaN lattice is 30° twisted with respect to sapphire and there is approximately 14% mismatch for GaN on sapphire lattice. Later, Si and SiC were also adopted as substrates for GaN.

Heteroepitaxy, when a crystal is grown on foreign material, is always serious complication, since it is difficult to find substrate with sufficiently similar properties such as lattice constant, good temperature stability or coefficient of thermal expansion. Sapphire substrates are most commonly used substrates for luminescence applications of nitrides, SiC or Si substrates are preferred for electronic applications. Although widely used, none of these substrates have ideal parameters and high dislocation density is formed in heteroepitaxial GaN prepared on them.

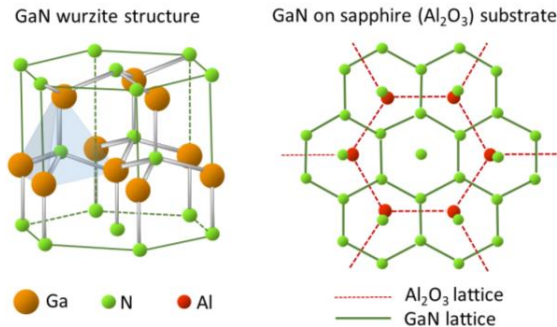


Fig. 2. Wurzite structure of GaN and coordination of GaN atoms on sapphire substrate.

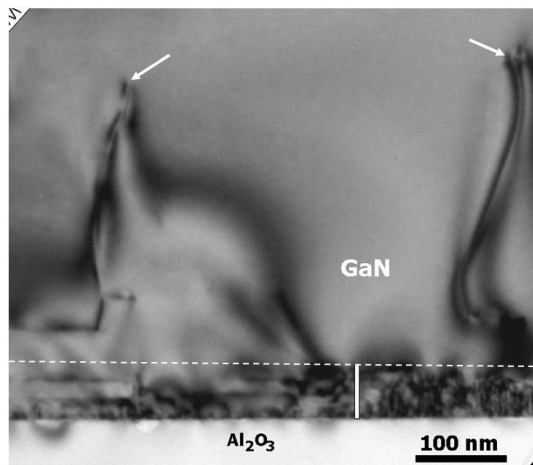


Fig. 3. TEM image of GaN buffer layer. Below the dotted line high density of dislocation mutually annihilating can be recognized. Only small part of dislocations propagates to upper layers, where some of them can also annihilate (see arrows).

It was one important invention of Nobel Prize 2014 winners that dislocation density can be suppressed when GaN nucleation on sapphire is done at much lower temperature than the optimal one for GaN epitaxy. In such a case, rough epitaxial surface is formed. The rough surface causes, that dislocations bend and annihilate with each other during subsequent epitaxial process at higher temperature. The footprint of this process can be recognized on transmission electron microscopy (TEM) image of GaN buffer layer prepared on sapphire substrate in our laboratory (Fig. 3). The region with strong mutual annihilation of dislocations is

below the dotted line. Only small part of dislocations propagates to upper layers, where some of them can also annihilate (see arrows).

The second obstacle was preparation of p-type GaN, which is necessary in all LED structures. Doping GaN by Mg did not work and no expected p-type conductivity was observed in Mg doped GaN. The solution was easy, when it was found that H atoms, bound to N, compensate Mg acceptors: by annealing at 800°C in N₂ atmosphere hydrogen was desorbed from GaN and p-type conductivity was achieved.

The last task was to shift the emitted light from UV to blue spectral region by replacing some Ga atoms in the crystal structure by bigger In, see Fig. 4. After many experiments it was found that In incorporation requires pure N₂ atmosphere and lower temperature of epitaxy. The blue LED production could start.

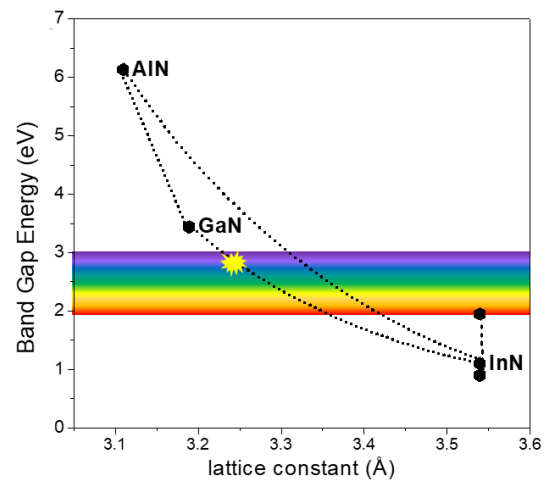


Fig. 4. Band gap energy versus lattice parameters of nitride semiconductors. There is still uncertainty about InN band gap.

LUMINESCENT APPLICATIONS OF NITRIDES

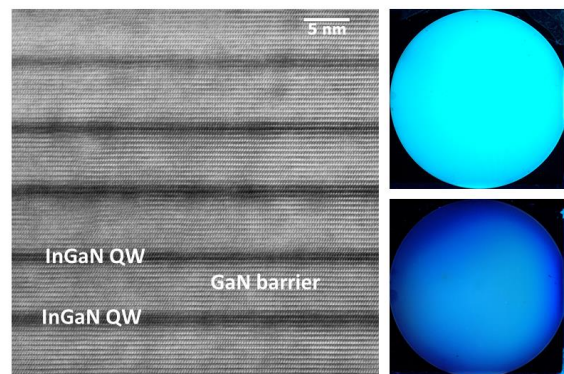


Fig. 5. InGaN/GaN multiple quantum well structures: structure image from high resolution transmission electron microscope and luminescence of similar structures with different QW properties.

Most of luminescence applications is based on InGaN quantum wells (QWs). QW is few nanometers

thick InGaN layer surrounded by barriers, usually by GaN, see Fig. 5. The wavelength of QW emission can be controlled by composition or thickness of InGaN layer. Luminescence of QWs with different parameters are shown on right side of Fig. 5. More detailed description of nitride QWs and their properties can be found in contribution of Jiří Oswald in this proceeding.

The blue LED was crucial for obtaining efficient white light source. The white light is usually obtained by combination of blue LED with yellow luminophore surrounding the LED, which is directly excited by the LED light. This source was at first most required as back light of coloured LCD displays essential for laptops. It helped also to development of smart phones. With increased production of white LEDs their price fell down and the LED bulb became so cheap that both, inner and outer LED lighting has massively replaced older light sources pushing even lower the white LED price (it decreased ten times between years 2009 and 2020). At this point it is necessary to mention, that we should take care about keeping a healthy circadian rhythm by proper artificial light quality. During the day the “colder” white light is suggested, while at evening “warm” white light is necessary with suppressed blue part of the spectrum, so that the body can produce melatonin, which is responsible not only for efficient resting but also for healing mechanisms in our bodies.

ELECTRONIC APPLICATIONS

Although the luminescent applications of nitrides are so widely spread, it is expected that dominant field of nitride applications will be in electronics. Nitrides offer interesting combination of properties which will be required in near future. They are suitable for high power as well as for high frequency applications. The achieved cutoff frequency of nitride transistors on SiC substrates is nowadays around 400 GHz [3]. These properties will be gradually more required in wireless, especially in 5G.

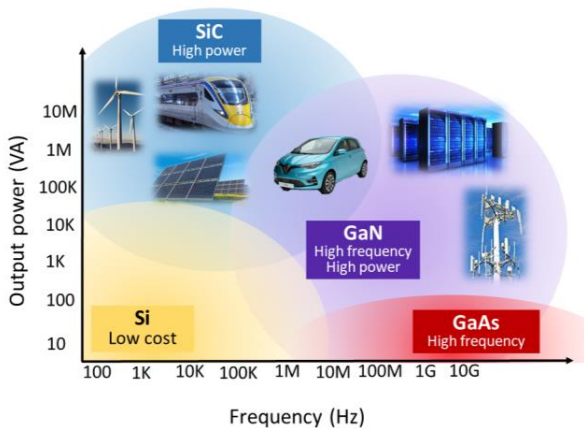


Fig. 6. Graphical illustration of competition of semiconductors with respect to the required power and frequency of particular applications.

networks and in large dataservers used for instance for cloud data storage. There is also a big potential for

nitride electronics in electromobility.

However, nitrides are not the only one semiconductors suitable for high power application or high frequency applications, see Fig. 6. For high frequencies GaAs based electronics with InGaAs electron channel is often used. The cutoff frequency of these transistors is even higher than in case of nitrides, the achieved values are 1.3 THz and were obtained for a 15 nm gate length HEMT [4]. However, they are not suitable for high power applications. On the other hand for high power SiC is also suitable. It has very similar parameters, such as high band gap energy and consequently also high break down voltage. The advantage of SiC is availability of substrate for epitaxy, which improves the SiC epitaxial layer quality in comparison to GaN prepared on Si or SiC substrates.

On the other hand, GaN has two important advantages. First, it enables to make heterostructure by combining GaN with related semiconductors, such as AlGaIn, AlInN or InGaIn. Second, there is a strong polarization field in wurzite lattice formed between interfaces in heterostructure. Thanks to the polarization field two dimensional electron gas (2DEG) is formed on AlGaIn/GaN interface with the electron density in the order of 10^{13} cm^{-2} .

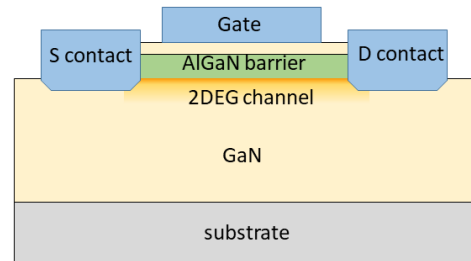


Fig. 7. Scheme of basic “normally open” nitride HEMT structure with 2DEG formed in GaN under AlGaIn barrier.

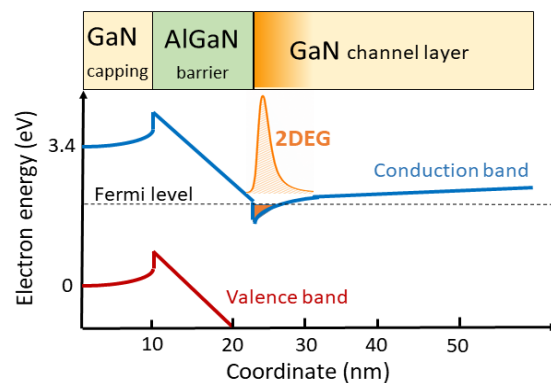


Fig. 8. Scheme of conduction band edge profile on the cross section of basic “normally open” HEMT structure with 2DEG formed below AlGaIn/GaN interface.

Such a high electron density is screening the coulombic field of ionized impurities and decreases electron scattering on ionized impurities in the material. Thus, the electron mobility is increased and transistors

with 2DEG are suitable for high frequency applications. The basic scheme of unipolar transistor which takes advantage of such 2DEG is shown in Fig. 7. The scheme of band gap alignment profile on the cross section of HEMT structure is shown in Fig. 8.

There is a competition between these two materials, GaN and SiC, see Fig.6. Nowadays SiC is winning in purely power applications, such as solar cell and wind power station invertors or in railway traction. GaN is used in radar stations, in base stations of wireless networks, in huge dataservers used for instance for cloud data storage.

FUTURE PERSPECTIVES

Surprisingly, although the luminescent applications of nitride semiconductors have been produced for thirty years, there are still a lot of challenges, unsolved problems and questions which need to be answered. Many questions are connected with InGaN layers. There is still a long time discussion about the InN band gap energy. It was reported to be in the interval 0.8-1.9 eV. The last reported values are 0.66 eV [5]. It is still not clear, why presence of In atoms in InGaN layers strongly increases luminescence efficiency. Structures with InGaN layers have very strong luminescence efficiency despite a high dislocation density, which would be detrimental for luminescence in other semiconductors. It is interesting, that the luminescence efficiency is even more enhanced when In containing layers are also placed below the luminescent active region and there is a vivid discussion about this problem among scientists. Another unsolved question is, why In requires purely N₂ atmosphere to get incorporated into the crystal. If only small concentration of H₂ is present in reactor atmosphere during epitaxy, almost no In atoms are incorporated into the layers.

Efficient nitride deep UV and green LEDs or lasers are a big challenge for technologists. Production of deep UV LED complicates impossible p-type doping of wide band gap AlGaIn and In containing layers cannot be used to increase the luminescence efficiency. Green laser production is not only difficult due to inefficient incorporation of In into the layers, but also due to the strain in InGaIn layers with high In content, and high polarization field in InGaIn QWs. So there is a lot of challenging work in the scientific field.

In industrial application of nitrides, very tough competition takes place in the field of electromobility where the winner is not decided, yet. However, a big increase in GaN production is expected with connection to the new 5G or 6G networks. Higher bandwidth will enable higher capacity, which means increased number of connected devices. This network will therefore have higher power requirements. GaN based HEMT circuits are supposed to be essential for 5G base stations. Additionally, electromagnetic waves used in the second frequency range of 5G network (24.25 - 52.6 GHz) have shorter propagation distances in comparison to LTE frequencies. This will increase density of base stations and further increase the GaN HEMT production. Thus,

it is probable that development of 5G network will reduce the price of GaN based electronics, which may finally help GaN to win the battle for electromobility. There was already the first “all GaN vehicle” designed by Japanese engineers, which has all electronics as well as luminescence devices based on nitrides, see Fig. 9.



Fig. 9. The first “all GaN vehicle” designed by Japanese engineers.

Concerning luminescence applications, nitride LEDs are slowly replaced by organic semiconductor LEDs in LCDs. However, nitrides are unbeatable in high efficiency and high luminosity applications, in outer, inner or automotive lighting, in projectors etc.

Very controversial is a new application of LEDs in so called “pink green houses”, which are in fact vegetable factories, where plants are constantly illuminated by light with wavelength suitable for photosynthesis (red and blue light). On the other hand, such farming is causing serious light pollution at night, see Fig. 10.



Fig. 10. “Pink green house” for vegetable production and light pollution produced by this farming.

Scientists are nowadays trying to develop short wavelength UV LED, which could help to kill bacteria and viruses and could offer very efficient way of disinfection in hospitals or air conditioning devices.

ACKNOWLEDGMENT: The authors acknowledge the support of the MSMT project no. NPU LO1603 – ASTRANIT.

REFERENCES

1. H. Morkoc: Nitride Semiconductor devices: Fundamentals an Applications (Wiley VCH Verlag &Co. KGaA – 2013).
2. I. Pelant, J. Valenta, Vesmír **92**, 612 (2013).
3. M. Cook, Semicon. Today, Compounds & Adv. Silicon **8** (May/June 2013).
4. M. Mohapatra, Internat. J. of Nano and Biomat. **5** (2014).
5. P. Huang, J. Mater. Chem. **A 4**, 17412 (2016).

NUCLEAR METHODS FOR ASTROPHYSICAL PURPOSES

G. D'Agata, dagata@ujf.cas.cz, J. Mrazek, V. Burjan, A. Cassisa, Nuclear Physics Institute of the Czech Academy of Sciences, Husinec - Řež, čp 130, 250 68 Řež, Czech Republic

INTRODUCTION

The production of the elements present in our Universe – apart from H, He and partly Li – is mainly due to the processes that take place in stars [1, 2]. In first approximation, a star can be considered as a system of self-gravitating particles, whose equilibrium can be described using the *virial theorem*: to remain at thermal equilibrium, a star spends half of the energy gained by contraction to rise its temperature, while the other half is lost by radiation. Inside the heated plasma, the particles collide producing energy via fusion reactions, giving rise to their evolution and to the nucleosynthesis of the elements. Those are also responsible for the neutrino fluxes from stars. The probability for a $A(x, c)C$ fusion process occur is governed by the Maxwell-Boltzmann distribution, $P \propto \exp(-E/kT)$, with energies E of the particles involved between eV and some hundreds keV. The interacting particles still abide to the laws of quantum mechanic, so the Coulomb (usually some MeV) and/or centrifugal barriers – arising from nuclear charges and angular momenta in the entrance channel $A+x$ – will strongly inhibit the reaction. For reactions between charged particles, the probability of interaction is governed by the tunnel effect [3], $R \propto \exp\left(-\sqrt{E_G/E}\right)$, E_G being *Gamow energy* $E_G = 2\mu c^2 (\pi\alpha Z_A Z_x)^2$, where μ is the center-of-mass of the interacting particles, Z_A and Z_x are their charges, α is the fine structure constant (1/137) and c is the speed of light. The convolution of the Maxwell-Boltzmann distribution and the tunnelling probability will give rise to a region of energies (the *Gamow window*) at which it is most probable that the reaction takes place at a certain the temperature. The main purpose of nuclear astrophysics is therefore to study such low-energy processes with the aim to better understand the stellar evolution and the chemical enrichment of the Universe. It is clear that the probability for a reaction to occur at low energies – usually expressed with the cross-section $\sigma(E)$ – is very small (order of nanobarn or lower). An experimental study of such processes via standard direct methods is therefore a challenge, given that the amount of nuclei involved in the reaction will be much lower in our laboratories than the one present in stars. To overcome those difficulties many experimental procedures can be employed: the beam intensity, the target density and the solid angle range spanned by the detectors can be increased in order to maximize the number of particles produced and detected. Those experimental procedures have nonetheless some drawbacks: increasing the beam intensity and the target density enhances the sheer number of particles involved in the the reactions of interest, but in the first case a spacial charge on the target is produced, heating it up and modifying its structure (density and composition), while increasing the density of the target the angular straggling and energy loss strongly reduce the reso-

lution. The solid angle range can also be increased, but there are limitations regarding the detection at low angles (near the beam) and the extreme count rates. Another possibility would be to increase the signal-to-noise ratio by reducing the background coming from cosmic rays, environmental radioactivity or from electric devices: material that can absorb neutrons or γ are therefore needed, and the measurement can be also performed in underground laboratories like in Laboratori Nazionali del Gran Sasso (L'Aquila - Italy) [4], in order to minimize the contribution from noise. Even with this procedures and equipment, measurements at low energies at very low energies are hard to perform – when not virtually impossible – so direct measurements usually rely on extrapolation of the cross-section, performed from data at higher energies and in terms of the astrophysical $S(E)$ -factor: $S(E) = E \sigma(E) \exp(2\pi\eta)$, where $\exp(2\pi\eta)$ represents the inverse of the Gamow factor ($\eta = \alpha Z_A Z_x \sqrt{\mu c^2 / 2E}$ being the Sommerfeld parameter) and removes the dependence of $\sigma(E)$ from the Coulomb barrier, making extrapolation easier. The $S(E)$ -factor has large uncertainties, for example due to the presence of unknown resonances or to the tail of sub-threshold ones in the extrapolation region. Furthermore, measurements at low energies suffer from the presence of electron screening effects [5], that increases exponentially the measured cross-section. To investigate the reaction the cross-section at low energies, indirect methods are then used: those allow to have access to the complete information regarding the cross-section and reaction rate of astrophysical interest.

NUCLEAR ASTROPHYSICS WITH INDIRECT METHODS

Among the indirect methods for nuclear astrophysics, the *Trojan Horse Method* (THM) [6] has been widely used to study the resonant capture of astrophysical interest, while the *Asymptotic Normalization Coefficients* (ANC) [7] method can be applied to determine the non-resonant capture contribution.

The THM allows to extract the bare nucleus cross section of a certain $A+x \rightarrow c+C$ resonant reaction of astrophysical relevance at low energies from a suitable three-body one in the exit channel $A+a \rightarrow c+C+S$, using the so-called *Quasi-free* (QF) mechanism. This is done assuming that the TH nucleus a has a cluster structure $a = x \oplus S$, where x is called participant and S is the spectator. If the bombarding energy E_A is higher than the Coulomb barrier between A and a , its effect (along with the electron screening) is negligible. Once the three body reaction is detected – usually using Position Sensitive silicon Detectors – and identified (via ΔE -E technique), the presence of the QF contribution must be ascertained, and the most sensible of all the kinematic variables is used: the shape of the momentum distribution of the S particle inside the cluster, $|\varphi(\mathbf{p}_S)|^2$. This quantity, in QF mechanism, must remain the same in the cluster and after the re-

action, where it can be reconstructed from the other variables. In this condition, the two-body cross-section can be written in terms of the triple-differential one

$$\left(\frac{d\sigma}{d\Omega}\right)_l^{HOES} \propto \frac{d^3\sigma}{dE_{C.M.}d\Omega_c d\Omega_C} \left(KF |\varphi(\mathbf{ps})|^2\right)^{-1} \quad (1)$$

where KF is a kinematic factor. The extracted cross-section, corrected by the penetration factor has then to be normalized to direct data at higher energies to be expressed in absolute units (barn).

In the ANC method, the direct capture part of the cross-section for a certain reaction $X + a \rightarrow Y + \gamma$ can be derived from the transfer one $X + A \rightarrow Y + b$, where $A = a \oplus b$ and $Y = X \oplus a$. In Distorted Wave Born Approximation (DWBA), the overlap function of the $X + a \rightarrow Y$ process can be written as

$$I_{Xa,l_Y,j_Y}^Y(r_{Xa}) = S_{Xa,l_Y,j_Y}^{1/2} \phi_{n_Y,l_Y,j_Y}(r_{Xa}) \quad (2)$$

S being the spectroscopic factor, while ϕ is the bound-state wave function. The experimental differential cross-section (in DWBA) can be written in terms of the theoretical one (σ^{DWBA}) as

$$\frac{d\sigma^{exp}}{d\Omega} = \sum_{j_Y,j_A} S_{Xa,l_Y,j_Y} S_{ba,l_A,j_A} \sigma_{l_Y,j_Y,l_A,j_A}^{DWBA} \quad (3)$$

where the two S represent the spectroscopic factors for the two reaction vertexes, respectively: one of the two is usually known, while the other has to be experimentally determined by the analysis of angular distributions (for example via elastic scattering). Regarding the S , although it is still considered a strong tool in nuclear physics, is dependent from the Optical Model parameter used, and different families of potential can give strongly different results. As pointed out [8], the direct part of the radiative cross-section at low energies and the direct transfer reaction mentioned above can have the same radial overlap integrals if the capture occurs at large distances from the nucleus (asymptotic region, $r_{Aa} > R_n$). In these conditions, the overlap integral and bound-state wave function of the entrance channel will be

$$I_{Xa,l_Y,j_Y}^Y(r_{Xa}) \rightarrow C_{Xa,l_Y,j_Y}^Y \frac{W_{-\eta,l_Y+\frac{1}{2}}(2k_{Xa}r_{Xa})}{r_{Xa}} \quad (4)$$

$$\phi_{Xa,l_Y,j_Y}(r_{Xa}) \rightarrow b_{Xa,l_B,j_B}^Y \frac{W_{-\eta,l_Y+\frac{1}{2}}(2k_{Xa}r_{Xa})}{r_{Xa}} \quad (5)$$

where W is the Whittaker function, C is the ANC and b is the single-particle ANC. The same is valid for $a + b \rightarrow A$. Substituting Eq. 4 and Eq. 5 in Eq. 2 and Eq. 3, the experimental cross-section is equal to

$$\frac{d\sigma}{d\Omega} = \sum_{j_Y,j_A} (C_{Xa,l_Y,j_Y}^Y)^2 (C_{ba,l_A,j_A}^A)^2 \frac{\sigma_{l_Y,j_Y,l_A,j_A}^{DWBA}}{b_{Xa,l_Y,j_Y}^2 b_{ba,l_A,j_A}^2} \quad (6)$$

The ANC have a small dependence on the chosen nucleon binding potential [9], so the ratio in Eq. 6 will be weakly dependent from b^2 . Both methods are extremely useful in getting the correct values of $\sigma(E)$ and $S(E)$ at low energies of astrophysical interest and

to reduce the uncertainties (see for example [10, 11, 12] and reference therein for THM and [13, 14, 15] and reference therein for ANC).

ACKNOWLEDGMENT: This work was supported by MEYS Czech Republic under the project EF16-013/0001679.

REFERENCES

1. E. M. Burbidge, G. R. Burbidge, W. A. Fowler and F. Hoyle, Rev. Mod. Phys. **29**, 547 (1957).
2. W. A. Fowler, Rev. Mod. Phys. **56**, 149 (1984).
3. G. Gamow, Zeitschrift für Physik **51**, 204 (1928)
4. C. Brogini, D. Bremmer, A. Guglielmetti, et al., Annual Review of Nuclear and Particle Science **60**, 53-73 (2010).
5. F. Strieder, C. Rolfs, C. Spitaleri and P. Corvisiero, Naturwissenschaften **88**, 461 (2001).
6. C. Spitaleri, Problems of Fundamental Modern Physics, II : Proceedings, Ed. by R. Cherubini, P. Dalpiaz, and B. Minetti, p. 21 (World Sci., 1991)
7. A. M. Mukhamedzhanov and R. E. Tribble, Phys.Rev. C **59**, 3418 (1999).
8. A. M. Mukhamedzhanov and N. K. Timofeyuk., JETP. Lett **51** (1990).
9. A. M. Mukhamedzhanov, H. L. Clark, C. A. Gagliardi et al., Phys. Rev. C **56**, 1302 (1997)
10. G. G. Rapisarda, C. Spitaleri, A. Cvetinovic et al., EPJA **11**, 189 (2018).
11. R. G. Pizzone, C. Spampinato, R. Sparta, et al., EPJA **56**, 11 (2020).
12. G. D'Agata, R. G. Pizzone, M. La Cognata, et al., ApJ **860**, 1 (2018).
13. V. Burjan, Z. Hons, V. Kroha, et al., EPJA **55**, 7 (2019).
14. A. M. Mukhamedzhanov, V. Burjan, M. Gulino et al, Phys. Rev. C **84**, 2 (2011).
15. G. G. Kiss, M. La Cognata, C. Spitaleri, et al., Phys. Lett. B **807**, 135606 (2020).

THE PROTON AND DEUTERON ACTIVATION AT NPI AND SPIRAL2/NFS FRANCE

E. Šimečková, simeckova@ujf.cas.cz, NPI CAS Řež, R. Běhal, behal@ujf.cas.cz, NPI CAS Řež, V. Glagolev, glagolev@ujf.cas.cz, NPI CAS Řež, J. Mrázek, mrazek@ujf.cas.cz, NPI CAS Řež, J. Novák, novak@ujf.cas.cz, NPI CAS Řež, M. Štefánek, stefanik@ujf.cas.cz, NPI CAS Řež

INTRODUCTION

Studies of excitation functions of charged particle reactions are of considerable significance for testing of nuclear models. The evaluated data libraries (e.g. TENDL [1]) – as a part of various computing programs serving for careful planning the construction, life cycle and decommission phases of nuclear facilities – need high accuracy experimental cross section data.

Number of systematic measurements of the proton and mainly deuteron activation were performed at NPI. Since the deuteron energy is limited by 20 MeV at NPI, we intend to continue these measurements at newly built facility NFS/SPIRAL2 in France. Since the deuteron beam is not yet available at SPIRAL2, we plan to perform proton activation on iron as the first experiment to continue recently conducted research at NPI.

Iron belongs to the most common structural material. The proton activation cross sections $p + {}^{\text{nat}}\text{Fe}$ were measured previously in many works and data are presented in EXFOR database. Nevertheless there are some gaps or misunderstanding in the experimental data.

One such case is in population of isomeric level and ground state of ${}^{\text{nat}}\text{Fe}(p,x){}^{58}\text{Co}$. The whole analysis of isomeric cross section ratios may contribute to the correct understanding of the population of the excited states in nuclei. Moreover, the short-lived isomeric states in ${}^{52,53}\text{Fe}$ are populated in the other reactions on ${}^{\text{nat}}\text{Fe}$.

EXPERIMENT AT NPI

The proton activation cross sections $p + {}^{\text{nat}}\text{Fe}$ reaction were recently measured in NPI CAS Řež. Experiment was supported by CANAM infrastructure.

The irradiation was carried out using an external proton beam of the variable energy cyclotron U120M operating in the negative-ion mode of acceleration. The activation cross sections were measured by a stacked-foil technique. The collimated proton beam impinged the stack of foils placed in a cooled reaction chamber that serves also as a Faraday cup. The stack is composed of investigated foils (Fe) interleaved by Cu foils (serving as an additional monitor and for energy attenuation). This method enables a simultaneous measurement of a number of data points. The mean energy, the energy thickness and the energy spread in each foil were simulated by SRIM 2008 package [2].

Cross sections were calculated from the specific activities, measured by two calibrated HPGe detectors, corrected to the decay using total charge and foil characteristics as well. Activated isotopes were identified on the basis of $T_{1/2}$, γ -ray energies and intensities [3].

We determined production cross sections for ${}^{55,56,57,58,58\text{m}}\text{Co}$ and ${}^{52\text{m},52,54,56}\text{Mn}$ in the agreement with

data of previous authors.

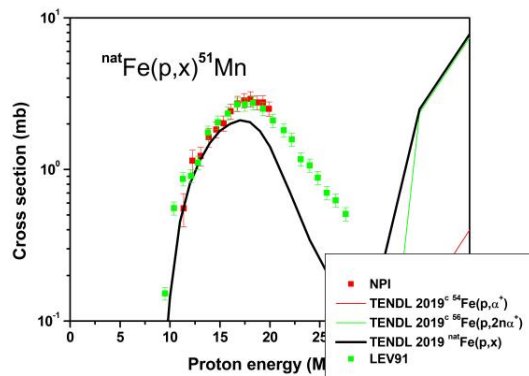


Fig. 1. Excitation function of the ${}^{\text{nat}}\text{Fe}(p,x){}^{51}\text{Mn}$ reaction

In earlier experiments, there was observed an activity of decaying ${}^{51}\text{Cr}$ (27.7 d) in the activation $p + {}^{\text{nat}}\text{Fe}$. This was assigned to ${}^{\text{nat}}\text{Fe}(p,x){}^{51}\text{Cr}$ (threshold 17.7 MeV) reaction, however, it appears that the part of activity of ${}^{51}\text{Cr}$ is a secondary decay of ${}^{51}\text{Mn}$ from ${}^{\text{nat}}\text{Fe}(p,x){}^{51}\text{Mn}$ reaction. The reaction ${}^{\text{nat}}\text{Fe}(p,x){}^{51}\text{Mn}$ itself is difficult to observe by the activation method, because the strongest gamma transition following the decay of ${}^{51}\text{Mn}$ (46 min) has the intensity 0.26 %.

The recent experiment in NPI and the decay curve analysis is in agreement with [4] and of the prediction of TENDL 2019 for ${}^{\text{nat}}\text{Fe}(p,x){}^{51}\text{Mn}$ reaction (Fig. 1).

NFS/SPIRAL2

NFS (Neutron For Science) is a component of the SPIRAL2 facility [5] using the newly built linear accelerator LINAC producing light ion beams (p,d,α). The NFS facility is mainly composed of two underground areas. The first is a converter hall where, in addition to neutron sources, a charged particle irradiation chamber is placed. The TOF area is an experimental room separated from the converter hall by a 3 m thick wall of concrete.

The system for irradiation by charged particles for NFS/SPIRAL2 was built within a program SPIRAL2-CZ that is a framework of a Czech participation in GANIL/SPIRAL2. The irradiation chamber was developed, constructed and tested in NPI and installed in NFS/SPIRAL2 Ganil.

The particle irradiation system consists of an irradiation chamber (IC) (located on beam line in the converter hall), HPGe detector system and a sample storage located in TOF area. Individual parts are connected by pneumatic transfer system (PTS) (developed in KIT Karlsruhe and adapted for the charge particle sample holder and equipped with air-brakes at every ending point). This construction enables to

remotely transfer irradiated samples between IC and detector.

The IC is based on an airlock system composed of two vacuum chambers (Fig.2). One chamber is equipped by a beam-target system and is permanently a part of the NFS beam line. The other one is equipped by a sample receive/send system and a manipulator that transfers a sample to/from the beam target system of the first chamber.

Beam-target system consists of an entrance collimator, a cooled rotating degrader with twelve selectable positions, an anti-scattering collimator (electrode), a sample lock system with a suspension and a cooled Faraday cup. The degrader will allow for a fast change of beam energy at the expense of the energy straggling. The cooled Faraday cup assembly serves to accurately measure the charge.

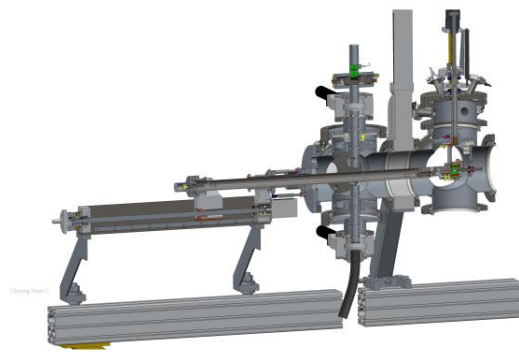


Fig. 2. The irradiation chamber. It is composed of two vacuum chambers separated by an interlock valve. The right chamber is a part of the beamline and contains a beam-target system. The left one contains a system for receiving/sending samples and equipped with the manipulator. Sample holders are green.

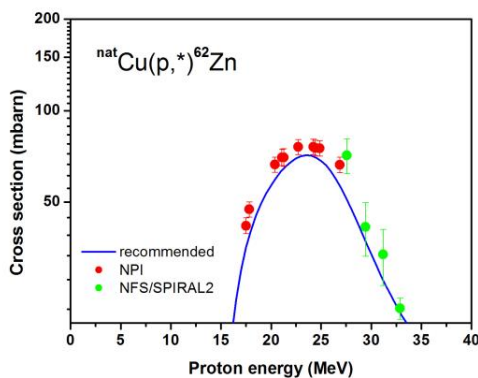


Fig. 3. Comparison our experimental values to the monitor reaction [6]

Sample holder is an aluminium cylinder (19 mm in diameter and 40 mm long) with hole (15 mm) in mid-height so that it can house a foil or a stack of foils. The inner diameter of the steel bolt fixing the foils is 11 mm. The correct orientation in the beam (or detector) is ensured by two magnets fixed in the body of the sample holder. The delivering time of sample holder from IC to the detector is of about 42 s.

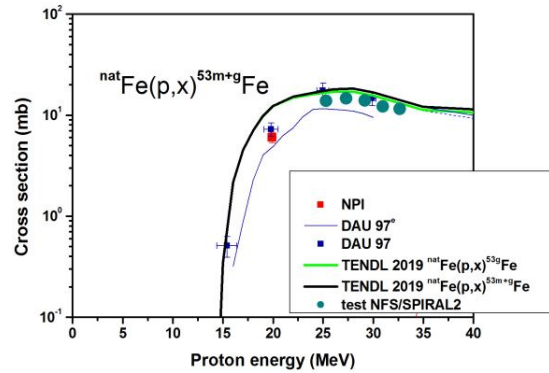


Fig. 4. Excitation function of the ${}^{\text{nat}}\text{Fe}(p,x){}^{53}\text{Fe}$ reaction

The entire cycle of irradiation and measurement is remotely controlled by the program.

TEST EXPERIMENT AT GANIL

The first proton beam was delivered from the LINAC at the autumn of 2019. The IC with PTS was commissioned (met safety rules) by the end of December and the first spectra were obtained.

The single Cu and Fe foils were irradiated by proton beam (33MeV initial energy) in several runs using various degraders. The results show satisfactory agreement with previous data and ability to study production of short-lived isotopes (see Fig. 3 and Fig. 4).

CONCLUSIONS

The ability and the reliability of the charge particle irradiation system were shown. The system enables systematic activation measurements in SPIRAL2/NFS as well as measurements of isotopes with short half-lives in (sub)minutes region. We plan to continue the study of $p + {}^{\text{nat}}\text{Fe}$ (${}^{54}\text{Fe}$) cross sections.

ACKNOWLEDGMENT: Authors are indebted to GANIL/SPIRAL2 technical staff, which provided help and cooperation during various phases of the project. The authors acknowledge the MEYS project SPIRAL2-CZ, CZ.02.1.01/0.0/0.0/16_013/0001679.

REFERENCES

1. A.J. Köning et al., Nuclear Data Sheets **155**, 1 (2019).
2. J.F. Ziegler, J.P. Biersack, D.M. Ziegler, SRIM-The stopping and Range of Ions in Matter, computer code SRIM (2008).
3. S.Y.F.Chu et al., The Lund/LBNL Nuclear Data Search (1999).
4. V.N.Levkovskij: Act. Cs. by Protons and Alphas, (Moscow – 1991).
5. X.Ledoux et al., Nuclear Data Sheets **119**, 353 (2014).
6. A. Hermanne et al., Nuclear Data Sheets **148**, 338 (2018).

DEVICES FOR NUCLEAR DATA MEASUREMENTS WITH COLLIMATED FAST NEUTRON BEAMS GENERATED ON U-120M CYCLOTRON

M. Ansorge, ansorge@ujf.cas.cz, NPI CAS, 250 68 Řež, Czechia, J. Novák, M. Majerle, D. Koliadko

INTRODUCTION

At the Nuclear Physics Institute of the CAS the new 1.6 m long collimator coupled to the new neutron converter (based on $p+^9\text{Be}$ reaction with 0.5 - 2.5 mm thin Be foil) driven by isochronous cyclotron U-120M was constructed and tested during recent years. The flux of the fast collimated neutrons is expected to reach 10^6 n/cm²/s at 2 m distance from a source behind the collimator. The collimated quasi-monoenergetic (QM) beams of fast neutrons (energies up to 33 MeV) are useful in neutron induced reaction measurements where detection probes have to be shielded from the neutron radiation. Motivated by the development of future fission and fusion energy projects and nuclear physics itself the nuclear data measurements of cross-sections (CS) for nuclear reactions induced by fast neutrons are under preparation.

COLLIMATED NEUTRON BEAM SOURCE

The collimator can be opened in two diameter regimes, 3 cm and 9 cm respectively. Best collimation properties are secured with inner parts inserted (i.e. final diam. is 3 cm). The inner part of the collimator consists of several iron and polyethylene tubes which have the decreasing outer diameter along the flight path of the beam. The collimator wall consists of a mixture of iron and water shielding.

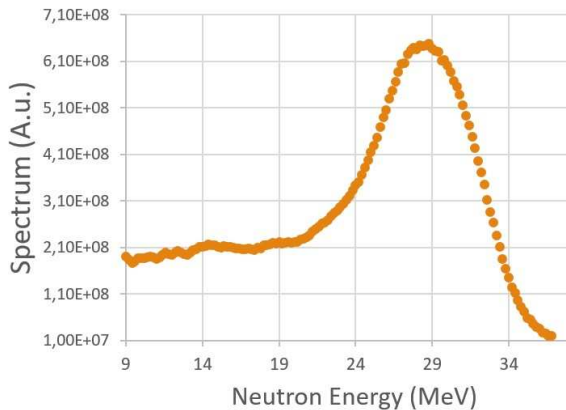


Fig. 1. Neutron Energy Spectrum at 2.5m distance on collimated beam $p+^9\text{Be}$ (2.5 mm) $E_{\text{proton}} = 33$ MeV

Neutron converter consists of the thin foil of the ^9Be (0.5 mm or 2.5 mm) which is backed by a thick graphite proton beam stopper. The FWHM of the QM-peak and overall shape of the neutron energy spectrum depends on the foil thickness and kinetic energy of primary protons. In Fig. 1 the QM-spectrum produced in 2.5 mm thin beryllium target at proton energy 33 MeV is shown. The energy neutron spectrum was measured by Time-of-Flight (ToF) technique [2] with standard 2×2 inches scintillation probe (NE-213)

placed into the beam axis at 2.5 m distance from the source and behind the collimator opened with 3 cm diameter. The beam profile shown in Fig. 2 was measured with small ($5 \text{ mm} \times 5 \text{ mm} \times 20 \text{ mm}$) stilbene crystal at the same distance and with the same collimator setup.

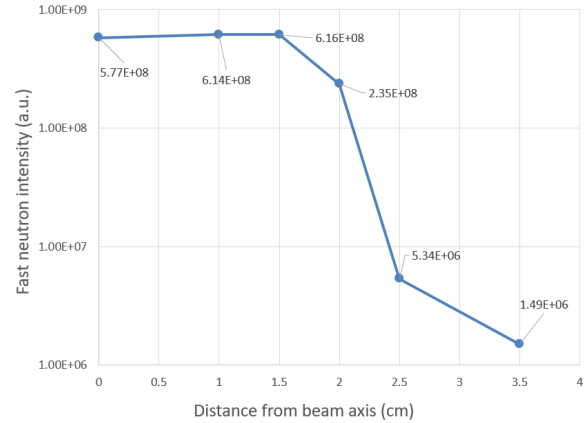


Fig. 2. Relative intensity of fast neutrons with respect to the distance from the neutron beam axis.

In the perpendicular distance to the collimated neutron beam axis of 3.5 cm the active volume of stilbene scintillator was spreading from the position 3.25 cm to 3.75 cm. At this position the neutron flux was approx. 400 times lower compared to the central position at 0 cm.

DETECTION SYSTEMS ON COLLIMATED BEAMS OF FAST NEUTRONS

The collimated fast neutron beams allow performing the on-beam neutron induced reaction product measurements with semiconductor detection systems which are usually very sensitive to neutron radiation. Two new detection systems are under the final stages of development at the Department of Nuclear Reaction at NPI CAS in Řež.

Array of HPGe detectors for on beam γ -measurements

The new array will consist of four HPGe detectors placed around the central axis of the collimated beam of fast neutrons. A similar detection system was successfully used for prompt γ -measurements at GELINA with the GAINS array [1]. The system is under development and will be able to measure the delayed gammas of residuals with decay times down to ms. Experiments with the detection of prompt gammas are planned as well. The detection system will be most efficient in the neutron energy range of 10-33 MeV. In Fig. 3 the photo from the first test of HPGe detectors placed behind the collimator is shown.



Fig. 3. First on-beam tests of new HPGe detectors placed behind the collimator.

Chamber for Light Ion Detection

Inspired by Medley setup [3] the new vacuum chamber for detection of light ions (p , d , t , ${}^3\text{He}$, α) produced in nuclear reactions induced by fast neutrons (up to 33 MeV) was constructed at NPI CAS. The chamber will allow to perform the measurements of double-differential cross sections for reactions (n , cp). The ToF method will be used for primary neutron beam energy determination and precise positioning of the rotational table is used for angle differentiation. The central sample holder can be equipped with four different targets. The chamber is equipped with dE-E Si-



Fig. 4. The new vacuum chamber placed into neutron beam axis behind the collimator

detector telescopes for distinguishing between charged particle types. The CAEN V1730 digitizer is used for data acquisition. In Fig. 4 photo of the new chamber is shown.

During the first on-beam tests the detection system exhibited good ability to measure the energy distribution of charged particles and the reasonable separation of particle types was achieved. It was also shown that time resolution of detected events will be better than 4 ns which will be sufficient for separation of QM-peak in neutron energy spectra during the ToF technique.

The detection system is expected to be used for various experimental set-ups and therefore the Geant4 simulation model was prepared alongside the real detection unit. The first version of the Geant4 model was described here [5] and it should be a valuable tool

for future experiment preparations as well as measured data analysis.

Transmission measurements

The collimation system proved to be an important part of transmission measurements which were recently conducted at NPI CAS. The scintillation probe NE-213 together with ToF technique was used to determine the decrease in intensity of QM-neutrons when the transmission sample was inserted into the beam axis. The total neutron cross-section values for the interaction of fast neutrons on liquid oxygen were measured and are published [4]. More detailed experimental data for ${}^{nat}\text{O}(n,\text{tot})$ CS were measured recently with the white neutron source and will be published soon.

CONCLUSION

The new neutron converter coupled to the collimator was constructed and basically described. Two detection systems are at the final stage of development at NPI CAS. New valuable nuclear data measurements of reaction products induced by fast neutrons with energies from 10 to 33 MeV are planned. Methodology of transmission measurements was successfully implemented and used. In next years the U-120M cyclotron should be upgraded with a bunching mechanism to achieve microsecond (instead of ≈ 40 ns) distances between single pulses of accelerated protons. This feature will allow the measurements with ToF technique at higher distances with better energy resolution and without frame overlap of detected neutrons.

ACKNOWLEDGMENT: This work was supported by OP RDE, MEYS, CZ under the project CANAM, EF16_013/0001812. This work was supported by project of the MEYS Spiral2-CZ, CZ.02.1.01/0.0/0.0/16_013/0001679.

REFERENCES

1. C. Borcea et al., EPJ Web Conf. **146**, 11004 (2017).
2. J. Novák, EPJ Web Conf. **239**, 17020 (2020).
3. S. Pomp et al., EPJ Web Conf. **8**, 07013 (2010).
4. M. Ansorge et al., EPJ Web Conf. **239**, 20008 (2020).
5. M. Ansorge: Geant4 model reakční vakuové komory CLID. (2019) ISBN 978-80-02-02895-6.

EFFECTS OF HIGH PRESSURE ON THE RADIOACTIVE DECAY

A. Cassisa, cassisa@ujf.cas.cz, Nuclear Physics Institute of The Czech Academy of Sciences, Řež 130, Řež 250 68, Czech Republic, F. de Oliveira Santos, GANIL, CEA/DRF-CNRS/IN2P3, Bvd Henri Becquerel, 14076 Caen, France, J. Mrazek, G. D' Agata, E. Šimečková, Nuclear Physics Institute of The Czech Academy of Sciences, Řež 130, Řež 250 68, Czech Republic

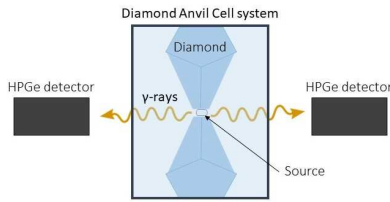


Fig. 1. Scheme of the experimental setup.

INTRODUCTION

The half-life of the radioactive elements has always been treated as a constant. In the mid-20th century, nonetheless, Segré and Daudel have found that it might be dependent on environmental conditions. This stimulated a lot of theoretical and experimental investigations regarding the possible influence of temperature, pressure, chemical composition and magnetic fields on the decay [1]. These studies shown that the most sensitive cases are those that involve the orbital electrons, i.e., the electron capture and internal conversion. One of the first important result was obtained by Gogarty et al. (1963): the authors found out that ${}^7\text{Be}$ -that decays via electron capture- at high pressure (100 kbar) decreases its half-life by 0.2% [2]. The possibility to influence the half-life of radioactive elements can have consequences in the improvement of radioactive waste treatment, on the theoretical description of electron screening effect and on the accuracy of radioactive dating of geological events. For those reasons, we prepare a test measurements with several unstable nuclei. The test will be performed at the Nuclear Physics Institute of the Czech Academy of Science using a diamond anvil cell (DAC) system. This system is able to reach pressures of 500 kbar. In this work, the preliminary study of the sensitivity of our experimental setup will be presented.

PREPARATION OF THE TEST

The typical diamond anvil cell (DAC) used in high-pressure experiments consists of two diamond surfaces that are used to compress the sample placed in-between of them. To test the experimental set-up, we arranged two options: a ${}^7\text{Be}$ sample (half-life 53 days) that decays via electron capture, and a ${}^{22}\text{Na}$ one (half-life 2.6 years), that decays via β^+ and therefore it is less sensitive to environmental conditions. Furthermore, the ${}^7\text{Be}$ sample decay in high pressure conditions has also been studied extensively [1]. The experimental setup consists of a DAC system and two 40% HPGe detectors (set-up sketched in the Figure 1). We will collect the gamma rays from the sources and calculate the difference between the decay rate of the sample under different pressures. For both chosen elements, the

expected change in the decay time is very small: 1% for the Beryllium sample [2] and 0.1% for the Sodium one [3]. The first one has been experimentally measured, while the second is based on theoretical models [4]. The experimental uncertainties must therefore be kept below 0.1%. For this reason it is crucial take into account all the sources of errors, an optimal starting point is the correct treatment of pile-up events and the dead-time. A pile-up event occurs when (at least) two signals arrive at the detector within the time window needed by the system to detect and evaluate one event. Dead-time can be defined as the time window at wich a detection system is not able to detect and store events. To reduce both pile-up events and dead-time to the minimum, we decided to use a digital signal processing, using a digitizer that is best suited for high resolution detectors and high counting rates (CAEN digitizer V1724).

This choice allows to tune all parameters involved in the digitalization process of the signal. The incoming signal is processed by two different filters. The first one is the timing and triggering filter (TTF), consisting of an RC filter that allows to reject the high frequency noise and a CR2 filter that changes the signal into a bipolar one. Its zero-crossing is used to determine the Time Stamp. The second one is an energy filter based on the Jordanov trapezoidal filter: the so-called Digital Pulse Processing for Pulse Height Analysis (DPP-PHA). The DPP-PHA is a fast recursive digital algorithm that is optimized for high resolution spectroscopy. It is able to convolute the typical exponential decay signal into a trapezoid with a flat top, its height is proportional to the amplitude of the signal. The implementation of this filter allows a pile-up rejection to a certain extent. We can recognise different pile-up events thanks to the definition of two time windows:

- The PKRUN is a window that contains the whole trapezoid of the signal;
- The PKTIME is a window containing only the part of the trapezoid, where the peak height is evaluated.

When two trapezoids related to different events overlap, one or both events may be flagged as pile-ups. Three main cases can appear in such a case (Fig. 2):

1. the overlap occurs after the PKTIME and before the end of the PKRUN of the first trapezoid, the second PKTIME cannot be evaluated correctly and it is flagged as pile-up (single zeroes);
2. the overlap occurs before the end of the PKTIME of the first trapezoid, both trapezoids are flagged as pile-ups (double zeroes);
3. the overlap occurs before the flat-top of the first trapezoid, the two pulses are too near to be separated. The pile-up is not recognized and the two

signals are treated as one, with the energy value being the sum of the two energies (visible pile-ups).

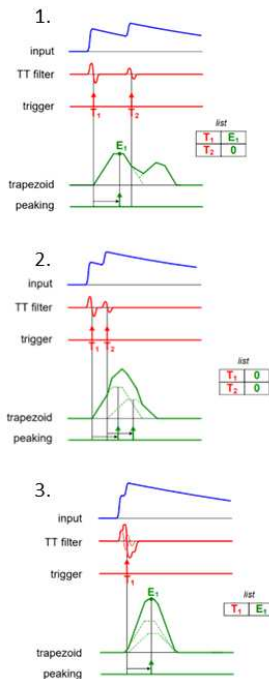


Fig. 2. Three different cases of pile-up event in the digital ADC.

FIRST RESULTS

In order to gain a deeper understanding on pile-up and lost event treatment, we performed a detailed analysis using different detectors and sources. We used silicon detector with an alpha source -where the spectrum of the incoming particles is simple- and an HPGe detector with a ^{22}Na source. In the second case we studied

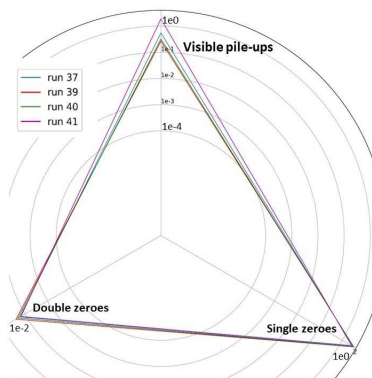


Fig. 3. Using different configurations of the digitizer parameters is possible to reduce the pile-ups and lost events.

the number and frequency of the single and double zeroes as a function of the time and the rate. Also, we studied the differences of lost and pile-up events for different digitizer parameters. With all those informations we developed a program that simulates digitizer

TAB. 1. Summary table with the differences between experimental data and the noises prediction performed by our simulation.

Index name	Experimental	Simulated
Tot. Events	2836705	2822275
Tot. Non Zero events	2822450	2807845
Tot. Zero events	14255	14430
Single Zeroes	14103	14293
Double Zeroes	73	67

response, in order to find the best values of the parameters (Fig. 3). The obtained results are summarized in Table 1. The results show a good agreement of the simulations with the experimental data.

CONCLUSIONS

A test of a diamond anvil cell (DAC) system is under preparation at NPI of the CAS. The goal is to measure the effects of high pressure on the decay half-life of radioactive elements. To test the precision and accuracy of the system we chose two samples: ^7Be , and ^{22}Na . The precision needed is about 1% for the ^7Be and 0.1% for the ^{22}Na . It is challenging to minimize all possible error sources. To reduce the uncertainty, the first step is to minimize the electronics noises and understand in detail to the response of the electronics. The simulation developed for this purpose shows an agreement with the experimental tests. We plan to further proceed with tests of stability.

ACKNOWLEDGMENT:

This work was supported by MEYS Czech Republic under the project SPIRAL2-CZ, EF16_013/0001679.

REFERENCES

1. G.T. Emery , Annu. Rev. Nucl. Sci. **22**, 162 (1972).
2. W. B. Gogarty et al., Office of Naval Research Technical Report **7**, (1963).
3. K.K.M. Lee, G. Steinle-Neumann, Earth and Planetary Science Letters **267**, 628-636 (2008).
4. W.B. Holzapfel, Europhys. Lett. **16**, 67 (1991).

MEASUREMENT OF OPEN-CHARM HADRONS IN Au+Au COLLISIONS AT $\sqrt{s_{NN}} = 200$ GeV BY THE STAR EXPERIMENT

J. Vanek for the STAR Collaboration, vanek@ujf.cas.cz, Nuclear Physics Institute of the Czech Academy of Sciences, Prague, Czech republic

PHYSICS MOTIVATION

One of the main goals of the heavy-ion program at the STAR experiment is to study properties of the Quark-Gluon Plasma (QGP). Charm quarks are an excellent probe of the QGP as they are produced at very early stages of ultra-relativistic heavy-ion collisions and therefore experience the whole evolution of the hot and dense medium. STAR is able to study production of charm quarks through a precise topological reconstruction of open-charm hadron decays utilizing the Heavy Flavor Tracker (HFT) [1].

Various measurements are used to study interactions of charm quarks with the QGP. In these proceedings, we present a selection of recent results on open-charm hadron production from the STAR experiment. In particular, we discuss the nuclear modification factors (R_{AA}) of D^\pm and D^0 mesons which give access to the charm quark energy loss in the QGP. We show the Λ_c^\pm/D^0 and D_s/D^0 yield ratios which help us better understand the charm quark hadronization process in heavy-ion collisions. In addition, we present the rapidity-odd directed flow of D^0 mesons, which can be used to probe the initial tilt of the QGP bulk and the effects of the early-time magnetic field.

RESULTS

Figure 1 shows the R_{AA} of D^0 [2] and D^\pm mesons as a function of transverse momentum (p_T) in 0-10% central Au+Au collisions. Both open-charm mesons show a significant suppression at high p_T which suggests strong interactions of the charm quarks with the QGP. The R_{AA} evolution in low to intermediate p_T region suggests a large collective flow of charm quarks [2].

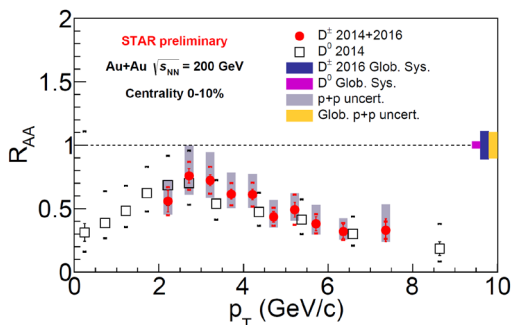


Fig. 1. R_{AA} of D^0 [2] and D^\pm mesons as a function of p_T in 0-10% central Au+Au collisions at $\sqrt{s_{NN}} = 200$ GeV.

The presence of the QGP may also influence the charm quark hadronization. In order to study that, STAR has measured the Λ_c^\pm/D^0 yield ratio as a function of number of participants (N_{part}) [3] as shown in Fig. 2. In central collisions, the ratio shows an enhancement with respect to PYTHIA 8.2 p+p calculations (Monash tune [4]) with and without color reconnection

(CR) [5]. The centrality dependence follows a similar trend as baryon to meson ratio of light flavor hadrons [6, 7]. The data are reasonably reproduced by the Catania model incorporating coalescence and fragmentation hadronization of the charm quarks [8].

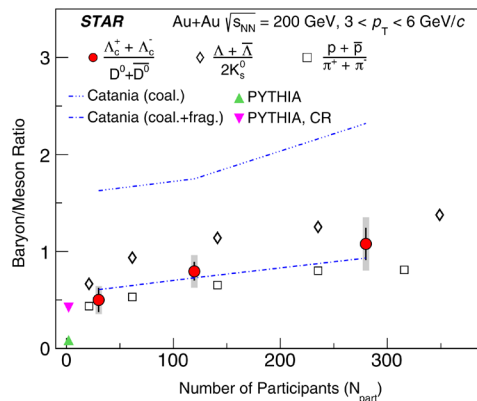


Fig. 2. Λ_c^\pm/D^0 yield ratio as a function of number of participants N_{part} . The open-charm hadron data are compared to measurements of light flavor hadrons [6, 7], PYTHIA calculation and the Catania model incorporating coalescence and fragmentation hadronization of the charm quarks [8]. Taken from Ref. [3].

To get more detailed information about hadronization of charm quarks, STAR has also measured the D_s/D^0 yield ratio, as shown in Fig. 3. The ratio is enhanced with respect to a PYTHIA 8.2 calculation, suggesting enhanced D_s production in Au+Au collisions with respect to p+p collisions. The data are qualitatively described by various models incorporating coalescence and fragmentation hadronization [8, 9, 10].

Theoretical calculations predict that the charm quarks could also be used to probe the initial tilt of the QGP bulk and the electromagnetic (EM) field induced by the passing spectators [11]. The former leads to a large negative slope of the directed flow versus rapidity (dv_1/dy) of open-charm mesons, and the latter to a negative slope for D^0 and a positive slope for \bar{D}^0 . When combined, the slope is predicted to be negative for both D^0 and \bar{D}^0 but larger for D^0 than for \bar{D}^0 in Au+Au collisions at $\sqrt{s_{NN}} = 200$ GeV. The STAR results on D^0 and \bar{D}^0 v_1 are shown in Fig. 4. The current precision of the measurement is not sufficient to conclude on the EM induced splitting, but the dv_1/dy slope is indeed negative and significantly larger than that of light-flavor mesons, as discussed in Ref. [12].

CONCLUSIONS

The STAR experiment has extensively studied the production of open-charm hadrons in Au+Au collisions at $\sqrt{s_{NN}} = 200$ GeV through a precise topological reconstruction of their hadronic decays, uti-

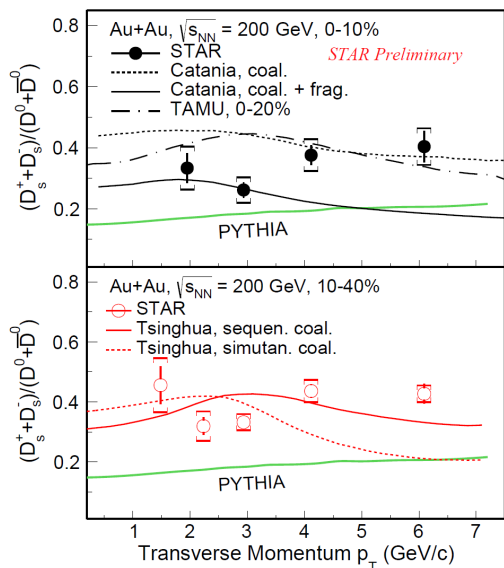


Fig. 3. D_s/D^0 yield ratio as a function of p_T . The data are compared to various models incorporating coalescence and fragmentation hadronization of charm quarks [8, 9, 10] and PYTHIA p+p calculations.

lizing the HFT. The latest results show that the D^0 and D^\pm mesons are suppressed in central Au+Au collisions, suggesting a substantial energy loss of the charm quarks in the QGP. The QGP seems to influence the charm quark hadronization. The STAR results on the Λ_c^\pm/D^0 and D_s/D^0 yield ratios are in qualitative agreement with theoretical models incorporating coalescence and fragmentation hadronization of charm quarks. The measured D^0 dv_1/dy slope is qualitatively consistent with hydrodynamical model calculations with tilted QGP bulk [11].

ACKNOWLEDGMENT:

This work was also supported from European Regional Development Fund Project "Center of Advanced Applied Science" No. CZ.02.1.01/0.0/0.0/16-019/0000778 and by the grant LTT18002 of Ministry of Education, Youth and Sports of the Czech Republic.

REFERENCES

1. D. Beavis et al., Technical Design Report, 2011. Available online: <https://drupal.star.bnl.gov/STAR/starnotes/public/sn0600>(accessed on 6 September 2019).
2. J. Adam et al., [STAR Collaboration], Phys. Rev. C **99**, 034908 (2019).
3. J. Adam et al., [STAR Collaboration], Phys. Rev. Lett. **124**, 172301 (2020).
4. P. Skands, S. Carrazza, J. Rojo, Eur. Phys. J. C **74**, 3024 (2014).
5. C. Bierlich, J. R. Christiansen, Phys. Rev. D **92**, 094010 (2015).
6. B.I. Abelev et al., [STAR Collaboration], Phys. Rev. Lett. **97**, 152301 (2006).
7. G. Agakishiev et al., [STAR Collaboration], Phys. Rev. Lett. **108**, 072301 (2012).
8. S. Plumari et al., Eur. Phys. J. C **78**, 348 (2018).

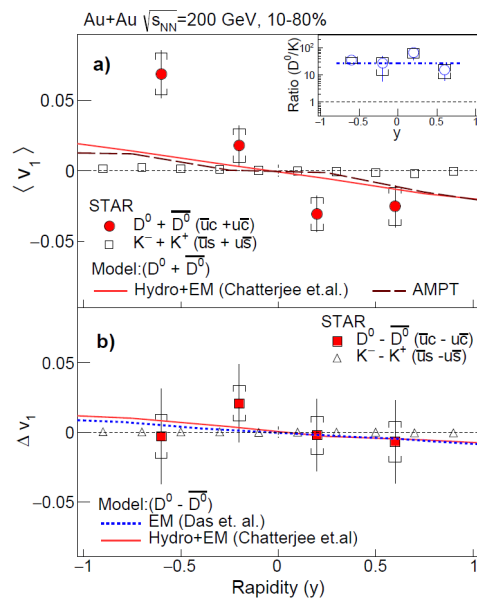


Fig. 4. (a) Directed flow of D^0 and \bar{D}^0 mesons at $p_T > 1.5$ GeV/c as a function of rapidity in 10-80% central Au+Au collisions at $\sqrt{s_{NN}} = 200$ GeV, compared to calculations of a hydrodynamic model with an initial EM field [13] and the AMPT model [14]. (b) Difference in v_1 between D^0 and \bar{D}^0 compared to a model prediction with only the initial EM field [13] and one that combines EM effects with hydrodynamics [11]. The D^0 data are compared to measurement of charged kaons [15]. Taken from Ref. [12].

9. M. He et al., Phys. Rev. Lett. **110**, 112301 (2013).
10. J. Zhao et al., arXiv1805.10858, (2018).
11. S. Chatterjee, P. Bozek, Phys. Lett. B **798**, 134955 (2019).
12. J. Adam et al., [STAR Collaboration], Phys. Rev. Lett. **123**, 162301 (2019).
13. S.K. Das et al., Phys Lett B **768**, 260 (2017).
14. M. Nasim, S. Singha, Phys. Rev. C **97**, 064917 (2018).
15. L. Adamczyk et al., [STAR Collaboration], Phys. Rev. Lett. **120**, 062301 (2018).

RECENT RESULTS OF INCLUSIVE JET PRODUCTION IN Au+Au COLLISIONS AT $\sqrt{s_{NN}} = 200$ GeV BY THE STAR EXPERIMENT

R. Licenik (for the STAR Collaboration), licenik@ujf.cas.cz, Nuclear Physics Institute of the Czech Academy of Sciences, Prague, Czech republic

INTRODUCTION

Jets are an excellent probe of the Quark-Gluon Plasma (QGP) - an exotic state of matter created in high-energy nucleus-nucleus collisions. They are created at the very early stage in the collision during hard parton-parton scatterings, which means that they experience the entire evolution of the system. In addition, their production cross section in proton-proton collisions is calculable by perturbative Quantum Chromodynamics. The modification of jet production as the result of parton interactions with the QGP medium (jet quenching) was first studied via suppression of high-transverse momentum (high- p_T) hadrons [1], which provided a clear evidence of QGP formation in Au+Au collisions at top RHIC energies. Since then, detailed measurements with reconstructed jets have been carried out in Pb+Pb collisions at the LHC [2, 3, 4]. These proceedings focus on the recently reported results of inclusive charged-particle jet production in Au+Au collisions at $\sqrt{s_{NN}} = 200$ GeV by the STAR experiment at RHIC [5] and also on the ongoing analysis of fully-reconstructed jets, which is expected to bring extended kinematic reach and improved precision.

DATASET AND ANALYSIS

The analysis uses the STAR detector [6], a multi-purpose large-acceptance system utilizing a solenoidal magnetic field. Charged-particle tracks and their momenta are reconstructed in the Time Projection Chamber (TPC) [7]. The Barrel Electromagnetic Calorimeter [8] is used to measure the energy deposited by neutral particles and also provides online triggers. The STAR detector offers a full azimuthal coverage within pseudorapidity range $|\eta| < 1$. The dataset for the charged-particle jet analysis amounts to $\sim 6 \mu\text{b}^{-1}$ of Au+Au collisions at $\sqrt{s_{NN}} = 200$ GeV recorded with the minimum-bias trigger in year 2011, while the fully-reconstructed jet analysis uses a 5.2 nb^{-1} dataset of Au+Au collisions at the same energy recorded in 2014 using the High-Tower trigger, requiring a signal threshold of ~ 4 GeV in a single BEMC tower. Charged-particle jets are reconstructed from TPC tracks (see [5] for analysis details), while fully-reconstructed jets also include the energy from BEMC clusters (3×3 towers), corrected for hadronic energy deposition. The clusters' transverse energy was limited to $0.2 < E_T < 30.0$ GeV. Jets are reconstructed using the anti- k_T algorithm [9] with resolution parameters $R = 0.2, 0.3, 0.4$. The combinatorial-jet background in both analyses is suppressed by imposing a cut on the transverse momentum of the hardest particle ($p_{T,\text{lead}}$) in a jet. However, this cut also introduces a bias into the fragmentation of the surviving jet population. This bias is estimated by varying the $p_{T,\text{lead}}$ cut and physics results are discussed in the

unbiased region.

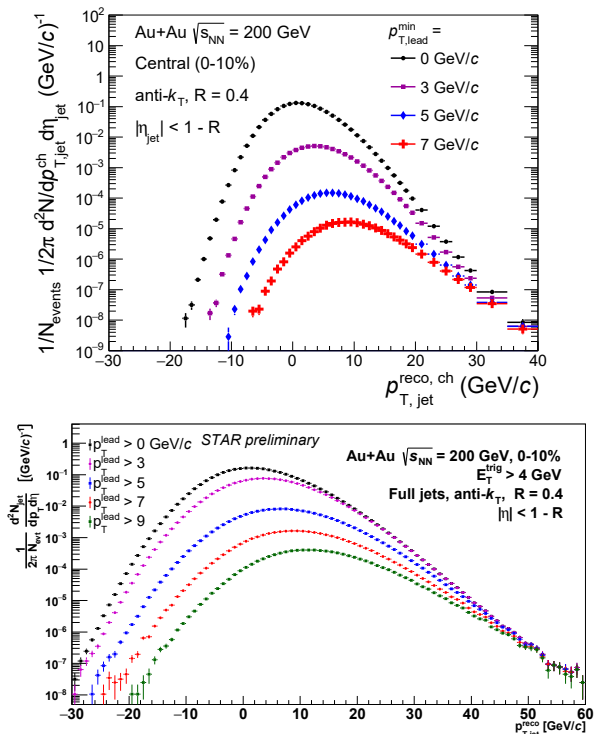


Fig. 1. Uncorrected distributions of charged-particle [5] (top) and fully-reconstructed (bottom) jets as a function of $p_{T,\text{jet}}^{\text{reco}}$ in 0-10% Au+Au collisions at $\sqrt{s_{NN}} = 200$ GeV. Different colors represent different values of $p_{T,\text{lead}}$.

RESULTS

Figure 1 shows the charged-particle (top) and fully-reconstructed (bottom) jet distributions as a function of $p_{T,\text{jet}}^{\text{reco}} = p_{T,\text{jet}}^{\text{raw}} - \rho \cdot A$, where $p_{T,\text{jet}}^{\text{raw}}$ is the raw jet p_T given by the jet finder, A is the jet area and ρ is the median background energy density (calculated event-wise), for $R = 0.4$ in central Au+Au collisions. It can be seen that the $p_{T,\text{lead}}$ cut significantly reduces the combinatorial background, especially at low $p_{T,\text{jet}}^{\text{reco}}$. The distributions also indicate the extended kinematic reach of the fully-reconstructed-jet analysis. However, since this analysis is a work in progress, we only show corrected results from the charged-particle jet analysis. Corrections are applied for the smearing effects of the high-multiplicity environment and instrumental effects using the SVD and Bayesian unfolding methods (details in [5]).

Figure 2 shows charged-particle jet R_{CP} , the scaled ratio of yields in central to peripheral collisions, which exhibits a similar level of suppression as charged hadrons at RHIC [10] and LHC energies [11] and as charged-particle jets at the LHC at higher $p_{T,\text{jet}}^{\text{ch}}$ [2], with weak $p_{T,\text{jet}}^{\text{ch}}$ dependence. Figure 3 shows charged-

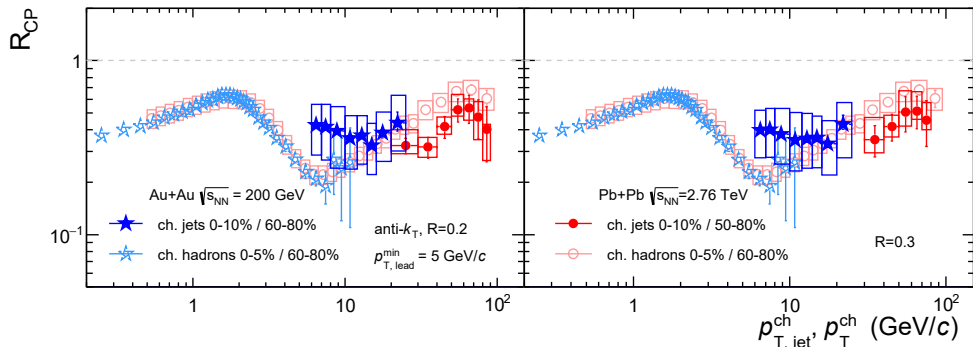


Fig. 2. R_{CP} of charged-particle jets reconstructed with $R = 0.2$ (left) and 0.3 (right) and $p_{T,lead} > 5$ GeV/c (solid stars) [5]. Also shown are measurements of R_{CP} for charged-particle jets at the LHC (solid circles) [2] and inclusive charged hadrons at RHIC (open stars) [10] and the LHC (open circles) [11].

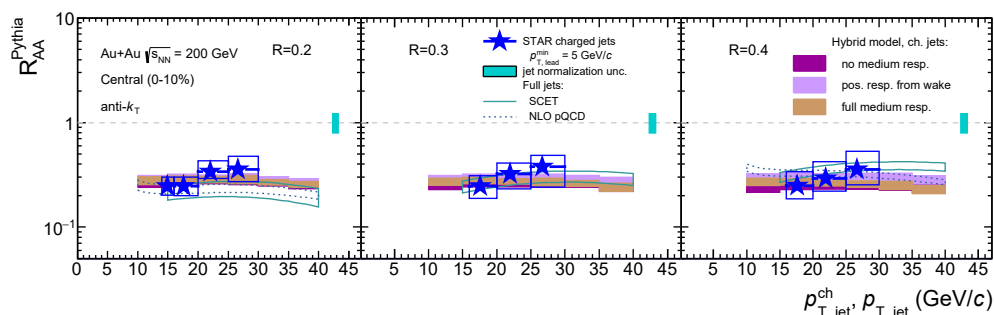


Fig. 3. R_{AA}^{PYTHIA} as a function of $p_{T,jet}^{ch}$ for charged-particle jets at STAR reconstructed with $R = 0.2$ (left), 0.3 (middle) and 0.4 (right), and $p_{T,lead} > 5$ GeV/c [5]. Bands represent theory calculations [13, 14, 15, 16].

particle jet R_{AA}^{PYTHIA} , which measures the yield suppression for central Au+Au collisions compared to $p+p$ baseline calculated by PYTHIA 6 (Perugia 2012, further tuned by STAR [12]). Calculations based on jet quenching models are largely consistent with the measured value of R_{AA}^{PYTHIA} within uncertainties, which motivates more precise measurements to distinguish among them.

CONCLUSIONS

We have discussed the recently reported results of charged-particle jet production in Au+Au collisions at $\sqrt{s_{NN}} = 200$ GeV by the STAR experiment. The R_{CP} shows large suppression, consistent with similar measurement at the LHC and also with charged hadron results at RHIC and the LHC. The R_{AA}^{PYTHIA} also shows large suppression consistent with models incorporating jet-quenching mechanisms. The ongoing fully-reconstructed jet analysis is expected to increase the kinematic reach and precision of STAR inclusive jet measurements.

ACKNOWLEDGMENT: This work is supported by the project LTT18002 of the Ministry of Education, Youth and Sport of the Czech Republic.

REFERENCES

1. STAR Collaboration, Phys. Rev. Lett. **91**, 072304 (2003).

2. ALICE Collaboration, J. High Energy Phys. **30**, 013 (2014).
3. ATLAS Collaboration, Phys. Lett. **B 790**, 108 (2019).
4. CMS Collaboration, Phys. Rev. **C 96**, 015202 (2017).
5. STAR Collaboration, arXiv:2006.00582 [nucl-ex].
6. K. Ackermann et al., Nucl. Instrum. Meth. **A 499**, 624 (2003).
7. M. Anderson et al., Nucl. Instrum. Meth. **A 499**, 659 (2003).
8. M. Beddo et al., Nucl. Instrum. Meth. **A 499**, 725 (2003).
9. M. Cacciari et al., J. High Energy Phys. **04**, 063 (2008).
10. STAR Collaboration, Phys. Rev. Lett. **91**, 172302 (2003).
11. ATLAS Collaboration, J. High Energy Phys. **09**, 050 (2015).
12. STAR Collaboration, Phys. Rev. **D 100**, 052005 (2019).
13. I. Vitev, B.-W. Zhang, Phys. Rev. Lett. **104**, 132001 (2010).
14. Y.-T. Chien et al., Phys. Rev. **D 93**, 074030 (2016).
15. Y.-T. Chien, I. Vitev, J. High Energy Phys. **05**, 023 (2016).
16. J. Casalderrey-Solana et al., J. High Energy Phys. **03**, 135 (2017).

SEARCH FOR JET QUENCHING EFFECTS IN HIGH-MULTIPLICITY PROTON-PROTON COLLISIONS AT $\sqrt{s} = 13$ TeV

F. Krizek for the ALICE Collaboration, krizek@ujf.cas.cz, Nuclear Physics Institute of CAS, Husinec-Řež, CZ 250 68

INTRODUCTION

Observed collective behavior in final state of small collision systems such as pp or p-Pb is one of the important discoveries done at the CERN Large Hadron Collider [1]. Yet, origin of this effect remains unknown. Its possible association with quark-gluon plasma (QGP) formation needs to be confirmed by an unambiguous observation of jet quenching in small systems.

Current understanding of the jet quenching effect [2] is based on a picture, where a high-energetic parton interacts with the QGP and undergoes energy losses. Such interaction leads to suppression of hadrons and jets with a high transverse momentum (p_T). Furthermore, it causes a substructure modification of the resulting jets and deflection of their momenta w.r.t. initial direction. The latter effect increases on average azimuthal acoplanarity of produced dijets and it should enlarge on average also the azimuthal opening angle between a high- p_T hadron and a jet in recoil.

ANALYSIS

In this paper, we discuss searches for jet quenching phenomenon in high-multiplicity pp collisions at $\sqrt{s} = 13$ TeV as measured by the ALICE experiment at CERN. The ALICE detector is described in detail in [3]. The analysis is based on two data sets recorded with two different trigger conditions, which select minimum bias events (MB) and high-multiplicity events (HM). Both triggers were based on signals provided by the V0A and V0C scintillator arrays which cover the forward ($2.8 < \eta < 5.1$) and backward ($-3.7 < \eta < -1.7$) pseudorapidity interval, respectively. The MB trigger required a time coincidence of signals from V0A and V0C. The HM trigger selected events, where the sum of V0A and V0C multiplicity signals (denoted V0M) exceeded at least 5 times the mean MB value (denoted $\langle V0M \rangle$). In the off-line analysis, $V0M / \langle V0M \rangle$ of HM events was further constrained to the range 5–9 to suppress residual pile-up.

Jet quenching should lead to average increase in the azimuthal opening angle enclosed by a high- p_T hadron and a recoiling jet. Thus in HM events one expects to see broadening of the corresponding distribution relative to MB. The distribution of the opening angle was measured by means of the hadron-jet correlation technique [4] that allows for data-driven statistical subtraction of the jet yield, which is uncorrelated to a high- p_T hadron. The high- p_T hadrons were selected from exclusive ranges $20 < p_T < 30$ GeV/c and $6 < p_T < 7$ GeV/c. These ranges will be denoted as TT{20, 30} and TT{6, 7}, respectively. Pseudorapidity of these high- p_T hadrons was constrained to $|\eta| < 0.9$. If there were more candidates for such a track in a given event, one of them was chosen by random.

Jets were reconstructed from charged-particle

tracks using the anti- k_T algorithm with a cone radius of $R = 0.4$ [5]. A low, 150 MeV/c infrared cutoff on p_T of jet constituents was applied. Pseudorapidity of produced jets was constrained to the range $|\eta_{\text{jet}}| < 0.5$. Jet p_T was corrected for the estimated contribution of the mean underlying event on event by event basis.

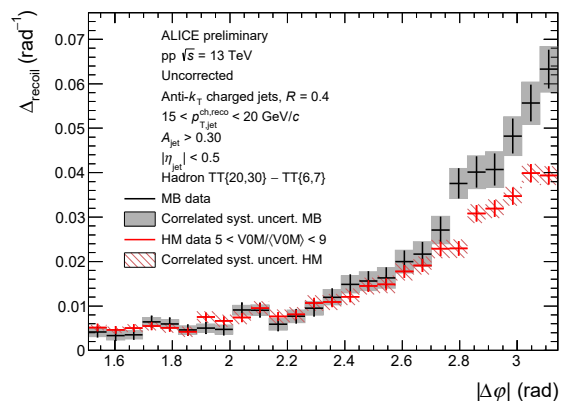
Jets which are formed by particles from the underlying event are uncorrelated with the chosen high- p_T hadron. From experiment it follows that the yield of such jets normalized per the number of selected high- p_T hadrons is largely independent of p_T of these hadrons [4]. Their contribution to the distribution of the hadron-jet azimuthal opening angle can be removed by constructing the following observable

$$\Delta_{\text{recoil}} = \frac{1}{N_{\text{TT}}} \left. \frac{dN_{\text{jet}}}{d\Delta\varphi} \right|_{\text{TT}\{20,30\}} - \frac{1}{N_{\text{TT}}} \left. \frac{dN_{\text{jet}}}{d\Delta\varphi} \right|_{\text{TT}\{6,7\}}, \quad (1)$$

where $\Delta\varphi$ is the azimuthal angle enclosed by the high- p_T hadron and a jet, and $1/N_{\text{TT}} \times dN_{\text{jet}}/d\Delta\varphi|_{\text{TT}}$ represents the jet yield associated to high- p_T hadrons from the given p_T bin normalized per the number of such hadrons.

RESULTS

Figure 1 shows a raw Δ_{recoil} distribution as measured in HM and MB events for jets with p_T in the range 15–20 GeV/c. The data suggest that jets, which are nearly back-to-back in azimuth w.r.t. the high- p_T hadron, are suppressed in HM events relative to MB. Similar suppression is seen also for other selected jet p_T ranges [6]. The observed behavior resembles jet



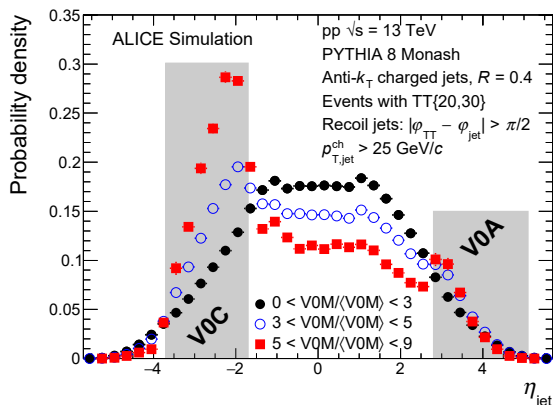
ALI-PREL-339704

Fig. 1. Raw Δ_{recoil} distributions as a function of the azimuthal opening angle between a high- p_T hadron and a jet in HM and MB pp collisions at $\sqrt{s} = 13$ TeV.

quenching; however, qualitatively similar behavior of the Δ_{recoil} distributions was obtained also for particle level HM and MB events generated with PYTHIA8 Monash [7] Monte Carlo event generator, which does not account for jet quenching, see [6].

The PYTHIA8 Monash event generator was thus

used to study possible origin of the observed phenomenon. In these simulations, recoil jets were studied in much wider pseudorapidity range $|\eta_{\text{jet}}| < 5.6$, which covers the V0A and V0C acceptances. Figure 2 presents pseudorapidity distributions of high- p_T recoil jets in events with different multiplicity bias. PYTHIA suggests that the HM trigger condition significantly enhances the probability to find a high- p_T recoil jet in the V0C array. This probability grows with $V0M/\langle V0M \rangle$. The observed asymmetry of the distributions raises from the asymmetric location of the V0C and V0A arrays w.r.t. the center of the ALICE detector. When no $V0M/\langle V0M \rangle$ bias is imposed, the distribution becomes symmetric.



ALI-SIMUL-347697

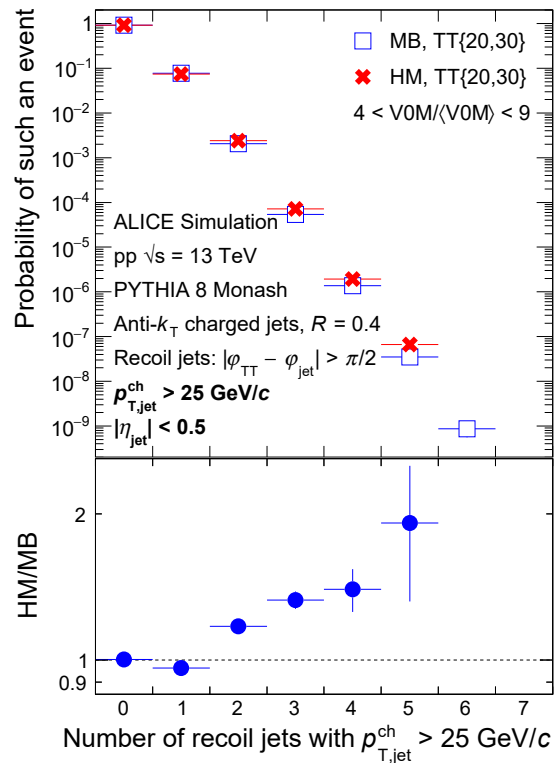
Fig. 2. Simulated pseudorapidity distributions of $p_T > 25$ GeV/c jets recoiling from a charged 20–30 GeV/c hadron in $pp \sqrt{s} = 13$ TeV collisions having different multiplicity bias. The multiplicity bias on an event is imposed by constraining $V0M/\langle V0M \rangle$. The pseudorapidity coverages of the V0A and V0C scintillator arrays are highlighted by gray boxes.

Furthermore, we studied abundance of MB and HM events, which have a given number of high- p_T recoil jets associated to a 20–30 GeV/c hadron, see Fig. 3. Pseudorapidity of the selected jets was constrained to $|\eta_{\text{jet}}| < 0.5$. The figure suggests that the probability to have multiple high- p_T jets in an event falls steeply both for the HM and MB requirement. The ratio of both spectra shows that HM suppresses events with a single recoil jet. On the other hand, the HM condition enhances the probability of multi-jet final states.

CONCLUSIONS

The suppression observed in Fig. 1 is thus due to events, in which the recoil jet is directed to the V0C or V0A array, where it induces the HM trigger. Such jet is then missing in the midrapidity to balance the high- p_T hadron. The observed effect thus results from the design of the ALICE HM trigger, but it can be expected that similar biases appear in all studies of small-collision systems, where high multiplicity is some detector is required. Quenching effects, if present, may be masked by such effects.

ACKNOWLEDGMENT: This research was funded by



ALI-SIMUL-347715

Fig. 3. Top panel: Probability to find a given number of high- p_T jets in MB and HM $pp \sqrt{s} = 13$ TeV events with a 20–30 GeV/c hadron. Bottom panel: Ratio of both spectra. PYTHIA 8 Monash particle level simulation.

the Ministry of Education, Youth, and Sports of the Czech Republic, grant number LTT17018.

REFERENCES

1. Khachatryan V. et al. (CMS Collaboration), *JHEP* **09**, 091 (2010).
2. Majumder, A., Van Leeuwen, M., *Prog. Part. Nucl. Phys.* **A66**, 41 (2011).
3. Aamodt, K. et al. (ALICE Collaboration), *JINST* **3**, S08002 (2008).
4. Adam, J. et al. (ALICE Collaboration), *JHEP* **09**, 1 (2015).
5. Cacciari, M., Salam, G.P., and Soyez, G., *JHEP* **04**, 063 (2008).
6. Jacobs, P. M. et al. (ALICE Collaboration), arXiv:2001.09517.
7. Skands, P., Carrazza, S., Rojo J., arXiv:1404.5630 [hep-ph].

IDENTIFYING HEAVY-FLAVOR JETS USING VECTORS OF LOCALLY AGGREGATED DESCRIPTORS

G. Ponimatkin, ponimatkin@ujf.cas.cz, Nuclear Physics Institute of the Czech Academy of Sciences, Prague, Czech republic

INTRODUCTION

The heavy-flavor jets which arise from hard scattered heavy quarks play an important role in many physics processes at collider experiments. Thus, the ability to identify such jets with high precision is crucial to many measurements, for example in studies of boosted objects at the LHC or studies of mass dependence of energy loss. At RHIC energies successful identification of heavy-flavor jets down to the low transverse momentum (p_T) can help with searches for the dead-cone effect [1] via Lund plane formalism [2, 3] and its modification via quark-gluon plasma medium [4] created in heavy-ion collisions.

Machine learning is an established way for solving such classification problems. The previous research on jet flavor identification utilized jet images [5] (for W/Z boson initiated jets) or p_T/DCA (distance of closest approach to the primary vertex) ordered sequences of particles [6] (for heavy flavor jet identification). The p_T/DCA ordering of particles in a jet is not physical and hence other methods are needed. One such method, called NetVLAD [7] is an efficient way for solving computer vision tasks that are using sets of vectors as an input.

TRAINING DATASET

Training data for pp collisions at $\sqrt{s} = 200$ GeV is simulated with the PYTHIA8 [8, 9] event generator at the center of mass energy $\sqrt{s} = 200$ GeV. We generate 2 datasets that contain light jets (those initialized by uds -quarks and gluons) and heavy-flavor jets (those coming from the fragmentation of c and b quarks). First dataset respects the realistic jet cross-section ratios and the second one with balanced number of jets represents an idealized benchmark case. In order to bring in the effects of the finite detector resolution, the transverse momentum and vertexing information of the particles are smeared using a Gaussian distribution via $p_T = \mathcal{N}(p_T, \sigma(p_T))$ [10], where $\sigma(p_T)$ and $DCA = \mathcal{N}(DCA, \sigma(\mathbf{p}))$ [11] with $\sigma(p_T)$ being the transverse momentum resolution and $\sigma(\mathbf{p})$ is vertex tracker resolution. After smearing, only the charged particles (protons, pions and kaons) with $0.2 < p_T < 30$ GeV/c and pseudorapidity $|\eta| < 1.0$ are accepted, since only charged particles leave hits in the vertex tracker.

JETVLAD MODEL AND ITS PERFORMANCE

We introduce the JetVLAD model, which takes a set of tracks, that are produced by the anti- k_T [14] jet reconstruction algorithm within the FastJet package [12, 13] and predicts if the jet originates from a light or heavy-flavor parton. Initially 4 combinations of the input variables were considered - track-

ing (p_T, η, φ), vertexing (DCA_{xy}, DCA_z), tracking and vertexing ($p_T, \eta, \varphi, DCA_{xy}, DCA_z$) and finally tracking and fragmentation ($p_T, \eta, \varphi, z, \Delta R, z(\Delta R)^2$). Here φ represent azimuthal angle of the track, DCA_{xy} and DCA_z are xy and z projections of the DCA , ΔR is the distance between track and jet axis and z is a total jet momentum fraction carried away by the track.

The tracking and vertexing inputs were chosen to yield optimal classification performance. The resulting model possesses 111608 of free parameters and only two hyper-parameters (number of layers in the model and number of clusters in the NetVLAD layer), which makes running this model computationally very efficient. The evaluation is done using standard metrics, namely the efficiency:

$$\text{Eff} = \frac{\text{TP}}{\text{P}}, \quad (1)$$

i.e. ratio of true-positives (correctly identified heavy-flavor jets) over positives (total number of heavy-flavor jets in the testing sample). This metric shows percentage of heavy-flavor jets algorithm can retrieve from the sample. Next metric is purity, given by

$$\text{Pur} = \frac{\text{TP}}{\text{TP} + \text{FP}}, \quad (2)$$

i.e. it is ratio of true-positives over true-positives and false-positives (light flavor jets that were identified as heavy-flavor) in the accepted sample. As the name suggest, this metric shows the background contamination in the selected sample. The last metric is rejection

$$\text{Rej} = \frac{\text{N}}{\text{FP}}, \quad (3)$$

where N is a total number of negatives in the sample (i.e light flavor jets) and FP is a number of false positive jets. This metric tells how many background jets are rejected per one false positive jet accepted. The results for selected working points and jet p_T ranges can be seen in the Table . Efficiency and rejection plots that were used for optimal input combination can be seen on Figure 1. The efficiency and purity plots for jets across different p_T ranges can be seen on Figure 2.

TAB. 1. JetVLAD classification performance in purity and rejection for different jet p_T ranges for the cross-section weighted (balanced) datasets with two working points based on efficiencies of 80% and 50%, respectively.

Range in jet p_T [GeV/c]	Tagging Efficiency	Signal Purity	Background Rejection
[5 - 10]	80%	83% (99%)	223 (268)
	50%	88% (99%)	540 (579)
[25 - 40]	80%	81% (99%)	322 (366)
	50%	85% (99%)	677 (740)

Figure 1 shows the background rejection as a function of the classification efficiency for different inputs.

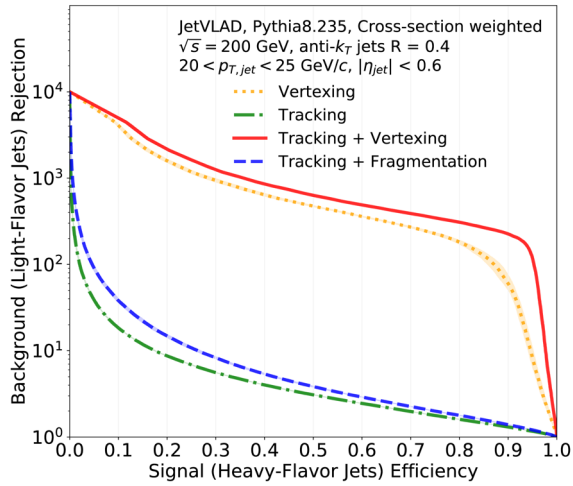


Fig. 1. Rejection vs efficiency plots for different input variables. The combination of tracking and vertexing information provides the best performance.

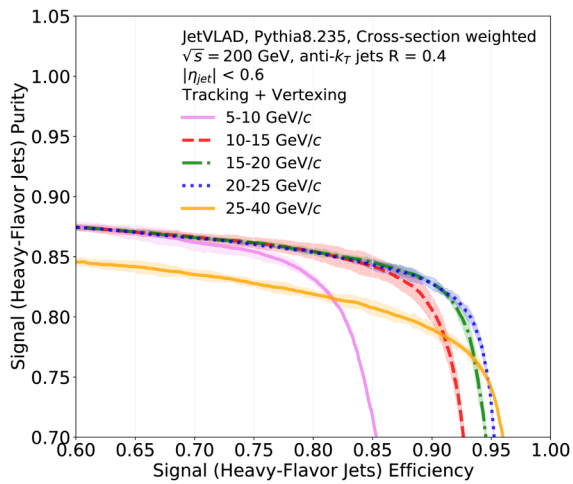


Fig. 2. Purity vs efficiency plots for different jet p_T ranges.

One can see that tracking and vertexing provides the best performance.

It is interesting to note, that vertexing alone provides a good model performance, but adding tracking information increases overall performance. Figure 2 shows that the model performance is changing slowly for different p_T ranges. The drop in the purity for the highest momentum range is due to the difference in jet kinematics, since at those momenta heavy-flavor jets are starting to resemble light jets.

CONCLUSIONS

We propose a novel jet tagging method suitable for RHIC energies which utilizes a set of tracks as an input making this tagger directly applicable to experiments for existing vertexing detectors and jet algorithms. The resulting method is computationally efficient and has a small number of hyper-parameters. The proposed method achieves 83% purity, background rejection rate of more than 200 and efficiency of 80% at lowest jet momenta. Such a performance enables

indentation of heavy-flavor jets at RHIC energies and provides the opportunity for new flavor tagged measurements.

ACKNOWLEDGMENT: This work is supported by the project LTT18002 of the Ministry of Education, Youth and Sport of the Czech Republic.

REFERENCES

1. Yu. L. Dokshitzer, D. E. Kharzeev, Phys. Lett. **B519**,199 (2001).
2. F. A. Dreyer, G. P. Salam, G. Soyez, JHEP **12**, 064 (2018).
3. L. Cunqueiro, M. Ploskon, Phys. Rev. **D 99**, 074027 (2019).
4. H. A. Andrews et al., J. Phys. **G 47**, 065102 (2020).
5. L. Oliveira, M. Kagan, L. Mackey, B. Nachman, A. Schwartzman, JHEP **07**, 069 (2016).
6. D. Guest, J. Collado, P. Baldi, S.-C. Hsu, G. Urban, D. Whiteson, Phys. Rev. **D 94**, 112002 (2016).
7. R. Arandjelovic, P. Gronat, A. Torii, T. Pajdla, J. Sivic, IEEE Transactions on Pattern Analysis and Machine Intelligence **40**, 1437 (2018).
8. T. Sjostrand, S. Mrenna, P. Skands, JHEP **05**, 026 (2006).
9. T. Sjostrand et al., Comput. Phys. Commun. **191** 159 (2015).
10. J. Rusnak: Jet Reconstruction in Au+Au collisions at RHIC (PhD thesis, Nuclear Physics Institute, The Czech Academy of Sciences - 2017).
11. STAR Collaboration, Phys. Rev. **C 99**, 034908 (2019).
12. M. Cacciari, G.P. Salam, G. Soyez, Eur. Phys. J. **C72**, 1896 (2012).
13. M. Cacciari, G.P. Salam, Phys. Lett. **B 641**, 57 (2006).
14. M. Cacciari, G.P. Salam, G. Soyez, JHEP **0804**, 063 (2008).

RECENT RESULTS OF Υ PRODUCTION MEASURED WITH THE STAR EXPERIMENT

L. Kosarzewski for the STAR Collaboration, kosarles@fjfi.cvut.cz, Faculty of Nuclear Sciences and Physical Engineering, Czech Technical University in Prague

INTRODUCTION

Upsilon (Υ) mesons are a good tool to study the nature of strong interaction and properties of quark-gluon plasma (QGP), created in ultra relativistic heavy-ion collisions [1]. Measurements of the production of these mesons in p+p collisions provide information about the quarkonium production mechanism. Such measurements serve also as a reference for studies of QGP, where Υ and J/ψ mesons are expected to dissociate at high temperatures [2] resulting in suppressed yields observed in heavy-ion collisions. This effect is due to Debye-like screening of color charges, which causes the bound states to dissociate. The level of suppression is estimated by measuring the nuclear modification factor:

$$R_{AA} = \frac{1}{\langle N_{coll} \rangle} \frac{d^2 N_{A+A}/dp_T dy}{d^2 N_{p+p}/dp_T dy} \quad (1)$$

where $\langle N_{coll} \rangle$ is the mean number of nucleon+nucleon collisions and the numerator and the denominator are differential yields vs. transverse momentum (p_T) and rapidity (y) in A+A and p+p collisions, respectively. Moreover, each of $\Upsilon(nS)$ has a different binding energy and dissociates at a different temperature, leading to a sequential suppression [3]. The measured Υ yields are also affected by feed-down contributions from heavier states, such as $\Upsilon(nS) \rightarrow \Upsilon(1S)\pi^+\pi^-$, $\chi_{bJ}(nS) \rightarrow \Upsilon(1S)\gamma$ and similar decays.

Furthermore, in A+A collisions there may be a contribution from a number of Cold Nuclear Matter (CNM) effects, which are unrelated to QGP. These effects include absorption in nucleus, comover interactions [4], coherent partonic energy loss [5], and modification of the nuclear parton distribution functions with respect to those of free nucleons. The last one shows shadowing and anti-shadowing effects [6], which could decrease or increase the parton (gluon) densities. All the above effects can be studied using p+A or d+A collisions.

Finally, studies of normalized yield $\Upsilon/\langle \Upsilon \rangle$ dependence on normalized charged particle multiplicity $N_{ch}/\langle N_{ch} \rangle$ allow to investigate interplay between hard and soft processes in high- N_{ch} p+p events. These studies have been performed by the CMS experiment at the LHC [7].

PRODUCTION IN P+P COLLISIONS

The STAR experiment has measured Υ production cross section in p+p collisions at $\sqrt{s} = 200$ GeV vs. rapidity (y) and $\sqrt{s} = 500$ GeV vs. p_T and y . Figure 1 shows the $\Upsilon(nS)$ rapidity-differential cross section in p+p collisions at $\sqrt{s} = 500$ GeV, where the newly measured $\Upsilon(2S)$ and $\Upsilon(3S)$ cross sections are presented along with $\Upsilon(1S)$. The $\Upsilon(1S)$ data are well described by Color Evaporation Model (CEM) [8] cal-

culations for inclusive $\Upsilon(1S)$. The same data are overestimated by a CGC+NRQCD [9, 10] calculation for directly produced $\Upsilon(1S)$.

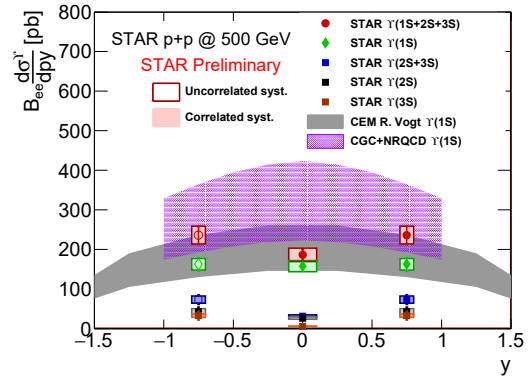


Fig. 1. $\Upsilon(nS)$ cross sections vs. rapidity (y) in p+p collisions at $\sqrt{s} = 500$ GeV, compared to model predictions for $\Upsilon(1S)$ [8, 9, 10].

The dependence of normalized $\Upsilon(1S)/\langle \Upsilon(1S) \rangle$ yield on normalized $N_{ch}/\langle N_{ch} \rangle$ was measured by STAR in p+p collisions at $\sqrt{s} = 500$ GeV. This is presented in Fig. 2 and compared to STAR J/ψ results at $\sqrt{s} = 200$ GeV [11], CMS $\Upsilon(1S)$ data [7], and ALICE data for J/ψ [12]. Both the Υ and J/ψ data follow similar trends at RHIC and the LHC, despite a large difference in the collision energies.

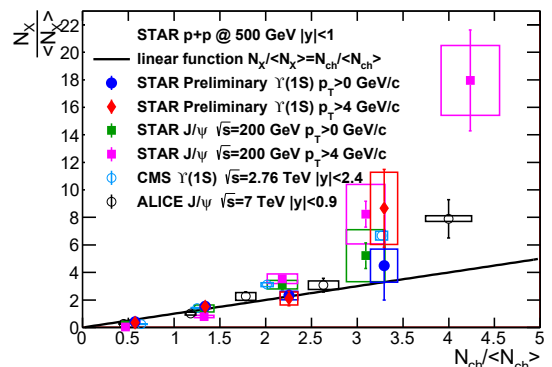


Fig. 2. Normalized yield $\Upsilon(1S)/\langle \Upsilon(1S) \rangle$ vs. normalized charged particle multiplicity $N_{ch}/\langle N_{ch} \rangle$. STAR results for $\Upsilon(1S)$ and J/ψ are compared to ALICE [12] and CMS [7] measurements.

SUPPRESSION IN AU+AU COLLISIONS

In Au+Au collisions at $\sqrt{s_{NN}} = 200$ GeV, the Υ R_{AA} is obtained by combining measurements in $\Upsilon \rightarrow e^+e^-$ and $\Upsilon \rightarrow \mu^+\mu^-$ decay channels. The resulting

R_{AA} of $\Upsilon(1S)$ vs. number of nucleons participating in a collision (a measure of centrality) N_{part} is shown in Fig. 3 along with the CMS data [13]. These results are compared to a model calculation [14], which includes QGP effects as well as regeneration and CNM effects.

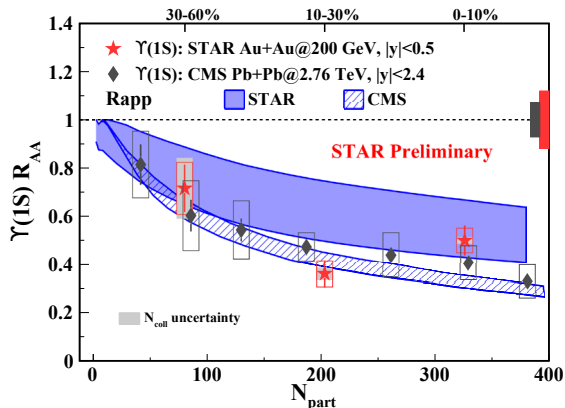


Fig. 3. Nuclear modification factor R_{AA} of $\Upsilon(1S)$ vs. number of participating nucleons N_{part} . The STAR data are compared to CMS results [13] and a model calculation [14].

The R_{AA} of $\Upsilon(2S+3S)$ is shown in Fig. 4 and compared to $\Upsilon(2S)$ measurements by CMS [13] as well as calculations by the same model [14].

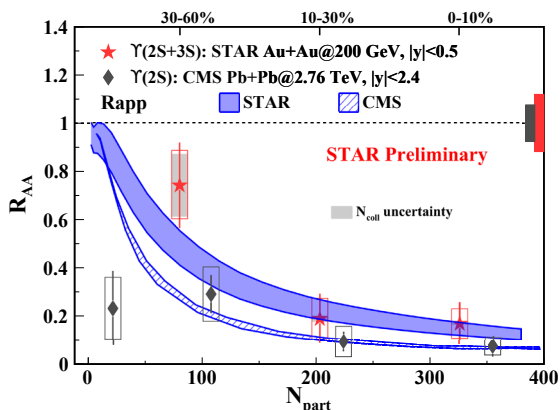


Fig. 4. Nuclear modification factor R_{AA} of $\Upsilon(2S+3S)$ vs. N_{part} . The STAR data are compared to CMS results for $\Upsilon(2S)$ [13] as well as a model calculation [14].

CONCLUSIONS

STAR experiment has measured Υ production in p+p collisions at $\sqrt{s} = 200$ GeV and $\sqrt{s} = 500$ GeV. The $\Upsilon(1S)$ data are well described by CEM model calculation [8] for inclusive $\Upsilon(1S)$, while overestimated by CGC+NRQCD model [9, 10] for direct $\Upsilon(1S)$. The charged particle multiplicity N_{ch} dependence was also studied, by measuring normalized $\Upsilon(1S)/\langle\Upsilon(1S)\rangle$ yield vs. $N_{ch}/\langle N_{ch}\rangle$. Similar trend is observed for $\Upsilon(1S)$ and J/ψ at RHIC and LHC experiments. This suggests similar phenomena happen for these particles even at different collision energies.

In Au+Au collisions at $\sqrt{s_{NN}} = 200$ GeV, the Υ production is measured both in dielectron and dimuon decay channels and the results are combined for better precision R_{AA} calculation. Both R_{AA} of $\Upsilon(1S)$ and $\Upsilon(2S+3S)$ is measured vs. number of participant nucleons N_{part} . The $\Upsilon(1S)$ data show a similar level of suppression at STAR and CMS, despite higher medium temperature reached at CMS. This could point to regeneration or CNM effects playing a role, and better constraints on these effects are needed. It should be also noted that most likely a large fraction of the observed suppression is due to the suppression of the feed-down contributions from the excited states. In central Au+Au collisions, $\Upsilon(2S+3S)$ R_{AA} is smaller than that of $\Upsilon(1S)$, consistent with the expectation of the sequential suppression. The $\Upsilon(2S+3S)$ data indicate a smaller suppression at RHIC than at LHC in peripheral collisions. All these data are qualitatively described by a model calculation [14], which includes the effects of Debye-like screening of color charges in hydrodynamic-modeled QGP with addition of regeneration and CNM effects.

ACKNOWLEDGMENT: This work was also supported from European Regional Development Fund-Project "Center of Advanced Applied Science" No. CZ.02.1.01/0.0/0.0/16-019/0000778 and by the grant LTT18002 of Ministry of Education, Youth and Sports of the Czech Republic.

REFERENCES

1. W. Busza, K. Rajagopal, W. van der Schee, Annual Review of Nuclear and Particle Science **68**, 339 (2018).
2. T. Matsui, H. Satz, Physics Letters B **178**, 416 (1986).
3. S. Chatrchyan, V. Khachatryan et al., Physical Review Letters **109**, 222301 (2012).
4. Z. Lin, C. M. Ko, Physics Letters B **503**, 104 (2000).
5. F. Arleo, S. Peign, Journal of High Energy Physics **122** (2013).
6. R. Vogt, Physical Review C **71** (2005)
7. S. Chatrchyan, V. Khachatryan et al., Journal of High Energy Physics, **4**, 103 (2014).
8. R. Vogt, Physical Review C **92**, 034909 (2015).
9. H. Han, Y.-Q. Ma, C. Meng, H.-S. Shao, Y.-J. Zhang, K.-T. Chao, Physical Review D **94**, 014028 (2016).
10. Y.-Q. Ma, R. Venugopalan, Physical Review Letters **113**, 192301 (2014).
11. J. Adam, L. Adamczyk et al., Physics Letters B **786** 87 (2018).
12. B. Abelev, J. Adam et al., Physics Letters B **712(3)**, 165 (2012).
13. V. Khachatryan, A. M. Sirunyan et al., Physics Letters B **770**, 357 (2017).
14. X. Du, M. He, R. Rapp, Physical Review C **96**, 054901 (2017).

NOVEL HIGH-LUMINOSITY FIXED-TARGET EXPERIMENT AT THE LHC

B. Trzeciak, BarbaraAntonina.Trzeciak@fjfi.cvut.cz, Faculty of Nuclear Sciences and Physical Engineering Czech Technical University in Prague

INTRODUCTION

Extraction of the multi-TeV proton and lead LHC beams with a bent crystal or by using an internal gas target allows one to perform the most energetic fixed-target experiment ever. pp , pd , pA , Pbp and PbA collisions can be studied with high precision and modern detection techniques over a broad rapidity range [1, 2].

A fixed-target mode with the 7 TeV LHC proton and 2.76 A TeV lead beams provides the center-of-mass (c.m.s.) energy per nucleon pair of $\sqrt{s_{NN}} = 115$ GeV for pp , pd and pA and $\sqrt{s_{NN}} = 72$ GeV for Pbp and PbA collisions, and the c.m.s. rapidity boost of 4.8 and 4.2 units, respectively. It offers a variety of polarised and nuclear targets, and high luminosities thanks to dense and long targets. Due to the large rapidity boost, the backward rapidity region ($y_{c.m.s.} < 0$) and so the high- x domain ($x \rightarrow 1$), where x is the momentum fraction of the parton in the target nucleon, are accessible with the standard experimental techniques.

IMPLEMENTATIONS

There are several technical implementations that can be considered in order to realise a fixed-target experiment with the LHC proton and lead beams [1]. The most promising and feasible solutions are: (i) an internal gas target (ii) a bent crystal splitting the beam halo onto an internal gas or a solid target. Both options can be installed in the existing LHCb or ALICE experiments. Feasibility of the possibility (i), however with low gas densities and without the target polarisation option, was already demonstrated by the SMOG system at LHCb [3] and the recently installed SMOG2 system [4]. In the case of the ALICE experiment, studies are ongoing on a possible implementation of a solid target coupled to a bent crystal mounted prior to the ALICE interaction point in the beam halo. Various target types from Be to W are considered with the target length of $\approx 100 \mu\text{m}$ up to 1 cm.

The expected luminosities with both detectors are promising for precise measurements and the ambitious physics program that is described in the next section. Depending on the utilized existing experimental setup and the target location, different $y_{c.m.s.}$ regions can be explored, as shown in Fig. 1 that presents center-of-mass rapidity acceptances for the ALICE and LHCb detectors. For the LHCb fixed-target mode, the target position is at the nominal Interaction Point (IP), i.e. $z_{\text{target}} = 0$, and for two other positions corresponding to $z_{\text{target}} = 0.4$ m and -1.5 m on the opposite side of the spectrometer. For ALICE, the acceptances are shown for a target located at the IP as well as at $z_{\text{target}} = -4.7$ m on the opposite side of the Muon spectrometer. A more detailed review of the possible technical implementations of the project can be found

in [1, 5].

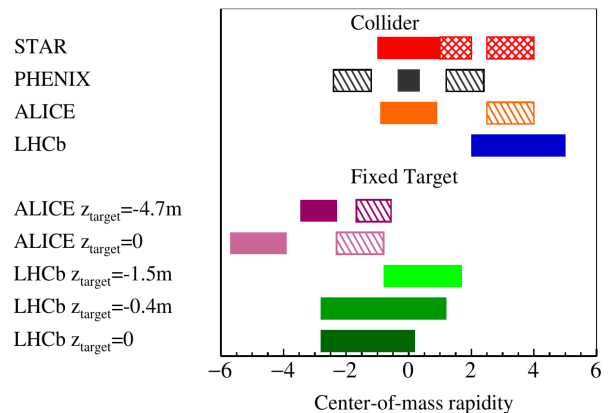


Fig. 1. Comparison of the kinematical coverages of the ALICE and LHCb detectors at the LHC and the STAR and PHENIX detectors at RHIC. For ALICE and LHCb, the acceptance is shown in the collider and the fixed-target modes for a 7 TeV proton beam (rapidity shift $\Delta y = 4.8$). spectrometer. The fully filled rectangles refer to detectors with particle identification capabilities, the double-hatched rectangles to electromagnetic calorimeters and the hatched rectangles to muon detectors. [1]

PHYSICS MOTIVATIONS

A fixed-target experiment utilizing the multi-TeV LHC proton and lead beams would greatly complement the current LHC collider programs, in the new energy domain between the SPS and the nominal RHIC collider energy. The main physics motivations for a fixed-target experiment at LHC are threefold: (i) the high momentum fraction (x) frontier in nucleons and nuclei (ii) the spin content of the nucleons (iii) studies of the hot and dense medium created in ultra-relativistic heavy-ion collisions down to the target rapidity region.

The light-quark parton distribution functions (PDF) in nucleons and nucleus can be probed using Drell-Yan measurements. Production of the open heavy-flavour hadrons and quarkonia is sensitive to the gluon content of the proton and nucleus. Their measurements would allow one to constrain the gluon PDF and nuclear PDF in the region of the high- x where the uncertainties are large [6]. In particular, studies of the still very poorly known gluon EMC effect would be possible with nuclear targets. Figure 2 presents the expected improvement on the gluon nPDF uncertainties, as encoded in nCTEQ15, with D^0 meson R_{pX_e} pseudo-data simulated using an LHCb-like detector setup [1, 7].

Moreover, at the high- x domain the predicted non-perturbative intrinsic source of the heavy-quark contribution of the nucleon [8] can influence the open heavy-flavour production [9]. This contribution can be verified with the proposed fixed-target experiment. These

⁰for the AFTER study group:
http://after.in2p3.fr/after/index.php/Current_member_list

studies are also of particular importance for the high-energy neutrino and cosmic ray physics. In addition, pp collisions with transversely polarised targets allow one to measure the Single Transverse Spin Asymmetries for Drell-Yan and heavy-flavour production, and in this way to access the quark and gluon Sivers functions in order to study the orbital angular momentum in the proton [10].

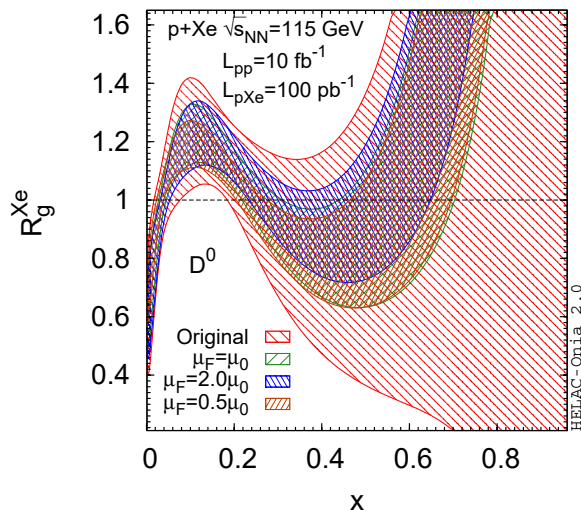


Fig. 2. nCTEQ15 gluon nPDFs (ratio of gluon densities in nCTEQ15/CT14 PDFs) before and after the re-weighting using fixed-target $D^0 R_{pXe}$ pseudo-data from LHCb-like simulations at a scale $Q = 2$ GeV.

A fixed-target program with a proton beam on different nuclear targets enables extensive studies of the Cold Nuclear Matter (CNM) effects, such as the nuclear modifications of the PDFs, energy loss or nuclear absorption in the nuclear medium. Good understanding of the CNM effects from pA collisions would also help in more precise studies of the properties of the deconfined hot and dense medium - Quark Gluon Plasma (QGP) - expected to be created in PbA collisions at $\sqrt{s_{NN}} = 72$ GeV. The wide rapidity coverage of such an experiment would allow one to access the longitudinal expansion of the medium and the phase diagram of the nuclear matter at different values of the baryon chemical potential (μ_B) [11, 12] which would be a complementary approach to the RHIC Beam Energy Scan programs. Measurements of the identified particle yields and azimuthal anisotropies (v_n) as a function of rapidity would help to access the temperature dependence of the medium shear viscosity while probing different energy densities.

Open-heavy flavour and quarkonium production is also of interest here as these probes can provide a good handle on the dynamic and thermodynamic properties of the medium, especially at mid-rapidity ($y_{c.m.s.} \approx 0$) where the yields are the highest [13]. Heavy quarks are created at the very early stage of the heavy-ion collisions in the initial hard scatterings and participate in the whole medium evolution losing their energy via radiative and collisional interactions with the medium. Studies of the sequential suppression of different bottomonium states, $\Upsilon(1S, 2S, 3S)$, have a potential to serve as the *medium thermometer* – with all

the caveats related to the dynamical effects beyond the static Debye-like screening of the $Q\bar{Q}$ potential in the coloured medium, which prevent the usage of the charmonium states as the thermometer.

CONCLUSIONS

In this contribution, we presented a proposal of a high-luminosity fixed-target experiment at the LHC. Possible technical implementations and the ambitious physics program were briefly discussed, more details can be found in the recent review [1].

ACKNOWLEDGMENT: This work was supported from The Czech Science Foundation, grant number: GJ20-16256Y.

REFERENCES

1. C. Hadjidakis et al., Phys. Rept. **527**, 1807.00603 (2018).
2. S. Brodsky et al., Phys. Rept. **522**, 1202.6585 (2013).
3. M. Ferro-Luzzi, Nucl. Instrum. Meth. **A 553**, 388 (2005).
4. LHCb Collaboration, CERN preprint CERN-LHCC-2019-005. LHCb-TDR-020 (2019).
5. C. Barschel et al., (CERN, Geneva - 2020).
6. A. Kusina et al., PoS HardProbes **2018**, 110, 1901.07950 (2019).
7. L. Massacrier et al., Adv. High Energy Phys. **2015**, 986348, 1504.05145 (2015).
8. R.S. Sufian et al., Phys. Lett. **B 808**, 135633 (2020).
9. S. Brodsky et al., Adv. High Energy Phys. **2015**, 231547 (2015).
10. D. Kikola et al., Few Body Syst. **58**, 139 (2017).
11. I. Karpenko, Acta Phys. Polon. **B 50**, 141 (2019).
12. V. Begun et al., Phys. Rev. **C 98**, 034905 (2018).
13. B. Trzeciak et al., Few Body Syst. **58**, 148 (2017).

ALICE - ITS UPGRADE

A. Isakov on behalf of the ALICE Collaboration, isakov@ujf.cas.cz, Nuclear Physics Institute of CAS, Husinec-Řež, CZ 250 68

INTRODUCTION

ALICE is one of the four big high-energy physics experiments, which take data at the LHC in CERN [1]. The main focus of this experiment is to study properties of nuclear matter under extreme energy densities and temperatures, which lead to creation of the quark-gluon plasma. In the upcoming Run 3, ALICE plans to focus on the measurement of open heavy-flavor hadrons, quarkonia, and vector mesons over a wide range of transverse momenta [2]. To achieve these physics goals the ALICE detector is undergoing an upgrade, which will allow for speeding up the readout rate to 100 kHz in Pb–Pb collisions and improving of tracking performance at the transverse momentum resolution in the region below 1 GeV/c.

The vital part of this program is an upgrade of the ALICE silicon vertex detector called the Inner Tracking System (ITS), which will be replaced by a new silicon tracker, entirely based on the ALPIDE monolithic active pixel sensor (MAPS) [3]. Schematic view of the new detector can be seen in Figure 1. The new detector will have seven layers of such pixel sensors, covering a total area of 10 m² segmented in $12.5 \cdot 10^9$ pixels. The 180 nm CMOS technology by TowerJazz, used to produce ALPIDE, enables to integrate a sensitive volume together with parts of front-end electronics in one silicon volume. The ALPIDE sensor has dimensions 3×1.5 cm² and pixel pitch 29×27 μm². The thickness of ALPIDE sensors in the Inner Barrel (IB) and Outer Barrel (OB) of ITS is 50 and 100 μm, respectively. The detector has low material budget (0.35% X_0 /layer for IB, 1.1% X_0 /layer for OB) to suppress multiple scattering for low- p_T particles. The upgraded detector will have radial span from 22 to 394 mm from the interaction diamond.

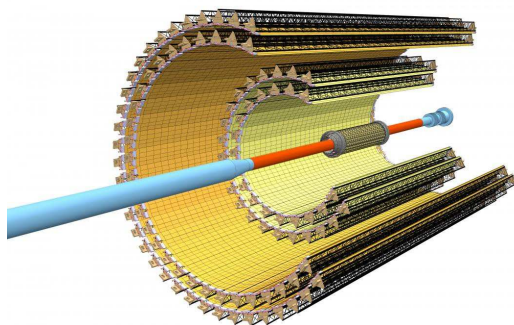


Fig. 1. Sketch of the upgraded ITS. The Inner Barrel is formed by the 3 concentric layers which are around the beam pipe. The Outer Barrel is formed by the 4 outer layers. Taken from [5].

It is expected that ALPIDE sensors of the innermost layer of the IB will obtain throughout Run 3 and Run 4 a Total Ionization Dose (TID) of 270 krad and a Non-Ionizing Energy Losses (NIEL) of $1.7 \cdot 10^{12}$ 1 MeV n_{eq} cm⁻² [5]. The project requires that the

sensors have to sustain radiation loads which are 10 times higher, while keeping keeping detection efficiency more than 99% and low value of fake-hit rate less than 10^{-6} hits/pixel/event. The radiation hardness of the ALPIDE sensor was tested using a 30 MeV proton beam from the cyclotron U-120M located in the Nuclear Physics Institute of the Czech Academy of Sciences [4]. After the accumulation TID of 2.7 Mrad, the irradiated sensor still meets project requirements on detection efficiency and noise level.

More details about the radiation hardness study of ALPIDE sensors can be found in [5].

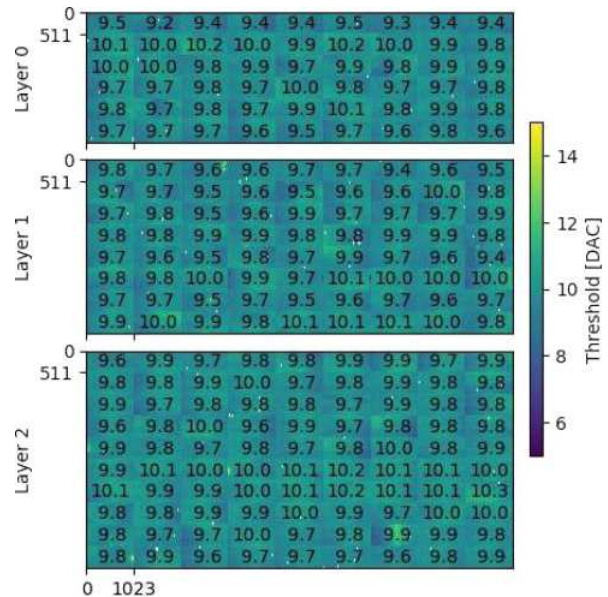


Fig. 2. Threshold map of the tuned ALPIDE sensors in the bottom half of the Inner Barrel. Threshold value is measured in DAC units, 1 DAC equals 10 e^- . Taken from [6].

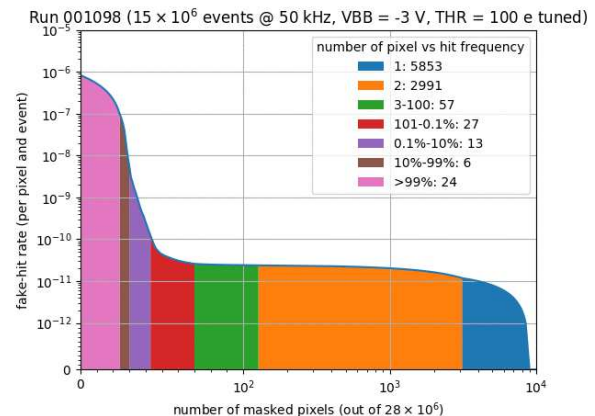


Fig. 3. Measurements of fake-hit rate for the half-layer 0 of IB, when masking a given number of the noisiest pixels. Taken from [6].

COMMISSIONING

The current status of the detector construction can

be described as follows. All half barrels of the detector are completed. Since February 2020 they are connected to services (cooling, readout etc.). The detector is undergoing a commissioning stage in an on-surface laboratory at CERN. The ITS commissioning carries out complete testing of the detector performance before its installation inside the ALICE cavern. It includes threshold scans, tests of noise performance, and measurements of temperatures and currents during detector operation and verification of time stability of those parameters. Figures 2 and 3 illustrate performance of the ITS IB during commissioning. The figure 2 presents the situation after the tuning, which enabled to achieve a uniform level of threshold for all IB sensors. Figure 3 shows evolution of fake hit rate when a given number of the noisiest pixels was masked out. Masking out the noisiest pixels significantly decreased the initial noise level. After removing of 41 problematic pixels, the noise level of 10^{-10} hits/pixel/event was achieved.

Since each half layer of ITS has overlapping staves, this geometry enables to reconstruct cosmic particle trajectories. During the early commissioning stage, the reconstruction of cosmic tracks was performed using an IB half-barrel. This measurement can be used to validate the correct chip alignment. Figure 4 shows a sketch to demonstrate how the track reconstruction is performed with a single half-layer.

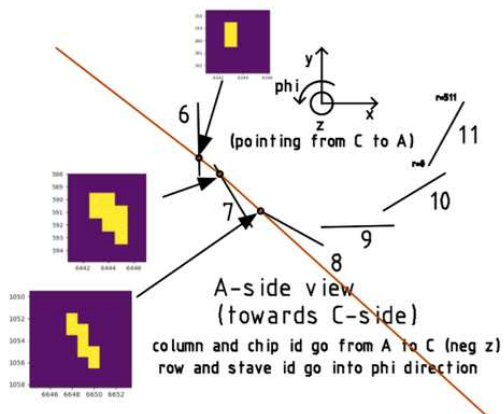


Fig. 4. Track reconstruction procedure for the first cosmic ray provided by the measurement in the half-layer 0 of the IB. Taken from [6].

CONCLUSIONS

In summary, the ALICE detector is undergoing a major upgrade to meet the requirements of the new physics program in the upcoming Run 3. The cornerstone of this upgrade is the replacement of the ITS by a new detector based on ALPIDE sensor. The new detector will enable to improve tracking efficiency for the low- p_T tracks and increase statistics for rare events. Currently, the ITS upgrade is approaching its final stage, and on-surface commissioning already has validated the stability of the detector parameters, such as temperature, currents, noise level, and chip alignment. The final installation of new ITS in the

ALICE cavern is scheduled for January 2021 with expected start of data taking in 2022.

ACKNOWLEDGMENT: This research was funded by the Ministry of Education, Youth, and Sports of the Czech Republic, grant number LTT17018.

REFERENCES

1. K. Aamodt et al. (ALICE Collaboration), JINST **3**, S08002 (2008).
2. B. Abelev et al., (The ALICE Collaboration), J. Phys. G: Nucl. Part. Phys. **41**, 087001 (2014) .
3. G. A. Rinella et al., (The ALICE Collaboration), Nucl. Instrum. Meth. **A 845**, 583 (2017).
4. F. Krizek et al., Nucl. Instr. Meth. Phys. Res. **A 894**, 87 (2018).
5. S. Kushpil et al., IEEE TNS **66**, 2319 (2019).
6. S. Kushpil et al., Nucl. Instrum. Meth. **A 979**, 164421 (2020).

OPEN-CHARM AND CHARM-TAGGED-JET PRODUCTION WITH ALICE AT LHC

J. Kvapil, jakub.kvapil@cern.ch, School of Physics and Astronomy, the University of Birmingham, Edgbaston, Birmingham, UK. B15 2TT

Charm quarks are mostly produced in hard partonic scattering processes in the early stages of hadronic collisions. Because of their large mass, their production cross section can be calculated using perturbative quantum chromodynamics down to zero transverse momentum p_T . Moreover, the study of the charm baryon-to-meson ratio provides unique information on the hadronisation mechanism. Measurements of charm-tagged jets add further information on the charm-quark fragmentation.

RESULTS

The ratio of the p_T -differential cross sections of Λ_c^+ baryon and D^0 meson in pp collisions at $\sqrt{s} = 13$ TeV is shown in Fig. 1 for two intervals of charged-particle multiplicity. The data show strong p_T and multiplicity dependence and are described within uncertainties by a tune of PYTHIA8 with colour reconnections beyond the leading colour approximation [1, 2]. On the other hand, the default version of PYTHIA8 [3], which is tuned to reproduce data from e^+e^- collisions, underestimate the ratios and does not reproduce their multiplicity dependence.

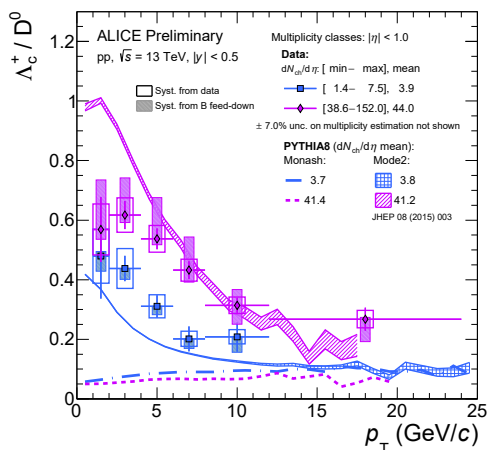


Fig. 1. The p_T -differential Λ_c^+/D^0 ratio for two multiplicity intervals in pp collisions at $\sqrt{s} = 13$ TeV compared to the default PYTHIA8 tune [1, 3] and to a tune with colour-reconnection beyond leading colour approximation [2].

The baryon-to-meson ratios $\Sigma_c^{0,+,++}/D^0$ and $\Xi_c^{0,+}/D^0$ are shown in Fig. 2 and 3, respectively. The PYTHIA8 tune with colour reconnection beyond leading-colour approximation describes the $\Sigma_c^{0,+,++}/D^0$ ratio, while it underestimates the $\Xi_c^{0,+}/D^0$ one. Jets are reconstructed using the anti- k_T algorithm and are tagged as D^0 -meson or Λ_c^+ -baryon jets if they contain a fully reconstructed D^0 meson or Λ_c^+ baryon. The parallel jet momentum frac-

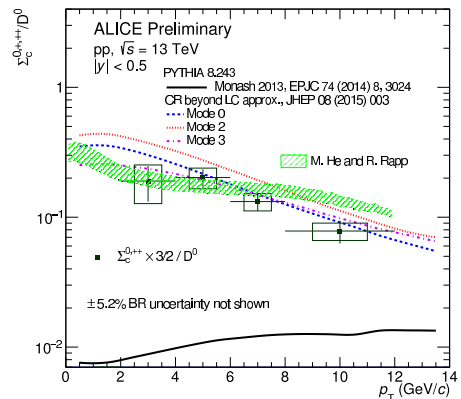


Fig. 2. The p_T -differential $\Sigma_c^{0,+,++}/D^0$ ratio in pp collisions at $\sqrt{s} = 13$ TeV compared to the default PYTHIA8 tune [1, 3] and to a tune with colour-reconnection beyond leading colour approximation [2].

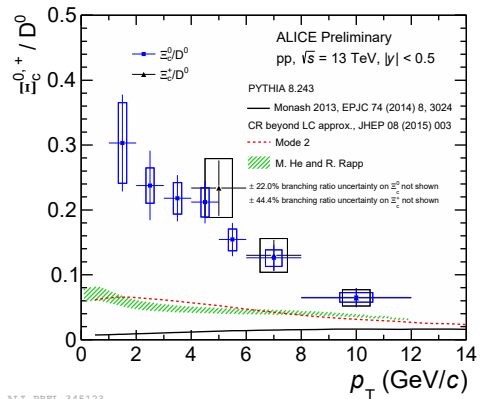


Fig. 3. The p_T -differential $\Xi_c^{0,+}/D^0$ ratio in pp collisions at $\sqrt{s} = 13$ TeV compared to the default PYTHIA8 tune [1, 3] and to a tune with colour-reconnection beyond leading colour approximation [2].

tion, $z_{\parallel}^{ch} = \frac{\vec{p}_D \cdot \vec{p}_{ch,jet}}{p_{ch,jet} \cdot p_{ch,jet}}$, is proportional to the emitted angle of the heavy-flavour particle with respect to the jet axis. The z_{\parallel}^{ch} probability densities of D^0 -tagged jets with $5 < p_{T,jet} < 7$ GeV/c and Λ_c^+ -tagged jets with $7 < p_{T,jet} < 15$ GeV/c for pp collisions at $\sqrt{s} = 13$ TeV are shown in Fig. 4 and 5, respectively. The POWHEG+PYTHIA6 model predicts harder fragmentation than the measured ones. In addition, the data favour models with colour reconnections beyond leading colour approximation.

One of the fundamental QCD effect is the so-called “dead-cone” [6], which suppresses gluon radiation at small angles with respect to the quark direction for massive quarks. Jets are declustered to access the hard

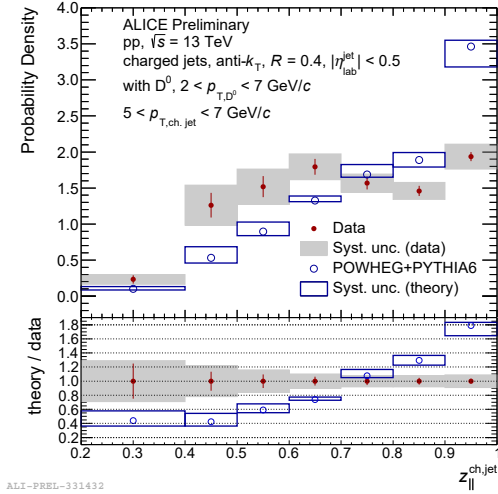


Fig. 4. Probability density distribution of the jet momentum fraction, z_{\parallel}^{ch} , carried by D^0 mesons measured in pp collisions at $\sqrt{s} = 13$ TeV for $5 < p_{T, \text{jet}} < 7$ GeV/c compared to POWHEG+PYTHIA6 predictions [4, 5].

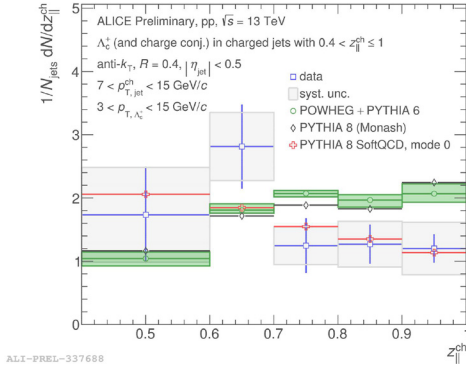


Fig. 5. Probability density distribution of the jet momentum fraction, z_{\parallel}^{ch} , carried by Λ_c^+ baryon measured in pp collisions at $\sqrt{s} = 13$ TeV for $7 < p_{T, \text{jet}} < 15$ GeV/c compared to expectations from POWHEG+PYTHIA6 [4, 5] and PYTHIA8 [1, 2, 3].

partonic splitting and the ratio of splittings angle distribution for D^0 -tagged and inclusive jets is reported in Fig. 6. Splittings with small angle are suppressed for D^0 -tagged jets with respect to inclusive jets. This is the first direct evidence of dead-cone at hadron colliders. Another consequence of the dead-cone effect, visible in Fig. 7, is the smaller number of leading-parton splittings n_{SD} for D^0 -tagged jets with respect to inclusive jets.

CONCLUSION

The hadronization of charm quarks is different in e^+e^- and in pp collisions and, in the latter, depends on the multiplicity of charged particles produced in the event. A tune of PYTHIA8 with colour reconnection beyond leading-colour approximation describes well the Λ_c^+/D^0 and $\Sigma_c^{0,+,++}/D^0$ baryon-to-meson ratios, while it fails to reproduce the $\Xi_c^{0,+}/D^0$ one. In

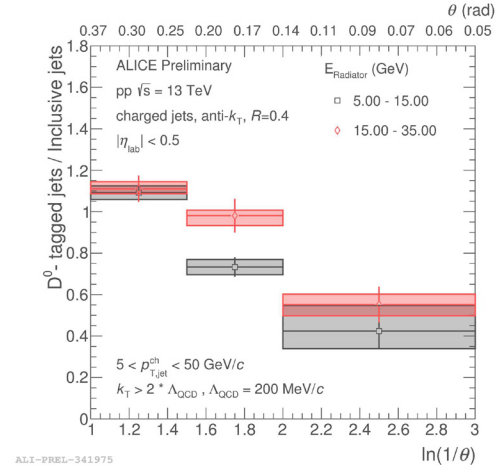


Fig. 6. Ratio of the splitting-angle distributions of D^0 -tagged jets and inclusive jets in pp collisions at $\sqrt{s} = 13$ TeV.

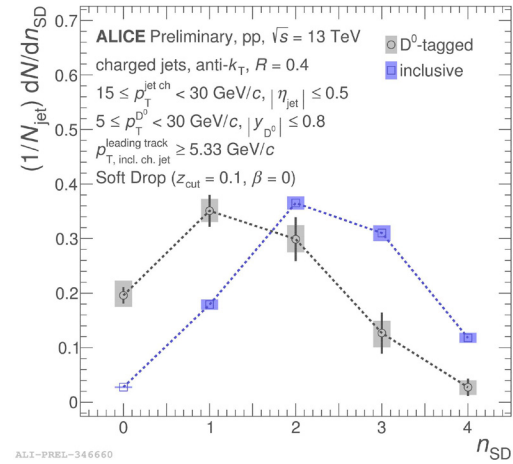


Fig. 7. Number of leading-parton splittings n_{SD} in pp collisions at $\sqrt{s} = 13$ TeV for D^0 -meson tagged and inclusive jets.

general, models predict harder fragmentation of charm quark in jets than what observed in data. Finally, the charm quark in jets splits less in comparison to inclusive jets mainly because of the dead-cone effect.

REFERENCES

1. T. Sjostrand, S. Mrenna, P. Z. Skands, Comput. Phys. Commun. **178**, 852 (2008).
2. J. R. Christiansen, P. Z. Skands, JHEP **08**, 003 (2015).
3. B. Andersson : The Lund Model. In: Cambridge Monographs on Particle Physics, Nuclear Physics and Cosmology (Cambridge University Press - 1998).
4. T. Sjostrand, S. Mrenna, P. Z. Skands, JHEP **05**, 026 (2006).
5. S. Frixione, P. Nason, C. Oleari, JHEP **11**, 070 (2007).
6. Y. Dokshitzer, V. Khoze, S. Troyan, Journal of Physics G: Nucl. Part. Phys. **17**, 1602 (1999).

ANALYSING MYSTERIOUS TURBULENCE

D. Duda, dudad@kke.zcu.cz, V. Yanovych, yanovichvitaliy@i.ua, V. Uruba, uruba@kke.zcu.cz, University of West Bohemia, Univerzitní 22, Pilsen Czech Republic

INTRODUCTION

It is often said that turbulence is the last unsolved problem of classical physics [1]. This is caused by its enormous complexity resulting from the mutual interactions of large number of *objects* of different sizes and strengths – the *vortices* and other *coherent structures*.

The classical definitions often mention the chaotic behavior [2]. In fact, turbulence is not chaotic: the laminar flow is chaotic, as the random thermal molecular motion averages out and the large-scale flow is governed only by external forces. In the case of turbulence, the molecular motion is organized over large distances (in comparison with molecular scale); the motion of molecules in one part of a vortex is connected with the opposite motion in the second part of this vortex. Therefore the entropy of the turbulent flow is smaller than that of corresponding laminar flow. The rise of turbulence (i.e. system of organized interacting structures) from the laminar flow (uniform motion, random at micro-scale) is one example of the *self-organization* problem [3]. The decreased entropy of the vortex system leads to faster increasing of total entropy as the organized structures are much more effective in mixing and transport of momentum or heat than the molecular diffusion alone.

We see the turbulence as an random chaotic process just because we do not understand it. Lets use a parable: imagine You are listening a speech in some language unknown for You. First You hear only a *chaotic* sequence of sounds, which is clearly different from *white noise*. As You study that language, You are able to recognize individual vocals, later on the words and even later the sentences carrying information. The idea of chaos comes never more into Your mind.

Contemporary methods of studying turbulent flows are mainly based on measuring some average quantity (velocity, pressure) and its variance or higher statistical moments. More advanced studies use frequency analysis (spectra [4]), correlation or structure functions [5] and powerful Eigen-decompositions (e.g. proper orthogonal decomposition POD [6]). In the light of the above mentioned parable, such trials of understanding are naive.

Therefore, we slowly develop an algorithm for identification of individual vortices. The idea is based on the assumption, that vortices are dominant coherent structures in the turbulent flow, thus the induced velocity field produced by the set of vortices might reconstruct the original measured velocity field. The properties of individual vortices (i.e. their fitting parameters: position, radius and circulation) are studied statistically.

MEASUREMENT OF TURBULENT FLOWS

We use the method of Particle Image Velocimetry (PIV), which is based on direct optical observation

of movement of small particles carried by the moving fluid. This method measures the instantaneous velocity in the entire field of view of a camera at the same moment. Therefore, this method is ideal for studying the coherent structures in the flow.

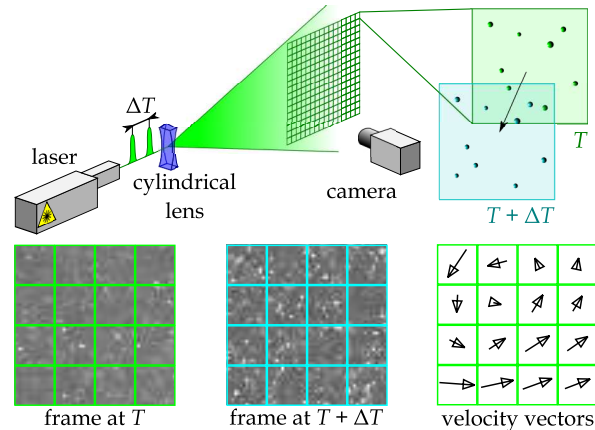


Fig. 1. The schematical sketch of the PIV method.

The particles (droplets of oil in our case) are illuminated by double pulsed laser, whose beam is defocused in one direction into a light sheet, as it is sketched in Figure 1. The pair of light pulses is separated in time by few microseconds and the shift of particles during this short time delay is measured. The higher velocity of particles, the smaller time delay is needed.

The spatial resolution depends on the used optics, but the field of view to the smallest recognizable scale (the grid size of the velocity vector array) to the field of view is in order of $\sim 10^1 - 10^2$, typically 32, 64 or 128; in the presented data we used 64. This ratio is definitely quite small in comparison with the possibilities of numerical simulations or with the needs of a real engineering applications.

INDIVIDUAL VORTEX IDENTIFICATION

Having the measured data in the form of a regular array of velocity vectors in a planar cut of 3D flow, we identify individual vortices by direct fitting the velocity array by Gauss vortex model. There are four fitting parameters: position x and y , vortex core radius R and circulation Γ . More technical details about the algorithm can be found in our article [7].

The instantaneous field of velocity fluctuations obtained by the PIV methodology and Reynolds decomposition¹ is further decomposed into the velocity field of finite number of individual macroscopic vortices plus the rest. The example is in Fig. 2. The rest contains the noise and the coherent structures, which are not vortices (e.g. divergent areas and areas of uniform motion), therefore its spectrum is flatter, but not entirely. It would be flat, if it contained white noise only.

¹fluctuating velocity $\mathbf{u}' = \mathbf{u} - \langle \mathbf{u} \rangle_T$.

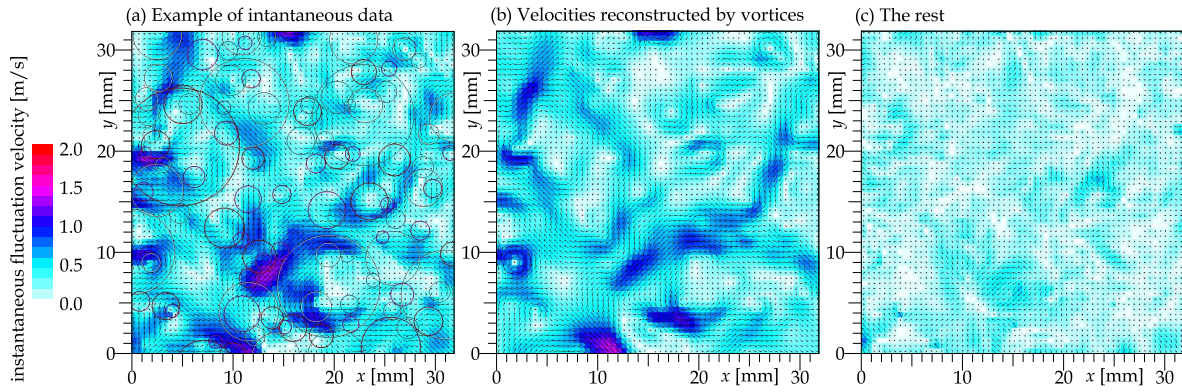


Fig. 2. Example of a single velocity field together with identified individual vortices (a), the velocity field of the vortices (b) and the remaining not covered by the vortices (c). Data is taken 76 mm, i.e. $4.7M$ from the grid of mesh parameter $M = 15.6$ mm.

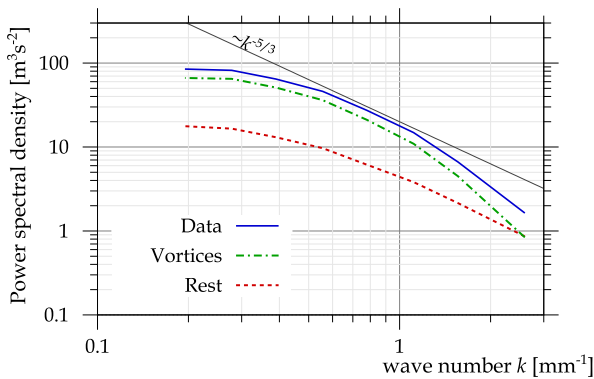


Fig. 3. Spatial spectrum [4] of original data (blue solid line), velocity field reconstructed by vortices (green dash-dotted line) and the rest (red dotted line). The black line represents the Kolmogorov scaling $k^{-5/3}$.

The instantaneous field of velocity fluctuations are presented in Fig. 3.

Fig. 4 shows the distribution of radii of vortices found in the example above. The number of larger vortices decreases as $\sim R^{-2.2}$ later with as $\sim R^{-3}$, while the distribution of small vortices falls very rapidly, as the majority of energy is carried by the larger vortices. With the increasing distance from the grid, there is no change in that distribution shape, only the location of the maximum shifts toward larger vortices. This is caused simply by the fact, that turbulence decays from bottom, i.e. the integral lengthscale grows with distance [8].

CONCLUSIONS

We introduce a new method of individual vortex identification and we use it to study turbulent flows from a different point of view than the standard ways based on mathematical processing of point velocities.

ACKNOWLEDGMENT: We thank for support to student Project SGS-2019-021

REFERENCES

1. U. Frisch: Turbulence: The Legacy of A. N. Kol-

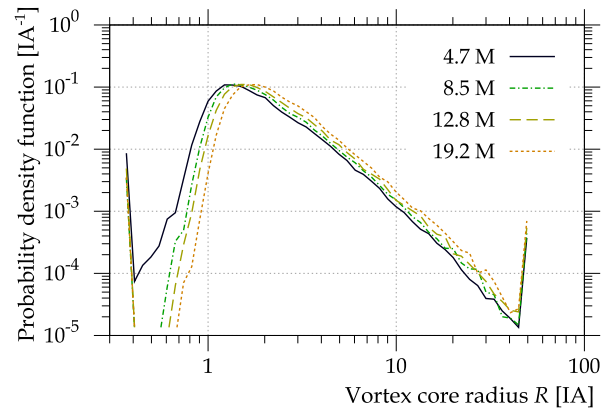


Fig. 4. Distribution of core radii of identified vortices. Black line represents vortices found in the example above, green does that at distance 133 mm = $8.5M$ from the grid, yellow at 200 mm = $12.8M$ and orange at 300 mm = $19.2M$. The peaks at the edges of the plot represents events out of the explored interval.

mogorov (Cambridge University Press, Cambridge - 1995).

2. S. B. Pope: Turbulent flows (Cambridge University Press, Cambridge - 2000).
3. D. Barkley et al: The rise of fully turbulent flow, Nature **526**, 550 (2015).
4. D. Duda, V. Uruba, ASME J. of Nuclear Rad. Sci. **5**, 030912 (2019).
5. E. O. Schulz-DuBois, I. Rehberg, Applied Physics **24**, 323 (1981).
6. V. Uruba, Entropy **21**, 2 (2019).
7. D. Duda, Topical Problems of Fluid Mechanics **2020**, 56 (2020).
8. T. Kurian, J. H. M. Fransson, Fluid Dynamics Research **41**, 021403 (2009).

EXPERIMENTAL STUDY OF EMERGENT GROUND STATE BEHAVIOUR IN RENi₅ (RE = Ce, Yb, Gd) SYSTEM

A. Dzubinska^{1,2}, andrea.dzubinska@upjs.sk, M. Reiffers³, M. Giovannini⁴, J. Rodríguez Fernández², R. Varga¹, J. I. Espeso², J. C. Gómez Sal²

¹CPM-TIP, UPJS, 040 11 Kosice, Slovakia

²Departament of CITIMAC, Faculty of Sciences, University of Cantabria, 390 05 Santander, Spain

³Faculty of Humanities and Natural Sciences, Presov University, 081 16 Presov, Slovakia

⁴Department of Chemistry, University of Genova, Via Dodecaneso 31, 16146 Genova, Italy

INTRODUCTION

In the early years of the 20th century, the study of physical properties in the low temperature range has started to develop. It is related to the emergent behaviour of matter due to the laws of quantum mechanics. Mentioned phenomena can be observed in the systems based on lanthanides and actinides [e. g. 1,2]. Because of the special properties of cerium (Ce) and ytterbium (Yb) and strongly correlated electron systems, new emergent anomalous behaviour can be under scientific attention.

Motivation for the study of RENi₅ (RE = Ce, Yb, Gd) system is the knowledge of ground state evolution among 3 different systems. One could expect the emergent behaviour arising due to existence of different physical interactions which could be connected with e.g. spin fluctuations, quantum criticality, Kondo effect or magnetocaloric effect. Their mutual competing can be tuned by magnetic field or pressure.

In this paper we experimentally studied magnetic and transport properties of substituted (Ce/Yb/Gd)Ni₅. On the other hand, we are working with other systems, where Ni atom is substituted by Cu, Pd or In. Prepared compounds are good candidates for the study of physical properties at low temperature regime.

EXPERIMENTAL DETAILS

The polycrystalline samples were prepared by two different methods. The first, samples with Ce and Gd were created by arc melting under pure argon. The second group consist from Yb-based material, where the single elements were enclosed in a tantalum crucible. After that, the crucible was sealed by arc welding under pure argon. Process of sample preparation was chaired by induction furnace under a stream of pure argon again.

The structural analysis has been studied by X-ray Bruker D8 Advance diffractometer and the surface analysis has been performed by Scanning electron microscope with X-ray energy dispersive spectroscopy system. Physical properties were studied by commercial device DynaCool (Quantum Design) in the temperature range in 2 K – 300 K with an applied magnetic field up to 9 T. Some of experiments need lower temperatures and Helium-3 refrigerator in the temperature range 40 mK – 300 K with applied magnetic field up to 9 T was used.

EXPERIMENTAL RESULTS AND DISCUSSION

During the investigation process mostly single-

phase samples have been prepared. This fact supports results plotted in Fig. 1, where the selected materials as an example of studied series is shown.

Fig. 1. shows the morphological analysis of two polycrystalline material prepared in two different ways. On the left, there is SEM image of Ce_{0.85}Gd_{0.15}Ni₅ bulk sample. The right side represents SEM morphological analysis of polycrystalline Yb_{0.8}Lu_{0.2}Cu₄Ni. The tables below them are the evidence, that the samples have required stoichiometric ratio.

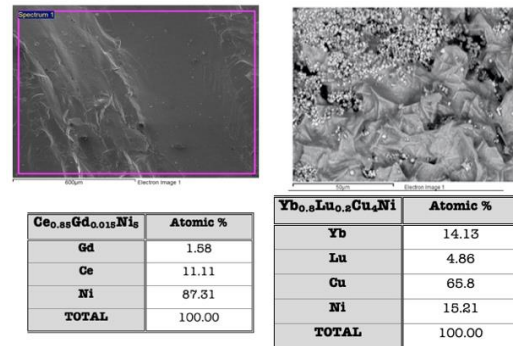


Fig. 1. SEM images of two selected polycrystalline samples.

Left side - Ce_{0.85}Gd_{0.15}Ni₅ and right side - Yb_{0.8}Lu_{0.2}Cu₄Ni. Obtained results are the evidence and summarized in the table below pictures, that sample has required stoichiometric ratio

From the structural point of view, there were observed several crystal structures depending on material. All of samples from RENi₅ (RE = Ce, Yb, Gd) crystallize in a hexagonal crystal structure of CaCu₅, so the Vegard law can be applied (see Fig.2.). The situation, where Ni atom is substituted by Cu, is different. Here were detected mixture of cubic MgCu₄Sn and its superstructure.

Magnetic measurements show magnetic ordering in whole prepared series of samples in studied system, except of CeNi₅, which is known as Stoner enhanced paramagnet. For the Gd_{1-x}Ce_xNi₅ system, where x = 0; 0.2; 0.5 and 0.8 an effective paramagnetic moment (μ_{eff}) and the value for saturation magnetization M_{SAT} were determined (TAB. 1). Increasing content of Ce decreases the value of M_{SAT} . However, the calculations taking the free ion values of Ce³⁺ and Gd³⁺ into account, gives the higher values than the experiment. In case of CeNi₅ there is no magnetic ordering and M_{SAT} does not exist. The possible explanation is that there are the non-magnetic Ce⁴⁺ ions in some positions presented. Experimentally determined valency of CeNi₅ varied from 3 to 3.5 [3].

Magnetic properties for samples based on Yb were investigated also. The most interesting results from these materials are plotted in Fig. 3. A broad

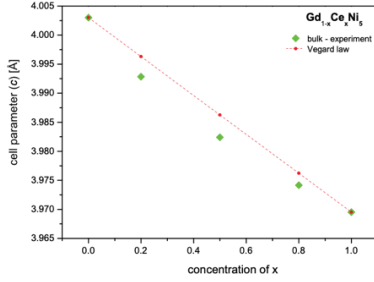


Fig. 2. The comparison of Vegard's law (red symbols) and obtained experimental data (green symbols) for bulk compounds of $Gd_{1-x}Ce_xNi_5$ system.

TAB. 1 The results of μ_{eff} and M_{SAT} of $Gd_{1-x}Ce_xNi_5$ system, where $x = 0; 0.2; 0.5$ and 0.8

$Gd_{1-x}Ce_xNi_5$	$x = 0$	$x = 0.2$	$x = 0.5$	$x = 0.8$
EFFECTIVE MAGNETIC MOMENT				
$Gd^{3+} = 7.94 \mu_B$ and $Ce^{3+} = 2.54 \mu_B, Ce^{4+} = 0 \mu_B$				
theory	$\mu_{eff} = 7.94$ $\mu_B/f.u.$	$\mu_{eff} = 6.86$ $\mu_B/f.u.$	$\mu_{eff} = 5.24$ $\mu_B/f.u.$	$\mu_{eff} = 3.62$ $\mu_B/f.u.$
experiment	$\mu_{eff} = 7.92$ $\mu_B/f.u.$	$\mu_{eff} = 7.16$ $\mu_B/f.u.$	$\mu_{eff} = 6.06$ $\mu_B/f.u.$	$\mu_{eff} = 4.33$ $\mu_B/f.u.$
SATURATION MAGNETIZATION M_{SAT} for $B = 9 T$				
$Gd^{3+} = 7 \mu_B$ and $Ce^{3+} = 2.14 \mu_B, Ce^{4+} = 0 \mu_B$				
theory	$M_{SAT} = 7$	$M_{SAT} = 5.588$	$M_{SAT} = 5.865$	$M_{SAT} = 3.002$
experiment	$M_{SAT} = 6.397$	$M_{SAT} = 5.421$	$M_{SAT} = 3.513$	$M_{SAT} = 1.33$

maximum is visible at temperatures close to 24 K. And this behavior is in an agreement with [4]. Moreover, the asymmetric shape of maximum with a tail at higher temperatures is probably due to the spin fluctuation effect [5]. It means, that alloy and compounds with multiple magnetic transitions might create new materials to attain magnetic refrigeration technology in broad temperature range with comparison of classical materials.

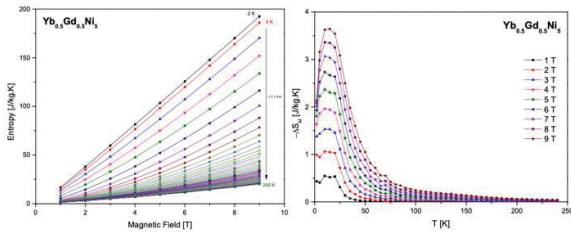


Fig. 3. Field dependences MCE data at different temperatures of $Yb_{0.5}Gd_{0.5}Ni_5$ (on the left). $-\Delta S_M(T)$ for the $Yb_{0.5}Gd_{0.5}Ni_5$ alloy for various magnetic field changes (on the right).

The magnetic field dependences of electrical magnetoresistivity (MR) for different temperatures for all samples are presented in Fig. 4. The magnetoresistance has been calculated from the field dependence of the resistivity data using the formula:

$$\frac{\Delta\rho}{\rho} (\%) = \frac{\rho(B) - \rho(0)}{\rho(0)} \times 100 \quad (1)$$

where $\rho(0)$ and $\rho(B)$ are the resistivities measured in various applied magnetic fields. All magnitudes are negative, except for $Gd_{0.8}Ce_{0.2}Ni_5$ compound at $T = 2 K$. Here, MR has a positive value.

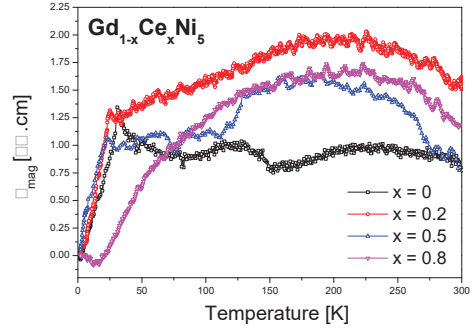


Fig. 4. $\rho_{mag}(T)$ of $Gd_{1-x}Ce_xNi_5$ ($x = 0; 0.2; 0.5$ and 0.8 system at $B = 0 T$).

Electrical transport properties for $Ce_{0.5}Yb_{0.5}Ni_5$ compound show that despite the maximum observed at heat capacity measurements ($T_c = 0.8 K$), electrical resistivity does not show the signs of transition temperature. The metal behaviour is detected.

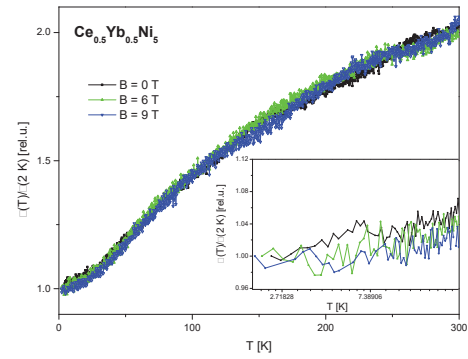


Fig. 5. Electrical resistivity measurements of $Ce_{0.5}Yb_{0.5}Ni_5$ compound. Inset shows low temperature detail in logarithmic scale.

CONCLUSIONS

This work deals with magnetic and transport properties study of emergent ground state behaviour mostly in $RENi_5$ ($RE = Ce, Yb, Gd$) system, where common factor is a rare earth. Collected experimental data show, that substitution of rare earth atoms in a compound has very important role. An interesting physical property can be observed due to acquired information.

ACKNOWLEDGMENT: This work was supported by the projects APVV-16-0079, VEGA 1/0611/18, VEGA 1/0053/19.

REFERENCES

1. Q. Si, F. Steglich, *Science* **329**, 1161 (2010).
2. G. R. Stewart, *Rev. Mod. Phys.* **73**, 797 (2001).
3. S. Raaen, R. D. Parks, *Solid State Commun.* **48**, 2 (1983).
4. A. Bajorek, G. Chełkowska, A. Chrobak, *Intermetallics* **32**, 384 (2013).
5. T. P. Rashid et al., *J. Applied Phys.* **122**, 093903 (2017).

MICROSTRUCTURE OF STEELS STUDIED BY MÖSSBAUER SPECTROMETRY

D. Košovský, xkosovsky@stuba.sk, M. Miglierini, marcel.miglierini@stuba.sk, Slovak University of Technology, Institute of Nuclear and Physical Engineering, Ilkovičova 3, 812 19 Bratislava, Slovakia, T. Kmječ, kmjec@mbox.troja.mff.cuni.cz, Charles University, V Holešovičkách 2, 180 00 Praha, Czech Republic

Steel is a material that is frequently found in general constructions of various components. In this research, we focus primarily on steel used in nuclear industry. In a long term, the material from which parts of a primary cooling circuit are constructed, has to withstand stresses stemming from different effects including high doses of radiation. At the same time, there is high temperature and pressure gradient in the walls of a reactor pressure vessel. Because of these effects, there is a need for detailed description of the steel's microstructure. To find out the attributes and to diagnose the structure of metallic materials, a large amount of nuclear-physical methods can be applied. One of the most sensitive is the Mössbauer spectroscopy. It makes use of nuclear properties of ^{57}Fe which belongs to the one of the most abundant elements in steels. This method is suitable mostly because of its high sensitivity as well as suitability to monitor hyperfine interactions. Using the Mössbauer spectra, we can determine e.g., valence states of Fe atoms, density of s-electrons and effective hyperfine magnetic fields created at the resonating nuclei [1]. The present study forms a background for the investigation of microstructural features of steels that are used in nuclear industry. In doing so, we have to prepare suitable fitting model for evaluation of the obtained Mössbauer spectra. This can be achieved by employing the results of the fitting applied to a model system. The latter is represented by a binary Fe-Cr alloy with well-defined Cr contents ranging from 1 at. % up to 50 at. %.

The original Fe and Cr material was melted using an arc in a vacuum apparatus with a copper matrix. After cooling down, the ingot had a homogenous structure and was shaped like a lens with a diameter of 20 mm and height of 10 mm. Next, the ingot was cut using a metallographic saw into discs with a thickness of 0.5 mm. Afterwards, the discs were ground with sandpapers and polished to mirror-like surface. Conversion electron Mössbauer spectroscopy (CEMS) measurements were carried out on a polished surface of the samples. A standard Mössbauer spectrometer with constant acceleration and equipped with a radioactive source of $^{57}\text{Co/Rh}$ was used. The values of isomer shifts are quoted with respect to the centre of the Mössbauer spectrum of an $\alpha\text{-Fe}$ calibration foil recorded at room temperature. The first approach of evaluation of Mössbauer spectra of Fe-Cr alloys with various Cr concentrations is based on binomial distribution. Using this theoretical model in a fitting software Confit [2] we have used input parameters such as line intensity, hyperfine field, line width and isomer shift of the particular spectral component as fitted variables. In order to obtain the number of individual spectral components, we had to first calculate the probability of Cr atoms occurrence in the BCC structure. This probability for the first nearest neighbour (NN) shell (1NN – denoted as m) and the second 2NN shell (n) is

$$P(m, n) = c_1 c_2 x^{(m+n)} (1-x)^{(Z_1+Z_2-(m+n))} \quad (1)$$

Coefficients c_1 and c_2 in equation (1) are given by a combination number that depends on the maximum and the actual number of Cr atoms in 1NN and 2NN, respectively. The mean value of hyperfine magnetic field $\langle B \rangle$ and isomer shift $\langle IS \rangle$ can be calculated as:

$$\langle B \rangle = \sum_{m,n} [P(m, n) B(m, n)] \quad (2.1)$$

$$\langle IS \rangle = \sum_{m,n} [P(m, n) IS(m, n)] \quad (2.2)$$

Probability values $P(m, n)$ give information about the number of components (sextets) that have to be taken into account. With rising concentration of Cr there is a need for higher number of sextets. The mean value of hyperfine magnetic field and isomer shift depends on concentration of Cr. In our case, Cr linearly decreases both quantities according to equ. (3) [3, 4]:

$$B(m, n) = B_0 - m\Delta B_1 - n\Delta B_2 \quad (3.1)$$

$$IS(m, n) = IS_0 - m\Delta IS_1 - n\Delta IS_2 \quad (3.2)$$

Taking the results of the calculated probabilities $P(m, n)$ into account and assuming that only spectral components with their relative area $> 2\%$ can be identified in the corresponding Mössbauer spectra, the number of sextets used for evaluation of the spectra varied from 2 (for 1 at. % Cr) up to 20 (for 50 at. % Cr).

Mössbauer spectrum of the sample with 2 at. % Cr is shown in Fig. 1 together with its three individual spectral components as an example of the applied fitting procedure for low concentrations of Cr based upon binomial distribution.

For binary iron alloys with high concentration of Cr the number of sextets as derived from binomial distribution is quite high and so is the number of the fitted variables. Thus, the fitting procedure might

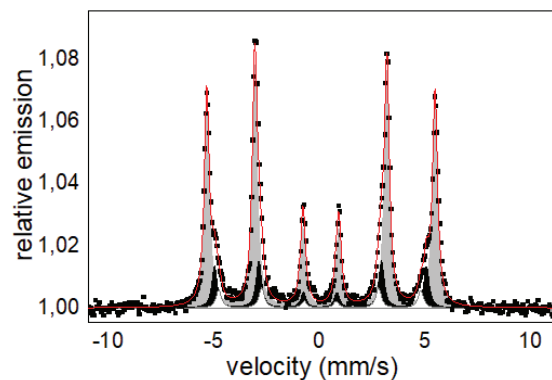


Fig. 1. Mössbauer spectrum of a Fe-Cr binary alloy with 2 at. % Cr measured by CEMS

become unstable. For this reason, we have applied a model, which considers Gaussian distribution of hyperfine magnetic fields rather than a discrete number of many sextets. Using this distribution, we have evaluated spectra with 25 and 50 at. % Cr. To interpret them, we have employed three distributed sextets. The first determining sextet had a fixed intensity $A_{31} = 0.333$ and a free intensity A_{21} . Line width was set to 0.25 mm/s. The following dependent sextets had, besides fixed widths, also fixed intensity ratio according to the first sextet. Mössbauer spectrum of the sample with a concentration of 25 at. % Cr is shown in Fig. 2 together with the individual distributed spectral components.

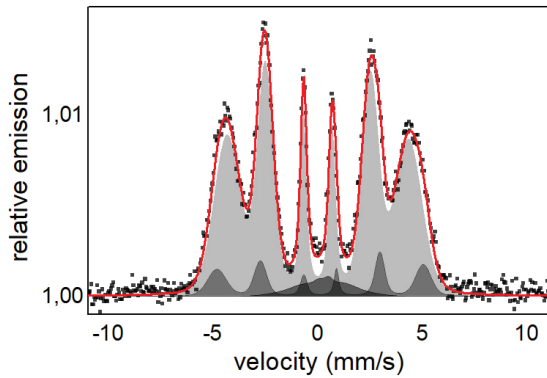


Fig. 2. Mössbauer spectrum of a binary alloy Fe-Cr with 25 at. % Cr measured by CEMS

From the study of the Fe-Cr samples we can say that the mean values of the investigated spectral parameters, viz. relative intensity ratio A_{21} , mean value of isomer shift $\langle IS \rangle$ and hyperfine magnetic field $\langle B \rangle$, decrease with at. % Cr. With a model based on binomial distribution and subsequent fitting we have obtained the results that are listed in Tab. 1 up to 25 at. % Cr. The following two rows ($x = 25$ and 50) represent the results obtained from fittings using Gaussian distributions.

TAB. 1. Values of spectral parameters corresponding to various Cr concentrations

x [%]	A_{21}	$\langle IS \rangle$ [mm/s]	$\langle B \rangle$ [T]
1	1.074	-0.012	32.7
2	1.105	-0.014	32.8
5	1.016	-0.015	32.0
10	0.967	-0.018	30.7
15	0.958	-0.024	30.3
25	0.979	-0.033	27.8
25	0.924	-0.030	26.5
50	0.713	-0.080	16.9

Linear decline of experimental values obtained for hyperfine magnetic field and isomer shift are plotted as a function of x (at. % Cr) in Fig. 3 and Fig. 4, respectively. The experimental points are analysed by linear fits according to eqn. (3). Values of $\langle B \rangle$ and $\langle IS \rangle$ obtained from fittings with a distribution model are plotted by red symbols. Even though the fitting model is different, the obtained values are satisfactorily positioned on the linear dependencies.

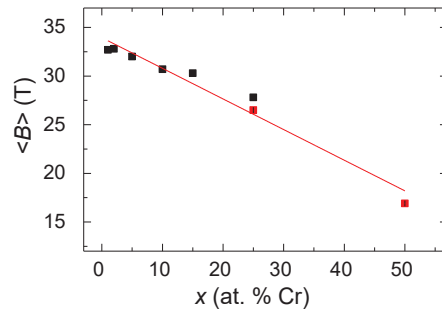


Fig. 3. Dependence of average hyperfine magnetic field $\langle B \rangle$ as a function of Cr concentration (x) in Fe-Cr binary alloy measured by CEMS

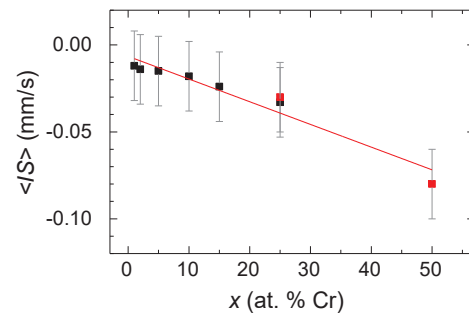


Fig. 4. Dependence of average isomer shift $\langle IS \rangle$ as a function of Cr concentration (x) in Fe-Cr binary alloy measured by CEMS

The aim of this work was to work out fitting models used for evaluation of Mössbauer spectra of metallic alloys that consist of two elements. Due to their considerable thickness, we have applied conversion electron Mössbauer spectrometry for measuring the investigated Fe-Cr samples. Using theoretical assumptions based on binomial distribution as well as Gaussian distribution of Cr in the nearest neighbouring shells of the resonant Fe atoms, average values of hyperfine magnetic field and isomer shift values were obtained. They satisfactorily match the predicted linear dependencies with respect to Cr concentration. The resulting models of evaluation are applicable not only to binary alloys with Cr but also to other metal elements such as Co, Mn, Ni, etc.

The results of this study and experience with fitting models will be used when Mössbauer spectra of real steels (e.g. PM-2000) used in nuclear industry will be evaluated within the current research project.

ACKNOWLEDGMENT: This work was supported by the grant VEGA 1/0130/20.

REFERENCES

1. Gutlich P. et al.: Mössbauer Spectroscopy and transition metal chemistry – fundamentals and applications (Springer - 2011).
2. T. Žák, Y. Jiraskova, Surf. Interface Anal. **38**, 710 (2006).
3. R. Idczak et al., Physica B **528**, 27 (2018).
4. R. Idczak et al., J. Nucl. Mater. **452**, 141 (2014).

STUDY OF MAGNETICALLY INDUCED CRYSTAL REORIENTATION OF Ni-Mn-Ga FERROMAGNETIC SHAPE MEMORY ALLOY

Š. Sukup^{1,3}, S. Heczko², O. Heczko³, heczko@fzu.cz

¹Archbishop Lyceum, Kroměříž, Czech Republic

²King's College London, Faculty of Natural & Mathematical Sciences, UK

³Institute of Physics CAS, 18121 Prague 8, Czech Republic

INTRODUCTION

In the past two decades Ni-Mn-Ga Heusler alloys have received great attention as these exhibit magnetic shape memory effects in low symmetry phases; modulated 10M and 14M and non-modulated martensite [1]. Here we focus on modulated 10M martensite [2]. These phases are formed upon martensitic transformation from high temperature parent Heusler cubic phase with L2₁ order. These materials belong to the multiferroic class of materials, in this case magnetoelastic multiferroics coupling ferromagnetism and ferroelasticity [3]. Owing to very highly mobile twin boundary separating differently oriented ferroelastic domains (twins), the martensitic twinned structure can be manipulated by magnetic field and stress resulting in large mechanically induced changes of magnetization and giant magnetically induced strain in 10M martensite about 6% [4]. Such large deformation, however, can be obtained only in single crystal as grain boundaries form the unsurmountable obstacles for twin boundary motion. The effect is also known as magnetically-induced reorientation (MIR).

Here we investigated the equivalence of magnetic and mechanical energy, i.e. the energy needed for the reorientation by a magnetic field and by mechanical force resulting in giant deformation.

EXPERIMENTAL

For experiment we used single crystalline samples of nominal composition Ni₅₀Mn₂₈Ga₂₂ from different sources including our own production. At room temperature all samples exhibit 10M modulated martensite structure with lattice constants $a \cong b > c$ in pseudotetragonal approximation. The rectangular samples were cut from single crystalline ingot along {100} planes of cubic parent phase and mechanically grinded and electropolished. To compare directly different modes of loading to induce reorientation the measurements were conducted on five samples by vibration sample magnetometer and custom-made stress-strain device.

RESULTS

From simple energy consideration the equivalence of mechanical and magnetic energy can be written as

$$E_{\text{mag}} = \sigma \cdot \varepsilon_0 \quad (1)$$

where σ is the mechanical stress and E_{mag} magnetic energy needed for reorientation and $\varepsilon_0 = 1 - c/a$ is the lattice distortion [5]. Experimentally the mechanical

energy can be evaluated from stress-strain diagram obtained during mechanical reorientation. Fig. 1 shows such curve measured during the gradual structure reorientation under compression stress from the single martensite twin variant with c-axis perpendicular to single variant with c-axis along the stress. The small peak on the onset signified the nucleation of initial twin boundary and the onset of reorientation. New boundaries were then nucleated during compression; however, the amount was not controlled.

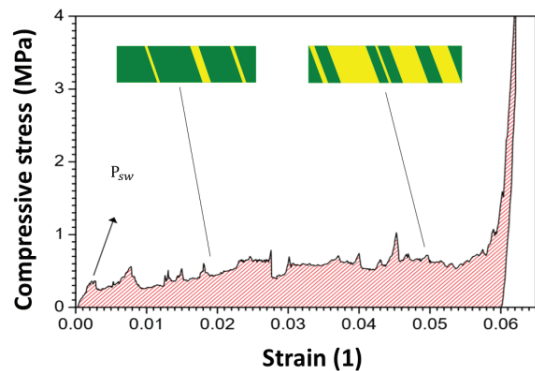


Fig. 1. Stress-strain curve of 10M martensite indicating by filling the energy needed for reorientation. The progress of twin variants redistribution is schematically shown in the inset.

The magnetic energy E_{mag} , driving force for reorientation, is a difference between the magnetic energy of the martensite twin variants having different orientation in magnetic field. The variant with c-axis (easy magnetization axis) along the field has lower energy than other variants with c-axes perpendicular to the field. Owing to the difference the variant with lower magnetic energy grows on the expense of other variants and the reorientation (MIR) occurred allowed by extremely low stress needed for twin boundary motion. Experimentally the energy needed for reorientation is given by the area between magnetization curves of differently oriented single variants and can be easily determined. This area is marked in Fig. 2. The figure also indicates the switching field H_{sw} in which the reorientation starts. Apparently in slowly growing magnetic field the whole reorientation is finished during single step. As the demagnetization factor was neglected in all measurement it may cause some systematic error resulting in the overestimation of magnetic energy [6].

The values of magnetic and mechanical energy needed for reorientation are summarized in Table 1 for several samples together with total average. It is apparent that magnetic energy needed for reorientation is invariably larger exceeding the mechanical energy of

about half. Still it is much lower than maximum magnetic energy, $\approx 170 \text{ kJ/m}^3$ available for reorientation determined from magnetocrystalline anisotropy.

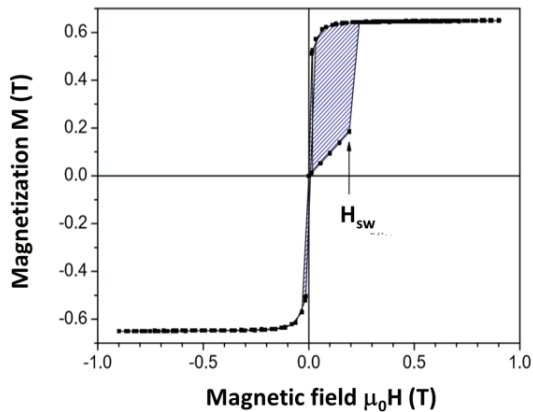


Fig. 2. Magnetization curves of single variant with c-axis (easy axis of magnetization) along and perpendicular to the magnetic field. At magnetic field marked H_{sw} the MIR occurred resulting in large jump in magnetization. The difference of magnetic energy is marked by blue filling.

It indicates that the reorientation takes place in middle of the range and no error from limits should arise. In any case the large difference is surprising but not totally unexpected. Previous experiments [7] dealing with only switching field already indicated that the onset of reorientation occurs in higher field than expected from the mechanical measurement.

TAB. 1. Average energy (from five measurements) needed for reorientation by mechanical and magnetic force

	Mechanical energy [kJ/m ³]	Magnetic energy [kJ/m ³]
Sample 1	45	79
Sample 2	60	83
Sample 3	36	69
Average	47	77

The values obtained from the experiment exhibited large scatter up to 20%. It can be mainly ascribed to the difficulties to secure the same fixture of the sample for each magnetic and mechanical measurement and random, uncontrolled nucleation of twin boundaries. Despite this, the observed difference between magnetic and mechanical energies is significant. It can be caused by fundamental difference in the experimental set-up. In magnetic experiment the reorientation is driven by gradually increasing magnetic field while in mechanical experiment the reorientation is controlled by strain. To have fully analogous experiment the reorientation in magnetic field should be controlled by magnetization which would assume variable magnetic field with quick feedback, which is difficult to realize in VSM. This is similar problem as dealing with re-entrant magnetization loop in purely magnetic studies [8]. One may also consider force (stress) controlled deformation which would be analogous to field measurement but it is also difficult to realize.

Being the magnetic field the independent variable we neglect the situation when the reorientation after overcoming the initial threshold may need much lower field to continue. In mechanical testing the mechanical force is determined in each stage of the reorientation. This can be the main reason why the magnetic energy for reorientation was much larger than the mechanical energy. Of course, one cannot exclude that the initial assumption (1) is not entirely true which demands further research.

CONCLUSIONS

In contrast with the phenomenological model [5] the calculated energy of magnetically induced reorientation or pseudoplastic deformation were considerably higher compared to the energy needed using mechanical force. The switching field of samples with nucleated twinning boundaries was also measured and compared to single variant crystals. Results only partly support modelling of the twinning stress and switching field [4-6]. The model-data discrepancies are an unresolved issue suggesting a need for modification of the model.

ACKNOWLEDGMENT: The work was done in the frame of activity "Otevřená věda" by Czech Academy of Sciences. O.H. thanks for support CSF No. 19-09882S.

REFERENCES

1. A. Sozinov et al., Appl. Phys. Lett. **102**, 021902 (2013).
2. L. Straka et al., Acta Mater. **59**, 7450 (2011).
3. J.D.M. Coey: Magnetism and Magnetic Materials (Cambridge University Press – 2010).
4. O. Heczko, Materials Science and Technology **30**, 1559 (2014).
5. A.A. Likhachev, K. Ullakko, The European Physical Journal **275**, 263 (2000).
6. O. Heczko et al., IEEE Magnetics Letters **6**, 1 (2015).
7. V. Kopecky et al., Acta Phys. Pol. **A 128**, 754 (2015).
8. S. Chikazumi: Physics of ferromagnetic materials (Clarendon Press, Oxford – 1997).

NITRIDE MULTIPLE QUANTUM WELL CHALLENGE

J. Oswald, oswald@fzu.cz, A. Hospodková, hospodko@fzu.cz, T. Hubáček, hubacekt@fzu.cz, K. Kuldová, kuldova@fzu.cz, J. Pangrác, pangrac@fzu.cz, Institute of Physics CAS, v.v.i., Cukrovarnická 10, CZ-16200, Prague 6, Czech Republic, F. Hájek, hajek@fzu.cz, Institute of Physics CAS, v.v.i., Cukrovarnická 10, CZ-16200, Prague 6, Czech Republic, Czech Technical University in Prague, FNSPE, Břehová 7, CZ-11519, Prague 1, Czech Republic.

INTRODUCTION

Nitride semiconductor heterostructures are widely used for light-emitting and laser diodes (LEDs and LDs) as well as for high-power and high-electron-mobility transistors. But efficient and fast luminescence of InGaN/GaN structures opens new application field of superfast scintillation detectors [1]. Unlike the LED case, nitride scintillation structure must be composed of high number of InGaN quantum wells (QW) due to high penetration depth of ionizing radiation. An increase in the number of QWs leads to a large increase of the strain energy in the structure due to various lattice constants of GaN and InGaN and a consequent increase in structural failures, which can lead to the collapse of the structure. Therefore, increasing the number of QWs is a major challenge that has not been solved yet.

EXPERIMENTAL

Structures were prepared on the Aixtron 3 × 2 CCS MOVPE apparatus equipped with LayTec EpiCurveTT system for in situ measurement of reflectivity, curvature and true temperature. Buffer layers were grown with trimethylgallium and ammonia precursors with a hydrogen carrier gas. The MQW region was prepared from triethylgallium, trimethylindium and ammonia precursors with a nitrogen carrier gas. Structures were grown on sapphire substrates with standard c-plane orientation. A low temperature GaN nucleation layer was grown at 550°C. Subsequently, 3 μm-thick undoped GaN buffer at 1050°C was grown. Before the growth of the MQW active region, a 1 μm-thick Si doped GaN layer was added to suppress band bending. The multiple QW active region consisted of 10 to 60 QWs prepared at 736°C and In content was close to 5%. QWs were separated by GaN quantum barriers (QB) prepared at 815°C. The thicknesses of QW and QB were around 1.5 nm and 5 nm, respectively. After each stack of five QWs and QBs, 25 nm-thick GaN separation layer was grown with the same growth temperature as for QB. The whole structure was always capped with a 12 nm thick GaN layer to isolate QWs from the surface states. Design of scintillation structure is shown in Fig. 1.

Photoluminescence (PL) spectra were measured at room temperature at two different excitation wavelengths. For 325 nm excitation wavelength, a confocal microscope (LabRAM HR Evolution, He–Cd laser) was used. For 375 nm excitation wavelength, a semiconductor laser LD- 375 was used and the detection was done using a combination of a double monochromator SDL-1 and a GaAs photomultiplier tube. Wavelength 325 nm enables excitation over GaN bandgap and the characteristic penetration depth is about 100 nm as opposed to 375 nm excitation which penetrates a few microns.

Cathodoluminescence (CL) measurements were performed in Philips XL30 ESEM with home-build CL setup including Avaspec ULS-TEC spectrometer with CCD detector.

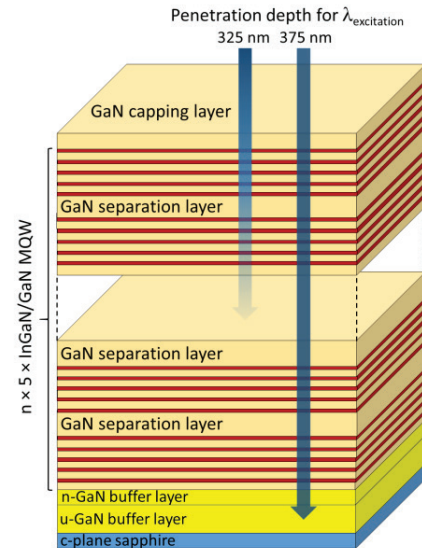


Fig. 1. Design of MQW scintillation structure with indication of different penetration depth of excitation wavelengths [2].

RESULTS AND DISCUSSION

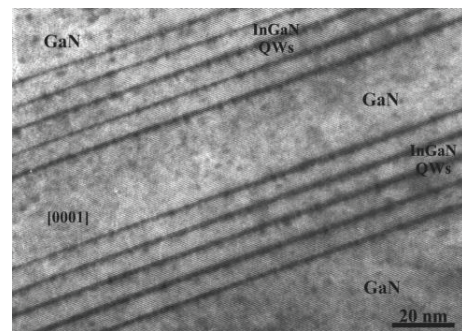


Fig. 2 High resolution TEM image of 2 x 5 MQWs.

High resolution transmission electron microscope (HRTEM) image of 2 x 5 MQWs is shown in Fig. 2, where dark lines are InGaN QWs. Weak fluctuation of In content can be seen (dark spots).

Resonant excitation of QWs at 375 nm penetrates through all the structure and PL from all QWs can be obtained similar to the case of excitation by ionizing radiation. Under this excitation, increased excitonic luminescence intensity without any saturation with QW number is observed (Fig. 3). We observed linear increase of intensity QW excitonic luminescence with the increasing number of QWs up to 60 [2].

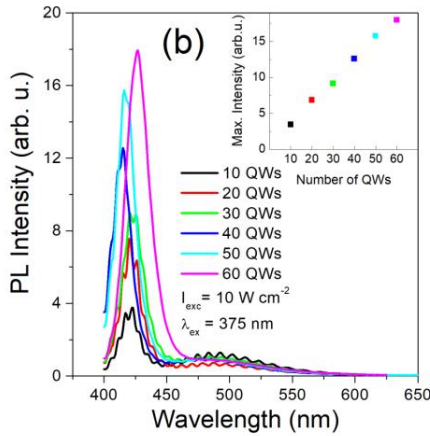


Fig. 3. Dependence of PL spectra on the number of QWs for 375 nm excitation. In the inset the dependence of PL intensity on number of QWs is shown [2].

This demonstrates the properly designed structure parameters and technology.

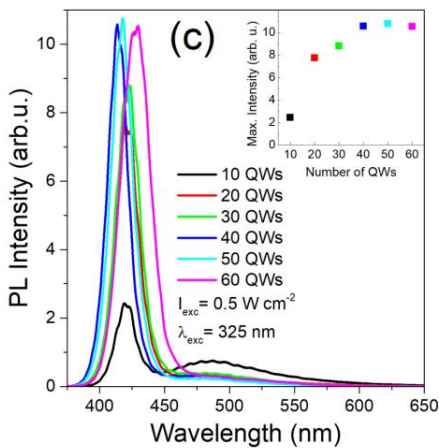


Fig. 4. Dependence of PL spectra on the number of QWs for 325 nm excitation. In the inset the dependence of PL intensity is shown [2].

The 325 nm excitation has energy above GaN band gap. It is thus highly absorbed in the structure. Approximately 90% of the excitation beam is absorbed in first 100 nm corresponding to about 10 topmost QWs. PL intensity is saturated with increasing number of QWs due to limited propagation of excitation light, Fig. 4. Origin and influence of defect band at 490 nm is discussed in detail in [2].

Decisive possible application of electron detection is CL. It was measured for the same set of samples with different number of QWs, see Fig. 5.

The dependence of CL intensity on the number of QWs is almost linear and only excitonic peak was observed. We compared CL spectra of our InGaN/GaN MQW structure with commercial YSO scintillator, see Fig. 6. Obtained integral intensities are comparable.

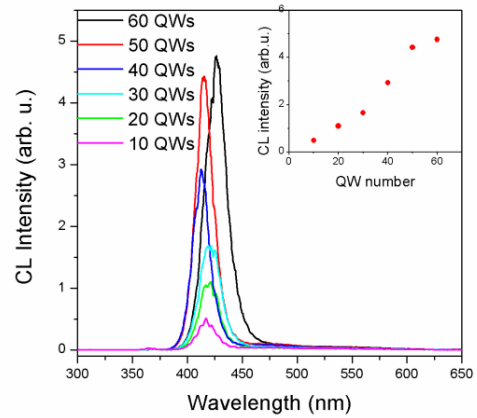


Fig. 5. Dependence of CL spectra on the number of QWs at acceleration voltage 20 kV. The dependence of integral CL intensity on number of QWs is shown in inset.

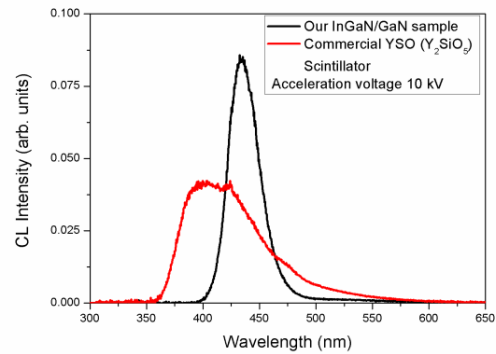


Fig. 6. Comparison of CL spectra of our InGaN/GaN MQW structure and commercial YSO scintillator.

CONCLUSIONS

We have prepared efficient luminescent InGaN/GaN structures with the high QW number.

We have obtained linear increased of PL intensity with increasing number of QWs in resonant excitation.

Cathodoluminescence intensity of our structures are comparable with commercial YSO scintillator.

ACKNOWLEDGMENT: The authors acknowledge the support of MSMT project no. NPU LO1603–ASTRANIT. The authors acknowledge Professor Philomela Komninou from Aristotle University of Thessaloniki for HRTEM measurements.

REFERENCES

1. A. Hospodková, et al. *Nanotechnology* **25**, 455501 (2014).
2. T. Hubáček, et al. *Journal Cryst. Eng. Comm.* **21**, 356 (2019).

DIELECTRIC SPECTROSCOPY OF FUNCTIONALIZED CARBON NANOTUBES

J. Kúdelčík, jozef.kudelcik@feit.uniza.sk, Department of Physics, Faculty of Electrical Engineering and Information Technology, Žilinská University, Univerzitná 1, 010 26 Žilina, Slovakia

Multi-wall carbon nanotubes (MWCNT) have a wide application due to their specific parameters. They can undergo chemical functionalization [1, 2] to enhance solubility in various solvents and to produce novel hybrid materials potentially suitable for applications. The functionalization can be done with various noble metal nanoparticles, such as Au, Ag, Pt, Pd, and their alloys [3, 4], and with magnetic nanoparticles (MNPs), such as Fe_3O_4 [5 - 7]. The saturation magnetization is significantly higher at functionalized samples due to the presence of nanoparticles of Fe_3O_4 with the relatively high magnetic moments that were attached to the wall of MWCNT. Thus, nanoparticles play the role of a starting point for changing the magnetization of the whole nanotube [7]. Oppositely the coercivity of these samples is noticeably lower in comparison with non-functionalized ones. This could be attributed to the small magnetic anisotropy of the nanoparticles.

The dielectric response measurements are a powerful method for the investigation of the electrical properties of various materials [8, 9]. Dielectric spectroscopy measurements as a function of frequency and the applied bias voltage offer the ability to investigate both bulk dielectric processes as well as the possible barrier contribution to the electrical properties at a wide temperature range. Polarization, phase transitions, electrical conductivity, and interfacial effects determine the dielectric behavior of either materials or composites [10, 11].

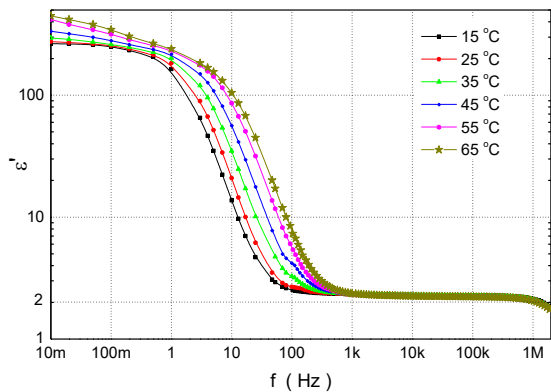


Fig. 1. The dependence of the real permittivity of fMWCNT/ Fe_3O_4 on the frequency for various temperatures at the constant electric field 140 kV/m.

For the measurement of the structural changes in MWCNTs functionalized (fMWCNTs) by Fe_3O_4 magnetic nanoparticles (20 – 25 nm) [7] diluted in transformer oil MOL TO 40A was used. Chemical vapor deposited MWCNTs were purchased from Sigma Aldrich Co. (length of 0.5 – 2 μm , the outer diameter of 20 – 30 nm, and the wall thickness of 1 – 2 nm). fMWCNT/ Fe_3O_4 were prepared by removal of carboxyl groups and by subsequent labeling with magnetic

nanoparticles. We used the sample with magnetic nanoparticles Fe_3O_4 of concentration 2.49 % mg/ml and MWCNT 0.22 % mg/ml. The sample had the density of 930.9 mg/ml. For measurement of these parameters, the LCR Meter QT 7600 Plus (QuadTech, USA) in the frequency range from 100 Hz to 1 MHz and IDAX 350 (Megger, UK) in the frequency range from 1 mHz to 10 kHz were used. The flat sample and the electrode system were placed in the oven where their temperature was stabilized. The studied fluid was placed in the liquid crystal cell ($d = 50 \mu\text{m}$ with $C_0 = 6.5 \text{ pF}$) fixed in the temperature stabilized block.

The real part of the complex permittivity of fMWCNT/ Fe_3O_4 measured at the constant electric field 100 kV/m is depicted in Fig. 1. The real permittivity (ϵ') at low frequencies was high and almost constant, and with increasing frequency, it decreased to stable value $\epsilon_\infty \approx 2$ (dielectric constant at high frequencies). The frequency area of decrease ϵ' was temperature-dependent. The decrease of ϵ' was caused by a relaxation process of polarization with a relaxation time τ or an eigenfrequency ($f_c = 1/(2\pi\tau)$). This process is related to the relaxation of the electric double layers (EDL) [12] around nanoparticles. Low-frequency maximums around 50 Hz were observed also by Nuzhnyy [9] or Špitalský [10]. This effect could be used in practice, e.g. when determining the temperature.

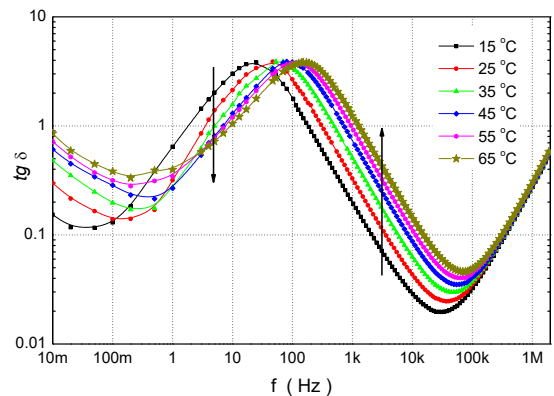


Fig. 2. Changes of acoustic attenuation for the jump change of the magnetic flux density to 200 mT for at various temperatures in samples No. H3.

The very high real permittivity of the fMWCNT in the low-frequency range originated from the low-frequency dispersion (LFD) mechanism [9, 10] and the presence of conductive magnetic nanoparticles causes its higher value. LFD has a similar mechanism as interfacial polarization but occurs at lower frequencies. In LFD mechanism, due to sufficiently low frequencies, nomadic charge carriers with low drift velocity also found sufficient time to move toward internal interfaces and pile up. This led to very large real permittivities. The increase of ϵ' can be also attributed to the formation

of large numbers of nanocapacitor structures allowing the composite to store the charges.

Fig. 2 shows the frequency dependence of dissipation factor at various temperatures. There are one local low-frequency maximum and two minima. The local maximum at the frequency ($f_{\delta} = f_c \sqrt{(\epsilon_s/\epsilon_{\infty})}$) relates to a relaxation process of polarization of EDL (ϵ_s – stable value at low frequencies). The whole development shifts to higher frequencies with increasing temperature. This shift is caused by an increase in the rotational and vibrational motion of nanotubes with temperature and thus a decrease in the relaxation time of their dipole polarization.

The full lines in Figs. 1 and 2 represent the Cole-Cole fits of experimental data. The Cole-Cole equation [12] is a relaxation model that is often used to describe dielectric relaxations, and it has the following form:

$$\epsilon^* = \epsilon_{\infty} + \frac{\Delta\epsilon}{1 + (j\omega\tau)^{\alpha}} + j \frac{\sigma}{\epsilon_0 \omega} \quad (1)$$

where ϵ^* is the complex dielectric constant, $\Delta\epsilon = \epsilon_s - \epsilon_{\infty}$, σ is the DC conductivity and α is the distribution parameter. The experimental data were fitted using the Origin 7.0 software. Cole-Cole parameters were obtained and listed in Tab. 1.

TAB. 1 Parameters from Cole-cole fit of the complex permittivity at various temperatures.

Temp (°C)	15	25	35	45	55	65
τ (s)	90	55	40	30	22	16
f_c (mHz)	1.8	2.9	4.0	5.3	7.2	10
f_{δ} (Hz)	25	45	66	86	125	163
α	.88	.85	.81	.69	.66	.66
σ (nS)	24	79	157	122	176	228
ϵ_s	250	238	246	266	307	315

The relaxation time decreased with increasing temperature and follows the Arrhenius law given by the relation:

$$\tau = \tau_0 \exp \{- E_A / kT\} \quad (2)$$

where τ_0 is the pre-exponential factor and E_A is the activation energy of the relaxation process. From the slope of the fit with a straight line of the dependence, $\tau(1/T)$, and according to Eq. (2), the activation energy was $E_A = 3,76$ eV.

Fig. 3 shows the frequency dependence of the relative permittivity in different electric fields. The change of the applied voltage from the range of 1 V to 5 V to the measuring capacitor corresponded to the change of the electric field intensity in the range from 20 - 140 kV/m. With an increase in voltage/intensity in the higher frequency range, we do not observe any change in the development. However, at frequencies below 100 Hz, there is a significant decrease in relative permittivity with voltage. This decrease is caused by several facts. In the first case, an increase in the intensity of the electric field in the measuring capacitor causes a decrease in the

effect of LDF and electrode polarization [10, 12]. As the intensity of the electric field increases, we also observe a shift of the whole development to the region of lower frequencies (indicated by an arrow). As the electric field increases, the electric dipoles of the nanoparticles have higher values, which have caused a higher depolarization field. This field further reduces the total intensity of the electric field and the eigenfrequency or relaxation maximum shifts towards lower frequencies. The next effect is caused by a decrease of charge carriers near of electrode due to an increase of drift velocity with an external electric field. At higher speeds for one half, they can hit the electrode and neutralize. We observe the same shift at the development and position of the local maximum $\text{tg } \delta$. Similar results are given in [9, 10].

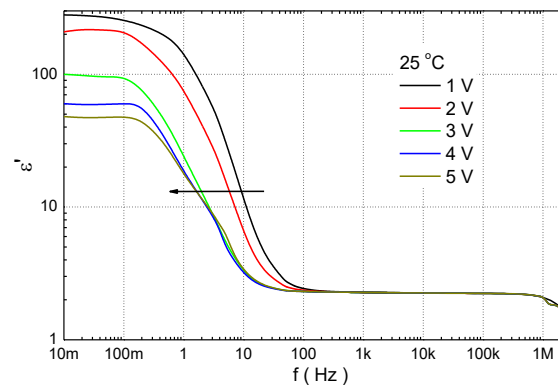


Fig. 3. Influence of the electric field on the relative permittivity of the sample at 25 °C

The dielectric spectroscopy was used to study the influence of the temperature and the electric field on the dielectric properties of fMWCNT/Fe₃O₄. The development of ϵ'' and $\tan \delta$ of studied magnetic fluid showed one low-frequency relaxation maximum at the eigenfrequency, which was associated with the electric double-layer around fMWCNT.

ACKNOWLEDGMENT: This research was supported by the project Slovak Grant Agency VEGA No. 2/0016/17 and fMWCNT/Fe₃O₄ was from M. Timko and P. Kopčanský, SAS Košice.

REFERENCES

1. I.Y. Jeon, et al., InTech 91 (2011).
2. B. Wu, Nano Today **6**, 75 (2011).
3. Z.J. Wang, Carbon **46**, 1687 (2008).
4. B. Zhang, Indian J. Chem. **A48**, 1345 (2009).
5. W. Zhao et al., Synthetic Metals **169**, 59 (2013).
6. B. Kaboudin, J. Organomet. Chem. **882**, 64 (2019).
7. Z. Mitróová et al., NANOCON (Olomouc – 2010).
8. M. Arjmad, Polym. Eng. Sci. **55**, 173 (2015).
9. D. Nuzhnyy, Nanotechnology **24**, 055707 (2013).
10. Z. Špitalský, Adv. Comp. Letters **19**, 179 (2010).
11. P. Hockicko et. al., J. Non-Cryst. Solids **440**, 26 (2016).
12. M. Rajňák et al., J. Chem. Phys. **146**, 014704 (2017).

QUANTUM DOTS GROWN BY METALORGANIC VAPOR PHASE EPITAXY

E. Hulcius, hulcius@fzu.cz, A. Hospodková, hospodko@fzu.cz, M. Slavická Zíková, zikova@fzu.cz, Institute of Physics of the CAS, v.v.i., Cukrovarnická 10, 162 00, Prague 6, Czech Republic

INTRODUCTION

This paper focuses on semiconductor quantum dots (QDs) embedded inside semiconductor heterostructures prepared by Metalorganic Vapor Phase Epitaxy (MOVPE) technology and is based on our contribution in [1]. Semiconductor direct-bandgap materials have much higher energy conversion efficiency than the light emission from atoms/molecules in a glass matrix or from some gases the other light sources, but they have a broad band or multimode light emission spectra. QDs created and embedded inside semiconductor heterostructures can fundamentally improve the quality of emitted light spectrum, temperature dependencies and efficiency of emission. The main technological procedure used for QD preparation is the self-assembled Stranski–Krastanov growth mode. Embedded MOVPE-prepared QDs are currently used for semiconductor lasers, optical amplifiers, LEDs and photodetectors. High extinction coefficient of QDs is promising for possible optical applications. QDs can operate like a single-electron transistor and show the Coulomb blockade effect. QDs have also been suggested for quantum information processing or solid-state quantum computation - they can be used as a single photon generators.

DEFINITION AND HISTORY

The first idea of QDs having properties different from that of the bulk material was published in 1981 and QDs were prepared in colloidal solution, but they were not embedded in a heterostructure yet.

MOVPE-grown QDs were reported in 1991, but with small response. MBE seems to be more suitable for attaining an exact layer thickness down to fractions of a monolayer. QD MOVPE papers published later attracted much more interest. An attempt to realize industrial MOVPE-prepared QD-based semiconductor lasers for fibre optic telecommunications appeared during the first years of this century (e.g. EU project DOTCOM 2002-05), but without an impact on the industrial production.

Semiconductor QDs exhibit unique electronic and optical properties, intermediate between those of bulk semiconductors and discrete atoms or molecules – see Fig. 1. The reason the size of QDs is comparable with the de Broglie wavelength of an electron in a crystal. Electrons (and holes) inside QDs behave differently from that found in a “bulk” material. The most important difference is that inside the QDs, electrons (and holes) can occupy only discrete energy levels due to strong localization; however, they also can be found nearby QDs with nonzero probability. The position of energy levels depends mainly on the smallest size of a QD. Thus, electron–hole recombination energy (the wavelength of the emitted radiation) depends on this size, often more than on the material bandgap energy, which is determining for wavelength emission from the

bulk material.

Reasons and examples of QD parameters for semiconductor lasers are as follows:

The emission from quantum levels in quantum wells and wires or QDs is monochromatic and still very efficient. One of the effects of strong quantum confinement are the discrete energy levels. Another effect is a lower threshold current density of a QD-based semiconductor laser, when achieving the inversion of population in QDs is needed for stimulated emission, as well as suppression of loss mechanisms such as Auger recombination and intervalence band absorption.

The photon energy (emitted wavelength) can be changed mainly by the size of QDs and not only by chemical composition. This is similar as in quantum well lasers, but the temperature dependence of these lasers is also much lower than for “classical” two-dimensional layered QW-based lasers.

Another very important property of QD-based semiconductor lasers is that very small QDs can emit single photons, necessary for quantum cryptography.

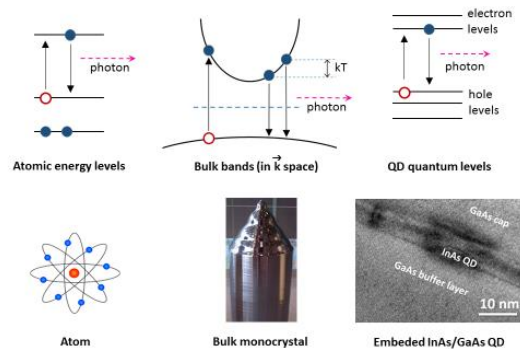


Fig. 1. Paradigm of quantum dots

MATERIALS AND STRUCTURES

The most common material combination for embedded QDs is InAs QDs in a GaAs matrix. The emission wavelength of these simple QDs is published up to 1250 nm. To further extend the emission wavelength, different kinds of strain-reducing layer materials such as InGaAs, GaAsSb or AlInAs are used to surround the InAs QDs. Useful material combinations are InAs QDs prepared on a InP substrate. To improve the electron localization in QDs lattice-matched buffers can be used, such as GaAsSb, InGaAs or AlAsSb.

GaSb QDs with the required simple hillock morphology were achieved, when InAs QDs were used as the seeding layer, see Fig. 2a. In this case, strong type II band alignment of carriers was obtained as is demonstrated in Figs 2 b–d. Fig. 3 depicts a QD capped by GaAsSb layer with low Sb content at during of the capping process. Dissolved amount of InAs during QD capping was so large that another unintentional QD layer was formed during the growth interruption after

the GaAsSb growth.

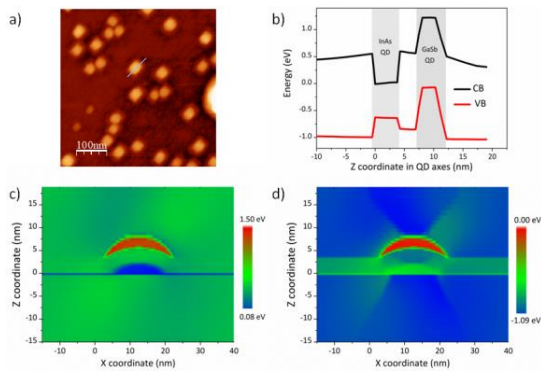


Fig. 2. AFM picture of hillock morphology of GaSb QDs when InAs QDs were used as the seeding layer (a), calculated band alignment of combined InAs and GaSb QDs along QD axes (b) map of band alignment for combined InAs and GaSb QDs of conduction (c) and valence (d) bands.

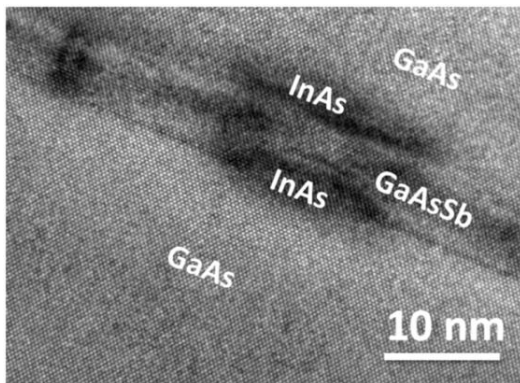


Fig. 3. HR TEM images of a QD capped by GaAsSb. TEM picture by Prof. P. Komninou Aristotle Univ. Thessaloniki.

GROWTH PROCEDURES

There are few papers about QDs prepared by liquid phase epitaxy. Krier et al., by Moiseev et al. with possible MIR-region applications, published them at 1999. Only exceptionally can we find papers about other epitaxial techniques, e.g. hydride vapor-phase epitaxy. However, the main stream is focused on MBE and MOVPE technology. The three growth technological procedures are used for MOVPE preparation of QDs embedded in the structure. Self-assembled Stranski–Krastanov growth mode on the flat surface - compound semiconductors with different lattice constants have to be used to reach tensile strain for self-assembled creation of QDs on the wetting layer. The second is formation of QDs in prepatterned inverted pyramids and the third is droplet epitaxy. To obtain reproducible growth of QDs is difficult, the problem is that the QD size, shape and their density are very sensitive to many technological parameters, such as growth temperature, growth rate, waiting time for QD formation, QD material precise dosage, growth rate and composition of the covering and buffer layers. The strong sensitivity of QD properties on so many growth parameters is the obstacle for wider industrial application of QDs.

SUMMARY AND FUTURE PERSPECTIVES

MOVPE-grown QDs have been prepared and studied by many MOVPE technological teams for more than 25 years, but their real current application is still limited. The situation is comparable with QWRs. In comparison with QWs, both of these structures are not mature. It is an open question if QDs will ever have a comparable impact on our lives as QWs (internet, laser diodes, QW-based devices in computers, mobile phones, etc.). It may happen that improvement of the final chip/device parameters in comparison with QW-based ones will not be sufficient to introduce new growth procedures and device constructions.

Materials that can be used for QD structures come from many semiconductor families like arsenide, antimonite, phosphide, telluride, and nitride binaries and ternaries. QD structure material choice (including substrate material like GaAs, Si, sapphire, SiC, perovskite, etc.) can drive emitted wavelength, influence temperature and structure stability, and, of course, the cost of devices. Complex internal QD device structures like QD size and shape (including layout in the case of QD arrays), SRLs and spacers (materials and thicknesses), QD layer multiplicity for stacking-layer structure, material and thickness of the capping layer, and the system of buffer layers can affect QD device parameters and their possible applications.

Future applications:

- QD-based single-photon or -electron devices. Mainly single-photon QD lasers for quantum cryptography.
- QD MIR photomultipliers can be more useful than for other QD photomultiplier wavelengths applications.
- QD long-life memories are very promising.
- Telecom lasers very probably for 1.3 μm , maybe also for 1.55 μm .
- We are not sure about the prospects of QD solar cells; this is at a very early stage of research with many exciting possibilities.

Future research:

- Extension of QD device wavelengths to the far-MIR and to the UV using different materials as well as size and shape of QDs.
- Improvement of structure parameters over the standard ones.
- The cost of devices has to be lowered, as usually, thus research of low-cost and mature (Si or GaAs wafers based?) technology has to be improved.

ACKNOWLEDGMENT: The authors acknowledge the support of MSMT project no. NPU LO1603 – ASTRANIT.

REFERENCES

1. S.J.C. Irvine, P. Capper (eds.): Metalorganic Vapor Phase Epitaxy (MOVPE): Growth, Materials Properties and Applications”, E. Hulicius, A. Hospodková, M. Zíková, Chapter 6: Quantum dots (John Wiley & Sons, Hoboken, NJ, 2020).

THE MOMENTUM SPECTRUM VERSUS THE PROBABILITY FLUX DIRECTION IN QUANTUM MECHANICS

J. Dittrich, dittrich@ujf.cas.cz, Nuclear Physics Institute CAS, CZ-250 68 Řež, Czech Republic

INTRODUCTION

Motivated by the studies of a scattering problem [1], the relation between the momentum direction given by its spectral support and the direction of the probability flux is examined in one-dimensional quantum mechanics. Simple examples show that they are locally uncorrelated in general for the Schrödinger and massive Dirac particles. They are correlated for the zero-mass Dirac particles.

SCHRÖDINGER EQUATION

A solution $\phi(t, x)$ of the one dimensional free Schrödinger equation can be written as

$$\phi(t, x) = (2\pi)^{-1/2} \int_{\mathbb{R}} e^{i(px - p^2 t)} \hat{\phi}(p) dp \quad (1)$$

in the units where the Planck constant $\hbar = 1$ and the particle mass $m = \frac{1}{2}$. Here $\hat{\phi}$ is the Fourier transform of the initial state $\phi(0, x)$. The probability density ρ and probability flux j are given by the formulas

$$\rho(t, x) = |\phi(t, x)|^2, \quad j(t, x) = 2\Im \left(\overline{\phi(t, x)} \partial_x \phi(t, x) \right).$$

The spectral projectors of the momentum operator act as

$$(\varphi, E_P(M)\psi) = \int_M \overline{\hat{\varphi}(p)} \hat{\psi}(p) dp.$$

Let us consider the initial state with

$$\hat{\phi}(p) = \sqrt{2\pi} \chi_{(M_1, M_2)}(p) + i\sqrt{2\pi} \chi_{(N_1, N_2)}(p)$$

where $0 \leq M_1 < M_2 < N_1 < N_2 < \infty$ and $\chi_{(m_1, m_2)}$ is the characteristic function of the interval (m_1, m_2) . The unessential normalization factor is skipped here. Numerically, values $M_1 = 0$, $M_2 = 1$, $N_1 = 2$, $N_2 = 3$ are used in the Figures. Using (1), the probability density and flux are calculated numerically.

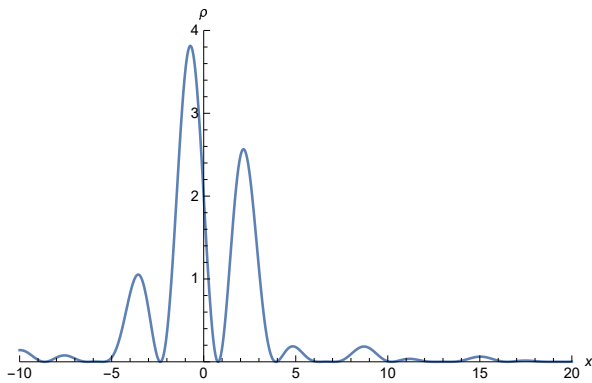


Fig. 1. Probability density $\rho(t, x)$ at the time $t=0$.

Apparently, regions with the negative current (i.e., in the direction opposite to the momentum) occur, e.g., at $t = 1$ around $x = 0.7$ (Fig. 4). This behavior may

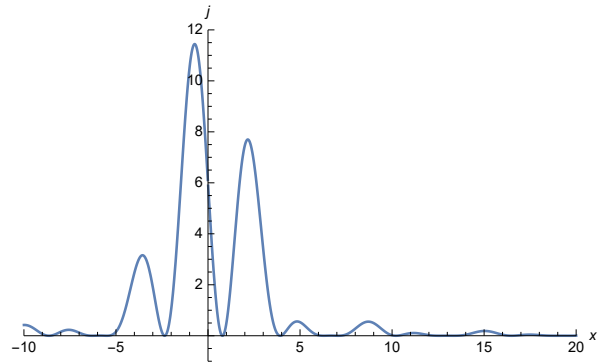


Fig. 2. Probability flux $j(t, x)$ at the time $t=0$.

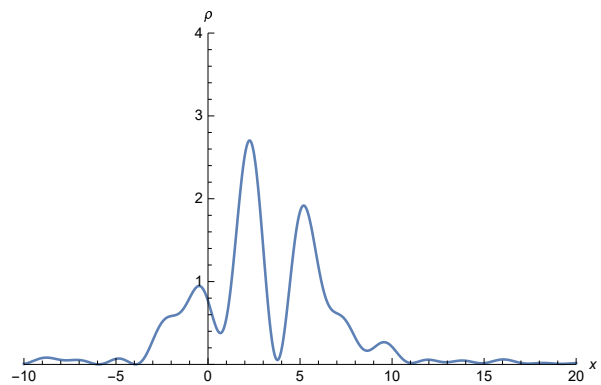


Fig. 3. Probability density $\rho(t, x)$ at the time $t=1$.

be interpreted as a motion of the peaks of the wave packet probability density to the right in the momentum direction but at the same time their spreading to the both sides. In the combination of the two processes, negative direction of the current may appear locally in the time and space.

DIRAC EQUATION - MASSIVE

Let us consider the Dirac equation for the 2-component spinors in the 1+1 dimensional space time with non-zero mass m . We use units where $\hbar = 1$ and $c = 1$ in this section. The Dirac 2×2 matrices are unique up to a similarity transformation as in the 4-dimensional space-time [2], so any of their representations may be used. Let us choose the Dirac equation in the form

$$(i\sigma_2 \partial_t - \sigma_1 \partial_x - m)\psi = 0 \quad (2)$$

where $\psi(t, x) \in \mathbb{C}^2$ and $\sigma_1, \sigma_2, \sigma_3$ are the usual Pauli matrices. Then probability density and flux are

$$\begin{aligned} \rho(t, x) &= \psi(t, x)^\dagger \psi(t, x) = |\psi_1(t, x)|^2 + |\psi_2(t, x)|^2, \\ j(t, x) &= \psi(t, x)^\dagger \sigma_3 \psi(t, x) = |\psi_1(t, x)|^2 - |\psi_2(t, x)|^2. \end{aligned}$$

The simple indefinite form of the current easily allows for the construction of states with momentum

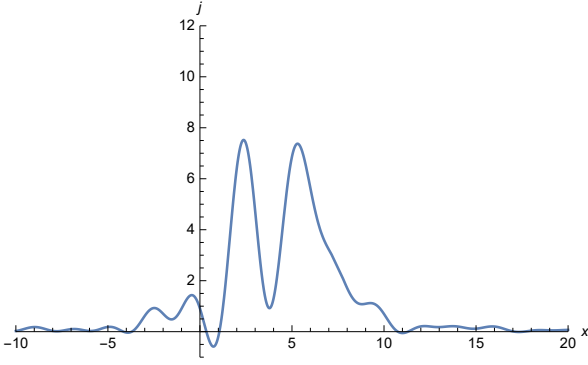


Fig. 4. Probability flux $j(t, x)$ at the time $t=1$.

spectral support in $[0, +\infty)$ but the current negative in some regions. These states are in general superpositions of positive and negative energy parts. We show an example that even states of momentum as well as energy spectral support in $[0, +\infty)$ but somewhere locally negative current exist.

The Hamiltonian corresponding to the equation (2) in the \mathbf{p} -representation has two eigenvalues $E_{\pm}(p) = \pm\sqrt{p^2 + m^2}$ corresponding to two eigen-spinors

$$\hat{\varphi}_{\pm}(p) = a_{\pm}(p) \begin{pmatrix} \mp im \\ (p^2 + m^2)^{\frac{1}{2}} \mp p \end{pmatrix},$$

$$a_{\pm}(p) = 2^{-\frac{1}{2}}(p^2 + m^2)^{-\frac{1}{4}}((p^2 + m^2)^{\frac{1}{2}} \mp p)^{-\frac{1}{2}}.$$

A state with both energy and momentum spectral support in $[0, +\infty)$ has at the time $t = 0$ initial form

$$\hat{\varphi}(p) = \hat{A}(p)\hat{\varphi}_+(p),$$

where $\hat{A} : \mathbb{R} \rightarrow \mathbb{C}$ is a function with support in $[0, +\infty)$. The time evolution of this state in the x -representation

$$\psi(t, x) = \frac{1}{\sqrt{2\pi}} \int_{\mathbb{R}} e^{i(px - \sqrt{p^2 + m^2}t)} \hat{A}(p)\hat{\varphi}_+(p) dp.$$

Let us choose a simple form

$$\hat{A}(p) = \sqrt{2E_+(p)(E_+(p) - p)} \chi_{(0, m)}(p)$$

so that

$$\psi(t, x) = \frac{1}{\sqrt{2\pi}} \int_0^m e^{i(px - \sqrt{p^2 + m^2}t)} \begin{pmatrix} -im \\ \sqrt{p^2 + m^2} - p \end{pmatrix} dp.$$

A normalization constant is again skipped here.

At $t = 0$, the upper component

$$\psi_1(0, x) = -i \frac{\sqrt{2}m e^{i\frac{mx}{2}}}{\sqrt{\pi}x} \sin \frac{mx}{2}$$

has zeroes, the first at $x = 2\pi/m$. Remembering the form of $j(t, x)$, there would be regions with negative direction of the flux if

$$\psi_2(0, 2\pi/m) = \frac{1}{\sqrt{2\pi}} \int_0^m e^{i2\pi p/m} \frac{m^2}{\sqrt{p^2 + m^2} + p} dp$$

would be nonzero. However, this is the case as the imaginary part of the last expression up to a positive factor equals

$$\int_0^m \frac{\sin(2\pi p/m)}{\sqrt{p^2 + m^2} + p} dp >$$

$$\left(\int_0^{m/2} + \int_{m/2}^m \right) \frac{\sin(2\pi p/m)}{\sqrt{m^2/4 + m^2} + m/2} dp = 0.$$

DIRAC EQUATION - MASSLESS

The Dirac equation (2) with $m = 0$ separates to the two uncoupled 1+1 dimensional analogs of the Weyl equations

$$(\partial_t + \partial_x)\psi_1 = 0 \quad , \quad (\partial_t - \partial_x)\psi_2 = 0$$

and the flux sign may be arbitrary in general. However, if we consider only states with energy as well as momentum spectral supports fully contained in $[0, +\infty)$ or $(-\infty, 0]$ the direction of the flux is the same as the direction of the momentum for the positive energy states and the opposite for the negative energy states.

The negative energy states are interpreted as the charge conjugated states of the antiparticles in quantum field theory. So we can formulate the result that for the massless neutrinos and antineutrinos in 1+1 dimensional space-time the directions of the momentum and the probability flux are the same.

CONCLUSIONS

Simple examples illustrate that the positive/negative momentum spectral support does not induce positive/negative direction of the probability current for Schrödinger and massive Dirac particles in 1+1 dimensional space-time.

For the massless Dirac particles, the current direction is positive/negative for the positive/negative momentum spectral support.

ACKNOWLEDGMENT: The work was supported by the NPI CAS institutional support RVO 61389005.

REFERENCES

1. J. Dittrich, Rev. Math. Phys. **32**, 2050029 (2020).
2. R.H. Good, Jr., Rev. Mod. Phys. **27**, 187 (1955).

PHYSICS AT FUTURE EIC EXPERIMENT

M. Krelina, michal.krelina@fjfi.cvut.cz, Czech Technical University in Prague, FNSPE, Brehova 7, 115 19 Prague, Czech Republic, J. Nemchik, nemcik@saske.sk, Czech Technical University in Prague, FNSPE, Brehova 7, 115 19 Prague, Czech Republic and Institute of Experimental Physics SAS, Watsonova 47, 04001 Kosice, Slovakia

INTRODUCTION

The future electron-ion colliders [1] will offer a detailed investigation of the hadronic and nuclear structure, including the non-linear Quantum Chromodynamics (QCD) and nuclear effects. They will represent a unique tool for the study of various processes, such as the vector meson production, deeply virtual Compton scattering, production of direct photons and Drell-Yan pairs, production of di-jets, etc.

In this report, we highlight the electroproduction of vector mesons off nucleon and nuclear targets, in particular heavy quarkonia, which are very effective for investigation of the corresponding production mechanism, as well as various nuclear effects inherent in heavy-ion collisions. We describe shortly the recent theoretical progress in determination of quarkonium wave functions [2, 3, 4], in predictions of nuclear shadowing at low Bjorken x_{Bj} [5] and present new results for the cross section in coherent quarkonium photoproduction off the nucleus.

PROTON TARGET

The elastic electroproduction of heavy quarkonia $\gamma^*N \rightarrow VN$ has been studied within the light-front (LF) color dipole formalism [3]. Here the the corresponding production cross section reads

$$\sigma^{\gamma^*p \rightarrow Vp}(x, Q^2) = \frac{1}{16\pi B} \left| \mathcal{A}^{\gamma^*p \rightarrow Vp} \right|^2, \quad (1)$$

where B is the diffractive slope in the process $\gamma^*N \rightarrow VN$, and the amplitude \mathcal{A} is given as,

$$\mathcal{A}^{\gamma^*p \rightarrow Vp} \propto \int dz d^2r \Psi_V^* \Psi_{\gamma^*} \sigma_{q\bar{q}}(r, z), \quad (2)$$

with Ψ_{γ^*} and Ψ_V denoting the wave functions related to $\gamma^* \rightarrow Q\bar{Q}$ and $Q\bar{Q} \rightarrow V$ transitions, respectively. Here $\sigma_{q\bar{q}}(r, z)$ is the dipole cross section representing the interaction of the $Q\bar{Q}$ photon fluctuations with a transverse size r with the target proton and the variable z is the photon momentum fraction carried by a heavy quark (antiquark).

The LF photon wave function is well described with no large uncertainties. Not so for the LF quarkonium wave function and $\sigma_{q\bar{q}}(r, z)$. However, the radial part of Ψ_V is well defined in the $Q\bar{Q}$ rest frame and can be obtained as a solution of the Schrödinger equation for various realistic $Q - \bar{Q}$ interaction potentials. Then its LF counter-part is acquired performing the Lorentz boost from the $Q\bar{Q}$ rest frame. Assuming a simple non-photon-like structure of the quarkonium wave function [2, 3, 4] in the $Q\bar{Q}$ rest frame, the corresponding Lorentz transform is also undergone for the spin-dependent part known as the Melosh spin rotation. The next ingredient of amplitude \mathcal{A} , the dipole cross section $\sigma_{q\bar{q}}$ cannot be derived from the first principles. Thus

we are obliged to adopt several popular parametrizations of $\sigma_{q\bar{q}}$ obtained from the fit of DIS HERA data. All these theoretical uncertainties related to the mass of heavy quark, to the form of $Q - \bar{Q}$ interaction potential, as well as to the choice of the phenomenological model for $\sigma_{q\bar{q}}$ have been analyzed in [3] and can be reduced by the future precise measurements at EIC. It was also found in [3] that the study of $\Psi'(2S)$ -to- $J/\Psi(1S)$ and $\Upsilon'(2S)$ -to- $\Upsilon(1S)$ ratios is very effective for minimization of the above uncertainties.

Another source of uncertainty is associated with the structure of $V \rightarrow Q\bar{Q}$ transition. The standard photon-like structure in the LF frame, frequently used in the literature, leads to an extra D -wave admixture in the quarkonium wave function in the $Q\bar{Q}$ rest frame. However, such a D -wave component contribution is not justified by any realistic nonrelativistic $Q - \bar{Q}$ potential model. In our studies [4] we have analyzed this contribution in the elastic electroproduction process $\gamma^*N \rightarrow VN$ by comparing the LF photon-like with the S -wave-only structure in the $Q\bar{Q}$ rest frame [2, 3]. For the $J/\Psi(1S)$ state this undesirable D -wave contribution causes a small 5–10% enhancement of electroproduction cross sections. However, the nodal structure of the $\Psi'(2S)$ wave function generates the boosting of D -wave effects with the corresponding undesirable 20–30% enhancement.

NUCLEAR TARGETS

In comparison to a nucleon, the nuclear targets provide us with additional information about the space-time pattern of production mechanism and the onset of various nuclear effects modifying the nucleus-to-nucleon ratio. Namely, the study of such ratio can reduce the above-mentioned uncertainties.

In coherent (elastic) $\gamma^*A \rightarrow VA$ and incoherent (quasi-elastic) $\gamma^*A \rightarrow VA^*$ quarkonium production, we included the higher twist quark shadowing related to the $Q\bar{Q}$ photon fluctuations, as well as the leading twist gluon shadowing (GS) associated with multi-gluon photon components [6]. For the former case, the onset of shadowing is controlled by the scale known as the coherence length (CL), which is given in the rest frame of the target nucleus as,

$$l_c = \frac{2\nu}{Q^2 + M_{Q\bar{Q}}^2}, \quad (3)$$

where ν and Q^2 is the energy and virtuality of the photon, and $M_{Q\bar{Q}}$ is the effective mass of the $Q\bar{Q}$ pair. This effect of coherence can also be interpreted as the lifetime of $Q\bar{Q}$ photon state. The maximal onset of shadowing requires long-lived photon $Q\bar{Q}$ fluctuations with $l_c \gg R_A$, where R_A is the nuclear radius. Otherwise one should apply corrections for the finite-CL which have been obtained and studied within a rigorous Green function formalism [5]. Besides, the GS

manifests itself at higher energies due to a larger effective masses of multi-gluon photon fluctuations.

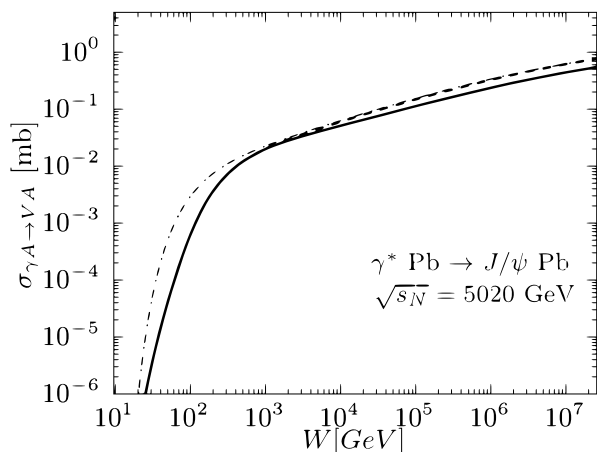


Fig. 1. Coherent J/ψ photoproduction at the LHC energy. The dot-and-dashed line represents model predictions in the high energy limit. The dashed and solid line includes additionally the finite-CL and GS corrections, respectively.

Taking into account all these nuclear phenomena (see [6] for more details), we can provide predictions for the LHC and future EIC experiments. As an example, in Fig. 1 we show our results for the cross section of the coherent process $\gamma Pb \rightarrow J/\Psi Pb$ at the LHC collision energy 5.02 TeV. Here, the dot-and-dashed line corresponds to maximal quark shadowing. The dashed line represents the finite-CL corrections, and the solid one includes GS additionally. Such a coherent charmonium photoproduction at the LHC energies was presently studied also in ultra-peripheral collisions (UPC) in [6].

One can see from Fig. 1 a weak onset of CL effects at small photon energies $W < 500$ GeV manifesting so importance of the finite-CL corrections. On the other side, the GS prefers larger photon energies reducing the nuclear cross section $\sigma_{\gamma Pb \rightarrow J/\Psi Pb}$. However, the corresponding magnitude of GS effects expected at the planned EIC experiments at BNL will be specified later after setting of all kinematical details during realization of the EIC project.

The Fig. 2 [6] shows the onset of particular nuclear effects in the $\gamma Pb \rightarrow J/\Psi Pb$ coherent process in UPC at the LHC energy 5.02 TeV. Here we treat the “ S -wave-only” structure of charmonium wave function in the $c\bar{c}$ rest frame. The dotted line represents our results for long-lived $c\bar{c}$ photon fluctuations. The dashed line includes additionally the spin effects and the difference between the solid and dashed line is a clear manifestation of GS effects at $y = 0$ and finite-CL corrections at large negative and positive rapidities.

Another theoretical investigation of coherent and incoherent electroproduction of vector mesons off a proton and off nuclear targets has been performed using the hot-spot model [7] for the nuclear profile function what corresponds to the possible existence of sub-nucleonic degrees of freedom of nucleons.

ACKNOWLEDGMENT: This work was supported by the project Centre of Advanced Applied Sciences with the number: CZ.02.1.01/0.0/0.0/16-019/0000778 (Czech Republic). Project Centre of Advanced Applied

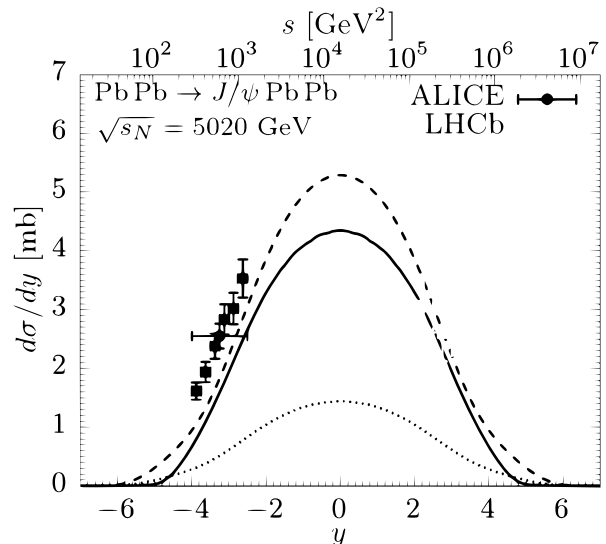


Fig. 2. Coherent J/ψ production in UPC at the LHC energy. The dot line represents model predictions in the high energy limit. The dashed and solid line includes additionally the spin rotation effects and the finite-CL and GS corrections, respectively.

Sciences is co-financed by European Union. J.N. work was partially supported also by the grant LTT18002 of the Ministry of Education, Youth and Sports of the Czech Republic, and by the Slovak Funding Agency, Grant 2/0007/18.

REFERENCES

1. A. Accardi *et al.*, *Eur. Phys. J. A* **52**, no. 9, 268 (2016); J. L. Abelleira Fernandez *et al.*, *J. Phys. G* **39**, 075001 (2012).
2. M. Krelina, J. Nemchik, R. Pasechnik, J. Cepila, *Eur. Phys. J. C* **79**, 154 (2019).
3. J. Cepila, J. Nemchik, M. Krelina, R. Pasechnik, *Eur. Phys. J. C* **79**, 495 (2019).
4. M. Krelina, J. Nemchik, R. Pasechnik, *Eur. Phys. J. C* **80**, 92 (2020).
5. M. Krelina, J. Nemchik, *Eur. Phys. J. Plus* **135**, 444 (2020).
6. B. Z. Kopeliovich, M. Krelina, J. Nemchik, I. K. Potashnikova, [arXiv:2008.05116 [hep-ph]].
7. M. Krelina, V. P. Goncalves, J. Cepila, *Nucl. Phys. A* **989**, 187 (2019); J. Cepila, J. G. Contreras, M. Krelina, J. D. Tapia Takaki, *Nucl. Phys. B* **934**, 330 (2018); J. Cepila, J. G. Contreras, M. Krelina, *Phys. Rev. C* **97**, 024901 (2018).

COMPARATIVE ELECTROCHEMICAL, OPTICAL AND X-RAY STUDIES OF POLYFLUORENE AND FLUORENE-BASED ALTERNATING COPOLYMER

K. Gmucová, katarina.gmucova@savba.sk, Institute of Physics, Slovak Academy of Sciences, Dúbravská cesta 9, 84511 Bratislava, Slovakia, K. Végső, karol.vegso@savba.sk, Institute of Physics, Slovak Academy of Sciences, Dúbravská cesta 9, 84511 Bratislava, T. Váry, tomas.vary@stuba.sk, Faculty of Electrical Engineering and Information Technology, Slovak University of Technology, 81219 Bratislava, Slovakia, V. Nádaždy, vojtech.nadazdy@savba.sk, Institute of Physics, Slovak Academy of Sciences, Dúbravská cesta 9, 84511 Bratislava, Slovakia

INTRODUCTION

In past years, the all-conjugated copolymers bringing together in one molecule hole- and electron-conductive parts became of utmost importance [1, 2]. The different copolymer parts have different stiffness values resulting in a different microstructure of the self-organized solution-processed thin film, and the relations between microstructure and electrical properties of such copolymers are strong.

Scherf and List reviewed the influence of both the main chain conformation changes and defect sites on polyfluorenes properties [3]. Admassie et al. studied a series of polyfluorene copolymers incorporating alternating electron-withdrawing (A) and electron-donating (D) groups [4]. Using quantum chemical calculations, the authors have proved the influence of various repeating electron-donating and electron-withdrawing groups on the HOMO and LUMO positions. Garcia-Basabe et al. studied the relationship between the microstructure of the polyfluorene based copolymer poly[2,7-(9,9-dioctylfluorene)-alt-4,7-bis(thiophen-2-yl) benzo-2,1,3-thiadiazole] (PFO-DBT) thin film and its transport properties [5]. The electronic structure of various PFO-DBT isomers varying by the up or down spatial orientation polydioctylfluorene, thiophene, benzothiadiazole, and, again, thiophene was described by DFT. Two most stable structures with almost identical relative energies were found.

MATERIALS AND EXPERIMENTAL SETUP

PFO and PFO-DBT thin films were spin-coated on ITO substrates in the glove box for 100 s up to a complete drying (PFO: from 1.5 wt% solution in toluene, spinning rate 20 rps, PFO-DBT: from 2.0 wt% solution in toluene, spinning rate 20 rps, both resulting in 100 nm thickness of the film). The thermal annealing of the thin film was performed at 110°C for 5 min. The electrochemical microcells were formed on ITO substrates with deposited thin films by attaching a cut micropipette tip bounding a working disc electrode of area 12 mm². The microcells were filled with the 0.1 M solution of NBu₄PF₆ in acetonitrile. The potential of the working electrode was recorded with respect to the reference Ag/AgCl electrode and recalculated to the local vacuum level assuming the Ag/AgCl energy vs. vacuum value of 4.66 eV.

The electronic structure was mapped by the energy-resolved electrochemical impedance spectroscopy (ER-EIS); the impedance/gain-phase analyzer Solartron analytical (model 1260) was used for this purpose [6, 7].

The density of states was mapped in the energy range from - 1.5 to - 7.0 eV vs. vacuum. The frequency was set to 0.5 Hz, the amplitude of AC voltage to 100 mV, and the sweep rate of the DC voltage ramp to 10 mV/s. The GIWAXS measurements were performed on a custom-designed Nanostar device (Bruker AXS, Germany) with a liquid Ga metal-jet X-ray source (Excillum, Sweden) generating high-intense Ga K α radiation with a photon energy of 9.25 keV. UV-Vis-NIR spectrophotometer (Shimadzu) with the spectral range 200 – 2200 nm was used to obtain absorbance spectra of studied thin films.

RESULTS AND DISCUSSION

The density of states (DOS) measured for the PFO and PFO-DBT as-prepared and thermally annealed thin films are shown in Fig. 1. The bandgap values of both polymers increased after the thermal annealing, while the LUMO energy was almost unchanged. A sharper DOS decrease was observed on the HOMO side of the spectrum. Moreover, the DOS changes in the forbidden gap of PFO-DBT (i.e., the lowering of defect states DOS) are more pronounced than those in the PFO thin film. The DOS in the PFO-DBT thin film was lower by $\sim 4 \times 10^{15} \text{ cm}^{-3} \text{ eV}^{-1}$, the DOS in the PFO thin film only by $\sim 2.5 \times 10^{15} \text{ cm}^{-3} \text{ eV}^{-1}$ [8].

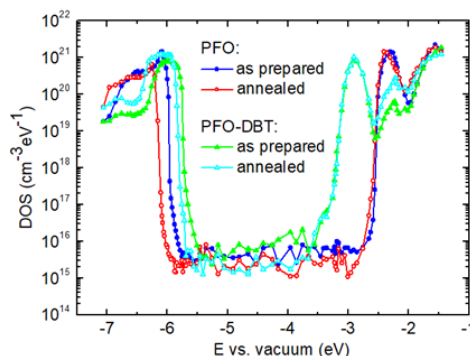


Fig. 1. ER-EIS spectra of PFO and PFO-DBT as prepared and thermally annealed thin films.

A comparison of the band gaps determined electrochemically with those obtained from UV-Vis absorption spectroscopy is shown in Fig. 2. As already mentioned in the literature, differences between the transport gap, electrochemical gap, and optical gap can be often observed. The data collected by Sworakowski et al. [9] showed that, on average, the CV measurements underestimate the gap energies by ca. 16 %, and the UV-

VIS optical spectroscopy underestimates the gap energies by ca. 37 % as compared to the gaps determined by UPS/IPES measurements.

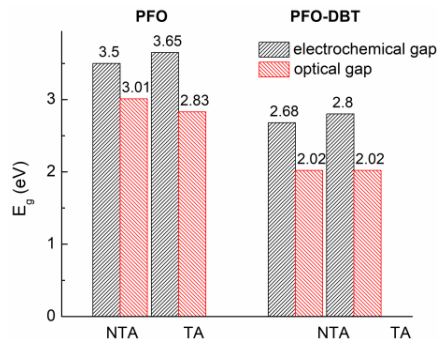


Fig. 2. Electrochemical and optical gaps of PFO and PFO-DBT as prepared and thermally annealed thin films.

Another issue highlighted in Fig. 1 is a stronger tendency to form structural defect states in the copolymer PFO-DBT films as compared to polymer PFO. The situation probably resides in a more complicated microstructure of the copolymer thin film caused by the presence of various isomers in its backbone chain [6]. The microstructure of films was studied by the X-ray method. The GIWAXS patterns of the PFO and PFO-DBT as-prepared and thermally annealed thin films are shown in Fig. 3.

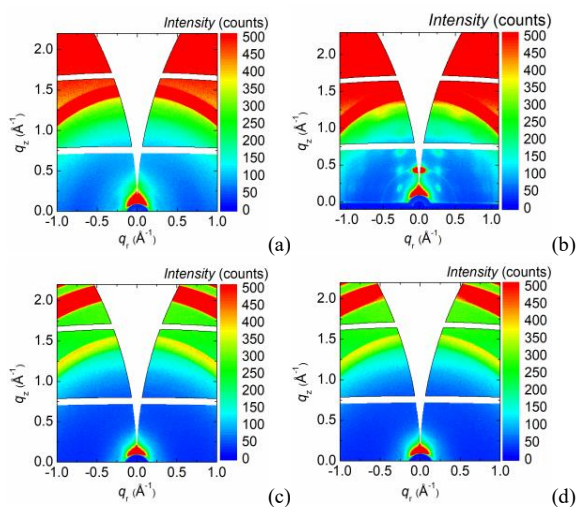


Fig. 3. GIWAXS patterns of (a) as prepared PFO thin film, (b) thermally annealed PFO thin film, (c) as prepared PFO-DBT thin film, and (d) thermally annealed PFO-DBT thin film.

An expressive formation of the crystalline structure due to thermal annealing of PFO thin film is visible in Fig. 3b. In this case, the impact of the altered chain geometry is manifested as the formation of β -phase in the PFO film [10, 11]. On the other hand, the isomers present in the PFO-DBT thin films, which vary by the up or down spatial orientation of chemical units in the molecular structure of the monomer [5], probably prevents the effective packing of molecules and formation of a crystalline structure during the thermal annealing.

CONCLUSIONS

The performed studies of PFO and PFO-DBT spin-coated films, both as prepared and upon annealing, have indicated an expressive thermal restructuring of the packing structure only for homopolymer PFO. The comparison between the information extracted from ER-EIS and GIWAXS measurements explicitly points out that combining these two methods is particularly appropriate.

ACKNOWLEDGMENT: This work was supported by the Scientific Grant Agency VEGA under Project No. 2/0163/17 and by the Slovak Research and Development Agency under the contract No. APVV-19-0465. This work was performed during the implementation of the project Building-up Centre for advanced materials application of the Slovak Academy of Sciences, ITMS project code 313021T081 supported by the Research & Innovation Operational Programme funded by the ERDF.

REFERENCES

1. D. Venkateshvaran, M. Nikolka, A. Sadhanala, V. Lemaur, M. Zelazny, M. Kepa, M. Hurhangee, A. J. Kronemeijer, V. Pecunia, I. Nasrallah, I. Romanov, K. Broch, I. McCulloch, D. Emin, Y. Olivier, J. Cornil, D. Beljonne, H. Sirringhaus, *Nature* **515**, 384 (2014).
2. T. Erdmann, S. Fabiano, B. Milián-Medina, D. Hanifi, Z. Chen, M. Berggren, J. Gierschner, A. Salleo, A. Kiriy, B. Voit, A. Facchetti, *Adv. Mater.* **28**, 9169 (2016).
3. U. Scherf, E. J. W. List, *Adv. Mater.* **14**, 477 (2002).
4. S. Admassie, O. Inganäs, W. Mammo, E. Perzon, M. R. Andersson, *Synth. Metals* **156**, 614 (2006).
5. Y. Garcia-Basabe, G. Kladnik, C. F. N. Marchiori, C. E. V. de Moura, L. Floreano, A. B. Rocha, L. S. Roman, A. Morgante, D. Cvetko, M. L. M. Rocco, *J. Phys. Chem. C* **121**, 25187 (2017).
6. V. Nádaždy, F. Schauer, K. Gmucová, *Appl. Phys. Lett.* **105**, 142109 (2014).
7. K. Gmucová, V. Nádaždy, F. Schauer, M. Kaiser and E. Majková, *J. Phys. Chem. C* **119**, 15926 (2015).
8. K. Gmucová, V. Nádaždy, T. Váry, *AIP Conference Proceedings* **1996**, 020014 (2018).
9. J. Sworakowski, *Synthetic Metals* **235**, 125 (2018), J. Sworakowski, K. Janus, *Organic Electronics* **48**, 46 (2017).
10. D. L. Huber, I. Avgin, *J. Polym. Sci. B: Polym. Phys.* **54**, 1109 (2016).
11. Q. Zhang, L. Chi, G. Hai, Y. Fang, X. Li, R. Xia, W. Huang, E. Gu, *Molecules* **22**, 315 (2017).

MAGNETIC, MAGNETOCALORIC, THERMAL AND TRANSPORT PROPERTIES OF $Gd_3Ni_2In_4$

K. Arun¹, T.P. Rashid¹, M. Reiffers², marian.reiffers@unipo.sk, A. Dzubinska³, R. Nagalakshmi¹

¹Intermetallics and Non-linear Optics Laboratory, Department of Physics, National Institute of Technology, Tiruchirappalli, 620 015, India

²Faculty of Humanities and Natural Sciences, Presov University, 081 16 Presov, Slovakia

³CPM-TIP, UPJS, 040 01 Kosice, Slovakia

INTRODUCTION

Nowadays, magnetic materials, which have a wide temperature range with several magnetic transitions, are suitable for very popular study of magnetocaloric properties. Such a broad range can be observed in materials with a second-order phase transition. One way to confirm this prediction is to study magnetic and magnetocaloric properties.

The attractive materials for the investigation are alloys and compounds with consist of rare earth. Among them the Gd-based materials are in the class of the goods candidates where an experiment and study of physical properties for potential practical applications are attractive.

For these reasons we choose $Gd_3Ni_2In_4$ material. Structural characterization was reported before in paper [1]. The most interesting results, which have been obtained, are presented in this contribution.

EXPERIMENTAL DETAILS

The polycrystalline sample was prepared by arc melting techniques using Centorr electric arc furnace under argon atmosphere. The individual pieces of starting elements have a high purity: 99.9 % for Gd, 99.99 % for Ni and 99.99 % for In. After the preparation process, the sample were enclosed in an evacuated quartz tube and subjected to annealing at 750 °C for 15 days.

The structural analysis has been studied by X-ray Bruker Panalytical Xpert PRO X-Ray Diffractometer with Cu-K α radiation ($\lambda = 1.54056 \text{ \AA}$) in the range $20^\circ \leq 2\theta \leq 80^\circ$. Both the homogeneity and the composition of the compound were analysed using scanning electron microscope (SEM) equipped with an energy dispersive X-ray (EDX) spectrometer.

Physical properties were measured by commercial device DynaCool (Quantum Design) in the temperature range from 2 K up to 300 K in an applied magnetic field up to 9 T.

EXPERIMENTAL RESULTS AND DISCUSSION

The first thing during the investigation process was performing of a Rietveld refinement. It was carried out to determine the phase purity (see in Fig. 1). The refinement result reveals that the $Gd_3Ni_2In_4$ compound has crystallized in single phase with hexagonal $Lu_3Co_2In_4$ -type $Gd_3Ni_2In_4$ with some Indium traces. The resulting lattice parameters ($a = 7.7051(6) \text{ \AA}$ and $c = 3.8093(4) \text{ \AA}$) obtained from the Rietveld refinement agree well with the previously result [1]. Back scattered electron (BSE) image confirms the absence of any other

impurity phases in the compound.

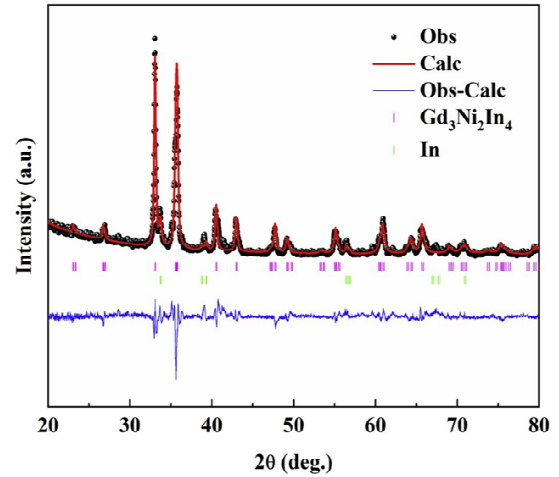


Fig. 1. The powder XRD pattern (black) of $Gd_3Ni_2In_4$ compound along with calculated pattern (red) and their difference (blue) [2].

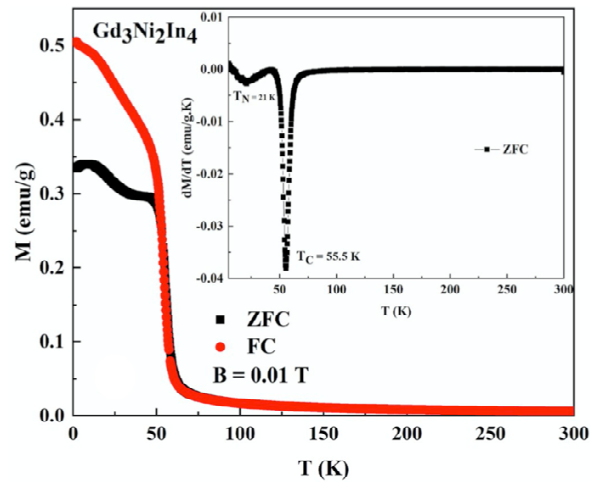


Fig. 2. Temperature dependence of magnetization at 0.1 T under ZFC and FC modes. Inset represents $dM(T)/dT$ with T_c and T_N [2]

The magnetization measurements performed between 2 K and 300 K are presented in Fig. 2. The transition temperatures have been observed at $T_c = 55 \text{ K}$ and $T_N = 21 \text{ K}$. In the present paper, the coexistence of antiferromagnetic and ferromagnetic competing interactions in compound might be the contributing component of thermomagnetic irreversibility [3, 4] which is discussed in further studies.

The magnetocaloric effect in the sample is qualitatively

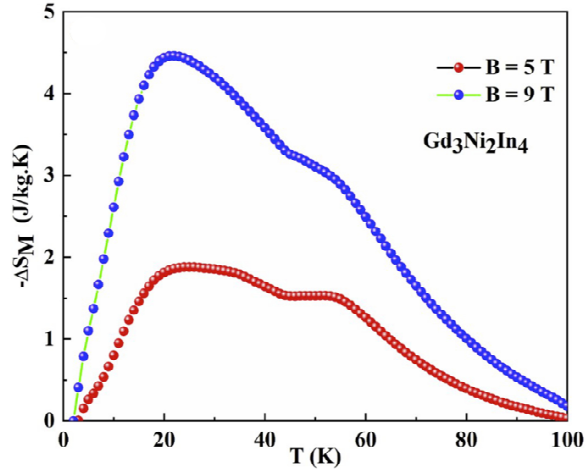


Fig. 3. Temperature variation of $-\Delta S_M$ (T) around ordering temperatures in magnetic field of $\Delta B = 5$ T and 9 T from heat capacity measurements [2]

vely estimated by calculating the change in magnetic entropy $-\Delta S_M$, with temperature in various applied magnetic fields which is shown in Fig. 3. Magnetic entropy was calculated from the well-known Maxwell equation. $C(T,0)$ and $C(T,B)$ represent the heat capacity data measured in various magnetic fields respectively. The presence of two successive transitions has resulted in broadening of MCE peak over a wide temperature range with $\Delta T_{FWHM} = 68$ K (in $\Delta B = 5$ T).

The $C(T)$ plot obtained without the application of external magnetic field, reveals two anomalies: one around 20 K and other around 50 K. As the strength of magnetic field grows, the minimum at 20 K shifts towards low temperatures confirming the existence of antiferromagnetic transition and the peak at 50 K is unaltered even at high fields as shown in inset Fig. 4.

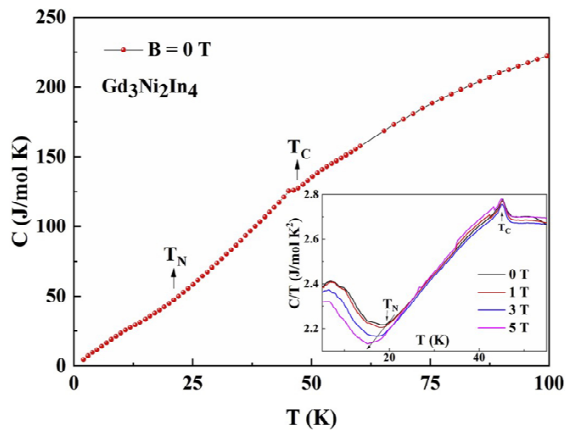


Fig. 4. Heat capacity temperature dependence of $Gd_3Ni_2In_4$ as a function of temperature. Inset shows the C/T vs T plot measured in various magnetic fields [2]

The field dependence magnetoresistance (MR) of the sample has been measured and results are plotted in Fig. 5. In the paramagnetic regime, the value of MR is not noteworthy whereas in the region closer to the transition temperature, $T_C = 55$ K, a small negative MR is observed and indicates ferromagnetic character.

Below T_C , MR linearly decreases with temperature and becomes positive around T_N . At the 2 K, MR reaches a value of 44 % in the magnetic field of 9 T. This is a signature of antiferromagnetic ordering of moments at low temperatures.

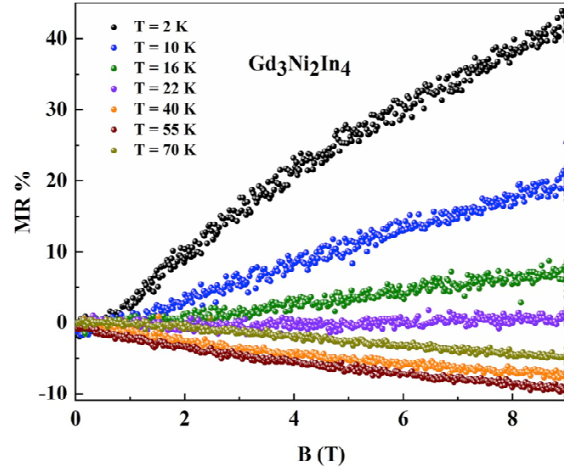


Fig. 5. MR of $Gd_3Ni_2In_4$ material measured in different applied magnetic field [2]

CONCLUSIONS

Based on obtained results, we can conclude that the magnetic, magnetocaloric, transport and thermodynamic properties of polycrystalline $Gd_3Ni_2In_4$ compound have been studied. The magnetocaloric properties indicate the applicability of the compound to the magnetic cooling in the low temperature range.

ACKNOWLEDGMENT: This work was supported by the projects APVV-16-0079, VEGA 1/0956/17 and the grant from Slovak Academic Information Agency (SAIA) under National Scholarship program.

REFERENCES

1. B. Heying et al., Z. Naturforschung B **71**, 1261 (2016).
2. K. Arun et al., Current Applied Physics **20**, 266 (2020).
3. N.K. Singh et al., Appl. Phys. **105**, 023901 (2009).
4. N.K. Singh et al, J. Appl. Phys. **99**, 08K904 (2006).

WIDE TEMPERATURE RANGE MAGNETOCALORIC EFFECT IN $\text{Dy}_{6.5}\text{Co}_2\text{Si}_{2.5}$

K. Arun¹, T. P. Rashid¹, I. Curlik², S. Ilkovic², sergej.ilkovic@unipo.sk, M. Reiffers², A. Dzubinska³, R. Nagalakshmi¹

¹Intermetallics and Non-linear Optics Laboratory, Department of Physics, National Institute of Technology, Tiruchirappalli 620015, India

²Faculty of Humanities and Natural Sciences, Prešov University, 081 16 Prešov, Slovakia

³Faculty of Natural Sciences, P. J. Šafárik University, 040 01 Košice, Slovakia

INTRODUCTION

Magnetocaloric effect (MCE) is one of the promising technologies for applications in refrigeration as energy efficient and environment-friendly alternative. For the materials interesting for the applications is the most important high value of the Refrigerant Capacity (RC), what can be done by maximizing of the magnetic entropy change ΔS_m and temperature span. Study of the MCE properties of the materials attracts the interest of the scientists because the giant MCE effect in $\text{Gd}_5\text{Si}_2\text{Ge}_2$ near room temperature were reported [1].

Alloys contains Gd are therefore from the one hand promising, but at the other hand they are from the practical point of view not reasonable. One of the usable approaches is to prepare “table-like” materials with multiple phase transitions [2, 3].

EXPERIMENTAL AND RESULTS

The $\text{Dy}_{6.5}\text{Co}_2\text{Si}_{2.5}$ alloy was synthesized by arc melting of the constituent elements having high purity (Dy, 99.9%; Ni and Si, 99.99%) in stoichiometric ratio in a water-cooled Cu hearth under purified argon atmosphere. The melted ingot was flipped and re-melted five times to ensure homogeneity. The as-cast sample was sealed in a quartz tube of high vacuum, annealed for 15 days at 800 °C, and then quenched to room temperature. The phase purity of the sample was determined by the X-ray powder diffraction (XRD) using of Rietveld refinement. Magnetic, thermodynamic, and transport measurements were performed on Quantum design DYNACOOOL device from 2 to 300 K and magnetic field up to 9 T.

Using of Rietveld-refined XRD analysis of $\text{Dy}_{6.5}\text{Co}_2\text{Si}_{2.5}$ alloy were identified three major phases Dy_5Si_3 (54.97 wt.%), $\text{Dy}_3\text{Co}_{2.2}\text{Si}_{1.8}$ (30.85 wt.%) and Dy_3Co (14.18 wt.%) (Fig. 1).

The temperature dependence of ZFC and FC magnetization $M(T)$ data measured in magnetic field $B = 0.01\text{T}$ are presented at Fig. 2. From the first order derivative of $M(T)$ (inset figure) were determined four temperatures of phase transitions (PT): $T_1 = 43\text{ K}$, $T_2 = 74.7\text{ K}$, $T_3 = 90.5\text{ K}$, and $T_4 = 132.4\text{ K}$.

Thanks to the known PT temperatures of Dy_3Co (29 K, 44 K) [4, 5] we can assume the presence of this phase in the prepared compound. PT at the temperature T_4 may be connected with the presence of the Dy_5Si_3 . Temperature T_2 seems to be far from any PT of alloy components thus may indicate $\text{Dy}_3\text{Co}_{2.2}\text{Si}_{1.8}$ phase [7]. We believe that the transition at 90.5 K is present as inherent characteristic of the prepared $\text{Dy}_{6.5}\text{Co}_2\text{Si}_{2.5}$ compound as a consequence of the multiple magnetic transitions. Higher applied magnetic field smeared out practically all phase transitions. Large bifurcation

between the FC and ZFC dependencies were observed because of the pinning of domain walls [8].

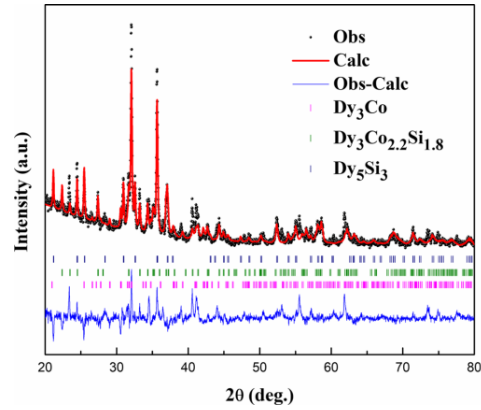


Fig. 1. XRD pattern of $\text{Dy}_{6.5}\text{Co}_2\text{Si}_{2.5}$ alloy

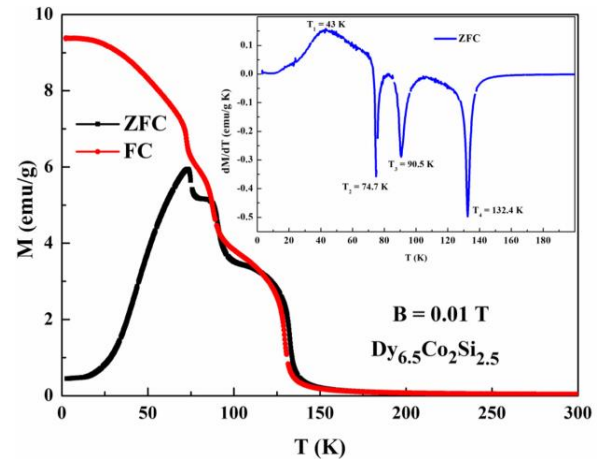


Fig. 2. Temperature dependence of magnetization

From the measurement of the temperature dependencies of heat capacity $C(T)$ were determined the PT temperatures, which are in consonance with the $M(T)$ measurement (Fig 3.). Application of magnetic field cause the smearing of the phase transitions what is in agreement with $M(T)$ measurement (inset Fig. 3).

Using of magnetization measurements were plotted Arrot plot as dependence of M^2 vs B/M (Fig. 4), which can be used for investigation of magnetocaloric properties. This plot gives information about the type of magnetic ordering as far as application limits of the compounds under study. Thanks to Banerjee criterion [9] can be distinguished the order of the phase transition according to the slope of the dependence. The slope is negative for second-order PT, otherwise PT is first-order.

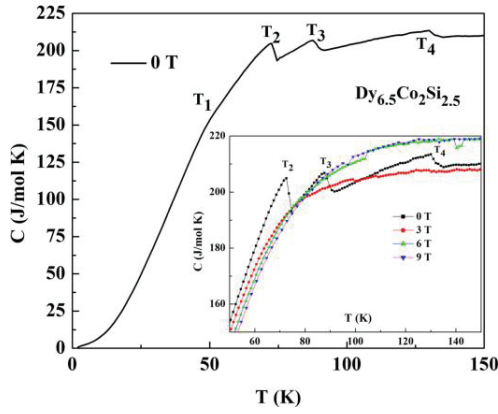


Fig. 3. Temperature dependence of heat capacity $C(T)$

Typical “S-shape” behavior below 47 K clearly seen on the Fig. 4 confirms first-order antiferromagnetic to ferromagnetic (metamagnetic) transition.

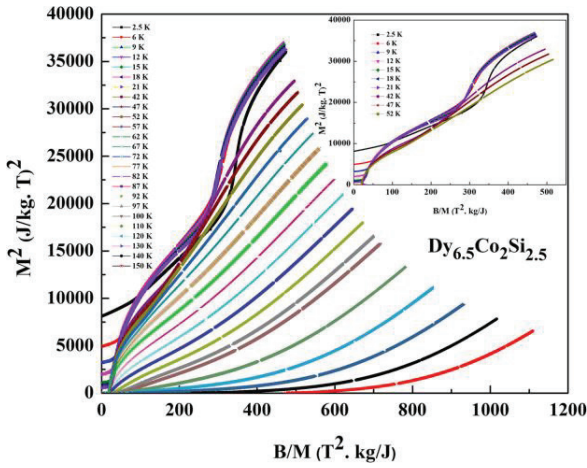


Fig. 4. Arrott plots in the vicinity of the magnetic transitions

Similar Arrott plot were reported in Dy_3Co [7] and $Dy_3Co_{2.2}Si_{1.8}$ [4]. At the other hand, the positive slope above 47 K indicates second-order magnetic phase transition which is favorable for MCE applications.

From magnetic measurements were calculated the magnetic entropy change (ΔS_M) as a function of temperature for various magnetic fields from isothermal magnetization data using Maxwell's relation:

$$\Delta S_m = \int_0^B \left(\frac{\partial M}{\partial T} \right)_B dB \quad (1)$$

The temperature dependence of $-\Delta S_M$ at Fig. 5 below 7.5 K change the sign from negative to positive with the increase of temperature due to the field-induced antiferromagnetic to ferromagnetic phase transition. The positive $-\Delta S_M$ is usually observed in magnetocaloric materials with first-order magnetic transition.

The maximum value of $-\Delta S_M$ was found 7.94 and 5.66 J/kg K for magnetic field change of 0 – 7 and 0 – 5 T, resp.. One of the most important characteristics of

the magnetocaloric materials is Refrigerant capacity (RC), which can be calculated as follows:

$$RC = -\Delta S_M^{max} \cdot \Delta T_{FWHM} \quad (1)$$

where $-\Delta S_M^{max}$ is the highest value of magnetic entropy and ΔT_{FWHM} is the full width at half maximum of the magnetic entropy peak, which defined the temperature span for chosen magnetic field change.

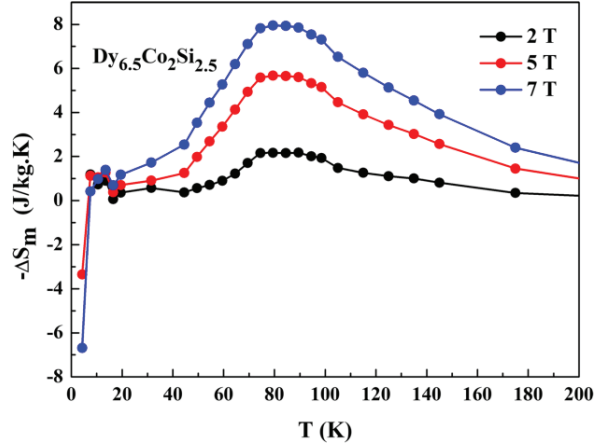


Fig. 5. Temperature-dependent magnetic entropy change

The RC value obtained for $Dy_{6.5}Co_2Si_{2.5}$ is 739 and 474 J/kg for magnetic field change 0 – 7 and 0 – 5 T, respectively is comparable or higher than in other already reported alloys. The temperature span is enlarged to 83.8 K thanks to the existence of four phase transitions in the presented alloy.

ACKNOWLEDGMENT: This work is the result of the Project implementation: University Science Park TECHNICOM for Innovation Applications Supported by Knowledge Technology, ITMS: 26220220182, supported by the Research & Development Operational Programme funded by the ERDF and also by VEGA 1/0956/17 and APVV-16-0079.

REFERENCES

1. V.K. Pecharsky, K.A. Jr. Gschneidner, Phys. Rev. Lett. **78**, 4494 (1997).
2. T.P. Rashid et al., J. Mater. Chem. Phys. **180**, 279 (2016).
3. D.C. Dos Reis et al., J. Magn. Magn. Mater. **424**, 84 (2017).
4. N.V. Baranov, A.N. Pirogov, A.E. Teplykh, J. Alloys. Compds. **226**, 70 (1995).
5. J. Shen et al., Appl. Phys. **A 99**, 853 (2010).
6. M. Falkowski et al., J. Magn. Magn. Mater. **331**, 144 (2013).
7. A.V. Morozkin et al., J. Magn. Magn. Mater. **389**, 157 (2015).
8. N.K. Singh et al., J. Appl. Phys. **101**, 093904 (2007).
9. B.K. Banerjee, Phys. Lett. **12**, 16 (1964).

NIHILNOVI – A NOT SO NEW APPROACH TO DATA VISUALISATION PROMOTING PORTABLE AND SIMPLE TEXT FORMATS

F. Dominec, dominecf@fzu.cz, Institute of Physics CAS, v.v.i., Cukrovarnická 10, CZ-16200 Prague 6, Czech Republic

INTRODUCTION

The ultimate aim of this project is nothing less than an appeal to the scientific community for wider adoption of open formats for data storage. Using human-readable text files or other standardized formats makes easier sharing the results across the world, their machine processing, as well as returning to them in the future when most software falls. Clearly, work of a scientist never ends with saving a file only: One will want to see the data plotted and export a nice graph thereof for publication; multiple files or columns may need to be plotted over each other and often also the data may need to be fitted, filtered or processed in a more sophisticated way. The usual approach is either to load them into a point-and-click application for scientific plotting like Origin or Scidavis, or to learn basics of programming and type the commands in a scientific math package like Mathematica, Matlab, Python or R.

However, none of these approaches is ideal: the former one becomes repetitive when manually handling larger datasets, and macro recording is only a partial remedy to it. The latter one leads to cumbersome programming in case of trivial tasks. Many programs (re)implement only a limited subset of mathematical or graphical functions required in science; the more advanced ones have graphical interfaces that hide useful functions in many-level menus. More often than not, such software tends to bind the researcher to proprietary data formats. According to the author's experience, all available choices of scientific software involve one or more described sacrifices.

PROPOSED SOLUTION

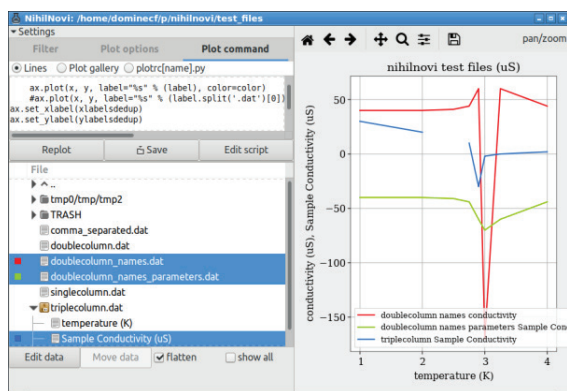


Fig. 1. Graphical user interface of *nihilnovi*

In an attempt to resolve the unfortunate situation described, the author presents a program named *nihilnovi*, with a single window containing a file browser, a code editor and a plotting area (Fig. 1). Selecting files in the file browser leads to immediate plotting of their contents in the right panel, which makes

data inspection as intuitive as viewing a photo gallery.

Importantly, the critical part of the Python code responsible for plotting is exposed to the user, who can write advanced commands for data processing and plotting (or paste them from included templates). This code is persistent with regards of file selection, and it allows processing multiple files at once. It can also be saved as a Python script, which enables not only its future development and re-use for new data, but also records step-by-step “lab notes” of the procedure used.

WHAT IS NOT NEW

Aside of its mixed clicking/programming workflow, the major novelty of the program is paradoxically in that it implements almost nothing new, employing the power of established software:

- It does not implement a new plotting library – Matplotlib [2] draws all high-quality plots both for the interactive on-screen plotting and for PDF export.
- It does not promote its custom scripting language – Python (version 3.0+) including numpy and other its powerful scientific modules have been a popular language for scientific use for over two decades.
- Also the suggested file formats for data input/output are simple ASCII files.
- Other input formats like Origin are also supported by means of existing libraries; a project dedicated to reverse engineering and documentation of binary formats [3] exists.

WHAT IS NEW

To author's dismay, development of *nihilnovi* was not possible without actually implementing some new features. One of newly written pieces of code provides the custom file/directory tree browser. More exactly, it is a *dataset/container* browser, since the concept of directory was extended also to *files* than can contain more than one dataset – i.e. a group of values. Therefore, a multi-column text file is treated similar to a directory containing three simple data files (see bottom left of Fig. 1). Likewise, an XLS file saved by Microsoft Office Excel is a container for one or more spreadsheets, which are in turn containers for columns. OPJ projects from Origin are also nested containers, as well as HDF5, GPX, ZIP and other file types for which the support is planned in future versions. One feature specific to this file browser is called *flattening* of containers. Whenever a directory (e.g. “tmp0” in Fig. 1) contains only a single object (e.g. “tmp”), their names are shown as joined into a single line. Such flattening is applied recursively, allowing to entirely hide containers that are void of accessible data. It minimizes the visual clutter in the file tree, especially in connection with the built-in filename

filtering. Another novel piece of code was required for an automatic DAT/CSV file reader. In practice, text files use different formatting – most importantly, a comma, tabulator, space or multiple spaces are used as column separators. The implemented routine guesses the formatting that leads to *most rectangular* data table, still being robust against row length irregularity due to intentionally missing values.

During loading of each file, its name and metadata are processed and stored to describe the resulting dataset. Such parameters can either be used for automatic labeling of the plotted curves, or can be assembled to form the third axis in case of e.g. a 3D-surface plot.

EXAMPLE: FABRY-PÉROT FRINGE REMOVAL

Coloured curves in Fig. 2 show experimental spectra of InGaN/GaN scintillator luminescence with two broad emission bands (≈ 415 and ≈ 490 nm). All spectra are modulated by Fabry-Pérot interference due to two interfaces of the gallium nitride epitaxial layer. This is unrelated to material – an optical artifact to be removed.

For illustration, Code block 1 shows a procedure that removes the fringes using Fourier transform, a task that would be rather tedious in graphical programs known to the author. Thanks to the script automatically adjusting to fringe density, it requires no user interaction

TAB. 1. Code block 1. Python3 code written into *nihilnovi* code editor to remove Fabry-Pérot fringes, as it is in Fig. 2, 3

```
def nGaN(wvl_nm):
    ## index of ref of GaN, from DOI 10.1063/1.1341212
    eV = [1.503, 2.757, 3.229, 3.395, 3.422]
    n = [2.359, 2.486, 2.643, 2.818, 2.893]
    energies = 6.626e-34*2.998e8/1.602e-19/1e-9 / wvl_nm
    return np.interp(energies, eV, n)

for x, y, param, label, color in \
zip(xs, ys, params, labels, colors):
    ## initially, x is free space wavelength
    ax.plot(x, y, label=label.split('@')[0], c=color)

    ## 1. convert wavelength in air to wavenumber in GaN
    x1 = 2*np.pi*nGaN(x)/(x*1e-9)

    ## 2. interpolate to new, equidistant x-axis
    x2 = np.linspace(np.min(x1), np.max(x1), len(x1)*2)
    y2 = np.interp(x2, x1[:-1], y[:-1])

    ## 3. FFT the spectrum into real-space domain
    xf = np.fft.fftfreq(len(x2), x2[1]-x2[0])
    yf = np.fft.fft(y2)

    ## 4. find and retouch the F.-P. component
    M = np.argmax(np.abs(yf[20:-20])) + 20
    retouch_value = (yf[M-5] + yf[M+5])/2
    yf[M-5:M+5] = retouch_value
    yf[len(yf)-M-5:len(yf)-M+5] = retouch_value

    ## 5. inverse FFT, re-interpolate wavenumber in
    ## GaN back to wavelength
    x3 = 2*np.pi*nGaN(x)/(x*1e-9)
    y3 = np.interp(x3, x2, np.fft.ifft(yf))
    ax.plot(x3[:-20], y3[:-20], color='black', lw=0.5)

ax.set_xlabel('free-space wavelength (nm)')
ax.set_ylabel('spectral intensity (A. U.)')
ax.set_yscale('log')
ax.legend(loc='best', prop={'size':6})
```

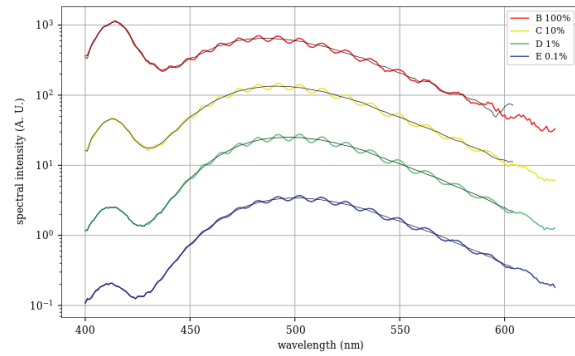


Fig 2. Example experimental spectra for different UV illumination intensities; coloured curves were measured, black overlay is the result of the adaptive Fabry-Pérot filter

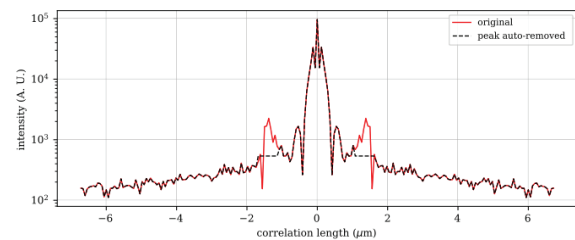


Fig 3. Diagnostic plot after steps #3 and #4 from the script. Note F.-P. filtering is *not* smoothing; in contrast, it selectively factors out the oscillations, keeping other spectral details.

Once this script was developed within *nihilnovi*, hundreds of spectral files can be processed with no further burden of the human user. Adding the yellow, green and blue spectral curves into Fig. 2 required holding the *control* key and selecting the files by mouse.

CONCLUSIONS

This article presents a program in which selecting of files often generates a publication-ready plot of data. Thanks to the mixed clicking/programming workflow, such simplicity of trivial tasks does not restrict the versatility of complex tasks. After three-year long development of *nihilnovi* in semiconductor laboratory, its author believes the project has reached such a state that it can be helpful to the scientific community. Therefore, it is published [1] as platform-independent free software, with all its dependencies being free software as well.

ACKNOWLEDGMENT: The author acknowledges the support of the Ministry of Education, Youth and Sports of the Czech Republic, project NPUI - LO1603 "ASTRANIT".

REFERENCES

1. F. Dominec: Nihilnovi source repository, <https://github.com/FilipDominec/nihilnovi/> (2020).
2. J. D. Hunter, Computing in Science & Engineering 9, 90 (2007).
3. M. Yakshin et al.: Kaitai struct documentation, <http://kaitai.io> (2020).

APPLICATION OF MACHINE LEARNING IN SINGLE CRYSTAL GROWTH

F. Hájek^{1,2}, hajek@fzu.cz, F. Dominec¹, dominecf@fzu.cz, A. Hospodková¹, hospodko@fzu.cz, J. Oswald¹, oswald@fzu.cz

¹Institute of Physics CAS, v.v.i., Cukrovarnická 10, CZ-16200, Prague 6, Czech Republic

²Czech Technical University in Prague, FNSPE, Břehová 7, CZ-11519, Prague 1, Czech Republic

INTRODUCTION

Development of a new material or device with required properties is a complex task usually accompanied with many attempts and discovering the dead ends. The performance of the material or device might be a complicated function of many input parameters like growth conditions, annealing conditions, postprocessing methods etc. Machine learning algorithms can be very efficient way to boost the development process in cheap and time-saving way [1]. Machine learning model can be trained on the available data and then used to predict material or device performance. This paper demonstrates capability of neural networks and regression trees to predict luminescence intensity from growth conditions of InGaN/GaN multiple quantum well (QW) structures and, consequently, improve its properties.

EXPERIMENTAL

InGaN/GaN samples were grown on the Aixtron 3×2 CCS MOVPE system equipped with LayTec EpiCurveTT apparatus for in situ measurement of reflectivity, curvature and true wafer temperature. Sapphire substrates with c-plane orientation were used for the growths. Buffer layers were grown with trimethylgallium and ammonia precursors with a hydrogen carrier gas. Additional details can be found elsewhere [2]. The precursor during active region growth were NH₃, triethylgallium and trimethylindium as sources for N, Ga and In respectively. Nitrogen carrier gas was used for active region growth. Studied structures contain stack of 5 QWs and barriers, separation layer and second stack of 5 QWs and barriers. The structure is capped with GaN layer.

Photoluminescence (PL) measurement were carried out with confocal microscope LabRAM HR Evolution, He-Cd laser (wavelength 325 nm) with used excitation density 0.05 Wcm⁻², objective 74CG, spot diameter 2 μ m and CCD detector Synapse with UV enhanced sensitivity. Both excitation and emission light were passed through objective and reflected laser light was filtered by in-build edge filter. Wavelength 325 nm (=3.8 eV) enables excitation over GaN bandgap and the characteristic penetration depth is about 100 nm [3]. Energy resolution is constant for all measurements and is about 0.1 nm. PL spectra of all samples were automatically fitted (Gaussian curve for QW luminescence band). Results of fitting along with growth parameters were used as input data for machine learning algorithms. Machine learning algorithms (neural networks, regression trees and different types of boosted trees) implanted in Sci-kit [4] Python library were used.

Details about the models can be found in the Sci-kit documentation [4].

RESULTS AND DISCUSSION

Datasets from more than 100 samples were randomly divided to training and test ensembles. To use neural network model, the input data were preprocessed: 15 input parameters (growth parameters) and one output parameter (QW luminescence intensity) were normalized with StandardScaler from Sci-kit library. Various types of neural network design were probed. The best prediction accuracy was achieved with two layers with 18 and 12 neurons, respectively, adaptive learning rate starting at 0.001 and activation function tangent hyperbolicus. To classify the machine learning predictions, the parameter explained variance score (EVS) between predictions on test ensemble and measured data was used. However, neural network gave rather poor prediction accuracy (Fig. 1).

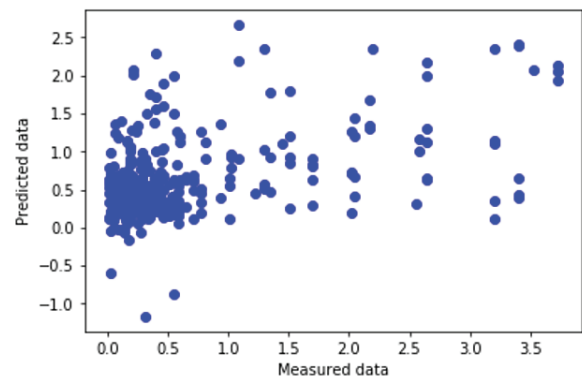


Fig. 1. Neural network prediction. EVS = 0.02.

For regression trees, data preprocessing is not necessary. Moreover, because the little computational time consumption in comparison to neural network, regression tree design can be easily optimized by fitting procedure for a given task. A single regression tree optimized main parameters were: maximal depth = 13, minimum samples split = 11 and minimum weighted fraction for leaf creating = 0.039. EVS for the single regression tree was as good as 0.62 (Fig. 2). However, few completely incorrect predictions can be found.

Next, regression tree boosting methods were examined. The procedure was the same as in the case of the single regression tree. Results from adaptive boosting and gradient boosting methods are shown in Fig. 3 and Fig. 4, respectively. Adaptive boosting was used to wipe out the completely incorrect predictions. However, the obtained EVS are little worse than in the case of single tree regression.

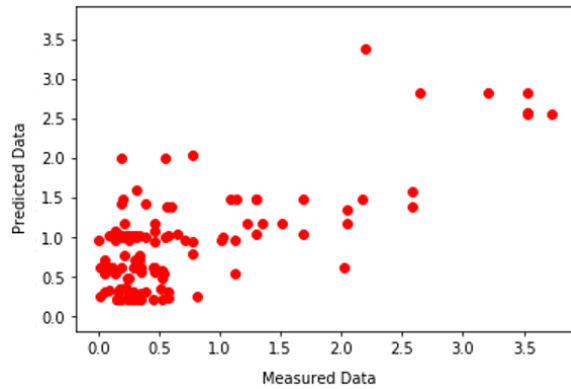


Fig. 2. Single regression tree prediction. EVS = 0.62.

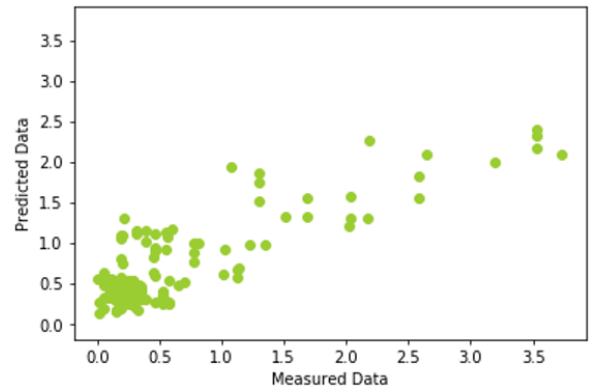


Fig. 5. Voting regressor prediction. EVS = 0.68.

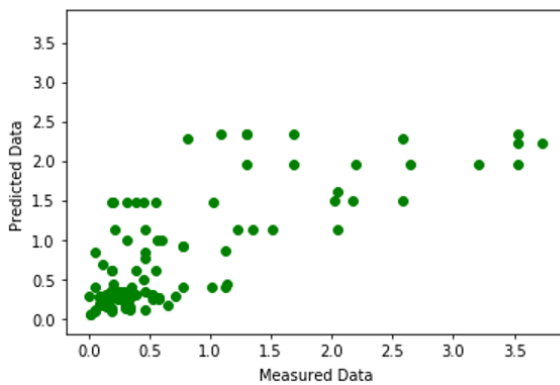


Fig. 3. Adaptive boosting tree prediction. EVS = 0.53.

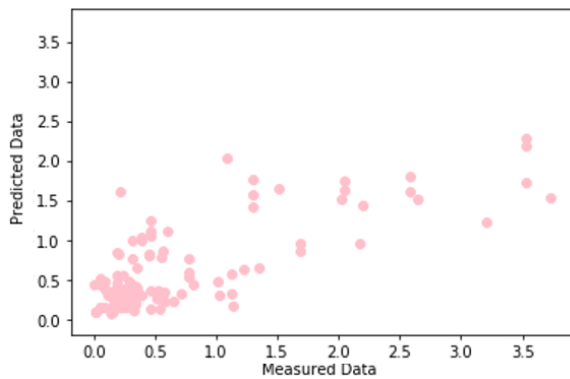


Fig. 4. Gradient boosting tree prediction. EVS = 0.57.

The best prediction accuracy was achieved with voting regressor. The estimators for the voting regressor were the three previously mentioned regression tree models. Linear dependence between predicted and measured values is evident, but the predicted values are underestimated. However, this problem can be easily solved by renormalization of the predicted values.

From comparison of neural networks and regression tree methods, the latter one performed great on our datasets. The main problem of neural network optimization is the computational time consumption which prevents fitting procedure to be run on personal computer. The second problem (for both methods) is the

small training dataset (around 100 samples). The last drawback of the machine learning algorithms can be wrong input parameters (wrong automatic fit of the complicated PL spectra with three bands) and possible missing input parameter (technical services and maintenance of the growth aperture, changing precursor sources, etc.)

The regression tree can be also useful in detecting the important growth parameters, as it is easily interpretable for human (in contrary to neural network). For example, growth time of barrier between QWs was shown as crucial parameter which was not expected.

CONCLUSIONS

Application of neural networks and different models of regression trees was shown on development of InGaN/GaN heterostructures with respect to their luminescence properties. The best prediction of luminescence intensity from growth parameters were obtained by voting regressor using different regression tree methods with EVS = 0.68. A single tree regression revealed growth time of barrier as very important growth parameter. The procedure demonstrated here is universal and cheap way of optimization which can be applied when new material or device for specific application is being developed.

ACKNOWLEDGMENT: The authors acknowledge the support of MSMT project no. NPU LO1603 – ASTRANIT.

Author would also like to thank Robert Horešovský for automatic fitting of PL spectra program development.

REFERENCES

1. T. S. Yao, et al. Chinese Physics Letters **36**, 068101 (2019).
2. T. Hubáček, et al. Journal of Crystal Growth **464**, 221 (2017).
3. J. F. Muth, et al. Applied Physics Letters **71**, 2572 (1997).
4. F. Pedregosa, et al. Journal of machine Learning research **12**, 2825 (2011).

IMPACT OF MACROSCOPIC PARTICLE COMPOSITION ON GAN EPITAXIAL GROWTH MORPHOLOGY AND LUMINESCENCE

K. Kuldová¹, kuldova@fzu.cz, F. Dominec¹, dominecf@fzu.cz, R. Novotný^{1,2}, novotnyra@fzu.cz, F. Hájek^{1,3}, hajek@fzu.cz, T. Košutová^{1,2}, kretkova@karlov.mff.cuni.cz, A. Hospodková¹, hospodko@fzu.cz, ¹Institute of Physics CAS, v.v.i., Cukrovarnická 10, CZ-16200 Prague 6, Czech Republic, ²Charles University, Faculty of Mathematics and Physics, Ke Karlovu 2027/3, CZ-12116 Prague 2, ³Czech Technical University in Prague, Faculty of Nuclear Sciences and Physical Engineering, Břehová 7, CZ-115 19 Prague 1

INTRODUCTION

While there is rich account in existing literature for nanoscopic defects in epitaxial gallium nitride (such as vacancies, dislocations and other atomic-scale disorders) [1, 2], as well as for mesoscopic morphological features that are visible with an optical microscope or with a SEM (such as v-pits, inversion domains, or trench defects) [3], not much investigation was dedicated to truly macroscopic defects of epitaxial growth than can be seen with naked eye.

The primary purpose of our laboratory work lies in the development of efficient and fast scintillator structures based on multiple InGaN/GaN quantum wells (MQW). During the preparation of these structures, great attention is paid to optimization of the growth parameters and to reduce the density of dislocations and point defects in this material [4].

In this article we describe two type of macroscopic defects on InGaN/GaN MQW structures caused by accidental contamination with dust particles during the structure growth. Understanding the impact of each of the contaminating elements is not only important for sample diagnostics, but it also provides insight into the complex physical and chemical processes during epitaxy.

EXPERIMENTAL

Preparation of 10 QW InGaN/GaN structure grown by metalorganic vapour phase epitaxy (MOVPE) atop of $\sim 5\mu\text{m}$ GaN buffer on a 2" sapphire substrate is described elsewhere [5]. Photoluminescence (PL) spectra was measured by confocal LabRAM HR Evolution system, excitation laser He-Cd $\lambda = 325\text{ nm}$, spot diameter $2\ \mu\text{m}$, scanning electron microscopy (SEM) by Philips XL30 ESEM with energy dispersive X-Ray (EDX) analysis, UV macro photography (UVMP) by 20 MPx camera with a 450 nm long-pass filter and 375 nm low intensity UV illumination, resolution $15\ \mu\text{m}$, and optical microscopy (OM) by Carl Zeiss Neophot32 optical reflection.

RESULTS AND DISCUSSIONS

Although cleanness is maintained during sample preparation, small uncoloured dots of diameter $\sim 0.1\ \mu\text{m}$ can be observed on some samples. After low intensity UV illumination, a much larger circular area of different colour appears around some of them, see Fig. 1, No. 1 and No. 2. In these two cases, the defect influence on the properties of the structure is large and far-reaching as we will show later. The third bright spot (No. 3) appears

in the SEM as a group of small GaN crystals ($\leq 5\ \mu\text{m}$) on bare sapphire substrate. The study of this defect is not the subject of this article.

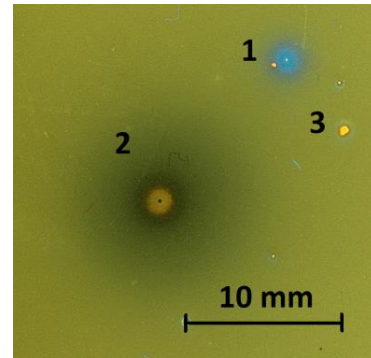


Fig. 1. UV macro photography of three different defects

Figure 2 shows the SEM images of the centres of defects No. 1 and 2, and their chemical composition performed by EDX analysis. In addition to the presence of GaN and sapphire (Al_2O_3), we find calcium (or CaO) in the centre of the first defect and Fe/steel in the second. A defective axis of the vacuum cleaner rotor in the apparatus was discovered as a source of iron contamination, calcium contamination is probably related to the reconstruction of the neighbouring laboratory.

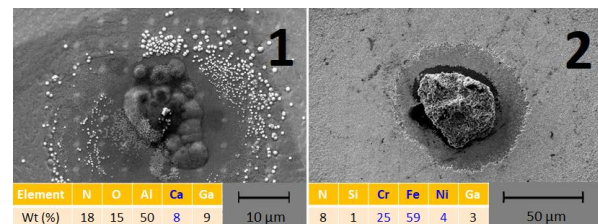


Fig. 2. SEM image of the centre of defects No. 1 and 2 from Fig. 1. In the inserts are the results of EDX analysis.

Both types of defects have a significant effect on 2D heterostructure growth (Fig. 3). They both have a centre with no (or only nanometrically thin) epitaxial layer surrounded by large circular area (diameter $\sim 500\ \mu\text{m}$) where 3D growth predominates over 2D. Unlike the iron defect, the calcium defect has this area raised by $2\text{-}3\ \mu\text{m}$ which is ten times more than the thickness of the MQW structure. This elevation must have been grown already during the growth of the GaN buffer. In [6], calcium is described as having very strong surface segregation and incorporating into the structure during low temperature growth only. The rough and damaged surfaces is

gradually getting smoother and the whole disturbed areas have a diameter of ~ 1 mm. Where defect No. 1 has an elevation, defect No. 2 has a depression that rises gradually to undisturbed surface.

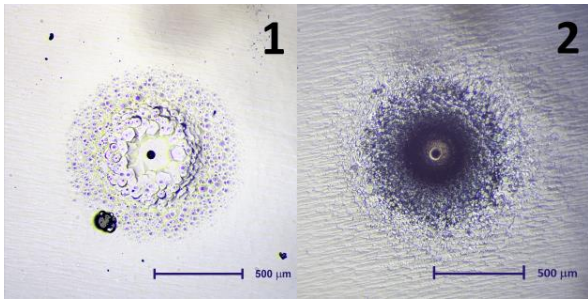


Fig. 3. OM image of defects No. 1 and 2 from Fig. 1.

Just as the morphology of the two defects differs, so does their impact on PL properties. Defect No. 1 with calcium impurity in the centre exhibits the blue shift of QW PL maximum in the region of impaired surface (see Fig. 4). This blue shift suggests that presence of Ca atoms decreases In incorporation into InGaN QWs.

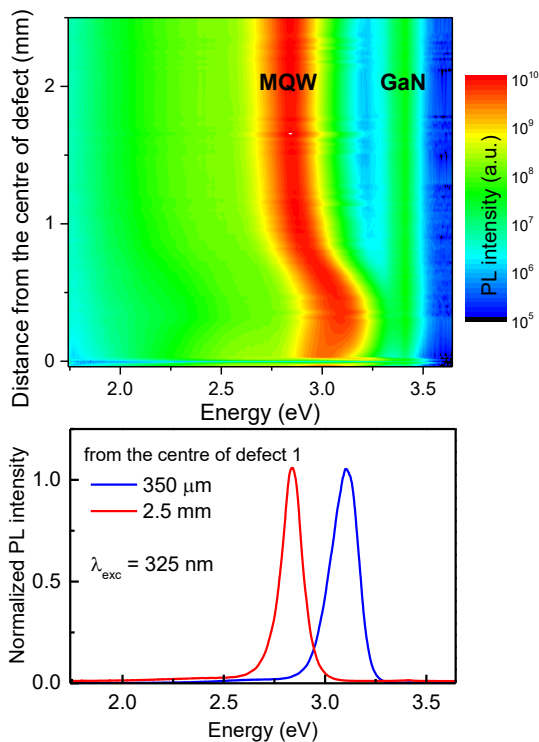


Fig. 4. PL map of the defects No. 1 and two PL spectra from this map: blue line - maximal blue shift at 350 μm , red line - spectrum of non-damaged area.

In contrast, defect No. 2 with Fe impurity shows practically no change in QW energy, but significant decrease in PL intensity. In Fig. 5 is compared PL integral intensity of MQW peak as function of the distance from the centre for both defects. We can see that the effect of calcium on the intensity of PL is small and, except for first 20-30 μm from the centre, practically does not change (this is also evident from the

map in Fig. 4).

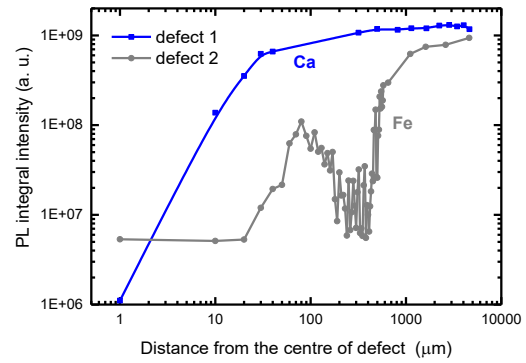


Fig. 5. PL integral intensity of the MQW as function of distance from defect No. 1 and No. 2.

On the other hand, the intensity of PL around Fe defect is low and reaches the intensity of the intact sample as far as 10 mm away from the centre of the defect. This is not surprising; Fe is known to quench luminescence in GaN [7]. Increase of PL intensity at ~ 100 μm can be explained by better light-extraction effect from 3D surface.

CONCLUSIONS

We have identified the elemental composition of two particles using EDX in an electron microscope. We have found particles of the 10-30 μm in size, composed of stainless steel (Fe+Cr+Ni) and calcium (Ca or Ca+O). Both particles cause a characteristic change in the epitaxial morphology in their vicinity, and change the luminescence properties of the sample on a much larger scale (1 – 10 mm), mainly Fe. Understanding defect composition helps to trace the sources of impurities in the laboratory. Their classification reduces the need for repeated study.

ACKNOWLEDGMENT: The authors acknowledge the support of the MSMT project no. NPU LO1603 – ASTRANIT.

REFERENCES

1. Ch. G. Van de Walle et al., *J. Appl. Phys.* **95**, 3851 (2004).
2. M. A. Reshchikov et al., *Phys. Rev. B* **90**, 235203 (2014).
3. O. Ambacher, *J. Phys. D: Appl. Phys.* **31**, 2653 (1998).
4. A. Hospodková et al., *J. Crystal Growth* **536**, 125579 (2020).
5. A. Hospodková et al., *J. Appl. Phys.* **121**, 214505 (2017).
6. E. C. Young et al., *Appl. Phys. Lett.* **109**, 212103 (2016).
7. A. Bonanni et al., *Phys. Rev. B* **75**, 125210 (2007).

SCHOOL MEASURING SYSTEM USING A MICROCONTROLLER

M. Choma, michal.choma@smail.unipo.sk, S. Ilkovič, sergej.ilkoVIC@unipo.sk, Prešov University, Prešov, Slovakia

INTRODUCTION

Microcontrollers are now widely spread to general public as a result of their low cost, simplicity and user support. Moreover, a microcontroller seems to be a suitable tool for building a school computer measuring system. Numerous manuals available on the Internet make it easy for less experienced users to work with microcontrollers. The selection of a particular microcontroller type for constructing the school computer measuring system corresponds to the requirements that depends on the resulting product. This paper presents the philosophy of a school computer measuring system and discusses the development process of the system. The authors also present the design of the system, which includes particular design of the printed circuit board and the 3D model of the device's case.

THE PROJECT PHILOSOPHY

The developing measuring system uses the microcontroller's built-in Wi-Fi module for the communication with the connected users. Using of this module the central Interface unit (BOX) acts as Access Point (AP) with running webservice service. By means of a smartphone (or other device with Wi-Fi technology) the user actively communicates with the measuring system. The webservice provides the bidirectional communication between measurement system and the user. This solution eliminates the requirement of expensive display element (e.g. display) into the measuring system and make use of native graphical potential of the users' devices, which greatly simplifies the design and construction of the measuring system. In addition, the whole design of the measuring system is based on requirements concerning its future implementation into the school environment and can be characterized as probeware (the application of probes, interface units, and software in education for the purpose of acquiring, displaying and analyzing data in real time [1]). The developing measuring system provides the user the possibility to measure and display measured data by means of graphs or gauges in real time. Subsequently, the measured data are being stored in the built-in internal memory, what reduces the external memory requirement. Thanks to this, the user has the possibility the data export and then process recorded data in arbitrary spreadsheet editor as regular CSV (comma separated value) spreadsheet.

THE SYSTEM DEVELOPMENT

The proposed measuring system consists of 4 basic parts, which are necessary for carrying out the measurement (Figure 1). They are namely interface unit, sensors, power supply and users' Wi-Fi devices (not included in the development process as far as they are

using only operational system-independent commercial web browser). The interface unit represents the core of the measuring system. It provides the communication between the user and the system. At the same time, it maintains a several functions: management of the Wi-Fi stack, taking care of http requests, management of sensors' communication, saving measured data to data storage, actualizing the status information on the LCD display and hardware control elements monitoring. The essential component of the interface unit is the ESP32-Wroom microcontroller from Espressif with built-in Bluetooth and Wi-Fi module [3]. The power supply voltage is 3.3 V. The basic microcontroller components are central processing unit (CPU), the operating and program memory, the oscillator, and the I/O peripherals.

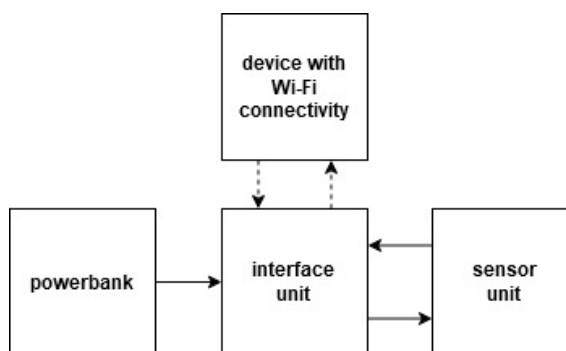


Fig.1. Block diagram of the measuring system

The ESP32-Wroom microcontroller features a 32-bit dual-core Xtensa LX6 microprocessor with Harvard architecture and 160/240 MHz clock frequency [4]. Microcontroller's non-volatile program memory is Flash memory type of 4MB size. This memory can be shared with the measured data. In this case the memory organization must be defined by the partition definition file (similar to the disk partition organization in the computers). The size of the available data for the measurement depends on the firmware size, what is compiled binary file. This approach is very comfortable, because the firmware update does not destroy the measured data. The data area is easily accessed via web interface in the web browser, using of third-party program. The other memory of this system is the volatile operating memory, which is much faster than the Flash memory. It is used for temporary storage of the running program (i.e. variable values) and within the selected microcontroller it represents its SRAM memory (static RAM memory) of 512 KB size [4].

Other components of the interface unit include a character display, voltage regulator, CAN (controller area network) transceiver, pushbuttons, connectors, and passive components - resistors and capacitors. The character LCD display is used for displaying the status information (AP login credentials, the web interface IP address, and the measurement status). The HT7333 voltage regulator from Holtek Semiconductor is used to

transform the input voltage from the power source or the power bank (5V) to the required voltage (3.3V) [5]. The Texas Instruments transceiver type SN65HVD233 DRG4 provides the connection to the CAN bus, through which the sensors communicate with the interface unit with the speed up to 1Mbps [6]. The transceiver is the interface between the microcontroller's built-in CAN controller and another sensors' CAN controller. The CAN communication [7] represents 2-wire bus with CANH and CANL signals, which are very resistant to electromagnetic interference, therefore this technology is widely used in automotive industry. The CAN bus transfer reliability is considered its biggest advantage. The nodes (devices connected to the CAN bus) can communicate by sending of the messages. Every message contains a specific identifier indicating the meaning of the transmitted message and its priority. The arbitration system eliminates the possibility of collision between two messages, what has no impact on the transfer rate.

SENSOR UNIT

Sensor is a device responsible for measuring the physical quantities. The communication between the Interface unit to sensor unit is done by CAN bus. Instructions are sending from the Interface unit to the Sensor unit and measured data and metadata (name of the sensor and the measured physical quantity, their abbreviations, measuring ranges, etc.) are sending in the opposite direction. The sensor unit, consists of an ESP32 microcontroller and all the necessary parts, like CAN transceiver, voltage regulator, pushbuttons, LED indicator, etc. The sensor unit is physically connected to the interface unit via USB socket. The system developer can choose the appropriate sensor depending on the physical quantity intending to measure. The Sensor unit can communicate with the sensors in several ways, what depends on the chosen sensor properties, i.e. A/D converter (built-in or external), I²C (Inter-Integrated Circuit), SPI (Serial Peripheral Interface) [2].

POSSIBILITIES OF USING THE MEASURING SYSTEM UNIT

The measuring system is primarily intended for its application in the school environment. Thanks to the interactive user interface, the measuring system is a suitable tool for demonstration experiments performed by teachers. Using interactive whiteboard (or projector) it is possible to display the user interface and thus the real - time measurement. In case the schools do not have an interactive whiteboard or any other tool for displaying the user interface, the teachers have a possibility to use smartphones. Multiple students can be connected to the 1 interface unit (in the mode of passive monitoring), and thus the measuring system appears to be a suitable tool for cooperative learning. The measuring system can also be used for outdoor education as a matter of fact that the measuring system is portable. In terms of the educational content of

physics, the measuring system offers time dependence measurement e.g. temperature, atmospheric pressure, force, acceleration.

CONCLUSIONS

The developed measuring system has many advantages especially thanks to ESP32 microcontroller. The microcontroller used within the sensor provides the possibility to work with analog or digital signal, making the system universal. The web interface makes the system simple, without any need to install proprietary software (only an internet browser is required, which is a part of the standard software in smartphones, tablets, or computers). For data processing can be used any program available to the user. The system offers two measurement regimes: time dependence of the selected physical quantity (Time based measurement) and dependence of two measured physical quantities (X-Y axis-based measurement). The environment can display measured physical quantities in semianalog way (gauges) and digital way and user have all measured data displayed in a graph. Data can be immediately exported to the connected device when the measurement is over. Due to the recent low cost of electronic components, the system is significantly cheaper than commercial systems. The system can be licenced on the open - source principle, and thus the possibility of participation in development or testing is welcome.

ACKNOWLEDGMENT: This work was supported by KEGA 009PU-4/2020.

REFERENCES

1. O. Lindwall, J. Bernhard: Approaching interactive engagement tasks (Padova, EARLI – 2003)..
2. Datasheet: ESP32 from https://www.espressif.com/sites/default/files/documentation/esp32_datasheet_en.pdf [cit. 20-02-2020]
3. Datasheet: ESP32-WROOM-32 from https://www.espressif.com/sites/default/files/documentation/esp32-wroom-32_datasheet_en.pdf [cit. 20-04-2020]
4. A. Maier, A. Sharp, Y. Vagapov, Internet Technologies and Applications (ITA). IEEE 143 (2017).
5. Datasheet: HT733 from <https://www.digchip.com/datasheets/parts/datasheet/196/HT7833-pdf.php> [cit. 20-04-2020]
6. Datasheet: SN65HVD233DRG4 from https://datasheet.lcsc.com/szlcsc/1810181627_Texas-Instruments-SN65HVD233DRG4_C61643.pdf [cit. 20-04-2020]
7. M. Di Natale et al.: Understanding and using the controller area network communication protocol: theory and practice (Springer Science & Business Media – 2012).

MODELLING CHANGE IN GRAVITATIONAL ACCELERATION AND ITS EFFECT ON PRESSURE IN LIQUID

M. Kováč, milan.kovac@fmph.uniba.sk, Comenius University in Bratislava, Faculty of Mathematics, Physics and Informatics, Mlynská dolina F1, 842 48

INTRODUCTION

Teachers, and hopefully students also, are familiar with enough number of experiments and demonstrations aimed at showing the dependence of hydrostatic pressure on the depth or density of a liquid.

The dependence of the pressure in a liquid on the depth is usually shown by immersing a tube in water. The tube is filled with air and connected to an air pressure sensor. We observe that with increasing depth, air pressure in the tube rises. The dependence of pressure at a certain depth on the density of a liquid is done very similarly. In this experiment, however, we do not change the immersion depth of the tube, but the liquid itself. Thus, we always measure the pressure at the same depth, first in water, then in sugar solution and finally in alcohol solution. In both experiments the liquid and the whole system are at rest. From experiments we conclude that the pressure below the surface is linearly dependent on the depth (quite decently, based on several depths and a relatively accurate measurement of pressure and depth) and also that it is linearly dependent on the density of the liquid (based on three densities).

In our version of the first experiment mentioned above, we will use a thin transparent tube. The tube is approximately 1 m long and connected to the pressure sensor at the bottom. By gradually adding water to the tube, depth of the water is increased as the level rises. Pressure of the liquid is measured at the bottom of the tube. Right after a proper examination of the dependence and evaluation of the measurement, we introduce a new possible subject of inquiry. We release the almost full tube with the attached pressure sensor from the stand and move it in the vertical direction. We notice that the pressure in the liquid rises and drops as the system moves up and down. This observation can lead to the assignment of an experiment planned by students themselves.

Such an experiment is usually meaningful for students when they perform the tasks associated with each of following phases [1]:

- Problem and hypothesis formulation
- Design of measurement method and apparatus
- Data collection
- Measurement evaluation

Example of such an assignment could be: Examine the dependence of the pressure in a liquid on the vertical motion of the system. (We will limit ourselves to the vertical direction, although after closing the tube it would be possible to extend the examination to the horizontal direction as well with similar results)

PROBLEM AND HYPOTHESIS FORMULATION

In order to observe this phenomenon in more detail, students can observe the change in pressure on the

graph as a function of time. With a systematic approach, they may notice that the change in pressure occurs as the system accelerates. Based on observations and experience from previous experiments, students formulate a hypothesis. At this stage, students do not have to converge to the idea that the dependence of pressure on system acceleration is linear.

We can slightly guide students in case they overlooked a knowledge they have already acquired. An example of such a hypothesis could be: Water at the bottom of an upwardly accelerated tube increases its density, and therefore the pressure increases. Liquids are almost incompressible and therefore density of the water at the bottom of the tube does not change.

DESIGN OF MEASUREMENT METHOD AND APPARATUS

At this point, students are challenged to design an apparatus that would allow evenly accelerated movement of the system in the vertical direction and the ability to change the acceleration. In addition to the mentioned system, we will also provide students with other equipment in the laboratory, which should at best include an acceleration sensor.

If students stagnate for a long time, we can draw their attention to the principle of operation of the elevator. We will focus on the counterweight for the cabin. The apparatus in such a case will therefore resemble Atwood's machine. On one side of the pulley there will be the thin transparent tube with water in which we will measure the pressure and on the other side there will be a counterweight. We can change the weight of the counterweight, and thus choose the acceleration of the system.

DATA COLLECTION

We guide students to make sure that they do not change the density of the liquid or the depth at which they measure pressure during the measurement. The methods of data collection and measurement depend on the apparatus and available equipment or sensors.

In the following, we describe our implementation of the experiment, which is one of the possible student solutions. We use a CMA Coach pressure and acceleration sensor to measure acceleration and pressure directly. When measuring, it is necessary to set a suitable measurement time and sampling frequency. The change in system acceleration and fluid pressure over time during one accelerated motion (one measurement) is shown in the graphs (Fig.1, Fig.2).

After we extracted needed data, we change weight of the counterweight, thus we change the acceleration of the system and perform the same measurement. We repeat the process as many times as possible. The graphs obtained from individual measurements must be

correctly interpreted and the required data extracted from them. The data are then recorded in a table.

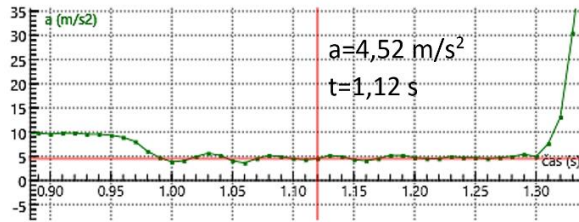


Fig. 1. Acceleration of the system vs time

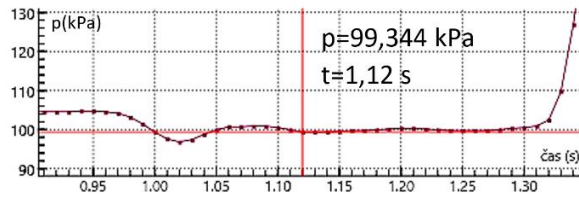


Fig. 2. Pressure in the accelerated liquid vs time

MEASUREMENT EVALUATION

The data recorded in the table will then be used to plot the dependence of the pressure in the fluid on the magnitude of the acceleration (Fig.3). By adding the trend line of the linear function to the graph, we verify the hypothesis. From the equation of the trend line it is possible to read the product $\rho \cdot h$ and value of the atmospheric pressure.

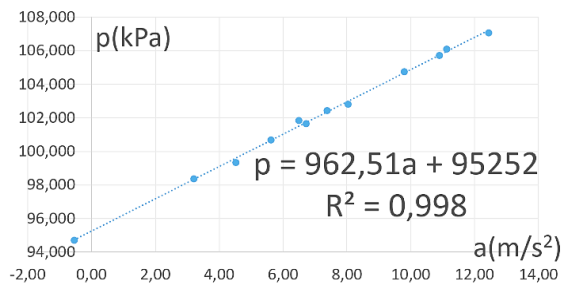


Fig. 3. Pressure in the liquid vs acceleration of the system

RESULTS AND IMPLICATION

An interesting conclusion for students can be reached when further examining the acceleration of the apparatus. Authors differ in defining weight. For purpose of the experiment we will use the following definition. Paul G. Hewitt defines weight as force exerted on a body by supporting surface [4]. By this definition, acceleration measured in the experiment was acceleration due to weight. So, by changing the acceleration of the system, weight of the system was changed. Another challenge for students may be to seek consequences or applications of the knowledge gained in this experiment. One of the consequences of the weightless state of a fluid will be the absence of buoyant force, which can be demonstrated by a simple experiment [2]. In our version of the experiment, an open container of water is used, in which the submerged

ping-pong ball is held from above by thin rods until the container is dropped (Fig.4). When the container drops, rods remain attached to the stand. During the drop, the ball falls together with the container and the water without emerging above the level of the water. This is because the ball is not subjected to any buoyant force, even though it is completely submerged in the water.

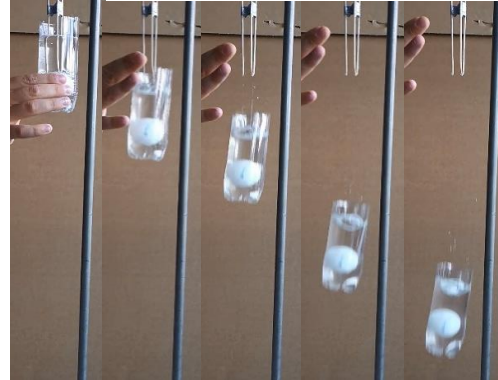


Fig. 4. Ping-pong ball in free-falling water

CONCLUSION

We presented an activity that can be implemented as an experiment planned by students themselves. Such an experiment can be a challenge for students. However, we believe that with enough scaffolding from the teacher, the proposed experiment can be beneficial for students. “The concept of scaffolding describes how children with the help of someone more knowledgeable to share and support their problem solving, can perform more complex tasks than they would otherwise be capable of performing on their own” [3]. In our proposed activity, we see the possibilities of developing student skills, especially in the design of equipment, interpretation of graphs, recording and processing of data, interpretation of measurement results. Finally, the experiment provides an opportunity to deepen students' ideas and knowledge of gravitational acceleration, pressure in fluids.

ACKNOWLEDGMENT: The author is grateful for the support from the Ministry of Education of Slovak Republic, project VEGA 1/0273/19, Tutoring and Scaffolding in the Preparation of Pre-Service Physics Teachers.

REFERENCES

1. J. Sliško, G. Planinšič, *Physics Education* **45**, 292 (2010).
2. R. Keith Sawyer, [ed.]: *The Cambridge Handbook of the Learning Sciences* (2nd. New York : Cambridge University Press – 2014) 44. 978-1-107-62657-7.
3. P. Demkanin: *Didaktika fyziky pre študentov magisterského štúdia a učiteľov v praxi* (Vydavateľstvo Univerzity Komenského – 2018) s. 66 978-80-223-4374-9.
4. P.G.Hewitt: *Conceptual physics* (Pearson – 2014) p. 166. 978-0-321-90910-7.

DEVELOPING THE CATEGORICAL SYSTEM OF BEHAVIOUR FOR STUDENT-LECTURER INTERACTION DURING PHYSICS DEMONSTRATIONS

A. Nikitin, alex.nikitin@seznam.cz, P. Káčovský, M. Snětinová, Department of Physics Education, Faculty of Mathematics and Physics, Charles University, Praha, Czech republic

INTRODUCTION

Even though the paradigm of experimenting in secondary and tertiary physics education is shifting towards more student-based approaches, demonstrational experiments still play an important role in education. At the authors' workplace, physics lecture demonstrations (DEMOs) have been performed for secondary school (ISCED 3) students on weekly basis for more than 30 years. Each performance takes around 75 minutes and is visited by a group of up to 90 students from different (usually two or three) schools. There are currently seven different physics topics to choose from.

Such a big activity offers suitable opportunity to study extrinsic factors that could influence students' perception of physics demonstration experiments. For this reason, a video study of DEMOs was performed and for purposes of this video study a widely applicable categorical system of behaviours was developed. This paper aims to present this categorical system.

VIDEO STUDIES IN PHYSICS EDUCATION

Video-based observation research methods have previously been used in several large-scale studies, such as TIMMS 1999 [1], IPN video study [2] or IRSE video study [3]. One of the results of those studies is – as we already stated at the beginning of this paper – that demonstration experiments still have a large role in science education. For example, according to IRSE video study [3] experiments are most conducted as either teacher demonstrations or pupils group work.

Video studies conducted in educational context are often focused either on hands-on experiments (e.g. [4]) or for analysis of normal school lessons (for example [5] or the well-known original Flanders' interaction analysis system [6]). Categorical system studying physics experiments in great detail was developed by M. Tesch [7] (as a part of IPN video study [2]), but once again it is intended for use in analysis of regular school lessons. Moreover, this system is focused solely on experiments themselves and lacks parts that would focus on the character of interaction between lecturer and audience.

CATEGORICAL SYSTEM FOR INTERACTION BETWEEN LECTURER AND AUDIENCE

Relatively early in development the decision was made to split our planned categorical system into two smaller subsystems so that the observer would not be forced to focus on too many too different parameters at once. To further support this decision there could be two major extrinsic factors that influence students' perception. Those are experiments themselves and communicational tools that the lecturer is using in interaction with audience.

In the first part of our research, we concentrated on the development of categorical system that focuses on the interaction between lecturer and audience. Figure 1 shows a diagram of this newly created system.

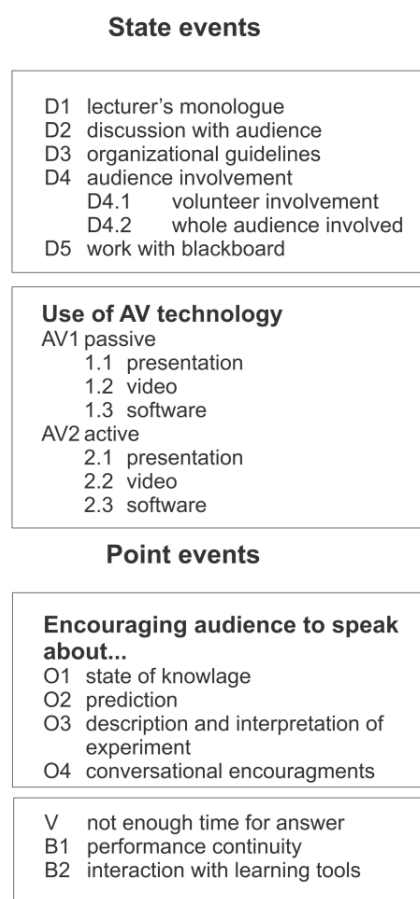


Fig. 1. Diagram of the system of categories for lecturer's interaction with audience

There are two different kinds of behaviour that we can observe. Those for which duration of behaviour is important and those for which duration is irrelevant. We call the first group *state events* and the other one *point events*.

State events consists of two major parts. First part is mainly trying to determine how much time lecturer communicates with audience and how much is he or she trying to "pull them into the performance". Audience is usually included into the performance either by discussion or by using volunteers during certain experiments. There are several experiments that require involvement of the whole audience. The other part of interval behaviours is the use of audio-visual (AV) technology, which studies what AV technology the lecturer works with and how much time is devoted to it. We differentiate whether those means of AV technology

are used passively (they are only switched on without active work with them) or actively (the lecturer uses or refers to them).

Point events study mainly questions with which the lecturer addresses the audience. Other means of encouraging audience to speak are also included. Furthermore, those behavioural categories study what objective the lecturer is trying to accomplish by those questions and whether he or she gives enough time to answer the questions in the first place.

BRIEF RESULTS

For the purposes of our research, we are using free software BORIS (Behavioural Observation Research Interactive Software) [8] to code videos. In the process of developing and testing the system we have used a time-unit Cohen's kappa [9] to measure agreement between observers. Cohen's kappa basically says, how much better an agreement between observers is compared to a chance agreement (for further information see [9]). IBM SPSS Statistics [10] was used to measure this coefficient. We consider value of the Cohen's kappa 0.80 as sufficient agreement. According to original Cohen's suggestions this value is considered almost perfect [11]. The system was developed to the point when Cohen's kappa between observers varies from 0.82 up to 0.91. We consider this a proof that the categorical system is well defined and hence applicable.

Based on data gathered via a video study with usage of just mentioned categorical system we can say that studied DEMOs performances are highly diverse.

First let us combine durations of behaviours **D2** and **D4** into a parameter called *audience inclusion*. There are performances that include audience into the show in almost 40 % of the whole performance duration. Yet there are performances for which duration of audience involvement makes only 1 % of the whole time.

When we combine active work with all types of AV technology (behaviours **AV2.1** to **AV2.3**) we can compare performances by their AV usage. They are also highly divergent in this parameter. The usage spans from none to over 50 % of performance duration.

When it comes to *instant events*, performances also significantly differ, especially when it comes to number of encouragements to speak per 10 minutes. The range is from 3 up to 22 encouragements per 10 min, which is more than two "questions" per one minute.

CONCLUSIONS

We have developed a categorical system for demonstration experiments that can be used to analyse various situations, e.g. science shows. This system will be enriched by its second, complementary part focusing solely on the experiments themselves. Categories of this second system will study phases and functions of individual experiments, type of data gathered during the performance, used materials, and it will track even thought-experiments as well. This system has already been developed and partially tested.

The categorical system focused on interaction between lecturer and audience has been used in a video study that is trying to identify extrinsic factors that largely influence students' perception. In this paper we have just briefly informed about the development of a new behavioural system and brief results of the previously mentioned video study. Detailed results of the video study and connection between character of performance and students' perception of the DEMOs will be discussed in a separate paper.

ACKNOWLEDGMENT: This work has been supported by Charles University Research Centre program No. UNCE/HUM/024.

REFERENCES

1. K.J. Roth et al.: Teaching Science in Five Countries: Results from the TIMSS 1999 Video Study (NCES 2006-011). (U.S. Government Printing Office, Washington D.C. – 2006).
2. T. Seidel et al., Zeitschrift für Pädagogik **52**, 765 (2006).
3. T. Janík et al., THE NEW EDUCATIONAL REVIEW **28**, 102 (2012).
4. D. Psillos, H. Niederrerr: Talking Physics in Labwork Contexts – A Category Based Analysis of Videotapes. Teaching and learning in the science laboratory (Kluwer Academic Publishers, Boston – 2002).
5. R. Santagata et al., Journal of Mathematics Teacher Education **10**, 123 (2007).
6. N. Flanders: Analyzing Teaching Behaviour (Addison-Wesley Pub. Co, Boston - 1970).
7. M. Tesch: Coding manual – Experiments in physics lesson. How to run a video study: Technical report of the IPN Video Study (Waxmann Verlag, Münster - 2005).
8. O. Friard, M. Gamba, Methods in Ecology and Evolution **7**, 1259 (2016).
9. R. Bakeman, V. Quera: Sequential analysis and observational methods for the behavioral sciences (Cambridge University Press, New York – 2011).
10. IBM Corp. Released 2019. IBM SPSS Statistics for Windows, Version 26.0. Armonk, NY: IBM Corp.
11. M. L. McHugh, Biochemia Medica **22**, 276 (2012).

PHYSICS FOR THE YOUNGEST AND THEIR TEACHERS

J. Houfková, jitka.houfkova@mff.cuni.cz, Charles University, Prague, Czech republic

What are the interests of the youngest "physicists" from kindergartens and primary schools? What do they like and what they can do? And what about their teachers? What can be developed in children through simple physics experiments? How does physics help teachers from different types of schools to work together? In answering the previous questions, the author draws on her many years of experience in introducing physics to preschool and primary school children and their teachers within her own author's program Fairytale Physics and within the activities of non-profit association for teachers Elixir to schools (Elixír do škol).

THE APPROACH TO SCIENTIFIC LEARNING OF YOUNG KIDS

The approach to the young children naturally varies from the approach to the older students. In order to be relevant young children's scientific learning must happen within a context they can make sense of. Scientific exploration is best cultivated through experiences that build on children's current interests and preoccupations [1]. Thus the models, metaphors and analogies used to help understand science to the little children should be related to their everyday experience and relevant to their current state of mental development. Figure 1 represents one example of such model – model of lungs.



Fig. 1. Model of lungs. (a) common model, (b) model adapted for smaller children

The main target of young children's encounter with science is not pure knowledge, more important is developing of positive relationship to science, love and joy from observing and discovering. Little children should closely watch and examine the nature and thereby create a positive emotional relationship with it [2]. The author's approach and experiences with the appropriate models, metaphors and analogies is in more detail discussed in [3].

THE PROGRAM FAIRYTALE PHYSICS

Hands on experimenting is one of many approaches to gaining the interest of children in science. Among

other benefits it helps to develop their fine motor skills and coordination, enhances their observation skills and boosts their language skills. Creating a positive attitude towards natural sciences, that will help the children not to lose their interest in them later in school, is invaluable, too.

The program Fairytale Physics was designed in 2008 by the author of this contribution and is continuously developed, broaden and widen until today. Parts of it are used by other preschool teachers and lecturers. Furthermore, teachers training courses were developed based on it. In 2013 and 2015 the program was rewarded by Czech Physical Society for popularisation of physics.

The basic idea behind the program is to show the children the beauty of physics through simple physics experiments that they can conduct themselves. Then to teach them this way about the observation, description, discussion, reasoning, hypothesis building and testing, team work, and all the things crucial to critical thinking. This is without any aim to create future scientists but with the hope to help to form future adults with ability to think critically and to reasonably navigate through their lives. As the preschool children are very inquiring, they want to know how things work and they love to do experiments. It is easy to catch their interest and motivate them to persist in science explorations and experimenting which are natural to them. They learn well by exploring of their own surroundings that they know and where they feel safe. That is the reason why the courses are preferably done in the preschools, in the class or school playground and garden. The whole workshop program is very interactive. It is based on doing hands on experiments and discussions with children. The workshops are aimed on basic physics topics concerning air and its properties, water and its properties, optics, heat, friction, magnetism and electricity. The content of selected topic was described in detail in [4]. The aids used for the experiments are as much as possible derived from things the children know, objects from preschool are used as much as possible. Most aids are from unbreakable materials as plastic or wood. Depending on the topic of the workshop and a given experiment the method of work differs. If it is possible each child tries the experiment him/herself (e.g. looking through a magnifying glass or playing with the Cartesian diver). Sometimes work in pairs is necessary (e.g. investigating how one magnet forces another to move or "calling" through "caps and thread telephones") and in some cases children work in groups (e.g. connecting simple electrical circuits). And some experiments are of course done only as demonstration conducted by teacher. Most of the experiments can be used to introduce and train basics principles of scientific work and approaches. The number of experiments at each workshop varies, but the experience gained over the years shows that lower number of experiments is better. A video capturing some glimpses of preschoolers

doing experiments can be seen at [5].

THE COMBINATION OF STORYTELLING AND PHYSICS EXPERIMENTS

The fairytales/stories where problems are not solved by magic but by physics experiments is another new approach to introducing physics experiments to kids. Physics experiments are placed into well-known children tales. This approach was successfully tested during the school year 2015/16 in cooperation of the author of this contribution with her student Aneta Čermáková in Aneta's bachelor thesis Motivation of preschool and younger school pupils to physics through stories [6]. Two well-known fairytales Dlouhý, Široký a Bystrozraký (The Tall, the Fat and the Sharp-eyed) and O kohoutkovi a slepičce (About the Rooster and the Hen) were enriched by eleven experiments. The experiments are always used to solve some difficult situations instead of magic. The modified stories were tested by different teachers. Children and teachers reacted to the stories very positively. The material for direct use for teachers is available at [7].

The surprise for the author of this contribution was the psychological effect of fairytales with experiments on the preschool and primary school teachers. It seems that the teachers fear performing experiments included in fairytales less than they are afraid of performing experiments on its own. In the school year 2019/20 the author of this contribution supervised another bachelor thesis dealing with storytelling and experiments [8]. Jana Doležalová set criteria according to which she selected five experiments that support the scientific thinking and wrote her own story that incorporates the experiments and motivate kids in doing them. She also created worksheets for additional individual work. The whole concept was tested with second graders in primary school and introduced to teachers that plan to use it in this coming year. The material for direct use for teachers is available at [9].

THE SUPPORT FOR TEACHERS

As the majority of preschool and primary teachers do not have training in science and science education they are often afraid to administer hands on experiments to their pupils and regularly include them to their class work. Thus it is important to offer them possibilities for further education. That can be done in various seminars organised by pedagogical centres and different educational institutions. Very efficient is also mutual support of interested teachers in teacher's peer support centres. Though the peer support of teachers has already become a recognized method of teacher development there are not many institutions in the Czech Republic that would enable it for science teachers. One of them that supports physics and IT teachers is the non-profit association Elixir to schools (Elixir do škol) [10] that among others organises monthly teacher's meetings. The author of this contribution is the guarantor of the physics content for pre and primary school teachers and two

years ago started the first centre dedicated for teachers from preschools to primary and junior high schools. Before that the Elixir centres were for junior and senior high schools and since then more such centres for teachers of younger kids were created.

The second impact of such centres is that they allow teachers from different types of schools to meet and get to know each other and new collaborations starts that leads to interconnecting of pupils from different classes from which all age categories of pupil's benefit. Among the collaboration is also lending aids from physics cabinets to teachers from lower school levels who do not have physics aids available.

CONCLUSIONS

Over the past years, the author found out that preschool and primary school children are capable of positive perceiving of physical experiments and that they are able to actively pursue appropriately chosen and designated experiments themselves. The models, metaphors and analogies for preschool and younger children must be based on their everyday experience and they must be as simple as possible what brings a lot of questions about their limits and accuracy and correctness. To allow the children the possibility to do experiments in preschool it is necessary to help their teachers to have at least basic understanding of physics phenomena and to gain some confidence in doing experiments. Teachers are assisted in this by various seminars organised by pedagogical centres and different educational institutions and by teachers peer support centres, e. g. centres organised by Elixir do škol.

REFERENCES

1. P. Brunton, L. Thornton: Science in the Early Years (SAGE Publications Ltd, London - 2015).
2. D. Krupová, I. Rochovská, Vědci v mateřské škole (Portál, Praha - 2015).
3. J. Houfková, AIP Conf. Proc. **2152**, 030008 (2019).
4. J. Houfková, Poradce ředitelky mateřské školy **4**, 42 (2018).
5. J. Houfková, D. Cejpková, Pohádková fyzika – ukázkové video (2016), http://kdf.mff.cuni.cz/~jitka/PohadkovaFyzika/promovideo_Pohadkova_fyzika_2016.mp4 [10-Sep-2020]
6. A. Čermáková: Motivation of preschool and younger school pupils to physics through stories (Bachelor thesis, MFF UK, Prague - 2016).
7. A. Čermáková: Motivace předškolních a mladších školních dětí k fyzice prostřednictvím příběhů – metodický materiál pro učitele, FyzWeb, <http://fyzweb.cz/materialy/cermakova/> [10-Sep-2020]
8. J. Doležalová: Využití příběhu propojeného s fyzikálními pokusy ve výuce na základní škole (Bachelor thesis, MFF UK, Prague - 2020).
9. J. Doležalová, Využití příběhu propojeného s fyzikálními pokusy ve výuce na základní škole - metodický materiál pro učitele, FyzWeb, <http://fyzweb.cz/materialy/dolezalova/> [10-Sep-2020]
10. Elixir do škol: <https://www.elixirdoskol.cz/>

THE SMÍCHOV INDUSTRIAL SCHOOL OF THE THIRD AGE

V. Krajčová, vera.krajcova@gmail.cz, Smichov secondary technical school, Preslova 72/25, Prague, Czech republic

INTRODUCTION

The Smíchov Secondary Industrial School (SSPŠ) has long been striving for the introduction of new forms of education, which are also related to the effort to become an open institution accessible to all generations. In the focus of all events are students of the school, who have the opportunity to develop in general, not only in usual classroom lessons, but also as assistants on workshop leaders for children from kindergartens and primary schools, and since 2015 also for seniors. The Smíchov Industrial School of the Third Age is a long-term project supported by a grant from the City of Prague, which in the form of regular lectures and workshops helps to develop the technical skills of seniors as well as social ties between the young generation and seniors.

INTERACTIVE SCIENCE CENTER ON SSPŠ (ISC)

At present, there is an increasing emphasis on competence education. In this perspective, the school is not just about teaching based on the transfer of knowledge from teacher to students, but about building the personality of man as a whole. The basic competencies include:

1. Learning competences
2. Competence to solve problems
3. Communicative competence
4. Social and personnel competences
5. Civic competence
6. Work competencies. [1]



Fig.1. Optical Experiments – juniors and seniors in interaction

This approach can be well ensured by interdisciplinary and intergenerational education. At the Smíchov Secondary Industrial School, we have been striving for this approach since 2013 by gradually building activities, which we have provisionally called the Interactive Science Center (IVC) [2]. This center includes several activities:

- STEM workshops for kindergartens and primary schools (for children 3 – 15 years),
- Physics teaching aids produced by students for their classmates in cooperation with universities

(graduation and student projects),

- Annual participation of active students in Science Camp in Bulgaria and Space Camp in Turkey,
- Lecture series: Modern physics and technology for primary and secondary school teachers, Physics, mathematics
- IT lectures and workshops for seniors (for adults aged 60 – 95 years),
- Hour class IT Handyman.

In this article, we will focus on activities aimed at seniors.

SMÍCHOV INDUSTRY OF THE THIRD AGE

The Smíchov Industrial School of the Third Age was founded in April 2017, when the first meeting of seniors, SSPŠ pupils (assistants) and a lecturer took place. The theme was The Best of a Physics Laboratory. Since then, 34 meetings have taken place focusing on various topics from physics (Nanotechnology, Astrophysics, Funny electrical circuits, Experiments in optics...), mathematics (Building curves, Financial mathematics...) and IT (Photography, 3D Modelling, Virtual Reality, Cyber Security...). Most of the topics were interdisciplinary, and then they belonged to STEM. The program is designed as an intergenerational activity – the lecturers (teachers from school, lecturers from the university, science popularization specialists), seniors and usually 2 – 3 assistants from among students are always attended at workshop. The Smíchov Industrial School of the Third Age currently has a permanent group of seniors from Prague 1. About 10 – 17 of them take part in each meeting with regard to the capacity of the room. The purpose of the program is to attract their attention to natural sciences. In 2020, the 4th year of the programme is taking place, which will be followed by the already planned 5th year from January 2021.



Fig.2. Funny Electrical Circuits – a junior and a senior in interaction

INTERGENERATIONAL EDUCATION

Learning competencies directly encourage the transfer of experience across generations. The idea of

intergenerational interconnection is not new. It is based on international research showing the disadvantage of older people, the misunderstanding of the younger generation and a number of negative stereotypes that favour youth over old age. All this leads to deterioration in the physical and mental health of the older generation. Research also suggests the need to connect the young and older generations. This can reduce inappropriate attitudes across generations [3].

At first glance, it might seem that the Smíchov Industrial School of the Third Age is purely about education of seniors. But this is not the case. It is an education system that is based on the word "between". So each of the three generations learns and the other generations learn.

SSPŠ teachers:

- To practice their organizational skills,
- To pass on their knowledge to people with many years of experience, which they do not normally encounter (they teach adolescents).

Seniors:

- learn to understand the young generation,
- return to their young years,
- have regular activity,
- they are not alone, they are part of the team,
- talk about workshops at home, show products to grandchildren and thus popularize physics.

SSPŠ students:

- get to know old age,
- learn to listen,
- learn patience and willingness,
- learn social contacts,
- learn physics.



Fig. 3. Graduates of the second year of the programme

So, each of the three generations takes something, that strengthens their competencies of all kinds.

“IT HANDYMAN (HODINOVÝ AJTÁK)”

Based on good experience with the Smíchov Industrial School of the Third Age and the demand of seniors for help with their personal equipment (setting up a PC or a tablet, installing a printer, replacing

hardware in a PC, etc.), a service called a “IT Handyman” (or “Hodinový ajták” in Czech), was created at SSPŠ. Within this assistance, SSPŠ only plays the function of a mediator, the service itself is held and arranged by the students themselves.

The service has two forms:

- students visit seniors at their home on the basis of an order – they repair a PC, they learn to control a mobile phone, they install equipment...
- consultations in the centres for seniors – by appointment, 2 – 3 students are available in the centres and solve problems with technology

Again, this is basically intergenerational education, where both parties learn from each other's competencies. SSPŠ students learn not to disappoint trust, patience and willingness and make their own decisions. On the other hand, seniors try not to look for the bad thing in the young generation and learn to work with new devices.

CONCLUSIONS

Intergenerational education with the state system includes teaching in secondary schools mainly to support relationships across generations. This article gave an example from practice where the education of seniors has been going on for several years as a normal part of school activities.

REFERENCES

1. Z. Bělecký: Klíčové kompetence v základním vzdělávání (Výzkumný ústav pedagogický, Praha – 2007) ISBN 978-80-87000-07-6.
2. V. Krajčová: Mezigenerační učení na SSPŠ. In: Moderní trendy v přípravě učitelů fyziky 9: Sborník příspěvků (Západočeská univerzita v Plzni, Plzeň – 2019).
3. A. Hatton-Yeo, T. Ohsako: Intergenerational programmes: Public, policy and research implications an international perspective [online]. (The UNESCO Institute for Education – 2020) 73 [cit. 2020-09-17]. Dostupné z: <https://eric.ed.gov/?id=ED458364>.

STUDENTS' SOLVING OF MULTIPLE-CHOICE TASKS FOCUSED ON GRAPH SLOPE INTERPRETATION OBSERVED BY THE EYE-TRACKING METHOD

M. Kekule, martina.kekule@seznam.cz, KDF MFF UK, V Holesovickach 2, 180 00 Prague

INTRODUCTION

Graphing literacy has been investigated in many studies in various research fields [1]. In physics education, we are mostly interested in scatterplots, which have several important features. Our study focused on the graph slope interpretation.

In several previous studies, typical students' misinterpretations of the graph slope have been identified [2]: Slope/height confusion, Variable confusion, Non-origin Slope Errors and Graph as a Picture or Real Situation Sketch Errors. Previous researches used typically interview or multiple-choice testing as a research method. Nowadays, we also employ the eye-tracking method, which allows us to get deeper insight into students' thinking processes. Particularly, we can track students' eye-movements and so to follow their attention. A typical methodological approach is embedded in novice-expert paradigm, where we compare problem solving strategies of experts and novices, and experts' strategies are considered to be the better one. In the educational field, we typically compare students who solved a task correctly and those who did not [2]. In the paper, we focused on differences among students who solved the whole test the best and who solved a task correctly as well.

METHOD

Eye-tracker Tobii TX300 ($f=300$ Hz, accuracy less than 0.5° of visual angle) was used. The infrared camera was placed under the 23-inch screen of the stimulus PC. Eye movements were recorded by Tobii Studio 3.2 and for identification of fixations inbuilt IVT filter was used. Eye movement was classified as a saccade when eye's velocity exceeded $30^\circ/s$. Minimum fixation duration was set on 60 ms. 37 students participated in the study, valid data from 32 participants (18 - 20 years old) were used for further analysis (47 % men, 53 % women).

TEST TASKS

Each student solved 8 tasks (task #2 was due to technical problems omitted from analysis). Five multiple-choice tasks were adopted from Beichner's TUG-K test [2], two tasks were adopted from previous studies [4], [5]. All tasks were focused on understanding of a slope in kinematics graphs, particularly, on position-time graphs and determining velocity.

DATA ANALYSIS

For each task we created so called AOIs (Areas of Interest). Each stem-text, stem-graph and each option was marked as a separate AOI. Because we compared two groups we did not need to take into account size of the areas and layout of the options. We created three

different students group in line with the expert-novice paradigm:

Correctly (1st) and incorrectly (2nd) answering students a particular task; students, who solved the whole test the best (3rd). As the eye-tracking metric, total fixations durations on a particular AOI was used.

RESULTS

Most participants solved a task in less than 1 minute. In order to complete a task, the best and worst performers needed the shortest time. Participants no. 20, 23 and 37 spent on tasks much more time than the others, so we did not include them into further analysis. Average total fixations duration on task #1, #3, #4, #5, #6, #7 and #8 is as follows:

23.8 s, 49.4 s, 43.2 s, 28.3 s, 37.3 s, 33.1 s, 34.4 s.

Groups of correctly and incorrectly answering students differ in their time (total fixations duration mean), which they spent on each task option. Fig. 1a and 1b show the means for both students' groups.

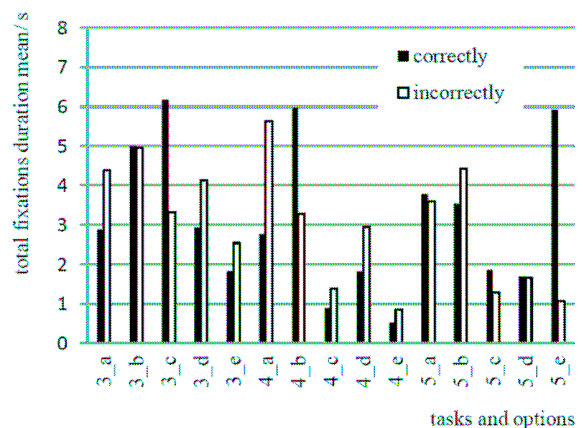


Fig. 1a. Total fixations duration mean (in s) of correctly and incorrectly answering students' groups spent on task options (task #3, #4 and #5)

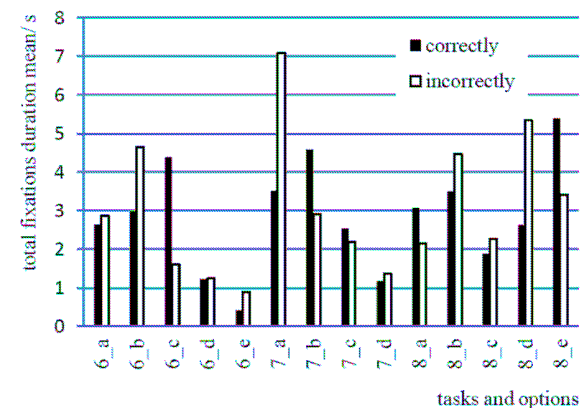


Fig. 1b. Total fixations duration mean (in s) of correctly and incorrectly answering students' groups spent on task options (task #6, #7 and #8)

Statistically significant differences were proved only for six task options. See Tab. 1. Incorrectly answering students spent more time on options, which are in line with typical misinterpretations. Particularly, they believe graph curves should have the same or similar shape if they describe one event (option 3_a), position/velocity/acceleration time graphs show trajectory of an object (options 7_a and 7_d), they show non-origin slope error (option 4_a).

Correctly answering students spent much more time on the correct options (5_e and 6_c). Moreover, incorrectly answering students paid to the correct option 5_e the least attention.

TAB. 1. Significant differences in total fixations duration means of correctly (group 1) and incorrectly (group 2) answering students spent on task options. Kolmogorov-Smirnov test, p-value < 0.05

task& option	Max Neg D	Max Pos D	mean 1	mean 2	Std.D. 1	Std.D. 2
3_a	-0.525	0.108	2.88	4.38	3.415	3.009
5_e	0.000	1.000	5.92	1.06	3.259	0.638
4_a	-0.667	0.048	2.77	5.64	1.234	2.789
6_c	0.000	0.789	4.39	1.61	1.937	0.920
7_a	-1.000	0.000	2.19	7.74	0.530	3.031
7_d	-0.833	0.000	0.60	1.42	0.225	0.470

We also focused on differences among the students, who correctly solved a task and the best performers. Students who got at least 80% of the maximum test score were included into the group (4 students). Fig. 2a and 2b shows the means for both students' groups. Statistically significant difference was proved only for one task option. See Tab. 2.

TAB. 2. Significant differences in total fixations duration means of correctly (group 1) answering students and the best performers (group 2) spent on task options. Kolmogorov-Smirnov test, p-value < 0.10

task& option	Max Neg D	Max Pos D	mean 1	mean 2	Std.D. 1	Std.D. 2
3_e	-0.000	0.750	2.34	0.84	1.288	0.487

CONCLUSIONS

Differences in students' attention allocation when they solved graphing tasks focused on the slope concept were investigated by the eye-tracking method. Correctly answering students spent always the most time on the correct options, whilst incorrectly answering students focused more on options, which we could consider as typical misinterpretations. The incorrectly answering students very often pay the least attention to the correct option! The best performing students spent much less time on options than the correctly answering students. Both students' groups recognize "nonsense" options and pay the least attention to them.

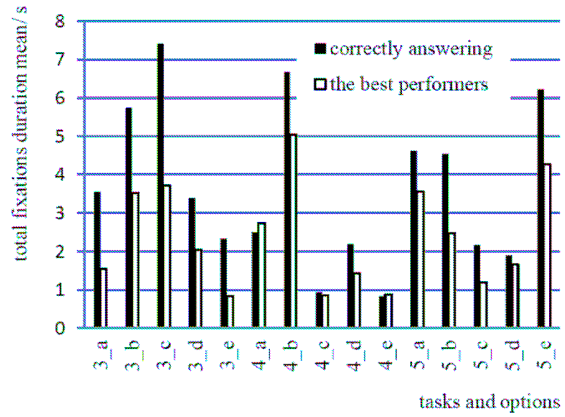


Fig. 2a. Total fixations duration mean (in s) of correctly answering students and the best performers spent on task options (task #3, #4 and #5)

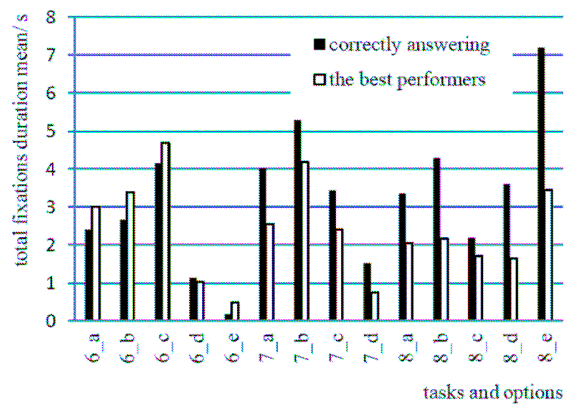


Fig. 2b. Total fixations duration mean (in s) of correctly answering students and the best performers spent on task options (task #6, #7 and #8)

REFERENCES

1. A. Susac, Physical Review, Physics Education Research **14**, 020109 (2018).
2. P. Klein et al., Physical Review, Physics Education Research **15**, 020116 (2019).
3. R. J. Beichner, American Journal of Physics **62**, 750 (1994).
4. J. Fenclova: Fyzikalni vedomosti nasich studentu, Studie CSAV **5** (Academia, Praha - 1980).
5. L. C. McDermott, M.L. Rosenquist, E. H. van Zee, Am. J. Phys. **6**, 503 (1987) .

BRIDGING COURSES FOR MATHEMATICS AND SCIENCE TEACHER STUDENTS

R. Holubová, renata.holubova@upol.cz, Faculty of Science, 17. listopadu 12, 77146 Olomouc, CZ, J. Slezáková, jana.slezakova@upol.cz, Faculty of Science, 17. listopadu 12, 77146 Olomouc, CZ

INTRODUCTION

Universities all over the world struggle to reduce the drop-out rates of the mathematics and science teacher students (approximately 75 % drop out, more than half of those drop out within the first year of their study). Several universities have introduced so-called bridging courses - courses designed to bridge the gap between what was learned in school and what is needed at university. An international survey on the existence and content of these courses was realized in the past six months. This survey was organized under the Erasmus project Bridge2Teach. Partners in this project are University of Vienna, Šiauliai University (Lithuania), Palermo University (Italy), University of Nitra (Slovakia), Palacky University Olomouc (Czech Republic). All universities are well-established schools providing pre and in-service teacher training in mathematics and science. The aim of this survey was to analyse the current status of bridging courses at various universities. An overview of the findings will be presented.

METHODOLOGY

The used methodologies in this research were as follow: 1. curricula and framework analysis, 2. interviews with staff teaching bridging courses, 3. questionnaires, 4. interviews with students attending bridging courses and students in the first semester on their study at the university. The interview was a semi-structured interview with the leading questions aimed on the expectations in the bridging course, and the reflection – if the expectations were fulfilled and if the course was useful. Transcripts of the interviews were summarized and analysed. The interviews took approximately 45 minutes each.

OUTCOME OF RESEARCH

The findings of the research will be presented for selected universities.

UNIVERSITY OF VIENNA

The university offers a wide number of bridging courses. The bridging course for the bachelor mathematics teaching program consists of a lecture “Introduction to Mathematics” (three 45-minute units per week, which corresponds to the length of the “Introduction into Mathematical Work” lecture for the bachelor mathematics program) and a preparatory tutorial (one 45-minute unit per week). The lecture and preparatory tutorial are held in the winter semester from early October to mid-December. Formally, both the lecture and the tutorial are not mandatory as such, but the final exam (7 ECTS) of the lecture is mandatory for

the students to pass, to be able to continue their studies. The Faculty of Physics offers a pre-course “Studying Physics” for both physics teacher and physics bachelor students, which takes place each year in September. The course is held as a 2 x 45-minutes-per-week-semester-equivalent. The course description lists as content: “Preparation of future physics students for the beginning of their studies. The course repeats the complete school physics and school mathematics.” The course is voluntary and does not accrue ECTS points for the study program. It exists since 2013.

The bridging course for the bachelor chemistry teaching program consists of a preparatory tutorial “Basic Chemistry Laboratory Course – preparatory tutorial” (one 45-minute unit per week, 1 ECTS) and a laboratory course “Basic Chemistry Laboratory Course – introductory lab course” (five 45-minute units per week, 5 ECTS). The lab course and preparatory tutorial are held in both the winter and summer semesters. Both the lab course and the tutorial are mandatory.

“Introduction to Biology” that forms the bridging course is held in the first four weeks of the semester. The lecture “Introduction to Biology Education” is held in the first two months of the semester. Formally, the lectures are not mandatory as such, but the combined final exam (6 ECTS) of the lectures is mandatory for the students to pass, to be able to continue their studies.

UNIVERSITY OF ŠIAULIAI

In Lithuania secondary education is not compulsory and lasts for two years (gymnasium 3rd and 4th forms or 11th and 12th secondary school classes. Students learn according to individual education plans. Students learn natural science subjects (physics, biology, chemistry) up to their 10th class. In the 11th - 12th class only one of these subjects or an integrated natural science course is compulsory. 140 hours are assigned to this general course. Therefore, students of a very different level of knowledge and abilities gather to Lithuanian university auditoriums.

For the students, who did not learn physics, chemistry or biology in the 11th - 12th classes, a possibility is given to choose from University offered extra subjects (up to 10 credits) to deepen physics, chemistry or biology knowledge. Besides, for the consolidation of knowledge, Holistic Natural Phenomena Understanding course is proposed in the programme, the main aim of which is: to develop entire, holistic world cognition and to motivate students for deeper nature phenomena understanding and interpretation, to evoke the willingness to explore.

This course is carried out in the first (autumn) semester of the first course. The size of it is 12 ECTS credits, 308 hours (lecture 48 hours, practice 56 hours, laboratory works 24 hours, independent work 180 hours). Interesting can be the fact that for the school

year 2020/21 there will be not science teacher students at this university.

UNIVERSITY OF PALERMO

In 2010 the Ministry of Education introduced a new university degree and a period of specialization and training in schools required for obtaining teacher qualification at the secondary level. Its name was "Tirocinio Formativo Attivo (TFA)". TFA programs are managed by universities in collaboration with local authorities at the regional level, and identify host schools where student teachers may complete their internship under the guidance of a school supervisor or tutor. Acceptance to TFA programs is competitive-applicants are required to pass an entrance examination, TFA course topics are defined at the national level and include pedagogical competencies, psychological competences, didactic competences, specific disciplinary contents, and active training and observation in a school under the guidance of an expert teacher tutor for approximately 400 hours. TFA programs also include an English language course (intermediate level B2) and a course in Information and Communication Technology (ICT) skills. TFA students must pass a final examination and submit a final written report on their training in order to obtain teacher qualification. Since 2019 in addition to the possession of a valid teaching qualification in a specific class, a one-year training and probation period accessible via a national public exam is necessary. There are also specific training programmes dedicated to Master's degree students to acquire 24 Credits in basic anthropological, psycho-pedagogy disciplines and teaching methodologies and technologies as an ulterior mandatory requirement to be admitted to the national public exam. Departments, in their offered training courses, give to Master's degree students the possibility to attend some course in Didactic of the discipline but, in many case, these are disconnected from each and fragmentary. Math and Science specific topics are studied during the specific Master degree course. Math/Science teacher training bridging courses are offered in the Master degree of the study. These courses do not fulfil the idea of bridging courses in their basic meaning.

PALACKY UNIVERSITY OLOMOUC

Mathematics teaching programme includes two bridging courses. Students in the first year of their study have to complete the compulsory subject Preparative Seminar in Mathematics (two hours per week) and the seminar Introduction to the Study of Mathematics (two hours per week). The content of these two subjects is focused on the solving of standard high school problems and deepening the knowledge of high school mathematics. The aim is to acquaint students with the principles associated with the study of mathematics (understand terms, symbols, mathematical text). A bridging course in Physics is not taught. But in the first

and second semester of the study a number of seminars in mathematics for physics students are offered. The subject Seminar in Mathematics for Physics Students is taught. The aim of the subject is to deepen the knowledge of high school mathematics, especially topics like functions, expressions, graphs, and differential calculus (derivative, integral, operators, differential equations). This seminar is addressed for students, which study the combination of science subjects and do not have mathematics (for example physics-chemistry, physics-biology, physics-geography etc). But the seminar is free also for physics-mathematics students if they feel the need to revise their high school mathematics knowledge. A variety of other seminars is offered by the Department of Experimental Physics for physics students, all of them are focused to overcome the gap between high school mathematics and the needs of the university level of the basic course of physics. Special biology and chemistry bridging courses are not taught.

CONCLUSIONS

The extent and framework of the courses varies widely – it can be a summer course, one-semester course in the beginning of the study, the course can be voluntary or mandatory. The crucial problem for science students at all universities seems to be insufficient knowledge of mathematics, especially in the case of physics students. They would welcome a bridging course before the beginning of the first semester because the majority of them have a problem to understand physics behind the mathematics of the solved problem.

A bridging course in physics would be useful too, because a great part of high schools do not teach physics in the fourth class (before the final exam - the graduation). Only an optional physics-chemistry seminar is taught (in the better case).

Within the project Bridge2Teach mentioned above bridging courses for mathematics and science teacher students will be prepared and workshops for lecturer (how to teach these courses) will be organized.

ACKNOWLEDGMENT: The manuscript is supported by the project ERASMUS+: Developing Bridging Courses for Mathematics and Science Teacher Students - Bridge2Teach.

REFERENCES

1. N. Barbieri. Teachers Training in Italy, 1st ed. (2019) Retrieved from http://www.uv.es/atlantid2011/2011_2012/Teachers%20Training%20in%20Italy%20by%20NS%20Barbieri.pdf
2. V. Lamanuskas: Report - Analysis of existing bridging courses in Lithuania. Erasmus + project materials (2019) (not published).
3. A. Ulovec: Report - Analysis of existing bridging courses in Austria. Erasmus + project materials (2020) (not published)
4. Palacky University study agenda <https://stag.upol.cz/portal/studium/prohlizeni.html>

STUDENTS' STRATEGIES FOR CREATING COMMENTS ON SILENT VIDEOS

S. Gorčáková, gorcakova@fmph.uniba.sk, K. Velmovská, velmovska@fmph.uniba.sk, Faculty of Mathematics, Physics a Informatics, Comenius University, Bratislava, Slovak Republic

INTRODUCTION

The constructivist model of knowledge, which is currently used in education in the form of inquiry-based learning, emphasize the development of understanding, the development of skills and competences related to activities that lead to the construction of knowledge [1]. However, during the education of didactics physics students, we often encounter a situation where the student prefers the educational strategies that he went through during his education and tends to imitate them. Therefore, we consider it important to provide continuous feedback to the students. One of the several opportunities where we can provide such feedback is the implementation of activities with silent video to the lessons. The inclusion of silent video in the training of physics teachers also helps to develop the verbalization of ideas [2]. Silent video is a type of task in which students record a commentary on a video, usually lasting one to two minutes, depicting a physical phenomenon, experiment, etc. [3].

SURVEY FOCUSED ON IDENTIFYING STRATEGIES FOR CREATING COMMENTS ON SILENT VIDEOS

Objective of survey: Preparing didactics physics students, we often encounter the fact that students choose teaching strategies in their outcomes, which they themselves experienced during their education. Our goal is to provide students with feedback. The task of this survey is therefore to identify the strategies chosen by students when commenting on silent videos.

Hypothesis of survey: It turns out that teachers in education tend to such educational strategies, which they themselves experienced as students, or which were then satisfying from their point of view. We believe that our students will also incline to some strategy in which they themselves participated, respectively which they consider appropriate. We therefore expect that:

Students choose the same strategy in each commentary on the three different silent videos.

Methods and sample of survey: The survey was conducted in March 2019 within the subject Methods of solving physical problems. It was attended by five first-year students of the master's degree in didactics of physics and supplementary pedagogical studies, who were given the task of recording a commentary on three silent videos - Cup, Electrostatics and Newton's Tube, which were created as part of the master thesis. [4] From the recorded comments, phenomenological analysis was made, which was focused on the specific strategies used by students to comment on silent videos.

Results of survey: The comments on the silent videos were made up of five students, who were marked with the letters A - E. The analysis of the individual students' comments is below. The comments are analysed in the same order for all students, as follows:

the first comment - on the silent video Cup, the second - Electrostatics, the last - Newton's tube.

Student A: In the first commentary on the silent video Cup, the student uses a lot of interjections, rhetorical questions and tries to interact with the listener. He first asks questions, later he answers them, so he explains the given phenomena that we see in the video to the listener. In the second commentary, he also asks questions to attract attention, just as in the first commentary he explains the phenomenon. The student approaches the third comment in the same way as the first two, but in addition he uses the contradiction with the expectation when he specifically draws attention to an often misconception.

Student B: At the beginning, his first comment contains a description of what is seen, later the student tries to explain what is really going on. The commentary contains many quiet places, but they do not serve as a space for thinking for the listener, because they do not follow a call to think or a question. This comment only contains declarative sentences. In the second comment, the student asks the listener a few questions with the following answer. The rest of the comment is just a very general statement of what is happening, unrelated to the specific situation. The third commentary in terms of strategies contains an explanation of the phenomenon without any interaction with the listener.

Student C: At the beginning of the first commentary, the student draws the listener's attention by telling him what he will learn. He further describes what is happening in the video, calling for attention to the details. The student waits for the second situation and then invites the audience to discuss. Finally, he explains the phenomenon. In the second commentary, as in the first, the student describes what is happening, asks the audience questions and invites them to discuss possible causes, but does not explain the phenomenon. In the third commentary, the student initially reveals what the phenomenon of the video is about but does not explain it further. He asks questions and gives the listener a task - to notice the details and discuss the causes.

Student D: His first commentary begins with the description of the phenomenon supplemented with rhetorical questions but not explaining the phenomenon. The student complements the commentary with music as a background, which is not disturbing. Similarly, he added music to the second and third commentaries. In the second commentary, he asks rhetorical questions, but also questions that are addressed directly to the listener, but not answered at all. In the third commentary, the student describes the phenomenon, asks questions, but their number is much smaller than in his previous two comments. The comment ends with an explanation.

Student E: His commentary only contains a description of what is seen and the assignment of the task to the listener - to think and discuss what is

happening in the video. It is the same in the second and third comments.

DISCUSSION

The results of the analysis of the comments suggest that the students chose the same strategy in creating all three comments. For student A, the effort to interact with the listener is noticed in all three comments. So, his comments are not just an ordinary explanation of the story, but the student tries to involve the audience in thinking. Such a strategy is typical for larger university lectures. The strategy chosen by student B, that was once used in schools, is still preferred by some teachers. It is a transmissive way of teaching, where the teacher presents the facts to the students, explains the phenomena and his students are mostly passive. The strategy perceived in student C comments has the attributes of strategy that is nowadays recognized. The student tries to actively involve the listener directly in the creation of commentary, leaves him space to think, invites him to discuss and so on. We think that this type of comment is the didactically best of the given comments. Student D approaches his comments in an original way, he tries to revive them in some way, so he complements the music as a background. He also addresses a few questions to the listener, but the listener is not forced to actively participate. Student E, like Student B, chooses a transmissive way of conveying knowledge.

Regardless of the content of the video, i.e. on the topic covered by the silent video, it was possible for each of the commentators to identify common features for all three comments, some of which we can assign to well-known teaching strategies. So, our expectations have been confirmed. We then provided the students with feedback along with the discussion.

CONCLUSIONS

Although students of didactics physics are guided during their studies to apply constructivist approaches in the teaching of physics, the results of the survey show that they often unwittingly choose the strategies that they were educated by during their compulsory education. The comments on the individual silent videos were divergent among the various students, and the strategies chosen by the students also differed from each other. During the discussion with the students about their comments, it turned out that constant feedback is extremely important for them, because it helps them to choose appropriate educational strategies.

ACKNOWLEDGMENT: This paper was elaborated with the support of the projects VEGA no. 1/0396/18 and UK/111/2020.

REFERENCES

1. B. A. Marlowe, M. L. Page: *Creating and sustaining the constructivist classroom - Second Edition* (California: Corwin Press – 2005) ISBN-13: 987-1-4129-1451-2

2. Cambridge university press. *Cambridge Dictionary online* (2016). Available on: <https://dictionary.cambridge.org/dictionary/english/verbalize> (2016).
3. F. Hreinsdóttir, B. Kristinsdóttir: *Using silent videos in the teaching of mathematics*. [online] In: S. Ceretkova (Ed.): *Staircase to Even More Interesting Mathematics Teaching*, p. 157 (Nitra, Slovakia: Constantine the Philosophers University in Nitra – 2016). Available on: <https://goo.gl/e9bnFn>
4. S. Gorčáková: *Implementácia tichých videí do prípravy študentov učiteľstva fyziky* (Master thesis. Bratislava, FMFI UK – 2019).

CONCEPTUAL PROBLEMS AND GRAPHICAL REPRESENTATION IN INTRODUCTORY COURSE OF QUANTUM PHYSICS

Z. Koupilová, zdenka.koupilova@mff.cuni.cz, P. Káčovský, petr.kacovsky@mff.cuni.cz, Department of Physics Education, Faculty of Mathematics and Physics, Charles University

INTRODUCTION

Recently, we have noticed a shift from traditional teaching style to more effective active-learning methods [1] also at university level, especially in introductory courses. Besides the transformation of the teaching style, finding suitable materials (conceptual tasks, questions for discussion, problems for group work or suitable tools for visualization) for such an approach have appeared as a big challenge.

Moreover, our course is intended for future secondary school physics teachers and therefore why we regard it to be important to use majority of materials in Czech so that future teachers have a possibility to learn the proper terminology. They will have to speak about basic quantum concepts without mathematical formalism (the only accurate quantum language) in their future practice.

In this paper, we want to bring tips for an activate-learning approach in teaching the introductory course in quantum physics gained in last ten years together with links to suitable materials.

CONCEPTUAL PROBLEMS

Conceptual problems, so called ConcepTests, were firstly introduced by prof. E. Mazur as a part of his Peer Instruction (PI) Method [2]. These are tasks aimed at core concepts of the theory, they can be simply formulated and solved rather by thinking than by complicated calculations. Mazur used mostly single-choice or multiple-choice questions. Nevertheless, we used open tasks more often. Two examples of our ConcepTest are in Tab. 1.

ConcepTests are very suitable for use in lessons utilizing PI method or group/class discussions. Moreover, we used them also as a part of home assignments for monitoring students' understanding of the previous lesson topics according to the Just-in-Time Teaching method [3].

CONCEPTUAL TESTS

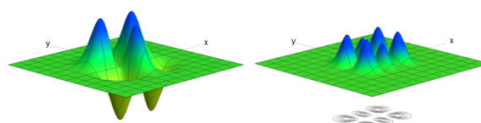
Conceptual questions (mostly single-choice ones) have been used for creating the so-called conceptual tests and they have been the internationally well-established research instrument in physics education research since 80's years of last century. The eight best assessed tests in quantum physics [4] differ in topics as well as in difficulty level. We prepared Czech version of the Quantum Mechanics Visualization Instrument (QMVI) [5] and Quantum Mechanics Survey (QMS) [6]. The QMS was administrated to students of our course in last four years. Their average score 38 % corresponds to the score of the undergraduate students in original version [6]. In addition, we asked students to assess their understanding the question (see fig. 1).

TAB 1: Examples of conceptual tasks

Consider the following eight states of a single particle:

1. The eigenstate of the \hat{H}
2. State with zero energy uncertainty
3. State with a sharp energy value
4. Particle energy does not change with its position.
5. If I measure energy in this state and immediately repeat the measurement on that particle, I will always get the same value in both measurements.
6. The measurement of energy does not affect the system.
7. The so-called stationary state.
8. In this state, the mean values of time-independent quantities are constant (regardless of whether or not they commute with the Hamiltonian).

Six of these options say the same thing, one is a generally true statement (valid for any state of one particle) and one is an absolute nonsense. Sort the statements out.



- 1) We see 2D graph of eigenstate and probability density. Is this an infinite rectangular well or a harmonic oscillator?
- 2) Determine the quantum numbers.
- 3) Calculate the energy of the state.

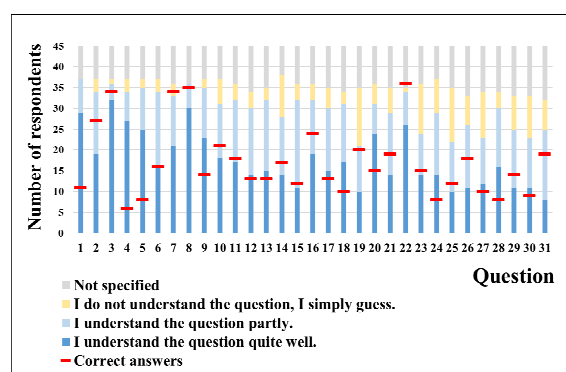


Fig. 1. Comparison of correct answers and perceived understanding of question

VISUALISATION TOOLS

Quantum physics is an abstract part of physics, so

students can benefit very much from proper visualization. Emphasis on graphics and interactive simulations is the most-visible difference between our course and other lectures. We use some well-known resources like Physlets Quantum Physics [7], PhET simulations [8] or Quantum Visualisation Projects (QuViS) [9].

Besides usage of the internationally well-known applets, we have prepared also our original ones – several small tools for visualisation of a specific thing and two larger projects. The first and older one is called *Orbitals* (fig. 2 left). [10] Four interactive programs (for Windows, prepared in LabView software) accompanied by workbook (10 pages, approx. 30 problems with explanatory text) present hydrogen atom eigenfunctions in a very detailed step-by-step approach. Our students work with them mostly as a home assignment.

The second project was a reaction on end of Java support in browsers when many useful Java applets remained unusable. One student of our course, Tomáš Škraban, programmed the “1D Quantum Potentials program” [11] displaying solutions of various 1D problems (fig 2 right) – infinite and finite rectangular well, rectangular step and barrier (with changeable shape, not necessarily symmetric) and linear harmonic oscillator. We can switch between probability density or real and imaginary parts of wave function display. In case of system with bound states, it is possible to show superposition of up to ten eigenstates. The time development is shown as an animation. For teaching purposes, it is also possible to display the solutions of Schrödinger equation for all energies.

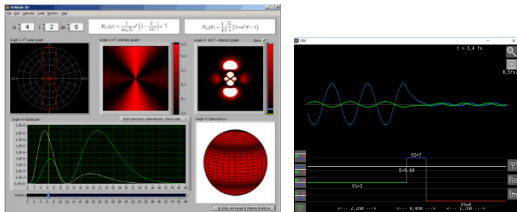


Fig. 2. Screenshot of *Orbitals* (left) and *1D potentials program* (right)

QuViS APPLETS IN CZECH

The collection of QuViS applets [9] is based on research of frequent student difficulties, furthermore their design and effectiveness are also verified [12]. The concept of these applets fit very well into our course. Nevertheless, the language barrier was an obstacle for some students, which limited the independent use of applets by the students themselves. Because the knowledge of Czech terminology is very important for future teachers, we decided to translate selected applets into Czech (fig. 3) with their authors' permission.

Since now, we have translated 17 applets and published them on the FyzWeb server [13]. They are divided into these topics: Classical systems, Basic concepts, One-dimensional potentials, Two-dimensional potentials, Momentum and spin and Entanglement and quantum information. We plan to translate about 30

applets in total and enrich all of them by suitable tasks or problems.

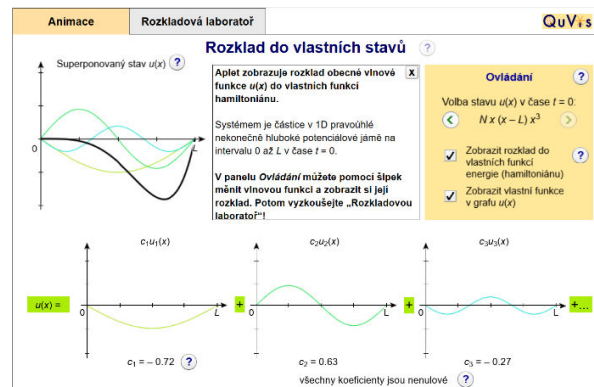


Fig. 3. An example of QuViS applet translated into Czech

CONCLUSIONS

In the article we present a comprehensive collection of conceptual tasks and suitable tools and visualizations created on the basis of other author's sources as well as materials developed directly in the mentioned course. These materials are freely available to anyone interested and can thus enrich teaching introductory courses in quantum physics at other schools.

ACKNOWLEDGMENT: Translation of applets and preparation of conceptual problems has been financially supported by the institutional development project of the Ministry of Education, Youth and Sports.

REFERENCES

1. R. Hake, *Am. J. Phys.* **66**, 64 (1998).
2. E. Mazur: *Peer instruction: a user's manual* (Prentice Hall, Inc., Upper Saddle River – 1997).
3. S. Simkins, M. H. Maier: *Just-in-Time Teaching: Across the Disciplines, Across the Academy* (Stylus Publishing, LLC, Sterling – 2010).
4. <https://www.physport.org/assessments/> [online, cit. Oct 9 2020].
5. R. Robinett, E. Cataloglu. *Am. J. Phys.* **70**, 3 (2002).
6. G. Zhu, C. Singh, *Am. J. Phys.* **80**, 3 (2012).
7. <https://www.compadre.org/pqp/> [online, cit. 9. 10. 2020].
8. <https://phet.colorado.edu/> [online, cit. 9. 10. 2020].
9. <https://www.st-andrews.ac.uk/physics/quvis/> [online, cit. 9. 10. 2020].
10. <http://kdf.mff.cuni.cz/~koupilova/orbitals/> [online, cit. 9. 10. 2020].
11. <http://fyzweb.cz/materialy/qm-potencialy/> [online, cit. 9. 10. 2020].
12. A. Kohnle et al., *Am. J. Physics* **80**, 148 (2012).
13. <http://fyzweb.cz/materialy/kvantovka/> [online, cit. 9. 10. 2020].

SMART BIOMETRIC RECORDING SYSTEM

A. Enikeev^a, J. Skopalík^{a,b}, j.skopalik@gmail.com, T. Parák^b, K. Švík^c, J. Kolářová^a, V. Čmiel^a, J. Mašek^d, masek@vri.cz,

^aDept. of Biomedical Engineering, Faculty of Electrical Engineering and Communication, Brno University of Technology, Brno, Czech Republic

^bDept. of Pharmacology and Toxicology, Faculty of Pharmacy, Masaryk University, Brno, Czech Republic

^cCentre of Experimental Medicine, Slovak Academy of Sciences, Bratislava, Slovakia

^dDept. of Pharmacology and Toxicology, VUVeL v.v.i, Brno, Czech Republic

INTRODUCTION

Lab rats and rabbits are traditional biophysical models for study of the orthopedic pathologies and curative effects. Traditional analysis of these pathologies is based on postmortem histological analysis or X-ray analysis or invasive biochemical bioptic sampling, however modern monitoring of orthopedic pathology needs also new methods based on quantification of functionality of body movement. The quantification could be realised in two different modes, the first mode is global quantification of whole-body movements (resulting in “tracking statistic” during the hours or days of movement in animal box). The second mode is the knee flexion quantification. Development of the complex tool for both of this quantitative analysis of movement was based on optimising the combination of optical detection system, mathematical image analysis and physical interpretation of the detected movement. The traditional veterinary lab cages (580 x 375 cm or 600 x 700 cm) were used due to standartisation.

SELECTING AND OPTIMISING OF OPTICAL METHODS

The selection of optical methods was based on a high number of evaluation steps on different combination of digital cameras and coloring or illumination of bottom of typical animal cage during the day (night phase not detected). The final decision-making moment rested in comparison of camera Microsoft HD3000 and Xiami MiHome on the optimised dark green cage (Fig.1). The camera was fixed on central position 60 cm above bottom of the box. The box had been innovated by transparent cover.



Fig. 1. Optimised geometry of the animal cage and camera and testing the optimal color of the bottom. Illumination was finalised in green cage as 65 Lux (measured at the bottom level)

PHYSICAL DESCRIPTION OF MOVEMENTS AND SELECTING AND OPTIMISING OF SOFTWARE FOR IMAGE ANALYSIS

Both types (rats and rabbits) models display maximum acceleration $1,2 \text{ m/s}^2$ and maximum speed $1,4 \text{ m/s}$. The time-lapse tracking of body should be related to the S = total distance summing all steps of body locomotion during defined several hours of monitoring, the graphs of average (m/s) distribution during the time the time and the trajectory (projected on the bottom of the cage, x and y axis are represented by orthogonal walls of the cage). Due to relative high ratio of body size to the box size, we could not take the animal body as dimensionless, we had to identify one objective point on body, which will be a good benchmark of body motility. After sets of tests, the mathematical centre of mass of graphical contour of animal body was taken as this objective benchmark for next all analysis.

The sufficient speed of recording was evaluated as 30 frames/s. Each single frame was processed by software utility created in Phyton (Fig. 2) in real time.



Fig. 2. Processing of each frame – optimal identification of animal body before computing the position of the mass centre

The identification of centre of mass and computing of x - y position had to be repeated by software 10times per second, at each of this time point the shift from the previous position was computed and the graphical

trajectory is generated in real time. Fig. 3 summarises the complex algorithm of software analysis in Python.

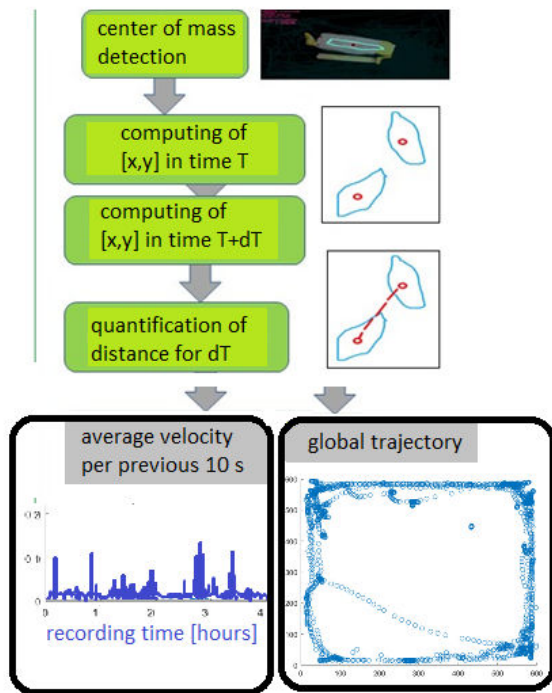


Fig. 3. Statistical overview of the animal trajectory and speed

DIGITAL ANALYSIS OF KNEE STRETCHING

Monitoring of knee functionality was additional analysis for better description of animal leg movement. This analysis was applied only to a rabbit (not smaller rat). The femur-tibia stretching (Fig. 3) was monitored using camera through the frontal transparent wall of the animal cage, recording of femur-tibia angle during the time is the merit of quantitative knee analysis. The “spinal direction” had to be orthogonal to the direction of camera view, if not the angle of the animal axis had to be identified from the image (marker with control distance d on Fig. 4) and apparent femur-tibia angle (angle define by f and t lines in Fig. 4) had to be recomputed to the real angle.



Fig. 4. Animal with knee markers and spinal markers (right picture) and software image analysis of the marked points and knee angle in each 0.1 s

RESULTS

These optimised combination of the hardware and software were tested on 5 rats with different pathology of knee and also on 6 rabbits (2 control, 4 with different

therapy on the of osteoarthritis) in animal unit. The markers and recording did not induce any irritation or stress reaction of the animals. The identification of a correct centre of mass and true trajectory was evaluated in more than 5000 frames (comparison with graphical results from manual detection), the (x, y) difference was smaller than 1 cm in 98 % of cases. Total difference of trace length per 500 s was under 25 cm (average difference under 3 % of total trace length). Average knee angle stretching of osteoarthritis rabbit was identified as 6° (per one rabbit step) in comparison to control rabbit with 22° (per one rabbit step). Moreover, the frequency of stretching during 6 hours was only 30 % in osteoarthritic knee.

CONCLUSIONS

The biomedical evaluation of pathological motility and regeneration in time are not effectively described in current biomedical and biophysical studies and they need the smart non-invasive methods for the objective quantification of the body motion and knee flexion. Modern imaging technologies and precise mathematical analysis with physical background bring possibilities to quantify the typical movement and produce “every-day objective documentation” of the pathological state.

ACKNOWLEDGMENT: The project was supported by Ministry of Education, Youth and Sports; project “FIT” CZ.02.1.01/0.0/0.0/15 003/0000495 and project FEKT-S-206195.

REFERENCES

1. Ch. Brenneis et al., Journal of the American Association for Laboratory Animal Science **56**, 18 (2017).

IT ACADEMY PROJECT IN THE LIGHT OF CHANGES IN PHYSICS EDUCATION

Z. Ješková, zuzana.jeskova@upjs.sk, M. Kireš, marian.kires@upjs.sk, Faculty of Science, Pavol Jozef Safarik University in Kosice, Šrobárova 1, 040 01 Košice, Slovakia

INTRODUCTION AND BACKGROUND

Rapid changes in economy and technology and their effect on the workplace call for changes in educational system. These problems of how 21st century education should look like are still in the main focus of educators. Although there are many approaches to this issue, it is generally agreed, that students should master the skills including critical thinking and problem solving skills, creativity and reasoning [1 - 4]. In accordance with 21st century educational goals, the concept of student-centred active learning and inquiry-based education (IBSE) is expected to promote learning of modern day students. The skills of problem solving, reasoning and critical thinking are involved in the whole process of inquiry from identifying a question, formulating hypothesis, gathering data, testing and evaluating hypothesis and drawing conclusions. This approach represents the basis how physics and science research is conducted and it is also already established in instruction for several decades. However, some education experts have noted that most 21st century's students are still being taught by teachers using 20th-century pedagogical practices in 19-century school organisations [4, 5]. It seems that this long-time effort supported by numerous national and international projects towards implementation of IBSE still does not guarantee the systematic implementation of desired instructional strategies. The national project IT Academy [6] (2016-2021), besides several other goals, has an ambition to help in motivation teachers towards wide implementation of inquiry-based science education methods and strategies. This particular goal is reflected in two ways: a) developing teaching and learning materials based on IBSE approach, b) education of teachers to master the methods and strategies of IBSE. It is already known that IBSE can be strongly enhanced by using digital tools to solve problems in order to collect, process and analyse data from experiments and to design and analyse models of studied phenomena. For this reason, digital tools are widely implemented in designing teaching and learning materials as well as in the teacher training programmes.

TEACHING AND LEARNING MATERIALS

The large number of teaching and learning materials has been developed for physics teaching at lower and upper secondary school level. They were developed on the basis of design-based research principles. The lessons designed by experienced teachers or experts in physics education were offered to physics teachers for trialling in the classroom. The lessons were subjected to two-round verification. After the first round the teaching and learning materials were adapted and modified based on teachers' comments for the second round of implementation. They have been modified again to create the final version of the developed lessons (fig. 1).

The materials are developed for individual lessons (about 80 physics lessons for lower and 50 physics lessons for upper secondary physics classes). The materials involve teachers' guide, working sheets for students, supplementary materials and multimedia and digital resources.

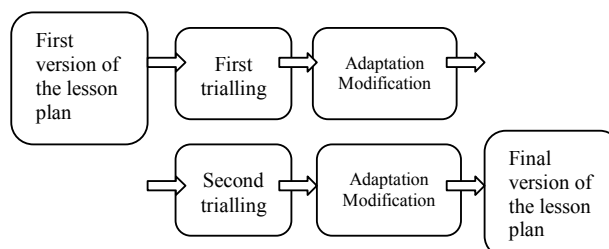


Fig. 1. Two-round design of lesson plans

Teachers' guides is complemented by an overview sheet where the learning goals, methods, tools and materials, necessary prior knowledge and skills and main misconceptions are communicated briefly. The teachers' guide itself contains a detailed lesson plan with proposed activities to provide knowledge and support to help understand and implement teaching plan, present alternatives and freedom of choice and engage teachers in ongoing reflection [7].

TAB. 1. Example of an activity at guided inquiry level

Inquiry phase	Research question: How much work is done by a weightlifter?
Conception, planning and design	-planning experiment -measuring time and position with the help of videomeasuring tools -predicting results (position vs. time graph)
Implementation	-manipulating software -collecting data by videomeasurement
Analysis and interpretation	-determining relationship between variables -what kind of motion is executed by the weight? -what is the acceleration in separate phases of weightlifting? -what net force is acting on the weight during its motion? -what force does the weightlifter generate? -what distance does the weight move? -what work is done by weightlifter?
Communication	Elaborating formal report about the gained result
Application and follow-up	What power is generated by the weightlifter?

Most lessons are designed using inquiry approach. The designed investigations are enhanced by digital tools, namely sensors and videomeasurement for data collecting (in certain cases data are collected using remote-controlled experiments) and software for data processing and analysis and also modelling tools involving simulations. Lessons are also supplemented by formative assessment tools.

The lesson starts with a research question for students to solve. They go gradually through the stages of inquiry cycle based on the framework of inquiry skills [8] (tab.1). Each lesson is designed at a certain level of inquiry depending on how much information is provided to students and how much guidance is provided by teacher. Most lesson plans are following the structure of confirmation inquiry (students are provided with the question, procedure and the result are known in advance) and guided inquiry (question and procedure is known, however the result and its explanation is generated by students). Related to the inquiry level more or less detailed students' worksheet guides students through the investigation posing questions and assignments for students to solve.

In fig. 2 the result of videomeasurement of the weightlifting is presented. After gathering data students follow with data analysis as suggested by questions in table 1.

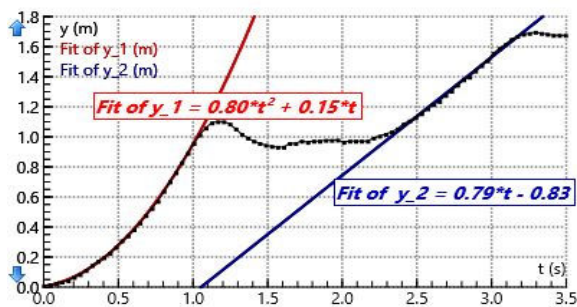


Fig. 2. Results of measuring the position of weight in the activity How much work is done by a weightlifter?

PHYSICS TEACHER EDUCATION PROGRAMME

In order to achieve the wide implementation of developed teaching and learning materials teachers must be motivated and educated in the field of corresponding methods and strategies to teaching.

TAB. 2. Physics teacher education programme structure

IBSE, introduction do digital technologies in physics education
Measuring with sensors, processing and analysing data
Measuring on videorecording
Computer modelling
IBSE and formative assessment

For this purpose, the in-service teacher education programme has been designed. It is based on the same concepts as teaching and learning materials, i.e. teachers

learn about the basic principles of IBSE, master the skills to use digital technologies and they are introduced the formative assessment tools and its importance for IBSE. The programme has a modular structure (tab.2) and is built as a blended course with present and distant parts with the extend of 50 hours (40/10) for the upper secondary school teachers and 40 hours (30/10) for the lower secondary school teachers.

The training is conducted the way that the teachers participating at the programme usually play a role of students conducting the activity. The learning scenario is then analysed with the lecturer in order to recognize the important inquiry elements, the benefits of digital tools and formative assessment tools to identify students' misconceptions. At the end of the programme teachers design their own lesson plan based on IBSE approach using one selected digital tool.

There are altogether almost 100 physics teachers who completed the teacher education programmes so far.

CONCLUSION

The collection of teaching and learning materials will be published online for teachers to use. The developed teacher education programmes will be running also in the following year. It will be complemented by one-day seminars or online webinars in order to attract participation of more teachers. We hope that the project effort helps in gaining teachers' self-confidence towards wide implementation of innovative strategies to promote learning of modern day students.

ACKNOWLEDGMENT: This paper was made in the framework of the national project IT Academy – Education for the 21st century that is supported by European social fund and European regional development fund under the Operational Programme Human resources.

REFERENCES

- Ch. Fadel 21st Century Skills: How can you prepare students for the new Global Economy? OECD. Learning in the 21st century, Research, Innovation and policy, OECD Publishing (2008).
- L. Bao, K. Koenig, Discip. and Interdiscip. Sci. Educ. Res. **1**, 2 (2019).
- The Future of education and skills, Education 2030, The Future we want, OECD position paper, OECD Publishing (2018).
- OECD Future of Education and Skills 2030, OECD Learning Compass 2030, A series of concept notes, OECD Publishing (2019).
- A. Schleicher, World Class, How to Build a 21st-Century School System, OECD Publishing (2018).
- IT Academy project, <http://itakademia.sk/>
- Learning Portal: Planning education for improved learning outcomes, available on <https://learningportal.iiep.unesco.org/> (2018).
- Z. Ješková et al., Journal of Baltic Science Education **15** (5), 559 (2016).

RESEARCH ON LEVEL OF STUDENTS' EDUCATIONAL INTEREST IN PHYSICS

A. Křučarová, andrea.klucarova@smail.unipo.sk, V. Šebeň, vladimir.seben@unipo.sk

To many people, the simple act of pronouncing the word physics literary sends chills down their spines. This concerns not only primary- or secondary-school students, but also people of productive and post-productive age. Some students are afraid of physics, others have respect for it, and there also exist such individuals who feel aversion towards it. Generally, students' interest in science subjects is worldwide decreasing [1]. According to pedagogical research provided by Dopita and Grecmanová [2] students show very little interest in physics study and they are not willing to spend their time studying it. A year later Mandíková [3] published that students' attitude towards physics is more negative than positive. We know from pedagogical experience that the level of interest varies from one person to another and can be of various degrees and forms. The most significant sign of interest can be considered the voluntary student-initiated incorporation of physics into their free-time activities, such as active participation in extra-curricular activities, out-of-school interest groups focused on physics topics or participation in physics competitions. Due to the fact that year after year there is a gradual decrease in the number of student competitors of the Physics Olympiad, we decided to examine what level of educational interest in physics is currently the most developed among primary-school students.

EDUCATIONAL INTEREST

Currently, an effort to activate the cognitive functions as well as cognitive activity of students is put into the foreground in pedagogical field. This happens in order to reduce the traditional model of education, in which students find themselves mostly in a position of passive participants of the teaching-learning process. Their cognitive activity is strongly influenced by educational interest. The more interested in studying the students are, the more activated their cognitive functions will become. For this reason, educational interest plays a very important role in developing student's attitude towards any school subjects. Moreover, the teachers largely participate in formation of student's educational interest and also its subsequent development through their motivational influence on students. The role of the teacher is besides providing the students with knowledge, also to arouse students' interest in the subjects they teach, to arouse students' interest in a certain scientific topic, and in case of already existing interest, to constantly support this interest [4].

Interest is generally considered to be one of the most influential motivating factors determining students' desire to learn. It is one of the most important conditions stimulating creativity and a creative attitude towards the activity being provided. We know from personal experience that any activity done with reluctance or by force, even though it misses a sign of students' interest in providing such an activity, is ineffective. In addition,

it is scientifically proven that interest supports the development of intellectual side of students, increases their ability to maintain attention for a longer time and, last but not least, the ability to be able to concentrate [5]. By interest we mean a conscious, voluntary, long-lasting and continuous focus of human activity on a specific area of cognition and active self-realization [6]. Educational interest is firstly encountered in the research papers and other works of Ščukinová [7]. She defines educational interest as "*a person's individual selective focus on self-studying, learning about objects, phenomena and facts of the world we live in, activating his/her mental processes, active work as well as cognitive possibilities.*" The object of educational interest concerns various areas related to human cognitive activity. One interest may differ from another in its intensity, breadth and depth of focus. Wide educational interest evokes a general interest in acquiring new information and knowledge. In the case of a deeper focus of educational interest, we already talk about narrowing the interest to a specific school subject or to a certain thematic unit. With regard to the degree of interest development and its nature, we distinguish three main levels of educational interest development: high, medium and low (situational) level. It is important for teachers to be able to correctly determine the appropriate level of their students' interest in the subject they teach at school [5].

METHODOLOGY

Pedagogical research has been done by the questionnaire method of obtaining statistical data. The authors of this paper have prepared a non-standardized questionnaire, which was used for conducting the research. The aim of this research was to determine the current level of primary-school students' educational interest in physics. The whole process of designing the questionnaire, preparing suitable questions as well as formulating possible answers was inspired by Lanina's methodology. Due to the fact that this methodology is based on the assumption concerning the existence of educational interest, Lanina [8] defines exactly three levels of interest: low, medium and high. However, in order to obtain more accurate results, we had to take into consideration that for quite a long time, physics has been one of the least popular school subjects. For this reason, we have added to the above-mentioned levels of interest another one, the so-called zero level of educational interest, which represents the student's complete disinterest in physics. Moreover, we have divided level-1 and level-3 into two sublevels. The questions in the questionnaire were focused on finding out students' emotional feelings towards the subject of physics, their attitude to experimental activities and to their independent scientific research work as well. In addition, students were asked to comment on issues concerning their primary motivation for studying

physics at home, also questions about attending some physics extra-curricular subject, and last but not least, about the possibility of becoming a professional worker in some physics field. Items of the questionnaire provided closed answers with one option to be chosen.

RESEARCH RESULTS

The research was conducted during January and February 2020 at the selected primary-schools in the Region of Prešov. The respondent sample consisted of students attending the 7th, 8th and 9th grade. From the number of returned questionnaires we formed the statistical group of 194 respondents. It consisted of 86 girls and 108 boys. Statistical analysis of questionnaires revealed six levels of physics-oriented educational interest among the primary-school students. They are presented in the following table:

TAB. 1. Table of educational interest levels

Interest level	Interest type	% frequency
0	total disinterest	5.2
1a	situational-low	12.9
1b	situational-high	38.7
2	medium	29.4
3a	high-standard	9.8
3b	high-maximum	4.1

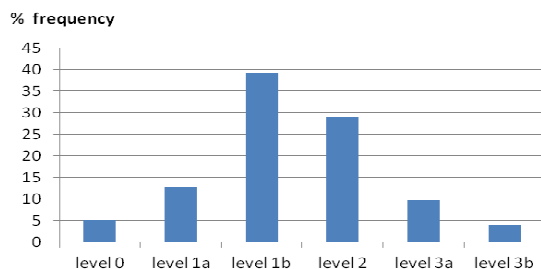


Fig. 1. Graph showing the percentage frequency of developed educational physics interest of primary-school students

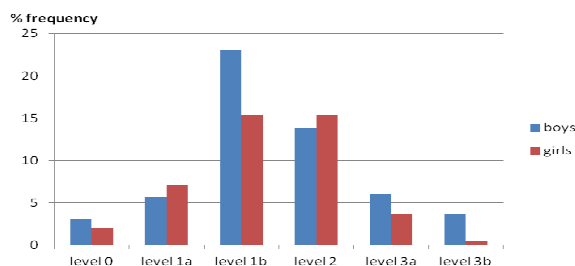


Fig. 2. Graph comparing the percentage frequency of developed educational physics interest of boys and girls

The results showed that most frequent type of educational interest is situational interest of a higher level. This interest level dominates at a total number of 38.7 % of students surveyed. More than half of them are boys representing about 60 %. The second most frequent level of educational interest in physics was confirmed in less than 30 percent of research-group students. It corresponds to the level-2 interest, in which students

show characteristics typical for a medium level of educational interest. Almost 13% of students show signs of situational interest of lower sublevel. This degree is typical for students whose cognitive interest in physics is not very developed.

CONCLUSIONS

Research results showed that the current most frequent level of students' educational interest in physics has reached the level of a higher situational interest. This means that students consider physics more interesting in comparison with other school subjects, however; they usually do not take part in extra-curricular physics activities. Students are amazed mainly by visual or sound effects of physics experiments. They do not like individual experimental work, but prefer group work. Last but not least, these students rarely understand the laws of physics and its principles. They are motivated to study predominantly by external motivational factors such as desire to get a good mark or, otherwise, effort to avoid getting a bad mark or being punished. The authors of this paper consider situational level of interest a sufficiently stable basis for its continuous development. Therefore, teachers should keep on supporting, stimulating students' interest with various motivational techniques. Moreover, it is important to create a non-violent environment in order to develop their educational interest continuously. Otherwise, there is a risk of a further decrease in the level of students' interest in physics, which may finally result in a complete loss of interest. As a matter of fact, that early suppression of any undesirable phenomenon and the prevention of its occurrence are always easier than the later elimination of consequences, thus it is better to prevent the loss of students' interest in physics.

ACKNOWLEDGMENT: This research was supported by the Grant Agency of Prešov University; project no GaPU 22/20.

REFERENCES

1. J.M. Ramsden, *Int. J. Science Educ.* **20**, 125 (1998).
2. M. Dopita, H. Grecmanová, *e-Pedagogicum* **8**, 31 (2008).
3. D. Mandíková, *Pedagogika* **59**, 380 (2009).
4. V. Šebeň: *Fyzika v záujmovej činnosti žiakov*. (Prešov: FHPV PU – 2007). ISBN 978-80-8068-690-1.
5. V. Šebeň, I. Šebeňová: *Poznávaci záujem a záujmová činnosť vo výchove mimo vyučovania*. In: *Námety pre prírodovednú a technickú záujmovú činnosť*. (Prešov: Pedagogická fakulta PU – 2011) ISBN 978-80-555-0433-9.
6. Z. Helus: *Psychologie* (Praha: Fortuna – 2003). ISBN 80-7168-876-2.
7. G. I. Ščukinová: *Pedagogičeskiye problemy formirovaniya poznatel'nykh interesov učaščichsja*. (Moskva: Pedagogika – 1988).
8. I. J. Lanina: *Metodika razvitiya poznatel'novo interesa učaščichsa pri obučenii fizike*. (Leningrad: Prosvěščenje – 1984).

WAYS TO EVALUATE STUDENTS' ARGUMENTS IN TEACHING PHYSICS IN PRIMARY SCHOOL

T. Kiss, kissstunde@gmail.com, K. Velmovská, velmovska@fmph.uniba.sk, Faculty of Mathematics, Physics and Informatics, Comenius University, Bratislava, Slovak Republic

INTRODUCTION

Argumentation is a part of our everyday life. It is a part of the communication we use in everyday life, for example to defend our opinions or express our thoughts. It is important for children to engage in argumentation also during school attendance. Speaking of teaching physics, students should express their views or provide their claims with use of facts when solving a physical problem. They should also hypothesize and explain different phenomena and events.

DEFINITION OF THE CONCEPT OF ARGUMENTATION

In the literature we could find various approaches of authors to define the concept of argumentation. Different authors perceive argumentation in different ways. They understand it as a form of proving, thought process expressed by words confirming that a claim is true or false to convince someone. Others emphasize the relationship of support between the premises and the conclusion [1 - 7].

Based on these definitions we defined in our work the concept of argumentation as well. From the point of view of teaching physics by argumentation we understand, that the student gives an explanation or clarification of a physical phenomenon, based on assumptions – known and valid facts, rules and laws of physics, or draws conclusion based on facts, information obtained (for example by measurement) and gives evidence for hypotheses.

WAYS TO EVALUATE ARGUMENTS

In the literature we could find different structures of argumentation text. In this article we are dealing with two of these structures.

The first structure is a three-parts structure of argumentation text by authors Palenčárová and Kročítý [8]. We can schematically describe this structure as C + E + R, where C denotes a claim or thesis, E denotes an evidence, arguing or clarifying and R denotes reasoning, summarizing claim, conclusion and solution, instructions for possible solutions, call to action. These parts can be repeated, the order is not determined exactly, so the parts can interchange and complete each other. Within the process of teaching physics, we could imagine this three-parts structure as follows. The first phase (C) is the stating a hypothesis, so the claim before the beginning of a given measurement. In the second phase (E) students observe the given phenomenon, take measurements, process obtained data and obtain some argument or evidence to draw a conclusion in the last phase (R) and justify whether their expectations from the first phase were correct or not.

This procedure is in accordance with the definition of scientific argumentation [7], because the students with the help of findings (some empirical evidence, which they obtained during observation and measurement - scientific method) make a decision on the correctness of the assumption (hypothesis).

The three-parts structure in teaching physics could be imagined even without the experimental phase – without realisation of measurement. Students make a conclusion while relying on known facts and claims.

The second scheme, which we are dealing with is from the author Toulmin [9] and consists of six parts which could be used to develop, analyse and categorize the argument: claim, grounds, warrant, backing, qualifier, rebuttal. The connection between these parts is shown in Fig. 1.

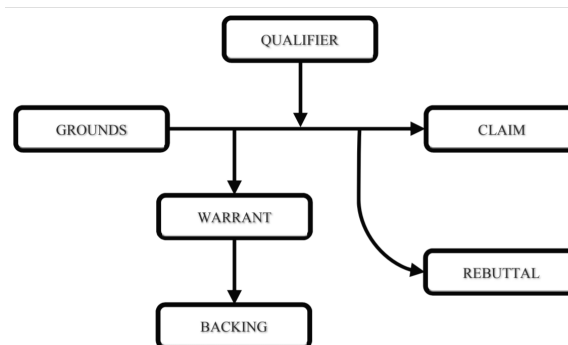


Fig. 1. Toulmin's scheme [10]

In the next step, we evaluate the students' answers according to both structures. In our article, according to the three-part structure, students could get 6 points at maximum in total, 3 points for the structure of the answer and 3 points for the correctness of the answer. Concerning the structure of the answer, every answer was divided into three parts based on three-part structure C + E + R. For each single part, not speaking of correctness, the students could get 1 point. In the following, we checked the correctness of each single part. In the case of correct answer, we gave score of 1 point. In this way, students could obtain 3 + 3 points, so 6 points in total for answering the given task.

In the same manner we evaluated the answers based on Toulmin's scheme, but because this scheme has six parts, the students were able to get 6 + 6 points, so 12 points in total.

EVALUATION OF CONCRETE STUDENTS' ANSWERS

The students of the 6th to the 9th grade of primary school were given a test consisted of tasks with open-ended questions. The task, which we present below, was focused on the behaviour of bodies in liquids. Students

were supposed to write their explanations and the reasons for them. Therefore, they were supposed to use argumentation skills.

The wording of this task is as follows: *Michael noticed that his grandmother left oil and water on the table. He found two identical test tubes in the cabinet. He poured some water into one test tube and closed it. Then he immersed it into an aquarium filled with water. The test tube stabilized in the water in a vertical position and it was floating vertically on the surface of the water. He filled the second test tube with oil to the same height and immersed it into an aquarium filled with water. The test tube with oil also stabilized in a vertical position. Compare immersion depths of these test tubes and explain your answer!*

In the following table 1 we present a concrete student's answer to the given task, which we tried to evaluate according to both structures: *The test tube with oil was less immersed than the tube with water. Because the oil has a lower density than the water, the oil is less immersed.*

TAB. 1. Evaluation of students' answer according to both structures

C + E + R			TOULMIN		
structure		2	structure		2
claim	The oil has a lower density than the water.	1	claim	The test tube with oil was less immersed than the tube with water.	1
evidence		0	grounds	The oil has a lower density than the water.	1
reasoning	The test tube with oil was less immersed than the tube with water.	1	warrant		0
total		4	backing		0
			qualifier		0
			rebuttal		0
			total		4

There were students who scored 0 points for this task. It is for the reason, that they either did not write any answer, or the answer they wrote was not related to the task. If the student wrote only conclusion, he or she could receive 1 or 2 points - 1 point for the structure and 1 point for the correctness. We also found answers, with some other information in addition to the conclusion. According to the structure C + E + R, when the student's answer contains claim and reasoning, he/she has 2 points for the structure, and according to the correctness he/she can get another 2 points. In the table above you can see the best answer of this task. According to the structure C + E + R, the student's answer contains claim and reasoning, and because both parts were correct, he/she received a total 4 points. In this answer, as in the most cases, the connection between claim and reasoning – so the evidence is missing – therefore the student could not receive 6 points, the maximum number of points.

Specifically, in this answer we miss the fact, that the student did not explain, that liquid with the same volume, but with a higher density has a greater weight and the immersion of the body is related to its weight. Speaking of Toulmin's scheme in the given example, because student's answer was too short, it received the same number of points as in the case of C + E + R.

CONCLUSIONS

Based on the evaluation of students' answers we can say that the maximum points – 6 or 12 points – was not received by any student. Furthermore, we can notice, that student's answers are quite short, and sometimes it is difficult to divide them into three parts, not yet into six parts. Therefore, we assume, that Toulmin's structure could be rather found in argumentation text where student expresses and justifies his or her opinion on the topic. In the task with the test tubes Toulmin's scheme could not be found, so in the following we want to assign another task, in which the students have more "freedom" to write their opinion.

ACKNOWLEDGMENT: This paper was elaborated with the support of the projects VEGA no. 1/0396/18.

REFERENCES

1. G. Brukker, J. Opatíková, Veľký slovník cudzích slov (Robinson s.r.o., Bratislava - 2006).
2. K. Hincová, A. Húsková, Slovenský jazyk pre 1. – 4. ročník stredných škôl (Slovenské pedagogické nakladateľstvo, Bratislava - 2009).
3. T. Nagy, S. Nagyová, P. Likavský, Umenie prezentácie a komunikácie (PF UK, Bratislava - 2010).
4. R. Staněk, Lekce 4: Argumentace (Brno - 2011).
5. S. Šaling, M. Ivanová-Šalingová, Z. Maníková: Slovník cudzích slov pre školu a prax (SAMO, Veľký Šariš – 1997).
6. J. Tomášková: Argumentácia v škole i bežnom živote (Metodicko-pedagogické centrum v Bratislave, Bratislava - 2015).
7. L. Bielik: Logika, argumentácia a evidencia (Bratislava - 2016).
8. J. Palenčárová, P. Kročický: Akademická príručka na tvorbu odborných textov (Vysoká škola manažmentu v Trenčíne, Trenčín - 2015).
9. Changing Minds, Toulmin's Argument Model (2019), [quoted. 12-02-2019]. Available online: http://changingminds.org/disciplines/argument/making_argument/toulmin.htm
10. S. E. Toulmin, The Uses of Argument (Cambridge University Press, Cambridge - 2003).

PROBLEMS OF EVALUATION OF STUDENTS' SCORE IN NON-STANDARDIZED ACHIEVEMENT TEST

J. Čevajka, jakub.cevajka@uniba.sk, K. Velmovská, klara.velmovská@uniba.sk, Comenius University in Bratislava, Faculty of Mathematics, Physics and Informatics, Mlynská dolina F1, 842 48

INTRODUCTION

Assessment of students in the teaching process is one of the responsibilities of the school and a mandatory part of the teacher's work. Petty [1] states that students' assessment can serve a variety of purposes. Through assessment, we can classify students' performance, help select candidates for jobs, or provide students with the goal of their education. Arends [2] states that what score students achieve in a test, what grades they receive and what judgments their teachers make about their potential, has important and long-lasting consequences for the students themselves as well as society. Arends [2], based on studies, states that teachers devote ten to thirty three percent of total working time to the process of assessment and evaluation of students. It is therefore a significant part of the teacher's work and at the same time one of the most important and sensitive work activities of a teacher. Teachers consider the assessment process to be one of the most challenging tasks of the teaching profession. Students' assessment is ranked among the most difficult tasks of their work, especially by beginning teachers [3]. *"Primary school teachers consider students' assessment to be one of the five most difficult components of pedagogical activity and the fourth most difficult activity for beginning teachers."* [4]

METHODS OF SURVEY

We decided to do survey aimed at evaluation of students' score by university students of physics teaching programme. The task of the survey was to compare the individual evaluations of the proposed non-standardized achievement test by students of physics teaching between them and with the evaluation according to the proposed mark scheme. The achievement test consisted of seven tasks, namely two closed tasks, four computational tasks and one task for a short verbal answer. This test was part of a summative assessment of first-year students of a 5-year bilingual gymnasium and focuses on the topic of buoyant force and Archimedes' law. Students took the test in one lesson for 40 minutes.

From the solved tests, we selected ten, which we assigned to university students in the first year of master's studies for evaluation. University students had to evaluate the tests without a mark scheme and correct answers. Their task was to design the evaluation of individual tasks, to evaluate student solutions and to give the overall evaluation of individual students in percentages. We set two hypotheses in the survey:

H1: Evaluation of the achievement test by students of physics teaching will be divergent.

H2: Evaluation of the achievement test by students of physics teaching will be incomparable with the evaluation according to the proposed mark scheme.

We collected data from two academic years and 16 university students from Faculty Mathematics, Physics and Informatics of Comenius University in Bratislava participated in the survey.

PROCESSING AND INTERPRETATION OF SURVEY RESULTS

After the evaluation process, we collected data from students, namely the overall evaluation of individual student solutions in percentages and the maximum possible number of points for individual tasks of the achievement test. We processed the obtained data so that the final evaluation of one student represented the arithmetic mean of evaluations from all evaluators (university students). As an indicator of the divergence of university students' evaluation, we chose the standard deviation. The standard deviation indicates the range of values in which most of the obtained data lie. The lower interval limit of values is obtained by subtracting the standard deviation from the mean and the upper interval limit by adding the standard deviation to the mean.

From the obtained interval limits, we found that most of the evaluations of students by university students lie in intervals with a width of approximately 8.40 to 30.00 percentage points. However, it is necessary to distinguish at what value the width of the interval is inappropriate and thus the evaluation does not meet the condition of objectivity. Based on the percentage points obtained, students in most schools are usually placed in evaluation classes, ie they get a grade from 1 to 5. Grading scales are set by schools differently and are usually available on the school website or in the school rules. After comparing the limits of the evaluation intervals for individual students obtained in our survey with the classification scales from three Bratislava gymnasiums, we found that some of the student's evaluations exceed two to three classification levels. The largest standard deviation of evaluation by university student cause the difference in grades from grade 2 to grade 3, or from grade 2 to grade 5, depending on the particular gymnasium. In the case of just one student, the evaluation by university students is in the range of one classification level at all three selected grammar schools, namely at grade 1.

Based on the above facts, we can state that the evaluation of student's achievement in the achievement test by university students is quite different, divergent, and therefore we do not reject hypothesis H1.

To verify the H2 hypothesis, we decided to statistically compare sets of different data. A more detailed description of the created mark scheme for the survey test and more information about survey data is given in the work of Čevajka [5]. We evaluated the achievement of students in the achievement test according to the proposed mark scheme. We statistically

compared this data set with the means we obtained from the evaluation by university students. We also compared the evaluation according to the proposed mark scheme with the evaluation of each evaluator (students of physics teaching). We processed the data in statistical program R. To compare the data, we chose Wilcoxon paired test for data that do not come from normal distribution. The null hypothesis to hypothesis H2 is:

H02: Arithmetic mean of evaluations by university students for individual students will be comparable with the evaluation according to the proposed scheme.

We verified the null hypothesis using the Wilcoxon test. The resulting p value was 1.953×10^{-3} . Since p value is less than 0.05, we reject the null hypothesis and do not consider the data to be comparable.

We also statistically compared the evaluation of students' achievement by individual evaluators (university students) with the evaluation according to the mark scheme. We proceeded in the same way as in the previous comparison and determined the second null hypothesis H02 for hypothesis H2 as follows:

H02a: The evaluation of students' achievement by individual university student will be comparable to the evaluation according to the proposed mark scheme.

From the results of statistical research, we found that we do not reject the null hypothesis in nine cases and reject it in seven cases. This means that the evaluation of the nine evaluators was comparable to the evaluation according proposed mark scheme and the evaluation of the seven evaluators was not comparable to evaluation according the proposed evaluation mark scheme. However, from the results of the statistical research we do not reject the H2 hypothesis, even though most of the evaluations of university students are comparable to the evaluations according to the proposed mark scheme. Student evaluations were so divergent that the data obtained as mean of student evaluations for individual students were not comparable to the evaluation according to the proposed scheme. For this fact, we decided not to reject hypothesis H2.

CONCLUSION

The results of the survey confirm the mentioned facts about the complexity of the evaluation process. Several factors enter the evaluation process, from the concept of the educational process and its goals to the teacher's personality. As the first factor of divergence in the evaluation of students' score, we see in the considerable predominance of open tasks in the proposed achievement test. According to Lapitková [6], the use of open tasks decreases the objectivity of the test, and thus also the objectivity of the evaluation. Chráska [7] also states that the disadvantage of open tasks is in the non-objectivity of their evaluation. However, it states that it is possible to set up an evaluation structure so that these tasks can be evaluated almost objectively. We believe that no divergence would be in the evaluation of achievement tests by university students if they had the mark scheme we proposed.

After evaluating the tests by university students, we

had a discussion with these students, in which they had to describe the difficulties associated with the task of evaluation. These problems related to the evaluation of open tasks and the lack of evaluation structure. These problems arose in determining the criteria for evaluating individual test tasks. The evaluation criteria say what the task is to test, i.e. they are related to the validity of the evaluation. The evaluation criteria result from the objectives of the teaching process itself, and thus the test tasks are intended to test the skills, competences and knowledge that have been developed through teaching. We therefore believe that in this case, the lack of university students' experience in the process of evaluating, which they will gain through practice, has manifested itself. We believe that the evaluation process is also influenced by the teacher's personality and current mood. Although these factors should not be part of the evaluation of student achievement, but university students described them in the discussion as factors influencing their evaluation. For a specific test, there were differences in the evaluation of the same solution by several classification levels.

The problem of evaluating test tasks could be eliminated if teachers had access to test tasks that have undergone standardization, their aim for assessment and the structure and method of assessment were clear.

Berová [8] states that in 2014, a total of 14 500 tasks from various subjects were created in the project of NUCEM, of which 660 are created for teaching physics and science. However, the resulting tasks have not been implemented in the teaching process and teachers in practice do not have access to these tasks. However, the tasks created in the project, together with the methodology of their evaluation, could offer teachers standardized, objective and valid tools for evaluation.

ACKNOWLEDGMENT: This paper was elaborated with the support of the projects VEGA no. 1/0396/18 Aspects of Critical Thinking Development in Science Education.

REFERENCES

1. G. Petty: Moderní vyučování (Portál s.r.o., Praha - 2008).
2. R. Arends: Learning to Teach (McGraw-Hill, Inc., USA - 1991).
3. R. Jedlička. et. al.: Pedagogická psychologie pro učitele (Grada Publishing, a.s., Praha - 2018).
4. R. Orosová, et. al.: Hodnotenie v prírodovedných predmetoch v podmienkach slovenského školstva, (2019).
5. J. Čevajka: Klasifikácia výkonu žiaka v didaktickom teste (Rigorózná práca, Bratislava – 2020).
6. V. Lapitková, et. al.: Hodnotenie žiackych výkonov v reformovaných prírodovedných programoch základnej školy (Vydavateľstvo Michala Vašečka, Prešov - 2011).
7. M. Chráska: Metody pedagogického výzkumu (Grada Publishing, a.s., Praha - 2016).
8. M. Berová: Tvorba úloh a testov z prírodovednej gramotnosti (2014).

SOLID-STATE ^1H NMR STUDY OF CORNSTARCH PLASTICIZED WITH UREA AND GLYCEROL DURING AGEING

N. Šmidová, natalia.smidova@tuke.sk, M. Kovaľáková, maria.kovalakova@tuke.sk, V. Hronský, viktor.hronsky@tuke.sk, Department of Physics, Faculty of Electrical Engineering and Informatics, Technical University of Košice, Park Komenského 2, 042 00 Košice, Slovakia

INTRODUCTION

There has been a growing interest in utilization of starch-based materials in non-food applications which have been reviewed recently [1, 2]. Especially, thermoplastic starch (TPS) often attracts attention as low cost bioplastics although TPS brittleness which can be even increased due to free volume relaxation (physical ageing) and/or retrogradation during material storage. This impedes its wide use.

Two structural forms of α -D glucose units, amylose and amylopectin, are the main constituents of native starch which occurs in semi-crystalline form in nature. To obtain a moldable TPS material, native starch is processed at high temperature under shear stress with addition of plasticizers such as low molecular weight polyols (e.g. glycerol) and/or amide-containing molecules (e.g. urea, formamide). During this process called plasticization, native starch crystallinity is usually completely destructed and hydrogen bonds between hydroxyl groups of starch chains are replaced by hydrogen bonds between plasticizers and starch whereby urea forms stronger and more stable bonds with starch than glycerol [3].

Starch-based materials structure is sensitive to ageing and time dependent changes in their structure are of great importance for their use as bioplastics. When TPS is stored above its glass transition temperature (T_g), it is prone to retrogradation, i.e. starch chains recrystallize when sufficient amount of water is available. In contrast, physical ageing can also occur at temperatures below T_g and it is accompanied by a local rearrangement of starch chains to a lower volume and energy configuration without the change in crystallinity. TPS plasticized with glycerol, a conventional plasticizer, was shown to retrograde which results in TPS embrittlement [4] while urea prevents starch retrogradation [5]. However, urea is a solid and it does not add much flexibility to plasticized starch. Therefore, a combination of both above-mentioned plasticizers could suppress the TPS retrogradation and makes TPS flexible.

Solid-state magic-angle spinning (MAS) ^1H NMR technique was used to characterize molecular mobility and hydrogen bonds interactions in starch plasticized with glycerol and urea during one-year storage in this study for better understanding of ageing of such systems.

EXPERIMENTAL

Native cornstarch Meritena[®] 100, Brenntag, Slovakia was used for preparation of TPS. Suspension of starch, urea, glycerol and water at weight ratio of 1:0.35:0.35:2.3 was stirred at 70°C and then dried at

100°C for 5 hours. The plasticized material was then kneaded in a laboratory mixer Plastograph Brabender PLE 331 for 10 min at 130°C and 100 rpm. One-millimeter-thick slab was prepared by compression moulding at 130°C under a pressure of 100 kPa and then was stored in a plastic bag at 22°C. The sample was prepared at the Polymer Institute of the Slovak Academy of Sciences, Bratislava.

MAS ^1H NMR measurements were performed on a Varian solid-state NMR spectrometer (VNMRS 400, Palo Alto, CA, USA) working at the ^1H resonance frequency of 400 MHz. Duration of ^1H $\pi/2$ pulse was 2.9 μs . A recycle delay of 10 s and acquisition times of 20 - 80 ms were applied. A probe-head equipped with 4 mm rotor spinning at 10 kHz was used for measurements. The chemical shifts were referenced to tetramethylsilane using adamantane as an external standard. The NMR spectra were analyzed using Mestrelab Research Mnova 9.0 software.

RESULTS AND DISCUSSION

MAS ^1H NMR spectra of the TPS sample were measured several times throughout one year and are shown in Fig. 1. Signals observed at ~ 5.8 ppm, 5.3 ppm, 4.7 ppm and 3.8 ppm are related to relatively mobile hydrogen nuclei of urea (U), glycerol OH groups (G(OH)), water (W) and glycerol CH/CH₂ groups (G(CH)), respectively [6]. Starch hydrogen nuclei contribute only to broad background due to strong dipolar interactions in starch chains which are much less mobile than molecules of plasticizers and water.

During plasticization, hydrogen bonds between hydroxyl groups in starch are disrupted and new H-bonds with molecules of plasticizers are formed. In the spectrum measured one day after sample preparation, G(OH) and W signals are not resolved indicating interactions with starch. In contrary, U signal is well resolved in this spectrum, meaning that hydrogen nuclei of urea are mobile and thus they are probably not involved in H-bonds with starch. However, it is well known that urea forms stronger H-bonds with starch than glycerol whereby the bond involves either hydroxyl oxygen in starch and amino hydrogen in urea or carbonyl oxygen in urea and hydroxyl hydrogen in starch [3]. In our case when the amount of urea is relatively large we propose that H-bond is formed between carbonyl oxygen in urea and hydroxyl hydrogen in starch. In other words, during plasticization urea reacted with starch preferentially through carbonyl oxygen prior to glycerol which could then form H-bonds with free O in the OH starch groups. When all H-bonding sites in starch became occupied the excess of urea and glycerol was solvated glycerol-urea-starch complex.

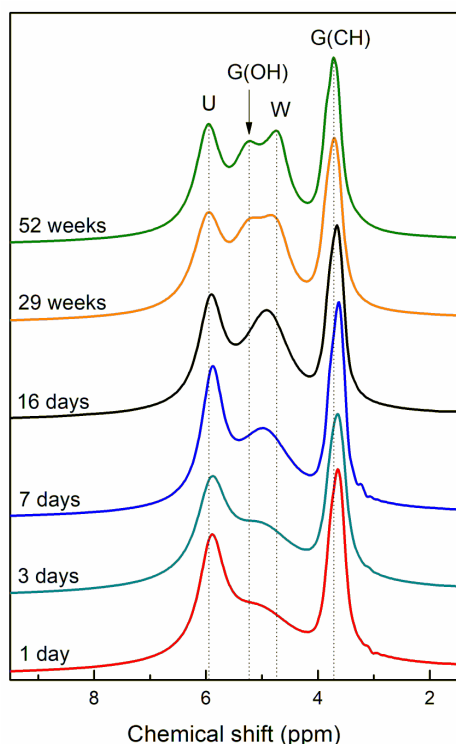


Fig. 1. MAS ^1H NMR spectra of the TPS sample aged as indicated. Chemical shifts of hydrogen nuclei related to urea (U), glycerol (G(OH), G(CH)) and water (W) are depicted

During ageing of the sample, G(OH) and W signals significantly narrowed (Fig. 1) in contrast with U and G(CH) signals. To detect changes in signals width and intensity, spectra of the sample aged 1 day and 52 weeks were deconvoluted. They were resolved in four lines with a Lorentzian profile; these are associated with U, G(OH), W and G(CH) signals; and one broad line with a Gaussian profile related to starch hydrogens and probably also firmly bound water molecules trapped within starch structure. The ratio of intensity of G(OH) signal to G(CH) signal was kept 0.6 which is the value drawn from glycerol molecular structure. Similarly, the intensity ratio of U signal to G(OH) and G(CH) signals was close to 1.3 in agreement with theoretical value calculated for the same weight amount of urea and glycerol in the sample. The intensity of the signals related to urea respectively glycerol did not change in spectral deconvolutions after 52 weeks since both urea and glycerol are non-volatile plasticizers. On the other hand, intensity of water signal slightly increased due to absorption of water from air during sample storage. Widths of the signals related to respective hydrogen nuclei gained from deconvolutions are shown in Fig. 2.

G(CH) signal is the narrowest (~ 120 Hz) compared to other signals because hydrogens in CH and CH_2 glycerol groups do not form H-bonds and thus are more mobile than other hydrogens. This signal is not affected by ageing of the sample. Neither width of U signal changed after 52 weeks; it was ~ 240 Hz, which means that urea formed stable bonds with starch involving carbonyl oxygen. By contrast, widths of G(OH) and W signals decreased to approximately half to a similar

value of 240 Hz. This could be explained by breaking of glycerol-starch H-bonds during sample ageing which were probably replaced by stronger urea-starch hydrogen bonds. As a consequence, more mobile glycerol molecules along with water molecules could form glycerol-rich domains with new network of hydrogen bonds between glycerol and/or water molecules.

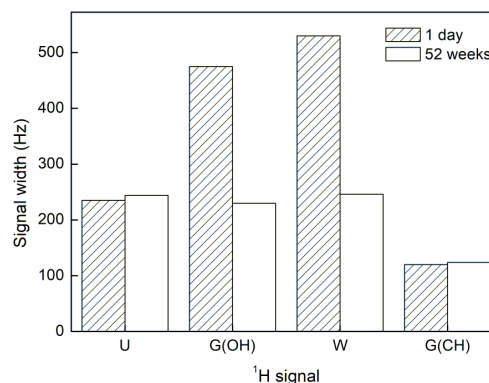


Fig. 2. Widths of the signals related to hydrogen nuclei in urea (U), glycerol (G(OH), G(CH)) and water (W) determined from deconvolution of MAS ^1H NMR spectra

CONCLUSIONS

MAS ^1H NMR spectra showed that in our TPS sample urea-starch hydrogen bonds established during plasticization preferentially involve carbonyl oxygen in urea and the bonds are stable throughout sample ageing. Phase separation of glycerol, i.e. formation of glycerol-rich domains took place in the sample after 29 weeks of storage resulting from disruption of glycerol-starch hydrogen bonds. This process was accompanied by slight water content increase causing higher mobility of glycerol molecules. Retrogradation of the sample did not occur as was found through XRD measurements (not shown) and thus, urea effectively prevented starch recrystallization.

ACKNOWLEDGMENT: This work was financially supported by the Slovak Grant Agency through the project VEGA No. 1/0570/17.

REFERENCES

1. M. A. Villar, S. E. Barbosa, M. A. García, L. A. Castillo, O. V. López: *Starch-Based Materials in Food Packaging: Processing, Characterization and Applications* (Academic Press, 2017).
2. H. Li, Y. Qi, Y. Zhao, J. Chi, S. Cheng, *Prog. Org. Coat.* **135**, 213 (2019).
3. X. Ma, J. Yu, J. Feng, *Polym. Int.* **53**, 1780 (2004).
4. J. J. G. van Soest, J. F. G. Vliegenthart, *Trends Biotechnol.* **15**, 208 (1997).
5. R. L. Shogren, C. L. Swanson, A. R. Thompson, *Starch/Stärke* **44**, 335 (1992).
6. A. Šoltýs, V. Hronský, N. Šmídová, D. Olčák, F. Ivanič, I. Chodák, *Eur. Polym. J.* **117**, 19 (2019).

VIDEO ANALYSIS IN STEM EDUCATION

P. Hockicko, peter.hockicko@feit.uniza.sk, G. Tarjányiová, gabriela.tarjanyiova@feit.uniza.sk, J. Kúdelčík, jozef.kudelcik@feit.uniza.sk Faculty of Electrical Engineering and Information Technology, University of Zilina, Univerzitná 1, Žilina, Slovakia

INTRODUCTION

STEM education focused on Science, Technology, Engineering and Mathematics includes the training of the university-educated students of a technical university who acquired skills in all the mentioned areas during the training. According to Bloom's taxonomy of cognitive goals, such education is realized at higher levels, such as analysis, application and evaluation. Video analysis, as one of the methods of teaching/learning, allows to develop mathematical skills in physical education and then prepare students with technical background for future engineering practice. The presented paper informs about the possibilities of using video analysis in teaching physics in engineering education. Using this method in teaching/learning process can improve students' understanding of the concept of force, the application of Newton's laws of motion, which was confirmed according to the results obtained from FCI (Force Concept Inventory) test [1-3].

VIDEO ANALYSIS

Nowadays, there are many programs and simulations to solve various real physical problems. Program Tracker [4] is free video analysis and modelling tool build on the Open Source Physics (OSP) Java framework. Video analysis using program Tracker in the educational process introduces a new creative method of teaching physics, makes natural sciences more interesting for the students [5]. Exploring the laws of nature in this way can be amazing for the students because this educational software is illustrative, interactive, inspires them to think creatively, improves their performance and it can help in studying physics. With the help of a high-speed camera (for the preparation of motion files - video experiments) and the program Tracker the students can study certain motion in detail. The video analysis gives the students simple and easy way to understand the process of movement. The program Tracker seems to be a useful modeling tool, too. The computer modeling enables the students to relate the results of measurements to theory, showing relations between the graphs obtained using a model and a measurement. A post-instruction assessment of the students' ability to interpret kinematics graphs indicated that groups which used video analysis tools, generally performed better than students taught via traditional instruction [6]. It has been confirmed that the competencies of the students have been more developed, and their knowledge has been more increased through working with program Tracker as opposed to groups taught by traditional methods [7 - 10]. Video analysis and modeling help the students to understand the natural sciences principles and natural phenomena more deeply, develop skills of abstraction and projection, awake

curiosity towards nature and the surrounding world and make physics a lot more fun.

All we need for a video analysis is a camera (mobile phone, tablet) to prepare motion files - video experiments. With the help of a high-speed camera and the program Tracker students can study certain motion in detail. They can observe various characteristics of the motion and learn the basics of classical physics while having fun. Video analysis gives students a simple and easy way to understand the process of movement.

A Casio Exilim EX-FH25 camera was used for preparing the video files. That camera allowed us to record videos with 30, 120, 240, 420 and 1000 frames per second (fps).

The main task of a video analysis is to build right conception of the natural phenomena and in the next step to use them for physical analysis. All we need is:

- a final video in the following formats: avi, mov, mpg
- to know the video's number of frames per second (fps) (for calculation of Δt)
- real dimensions in the video, for example 1 meter

By means of the Tracker students can detect the relationship between physical quantities and describe a motion using time dependencies. The Tracker offers time dependencies of 24 physical quantities (and/or we can define other) and data processing by means of graphs and tables. From the number of frames per second (30 fps or 120 fps usually) the time is deduced ($\Delta t = 0.033$ s or $\Delta t = 0.0083$ s) while the position can be measured in two dimensions (x, y) using a calibrated video image. The autotracking function in this program allows accurate tracking without a mouse.

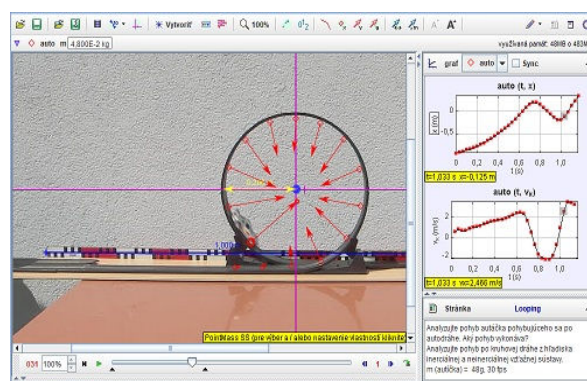


Fig. 1. Analysis of rotation motion according to the centre of the coordinate system

Using this interactive program Tracker, we can explain the solution of the problem from the point of view of the inertial and non-inertial reference system (Fig. 1). Program Tracker offers two types of models: analytic and dynamic. The analytic one defines position functions of time, while the dynamic one defines force functions and initial conditions for numerical solvers.

RESULTS FROM FCI TEST

The program Tracker was actively used during lecture from Physics at the Faculty of Operation and Economics of Transport and Communications (Air transport department) in the last academic year 2019/20 (full time Master's degree level, study program: Technology of Aircraft Maintenance, course ID: 13P168, Physics). The subject Physics consists of 3 - 3 - 0 (lectures - exercises - labs) lessons per week, presence study. The semester consists of 13 weeks. The lectures were conducted in an interactive way aimed at clarity - using real-life videos related to the topic. All videos were analysed with the program Tracker (using VAS method [9, 10]). We used Force Concept Inventory (FCI) test to verify students' knowledge of physics (kinematics and dynamics) [11]. It contained 30 qualitative multiple choices tasks that focused on conceptual understanding of Newtonian mechanics.

The pre-test was carried out at the beginning of the semester during the first week, post-test was carried out at the end of the semester and it was attended by 26 students who participated in the both pre- and post-test.

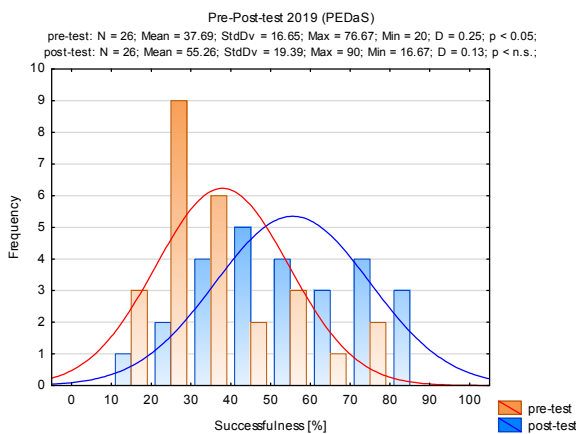


Fig. 2. FCI score of pre- and post-test

TAB. 1. t-Test: Paired Two Sample for Means.

	Pre-test	Post-test
Mean	37.69	55.26
Variance	277.13	376.15
Observations	26	26
Pearson Correlation	0.62	
df	25	
t Stat	-5.64	
P(T<=t) one-tail	3.58E-06	
t Critical one-tail	1.71	
P(T<=t) two-tail	7.17E-06	
t Critical two-tail	2.06	

Results presented in Fig. 2 and Tab. 1 indicate that there is a statistical difference in the mean of post-test and pre-test FCI score at the end and beginning of the semester.

DISCUSSION

As the authors claim it is necessary to point out that 60 % of FCI test, for empirical reasons, is minimal threshold so that a student could continue in understanding Newtonian mechanics effectively. Below this threshold, a student's grasp of Newtonian concepts is insufficient for effective problem solving. Otherwise a student is not able to overcome difficulties which caused him/her misconception and thus he/she learns physics by heart. 80 – 85 % FCI score represents the mastery level when a student thinks in terms of intentions and Newtonian physics [11, 12].

CONCLUSIONS

The use of interactive methods in teaching physics has significantly influenced the level of students' knowledge. Our results confirmed that there is the statistical difference in the mean of post-test and pre-test FCI score at the end and beginning of the semester. Watching real physics concept videos and their subsequent video analysis had a positive impact on the growth of knowledge and improving of conception of Newtonian mechanics at the end of the semester.

ACKNOWLEDGMENT: This work was supported by the Slovak Grant Agency KEGA through the project No. 029ŽU-4/2018. We like to thank David Koch from Arizona State University for providing the FCI test.

REFERENCES

1. M. Pinxten, et al, Proceedings of the 45th SEFI Annual Conference 2017, Portugal, 389 (2017).
2. P. Hockicko, G. Tarjányiová, Proceedings of 11th International Conference ELEKTRO 2016: Slovakia, (2016), IEEE Catalog Number: CFP1648S-DVD, 2016.
3. M. Pinxten, et al, 44th Annual Conference of the European Society for Engineering Education - Engineering Education on Top of the World: Industry-University Cooperation, SEFI 2016 (2016).
4. Program Tracker: <https://physlets.org/tracker/>
5. D. Brown, A. Cox, The Physics Teacher **47**, 145 (2009).
6. R.J. Beichner, American Journal of Physics **64**, 1272 (1996).
7. P. Hockicko, Proceedings of the 40th SEFI Annual Conference Engineering Education 2020: Meet the Future, 2012, Thessaloniki, Greece, (2012).
8. J. Ondruš, P. Hockicko, Transport and Telecommunication **16**, 127 (2015).
9. P. Hockicko, L. Krišťák, M. Němec, European Journal of Engineering Education **40**, 145 (2015).
10. P. Hockicko, B. Trpišová, J. Ondruš, Journal of Science Education and Technology **23**, 763 (2014).
11. D. Hestenes, M. Wells, G. Swackhamer, The Physics Teacher **30**, 141 (1992).
12. A. Savinainen, P. Scott, Physics Education **37**, 53 (2002).

COLLECTION OF SOLVED PHYSICS PROBLEMS AND COLLECTION OF PHYSICS EXPERIMENTS

M. Snětínová, marie.snetinova@mff.cuni.cz, P. Káčovský, petr.kacovsky@mff.cuni.cz, Z. Koupilová, zdenka.koupilova@mff.cuni.cz, D. Mandíková, dana.mandikova@mff.cuni.cz, Department of Physics Education, Faculty of Mathematics and Physics, Charles University, Prague, Czech republic

INTRODUCTION

Solving physics problems is one of the key abilities which students should reach during their physics education. To reach this goal it is necessary to invest quite a lot of time to train this skill during lessons. Moreover it is very hard to train problem solving without the help of a tutor or without specially designed materials. The lack of suitable materials was the starting impulse for creating a Collection of Solved Problems specially aimed to develop problem-solving skills fourteen years ago.

The second Collection, the Collection of Physics Experiments, currently contains more than 160 published detailed experimental instructions. These are intended as inspiration for teachers, especially at the primary and secondary school level. Experimental descriptions contain methodological and technical notes, sample results or short video sequences of the given experiments. Both Collections are interconnected and have their English versions.

COLLECTION OF SOLVED PROBLEMS

As it was written above, the structure of problem solutions is specially designed to substitute tutor's help during lesson, to show readers how to think about the problems and encourage students to solve at least some parts of a problem independently. There are various hints, notes with laws and formulas, plots and other tools supporting students' effort before detailed solution. To fulfil our intention, we have developed our own web interface for these problems that does not show the entire solution at first (see Fig. 1). [1]

Nowadays the database contains more than 900 fully solved physics problems in Czech, more than 100 problems in Polish and nearly 300 problems in English (see Tab. 1). Further problems are still being translated. Problems are arranged according to the topic they are dealing with. The level of problems is from lower secondary school to university. Readers can filter problems not only according to their topics and levels, but also according to special ways the problems are solved (graphically, qualitatively, ...) or according to specific cognitive functions that are developed by the problems.

TAB. 1. Numbers of problems and experiments in topics

	Problems		Experiments	
	Czech	Eng.	Czech	Eng.
Mechanics	235	96	7	
Electromagnetism	280	90	51	12
Thermodynamics	152	74	73	37
Optics	67	18	29	5
Others	170		6	

Fig. 1. Example of the task *Current-carrying wire in a magnetic field* (code 287)

Apart from physics problems, there are two Collections of math problems, both on university level.

PROBLEMS FROM PISA RESEARCH

In the last two years, problems released from the international PISA research have become part of the Collection of Solved Problems. The problems used in PISA tests differ in their structure and focus from the problems commonly used in our schools. They are more complex and based on real situations; the assignment consists of extensive text, graph, picture or other written material to which the questions relate. The problems are supplemented not only with solutions, but also with additional comments to match the style of the Collection.

We want to make PISA problems accessible to a wider number of teachers and students in this way. Nowadays, 10 classic PISA problems have been published and 2 new problems with interactive elements (from PISA 2015) are prepared.

INTERACTIVE COMPONENTS OF PROBLEMS

We use the fact that the Collection is exclusively electronic and in recent years, we prepared interactive elements created in GeoGebra or Wolfram Mathematica (as CDF modules) for a still-increasing number of problems. These elements serve various purposes, e.g. they help to create a correct geometric idea of the problem; they simulate a mental process solving the problem; they graphically show the solution for other

values than those specified etc. (see Fig. 2). If it is suitable, an interactive element is accompanied by questions or tasks, so that the readers can not only freely “play” with the interactive element, but also work purposefully and deepen their understanding of the issue.

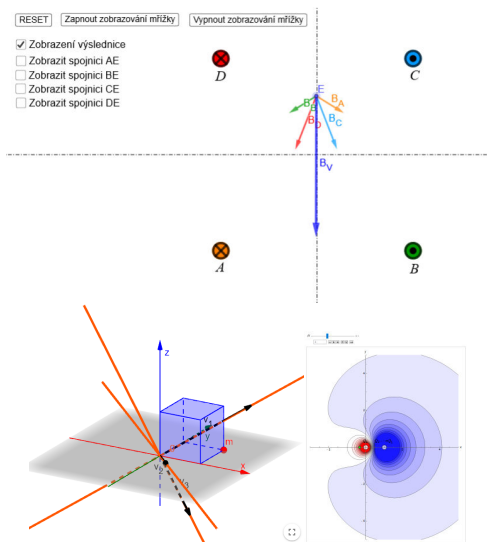


Fig. 2. Three examples of interactive problems' components

COLLECTION OF PHYSICS EXPERIMENTS

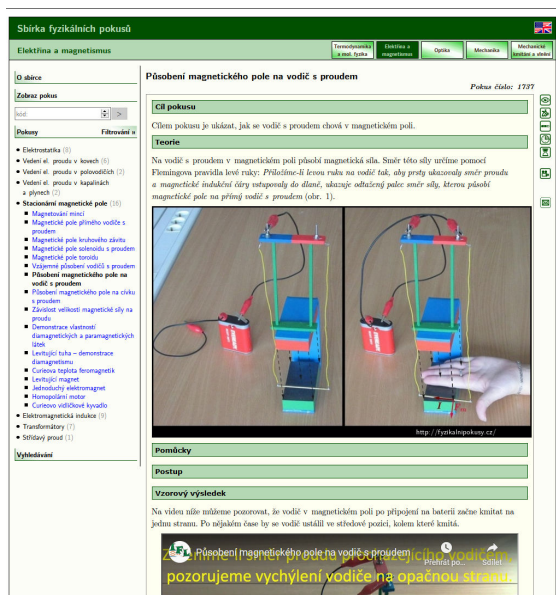


Fig. 3. Example of experiment description *Wire in magnetic field* (code 1737); supplementing problem code 287 in fig. 1

In 2015 the Collection of Physics Experiments was created using the same interface and database. The purpose of this collection is to be an inspiration for teachers, especially at the primary and secondary school level. The description of experiments is written in great detail, supplemented by technical and methodological notes, photos and video sequences capturing the exemplary performance (Fig 3) [2]. The use of the same web interface allows easy connection of problems and

experiments with the same topic. Nowadays, the Collection contains more than 160 experiments; about 50 of them translated also into English (Tab. 1).

ATTENDANCE

We monitor access to the Collections using Google Analytics tools. On school days, the Czech part of the Collection of Solved Problems shows almost a thousand unique approaches per day and the Czech part of the Collection of Physics Experiments over 200 accesses per day. In the year-on-year comparison, the number of approaches has a steady or slightly increasing trend.

Fig. 4 shows the daily number of accesses for the last 16 months that copy the school days. Furthermore, it is evident that during the period of distance learning at all types of schools in the Czech Republic in the period March-June 2020, the number of accesses to both Collections more than doubled.

Both Collections have a similar rate of immediate abandonment (approximately 85 %), an average number of pages viewed per access (1.5) and a connection length (1 minute), but also a rate of return of around 20 %. From all the indicators, we conclude that the Collections are a material widely used by students and teachers.



Fig. 4. Time development of daily unique hits to Czech parts of both Collections (March 2019 – August 2020)

ACKNOWLEDGMENT: The development of the Collections has been financially supported by the IRP of the Ministry of Education, Youth and Sports.

REFERENCES

1. Z. Koupilová et al., Eur. J. Phys. **38**, 055801 (2017)
2. Z. Koupilová, P. Káčovský: In Selected Papers from the 20th International Conference on Multimedia in Physics Teaching and Learning (European Physical Society, Munich – 2016).

PARTICIPATION OF CZECHOSLOVAKIA IN THE ESTABLISHMENT OF THE JOINT INSTITUTE OF NUCLEAR RESEARCH (DUBNA, RUSSIA)

E. Těšínská, tesinska@cesnet.cz, Czech Academy of Sciences, Institute of Contemporary History, Prague

INTRODUCTION

Former Czechoslovakia became one of eleven signatory countries of the Convention on the Establishment of the Joint Institute of Nuclear Research (JINR, Dubna, Russia) in March 1956. Václav Votruba (1909–1990), the theoretical physicist from Czechoslovakia, was elected one of first two Vice-Directors of JINR. Based on primary archive sources a brief history of these events is described.

SOVIET PROPOSAL FOR THE ESTABLISHMENT OF AN EAST INSTITUTE OF NUCLEAR RESEARCH

Czechoslovakia was invited to participate in the establishment of an East Institute of Nuclear Research, intended as a parallel to the Laboratory of the European Organization for Nuclear Research (CERN, Meyrin, Switzerland), by a “commemorative note” of 18 January 1956 sent by N. S. Khrushchev (First Secretary of the Central Committee of the Soviet Communist Party) to A. Novotný (First Secretary of the Central Committee of the Czechoslovak Communist Party).

The Soviet invitation was a response to the question about participation of East European countries in CERN, which had been mentioned during the First International Conference on Peaceful Use of Atomic Energy held in Geneva in August 1955.

CZECHOSLOVAK GOVERNMENTAL DELEGATION TO THE CONFERENCE ON THE INSTITUTE IN MOSCOW

The commemorative note constituted a proposal to establish an East Institute of Nuclear Research in the USSR, based on facilities and staff of two already existing institutes of the Soviet Academy of Sciences in the Moscow region, namely the Institute for Nuclear Problems, which operated a 580 MeV synchrocyclotron and the Electro-Physical Laboratory with a 10 GeV proton synchrotron under construction.

Czechoslovak party and governmental bodies agreed and accepted the Soviet invitation. An official delegation was nominated to take a part at an upcoming conference on the Institute in Moscow: its members were F. Vlasák (Minister of Energetic, head of the delegation), J. Baier (acting Vice-President of the Czechoslovak Governmental Committee on Research and Peaceful Use of Atomic Energy), Č. Šimáně (Director of the Nuclear Physics Institute, NIP), V. Petržílka (Corresponding Member of the Czechoslovak Academy of Sciences, Professor and Dean of the Faculty of Technical and Nuclear Physics of Charles University), F. Kovář (Counsellor for nuclear energy issues at the Czechoslovak Embassy in Moscow)

and experts: L. Trlifaj (Head of the Theoretical Department of NIP), J. Váňa and M. Seidl (Director of the Research Institute of Vacuum Electro-Engineering and Head of the Institute’s Accelerator Department respectively).

The delegation was authorised to put forth a proposal at the conference that a proton accelerator with the capacity of at least 50 GeV and an electron accelerator of several GeV are built in the Institute to become its new powerful experimental devices. The proposal was not submitted as the Soviet delegation had presented a project of the Institute’s development for the next 3 - 4 years, which included construction of a nuclear reactor of high neutron flux and an ion accelerator for energy higher than 6 - 7 MeV/nucleon.

COURSE OF THE MOSCOW CONFERENCE

The conference on the East Institute of Nuclear Research took place in Moscow on 20 – 26 March 1956 with the participation of governmental delegations of eleven East-block countries (Albania, Bulgaria, People’s Republic of China, Czechoslovakia, GDR, Democratic People’s Republic of Korea, Hungary, Mongolia, Poland, Rumania and USSR).

At the first session on 20 March the Soviet proposals were presented by D. I. Blokhintsev (on the location of the Institute and construction of its new experimental facilities), S. K. Tzarapkin (on principles of the Institute financing) and A. V. Topchiev (on the organization and administration of the Institute). Discussion about the Soviet proposals followed in next sessions. On 21 March an excursion was organized to the Institute of Nuclear Problems and the Electro-Physical Laboratory of AS USSR in Moscow region (future town of Dubna).

J. Baier spoke in the discussion on behalf of the Czechoslovak delegation on 22 March. He called the establishment of the Institute another step of the Soviet aid provided to people’s democratic countries in the field of research and peaceful use of the nuclear energy. He welcomed that not only high energy physics but also applied physics would be developed in the Institute, including research into materials for nuclear reactors. He supported the opinion pronounced in the discussion that the Institute should work (and coordinate cooperation of its member states) also in the field of cosmic rays. As to the Czechoslovak participation in the Institute he stated: „*The contribution of Czechoslovakia in the field of nuclear physics will not be big in the beginning of the Institute. Yet, there are some rather good theoretical physicists in Czechoslovakia. In addition, Czechoslovak engineers, who have already proved their capacities in related fields and in construction of accelerators, might also be helpful. Czechoslovak engineering industry, for which manufacturing of nuclear engineering is one of*

the fundamental perspective tasks and which has good preconditions for manufacturing electrical equipment and nuclear physics and technique instruments, might also be of help."

SIGNATURE OF THE CONVENTION AND ELECTION OF THE FIRST DIRECTORATE

F. Vlasák, authorized by the Czechoslovak Government for this, signed the Convention on the Establishment of the East Institute of Nuclear Research at the closing session of the Moscow conference on 26 March 1956. Consequently, the first Directorate of the Institute was elected: Director D. I. Blokhintsev (USSR) and two Vice-Directors M. Danysz (Poland) and V. Votruba (Czechoslovakia). The Directorate was assigned the task to work out the draft statutes of the Institute within three months. In an additional session on the same day the name of the Institute was changed to the Joined Institute of Nuclear Research (JINR), so that no antimony between the West and the East was incorporated.

NOMINATION AND ELECTION OF V. VOTRUBA VICE-DIRECTOR OF JINR

V. Votruba did not take part in the Moscow conference on JINR; he was on business in Bulgaria at that time. It was Soviet academician Topchiev who came with the idea to nominate a Czech scientist for the post of one Vice-Director of the Institute. After a quick consultation of this issue by telephone with V. Kopecký in Prague and V. Votruba in Sofia (Bulgaria), the Czechoslovak delegation nominated V. Votruba to the post.

In the world of theoretical physics Václav Votruba (1909–1990) had already been a renowned figure. He had published (both in Czech and in a foreign language) papers on theory of relativity, quantum electrodynamics and theory of elementary particles, e.g. on the problem of electron triplet, on a generalized theory of nucleons and mesons, on the decay of mesons μ (in co-authorship with Č. Muzikář), on a classification of elementary particles based on isotopic spin (with M. Lokajíček and Ch. J. Christov). He was Corresponding Member of the CSAS, Professor of Theoretical Physics at the Faculty of Technical and Nuclear Physics of ChU, in February 1956 he was awarded the academic research degree Doctor of Science.

TENURE OF THE OFFICE BY V. VOTRUBA

V. Votruba took up the post of Vice-Director of JINR on 1 September 1956. The term of office of first two Vice-Directors was two years and terminated in March 1958. Votruba did not want to run for the second time. His reasons were both professional and personal: there was an urgent need for a professor of theoretical physics at Charles University after the death of professors V. Trkal (in 1956) and Z. Matyáš (in 1957); he also could not imagine to stay in Dubna without his family. The Scientific Council of JINR, however, did

not prepare other nominations to the posts of Vice-Directors. So, by a resolution of the Committee of the Plenipotentiaries of the Governments of the JINR Member States, the term of office of both Vice-Directors was prolonged till March 1959.

In the position of the Vice-Director of JINR Votruba participated in a number of events, e.g. he took part (as an observer on behalf of JINR) in the First General Conference of the IAEA in Vienna in 1957, he was a member of the JINR delegation at the Seventh and the Eighth Annual International Conferences on High Energy Physics (in 1957 in Rochester, USA, and in 1958 organized by CERN in Geneva).

VISIT OF THE CZECHOSLOVAK PRESIDENT A. ZÁPOTOCKÝ IN JINR

On 28 January 1957 the Czechoslovak Governmental delegation headed by President of Czechoslovakia Antonín Zápotocký, which was on one-week official visit in the USSR, visited JINR in Dubna. V. Votruba together with Director D. I. Blokhintsev met the delegation and showed them round the campus of the Institute and its main experimental devices.

V. Votruba took the advantage of the personal encounter with President Zápotocký to remember him and repeat his plea for release from prison Czechoslovak physicist M. Lokajíček (1923–2019), Votruba's former research assistant. M. Lokajíček was arrested in February 1954 and sentenced to seven years of prison in June of that year for taking part in meetings of a catholic organization aimed to religious education of the youth.

V. Votruba requested an audience with President Zápotocký in the case of M. Lokajíček already by a letter of 10 January 1955. He wrote that Lokajíček was one of the most talented Czechoslovak young scientists in the field of nuclear physics and his elimination from professional work and international competition was bringing about considerable damage and loss to the Czechoslovak physics.

The requested audience was not granted to V. Votruba in 1955. Nevertheless, after the repeated request submitted during the meeting with A. Zápotocký in Moscow in January 1957, the judicial proceedings with M. Lokajíček were re-examined, and M. Lokajíček was released from prison in June of the same year.

FUTHER ENGAGEMENT OF V. VOTRUBA IN CZECHOSLOVAK COOPERATION WITH JINR

V. Votruba took part in Czechoslovak cooperation with JINR also in next years. In 1961–1963 he was a member of the Scientific Council of JINR. He also was a member of the Commission for Cooperation with JINR, which was set up in November 1962 as an auxiliary body of the Czechoslovak Plenipotentiary for JINR of that time academician and Vice-President of CSAS J. Kožešník.

REFERENCES

The outline is based on documents from archives in CR and from the Archive of JINR in Dubna.

CALDEIRA-LEGGET MODEL FOR PARTICLE-BATH SYSTEMS IN THE PRESENCE OF A MAGNETIC FIELD

V. Lisý, vladimir.lisy@tuke.sk, J. Tóthová, jana.tothova@tuke.sk, Department of Physics, Faculty of Electrical Engineering and Informatics, Technical University of Košice, P. Komenského 2, 04200 Košice, Slovakia

INTRODUCTION

The current interest of physicists to the problems of Brownian motion (BM) of charged particles in magnetic fields is mainly due to the necessity of taking into account the memory effects in the particle dynamics [1]. In all the papers published so far, the corresponding equations of motion for the Brownian particles (BP) are, however, just postulated. Moreover, the effect of the magnetic field on the particles that surround the BP is not considered. The present work represents an attempt towards the creation of the theory that takes into account also the influence of the external field on the motion of the particles of the medium in which the tagged BP is immersed. At this stage, we develop the approach presented in [2] and within a modified Caldeira-Leggett (CL) [3] particle-bath model treat the medium as a gas of particles, whose interaction with the BP expectedly affects the dynamics of the BP.

PARTICLE-BATH SYSTEMS IN THE PRESENCE OF A MAGNETIC FIELD

Consider a particle, linearly coupled with N oscillators, which are not coupled to each other. The system is placed in a magnetic field \mathbf{B} oriented parallel to the axis z . The bath oscillators with eigenfrequencies ω_i and masses m_i carry net charges q_i , and the charge of the BP of mass m is Q . The strength of coupling between the BP and the i th oscillator is c_i . The positions of the bath particles and the BP are $\mathbf{r}_i = (x_i, y_i, z_i)$ and $\mathbf{r} = (x, y, z)$, and momenta $\mathbf{p}_i = (p_{xi}, p_{yi}, p_{zi})$ and $\mathbf{p} = (p_x, p_y, p_z)$, respectively. In the frame of the CL model [3], the dynamics of the system is described by the coupled equations of motion with magnetic forces,

$$\dot{\mathbf{r}} = \frac{\mathbf{p}}{m}, \quad \dot{\mathbf{p}} = \sum_i m_i c_i \left(\mathbf{r}_i - \frac{c_i}{\omega_i^2} \mathbf{r} \right) + Q \dot{\mathbf{r}} \times \mathbf{B}, \quad (1)$$

$$\dot{\mathbf{r}}_i = \frac{\mathbf{p}_i}{m_i}, \quad \dot{\mathbf{p}}_i = -m_i \omega_i^2 \mathbf{r}_i + m_i c_i \mathbf{r} + q_i \dot{\mathbf{r}}_i \times \mathbf{B}. \quad (2)$$

The method of solution of these equations is described in detail in the Appendix of Ref. [4]. Along the axis z , the motion of the particles is not affected by the magnetic field. Along the x axis, the equation for the BP motion is

$$m \dot{v}_x(t) = QB v_y(t) - \int_0^t v_x(t') G(t-t') dt' + \int_0^t v_y(t') H(t-t') dt' + f_x(t). \quad (3)$$

The equation for $v_y(t)$ has the same form with x changed to y , Q to $-Q$, and H to $-H$. The zero-mean

projections of the random force $f_x(t)$ and $f_y(t)$ are determined by the initial positions and velocities of the particles in the system [4]. Equation (3) is of the form of generalized Langevin equation (GLE) [5] but with two memory functions, $G(t)$ and $H(t)$. Denoting $\Omega_i = q_i B / m_i$, $\gamma_i = (\Omega_i^2 + 4\omega_i^2)^{1/2}$ and $\gamma_i^\pm = \gamma_i \pm \Omega_i$, $G(t)$ is expressed as

$$G(t) = 2 \sum_{i=1}^N \frac{m_i c_i^2}{\gamma_i} \left[\frac{\cos(\gamma_i^+ t / 2)}{\gamma_i^+} + \frac{\cos(\gamma_i^- t / 2)}{\gamma_i^-} \right]. \quad (4)$$

$H(t)$ is obtained if in (4) the functions $\cos(\dots)$ are replaced by $\sin(\dots)$ and the second term is with sign $-$.

Equations (3) and (4) possess large possibilities for the predictions of the behavior of systems of charged particles in the magnetic field. Specific solutions for the correlation functions describing the random motion of the BPs (such as the velocity correlation function (VCF) $C_{v_\alpha v_\beta}(t) = \langle v_\alpha(t) v_\beta(t_0 + t) \rangle$) require knowledge of c_i and the distribution function for the frequencies $\{\omega_i\}$ for concrete systems. However, some results of a general character can be obtained just assuming that the system is conditioned to be stationary, without restricting it to be in thermal equilibrium. So, if Eq. (3) is multiplied by $v_x(0)$ and the conjugated equation for $v_y(t)$ by $v_y(0)$, and statistically averaged, one obtains equations for $C_{v_\alpha v_\alpha}(t)$ ($\alpha = x, y$), $C_{v_x v_y}(t) = \langle v_x(t) v_y(0) \rangle$ and $C_{v_y v_x}(t) = \langle v_y(t) v_x(0) \rangle$. With the use of $C_{v_\alpha v_\alpha}(0) = 0$, the causality principle (due to which $\langle v_\alpha(0) f_\alpha(t) \rangle = 0$ for $t > 0$) and equipartition, $C_{v_\alpha v_\alpha}(0) = k_B T / m$, the VCFs can be found. It is suitable to use the Laplace transform $\tilde{C}_{v_\alpha v_\alpha}(s) = \int_0^\infty C_{v_\alpha v_\alpha}(t) e^{-st} dt$. Then

$$\tilde{C}_{v_\alpha v_\alpha}(s) = k_B T \frac{ms + \tilde{G}(s)}{[ms + \tilde{G}(s)]^2 + [QB + \tilde{H}(s)]^2}. \quad (5)$$

The expression for $C_{v_x v_y}(t) = -C_{v_y v_x}(t)$ differs only by the numerator, which is $QB + \tilde{H}(s)$. These functions are related to all other relevant correlation functions, such as the positional autocorrelation function $C_{xx}(t) = \langle x(0)x(t) \rangle$, the mean square displacement (MSD) $X(t) = 2[C_{xx}(0) - C_{xx}(t)]$, or the time-dependent diffusion coefficient $D_x(t) = \dot{X}(t) / 2$ [6]. Analogous relations hold for the y -direction. Moreover, if we multiply Eq. (3) by $f_x(0) = m \dot{v}_x(0) - QB v_y(0)$ and the equation for $v_y(t)$ by $f_y(0) = m \dot{v}_y(0) + QB v_x(0)$ and average the results, the time correlation functions of the random forces $C_{f_\alpha f_\alpha}(t) = \langle f_\alpha(t) f_\alpha(0) \rangle$ can be expressed

through the already derived VCFs. Due to stationarity, we obtain the fluctuation-dissipation theorem [6]

$$C_{f_\alpha f_\alpha}(t) = k_B T G(t), \quad \alpha = x, y. \quad (6)$$

The important difference from Kubo's relation [6] is in the explicit dependence of the memory function on the external field. The role of the memory function is played only by $G(t)$. When there is no response of the bath, $\Omega_i = 0$, $H(t) = 0$, and Eqs. (3)-(5) coincide with the previously used equations for the BM of particles in a magnetic field with the memory function $G(t)$ [7].

EVALUATION OF MEMORY FUNCTIONS AND TIME CORRELATION FUNCTIONS

To calculate the memory functions, the VCFs, and other correlation functions that are necessary to describe the dynamics of concrete systems, one has to specify the strengths of coupling c_i and the distribution $h(\omega_i)$ of the oscillators' eigenfrequencies ω_i . For example, $h(\omega_i)$ can be considered as continuous, the sums in $G(t)$ and $H(t)$ replaced by an integral, $\sum_i f(\omega_i) \rightarrow \int f(\omega) h(\omega) d\omega$, and c_i taken to be constant. For simplicity, we suppose that the masses m_i are equal, $m_i = \mu$. Then, when the bath does not respond to the external field, $G(t)$ from (4) reads $G_0(t) \approx \mu c^2 \int_0^\infty d\omega h(\omega) \omega^{-2} \cos(\omega t)$. As an example, we consider the often used fractional memory function [8] $G_0(t) = \xi_\varepsilon \varepsilon t^{\varepsilon-1}$, where $t > 0$ and $1 > \varepsilon > 0$. The corresponding frequency distribution is

$$\frac{h(\omega)}{\omega^2} = g_\varepsilon \frac{\omega^{-\varepsilon}}{\mu c^2}, \quad g_\varepsilon = \frac{2\xi_\varepsilon}{\pi} \frac{\Gamma(1-\varepsilon/2)\Gamma(1+\varepsilon/2)}{\Gamma(1-\varepsilon)}, \quad (7)$$

where $\Gamma(x)$ is the gamma function. The equation for $G(t)$ is

$$G(t) = g_\varepsilon \int_0^\infty \omega^{-\varepsilon} \left\{ \cos[\gamma(\omega) \frac{t}{2}] \cos\left(\frac{\Omega t}{2}\right) + \frac{\Omega}{\gamma(\omega)} \sin[\gamma(\omega) \frac{t}{2}] \sin\left(\frac{\Omega t}{2}\right) \right\} d\omega \quad (8)$$

and $H(t)$ is given by a similar equation with $\cos(\Omega t / 2)$ replaced by $\sin(\Omega t / 2)$ and $\sin(\Omega t / 2)$ by $-\sin(\Omega t / 2)$. If $\Omega = 0$, it follows from these equations that $G(t) = G_0(t)$ and $H(t) = 0$. For $\Omega \neq 0$, the long-time asymptotes of $G(t)$ and $H(t)$ can be obtained noting that the main contributions to the integrals of the rapidly oscillating functions are given by small ω . At $\Omega t \gg 1$ this gives the decay $\sim t^{-(\varepsilon-1)/2}$. The numerical results for $G(t)$ (8) and $H(t)$ are illustrated in Fig. 1.

The time dependence of the VCF is $C_{v_\alpha v_\alpha}(t) \sim t^{-(3+\varepsilon)/2}$ and the MSD shows a sub-diffusive behavior $X(t) = Y(t) \approx 2D_\varepsilon t^{(1-\varepsilon)/2}$ with the "diffusion coefficient"

$$D_\varepsilon = \frac{\Gamma(1-\varepsilon)\Gamma[(3+\varepsilon)/4]\Gamma[(1-\varepsilon)/4]}{2\Gamma^3[(1+\varepsilon)/2]\Gamma^3[(1-\varepsilon)/2]} \frac{k_B T}{\xi_\varepsilon |\Omega|^{(1-\varepsilon)/2}}. \quad (9)$$

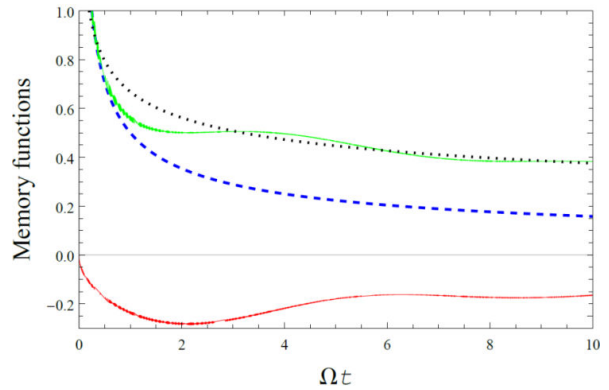


Fig. 1. Memory functions $G(t)$ (upper full line) and $H(t)$ (lower full line) for the fractional distribution of bath frequencies. The no-response function $G_0(t)$ (dashed line) and the long-time asymptote of $G(t)$ (dotted line) are also shown. All the functions are normalized to $\xi_\varepsilon \Omega^{1-\varepsilon}$ and calculated for $q > 0$ and $\varepsilon = 0.5$.

CONCLUSION

As distinct from all the previous papers on the BM of charged particles across a magnetic field, in this work, we consider the possibility that the external field affects the dynamics of the charged bath particles surrounding the tagged BP. Since the bath particles are coupled to the BP, the magnetic field has not only the direct effect on the stochastic motion of the BP but an indirect one through the bath particles as well. These effects are elaborated in detail within a modified CL model. The approach opens many possibilities for the calculation of the relevant correlation functions, as well as for the development of the model itself. For example, a more realistic description of the BM under external force fields requires also the inclusion of nonlinear effects due to the interactions between the bath particles.

ACKNOWLEDGMENT: This work was supported by the Scientific Grant Agency of the Slovak Republic through grant VEGA 1/0250/18.

REFERENCES

1. J.C. Hidalgo-Gonzales, J.I. Jiménez-Aquino, M. Romero-Bastida, *Physica A* **462**, 1128 (2016).
2. V. Lisý, J. Tóthová, *Acta Phys. Pol. A* **137**, 657 (2020).
3. A.O. Caldeira, A.J. Leggett, *Quantum tunneling in a dissipative system*, *Ann. Phys. (N.Y.)* **149**, 374 (1983).
4. J. Tóthová, V. Lisý, *Physica A* **559**, 125110 (2020).
5. R. Kubo, *Rep. Progr. Phys.* **29**, 255 (1966).
6. J. Tóthová et al., *Eur. J. Phys.* **32**, 645 (2011).
7. V. Lisý, J. Tóthová, *Transp. Theory Stat. Phys.* **42**, 1 (2013).
8. R. Mankin et al., *Phys. Rev. E* **97**, 012145 (2018).

BROWNIAN MOTION IN A BATH AFFECTED BY AN EXTERNAL HARMONIC POTENTIAL

J. Tóthová, jana.tothova@tuke.sk, V. Lisý, vladimir.lisy@tuke.sk, Department of Physics, Faculty of Electrical Engineering and Informatics, Technical University of Košice, P. Komenského 2, 04200 Košice, Slovakia

INTRODUCTION

The Brownian motion of a particle in a bath of other particles is effectively described by the generalized Langevin equation (GLE). Following Kubo [1], usually it is assumed that external forces acting on the system do not affect the random thermal force that enters the GLE: the action of such forces is restricted to the Brownian particle (BP). However, there are physical situations, when also the bath particles respond to the external field [2, 3]. In this contribution, we show that if the bath is affected by a harmonic potential, the modified particle-bath model [4] leads to the GLE for which Kubo's fluctuation-dissipation theorem (FDT) [1] remains valid but both the thermal force and the associated memory function are affected by the confinement potential. The correlation functions describing the random motion of the BPs change in comparison with those in the original model as well. Specific solutions for these functions are obtained depending on the frequency distribution of the bath oscillators and their coupling to the BP.

MODIFIED PARTICLE-BATH MODEL

In the particle-bath model [4], noninteracting bath oscillators are linearly coupled to the BP. The system is in a harmonic field but the bath particles do not feel it. In our approach, both the BP and the oscillators respond to the external field. For the motion along the axis x , the modified Hamiltonian of the system reads

$$H = \frac{p^2}{2m} + \frac{1}{2} \kappa x^2 - Qx + \frac{1}{2} \sum_{i=1}^N \left[\frac{p_i^2}{m_i} + m_i \omega_i^2 \left(x_i - \frac{c_i x}{\omega_i^2} \right)^2 + \kappa_i x_i^2 \right] - \sum_{i=1}^N q_i x_i. \quad (1)$$

Here, c_i are the strengths of coupling between the BP and the oscillators with eigenfrequencies ω_i , p , and p_i stay for the BP and oscillator momenta, respectively. The effects of the external field on the BP of mass m and the bath particles of masses m_i are distinguished by different elastic constants κ and κ_i . The Hamiltonian includes linear terms in the positions of the particles. The quantities proportional to Q and q_i representing the contributions that accompany the harmonic terms could result from the interaction of the particles in an electric field (if the particles are in a laser beam creating a potential well for the BP but interacting also with the bath particles). The generalization of the model [4] does not violate the linearity of the theory and allows obtaining analytical results. From (1), by the standard way one obtains the equations $\dot{x} = p/m$, $\dot{p} = -\partial H / \partial x$ for the BP, and $\dot{x}_i = p_i/m_i$, $\dot{p}_i = -\partial H / \partial x_i$ for the bath

particles. It is suitable to solve the resulting equations of motion by the method described in detail in [5, 6]. The final equation for the BP is obtained in the form of the GLE,

$$m\dot{v}(t) + \kappa' x(t) + \int_0^t d\tau \Gamma(t-\tau)v(\tau) = \sum_i \frac{c_i}{\gamma_i} \int_0^t d\tau \sin[\gamma_i(t-\tau)] q_i(\tau) + Q(t) + f(t), \quad (2)$$

where $\kappa' = \kappa + \sum_i (c_i / \omega_i \gamma_i)^2 \kappa_i$, $\gamma_i^2 = \omega_i^2 + \kappa_i / m_i$ and $\Gamma(t) = \sum_i m_i c_i^2 \gamma_i^{-2} \cos(\gamma_i t)$. When the bath does not feel the external field, then $\kappa_i = 0$, $\gamma_i \rightarrow \omega_i$ and we return to the memory function $\Gamma(t)$ found in [4]. The random thermal force $f(t)$ in (2) has the same form as in [4] if ω_i is replaced by γ_i . The solution of (2) for the velocity correlation function (VCF) $C_{vv} = \langle v(0)v(t) \rangle$,

$$\tilde{C}_{vv}(s) = \int_0^\infty e^{-st} C_{vv}(t) dt = k_B T [ms + \tilde{\Gamma}(s) + \kappa' s^{-1}]^{-1}, \quad (3)$$

is determined by κ' and does not depend on q_i and Q . It can be obtained if (2) is multiplied by $v(0)$ with $\langle v(0) \rangle = 0$, by using the equipartition theorem $C_{vv}(0) = k_B T / m$ and $\langle v(0)f(t) \rangle = 0$ (causality). If q_i and Q are nonzero, the mean velocity of the BP, $V(t) = \langle v(t) \rangle$, is nonzero as well. It is determined averaging Eq. (2),

$$\tilde{V}(s) \left[ms + \tilde{\Gamma}(s) + \frac{\kappa'}{s} \right] = \sum_i c_i \frac{\tilde{q}_i(s)}{s^2 + \gamma_i^2} + \tilde{Q}(s). \quad (4)$$

The mean displacement of the BP is $\langle x(t) \rangle = \int_0^t V(t') dt'$ and $\langle x(t) \rangle^2$ must be added to the mean square displacement (MSD) obtained from (2) when the first two terms on the right-hand side are absent. Since $\Gamma(t)$ must go to zero as $t \rightarrow \infty$, due to the final value theorem $s\tilde{\Gamma}(s) \rightarrow 0$ at $s \rightarrow 0$. Thus, $\tilde{\Gamma}(s)$ tends to zero more slowly than $1/s$. The stochastic part of the MSD, determined from (3) as $2\tilde{C}_{vv}(s)/s^2$ [7], thus at small s behaves as $2k_B T / \kappa' s$, which in the time domain at $t \rightarrow \infty$ corresponds to $2k_B T / \kappa'$.

FLUCTUATION-DISSIPATION THEOREM

If there is no external force acting on the system, the FDT is easily obtainable from the GLE [1]. For the case when all κ_i equal to κ and $q_i = Q = 0$ the FDT was derived in [3]. Here, we use a different way to prove the FDT noting that the Hamiltonian (1) is identical to that

with ω_i replaced by γ_i and κ in the second term by κ' . Assuming as in [4] that at $t = 0$ the system was in thermal equilibrium, we use this Hamiltonian to calculate the average of $\langle f(t)f(t') \rangle$. Since the terms with $i \neq j$ in the sum $\sum_{i,j}$ give zero, after substitution of the means $\langle [x_i(0) - c_i x(0) / \gamma_i]^2 \rangle = k_B T / (m_i \gamma_i^2)$ and $\langle \dot{x}_i^2(0) \rangle = k_B T / m_i$ in $\langle f(t)f(t') \rangle$, one obtains

$$\frac{\langle f(t)f(t') \rangle}{k_B T} = \sum_i m_i c_i^2 \gamma_i^{-2} \cos[\gamma_i(t-t')] = \Gamma(t-t'). \quad (5)$$

This proves that the correlation function of the thermal force obeys the condition of stationarity and that the second FDT [4] holds also in the case of the presented modified particle-bath model.

EVALUATION OF κ' AND $\Gamma(t)$

Analytical estimations of $\Gamma(t)$, VCFs and other correlation functions used to describe the BP dynamics can be done in different ways. Here we consider c_i as independent on ω_i and the frequency distribution $h(\omega_i)$ continuous [4] so that the sums can be replaced by integrals: $\sum_i f(\omega_i) \rightarrow \int f(\omega)h(\omega)d\omega$. Then, for equal masses and coupling constants ($m_i \equiv \mu$, $c_i \equiv c$) and the bath not responding to the external field, $\Gamma_0(t) \approx \mu c^2 \int_0^\infty d\omega h(\omega) \omega^{-2} \cos(\omega t)$. For a chosen model of $\Gamma_0(t)$, Inverting this expression, $h(\omega)$ can be determined and, in the first approximation, used to calculate the desired quantities in the more general case of the bath responding to the external field. So, for a popular memory function $\Gamma_0(t) = (\xi/\tau) \exp(-t/\tau)$, which corresponds to the Ornstein-Uhlenbeck stochastic process [8], we get $h(\omega) = (2\xi\omega^2 / \pi\mu\tau^2 c^2) / (\omega^2 + \tau^{-2})$. Here, τ is the correlation time of the thermal force and ξ is the friction coefficient of the BP when $\tau \rightarrow 0$. For such $h(\omega)$ the elastic constant in (2) will be

$$\kappa' = \kappa + c^2 \bar{\kappa} \int_0^\infty d\omega \frac{h(\omega)}{\omega^2(\omega^2 + \bar{\kappa}/\mu)}, \quad (6)$$

where all the constants κ_i are considered equal, $\kappa_i \equiv \bar{\kappa}$. From this formula, we get in the case of the SLE, when $h(\omega) = 2\xi\omega^2 / \pi\mu c^2$, the modified elastic constant in the form $\kappa' = \kappa + \xi\sqrt{\bar{\kappa}/\mu}$. For the GLE when $\tau \neq 0$, Eq. (6) gives $\kappa' = \kappa + \xi\alpha / [\tau(1+\alpha)]$, where $\alpha^2 = \tau^2 \bar{\kappa} / \mu$.

Analytical results for the new memory function can be obtained from the integral

$$\Gamma(t) = \mu c^2 \int_0^\infty d\omega \frac{h(\omega)}{\gamma^2(\omega)} \cos[\gamma(\omega)t], \quad (7)$$

where $\gamma^2 = \omega^2 + \bar{\kappa}/m$. The integral can be exactly calculated using the Laplace transform as in (3),

$$\tilde{\Gamma}(s) = \frac{\xi}{\tau s} \left[\frac{1}{1+\alpha} - \frac{1}{1+\sqrt{\alpha^2 + (\tau s)^2}} \right]. \quad (8)$$

When there is no response ($\alpha = \bar{\kappa} = 0$), $\tilde{\Gamma}(s) = \xi / (\tau s + 1)$. At $t \rightarrow 0$ we have from (7) $\Gamma(0) = (\xi/\tau) / (1+\alpha)$, in agreement with the $s \rightarrow \infty$ limit of $s\tilde{\Gamma}(s)$ from (8), as well as $\Gamma(0) = \xi/\tau$ for the standard Langevin equation (SLE) and the no-response bath. At $s \rightarrow 0$, $\tilde{\Gamma}(s) \approx \xi s \tau [2\alpha(1+\alpha)^2]^{-1}$ that corresponds to the result for the SLE $\tilde{\Gamma}(s) \approx \xi s / [2\sqrt{\bar{\kappa}/\mu}]$. The long-time behavior of the memory function can be obtained directly from (7) as for integrals of rapidly oscillating functions. The asymptote of $\Gamma(t)$ at $t \gg \tau$ is

$$\Gamma(t) \approx -\frac{2\xi}{\sqrt{\pi\alpha\tau}} \left(\frac{t}{\tau}\right)^{-3/2} \left[\cos\left(\alpha\frac{t}{\tau}\right) + \sin\left(\alpha\frac{t}{\tau}\right) \right]. \quad (9)$$

In the case of the SLE, a similar result is obtained from (7) at $\tau = 0$:

$$\Gamma(t) \approx -\frac{2\xi}{\sqrt{\pi}} \left(\frac{\mu}{\bar{\kappa}}\right)^{1/4} \left[\cos\left(\sqrt{\frac{\bar{\kappa}}{\mu}}t\right) + \sin\left(\sqrt{\frac{\bar{\kappa}}{\mu}}t\right) \right] t^{-3/2}. \quad (10)$$

CONCLUSIONS

In conclusion, we have derived the generalized Langevin equation and the second FDT for the Brownian motion in a harmonic potential. This situation can be realized by optical traps. As distinct from Kubo's assumption for the GLE, the external force $-\kappa x$ affects the random force $f(t)$. Its time correlation function and the memory function $\Gamma(t)$ thus depend on the elastic constant κ . We have also proposed a method of the calculation of $\Gamma(t)$ and the relevant time correlation functions. The results could be important for new studies and interpretation of experiments on different systems whose description is related to the theory of the stochastic motion under external force fields.

ACKNOWLEDGMENT: This work was supported by the Scientific Grant Agency of the Slovak Republic through grant VEGA 1/0250/18 and by the Ministry of Education Agency for Structural Funds of the EU, project No. 26210120012.

REFERENCES

1. R. Kubo, Rep. Progr. Phys. **29**, 255 (1966).
2. B. Cui, A. Zaccane, Phys. Rev. E **97**, 060102 (2018).
3. V. Lisý, J. Tóthová, Results Phys. **12**, 1212 (2019).
4. R. Zwanzig, Nonequilibrium Statistical Mechanics (Oxford University Press, New York - 2001).
5. J. Tóthová, A. Šoltýs, V. Lisý, J. Molecular Liquids **317**, 113920 (2020).
6. J. Tóthová, V. Lisý, Physica A **559**, 125110 (2020).
7. J. Tóthová et al., Eur. J. Phys. **32**, 645 (2011).
8. P. Bialas, J. Łuczka, Entropy **20**, 123 (2018).

THERMAL TREND OF THE BIPARTITE ENTANGLEMENT IN THE SPIN-1/2 ISING-HEISENBERG PLANAR LATTICE OF INTER-CONNECTED TRIGONAL BIPYRAMIDS

L. Gálisová, galisova.lucia@gmail.com, Institute of Manufacturing Management, Faculty of Manufacturing Technologies with the seat in Prešov, Technical University of Košice, Bayerova 1, 080 01 Prešov, Slovakia

INTRODUCTION

Bipartite quantum entanglement belongs to hot topics of modern physics mainly due to its significant role in quantum information theory [1]. However, this quantum-mechanical correlation is most often theoretically studied in one dimension (1D), as quantum spin chains are the simplest models for its study at zero as well as finite temperatures [2]. In two-dimensional (2D) models, the bipartite entanglement is examined mainly in the ground state or at very low temperatures [3].

Inspired by the last fact, in this paper we will examine the bipartite quantum entanglement in the exactly solved 2D spin-1/2 Ising-Heisenberg lattice formed by identical trigonal bipyramids [4]. As we have only recently demonstrated in [5], this mixed-spin model represents a suitable playground for exact study of the phenomenon not only in the ground state, but also at finite temperatures.

MODEL

We consider the spin-1/2 Ising-Heisenberg model on the infinite 2D lattice formed by trigonal bipyramidal plaquettes, which is schematically depicted in Fig. 1. The common vertices (white circles) of six nearest-neighbouring plaquettes are occupied by the Ising spins $\sigma = 1/2$, while others (blue circles) are occupied by the Heisenberg spins $S = 1/2$. The total Hamiltonian of the model can be written as a sum of $Nq/2$ plaquette Hamiltonians $\hat{\mathcal{H}} = \sum_{j=1}^{Nq/2} \hat{\mathcal{H}}_j$, where N is the total number of the Ising spins ($N \rightarrow \infty$), q labels the number of the nearest-neighbouring bipyramidal plaquettes having common vertex ($q = 6$ for the present model) and each plaquette Hamiltonian $\hat{\mathcal{H}}_j$ involves all the exchange interactions realized within the respective Ising-Heisenberg trigonal bipyramid:

$$\hat{\mathcal{H}}_j = -J_H \sum_{k=1}^3 [\Delta (\hat{S}_{j,k}^x \hat{S}_{j,k+1}^x + \hat{S}_{j,k}^y \hat{S}_{j,k+1}^y) + \hat{S}_{j,k}^z \hat{S}_{j,k+1}^z] - J_I \sum_{k=1}^3 \hat{S}_{j,k}^z (\hat{\sigma}_j^z + \hat{\sigma}_{j+1}^z). \quad (1)$$

In above, $\hat{S}_{j,k}^\alpha$ ($\alpha = x, y, z$) and $\hat{\sigma}_j^z$ are spatial components of the spin-1/2 operators related to the Heisenberg and Ising spins, respectively, J_H marks the XXZ Heisenberg interaction inside the Heisenberg triangles, Δ is the exchange anisotropy parameter in this interaction, and J_I labels the Ising-type interaction between the nearest-neighbouring Ising and Heisenberg spins.

The general version of the 2D spin-1/2 Ising-Heisenberg lattice with q inter-connected bipyramidal plaquettes has been exactly solved in our recent paper [4] under the periodic boundary conditions $\hat{S}_{j,4}^\alpha \equiv \hat{S}_{j,1}^\alpha$, $\hat{\sigma}_{Nq/2+1}^z \equiv \hat{\sigma}_1^z$ by means of the gener-

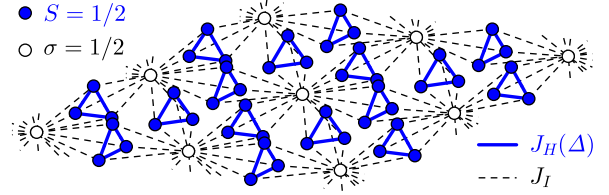


Fig. 1. The part of the studied spin-1/2 Ising-Heisenberg lattice. Blue (white) circles show lattice sites occupied by the Heisenberg (Ising) spins and blue solid (black dashed) lines label the Heisenberg (Ising) exchange interactions.

alized decoration-iteration transformation method [6]. Thanks to the identical exchange coupling $J_H(\Delta)$ between the Heisenberg spins, which clearly indicates the same bipartite quantum entanglement in the Heisenberg triangles, some of the physical quantities from Ref. [4], namely the spatial components of the pair correlation function $C_\Delta^{xx} = \langle \sum_{j=1}^3 \hat{S}_{j,k}^{x(y)} \hat{S}_{j,k+1}^{x(y)} \rangle$, $C_\Delta^{zz} = \langle \sum_{j=1}^3 \hat{S}_{j,k}^z \hat{S}_{j,k+1}^z \rangle$ and the spontaneous magnetization $M_\Delta = \langle \sum_{j=1}^3 \hat{S}_{j,k}^z \rangle$, can directly be used for a rigorous calculation of the concurrence [7]:

$$\mathcal{C} = 2 \max \left\{ 0, \frac{2}{3} |C_\Delta^{xx}| - \sqrt{\left(\frac{1}{4} + \frac{C_\Delta^{zz}}{3} \right)^2 - \frac{M_\Delta^2}{9}} \right\}. \quad (2)$$

As will be demonstrated in the following section, the quantity (2) represents very suitable tool for a comprehensive investigation of the bipartite entanglement in the considered 2D mixed-spin model.

RESULTS AND DISCUSSION

Let us proceed to the analysis of the bipartite quantum entanglement in the spin-1/2 Ising-Heisenberg model displayed in Fig. 1 by considering the ferromagnetic exchange interactions $J_H > 0$, $J_I > 0$. As reported in our recent article [4], the ground state of this particular version of the model is constituted by either the spontaneously ordered quantum ferromagnetic phase |QF> = $\prod_{j=1}^{3N} |\uparrow\rangle_{\sigma_j} \otimes \frac{1}{\sqrt{3}} (|\uparrow\uparrow\downarrow\rangle_j + |\uparrow\downarrow\uparrow\rangle_j + |\downarrow\uparrow\uparrow\rangle_j)$ or the spontaneously ordered classical ferromagnetic phase |CF> = $\prod_{j=1}^{3N} |\uparrow\rangle_{\sigma_j} \otimes |\uparrow\uparrow\uparrow\rangle_j$. The QF phase is stable in the zero-temperature parameter region $\Delta > J_I/J_H + 1$. Otherwise, the CF phase appears.

A strength of the bipartite entanglement between the Heisenberg spins, which can be observed only in the QF phase and its thermal trend can be fully understood from the density plot of the concurrence (2) displayed in Fig. 2 in the $\Delta - k_B T/J_I$ plane for the model with equal Ising and Heisenberg exchange interactions $J_H = J_I$. In this figure, the blue dashed curve delimiting the entangled region with $\mathcal{C} > 0$ was obtained from Eq. (2) by solving the equation $\mathcal{C} = 0$ and the critical

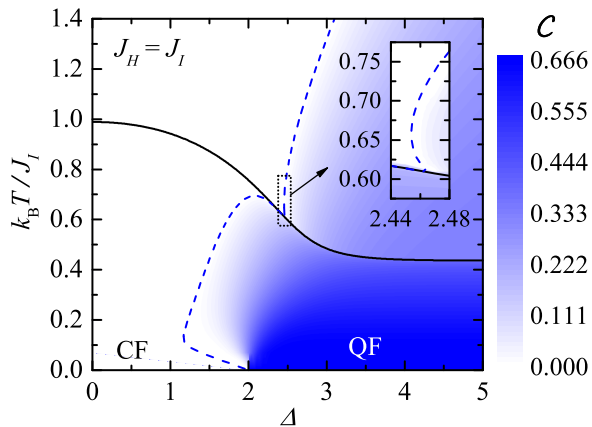


Fig. 2. The density plot of the concurrence \mathcal{C} in the $\Delta - k_B T / J_I$ plane for the model with $J_H = J_I$. The blue dashed curve is the threshold between the entangled ($\mathcal{C} > 0$) and non-entangled ($\mathcal{C} = 0$) regions and the black solid curve shows the critical temperature of the model.

temperature of the model (black solid line) is the solution of the exact critical condition $J_{eff} / (k_B T_c) = \ln 3$ for the isotropic spin-1/2 Ising triangular lattice [8] (J_{eff} is given by Eq. (6) in Ref. [4]). It is obvious from Fig. 2 that the bipartite entanglement of the Heisenberg spins, which can be observed in the QF phase at zero temperature, is unsaturated ($\mathcal{C} = 2/3$), but much more resistant to temperature than the respective spontaneous long-range spin order. In fact, it persists far above the critical temperature of the studied model. Due to thermally induced fluctuations to energetically close quantum Heisenberg spin states, a weak quantum entanglement can also be detected above the CF phase near the ground-state boundary CF-QF, as evidenced by the pronounced C-shaped dependence of the blue dashed curve below critical temperature at the exchange anisotropies $\Delta \in (J_I / J_H, J_I / J_H + 1)$. The second, almost unobservable C-shaped dependence of the blue dashed curve indicating a remarkable thermally induced re-appearance of the entangled Heisenberg states can be found slightly above the critical temperature of the model within very narrow range of $\Delta > J_I / J_H + 1$ (see the inset in Fig. 2). All above findings can be seen once again and in more detail in Fig. 3, which shows typical temperature dependencies of the concurrence \mathcal{C} for four representative values of the exchange anisotropy Δ under the assumption of the same condition for the interaction constants J_H, J_I as considered in Fig. 2.

CONCLUSIONS

In the present paper, the thermal trend of the bipartite quantum entanglement in the ferromagnetic spin-1/2 Ising-Heisenberg model on 2D lattice consisting of trigonal bipyramidal plaquettes has been examined with the help of the quantity called concurrence. It has been demonstrated that the unsaturated bipartite entanglement observed in the spontaneously ordered QF ground state persists even far above the critical temperature of the model. In

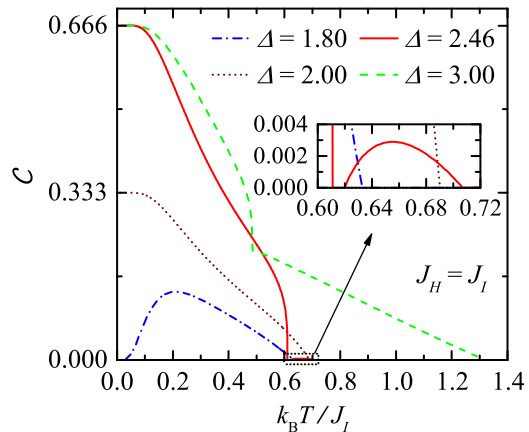


Fig. 3. Typical thermal variations of the concurrence \mathcal{C} for the model with $J_H = J_I$ and four representative values of the exchange anisotropy parameter Δ .

addition, the entangled Heisenberg spin states can also be thermally activated above the CF ground state in a vicinity of the ground-state boundary with the QF phase and restored slightly above the critical temperature of the model. The observed temperature-invoked activation and re-entrance of the bipartite quantum entanglement between spins in a vicinity of the first- and second-order phase transitions, respectively, seems to be general feature of 2D regular lattices involving the symmetric ferromagnetic Heisenberg triangular clusters inter-connected through the Ising spins. As a matter of fact, the same trend has been recently independently observed in the spin-1/2 Ising-Heisenberg models on the 2D lattice with four bipyramidal plaquettes being inter-connected via common vertex [5] and the triangulated Hutsimi lattice [9].

ACKNOWLEDGMENT: This work was financially supported by the grants Nos. APVV-16-0186 and VEGA 1/0301/20.

REFERENCES

1. M. A. Nielsen and I. L. Chuang: Quantum Computation and Quantum Information (Cambridge University Press, Cambridge - 2000).
2. L. Zhou, H. S. Song, Y. Q. Guo, C. Li, Phys. Rev. A **68**, 4567 (2003).
3. T. Roscilde, P. Verrucchi, A. Fubini, S. Haas, V. Tognetti, Phys. Rev. Lett. **94**, 147208 (2005).
4. L. Gálisová, J. Phys.: Condens. Matter **31**, 465801 (2019).
5. L. Gálisová, Phys. Lett. A **384**, 126629 (2020).
6. J. Strečka, Phys. Lett. A **374**, 3718 (2010).
7. L. Amico, A. Osterloh, F. Plastina, R. Fazio, G. M. Palma, Phys. Rev. A **69**, 022304 (2004).
8. R. M. F. Houtappel, Physica **16**, 425 (1950).
9. C. Ekiz, J. Strečka, Acta Phys. Pol. A **137**, 592 (2020).

PHASE BIREFRINGENCE DISPERSION FUNCTION AS A COMPLEMENTARY TOOL FOR INVESTIGATION OF NEMATIC LC STRUCTURE

N. Tarjányi, norbert.tarjanyi@feit.uniza.sk, M. Veveričik, vevericik@fyzika.uniza.sk, D. Káčik, daniel.kacik@feit.uniza.sk, Department of Physics, Faculty of Electrical Engineering and Information Technology, University of Žilina, Univerzitná 8215/1, 010 26 Žilina, Slovakia

INTRODUCTION

Nematic liquid crystals (NLC) represent a very important class of materials that found naturally their utilization as polarizers, displays, and modulators due to their unique molecular structure and ability to respond to external fields. Interest in LCs is not fading even today. Many researchers are trying to improve their basic properties, for example by dyes [1] or by doping with various kinds of nanoparticles [2], so that they can better respond to electric and/or magnetic fields and serve as new kinds of retarders and switches [3]. One of the natural properties of a liquid crystal is its birefringence. Often, this feature is used for the construction of polarizing elements, light intensity or phase modulators, and sensors but also it has the potential to be used as an additional tool for the study of electronic absorption bands of LC in the UV and near-UV region. Such an approach is suggested in the contribution.

SAMPLE PREPARATION AND EXPERIMENT

The material we studied was a thin film of nematic liquid crystal, 6CHBT with the mean value of birefringence being around 0.15 [4], thus belonging to a group of mid-birefringence materials [5]. Since the optical anisotropy of the crystal vanishes at temperatures above 43°C [4] the investigation was performed at the temperature of 24.5 °C. The samples were prepared using special glass cells provided by the Military University of Technology, Warsaw. The glass plates forming the cell were separated by built-in spacers (50 ± 0.1) μm thick. To obtain the sample exhibiting birefringence the inner surfaces of the cell were treated in a way ensuring uniform planar LC molecules alignment with no or only negligible pretilt.

The apparatus for investigation consisted of a halogen lamp with an integrated collimating lens, a set of two plane polarizers designed for polarizing light in the visible spectral range, and an optical spectrum analyzer (OSA) HR2000⁺ (from Ocean Optics). The liquid crystal cell fixed on a rotary stage with an opening enabling the illumination of the cell was placed in between the crossed plane polarizers. Light from the halogen lamp impinged the first polarizer, propagated through the LC sample and was collected by an optical fiber with a core diameter 400 μm and a numerical aperture 0.39 placed behind the second polarizer (Fig. 1). It stems from the theory that in case of a uniaxially birefringent sample, which is placed between two crossed plane polarizers, the intensity of light behind the second polarizer can be expressed [6]

$$I(\lambda) = I_0(\lambda) \cdot \left\{ \sin \left[\frac{\pi t}{\lambda} \Delta n(\lambda) \right] \right\}^2, \quad (1)$$

where $I_0(\lambda)$ denotes the input spectral distribution of light intensity, t is the sample thickness, Δn is the sample phase birefringence, and $I(\lambda)$ represents the spectral distribution of intensity detected at the output.

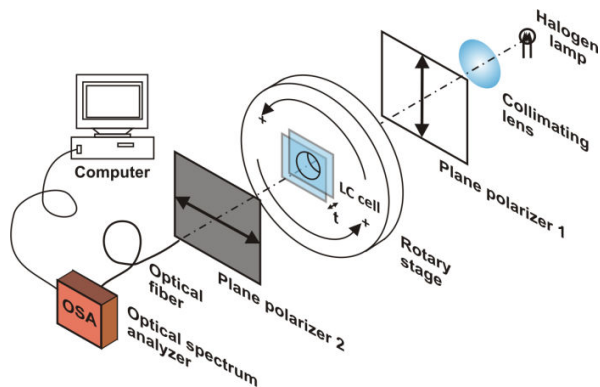


Fig. 1. A sketch of apparatus used for investigating the birefringence of 6CHBT liquid crystal

As Eq. (1) states the output intensity depends on the wavelength λ of light, the thickness t of the sample, and its birefringence Δn . By rotating the stage with the sample we found its proper position for which a well detectable characteristic channeled spectrum emerged at the OSA. The signal was recorded by the optical spectrum analyzer with a 0.5 nm resolution (Fig. 2).

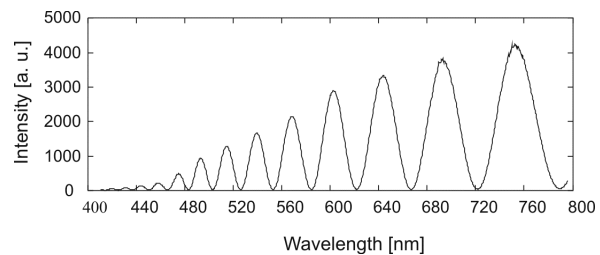


Fig. 2. The measured channeled spectrum.

PHASE BIREFRINGENCE

The dispersion of phase birefringence $\Delta n(\lambda)$ can be determined from the measured channeled spectrum using Eq. (1) and an appropriate model describing the birefringence of the liquid crystal. According to a general polarizability model [7], the phase birefringence dispersion of LC in the spectral region of wavelengths without resonant frequencies can be expressed by

$$\Delta n(\lambda, T) \approx \sum_j G_j(T) \frac{\lambda^2 \lambda_j^2}{\lambda^2 - \lambda_j^2}, \quad (2)$$

where parameters λ_j and $G_j(T)$ determine the position of the resonance within the j^{th} absorption band and its

strength, respectively. The phase birefringence dispersion (particularly, the parameters λ_j and $G_j(T)$) was found by fitting the measured channeled spectrum with the function described by Eq. (1) in which the phase birefringence $\Delta n(\lambda)$ had the form expressed by Eq. (2). The initial values of the mean resonance wavelengths λ_j used in the fitting process were chosen according to the known absorption spectrum of 6CHBT [8]. We started the fitting process assuming the existence of only one absorption band in the UV region. As the difference between the measured and the calculated channeled spectrum was about 10 % in the rather broad spectral range, we revisited the assumption and included another absorption band into the fitting. The discrepancy between the measured and the calculated spectrum dropped down to less than 2.5 % in the case of a 2-bands model and the result of the fitting, in this case, is shown in Fig. 3.

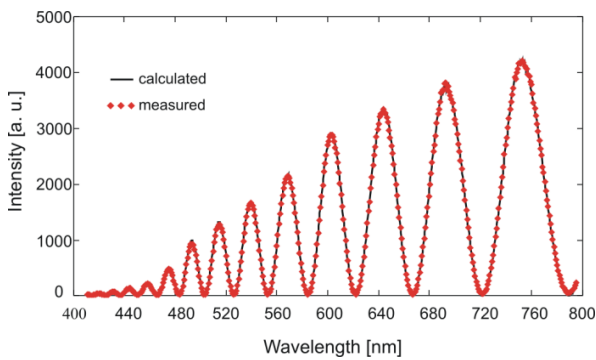


Fig. 3. The measured channeled spectrum fitted by the calculated one using Eq. (1) and Eq. (2)

RESULTS AND DISCUSSION

Table 1 shows the particular values of the parameters λ_j , $G_j(T)$ obtained by the fitting in cases of the considered 1- and 2-bands models. Values of the mean resonance wavelengths λ_j fit well into the regions typical for 6CHBT as well as for LCs in general [9].

TAB. 1. Values of the obtained fitting parameters.

	1-band model	2-bands model
λ_1 [nm]	219.31	107.34
G_1 [nm ⁻²]	$2.72 \cdot 10^{-6}$	$5.12 \cdot 10^{-6}$
λ_2 [nm]	-	256.67
G_2 [nm ⁻²]	-	$1.11 \cdot 10^{-6}$

Fig. 4 shows the phase birefringence dispersions calculated according to Eq. (2) using the parameters listed in TAB.1. Though the curves plotted in Fig. 4 look quite similar at first glance, they are not the same. The deviation between them is illustrated by their ratio plotted in Fig. 5. For clarity, there is also plotted a curve representing the unity which expresses the case when the two dispersion curves would be the same. Thus, it can be seen that the deviation between dispersion curves calculated according to 1- and 2-bands models is a maximum of 1%. Nevertheless, the deviation between the measured and the calculated channeled spectrum, which is less than 2.5% in our case, is decisive.

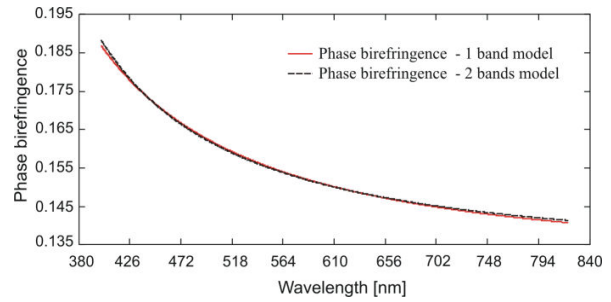


Fig. 4. Phase birefringence calculated according to Eq. (2)

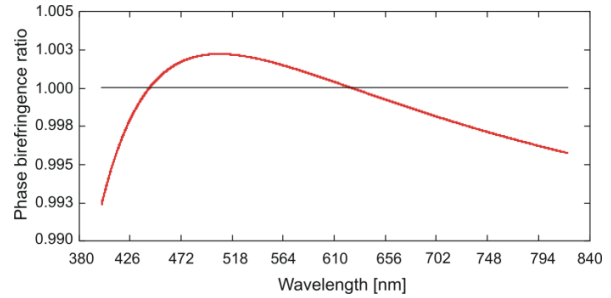


Fig. 5. The ratio between phase birefringence dispersions calculated according to 1- and 2-bands models.

CONCLUSIONS

We investigated the phase birefringence dispersion of pure 6CHBT liquid crystal in the visible spectral range and at the temperature of 24.5 °C. The phase birefringence dispersion $\Delta n(\lambda)$ was determined by fitting the calculated channeled spectrum to the measured one. The deviations between the measured and the calculated spectra were about 10% in the case of a 1-band model and less than 2.5% in the case of 2-bands model, and stayed unchanged also in case of a 3-bands model. Such a good match promises to use the approach as a complementary investigation method of LC optical properties to the existing absorption or ellipsometric measurements, the aim of which is to characterize the optical properties of a liquid crystal sample.

ACKNOWLEDGMENT: This work was supported by the Slovak Research and Development Agency under the Contracts no. APVV-15-0441 and APVV-19-0602, and projects VEGA 2/0016/17 and VEGA 1/0069/19.

REFERENCES

1. M. S. Zakerhamidi et al., *J. Mol. Liq.* **221**, 608 (2016).
2. Y. Shen et al., *Appl. Sci.* **9**, 2512 (2019).
3. K. Bednarska et al., *Opt. Mater.* **98**, 109419 (2019).
4. A.W. Domański et al., *Opto-Electron. Rev.* **14**, 305 (2006).
5. G. Pathak et al., *Opto-Electron. Rev.* **26**, 11 (2018).
6. M. Born, E. Wolf: *Principles of Optics* (Cambridge University Press, Cambridge - 1999).
7. Sh.-T. Wu, *Phys. Rev. A* **33**, 1270 (1986).
8. Ch.-H. Wen et al., *Liq. Cryst.* **31**, 1479 (2004).
9. T. Hanemann et al., *Liq. Cryst.* **11**, 917 (1992).

COMPLEX VOLUME CHANGES INDUCED BY HIGH PRESSURE AND EXTERNAL MAGNETIC FIELD IN Ni₂MnSn-BASED HEUSLER ALLOY

J. Kamarád, kamarad@fzu.cz, J. Kaštil, kastil@fzu.cz, Z. Arnold, arnold@fzu.cz, M. Mišek, misek@fzu.cz, Institute of Physics ASCR, v.v.i., Na Slovance 2, 182 21 Prague 8, Czech Republic, O. Isnard, olivier.isnard@neel.cnrs.fr, Institut NEEL CNRS/UGA, Grenoble, France

INTRODUCTION

The Heusler Ni₂Mn_{1+x}Sn_{1-x} alloys exhibit structural martensitic transformation from cubic austenite (A) phase above room temperature into orthorhombic martensite (M) phase at lower temperature as far as their composition lies in a range, $0.4 \leq x \leq 0.6$. The martensitic transformation is accompanied by large anomalies in properties of alloys, including significant changes of volume, magnetization and transport properties [1,2]. The mentioned volume changes were a motivation to study an effect of high pressure on magnetization of the Ni_{1.92}Mn_{1.56}Sn_{0.52} (with an excess of Mn) alloy in wide range of temperature, magnetic field and pressure together with an investigation of related magnitudes as thermal expansion and forced volume magnetostriction.

EXPERIMENTAL

Polycrystalline Ni_{1.92}Mn_{1.56}Sn_{0.52} alloy was prepared in a vacuum by electric induction melting. The used high-pressure cell made from non-magnetic CuBe bronze ensures hydrostatic conditions up to 1.2 GPa at room temperature [3]. The SQUID-magnetometer MPMS-7T (QD Co.) magnetometer from 2 K to 400 K at field up to 7 T. Magnetostriction was measured by a strain-gage-bridge up to field 14 T in the Measuring System (PPMS-14T, QD Co.) and by a dilatometer utilizing capacitance cell and cryostat with 6 T magnet.

RESULTS

The ferromagnetic state of the austenite phase of the alloy was detected below $T_C = 320$ K. With decreasing temperature, the structural A-M transition was observed at $T_{A-M} = 282$ K and the reverse M-A transition was found with a temperature hysteresis at $T_{M-A} = 294$ K. The M-A transformation is accompanied by an increase of volume of the alloy, see Fig. 1. External magnetic

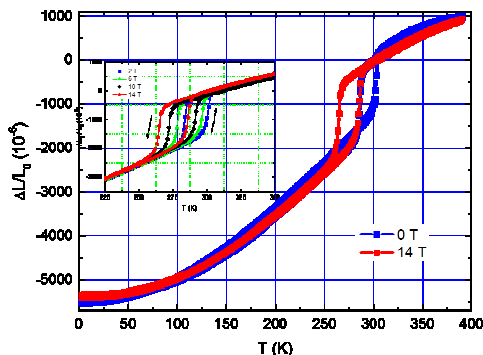


Fig. 1. Thermal expansion at zero and high magnetic fields

field supports ferromagnetism of austenite and both transition temperatures decrease in field, $dT_{M-A}/dH = -1.3$ K/T. On the other hand, stability of martensite phase of the alloy (with lower volume) as well as transition temperatures T_{A-M} , T_{M-A} increase significantly under pressure, $dT_{M-A}/dP = +18$ K/GPa⁻¹.

The pronounced decrease of magnetization of martensite phase under pressure, $d \ln M / dP = -18.7 \times 10^{-3}$ GPa⁻¹, has been observed at low temperature, see Fig. 2. In contrast, pressure dependence of magnetization of the austenite phase of the stoichiometric Ni₂MnSn alloy at low temperature is very slight, $d \ln M / dP = -2.5 \times 10^{-3}$ GPa⁻¹, [2]. This unequal pressure dependence of magnetization of the studied alloys points to a more localized character of magnetism in austenite phase of the stoichiometric Ni₂MnSn compound and to an itinerant character of magnetism in martensite phase of the off-stoichiometric alloy. Simultaneously, low value of magnetization, $M(5K, 0, 0) = 1.61$ μ_B/f.u., and high value of the high-field susceptibility, $\chi_{hf} = 3.8 \times 10^{-4}$, verifies a presence of antiferromagnetic interactions in the off-stoichiometric Ni₂Mn_{1+x}Sn_{1-x} alloys with an excess of Mn.

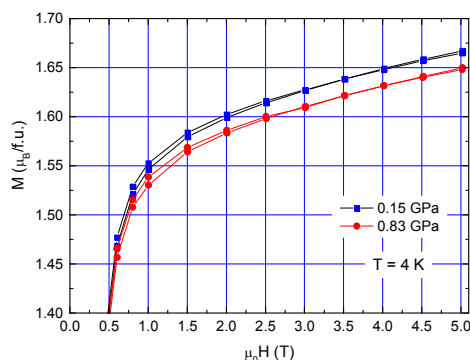


Fig. 2. Pressure dependence of magnetization $M(5K, H, P)$ of martensite phase of the alloy

The general effect of magnetic field on volume of magnetic materials, the forced volume magnetostriction, is simply related to the pressure effect on magnetization of these materials by the Maxwell relation,

$$d\omega/dH = -\rho dM/dP \quad (1)$$

where ρ is mass density and $\omega = \Delta V/V_0 = 3x\Delta L/L_0$, that has been measured at temperature 6 K by the strain-gage-bridge in field up to 14 T. The strain-gage bridge was oriented with a sensitive direction parallel to applied magnetic field. The dependence $\Delta\omega(H)$ exhibits a strictly linear character at fields above 2 T (see Fig. 3) and the forced volume magnetostriction of martensite of the alloy can be expressed by a value $d\omega/dH = (6.85 \pm$

$0.05) \times 10^{-6} T^{-1}$. The volume changes induced by magnetic field above 2 T are isotropic, so, the strain-gage-bridge provides relevant data in the case of polycrystalline alloy.

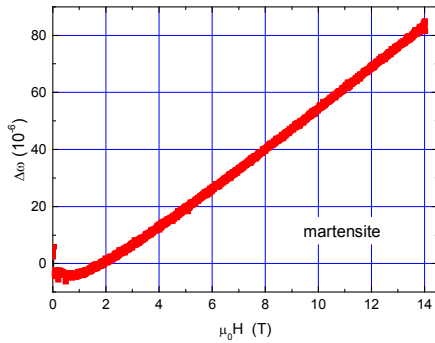


Fig. 3. The forced volume magnetostriction of martensite of the alloy at temperature 6 K

Using the equation (1), the determined value of the forced volume magnetostriction leads to value of $dM/dP = -4.05 \times 10^{-2} \mu_B/f.u.GPa^{-1}$ that well agrees with measured value of pressure dependence of saturated magnetization of martensite at temperature 4 K and with value of $dM/dP = -4.85 \times 10^{-2} \mu_B/f.u.GPa^{-1}$ presented in [4].

A complex microstructure of martensite phase of the $Ni_{1.92}Mn_{1.56}Sn_{0.52}$ alloy originates from crystalline twins that are induced in course of the martensitic diffusionless transformation of the alloy. Due to the complex microstructure of the alloy, magnetostriction of its martensite phase is anisotropic at low magnetic field, see Fig. 4. The field induced dilatation ΔL of zero-field cooled samples was measured at temperature 3 K along magnetic field ($H 0^\circ$) and perpendicularly to external field ($H 90^\circ$). The easy magnetization direction (EMD) of martensite phase is parallel with the shortest lattice parameter of the orthorhombic structure of the twins. When the magnetocrystalline anisotropy energy is strong enough, crystalline twins are turned by external field with EMD into the field direction and so, a dilatation

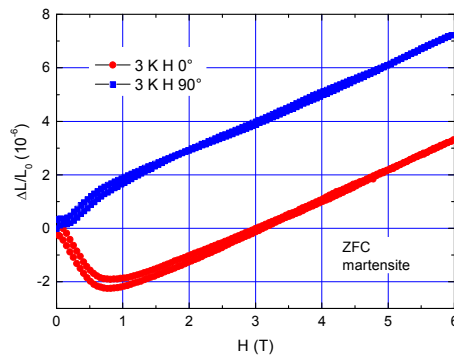


Fig. 4. The low field anisotropic magnetostriction of martensite phase of the alloy

measured along external field is negative. *Vice versa*, a dilatation measured in direction perpendicular to

external field is positive. With increasing magnetic field, changes of microstructure of martensite phase increase, but simultaneously, they induce an increase of elastic energy that inhibits further turning of twins [5]. As can be seen in Fig. 4, the isotropic forced volume magnetostriction starts to dominate in a range of magnetic field above 2 T.

CONCLUSIONS

The structural martensitic transformation of the Heusler $Ni_{1.92}Mn_{1.56}Sn_{0.52}$ alloy is strongly reflected within thermal expansion measurement by a very sharp step-like change of $\Delta L/L_0$. The calculated change of volume ($\Delta V/V_0 = 3 \times \Delta L/L_0 = 0.55\%$) well agrees with the volume change determined by x-ray diffraction experiments [2].

The pronounced decrease of magnetization of the alloy under pressure at low temperature points to an itinerant character of magnetism of martensite phase of the alloy, in contrast to a more localized character of magnetism in austenite phase of the stoichiometric Ni_2MnSn compound.

The measured forced volume magnetostriction of the alloy exhibits a strictly linear character at fields above 2T up to field 14 T, An excellent agreement of the observed value of the forced volume magnetostriction with the pressure effect on magnetization of the alloy has been confirmed using the Maxwell relation. This verifies both, the isotropic character of magnetostriction in magnetic field above 2 T and the legitimacy of the used methodology of volume changes determination.

The anisotropic magnetostriction was observed at magnetic field below 2 T. It arises from a turning of crystalline twins in martensite phase of the alloy into external field direction due to strong magnetocrystalline interaction. This model was originally described in the case of Ni_2MnGa -based alloys [5], but, it can be used here too.

ACKNOWLEDGMENT: This work was carried out with the support of: i) the Grant Agency of CR, grant No.: 20-16130S, ii) the program of Czech Research Infrastructures (project no. LM2018096) and iii) the project of MEYS, SOLID21 in Operational program EU.

REFERENCES

1. Y. Sutou, Y. Imano, N. Koeda, T. Omori, K. Ishida, K. Oikawa, Appl. Phys. Lett. **85**, 4358 (2004).
2. J. Kaštil, J. Kamarád, O. Isnard, Y. Skourski, M. Mišek, Z. Arnold., J. Alloys and Comp. **650**, 248 (2015).
3. J. Kamarád, Z. Machátová, Z. Arnold, Rev. Sci. Instrum. **75**, 5022 (2004).
4. Y. Chieda, T. Kanomata, K. Fukushima, K. Matsubayashi, Y. Uwatoko, R. Kainuma, K. Oikawa, K. Ishida, K. Obara, T. Shishido, J. Alloys Compd. **486**, 51 (2009).
5. R.C. O'Handley, J. Appl. Phys. **83**, 3263 (1998).

NEW VIEW ON THE ORIGIN OF HIGH CONDUCTIVITY OF POLYANILINE FILMS PROTONATED BY HYDROCHLORIC ACID

R. Rutsch, ryby19@outlook.com, J. Toušek, tousek@karlov.mff.cuni.cz, J. Toušková, touskova@karlov.mff.cuni.cz, Faculty of Mathematics and Physics, Charles University, 18200 Prague 8, Czech Republic

INTRODUCTION

Polyaniline (PANI) is a material known for its huge range of obtainable conductivities. In general, three types of charge carriers are considered in PANI salt, namely holes, polarons and protons. Many authors attribute the high conductivity of acid doped PANI to polarons [1 - 3].

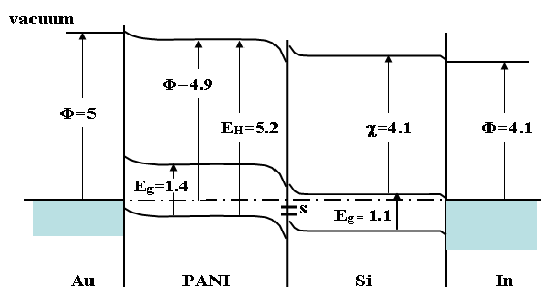


Fig. 1. The band diagram of PANI/Si heterojunction. Φ are the work functions, χ is the affinity of Si, E_H is the energy at the HOMO level, E_g are the band gaps and s shows the occupied states at the PANI/Si interface (energy is in eV)

It is well-known for its good stability low cost for production and wide range up to the difference of ten magnitudes of obtainable conductivities, that can be achieved by appropriate degree of protonation with strong acids (i. e. hydrochloric or camphorsulfonic) [4, 5]. The explanation of high achieved conductivity (several $S.cm^{-1}$) and transport mechanism differs from author to author. In general three type of charge carriers are assumed, namely polarons, holes (material exhibits p-type conductivity) and ions (protons).

In this paper we conduct the experiments to find the conductivity of each type of charge carriers separately and to determine their contribution to overall conductivity. The PANI layers were deposited in situ on n-type Si substrate as it was described in our previous work [6] from solution of aniline hydrochloride (0.2 M) with ammonium peroxydisulfate (0.25 M) in aqueous medium. The thickness of the PANI layer measured by atomic force microscope was 160 nm.

The overall conductivity of PANI layer was measured on glass substrate in the direction of the substrate by four-terminal resistance method with ohmic gold electrodes in alternating current regime. Several frequencies were utilised and values were extrapolated to zero frequency leading value (1.9 – 3.5) $S.cm^{-1}$.

MOBILITY MEASURED BY IMPEDANCE SPECTROSCOPY

As described in detail in our previous publication [6] the mobility of holes and polarons were measured by impedance spectroscopy on Au/PANI/Si/In structure.

The currents injected from the electrodes are non-stationary space charge limited currents transporting holes and polarons. Peak frequencies ω_{max} gives the carrier transit time $\tau = 1/\omega_{max}$ and shifts to higher values with increasing voltages. Voltage dependence of the transit time enables to obtain mobility μ as a function of the electric field E . Assuming moderate dispersion:

$$\mu = \frac{d}{0.44\tau E} \quad (1)$$

d is the thickness of the sample, linear dependence of $\mu/E^{1/2}$ was found indicating Poole-Frenkel mechanism. By interpolation for zero voltage mobilities were found: $\mu_{holes} = 1.8 \times 10^{-6} \text{ cm}^2V^{-1}s^{-1}$ and $\mu_{polarons} = 2.7 \times 10^{-7} \text{ cm}^2V^{-1}s^{-1}$.

V-A CHARACTERISTIC

The Au/PANI/Si/In structure polarized in the forward direction blocks electrons from Si wafer from entering PANI and therefore enables to determine the conductivity of PANI without the influence of the ions. This conductivity was evaluated from the forward direction of V-A characteristic. The analytical expression for charge transport including emission and diffusion currents for forward direction gives expression:

$$J = \frac{J_0 J_S \{ \exp[(U - JR_S)/nkT] - \exp[-e(n-1)(U - JR_S)/nkT] \}}{J_0 \exp[-e(n-1)(U - JR_S)/nkT] + J_S} + \frac{U - JR_S}{R_{Sh}} \quad (2)$$

where R_S , R_{Sh} are the series and shunt resistances, respectively, e is the electron charge, k is the Boltzmann constant, T is the absolute temperature, J_0 and J_S are the emission and diffusion currents, respectively. The factor n characterizes distribution of the diffusion potential V_D between the two parts of the junction. RSBY fitting the theory to experiment n , R_S , R_{Sh} were obtained and using the area of the electrodes and thickness of the sample the hole conductivity $8.2 \times 10^{-7} \text{ S.cm}^{-1}$ was evaluated.

DIELECTRIC SPECTROSCOPY

We studied polarization of PANI/Si under the electric field. Mobility of protons in the PANI layer was determined by dielectric measurement [7]. The given structure of PANI is not permeable for ions, therefore mobility of protons was calculated by determining dielectric relaxation time τ_{EP} from the permittivity spectra:

$$\mu_{protons} = \frac{ed^2 \epsilon_R}{4\epsilon_0 \epsilon_{EP} \tau_{EP} kT} \quad (3)$$

giving value $2.3 \times 10^{-7} \text{ cm}^2 \text{V}^{-1} \text{s}^{-1}$ where ϵ_{REF} represents real part of permittivity influenced by polarization for lower frequency limit, d is thickness of the material and τ_{EF} is dielectric relaxation time evaluated from imaginary part of the permittivity spectra. The concentration of free protons p can be determined from dielectric spectra and the equation for Debye screening length L_D :

$$L_D = \frac{1}{e} \left(\frac{\epsilon_R \epsilon_0 kT}{p} \right)^{1/2} \quad (4)$$

where ϵ_R is permittivity without electrode polarization and ϵ_0 is the vacuum permittivity and for the L_D it holds:

$$d/L_D = \epsilon_{REF}/\epsilon_R \quad (5)$$

The evaluated concentration $7.1 \times 10^{18} \text{ cm}^{-3}$ corresponds to DC conductivity of protons $2.6 \times 10^{-7} \text{ S.cm}^{-1}$.

TAB. 1. Measured conductivities

	$\sigma \text{ (S.cm}^{-1}\text{)}$
Conductivity caused by protons	2.6×10^{-7}
Conductivity caused by holes and polarons	8.2×10^{-7}
Conductivity measured by four probe ohmic electrodes method	1.9 - 3.5

PROPOSED MODEL

To explain a huge difference between conductivities measured by the four probe ohmic electrode method and conductivities evaluated from the current - voltage characteristics of Au/PANI/Si/In structure and the dielectric spectroscopy, a new model was proposed. Our model assumes that H^+ and Cl^- ions cause redox reactions at the electrodes: hydrogen ions are reduced at the cathode, chlorine ions are oxidized at the anode (see Fig. 2). The neutral chlorine and hydrogen molecules diffuse between the electrodes and react with each other transporting electrons in this way. The atoms and molecules are much more mobile than the ions because they are not influenced by the Coulomb forces. The unbounded hydrogen and chlorine are very probably responsible for the high conductivity of the PANI material. These reactions do not take place in the Au / PANI / Si / In structure polarized in the forward direction, because the electric field at the PANI / Si interface prevents electrons from penetrating into the PANI and thus prevents the conversion of hydrogen ions into atoms.

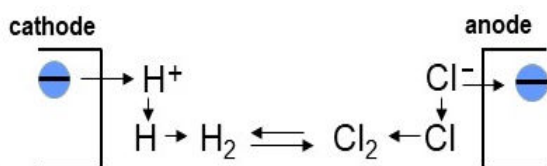


Fig. 2. Illustration of proposed model for transport of the current

CONCLUSIONS

The conductivity of $(1.9 - 3.5) \text{ S.cm}^{-1}$ was measured in protonated PANI with four gold electrodes in the plane of the substrate. The contributions of polarons and holes were determined from Au/PANI/Si/In structure that is not permeable for ions. The impedance measurements give: $\mu_{\text{holes}} = 1.8 \times 10^{-6} \text{ cm}^2/(\text{V.s})$ and $\mu_{\text{polarons}} = 2.7 \times 10^{-7} \text{ cm}^2/(\text{V.s})$. From the analytical expression for current-voltage characteristics [8] the serial resistance and conductivity of holes with small contribution of polarons were determined: $\sigma = 8.2 \times 10^{-7} \text{ S.cm}^{-1}$. Since in the PANI /Si structure ions cause polarization, it is possible to determine their concentration from dielectric spectra: $p = 7.1 \times 10^{18} \text{ cm}^{-3}$. Then, from the evaluated mobility $\mu_{\text{protons}} = 2.3 \times 10^{-7} \text{ cm}^2 \text{V}^{-1} \text{s}^{-1}$ corresponding conductivity $2.6 \times 10^{-7} \text{ S.cm}^{-1}$ was calculated. To explain discrepancy in the conductivity of holes, polarons and ions and conductivity measured on PANI/Au structure we suggested model, where ions have a dual function: firstly, they themselves participate in conductivity and secondly they generate neutral particles of hydrogen and chlorine by redox reaction at the electrodes. These diffuse between the electrodes and transport charge through reactions with each other. The neutral hydrogen and chlorine particles are not influenced by the Coulomb forces therefore are more mobile than ions.

ACKNOWLEDGMENT: This work was supported by grant GAUK no. 190119 of the Grant Agency of Charles University in Prague and SVV - 260 579 financed by Ministry of education of Czech Republic.

REFERENCES

1. Y. Harima, R. Patil, K. Yamashita, N. Yamamoto, S. Ito, A. Kitani, Chem. Phys. Lett. **345**, 239 (2001).
2. M. Chipara, G. Aldica, D. Hui, M. Dimonie, K. T. Lau, L. Georgescu, I. Munteanu, H. Maroscoiu, J. Optoelect. Adv. Mater. **6**, 297 (2004).
3. J. Kim, S. Park, and N. F. Scherer, J. Phys. Chem. **B112**, 15576 (2008).
4. V. J. Babu, S. V. Vempati and S. Ramakrishna, Mater. Sci. Appl. **4**, 1 (2013)
5. Zh. A. Boeva, V. G. Sergeev, Polym. Sci. **C56**, 144 (2014).
6. J. Toušek, J. Toušková, R. Rutsch (Chomutová), I. Křivka, M. Hajná, and J. Stejskal, Synth. Met. **234**, 161 (2017).
7. R. J. Klein, S. Zhang, S. Dou, B. H. Jones, R. H. Colby, J. Runt, J. Chem. Phys. **124**, 144903 (2006).
8. J. Toušková, D. Kindl, E. Samochin, J. Toušek, E. Hulicius, J. Pangrác, T. Šimeček, Z. Výborný, Sol. En. Mat. & Sol. Cells **76**, 135 (2003)

MÖSSBAUER SPECTROMETRY IN THE STUDY OF METALLIC GLASSES

M. Miglierini, marcel.miglierini@stuba.sk, Slovak University of Technology, Institute of Nuclear and Physical Engineering, Ilkovičova 3, 812 19 Bratislava, Slovakia, M. Cesnek, martin.cesnek@fjfi.cvut.cz, Department of Nuclear Reactors, Czech Technical University in Prague, V Holešovičkách 2, 180 00 Praha, Czech Republic

Mössbauer spectrometry is one of few analytical tools that can describe disordered amorphous systems. This can be done via hyperfine interactions between nuclei and electron shells which sensitively probe local short-range order arrangement [1]. Experiments performed in a broad range of temperatures provide information on the evolution of microstructure. This is reflected by continuous modification of hyperfine interactions from magnetic dipole towards electric quadrupole ones. Eventually, the Curie temperature of the investigated metallic glass can be determined.

Metallc glasses are still attracting the interest of researchers namely for their very good soft magnetic properties [2, 3]. With the aim to enhance their practical applications, new compositions are continuously scrutinized [4]. Here, we present Mössbauer spectrometry study of a novel Fe-based metallic glass with addition of Co and P prepared in a form of ribbons by conventional method of planar flow casting. Samples in as-quenched state as well as after annealing at selected temperatures are investigated.

Amorphous $\text{Fe}_{51}\text{Co}_{12}\text{Si}_{16}\text{B}_8\text{Mo}_3\text{P}_8$ (at. %) alloy was produced in a form of 6 mm wide and about 0.02 mm thick ribbons using rapid solidification on a cooper quenching wheel. The amorphicity of the as-quenched material was verified by X-ray diffractometer working with CoK_α radiation. Mössbauer spectra were recorded in transmission geometry using a constant acceleration driver equipped with a $^{57}\text{Co}(\text{Rh})$ radioactive source. Spectra were recorded at temperatures from 4.2 K to 415 K, eventually in external magnetic field of 6 T oriented parallel to the ribbon plane. Mössbauer spectra were analysed by least-square fitting procedure using the NORMOS [5] and CONFIT [6] fitting softwares. Velocity calibration was accomplished by a 12.5 μm thick bcc-Fe foil. Isomer shift values are quoted with respect to the centre of its Mössbauer spectrum taken at room temperature.

Along with as-quenched ribbons also thermally treated samples were analysed. Ribbons 3 - 4 cm in length were annealed at 573 K and 673 K for 1 hour.

Examples of Mössbauer spectra recorded from as-quenched sample at 300 K, 4.2 K, and at 4.2 K in external magnetic field of 6 T are shown in Fig. 1 together with the derived distributions of hyperfine magnetic fields, $P(B)$. The spectra exhibit broad absorption lines characteristic for amorphous systems.

At 4.2 K, the individual lines are better separated one from another due to low temperature. Consequently, the average hyperfine magnetic field, $\langle B \rangle$, has increased from 11.0 T at 300 K up to 17.3 T at 4.2 K. This is documented also by a shift of $P(B)$ distribution towards higher B -values at 4.2 K.

It should be noted, that in the in-field experiments, the value of $\langle B \rangle$ represents an effective magnetic field that locally acts upon the resonant atoms. It results from

mutual interaction of the internal hyperfine magnetic field and the external one. Due to antiferromagnetic coupling, $\langle B \rangle$ decreases down to 11.7 T, nearly the same value as at 300 K. Still, contribution of high B -values is visible namely at the corresponding $P(B)$.

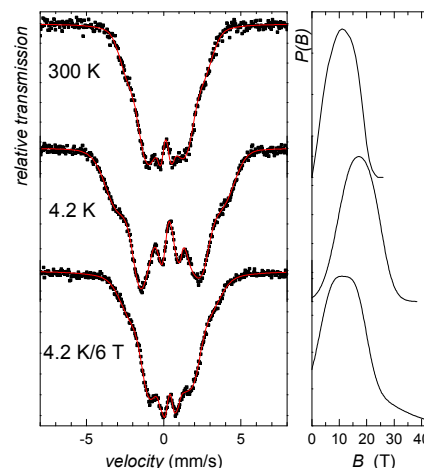


Fig. 1. Mössbauer spectra (left) and corresponding $P(B)$ distributions (right) of the as-quenched sample recorded at 300 K, 4.2 K, and at 4.2 K in external magnetic field of 6 T

Similar behaviour of Mössbauer spectra was observed in the sample annealed at 573 K/1 hr. The obtained $\langle B \rangle$ -values are of 11.5 T, 17.4 T, and 11.7 T for experiments performed at 300 K, 4.2 K, and at 4.2 K in 6 T, respectively. Thus, annealing had only a minor effect on the values of average hyperfine magnetic field. However, notable differences were unveiled in the position of the net magnetization.

In the as-quenched sample, magnetic spins were preferentially oriented by $\sim 24^\circ$ out of the ribbon plane and their arrangement was not changed when the temperature dropped from 300 K down to 4.2 K. External magnetic field of 6 T has aligned the spins into its direction, i.e., in the plane of the sample, as expected.

Situation is remarkably different in the annealed sample. The original angle of $\sim 28^\circ$, which is very close to that of the as-quenched sample, has increased to $\sim 33^\circ$ at 4.2 K which corresponds to almost random orientation of spins. The behaviour of spins in the annealed sample is even more remarkable when external magnetic field was applied. Here, deviation of the spins from the expected in-plane position was unveiled and it amounts $\sim 10^\circ$. Thus, a conclusion can be proposed that the annealing affects the structural short-range order which is demonstrated in the positions of the spins.

Evolution of magnetic microstructure was followed by adopting Mössbauer spectrometry at different temperatures. As a consequence, originally magnetic dipole hyperfine interactions, which are represented by sextets in the Mössbauer spectra, continuously collapsed

and, finally, only pure electric quadrupole interactions were observed. They are represented by doublets and indicate loss of ferromagnetism and transformation of the sample into paramagnetic state. Quantification of the respective spectral parameters provides the value of Curie temperature.

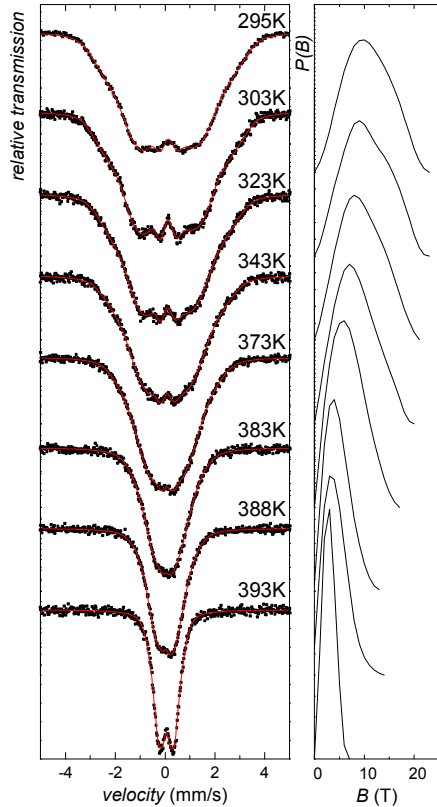


Fig. 2. Mössbauer spectra (left) and corresponding $P(B)$ distributions (right) of the sample annealed at 673 K/1 hr recorded at the indicated temperatures

Variations in the character of hyperfine interactions with temperature are demonstrated in Fig. 2 where Mössbauer spectra of sample annealed at 673 K/1 hr are shown. Continuous narrowing of the spectra with rising temperature of measurement can be clearly seen. At the same time, $P(B)$ distributions are also getting narrower and their maxima are shifted towards lower B -values.

Average $\langle B \rangle$ -values of $P(B)$ are plotted in Fig. 3 as a function of temperature. Curie temperature can be derived from the temperature dependence of $\langle B \rangle$ according to the formula:

$$\langle B \rangle(T) = \langle B \rangle(0) (1 - T/T_C)^\beta \quad (1)$$

where $\langle B \rangle(T)$ is average hyperfine magnetic field at temperature T , $\langle B \rangle(0)$ is saturation magnetic field at $T = 0$ K and β is a critical exponent which for the Heisenberg model equals 0.36. Using this approach, we have determined Curie temperatures of the as-quenched and annealed (673 K) samples to be of 392 K and 398 K, respectively.

Even though one can argue that determination of Curie temperature by Mössbauer spectrometry

performed in a broad temperature range is not an optimal way, it has one undisputable advantage. Namely, the shapes of the Mössbauer spectra that are governed by hyperfine interactions sensitively reflect the local atomic arrangement.

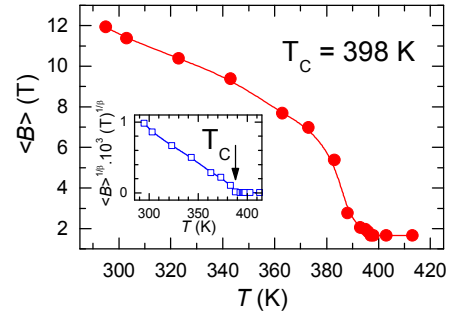


Fig. 3. Average hyperfine magnetic field, $\langle B \rangle$, plotted against temperature of measurement, T , as derived from $P(B)$ distributions of Mössbauer spectra of the sample annealed at 673 K/1 hr. The inset shows linearized dependence according to Eqn. (1)

In addition, because structural features are closely related to magnetic microstructure, Mössbauer spectrometry offers unique opportunity for detailed analysis namely of arrangement of local magnetic moments. Indeed, this information is hardly accessible by another technique.

In this work, we have demonstrated that Mössbauer spectrometry was able to unveil differences between arrangements of spins in the as-quenched and annealed samples. In the latter, close-to-random orientation of spins was observed at 4.2 K and external magnetic field of 6 T was not able to align all spins in its direction. These are consequences of modifications of the microstructure as confirmed by Mössbauer spectrometry.

ACKNOWLEDGMENT: This work was supported by the grants VEGA 1/0130/20, APVV-16-0079 and by the European Regional Development Fund-Project "Center for Advanced Applied Sciences" No. CZ.02.1.01/0.0/0.0/16_019/0000778.

REFERENCES

1. M.B. Miglierini, J. Dekan, M. Cesnek, I. Janotová, P. Švec, M. Bujdoš, J. Kohout, J. Magn. Magn. Mater. **500**, 166417 (2020).
2. H. Li, A. He, A. Wang, L. Xie, Q. Li, Ch. Zhao, G. Zhang, P. Chen, J. Magn. Magn. Mater. **471**, 110 (2019).
3. C. C. Cao, Y. G. Wang, L. Zhu, Y. Meng, X. B. Zhai, Y. D. Dai, J. K. Chen, F. M. Pan, Sci. Rep. **8**, 1243 (2018).
4. C.C. Cao, L. Zhu, Y. Meng, X.B. Zhai, Y.G. Wang, J. Magn. Magn. Mater. **456**, 274 (2018).
5. R. A. Brand, Nucl. Instr. Met. Phys. Res. **B 28**, 398 (1987).
6. T. Žák, Y. Jirásková, Surf. Interface Anal. **38**, 710 (2006).

PHASE TRANSFORMATIONS IN Al-Li-BASED ALLOY STUDIED BY IN-SITU TEM

M. Cieslar, cieslar@met.mff.cuni.cz, R. Krlk, rkralik96@gmail.com, S. Belejov, Sara.belejova@gmail.com, B. Kivsk, krivska.barbora@seznam.cz, M. lapkov, slapakova@karlov.mff.cuni.cz, L. Bajtoov, lucibajtos@gmail.com, J. vrkov, svrckovaj@gmail.com, Charles University, Faculty of Mathematics and Physics, Ke Karlovu 5, 121 16 Prague, Czech Republic

INTRODUCTION

Alloying of Al by Li brings a significant density reduction and an increase of Young modulus [1, 2], which are very attractive features for many spacecraft applications. Additionally, fracture toughness at cryogenic temperatures is improved compared to traditional Al alloys [3, 4, 5]. Li element could be present in a solid solution but the main strengthening effect is reached from the existence of a metastable Al_3Li phase (δ') [6, 7, 1, 8]. Other alloying elements which are often added to Al-Li alloys are Cu and Mg which contribute to a formation of another strengthening phases creating either Cu and Mg-based phases (e.g. Al_2Cu (θ'), Al_2CuMg (S') [9, 10]) or co-precipitating with Li and forming phases such as Al_2CuLi (T_1) and Al_6CuLi_3 (T_2) [6].

However, even though Li brings to Al alloys many benefits, a decrease in the ductility and formability with a noticeable anisotropy of mechanical properties are observed, limiting thus the commercial use of this type of alloys [1]. Anisotropic and inhomogeneous behavior are assigned mainly to a crystallographic texture, main features of main strengthening phases and a fiber grain structure formed during conventional casting and subsequent thermo-mechanical processing including multi-pass hot rolling or extrusion [11, 12].

In-situ transmission electron microscopy (TEM) annealing experiment is a possible option how to directly observe microstructural and phase changes at selected temperatures in thin foils for TEM, because they could simulate a constrained volume of thin (sub)grains.

EXPERIMENTAL DETAILS

A rolled plate prepared from a commercial AA2195 aluminum alloy in a peak-aged conditions with a composition given in Table 1 was used as an input material. Light optical microscopy (LOM) observations of

TAB. 1. Chemical composition in wt. %

Al	Cu	Li	Mg	Ag
96.0	3.7	0.8	0.4	0.3
Zr	Zn	Fe	Si	Ti
0.1	0.25	0.15	0.12	0.1

a grain structure were performed on specimens etched by Barkers solution using Zeiss Axio Observer metallographic microscope. Distribution of main strengthening particles, their crystallographic identification were acquired using JEOL JEM 2000FX electron microscope. In-situ annealing experiments were performed in a heating stage in JEOL 200FX electron microscope. Thin foils (30-100 nm thick) of solution treated (510 °C/530 min) material were in-situ annealed with an effective heating rate of 10 °C/min up to 400 °C.

RESULTS AND DISCUSSION

Results of LOM observations proved a presence of a pancake structure typical for rolled and heat treated materials (Figure 1) in the as-received plate. Partially recovered and partially recrystallized flat grains elongated in the rolling direction form a rather inhomogeneous pattern with average dimensions approximately (in μm) $1000 \times 400 \times 40$. Those dimensions are fairly large in comparison with a size of main strengthening particles (~ 100 nm). Therefore a rather homogeneous distribution of T_1 (Al_2CuLi) in $\{111\}$ and θ' (Al_2Cu) in $\{100\}$ systematic planes were detected by TEM. Rare Al_3Li (δ') precipitates appear in the material in accordance with recent works on 3rd generation of Al-Li based alloys [13].

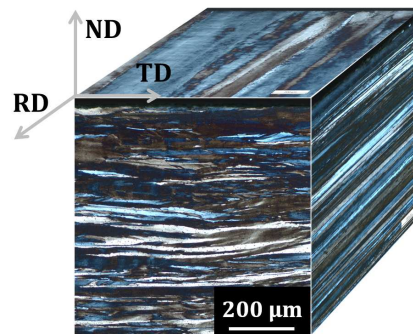


Fig. 1. LOM 3D micrograph of as-received plate structure in peak-aged conditions.

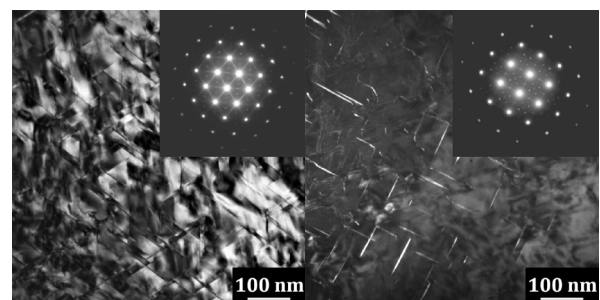


Fig. 2. TEM bright field (BF) and dark field (DF) micrographs of as-received plate microstructure in peak-aged conditions with SAED patterns showing intensive streaks reflecting the presence of plate-like particles in planes parallel to the electron beam.

The material after solution treatment contains only a dispersion of Ag particles (Figure 3a). First plate-like Cu-rich particles form in the foil at temperatures close to 200 °C (Figure 3b) and their ripening and further growth occur at higher temperatures (Figure 3c). However, only one family of plates lying in planes nearly parallel to the foil surface develops as

confirmed also by a diffraction pattern (compare Figure 3d with inset in Figure 2). The results of in-situ observations thus show that a constrained thickness of a material with a size comparable with a characteristic dimension of strengthening particles could significantly suppress their homogeneous distribution in all equivalent planes. A majority of flat profiles prepared by conventional casting methods followed by intensive rolling or extrusion could contain thin grains and subgrains with thicknesses not exceeding 200–500 nm, resulting thus in an amplification of anisotropy of mechanical properties.

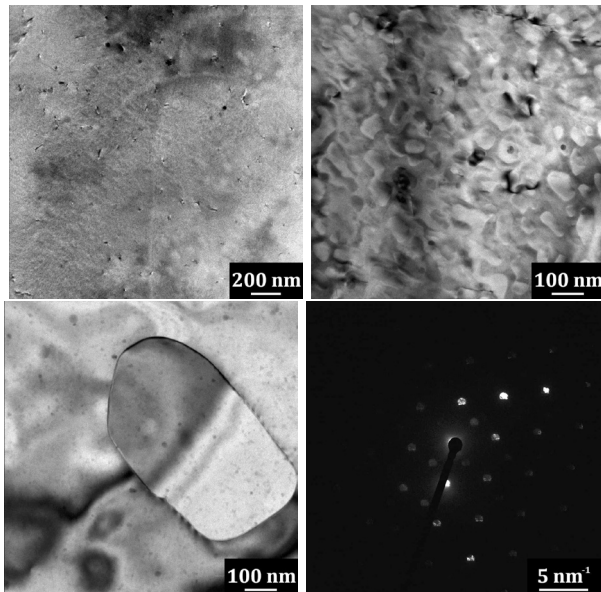


Fig. 3. TEM micrographs of T_1 plates in thin foil during isochronal annealing with an effective heating rate 10 K/min and SAED image near $[110]$ Al orientation. a) BF, 520 °C / 80 min; b) BF, 300 °C; c) BF, 400 °C; d) SAED, 400 °C

CONCLUSIONS

Formation of plate-like T_1 (Al_2CuLi) and θ' (Al_2Cu) precipitates is strongly affected by a constrained volume of a thin foil. Only plates laying in planes nearly parallel with the foil surface were formed. This anisotropic microstructure could generate anisotropy of mechanical properties, therefore less conventional casting and down-streaming processing including continuous casting to a final gauge without any subsequent rolling could be a promising procedure.

ACKNOWLEDGMENT: The financial support of GAR project 20-19170S, SVV-260582 and GAUK project 938120 are highly acknowledged.

REFERENCES

1. E. Lavernia, T. Srivatsan, F. Mohamed, J. Mater. Sci. **25**, 1137 (1990).
2. N. Prasad, A. Gokhale, P. Rao, Sadhana **28**, 209 (2003).
3. B. Kashyap, M. Chaturvedi, Mater. Sci. Eng. A. **281** 88 (2000).
4. H. Qin, H. Zhang, H. Wu, Mater. Sci. Eng. A. **625** 322 (2015).
5. A. Sverdlin, A. Drits, T. Krimova, K. Sergeev, I. Ginko, Adv. Mater. Process. **153** 49 (1998).
6. R. Rioja, J. Liu, Metall. Mater. Trans. A Phys. Metall. Mater. Sci. **43** 3325 (2012).
7. E. Lavernia, N. Grant, J. Mater. Sci. **22** 1521 (1987).
8. B. Bodily, M. Heinemann, G. Bray, E. Colvin, J. Witters., Advanced aluminum and aluminum-lithium solutions for derivative and next generation aerospace structures, SAE 2012 Aerospace Manufacturing and Automated Fastening Conference & Exhibition, 1874 (2012).
9. T. Srivatsan, E. Lavernia, N. Eswara Prasad, V. Kutumbarao, Quasi-Static Strength, Deformation, and Fracture Behavior of Aluminum-Lithium Alloys. In Aluminum-Lithium Alloys: Processing, Properties, and Applications (Elsevier Inc - 2014).
10. R.F. Ashton, D.S. Thompson, F.W. Gayle: The effect of processing on the properties of Al-Li alloys. In Aluminum Alloys – Their Physical and Mechanical Properties (EMAS, Warley - 1986).
11. K.V. Jata, A.K. Singh: Texture and Its Effects on Properties in Aluminum-Lithium Alloys. In Aluminum-Lithium Alloys: Processing, Properties, and Applications (Elsevier Inc - 2014).
12. H. Piehler: Fundamentals of Modelling for Metals Processing. In Fundamentals of modelling for metals processing (ASM Handbook - 2009).
13. Q. Zhang, C. Zhang, J. Lin, G. Zhao, L. Chen, H. Zhang, Mater. Sci. Eng. A **742** 773 (2019).

MONTE CARLO SIMULATIONS OF UPSILON MESON PRODUCTION

J. Bielcik, jaroslav.bielcik@fjfi.cvut.cz, J. Ceska, ceskajak@fjfi.cvut.cz, L. Kosarzewski, leszek.kosarzewski@gmail.com, M. Myska, miroslav.myska@fjfi.cvut.cz, Czech Technical University in Prague, Prague, Czech republic

INTRODUCTION

Quarkonia are an important probe into studying the properties of quark-gluon plasma. Proton-proton collisions serve as an essential baseline for studying the effects of quarkonia in proton-nucleon and nucleon-nucleon collisions. This poster presents the main characteristics of Upsilon mesons from Monte Carlo generation of proton-proton collisions at $\sqrt{s} = 500$ GeV. Monte Carlo event generators PYTHIA and Herwig were used to generate the data. Main aim of the simulations is to explore the dependence of normalised Upsilon meson yield on normalised event multiplicity. Normalised multiplicity dependence is a meaningful tool for understanding the particle production mechanisms and the interplay between soft and hard QCD processes.

MOTIVATION

Υ mesons are a quark-gluon plasma (QGP) probe. The observed production suppression at higher temperatures is caused by Debye-like colour screening of diquark potential [1], cold nuclear matter effects (e.g. shadowing, comover interaction or nuclear absorption [2]) and feed-down contributions.

Υ production mechanism is not yet well understood. The important ingredients are hard scattering (the production of $b\bar{b}$) and bound state formation (colour singlet and colour octet channels).

Current results from CMS and STAR can be seen on (Fig. 1).

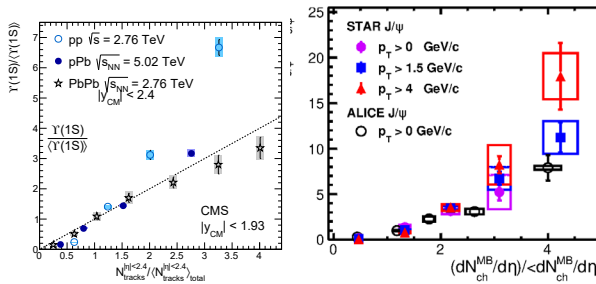


Fig. 1. Left: CMS results for Υ production dependence on charged particle multiplicity in pp @ $\sqrt{s} = 2.76$ TeV [3] Right: STAR results for J/Ψ in pp @ $\sqrt{s} = 200$ GeV [4].

This dependence is sensitive to the interplay between soft and hard processes, influence of multiparton interactions and possible parton saturation signatures.

NORMALISED MULTIPLICITY DEPENDENCE

Experimental observable $N_{\Upsilon} / \langle N_{\Upsilon} \rangle$ defined as:

$$N_{\Upsilon} / \langle N_{\Upsilon} \rangle = (N_{\text{MB}} / N_{\text{MB}}^{\text{bin}}) (N_{\Upsilon}^{\text{bin}} / N_{\Upsilon}) \quad (1)$$

$N_{\text{ch}} / \langle N_{\text{ch}} \rangle \dots$ self-normalised particle multiplicity;
 $N_{\Upsilon} \dots$ total number of events containing Upsilon meson;
 $N_{\Upsilon}^{\text{bin}} \dots$ number of Upsilon events in corresponding multiplicity bin;
 $N_{\text{MB}} \dots$ total number of minimum bias (MB) events;
 $N_{\text{MB}}^{\text{bin}} \dots$ number of MB events in corresponding $N_{\text{ch}} / \langle N_{\text{ch}} \rangle$ bin.

MONTE CARLO EVENT GENERATORS

Two Monte Carlo generators were used in this study: PYTHIA and Herwig.

The main features of PYTHIA include p_T ordered showers, Lund string hadronisation model and direct Upsilon production (dedicated matrix elements for Bottomonia).

Herwig's main features are angular ordered showers, string hadronisation and Upsilon production during hadronisation phase ($b\bar{b}$ matrix element).

SIMULATION

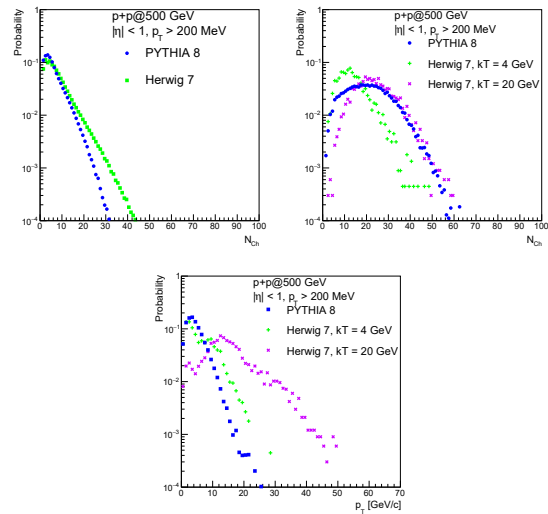


Fig. 2. Multiplicity distributions for MB (top left) and Upsilon(1S) (top right) events and p_T distributions for Upsilon events (bottom).

The study focuses on PYTHIA and Herwig simulations of pp collisions at 500 GeV. For minimum bias events non-single-diffractive SoftQCD events were chosen. Criteria for track selection were: $|\eta| < 1$, $p_T > 0.2$ GeV/c, stable ($\tau > 10$ mm/c) (STAR cuts). Only Upsilon within $p_T > 0$ or 4 GeV/c, electron decay channel only, both electrons within acceptance were selected. Only directly produced Upsilon(1S) were chosen - no feed-down contribution. Herwig production depends on b-parton k_{\perp} cut (4 or 20 GeV/c) - lower values result in spoiling track multiplicity while improving

Upsilon characteristics. This study also includes comparison to STAR preliminary data [5].

The multiplicity and p_T distributions can be seen on (Fig. 2).

RESULTS

Normalised event multiplicity of Upsilon yield was calculated using the equation (1). $N_{ch}/\langle N_{ch} \rangle$ binning was selected in correspondence to STAR preliminary data: 0-1, 1-2, 2-3, 3-8 and 8-100 (overflow bin).

The results can be seen on (Fig. 3).

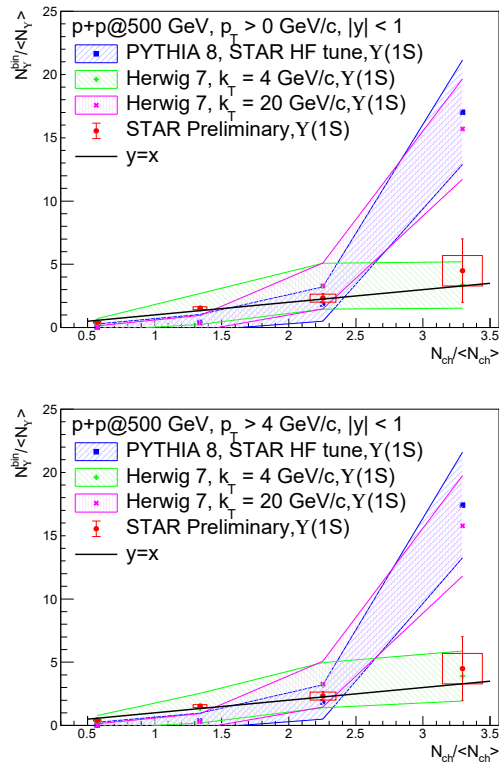


Fig. 3. Normalised Upsilon(1S) yield dependence on normalised multiplicity for PYTHIA and Herwig compared to STAR preliminary data [5]; Top: p_T integrated; Bottom: $p_T > 4$ GeV/c.

CONCLUSION

The minimum bias spectra differ significantly for PYTHIA and Herwig in larger multiplicities. Upsilon production in Herwig has limited validity. Both PYTHIA and Herwig ($k_{\perp} = 20$ GeV/c) predict stronger than linear increase in normalised Upsilon yield in dependence on normalised multiplicity. In comparison to STAR preliminary data [5] both PYTHIA and Herwig ($k_{\perp} = 20$ GeV/c) predict higher values for larger multiplicities, while underestimating smaller multiplicity values. The data suggests, that Upsilon mesons are produced in multi-parton collisions [6], due to stronger than linear increase predicted by PYTHIA and Herwig ($k_{\perp} = 20$ GeV/c).

ACKNOWLEDGEMENTS: The work was supported from the project LTT18002 of the Ministry of Ed-

ucation, Youth, and Sport of the Czech Republic and from European Regional Development Fund-Project "Center of Advanced Applied Science" No. CZ.02.1.01/0.0/0.0/16-019/0000778.

REFERENCES

1. S. Chatrchyan et al. [CMS], Phys. Rev. Lett. **109**, 222301 (2012).
2. Ziwei Lin, C.M. Ko, Phys. Lett. B **503**, 104 (2001).
3. S. Chatrchyan et al. [CMS], JHEP **04**, 103 (2014).
4. J. Adam, et al. [STAR], Phys. Lett. B **786**, 87 (2018).
5. L. Kosarzewski [STAR]: Overview of quarkonium production studies in the STAR experiment, Presented at FAIRness (2019).
6. J. Adam et al. [ALICE], JHEP **09**, 148 (2015).

SPECIFIC HEAT STUDY OF $[\text{Ni}(2aepy)_2\text{Cl}(\text{H}_2\text{O})]\text{Cl}\cdot\text{H}_2\text{O}$ – A SPIN-1 QUASI-ONE-DIMENSIONAL ANTIFERROMAGNET

M. Holub, mariia.holub@student.upjs.sk, E. Čížmár, erik.cizmar@upjs.sk, Institute of Physics, Faculty of Science, P.J. Šafárik University, Park Angelinum 9, Košice, Slovakia, S. Šterbinská, slavomira.sterbinska@student.upjs.sk, J. Kuchár, juraj.kuchar@upjs.sk, J. Černák, juraj.cernak@upjs.sk, Department of Inorganic Chemistry, Faculty of Science, P.J. Šafárik University in Košice, Moyzesova 11, 041 54 Košice, Slovakia

INTRODUCTION

Coordination complexes based on Ni(II) ions attracted major attention as model systems representing $S = 1$ antiferromagnetic (AFM) chains with a non-degenerate gapped ground state in the so-called Haldane phase [1-2]. The magnetic ground state of such a system is sensitive to the relative magnitude of the single-ion anisotropy (D) usually present in Ni(II) based systems and the intrachain exchange interaction (J) parameters. The D/J ratio dictates the system's placement in the complex phase diagram where the quantum-critical point (QCP) equal to $D/J = 1$ exists representing a topological quantum critical point. Experimentally, a most promising candidate $[\text{Ni}(\text{HF}_2)(3\text{Clpy})_4]\text{BF}_4$ ($3\text{Clpy} = 3\text{-chloropyridine}$) being close to $D/J = 1$ was recently suggested [3 - 4], however, there are still disputes whether this system approaches the critical point from the Haldane ($D/J < 1$) or quantum paramagnet (QPM, $D/J > 1$) phase. Since there are only a few examples very close to $D/J = 1$, further study of Ni(II)-based materials deserves attention.

STRUCTURE AND MAGNETIC PROPERTIES

The crystal structure of the studied complex $[\text{Ni}(2aepy)_2\text{Cl}(\text{H}_2\text{O})]\text{Cl}\cdot\text{H}_2\text{O}$, where $2aepy$ is 2-aminoethylpyridine, is ionic and is formed of $[\text{Ni}(2aepy)_2\text{Cl}(\text{H}_2\text{O})]^+$ complex cation, chloride anion, and water solvate molecule (Fig. 1). Hexacoordinate Ni^{2+} ions form zig-zag chains running along the crystallographic b -axis (Fig. 2) through the hydrogen bonds network [5].

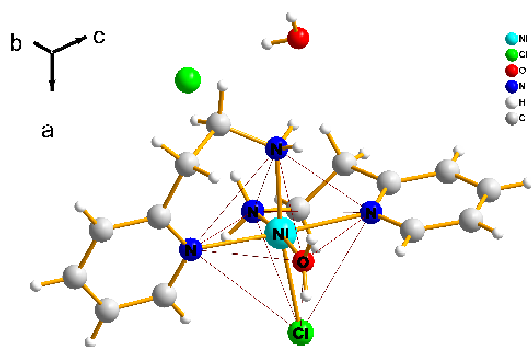


Fig. 1 View on the molecular unit of $[\text{Ni}(2aepy)_2\text{Cl}(\text{H}_2\text{O})]\text{Cl}\cdot\text{H}_2\text{O}$

The previous analysis of magnetic properties of the powdered sample of $[\text{Ni}(2aepy)_2\text{Cl}(\text{H}_2\text{O})]\text{Cl}\cdot\text{H}_2\text{O}$ in the temperature range between 1.8 – 300 K [5] revealed that the studied compound represents a possible candidate of an anisotropic $S=1$ AFM spin chain system in the vicinity of the quantum critical point between Haldane

and QPM phase. A maximum in the temperature dependence of susceptibility at 4.5 K typical for AFM spin systems was described by the spin-chain model [6] with magnetic parameters $D/k_B = 4.05$ K, $J/k_B = 3.55$ K, and $g = 2.35$.

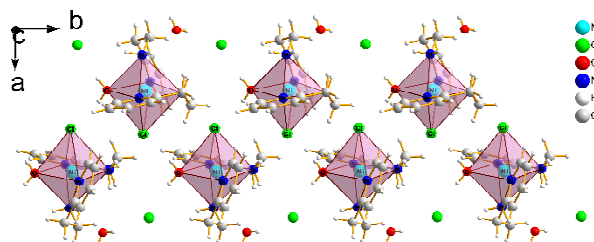


Fig. 2 Supramolecular arrangement of Ni(II) ions shown in the center of distorted coordination octahedra in the ionic crystal structure of $[\text{Ni}(2aepy)_2\text{Cl}(\text{H}_2\text{O})]\text{Cl}\cdot\text{H}_2\text{O}$ creates zig-zag chain motif along the crystallographic b -axis.

SPECIFIC HEAT STUDY

The estimation of the D and J parameters from the magnetic studies of powdered samples of Ni(II)-based anisotropic low-dimensional magnets is often ambiguous and high-quality single crystals are often unavailable. Several experimental methods need to be employed for a better understanding of their properties, the specific heat measurement being one of them. Besides, a very small energy gap in the excitation spectra of Haldane or QPM phase close to QCP at $D/J = 1$ for AFM spin chains is observable clearly only at very low temperatures. The presence of an energy gap between non-magnetic singlet ground state and excited magnetic triplet state can be also hindered by the long-range order (LRO) induced by weak inter-chain exchange interaction or rhombic anisotropy term [4]. The heat capacity of $[\text{Ni}(2aepy)_2\text{Cl}(\text{H}_2\text{O})]\text{Cl}\cdot\text{H}_2\text{O}$ was measured using a powdered sample in the form of a pellet in Quantum Design PPMS (Physical Property Measurement System) equipped with He-3 refrigerator in the temperature range from 0.38 K to 25 K in zero magnetic field. No hint of λ -like anomaly in the temperature dependence of the specific heat was observed down to the lowest experimental temperature limit that would suggest the absence of LRO. We should clarify that in our case the experimental data of total specific heat C_{mol} (shown in Fig. 3 as C_{mol}/T) consist of a phonon (C_{lat}) and magnetic (C_{mag}) contribution and for further analysis, the subtraction of C_{lat} from total specific heat is necessary to obtain the magnetic specific heat C_{mag} . For the correct simulation of the total specific heat in a wide temperature range (including high temperatures where phonon contribution eventually dominates) combined Debye-Einstein model

$$C_{lat} = \frac{3A_D}{\left(\frac{\theta_D}{T}\right)^3} \int_0^{\frac{\theta_D}{T}} \frac{x^4 e^x}{(e^x - 1)^2} dx + A_E \left(\frac{\theta_E}{T}\right)^2 \frac{e^{-\frac{\theta_E}{T}}}{\left(e^{-\frac{\theta_E}{T}}\right)^2} \quad (1)$$

was used for the description of C_{lat} with $x = \frac{\hbar\omega}{k_B T}$, where ω represents phonon frequency, θ_D and θ_E are Debye and Einstein temperature, respectively. Parameters A_D and A_E represent characteristic constants for Debye and Einstein model, respectively. The temperature dependence of the total specific heat was then analyzed by formula $C_{mol} = \frac{a}{T^2} + C_{lat}$ at temperatures above 10 K, where simple approximation for the high-temperature behavior of magnetic specific heat $C_{mag} = \frac{a}{T^2}$ of low-dimensional magnets (well above the maximum observed at 2.4 K) can be used. The fit of the model formula for C_{mol}/T to the experimental data yielded a following set of parameters: $A_D = 63.0$ J/Kmol, $\theta_D = 92.7$ K, $A_E = 105.7$ J/Kmol, $\theta_E = 165.1$ K and $a = 178.1$ JK/mol. After the subtraction of the phonon contribution, the C_{mag} shown in Fig. 3 can be analyzed further.

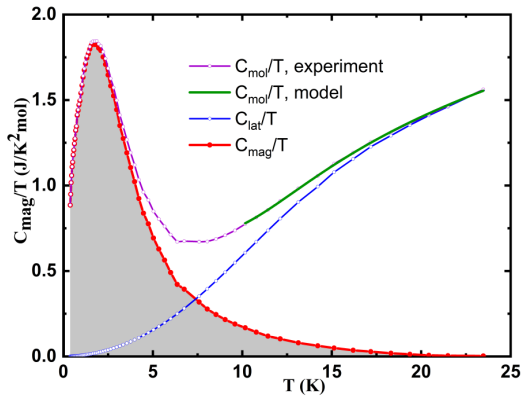


Fig. 3. Temperature dependence of the rescaled specific heat measured in zero magnetic field (purple line with symbols) showing the procedure of the subtraction of the phonon contribution (blue line with symbols). The green line represents the fit of high-temperature model for C_{mol}/T and the gray area represents magnetic entropy removed in the experimental temperature range calculated from magnetic specific heat (red line with symbols).

Using De Klerk's formula for a Heisenberg magnet [7], namely $CT^2/R = 3\Theta^2/(2z)$, where $\Theta = zJS(S+1)/(3k_B)$ and R is gas constant, the equation $a = (2/3)Rz/(J/k_B)^2$ is derived to estimate exchange coupling within this simple model from the high-temperature expansion of the magnetic specific heat for spin $S=1$. We obtain the value of the exchange coupling $|J/k_B| = 4.0$ K assuming isolated chains, where the number of next-nearest neighbors is $z = 2$, which is consistent with the estimates from the magnetic data (although the influence of single-ion anisotropy is here neglected). Next, the magnetic entropy at zero magnetic field $S_{mag} = 8.74$ J/Kmol was calculated by the

integration of C_{mag}/T in the experimental temperature range. It is very close to the theoretical prediction $S_{theor} = R \ln(2S + 1) = 9.13$ J/Kmol for a magnetic system with spin $S = 1$. The high-temperature contribution above 25 K to the magnetic entropy is negligible and the difference between S_{theor} and S_{mag} is small as evidence of a very weak inter-chain interaction. This would suggest an absence of LRO (non-magnetic ground state) or a possible transition into LRO located at very low temperatures that would allow observation of the energy gap from further low-temperature studies. The ongoing work is also focused on the analysis of temperature dependence of C_{mag} for better estimation of D , J , and possible next-nearest neighbor interaction within the chains. Since only simple numerical predictions for the specific heat of anisotropic $S = 1$ AFM spin chains exist in the literature, the Quantum Monte Carlo method will be employed for the simulations.

CONCLUSIONS

The *zig-zag* chains formed in the structure of $[\text{Ni}(\text{2aepy})_2\text{Cl}(\text{H}_2\text{O})]\text{Cl}\cdot\text{H}_2\text{O}$ can be distinguished. The studies of magnetic properties yield the set of parameters $D/k_B = 4.05$ K, $J/k_B = 3.55$ K, and analysis of the specific heat and magnetic entropy shows that inter-chain interaction is very small presumably preserving non-magnetic ground state down to very low temperatures. That suggests that the studied system is an excellent example to study the properties of anisotropic $S = 1$ AFM spin chains near the QCP between Haldane and QPM phase.

ACKNOWLEDGMENT: This work was supported by projects VEGA 1/0426/19, APVV-18-0197, and APVV-18-0016.

REFERENCES

1. F.D.M. Haldane, Phys. Lett. A **93**, 464 (1983).
2. F.D.M. Haldane, Phys. Rev. Lett. **50**, 1153 (1983).
3. J.L. Manson et al., Inorg. Chem. **51**, 7520 (2012).
4. D.M. Pajerowski et al., Phys. Rev. B **101**, 094431 (2020).
5. S. Šterbinská et al., Polyhedron **187**, 114654 (2020).
6. J. Brambleby et al., Phys. Rev. B **95**, 134435 (2017).
7. D. De Klerk, Physica **12**, 512 (1946).

SHORT-RANGE CORRELATION INVESTIGATION IN DEUTERON INDUCED REACTIONS

M. Janek¹, janek@fyzika.uniza.sk, V.P. Ladygin², A.V. Averyanov², E.V. Chernykh², D. Enache³, Yu.V. Gurchin², A.Yu. Isupov², J-T. Karachuk^{2,3}, A.N. Khrenov², D.O. Krivenkov², P.K. Kurilkin², N.D. Ladygina², A.N. Livanov², O. Mezhska⁴, S.M. Piyadin², S.G. Reznikov², Ya.T. Skhomenko⁵, G. Tarjanyiova¹, A.A. Terekhin², A.V. Tishevsky².

¹Physics Department, University of Zilina, Zilina, Slovakia, ²Joint Institute for Nuclear Research, Dubna, Russia, ³Advanced Research Institute for Electrical Engineering, Bucharest, Romania, ⁴University of P. J. Shafarik, Kosice, Slovakia, ⁵BSNRU, 308015, Belgorod, Russian Federation,

INTRODUCTION

One of the approaches to investigate the equation-of-state of dense nuclear matter is the study of the short-range correlations of nucleons in nuclei. Short-range correlations have densities comparable to the density in the center of a nucleon and they can be considered as the drops of cold dense nuclear matter. Dp elastic and dp breakup processes are investigated at Internal Target Station of Nuclotron; dp elastic process in angular range from 60 - 135 degree in c.m. in the energy range from 400 - 2000 MeV; dp breakup reaction in angular the range from 19 - 56 degree from 300 - 500 MeV. Results which comes from analyzing powers of dp elastic scattering show strong sensitivity to the short range spin structure of the isoscalar nucleon-nucleon correlations. Description based on relativistic multiple-scattering model provides reasonable agreement at small and large angles but the problem is related to angles between them.

RESULTS AND CONCLUSIONS

Polarization of deuteron beam is provided by polarization ion source (PIS). Ideal values of polarizations were $p_z, p_{zz} = (-1/3, \pm 1)$. PIS can provide unique opportunity for the studies of the spin effects and polarization phenomena in few body systems at Internal Target Station (ITS). Good values of vector and tensor polarizations were obtained at low energy polarimeter [1]. The polarization was flipped each spill between "up" and "down" and "no polarization". Polarization of deuteron beam was monitored continuously during whole experiment. Vector and tensor polarizations are obtained from the asymmetries and known values of analyzing powers of dp elastic reaction at energy of 270 MeV. Measured values of polarization for "+ mode" when tensor component is positive are: $p_z = -0.190 \pm 0.009$, $p_{zz} = 0.533 \pm 0.017$ and for "- mode": $p_z = -0.230 \pm 0.007$, $p_{zz} = -0.705 \pm 0.013$.

TAB. 1. Measured values of iT_{11} and T_{20} analyzing powers for four detector configurations. Detector configurations are determined by polar (θ_1, θ_2) and azimuthal (ϕ) angles. The azimuthal angle ϕ is the angle between the detector and beam direction.

con.	θ_1	θ_2	ϕ	iT_{11}	T_{20}
5,4	34.8	52.5	135	0.10 ± 0.02	0
6,3	36.8	50.4	45	0.11 ± 0.06	0
1,6	34.8	36.8	135	0.55 ± 0.15	0.13 ± 0.30
5,2	34.8	36.8	135	0.39 ± 0.13	-0.09 ± 0.27

iT_{11} analyzing power at 72.3° and 76.5° in cm was

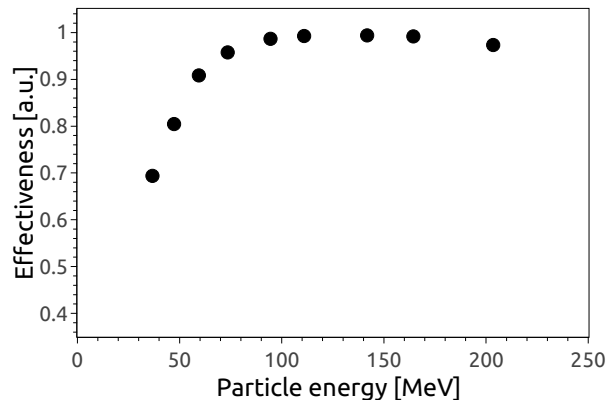


Fig. 1. Proton detector efficiency of $\Delta E - E$ detector No. III.

measured under pp quasi conditions, obtained values are 0.10 ± 0.02 and 0.11 ± 0.06 , respectively. They are in agreement with world pp - elastic scattering data within experimental errors. Combined values of last two rows of TAB. 1 of the vector iT_{11} and tensor T_{20} analyzing powers at polar angles of 34.8° and 36.8° and difference in azimuthal angles of 135° are 0.47 ± 0.10 and 0.02 ± 0.20 [2].

Two detector configurations, longitudinal and perpendicular, were used in order to investigate detector's efficiency of particle registration.

Longitudinal configuration is used to investigate possible variation of detector efficiency of particle registration due to misalignment. Results show that there is some efficiency decreasing which increases with detector misalignment.

Perpendicular configuration is used to investigate detector efficiency as a function of a depth in E - scintillator. Results obtained from simulations in ROOT and GEANT4 packages show that particles with energy 75 MeV and below stop at the beginning of the E - detector. Efficiency is decreasing with decreasing of position from photocathode of E scintillator. Efficiency as a function of particle's energy is shown in Fig. 1.

Cross section of dp elastic scattering and predictions of relativistic-multiple scattering model [3] at 1400 MeV was obtained. Δ isobar contribution improves the qualitative description of the cross section at 1400 MeV. Good agreement is observed up to 70°.

Angular dependence of dp elastic scattering of the vector A_y , tensor A_{yy} and A_{xx} at deuteron energy of 400, 700 (see Fig. 2) and 1000 MeV was obtained along with the predictions based on relativistic multiple scattering model. Large contribution which comes from double scattering term is observed, but it does

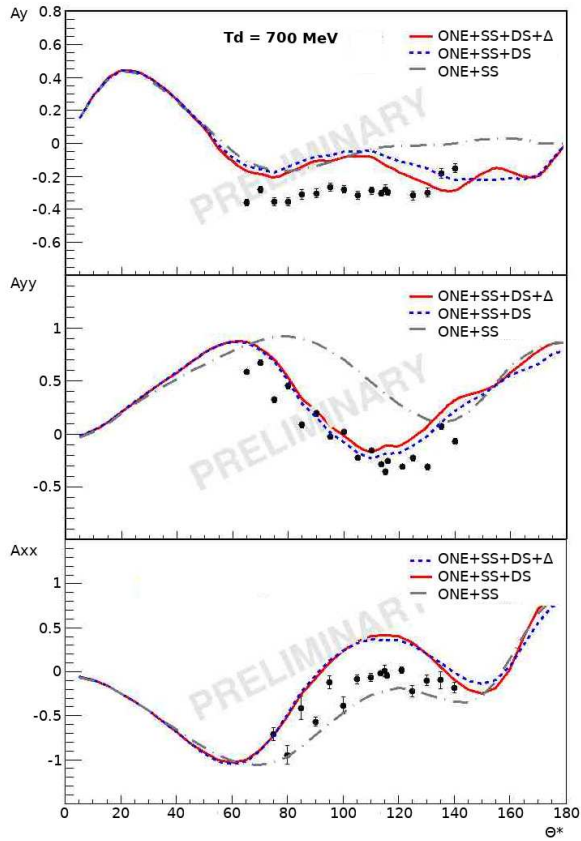


Fig. 2. Angular dependence of dp elastic scattering of the vector A_y , tensor A_{yy} and A_{xx} at deuteron energy of 700 MeV. Curves are predictions based on relativistic-multiple scattering model [3] when one nucleon exchange and single scattering term, additional double scattering term and Δ isobar are taken into account.

not improve the description of analyzing powers in all cases, rather at small angles. Moderate contribution which comes from Δ isobar is found at higher energies.

Preliminary results of the five fold differential cross section of dp breakup reaction investigated at 400 MeV for the case of detector arms placed at the angles of 27° and 43° , 31° and 43° , 35° and 43° , 39° and 43° are presented in Fig. 3. The systematic error (under evaluation) is mainly affected by the procedure of Polyethylene - Carbon subtraction, the solid angle of the detectors and the normalization coefficient determinations. One can see some structures in kinematic S -curve at the vicinity of ≈ 100 MeV and ≈ 260 MeV. The next step is to obtain results at other angles to investigate observed structure in recent data.

Possible future measurements on extracted beam of Nuclotron include the measurements of the tensor A_{yy} and vector A_y analyzing powers in inclusive deuteron breakup, $A(d, p)X$, at large transverse proton momenta [4] at the highest available energy at Nuclotron; of the tensor A_{yy} and vector A_y analyzing powers [5] (and, possibly, vector polarization transfer coefficient C_y^y [6]) in the inelastic deuteron scattering, $A(d, d')X$, in the vicinity of the baryonic resonances excitation; of the tensor A_{yy} and vector A_y analyzing powers in the inclusive pion production, $A(d, \pi^-)X$, also at the highest available energy at Nuclotron.

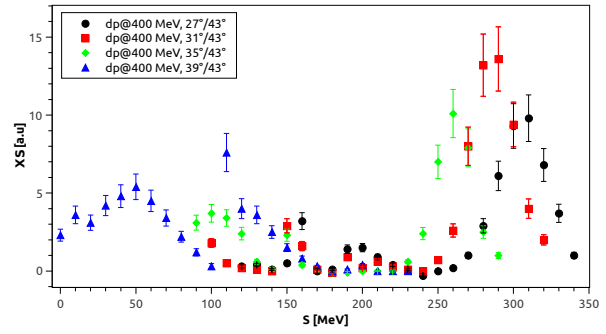


Fig. 3. Preliminary results of the five fold differential cross section of dp breakup reaction investigated at 400 MeV for the case of detector arms placed at the angles of 27° and 43° (black symbols), 31° and 43° (red symbols), 35° and 43° (green symbols), 39° and 43° (blue symbols), respectively. Only statistical errors are shown.

The inclusive measurements of the analyzing powers in inclusive deuteron breakup and the inelastic deuteron scattering in the vicinity of the baryonic resonances excitation can be also performed. Baryonic resonances spin properties can be studied at the energies between 2 and 6 GeV of the deuteron kinetic energy [6] [7].

Future spin studies require also advanced deuteron beam polarimetry to more detailed studies of reaction mechanisms and structure of short nucleon correlations of deuteron induced reactions at intermediate energies.

ACKNOWLEDGMENT: The work has been supported in part by the Ministry of Education, Science, Research and Sport of the Slovak Republic (VEGA Grant No. 1/0113/18), by the RFBR under grant No.19-02-00079a and by JINR- Slovak Republic cooperation programs in 2020.

REFERENCES

1. M. Janek et al., Few-Body Systems Vol. 58 Issue 2, 40 (2017).
2. M. Janek et al., Communications: Scientific letters of the University of Zilina **3**, 62 (2017).
3. N. B. Ladygina, Eur.Phys.J. **A52**, 199 (2016).
4. L. S. Azhgirey et al., Phys.Lett. **B387**, 37 (1996).
5. V. P. Ladygin et al., Phys. Atom. Nucl. **69**, 852 (2006).
6. V. P. Ladygin, N.B. Ladygina, Phys. Atom. Nucl. **65**, 182 (2002).
7. A. Jerusalemov et al., Eur. Phys. J. **A51**, 83 (2015).

PROPERTIES OF YELLOW BAND IN GaN LAYERS

T. Hubáček, hubacekt@fzu.cz, V. Jary, jary@fzu.cz, K. Kuldová, kuldova@fzu.cz, A. Hospodková, hospodko@fzu.cz, J. Pangrác, pangrac@fzu.cz, E. Hulicius, hulicius@fzu.cz, Institute of Physics, Czech Academy of Sciences v.v.i., Cukrovarnická 10, 162 00, Prague 6, Czech Republic

INTRODUCTION

Nowadays, gallium nitride (GaN) is the second most important semiconductor material after the silicon. GaN has found utilization in optoelectronic devices, such as blue light-emitting or laser diodes, or in high-power and high-frequency applications, such as high electron mobility transistors.

The most important technology, which is used for the growth of nitrides, is Metal Organic Vapour Phase Epitaxy (MOVPE). Since 1960s, when the first epitaxial GaN layers were prepared, a lot of research and improvements were done, but there are still plenty of open questions and challenges which need to be answered and solved.

MOVPE grown GaN layers are usually unintentionally n-doped, due to oxygen impurities (O_N) [1]. Increased fermi level energy in n-type semiconductor can also enhance formation of acceptors and these acceptor levels are responsible for different kinds of defect luminescence. It can be detrimental to some applications and suppression of these acceptor levels is essential.

Typical defect bands in the luminescence spectra of GaN layers are blue band (BB) and yellow band (YB). BB has maximum around 2.9 eV and Zn_{Ga} [2] or C_N-H_i [3] shallow acceptor levels were found as a source of this band. YB has maximum around 2.2 eV and source of this band is deep acceptor level 0.9 eV above valence band. C_N (and its complexes) [4,5] and V_{Ga} (and its complexes) [6, 7] were suggested as a source of deep acceptor level responsible for YB emission.

We studied influence of different technological parameters of MOVPE grown n-doped GaN layers on YB intensity. Different carrier gas (H_2 or N_2), type of Ga precursor (TMGa or TEGa), temperature and growth rate was investigated [8]. We found out that carrier gas has the most important impact on the YB intensity. From the positron annihilation spectroscopy measurements, we found out that nitrogen carrier gas influences clustering of V_{Ga} to big complexes and suppresses YB intensity significantly [8]. In this work, we continue in more detailed study of YB luminescence properties of one selected sample.

EXPERIMENTAL

Aixtron 3x2 CCS MOVPE apparatus equipped with LayTec EpiCurveTT system for in situ measurement was used for the preparation of structures. Sapphire substrate with c-plane orientation was used for the growth. Standard GaN nucleation and coalescence layer was grown on the substrate. On top, 1 μm thick GaN layer doped with silicon was grown from TMGa precursor in N_2 atmosphere. The growth temperature was 950°C, which is quite low for a sufficient

decomposition of TMGa molecules and thus carbon impurities should be incorporated in layer. Secondary-ion mass spectrometry (SIMS), provided by EAG laboratories, confirmed our expectation and carbon concentration in the sample was around $3 \times 10^{17} \text{ cm}^{-3}$.

The main characterization technique used in this article was temperature dependence photoluminescence (PL). PL spectra were measured using a custom-made spectrofluorometer 500M Horiba Jobin Yvon with a steady state deuterium lamp as an excitation source. The detection part of the setup involved a single-grating monochromator and a photon counting detector TBX-04. Measured spectra were corrected for the spectral dependence of detection sensitivity. PL measurements within the 8 - 500 K temperature region were performed using a closed cycle refrigerator (Janis Instruments).

Nanosecond nanoLED pulsed light source (Horiba) was used as an excitation source for the photoluminescence decay curves measurement. Measured curves were convoluted in SpectraSolve software package for determination of true decay curves.

RESULTS

Room temperature photoluminescence spectrum of our samples showed very intense YB and suppressed GaN excitonic band (see Fig. 2 in [8]). Based on the SIMS results, we expected that the source of the deep acceptor level responsible for YB in our sample should be carbon [8]. It is the most common impurity in MOVPE grown layers, especially in layers grown from TMGa precursor at lower temperature (below 1000°C).

In this article, low temperature photoluminescence spectrum was measured and from the results we tried to distinguish the source of the YB. Fig. 1 shows PL spectrum at $T = 8K$ of investigated sample.

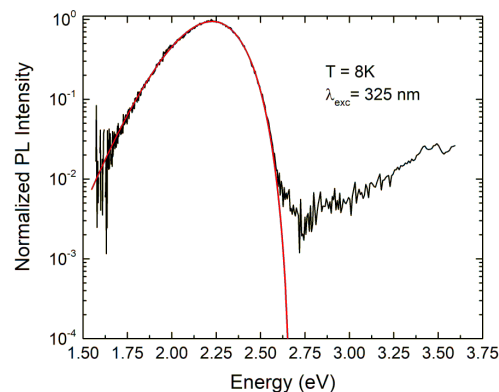


Fig. 1. PL spectrum at $T = 8K$ of n-doped GaN layer. The YB shape (red line) was calculated using equation (1) with the following parameters: $I_{\max} = 0.94$, $\hbar\omega_{\max} = 2.23 \text{ eV}$, $S_c = 6.9$ and $E_0^* = 2.67 \text{ eV}$.

For the analysis of the YB shape from the low temperature PL spectrum, we have used formula derived from one-dimensional configuration coordinate model [9]:

$$I(\hbar\omega) = I_{\max} \exp \left[-2S_e \left(\sqrt{\frac{E_0^* - \hbar\omega}{E_0^* - \hbar\omega_{\max}}} - 1 \right)^2 \right] \quad (1)$$

where S_e is the Huang-Rhys factor for the excited state, I_{\max} is the PL intensity at the band maximum, $E_0^* - \hbar\omega_{\max}$ is the relaxation energy in the ground state, $\hbar\omega_{\max}$ is the position of the YB maximum and $E_0^* = E_0 + 0.5 \hbar\Omega$, where E_0 is the zero phonon line and $\hbar\Omega$ is the energy of the effective phonon mode in the excited state [10].

Our data can be fitted using equation (1) with the parameters: $I_{\max} = 0.94$, $\hbar\omega_{\max} = 2.23$ eV, $S_e = 6.9$ and $E_0^* = 2.67$ eV. The simulated curve fits the measured data very well (see Fig. 1). Our results are in a good agreement with the parameters of YB shape in the Reshchikov's article [10]. In this article, MOVPE grown n-doped GaN layer were analysed and the shape of the YB was fitted with the same equation and parameters: $I_{\max} = 1$, $\hbar\omega_{\max} = 2.22$ eV, $S_e = 7.4$ and $E_0^* = 2.68$ eV. Strong YB in this sample was attributed to carbon-related defect (C_N) [10]. Our results (low temperature PL measurement and SIMS analysis) support the hypothesis about the C_N defect which is responsible for the YB in our sample.

We have also measured room temperature decay time of the YB. Measured decay curve and 3-exponential fit, is shown in Fig. 2.

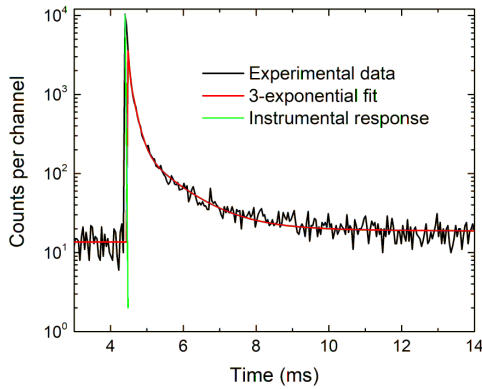


Fig. 2. Room temperature decay curve measured at 543 nm emission wavelength (YB maximum). Fit was provided according to equation (2) with three decay time components: 0.15, 0.98 and 47 ms.

Experimental data in Fig. 2 were fitted using equation (2). Data were fitted with three decay time components.

$$I = \sum_{i=1}^n A_i \exp \left[-\frac{t}{\tau_i} \right] \quad (2)$$

Decay time of the YB is in the range of hundreds of microseconds. The fastest component has 150 μ s decay

time and the relative light sum is around 35 %. Decay time of the YB in the same range was also observed in the article [11]. The second and the third component of the fit has 0.98 and 47 ms decay time and the relative light sum is around 28 % and 37 %, respectively.

Such a slow decay time of YB can be detrimental for some applications and YB luminescence should be suppressed as much as possible.

CONCLUSIONS

In this article, luminescence properties of n-doped GaN layer, grown with specific growth condition to obtain high carbon concentration in layer, were studied. Room temperature PL spectrum showed very strong YB intensity and suppressed GaN excitonic band.

Properties of YB were studied by low temperature PL measurement and decay time measurement. Shape of the YB was analysed with one-dimensional configuration coordinate model and it was shown that the YB properties are similar to properties of YB caused by carbon-related defect (C_N). Our PL results are in a good agreement with SIMS analysis, where higher carbon concentration was detected.

Decay time of YB is in the hundreds of microseconds. This value corresponds to published results of other groups. This slow defect band can be detrimental for some applications and needs to be suppressed.

In conclusion, low temperature PL measurement is a good tool for investigation the source of YB in different MOVPE grown GaN layers. Understanding of the origin of YB can help technologists to improve the growth process and eliminate YB source.

ACKNOWLEDGMENT: The authors acknowledge the support of MSMT project no. NPU LO1603 – ASTRANIT.

REFERENCES

1. T. Zhu, R.A. Oliver, Phys. Chem. Chem. Phys. **14**, 9558 (2012).
2. D.O. Demchenko et al., Phys. Rev. B **88**, 115204 (2013).
3. D.O. Demchenko et al., J. App. Phys. **119**, 035702 (2016).
4. J.L. Lyons et al., Appl. Phys. Lett. **97**, 152108 (2010).
5. D.O. Demchenko et al., Phys. Rev. Lett. **110**, 087404 (2013).
6. J.L. Lyons et al., Phys. Status Solidi B **252**, 900-908 (2015).
7. Z. Xie et al., Appl. Phys. Lett. **112**, 262104 (2018).
8. T. Hubáček et al., J. Cryst. Growth **531**, 125383 (2020).
9. M.A. Reshchikov et al., Phys. Rev. B **90**, 035207 (2014).
10. M.A. Reshchikov et al., Phys. Rev. B **94**, 035201 (2016).
11. C. Díaz-Guerra et al., J. Appl. Phys. **94**, 2341 (2003).

THE STUDY OF LATTICE DYNAMICS IN LOW-DIMENSIONAL QUANTUM MAGNETS WITH CHAIN-LIKE CRYSTAL STRUCTURE

O. Vinnik¹, olha.vinnik@student.upjs.sk, L. Lederová¹, livia.lederova@student.upjs.sk, R. Tarasenko¹, robert.tarasenko@upjs.sk, L. Kotvytska¹, liliia.kotvytska@student.upjs.sk, K. Zakuřanská², katarina.zakutanska@gmail.com, N. Tomašovičová², nhudak@saske.sk, A. Orendáčová², alzbeta.orendacova@upjs.sk, ¹Institute of Physics, P. J. Šafárik University, Park Angelinum 9, 04001 Košice, Slovakia, ²Institute of Experimental Physics of SAS, Watsonova 47, 04001 Košice, Slovakia

INTRODUCTION

Square lattice represents paradigm of two-dimensional (2d) magnetism. While ground-state and finite-temperature properties are well known [1], the study of the effects of spatial anisotropy within magnetic layer started only recently. Magnetic layers of quasi-two-dimensional quantum magnets Cu(en)Cl₂, Cu(tn)Cl₂, Cu(en)₂SO₄ and Cu(en)(H₂O)₂SO₄ (en = C₂H₈N₂, tn = C₃H₁₀N₂) were described within spin = 1/2 Heisenberg antiferromagnetic models on the rectangular and zig-zag-square lattice with nearest-neighbor intralayer couplings $J_1 > J_2$ [2, 3]. Both lattices interpolate between chain ($R = J_2/J_1 = 0$) and square lattice ($R = 1$). The largest spatial anisotropy ($R = 0.2$) and the strongest effect of interlayer coupling J' was observed in Cu(en)Cl₂, while somewhat lower R and much weaker J' was indicated in Cu(tn)Cl₂ and Cu(en)(H₂O)₂SO₄ ($R = 0.3 - 0.5$).

All studied compounds are characterized by one-dimensional polymeric structure. While in Cu(en)Cl₂ and Cu(tn)Cl₂ covalent ladders are packed to 3d structure via hydrogen bonds, in other two compounds the covalent chains are bound together via hydrogen bonds. Preliminary studies of lattice specific heat of Cu(en)Cl₂ and Cu(tn)Cl₂ up to 300 K revealed structural phase transition at 138 and 160 K, respectively [4]. Using existing vibrational data above 400 cm⁻¹, the specific heats were described as a sum of the contribution of averaged acoustic modes described within Debye approximation

$$C_{Deb} = 9Nk_B \left(\frac{T}{\theta_D} \right)^3 \int_0^{\theta_D/T} \frac{z^4 \exp(z) dz}{(\exp(z)-1)^2} \quad (1)$$

where $z = \hbar\omega/(k_B T)$ and optical modes described within Einstein theory

$$C_{Ein} = Nk_B \frac{z^2 \exp(z)}{(\exp(z)-1)^2}. \quad (2)$$

To achieve good agreement with experimental specific heat data, other optical modes with energies below 400 cm⁻¹ were numerically added. In both compounds, the deviation from the Debye function appeared already above 15 K indicating the presence of low-energy vibrational modes. The present work is focused on the comparative study of lattice subsystems in the chain-like materials Cu(en)₂SO₄ and Cu(en)(H₂O)₂SO₄. For that purpose, specific heat and Raman spectrum were investigated and analysed in the same manner as aforementioned ladder-like compounds. The main goal

of the work is specification of the temperature region in which acoustic modes dominate to find potential correlation between the formation of magnetic correlations and dominant lattice modes.

EXPERIMENTAL DETAILS

Single crystal specific heat measurements in zero magnetic field were performed from 2 to 300 K using commercial Quantum Design PPMS device. Measurements of addenda were performed for each sample separately. Raman spectra of polycrystalline samples enclosed in aluminum capsules were recorded at 300 K from 50 to 3000 cm⁻¹ in commercial Bruker FTIR spectrometer.

RESULTS AND DISCUSSION

Both compounds represent magnetic insulators, therefore only lattice (C_{latt}) and magnetic (C_{mag}) contribution to the total specific heat (C_{tot}) can be considered. Temperature dependence of specific heat of Cu(en)(H₂O)₂SO₄ (CUEN) was measured from 2 to 300 K. Unlike the aforementioned ladder-like compounds, no structural phase transition was observed in the interval between 2 and 300 K. Previous low-temperature analysis of magnetic specific heat of CUEN [5] revealed that the corresponding magnetic model deviates from the last term of high-temperature expansion $1/T^2$ below about 6 K. At higher temperatures, C_{latt} can be effectively approximated as $bT^3 + cT^5 + dT^7$ and at moderate temperatures, the approximation $C_{tot} \sim a/T^2 + bT^3 + cT^5 + dT^7$ can be applied. The fitting procedure in the interval from 6 to 15 K provided slightly different parameters than those reported in [5], probably due to some contribution of Apiezon in the previous experiment. The best agreement was found for $a = 24.4$ JK/mol, $b = 6.17 \times 10^{-4}$ J/(K⁴ mol), $c = 2.97 \times 10^{-6}$ J/(K⁶ mol), $d = -6.01 \times 10^{-9}$ J/(K⁸ mol). Then for evaluation of lattice specific heat below 6 K, the extrapolation of $bT^3 + cT^5 + dT^7$ was applied while above 6 K, $C_{latt} = C_{tot} - a/T^2$ was used (Fig. 1). Using standard relation

$$b = \frac{12}{5} \pi^4 Nk_B \frac{1}{\theta_D^3}, \quad (3)$$

Debye temperature $\theta_D = 146$ K was calculated. The value was applied for the evaluation of the contribution of acoustic phonons (Eq. 1) to the lattice specific heat. As can be seen in Fig. 1, the deviation of data from Eq. 1 appear already above 10 K, which indicates the activation of some low-energy optical modes. Considering infrared (IR) active modes [6] 102, 150,

227, 246, 256, 332, 406, 453, 474, 540, 625, 679, 762, 897, 964, 986, 1065 (in cm^{-1}) and Raman modes 68, 88, 107, 128, 151, 163, 170, 248, 296, 332, 413, 442, 454, 479, 487, 548, 599, 739, 799, 824, 863, 878, 925, 938, 959, 979, 1021, 1036, 1046 (Fig.2), the specific heat within Einstein approximation (Eq.2) was calculated. The resulting lattice specific heat is in good agreement with experimental data (Fig.1).

$$C_{latt} = C_{Deb} + \sum_i C_{Ein}^i \quad (4)$$

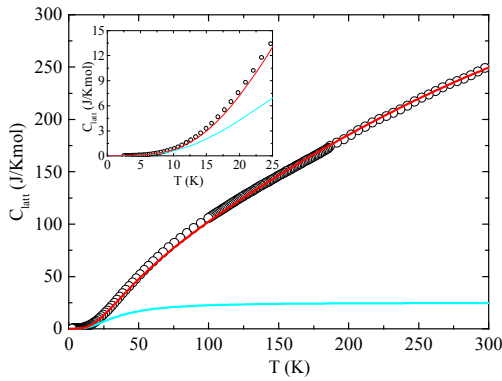


Fig. 1. Temperature dependence of lattice specific heat of CUEN single crystal. Cyan line represents Eq. 2, red line corresponds to Eq. 4. Inset: Zoom of the main plot at lowest temperatures

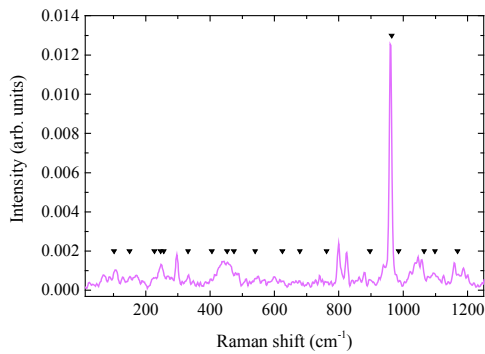


Fig. 2. Raman spectrum of polycrystalline CUEN. Symbols denote IR active modes

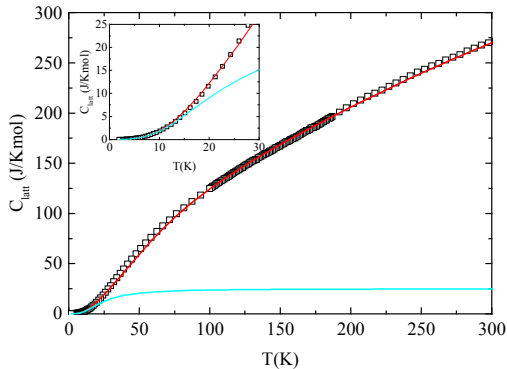


Fig. 3. Temperature dependence of lattice specific heat of $\text{Cu(en)}_2\text{SO}_4$ single crystal. The lines have the same meaning as in Fig. 1

The same approach was applied for $\text{Cu(en)}_2\text{SO}_4$. The

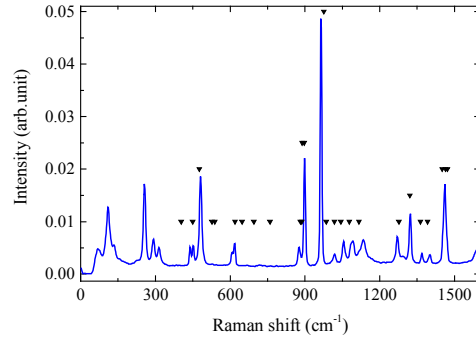


Fig. 4. Raman spectrum of polycrystalline $\text{Cu(en)}_2\text{SO}_4$. Symbols denote IR active modes

fitting $C_{tot} \sim a/T^2 + bT^3 + cT^5 + dT^7$ in the region between 10 and 24 K provided $a = 109.2 \text{ J/K mol}$, $b = 1.89 \times 10^{-3} \text{ J/(K}^4 \text{ mol)}$, $c = -1.12 \times 10^{-6} \text{ J/(K}^6 \text{ mol)}$, $d = 1.58 \times 10^{-10} \text{ J/(K}^8 \text{ mol)}$. Using Eq.3, $\theta_D = 100 \text{ K}$ was calculated and the contribution of acoustic phonons (Eq. 1) to the lattice specific heat was evaluated (Fig. 3). The deviation of data from Eq. 1 appear already above 15 K. Applying Eq. 2, the contribution of optical modes was calculated considering IR active modes [7] 403, 449, 476, 526, 538, 619, 647, 694, 759, 881, 887, 889, 896, 975, 985, 1018, 1043, 1078, 1116, 1276 (in cm^{-1}) and Raman modes 68, 74, 109, 132, 153, 169, 178, 188, 209, 223, 230, 255, 292, 313, 439, 450, 481, 608, 618, 876, 898, 963, 1017, 1054, 1092, 1133, 1270 (Fig. 4).

It should be noted that the validity of Curie-Weiss law in all mentioned compounds is limited to the temperatures where significant deviations from Debye function (Eq.1) appear. It seems that low-energy optical modes are responsible for the disturbing of magnetic correlations in these structurally and magnetically low-dimensional systems.

CONCLUSIONS

The study of lattice specific heat and vibrational spectra in structurally and magnetically low-dimensional Cu(II) based systems revealed that acoustic phonons dominate at temperatures up to about 10 - 15 K. Low-energy optical modes excited at higher temperatures probably cause the total disturbance of all magnetic correlations.

ACKNOWLEDGMENT: The work has been supported by VEGA grant 1/0269/17 and APVV-18-0197.

REFERENCES

1. U. Schollwöck, et al: Quantum Magnetism (Springer, Berlin- 2004).
2. L. Lederová et al, Phys. Rev. B **95**, 054436 (2017).
3. L. Lederová et al, Phys. Rev. B **100**, 134416 (2019).
4. L. Lederová et al, Proceedings of 24th Conf. of Slovak Physicists, 72, (2019).
5. L. Lederová et al, Acta Phys. Polonica A **137**, 955 (2020).
6. V. Manríquez et al, J. Chem. Cryst. **26**, 15 (1996).
7. R.Tarasenko, Thesis, (2013).

INTERDIFFUSION IN ALUMINUM-STEEL CLAD STRIP

B. Krivská, krivska.barbora@seznam.cz, M. Šlapáková, slapakova@karlov.mff.cuni.cz, M. Kihoulou, kihoulou@karel.troja.mff.cuni.cz, R. Králík, rkralik96@gmail.com, L. Bajtošová, lucibajtos@gmail.com, M. Cieslar, cieslar@met.mff.cuni.cz, Charles University, Faculty of Mathematics and Physics, 121 16 Prague, Czech Republic, O. Grydin, grydin@lwk.upb.de, M. Stolbchenko, stolbchenko@lwk.upb.de, M. Schaper, schaper@lwk.upb.de, Paderborn University, Chair of Materials Science, 33098 Paderborn, Germany

INTRODUCTION

Aluminum-steel composites are promising structural materials. Very thin diffusional seams form on the interface between aluminum and steel during cladding of flat Al-steel strips produced by twin-roll casting. Their thickness and phase composition are crucial parameters that influence bonding strength between the metals. The diffusion seam could be enhanced by supplemental annealing, however, there are some limitations. Diffusion seams could develop into hard but brittle continuous intermetallic layers during additional annealing, adhesive strength between steel and aluminum decreases abruptly and a delamination of the layers follows [1, 2].

The aim of the present work is to determine an effective interdiffusion coefficient from experimental concentration profiles and to simulate diffusion at the aluminum (EN AW-1070)–steel (1.4301 type) interface using Fick’s second law [3].

THEORETICAL BACKGROUND

The Fick’s second law provides a direct proportion between a mass flux and the gradient of concentration [4]

$$\frac{\partial c(x, t)}{\partial t} = \nabla \cdot (D \nabla c), \quad (1)$$

where c signs the concentration, D diffusion coefficient, x coordinate and t time.

Intermixing of the binary A-B system can be described by an interdiffusion coefficient, which generally depends on the concentration. Inverting of second Ficks law the interdiffusion coefficient could be determined by Boltzmann-Matano method [5].

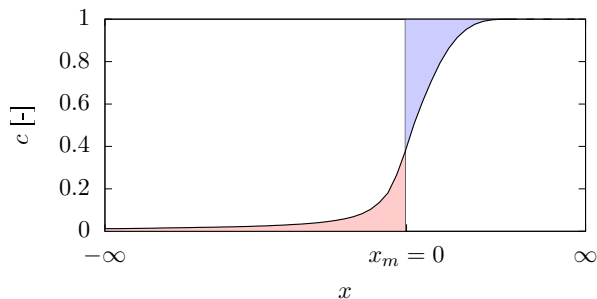


Fig. 1. Position of Matano plane results from a conservation condition which says that gain and lost the of the diffusing species (blue and red filled areas under the concentration curve) must be equal.

The non-linear partial differential equation 1 can be transformed to a nonlinear ordinary differential equation (ODE) by Boltzmann transformation. Integration

of the ODE leads to a relation between concentration profile $c(x)$ and a concentration dependent diffusion coefficient $D(c)$

$$D(c^*) = -\frac{1}{2t} \frac{\int_{c_L}^{c^*} (x - x_M) dc}{\left. \frac{dc}{dx} \right|_{c^*}}, \quad (2)$$

where c^* is a selected concentration and x_M denotes a so-called Matano plane (see Figure 1).

SIMULATION OF DIFFUSION

FEniCS software, which is designed for numerical solving of partial differential equations by a finite element method [6], was employed for diffusion simulations. Linear Lagrange elements were used for concentration function and Crank-Nicolson semi-implicit scheme with CourantFriedrichsLewy condition were applied for time discretization [7]. Diffusion coefficient present in diffusion equation was approximated by a piecewise constant function $D(c)$. Since the term $D(c)$ brings a nonlinearity to the equation, it was linearized by means of the previous time step. A resolution of 400 nodes was found sufficient for all calculations.

Since the system Al–steel is not a binary system a simplification was done by introducing “atoms of steel” including all elements apart from aluminum. Justification of such step is based on the shape of concentration profiles of Ni and Cr, which are similar to the one of Fe, indicating a similar value of their diffusion coefficients [8]. Si concentration was negligible in comparison with those of other elements. Diffusion coefficient was then evaluated from steel-concentration curves smoothed by Savitzky-Golay filter [9].

RESULTS AND DISCUSSION

Tests of programs for computation of diffusion coefficient and diffusion simulation on an analytical solution of the diffusion equation with a constant diffusion coefficient showed a limited precision of the method near $c = 1$ and $c = 0$. However, unless there were the flawed $D(c)$ tails, the analytical solution overlapped with the simulated profile.

Afterwards, the Boltzmann-Matano method was used for the evaluation of $D(c)$ from the smoothed steel-concentration profile using electron dispersion X-ray analysis (EDS). Diffusion coefficient, measured concentration profile and simulation are displayed in Figure 2 and 3.

Obtained $D(c)$ should be interpreted as an effective interdiffusion coefficient, which could in some way quantify the rate of the ongoing diffusion processes according to Fick’s second law, where a concentration gradient acts as a main driving force. Recent works on

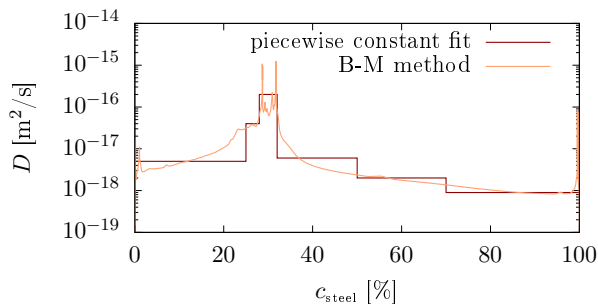


Fig. 2. Diffusion coefficient obtained from a concentration profile after 16 h annealing at 500 C.

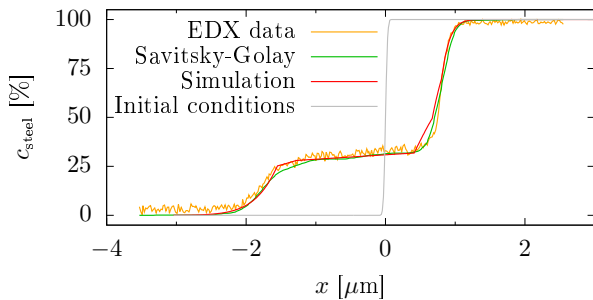


Fig. 3. Measured and simulated concentration profile after 16 h annealing at 500 °C.

Al-steel composites often refers to interdiffusion coefficients of aluminum in iron and of iron in aluminum. Since the published value of iron's diffusivity in aluminum is higher than that of aluminum in iron [8], they incline to a conclusion that diffusion proceeds towards aluminum and related formation of the intermetallic layer grows in Al [1, 2, 10] (see the concentration plateau in Figure 3). Plotting of the simulated concentration profile together with the initial condition shows that the intermetallic layer grows rather towards Al side, even though not fully unambiguously – the growth occurs on both sides of the Al-steel interface, but it is less developed on the steel side.

However, an accuracy of the calculations could be limited by several simplifications which had been done. The diffusion coefficient was calculated from some profiles by EDS in scanning electron microscope (SEM). Nevertheless, the shape of the profile could be significantly influenced by so-called interaction volume, which is larger than a volume defined by a diameter of the electron beam in SEM [11]. Moreover, in the case of Al-steel joint, a layer of several intermetallic phases forms during diffusion which makes the system more complex.

CONCLUSIONS

Boltzmann-Matano method enables to determine the interdiffusion coefficient $D(c)$ from a shape of the concentration-depth profile obtained after isothermal annealing. Applying this method on the Al-steel couple with developed Al-Fe rich intermetallic phase on the interface leads to an effective diffusion coefficient reaching its maximum at a composition of

the intermetallic phase layer. Using its piecewise fit in the solution of the diffusion equation provides a satisfactory agreement with measured concentration profile showing the growth of the intermetallics rather towards Al layer as it is stated in recent works. However, many simplifications have been done – the Al-steel joint is not a binary system and phase transformations proceeds during the diffusion. Legitimacy of using diffusion coefficient, i.e. consideration of the concentration gradient as a driving force of diffusion, should be further proven.

ACKNOWLEDGMENT: The financial support of GAR project 20-00355Y, SVV-260582 and German Research Foundation (DFG) in regard to the project SCHA 1484/21-1 are highly acknowledged.

REFERENCES

1. H.R. Akramifard, H. Mirzadeh, M.H. Parsa, Mater. Sci. Eng. A **613**, 232 (2014).
2. M. Stolbchenko, O. Grydin, M. Schaper, Adv. Eng. Mater. 21, 1800454 (2019).
3. A. Fick, Lond. Edinb. Dubl. Phil. Mag. **10**, 30 (1855).
4. P. Atkins, J. de Paula: Physical Chemistry (Oxford University Press, Oxford - 2006).
5. H. Mehrer: Diffusion in Solids (Springer-Verlag Berlin Heidelberg - 2007).
6. A. Logg, K.-A. Mardal, G. Wells: Automated Solution of Differential Equations by the Finite Element Method (Springer-Verlag Berlin Heidelberg - 2012).
7. A. Quarteroni, A. Valli: Numerical Approximation of Partial Differential Equations (Springer-Verlag Berlin Heidelberg - 1994).
8. H.R. Akramifard, H. Mirzadeh, M.H. Parsa, IJISSI **13**, 38 (2016).
9. A. Savitzky, M.J.E. Golay, Anal. Chem. **36(8)**, 1627 (1964).
10. R. Li and T. Yuan, X. Liu and K. Zhou, Scr. Mater. **110**, 105 (2016).
11. P.J. Goodhew, J. Humphreys, R. Beanland: Electron Microscopy and Analysis (Taylor & Francis, London - 2001).

CHARACTERIZATION OF THIN FREE-STANDING AL-MG FILMS

L. Bajtošová, lucibajtos@gmail.com, R. Králík, rkralik96@gmail.com, B. Krivská, krivska.barbora@seznam.cz, H. Libenská, libenska1@seznam.cz, J. Veselý, vesely@gjh.sk, M. Cieslar, cieslar@met.mff.cuni.cz,
Faculty of Mathematics and Physics, Charles University, Ke Karlovu 3, 12116 Prague, Czech Republic

INTRODUCTION

Components in micromechanical systems (MEMS) can be often exposed to large loads or a high frequency motion. For that reason, a prediction of their mechanical properties is considerably important. A change of mechanical behaviour in thin and multilayer films compared to the behaviour in bulk materials is a known and broadly examined phenomenon resulting mainly from low grain size and high-volume fraction of interfaces. A dependence of yield strength on grain size known as Hall-Petch relationship [1] based on a premise that dislocation pile-ups in fine grained materials contain fewer dislocations thus larger stress is necessary for the movement of dislocations in adjoining grain breaks down in materials with grains under a certain critical grain size [2,3]. For most metals, the critical size is expected to be below 10 nm [4], however experiments have shown inverse or reduced slope in Hall-Petch relationship for several times larger grain sizes [1,5]. A number of models explaining this behaviour including dislocation-based [6], diffusion-based [7], grain-boundary shearing [8] and two-phase based [9] models have been proposed.

However, experimental results [10,11] revealed observations contrary to the presumptions of many above mentioned models. New experimental results received by in-situ deformations in TEM could help to reach a better understanding of ongoing deformation processes. Nevertheless, detailed knowledge of the microstructure of thin films is a necessary prerequisite for such investigations.

A fabrication of thin metal layers with average grain size less than 100 nm is now possible by different methods, one of the most common includes physical vapor deposition methods, namely magnetron sputtering [12]. The magnetically enhanced diode sputtering exhibits various advantages such as high deposition rates or high purity and uniformity of deposited films.

Down to 100 nm thick free-standing Al films have been prepared and basic characterisation of grains size and preferred orientation has been made by atomic force microscopy, conventional and in-situ transmission electron microscopy and automatic phase and orientation mapping in TEM.

EXPERIMENTAL METHODS

Thin free-standing films were prepared from DC magnetron sputtered samples by dissociating the films from a glass substrate covered by photoresist. 50 nm, 100 nm and 150 nm thick films were made from a 3-inch AlMg target.

The films were characterised by AFM using Bruker Dimension Edge device in tapping mode, by TEM in BF and by Automated orientation phase mapping at TEM JEOL 2200FS equipped with "Spinning Star" electron precession with an ASTAR software package.

RESULTS

TEM observations (Fig. 1.) show uniformly sized grains of irregular round shape forming the films. Average grain size increases gradually with the film thickness from 30 nm for the 50 nm thick films to 60 nm for 150 nm thick films. As the film thickness increases, overlapping of several neighbouring grains can be noticed (Fig. 1. c). Furthermore, bright areas surrounding the grains are visible notably in 100 nm thick film (Fig. 1. b). This could be due to a different phase forming around the grain boundaries, however, the theory could not be confirmed by any of performed analysis.

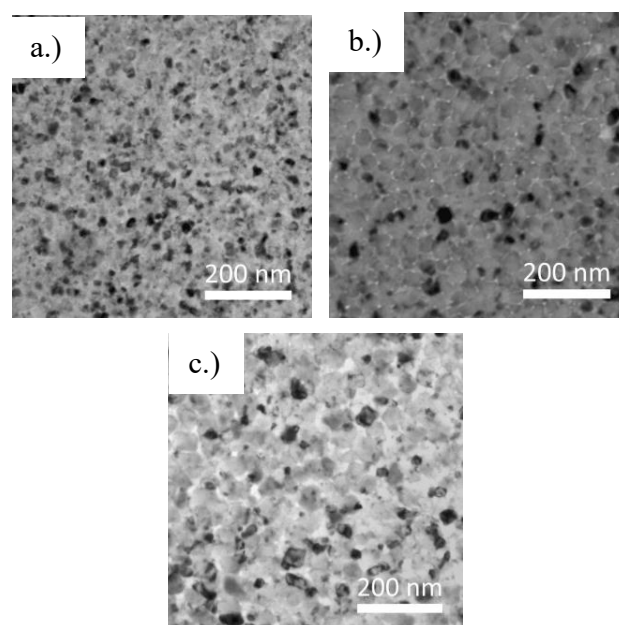


Fig. 1. TEM BF image of a) 50 nm, b) 100 nm, c) 150 nm thick film

AFM measurements (Fig. 2) show surface roughness in scale of tens of nm. Rather large changes in y direction obscure the surface shape and make the accurate determination of grain size impossible.

Grain orientation distribution maps obtained by Automated orientation phase mapping at TEM are shown in Fig. 3 and Fig. 4. Average grain size for 150 nm thick film corresponds with the TEM BF measurements (Fig. 3 a). However, in case of 50 nm thick films, the grains in orientation maps (Fig. 3. b) are considerably larger than the ones observed by conventional TEM images (Fig. 1 a). It is possible that several grains of the similar orientation are grouped together which results in seemingly one large grain in the colour-coded images. Moreover, the determination of grains size from orientation maps is problematic due to the large areas of

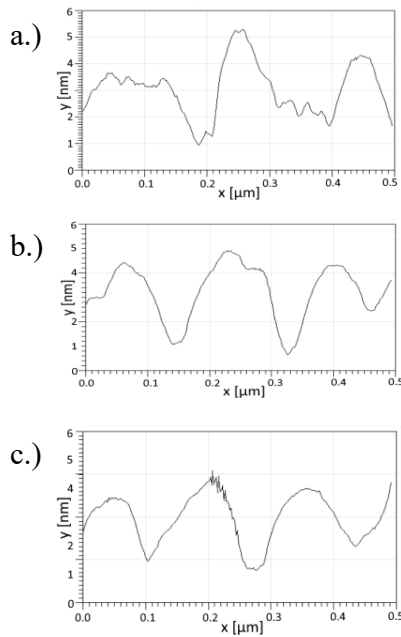


Fig. 2. Graphs of surface height y depending on horizontal coordinate x obtained from the AFM measurements for a) 50 nm, b) 100 nm, c) 150 nm thick film

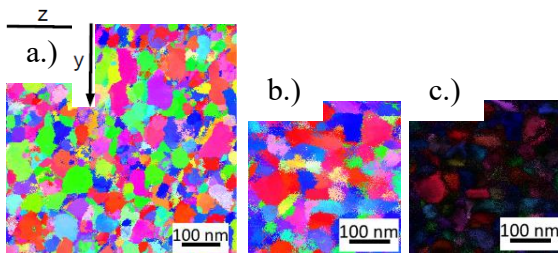


Fig. 3. ASTAR orientation maps of direction parallel to the sample surface for a) 150 nm, b) 50 nm thick films. c) ASTAR orientation map of 50 nm thick film with low reliability areas marked black

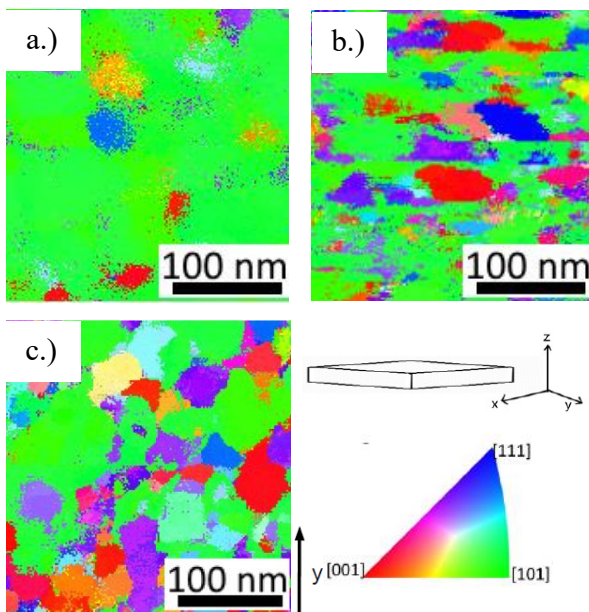


Fig. 4. ASTAR orientation maps of direction perpendicular to the sample surface for a) 50 nm, b) 100, c) 150 nm thick films

low orientation reliability caused by the overlapping of neighbouring grains (Fig. 3 c).

Orientation maps in the direction perpendicular to the sample surface (Fig 4.) reveal preferable grain orientation in direction [101], particularly for the 50 nm thick sample (Fig. 4. a). Slightly more sparsely, large grains of [001], [111] and other directions between also appear.

Maps in directions parallel to the surface x, y do not show any preferable orientation distribution (Fig. 3 a, b).

CONCLUSIONS

Preparation of thin Al films by DC magnetron sputtering onto a photoresist-covered glass substrate leads to evenly distributed grains with average size gradually increasing with the film thickness and direction [101] preferably oriented perpendicular to the sample surface.

ACKNOWLEDGMENT: Authors would like to acknowledge the support from Grant Agency of Charles University under the project 574120.

REFERENCES

1. E O Hall, Proc. Phys. Soc. B **64**, 742 (1951).
2. G.W. Nieman, J.R. Weertman, R.W. Siegel, Scr. Metall. **23**, 21070323 (1989).
3. A. H. Chokski, A. Rosen, J. Karch, H. Gleiter, Scr. Metall. **23**, 1679 (1989).
4. T.G. Nieh, J. Wadsworth, Scr. Metall. Mater. **25**, 955 (1991).
5. G.W. Nieman, J.R. Weertman, R.W. Siegel, J Mater. Res. **6**, 1012 (1991).
6. R.O. Scattergood, C.C. Koch, Scr. Metall Mater. **27**, 1195 (1992).
7. R.A. Masamura, P.M. Hazledine, C.S. Pande, J. Acta Mater. **46**, 4527 (1998).
8. H. Van Swygenhven, M. Spaczer, A. Caro, Acta Mater. **47**, 3117 (1999).
9. G.J. Fan, H. Choo, P.K. Liaw, E.J. Lavernia, Mater. Sci. Eng. A **409**, 243 (2005).
10. R.C. Hugo, H.H. Kung, J.R. Weertman, R. Mitra, J.A. Knapp, D.M. Follstaedt, Acta Mater. **51**, 1937 (2003).
11. H. D. Espinosa, R. A. Bernal, T. Filleter, Small **8**, 3233 (2012).
12. I. V. Tudose, F. Comanescu, P. Pascariu, S. Bucur, L. Rusen, F. Iacomi., E. Koudoumas, M. P. Suche, Functional Nanostructured Interfaces for Environmental and Biomedical Applications, 15 (2019).

RECRYSTALLIZATION OF A TWIN-ROLL CAST AA8079 ALUMINUM ALLOY AFTER HOMOGENIZATION

R. Králík, rkralik96@gmail.com, L. Bajtošová, lucibajtos@gmail.com, B. Krivská, krivska.barbora@seznam.cz, M. Cieslar, cieslar@met.mff.cuni.cz, Faculty of Mathematics and Physics, Charles University, Ke Karlovu 3, 121 16, Prague 2, Czech republic

INTRODUCTION

Recrystallization kinetics of solids can be described by the Johnson-Mehl-Avrami-Kolmogorov (JMAK) model. The model describes development of recrystallized volume fraction of a material during isothermal annealing. The JMAK equation can be simplified into the form given by equation 1, where $x(t)$ is the time dependent recrystallized fraction, C and k are temperature dependent constants and n is the temperature independent parameter of recrystallization kinetics [1 - 3].

$$x(t) = C \cdot \exp(1 - k \cdot t^n) \quad (1)$$

The kinetics parameter n is, in an ideal case, equal to 4. This applies for a single phase infinite material which contains no defects. This parameter decreases by 1 when dimension of growth of recrystallized grains is restricted by 1. However, real materials have finite volumes restricted by their surfaces and contain further defects such as primary phase particles, solute atoms and more. According to Humphreys et al. [4] all of these defects can further decrease the parameter n .

Aluminum alloys have had their recrystallization kinetics studied in the past. Parameters of kinetics close to 1 have been reported. However, this number strongly depends on the specific alloying elements and their concentrations [5, 6]. This is lower than predicted by the JMAK model due to the presence of obstacles of grain boundary motion in the materials. The AA8079 aluminum alloy contains iron and silicon as main alloying elements. Intermetallic particles containing iron are forming during solidification. Different sizes and distributions of these particles can affect recrystallization of the material through effects called Zener drag (ZD) and particle stimulated nucleation (PSN) [7, 8]. These particle distributions can be modified through different homogenization treatments [9].

EXPERIMENTAL METHODS

The AA8079 aluminum alloy contains approximately 1.06 wt.% Fe, 0.06 wt.% Si and less than 0.01 wt.% of Mn and Ti. The material was prepared by twin-roll casting. The as-cast material comes in a form of a 7 mm thick billet. This billet is then homogenized at 420 °C and 580 °C for 8 h in order to achieve different states of the material prior to further processing.

The homogenized materials were rolled to 600 μm and isothermally annealed at 250 °C, 275 °C and 300 °C for up to 16 h. Microhardness of the annealed materials was measured in order to determine recrystallized volume fraction $x(t)$ of the material through a simplified

model given by equation (2) [10]. Here, HV_0 , $HV(t)$ and HV_R are microhardness before annealing, at time t during the annealing, and after full recrystallization, respectively.

$$x(t) = (HV_0 - HV(t)) / (HV_0 - HV_R) \quad (2)$$

Microhardness was measured by a Qness Q10 microhardness measuring device. Light optical microscopy observations were performed with a Zeiss Axio Observer 7 microscope.

RESULTS AND DISCUSSION

Light optical microscopy reveals different particle distributions and morphologies at different temperatures of homogenization. The material homogenized at 420 °C (Fig. 1a)) contains fine particles distributed through the material. These fine particles are expected to control recrystallization by retarding boundary motion through ZD. The material homogenized at 580 °C (Fig. 1 b)) contains a mixture of coarse and fine particles. The coarse particles contribute to recrystallization control through PSN. Kinetics parameter can be evaluated from equation 1 by applying a logarithm twice and performing linear regression of the function in Avrami coordinates.

The material homogenized at 420 °C requires a temperature of at least 300 °C to fully recrystallize in the selected time interval (Fig. 2). However, at 300 °C the material recrystallized after 5 h annealing. The recrystallized fraction for the material annealed at 300 °C follows a typical S-shaped curve as expected from equation 1 and parameter n can be evaluated. The measured parameter was approximately 1.3, which is significantly lower than in the ideal case given by the JMAK model, but in accordance with findings of other authors [5, 6].

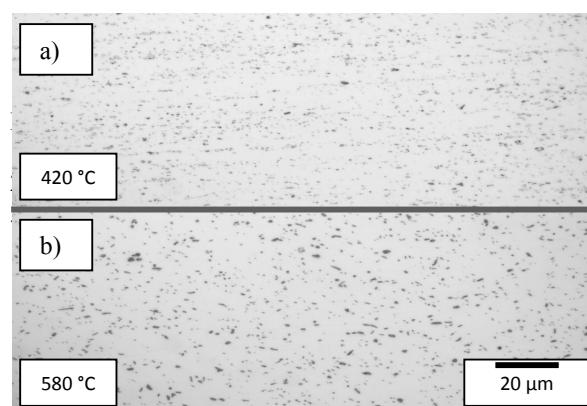


Fig. 1. LOM of intermetallic particles of the homogenized materials

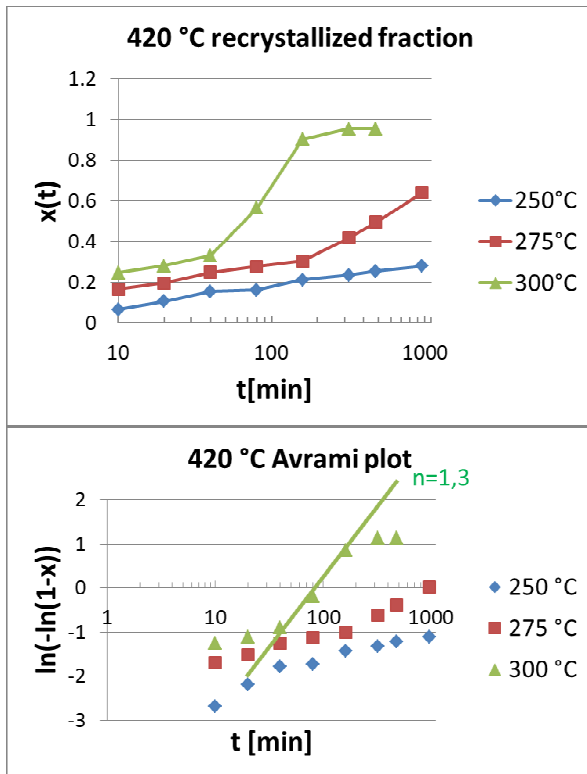


Fig. 2. JMAK analysis of the material homogenized at 420 °C

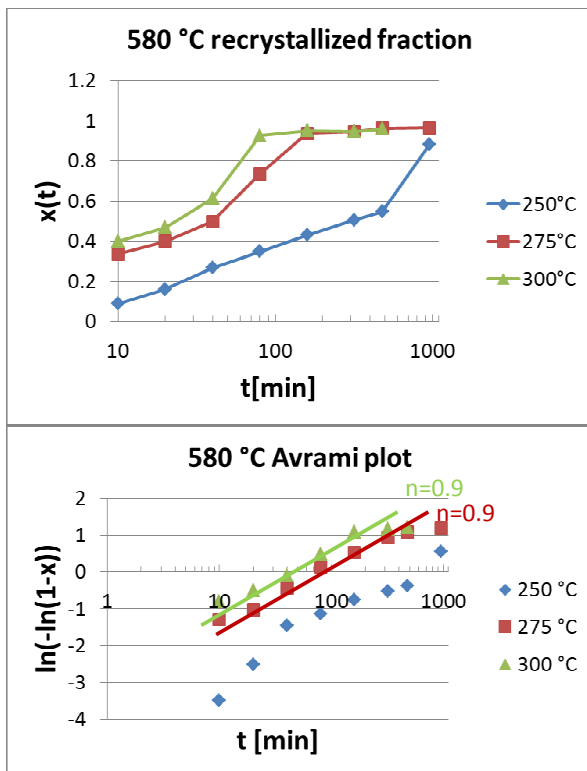


Fig. 3. JMAK analysis of the material homogenized at 580 °C

The material homogenized at 580 °C recrystallized fully during annealing at 300 °C and 275 °C. In both cases the material fully recrystallized within 3 h. However at 250 °C the material only began to recrystallize after an extended period of time and was

not fully recrystallized even after 16 h regardless of homogenization temperature. Parameter n was evaluated for the two successful cases. In both cases the parameter was approximately 0.9 which confirms the assumed temperature independence of the parameter [1 - 3].

CONCLUSIONS

Material with higher temperature of homogenization recrystallizes at lower temperatures and in shorter time as a consequence of PSN. Material with lower homogenization temperature has recrystallization hindered by higher influence of ZD. Neither of the materials recrystallizes at 250 °C within 8 h.

ACKNOWLEDGEMENT: The financial support of the GAUK project number 704119 and project FV20337 of Ministry of Industry and Trade is highly acknowledged.

REFERENCES

1. M. Avrami, J. Chem. Phys. **7**, 1103 (1939).
2. M. Avrami, J. Chem. Phys. **8**, 212 (1940).
3. M. Avrami, J. Chem. Phys. **9**, 177 (1941).
4. F. J. Humphreys, M. Hatherly: Recrystallization and related annealing phenomena (Pergamon – 2004).
5. M. Tajally, Z. Huda, Metal Science and Heat treatment **53**, 213 (2011).
6. S. Dutta, M. S. Kaiser, Procedia Engineering **90**, 188 (2014).
7. E. Nes, N. Ryum, O. Hunderi, Acta Metallurgica **33**, 11 (1985).
8. F. J. Humphreys, Acta Metallurgica **25**, 1323 (1977).
9. Y. Birol, Journal of Materials Processing Technology **202**, 564 (2008).
10. P. N. Kalu, D. R. Waryoba, Materials Science and Engineering: A **464**, 68 (2005).

NANOFLUID BASED ON A NEW GENERATION OIL

K. Paulovičová¹, paulovic@saske.sk, J. Tóthová², Jana.Tothova@tuke.sk, M. Rajňák^{1,2}, rajnak@saske.sk, M. Timko¹, timko@saske.sk, P. Kopčanský¹, kopcan@saske.sk, V. Lisý², Vladimír.Lisy@tuke.sk, ¹Institute of Experimental Physics SAS, Watsonova 47, 040 01 Košice, Slovakia, ²Faculty of Electrical Engineering and Informatics, Technical University of Košice, Letná 9, 042 00 Košice, Slovakia

INTRODUCTION

Magnetic fluids belong to special nanomaterials with many application possibilities. One of the fields of their use is the energy industry, where the demands on the performance of electrical equipment are constantly rising. As a result, there is a need to use modern insulation systems. Adding nanoparticles to conventional media could be one way to obtain them. In this study, we focused on the complex characterization of potential magnetic nanofluids (MNFs) based on isoparaffin hydrocarbons extracted from natural gas. These new-generation gas-to-liquid (GTL) derived electrical insulation fluids are cleaner, chemically stable, and the thermal conductivity values of these fluids are higher, indicating improved heat transfer properties [1]. For the preparation of MNFs, we used sterically stabilized nanoparticles of iron oxides with a volume fraction in samples in the range of 0.03 – 3.0 %. The saturation magnetization, magnetic susceptibility, density, and viscosity were investigated showing a significant enhancement with an increase of the volume fraction. Our experimental results show that the nanofluids prepared on the basis of the GTL technology have a stable colloidal character that is necessary for its application as a potential cooling medium in electro-energetics.

EXPERIMENTAL DETAILS

In this contribution, for the synthesis of iron oxides nanoparticles (IONPs) we used the bottom-up approach. The nanoparticles were obtained by the co-precipitation technique of water solutions of trivalent and bivalent iron salts in the molar ratio 2:1. The nucleation and growth of the spherical particles were carried out at 80 – 82°C in the presence of NH₄OH used as a precipitating agent. The surface of the magnetic nanomaterial was sterically functionalized by chemisorption of C₁₇H₃₃COOH (coating agent), ensuring hydrophobicity of their surface. The nanoparticles with the hydrophobic character were further used in the preparation of the basic nanofluid based on GTL oil (Shell Diala S4 ZX-I). The sample of MNF with the nonpolar character without any phase separation and sedimentation was prepared with a procedure described in [2], with minor modifications. Other MNFs with different volume fractions of the magnetic phase were prepared by dilution of the basic nanofluid by the GTL carrier liquid. The magnetic properties, exact concentration, and average diameter of IONPs were determined from the analysis of magnetization curves. The magnetization of the studied samples was measured by the vibrating-sample magnetometer (VSM) installed on a cryogen-free high field measurement system from Cryogenic

Limited. The magnetization curve as a function of the applied magnetic field showed the typical superparamagnetic behavior of single-domain magnetic nanoparticles at 289 K. At 1.8 K the blocked state is reflected in the hysteresis loop with the coercivity field of about 0.02 T [3]. The resulting magnetization curves of all experimental samples are depicted in Fig. 1. It shows that the saturation magnetization of individual samples increases with the growing volume fraction of IONPs in MNFs.

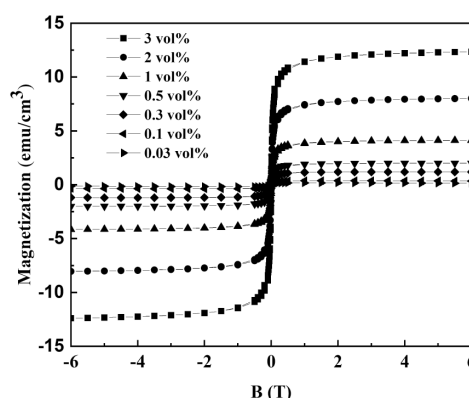


Fig. 1. The magnetic hysteresis loops (magnetization versus the applied magnetic field) of experimental samples with different volume fractions of IONPs.

The volume fraction of the solid magnetic phase was determined according to the relationship $\Phi_v = M_s / M_b$, where $M_b = 446 \text{ emu/cm}^3$ is the spontaneous magnetization of magnetite grains [4, 5]. The obtained values of saturation magnetization and other determined characteristics of the studied MNFs are summarized in Table I.

TAB. 1. The basic parameters of the prepared MNFs: M_s - saturation magnetization, Φ_v -magnetic volume fraction, ρ - density, η/η_0 -relative viscosity taken at room temperature.

Sample	M_s [emu/cm ³]	Φ_v [%]	ρ [g/cm ³]	η/η_0
GTL oil		-	0.807	-
NF	12.34	3	0.965	1.47
NF1	8.01	2	0.908	1.35
NF2	4.13	1	0.860	1.19
NF3	1.99	0.5	0.834	1.16
NF4	1.19	0.3	0.823	1.12
NF5	0.34	0.1	0.813	1.1
NF6	0.13	0,03	0.810	1.04

For the characterization of the size distribution of nanoparticles, we analyzed the data from the VSM measurements and the dynamic light scattering (DLS) method. Analyzing the VSM measurements we found

that the mean particle diameter was 10.3 nm. It was determined by fitting the magnetization curve using the Langevin function, which very closely describes the magnetic behavior of the same size IONPs [5]. The DLS method is a well-established technique to measure hydrodynamic sizes, polydispersities, and aggregation effects of nanoparticles dispersed in a colloidal suspension. This method is based on the measurement of the laser light scattering fluctuations due to the Brownian motion of the suspended NPs. It was carried out using a Malvern Zetasizer Nano ZS instrument by backscatter detection (173°) of a HeNe laser beam. The measurements yielded the average hydrodynamic particle diameter of 14.54 nm (Fig. 3). The obtained results reflect the effective coating and stabilization of nanoparticles with oleic acid.

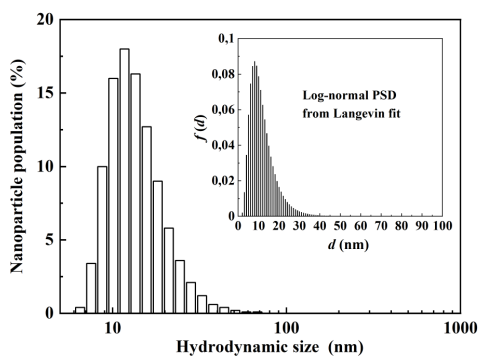


Fig. 3. Histogram of the particle diameters obtained from DLS and VSM method.

Rheological characterization was performed by a Physica Anton Paar GmbH MCR-502 rheometer using two parallel plates. The studied MNFs (solid loading from 0.03 up to 3 vol. %) and the carrier liquid shows an ideal viscous flow behavior, as can be seen in Fig. 4. In the range of the shear rate $1 - 110 \text{ s}^{-1}$, the shear stress linearly increases with the increasing shear rate. It is a display of the so-called Newtonian fluids, whose viscosity does not depend on the shear rate.

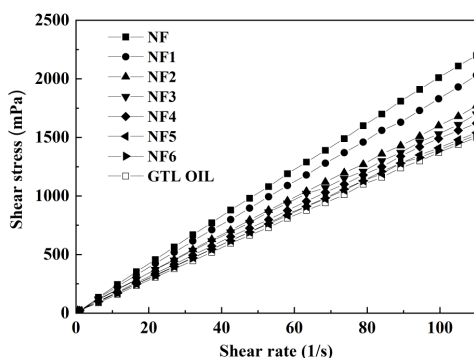


Fig. 4. Flow curves of the pure GTL oil and MNFs.

Basic dynamic magnetic properties of the investigated samples were determined by commercial AC susceptometer IMEGO-DynoMag at room temperature within the frequency range from 1 Hz to 250 kHz. The measurement of the dynamic magnetic

susceptibility, also referred to as AC magnetic susceptibility, is a sensitive tool for characterizing materials. Close to constant behavior of the frequency-dependent real component (χ') and the imaginary one (χ'') of the AC magnetic susceptibility for all studied MNFs is presented in Fig. 5. This nearly constant behavior reflects the polydisperse character of nanoparticles and the absence of any larger particle aggregates in the prepared nanofluids [6, 7].

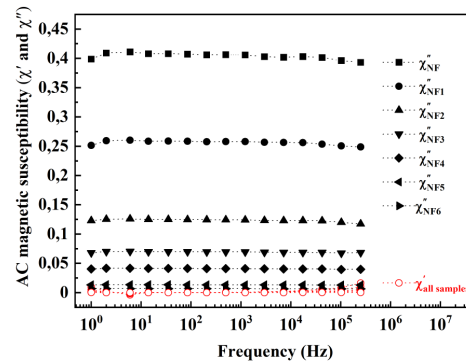


Fig. 5. Real and imaginary AC susceptibility at 289 K.

CONCLUSIONS

According to the experimental results, it was shown that the MNFs prepared on the basis of the GTL oil have a stable colloidal character that is necessary for its application as a potential cooling medium in high power electro-energetics.

ACKNOWLEDGMENT: This work was supported by the Slovak Academy of Sciences and Ministry of Education in the framework of the projects VEGA 1/0250/18 and VEGA 2/0011/20, by Slovak Research and Development Agency under the Contract No. APVV-18-0160, and European Regional Development Fund, projects ITMS2014+: 313011T548.

REFERENCES

1. W. Lu et al., IEEE Trans. Dielectr. Electr. Insul. **23**, 2450 (2016).
2. L. Vékás et al., China Particuology **5**, 43 (2007).
3. K. Paulovičová et al., Acta Phys. Pol. A **137**, 908 (2020).
4. K. Kebede et al., Mater. Sci. Eng. B **215**, 37 (2017).
5. Z. Rozynek et al., Eur. Phys. J. E **34**, 28 (2011).
6. R. Hamdi et al., J. Mol. Struct. **1175**, 844 (2019).
7. M. Rajnak et al., J. Appl. Phys. **114**, 034313 (2013).

STUDY OF RING-LIKE STRUCTURES IN PARTICLE EMISSION IN RELATIVISTIC NUCLEAR INTERACTIONS

A. Kravčáková, adela.kravcakova@upjs.sk, M. Vaľa, martin.vala@upjs.sk, S. Vokál, stanislav.vokal@upjs.sk, J. Vrláková, janka.vrlakova@upjs.sk, Faculty of Science, P.J. Šafárik University, Košice, Slovakia

INTRODUCTION

An important aim of nucleus collisions investigation at high energies is to search for a phenomena connecting with large densities obtained in such collisions. As an example, the transition from the QGP (quark - gluon plasma) back to the normal hadronic phase is predicted to contribute to fluctuations in the number of produced particles in local regions of phase space [1][2].

The goal of our work was to study the ring-like structures of produced particles in azimuthal plane. They occur if many particles are produced in a narrow region along the rapidity axis, which at the same time are almost regularly distributed over the whole azimuth (Fig.1b). The jet-like structures consist of cases, where particles are focused in both dimensions (Fig.1a).

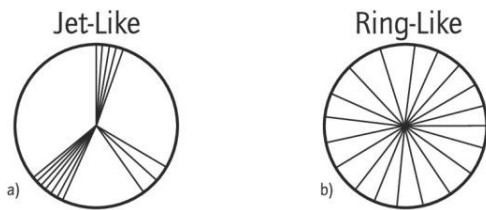


Fig. 1. Schema of the jet-like and ring-like structures in azimuthal plane. Primary track is perpendicular to figure plane

EXPERIMENT

The stacks of NIKFI BR-2 nuclear photoemulsions have been irradiated horizontally by ^{208}Pb beam at 158 AGeV/c (the CERN SPS experiment EMU12) and by ^{197}Au beam at 11.6 AGeV/c (the BNL AGS experiment E863).

The used photoemulsion method allows to measure:

- multiplicities of any charged particles, which include relativistic (N_s) particles with $\beta > 0.7$, projectile fragments (N_F) with $\beta \approx 0.99$ and target fragments (N_h) with $\beta < 0.7$;
- angles of particles with the resolution of 0.010 – 0.015 rapidity units in the central region, pseudorapidity is given by $\eta = -\ln\left(\tan\left(\frac{\theta}{2}\right)\right)$, where θ is the emission angle with respect to the beam direction,
- charges of projectile fragments (Z_F).

We analysed 628 $^{208}\text{Pb}+\text{Ag}(\text{Br})$ interactions divided into three centrality groups according to the number of relativistic particles ($350 \leq N_s < 700$, $700 \leq N_s < 1000$, $N_s \geq 1000$), and 1128 $^{197}\text{Au}+\text{Ag}(\text{Br})$ collisions also in three centrality groups ($100 \leq N_s < 200$, $200 \leq N_s < 300$, $N_s \geq 300$).

METHOD

A method we use to search for a ring-like structure was proposed in [3]. The multiplicity N_d of analyzed

subgroup of relativistic particles from an individual event is fixed. Each consecutive N_d tuple of particles along the η axis of individual event is characterized by a size $\Delta\eta = \eta_{max} - \eta_{min}$, where η_{min} and η_{max} are the pseudorapidities of the first and last particles in the subgroup and a density $\rho = N_d/\Delta\eta$.

To parameterize the azimuthal structure of the subgroup in a suitable way a parameter

$$S_2 = \sum(\Delta\Phi_i)^2 \quad (1)$$

has been suggested, where $\Delta\Phi$ is the difference between azimuthal angles of two neighboring particles in the investigated subgroup. For the sake of simplicity it was counted $\Delta\Phi$ in units of full revolutions $\sum(\Delta\Phi_i) = 1$.

The parameter S_2 is large ($S_2 \rightarrow 1$) for the jet-like, small ($S_2 \rightarrow 1/N_d$) for the ring-like structures and the expected value for the stochastic scenario with independent particles can be expressed as $\langle S_2 \rangle = 2/(N_d + 1)$.

Expected normalized $S_2/\langle S_2 \rangle$ distributions for different scenarios are schematically illustrated in Fig.2, using Gauss distributions.

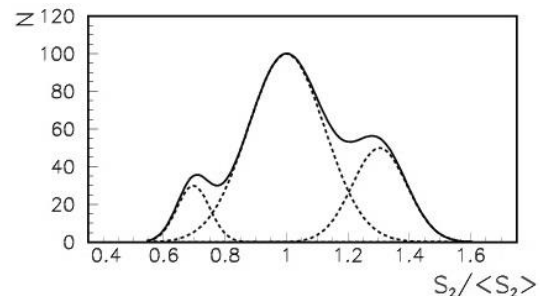


Fig. 2. The schematical normalized $S_2/\langle S_2 \rangle$ summary distribution from three effects (from the left to the right): ring-like, stochastic and jet-like effects distributions

RESULTS

The detailed study of ring-like substructures of the particles produced in 11.6 AGeV/c ^{197}Au interactions with Ag(Br) targets in emulsion detector has been done in [4]. Using the presented method, we obtained for central Au+Ag(Br) interactions normalized $S_2/\langle S_2 \rangle$ distribution (with additional criteria $\Delta\eta < 0.3$).

In Fig.3 it is fitted by three Gaussians. One can see a good agreement of experimental distribution and three Gaussians fit. Also the additional structure in the region on the left of the peak, where the ring-like substructures could give their contribution, is visible.

The experimental normalized $S_2/\langle S_2 \rangle$ distributions compared with the calculated ones by the FRITIOF model for the most central groups of events measured in ^{208}Pb and ^{197}Au induced collisions with Ag(Br) nuclei at 158 and 11.6 AGeV/c are presented in Fig. 4.

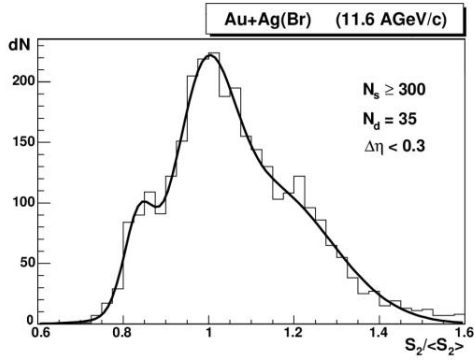


Fig. 3. The normalized $S_2/\langle S_2 \rangle$ distribution for central $^{197}\text{Au}+\text{Ag}(\text{Br})$ collisions fitted by three Gaussians.

The model distributions were aligned according to the position of the peak with the experimental one. Neither ring-like nor jet-like effects are part of the FRITIOF model, so model distributions are used as a statistical background.

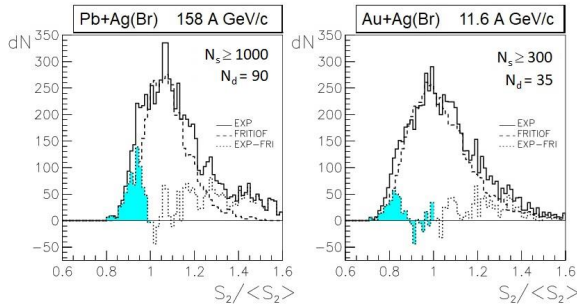


Fig. 4. The experimental and FRITIOF model normalized $S_2/\langle S_2 \rangle$ distributions for central ^{208}Pb and ^{197}Au induced collisions.

Both experimental distributions are shifted to the right, have a tail in the right part and are broader than the FRITIOF spectra. The left parts of both experimental distributions are not as smooth as in the model and there are some shoulders that refer to the surplus of the events in this region.

The results obtained from the experimental data after the subtraction of the statistical background are also shown. The resultant distributions have two very good distinguishable hills: the first, in the region $S_2/\langle S_2 \rangle < 1$, where the ring-like effects are expected and the second in the jet-like region $S_2/\langle S_2 \rangle > 1$.

The probability of the formation of the nonstatistical ring-like substructures can be estimated as a rate of the surface of the ring-like part to the full surface of the experimental distribution.

The estimated contribution of the ring-like effect to the experimental data as a function of N_d for $^{208}\text{Pb}+\text{Ag}(\text{Br})$ interactions and for the three centrality regions is presented in Fig.5.

These dependencies have several maxima situated nearly the same value of N_d . In the group with $N_s \geq 1000$ dependence slowly increases, while in the two other groups the dependences are decreasing.

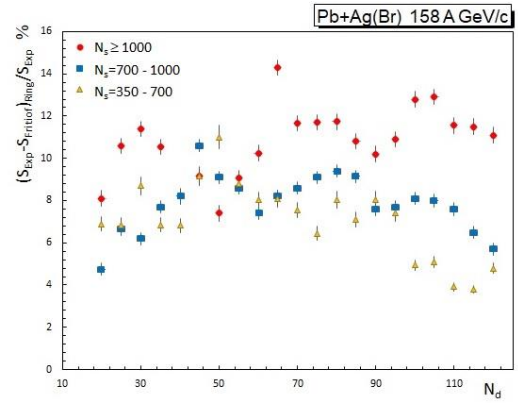


Fig. 5. The probability of ring-like structures as a function of N_d for different centralities.

CONCLUSIONS

The azimuthal ring-like substructures of produced particles from collisions of 11.6 AGeV/c ^{197}Au and 158 AGeV/c ^{208}Pb beams with Ag(Br) targets in the emulsion detector have been investigated.

The additional subgroups of produced particles in the region of the ring-like substructures ($S_2/\langle S_2 \rangle < 1$) in comparison to the FRITIOF model calculations have been observed.

The probability of the formation of a non-statistical ring-like substructures increases with increasing multiplicity of produced relativistic particles in interaction, which takes place for more central collisions and for larger primary energies and masses.

Our preliminary results for $^{208}\text{Pb}+\text{Ag}(\text{Br})$ collisions at 158 AGeV/c showed that the estimated contribution of the events with ring-like substructures is about 10-12% in the most central group of collisions with $N_s \geq 1000$. This value slowly decreases in two other groups of less central events with $N_s = 350 - 700$ and $N_s = 700 - 1000$.

ACKNOWLEDGMENT: This research was supported by the Ministry of Education, Science, Research and Sport of the Slovak Republic (VEGA No. 1/0113/18)

REFERENCES

1. E. Stenlund et al., Nucl. Phys. **A 498**, 541c (1989).
2. L. van Hove, Z. Phys. **C 21**, 93 (1984).
3. M. I. Adamovich, J. Phys. **G 19**, 2035 (1993).
4. G. I. Orlova, A. Kravčáková, S. Vokál, V. V. Prosin, in Proc. of the Hadron Structure 2002, Herľany, Slovakia, 22-27. Sept. 2002, Ed. by P. J. Šafárik University Košice, 155 (2003).

COR SYSTEM FOR COSMIC RAYS TRAJECTORIES IN MAGNETOSPHERE SIMULATION

D. Gecášek, daniel.gecasek@tuke.sk, Technical University, Košice, Slovakia, J. Genčí, jan.genci@tuke.sk, Technical University, Košice, Slovakia, P. Bobík, bobik@saske.sk, Institute of Experimental Physics, Slovak academy of sciences, Košice, Slovakia

INTRODUCTION

Cosmic rays are particles coming from space. The system COR (Cut-off rigidity) provides access for the wider scientific community to models of simulation of cosmic ray trajectories in the magnetosphere via a web interface. The system offers simulations of vertical directions or, from 576 directions covering half sphere (2π solid angle) with the center of the sphere in the point of interest. The simulation particle tracing is realized in combined internal (IGRF) and the external geomagnetic field (Tsyganenko 96 or Tsyganenko 05) covering the range of years 1968 to 2020. We call this Standard simulation module. There is also a module for simulation in an earlier period called the Historic simulation module that uses a couple of geomagnetic field approximations for the last two millennia (years from 0 to 1968) [1].

SYSTEM ARCHITECTURE

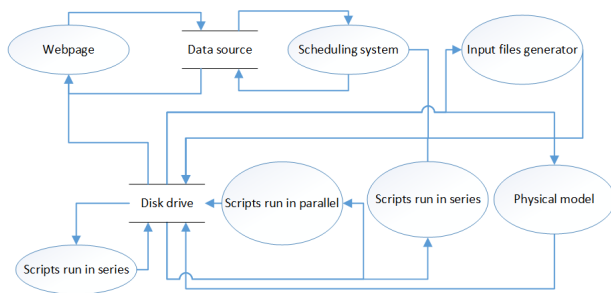


Fig. 1. Data flow diagram of COR system

The webpage cor.crmmodels.org is an interface for the user to interact with the system. Users can enter new requests for simulations, browse or download their results there. Anonymous users have access to limited functionality, they can only request single trajectory visualizations and browse existing results. Registered users can also request all types of possible simulations the system offers. A special kind of user, called privileged user, can enter requests for computationally intensive simulations.

The scheduling system reads requests from the data source and computes their results in a parallel environment. It also handles post processing of results and creation of visualizations. More complete information about the system architecture can be found in [2].

STARTING RIGIDITY VALUE OPTIMIZATION

Standard multidirectional simulation without starting rigidity optimization consists of 576 directions with rigidity step 0.01 GV and rigidity range

from 0.01 GV to 100 GV.

TAB. 1. Table of durations of simulation for selected positions with optimizations turned on or off.

Latitude	Longitude	Optimization	Duration
-60.15°	287.79°	No	14:04:31
-60.15°	287.79°	Yes	09:12:33
-10.05°	287.79°	No	05:05:36
-10.05°	287.79°	Yes	04:24:15
40.21°	287.79°	No	14:11:44
40.21°	287.79°	Yes	10:28:57

The table 1 above shows the durations of multidirectional simulations for selected points near the equator and further from it. There are also durations of simulations with starting rigidity optimization.

For equatorial positions without starting rigidity optimization, the simulation length is approximately 5 to 8 hours and for middle and high latitude positions it takes approximately 10 to 15 hours. With optimization, the length of simulation for equatorial positions shortens by approximately half to one hour and in the middle and high latitudes, it shortens by approximately 5 hours. As we can observe the duration of simulations is highly dependant on their position.

SYSTEM FEATURES

In the following section, we describe the features of the system available for the users.

Module for historical effective cutoff rigidity evaluation

The module allows users to evaluate magnetosphere transparency (cut off rigidity and spectrum of allowed and forbidden rigidities) for cosmic rays in the last two millennia. In the current version of the module, trajectories are simulated only for vertically incoming particles.

In figure 2 long term changes of effective vertical cutoff rigidities at the longitude 30° for selected latitudes of the southern hemisphere for years between 1 and 1901 CE are presented. The time of calculation is 1st January 00:00 for each point in time.

Simulations of the of multidirectional cosmic ray trajectories

The module evaluates trajectories for all incoming directions, represented by 576 directions uniformly covering the whole sky, and provides the user with all simulated data. The module also provides a user with a catalog of spectra of allowed and forbidden rigidities for all 576 evaluated directions, transmission function visualization, sky map of cut off rigidity visualization, and acceptance code visualizations.

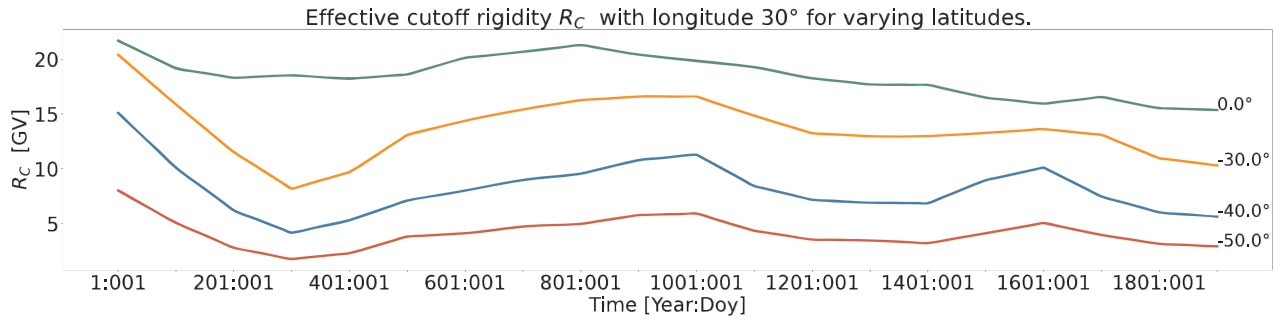


Fig. 2. Visualization of effective cutoff rigidity for years between 1 and 1901.

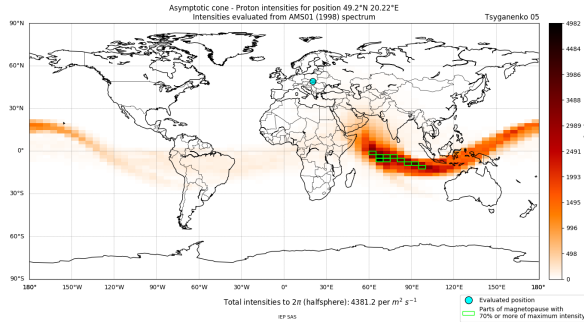


Fig. 3. Visualization of the acceptance cone for multidirectional trajectory simulation.

Figure 3 is an example of acceptance code visualization, provides information on which directions most of the particles that landed on the surface of the atmosphere above the simulated point came from. Acceptance cone of particles at magnetopause with intensities in different directions is shown. The figure also shows the value of the number of protons that reach a given point.

The figure illustrates the multidirectional approach of cosmic ray trajectories to a selected point in the Earth's magnetosphere. The used model for trajectories backtracking is described in [3].

Visualization of cosmic ray particle trajectory

For educational purposes, we added to the COR system a module for visualization of a single cosmic ray trajectory. The module allows visualization of trajectory for a particle with selected energy and incoming direction.

Example of the trajectory visualization for a proton with energy 2.859 GeV (rigidity 3.68 GV) coming to a position with latitude 50° and longitude 0°, from a direction with the zenith angle 10° and the azimuthal angle 70°.

SUMMARY

COR system at cor.crmmodels.org provides a wider scientific community with access to models for simulation of cosmic rays in Earth's magnetosphere. In this manuscript, we briefly describe the basic options and simulations provided by the COR system.

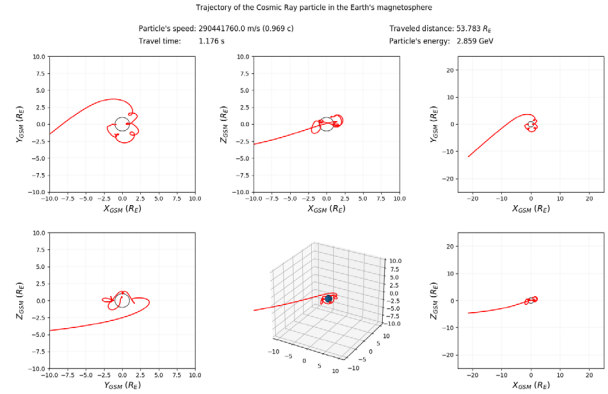


Fig. 4. Visualization of cosmic ray trajectory.

REFERENCES

1. P. Bobik et al., *Solar Physics*, 423 (2004).
2. D. Gecasek et al., *Electrical Engineering and Informatics* **10**, 401 (2019).
3. P. Bobik et al., *Physics and Modeling* **155**, 301 (2005).

SEARCH FOR PSEUDORAPIDITY FLUCTUATIONS IN HIGH ENERGY NUCLEAR COLLISIONS

J. Vrláková, janka.vrlakova@upjs.sk, S. Vokál, stanislav.vokal@upjs.sk, M. Val'a, martin.vala@upjs.sk
Faculty of Science, P.J. Šafárik University, Košice, Slovakia

INTRODUCTION

The existence of quark-gluon plasma (QGP) - a new phase of strongly interacting systems at high energy or density has been predicted in the framework of the quantum chromodynamics. The study of relativistic interactions has provided the opportunity to search for the signal of QGP. Large fluctuations of particle production have been expected in the transition from QGP to hadron phase [1, 2]. The study of particle production is a most useful tool for event characterization, for instance with respect to the centrality of the collision. Systematic studies of the variation with mass, energy, and impact parameter can provide the basis for the understanding of reaction mechanism [3].

EXPERIMENT

Nuclear interactions for various primary nuclei at different energies have been studied using horizontally exposed emulsion detector. Experimental data samples were collected by EMU01 and Dubna collaborations. The charged particles were classified according to the commonly accepted emulsion terminology into groups. The group of relativistic (shower) particles includes particles with $\beta > 0.7$ produced in the interactions as well as those knocked-out from the target nucleus. The polar (Θ) and azimuthal (Ψ) emission angles of all tracks have been measured. The value of pseudorapidity

$$\eta = -\ln \left[\tan \frac{\Theta}{2} \right] \quad (1)$$

has been calculated for each relativistic particle.

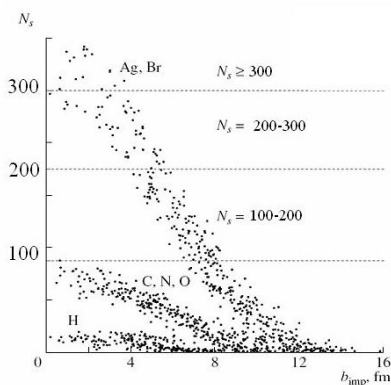


Fig.1. The dependences of N_s on b_{imp} for Au+Em interactions at 11.6 A GeV/c (FRITIOF model).

METHOD OF ANALYSIS

The method for measurement of fluctuations, which vanishes in the case of independent particle emission from

a single source, has been proposed in [6]. Event-by-event fluctuations of observables, which are defined as a sum of particle kinematics variables (rapidity or transverse momentum) and the summation runs over all produced particles of given event, can be studied by this method [7]. We can define a single particle variable as $z \equiv x - \bar{x}$, where

$$\bar{x} = \frac{1}{N_t} \sum_{k=1}^N \sum_{i=1}^{N_k} x_i, \quad (2)$$

N_k is particle multiplicity of the k^{th} -event, N is the total number of events, N_t is the total number of particles in all events. Also we define average multiplicity $\langle N_t \rangle = \frac{N_t}{N}$, so in Eq. (2) we sum over all events and over all particles from every events. The variable Z_k is multiparticle analog of z and can be defined as

$$Z_k = \sum_{i=1}^{N_k} (x_i - \bar{x}) \quad (3)$$

Then we define a quantity $\langle Z \rangle$ as

$$\langle Z \rangle = \frac{1}{N} \sum_{k=1}^N Z_k \quad (4)$$

The Φ quantity is defined as

$$\Phi = \sqrt{\frac{\langle Z^2 \rangle}{\langle N_t \rangle}} - \sqrt{\langle Z^2 \rangle} \quad (5)$$

where $\sqrt{\langle Z^2 \rangle}$ is the square of the 2nd moment of the inclusive z distribution. The quantity Φ measures the event-by-event fluctuations [7]. In case of study of pseudorapidity distribution of produced particles we can define $z = \eta_i - \bar{\eta}$. When the produced particles are independent each other, there are no correlations among particles and the Φ values vanishes. The non-zero values of Φ may attributed to the measure of correlations among produced particles [6,7].

ANALYSIS AND RESULTS

The Φ dependences for O+Em induced interactions at 4.5 - 200 A GeV/c have been studied using method of the quantity Φ . Experimental and Cascade evaporation model (CEM) data samples have been compared. We selected interactions with Ag(Br) targets, and we studied the groups of interactions with increasing number of relativistic particles $\langle N_s \rangle$ (Fig.2) for O+Ag(Br) interactions at 4.5 and 200 A GeV/c. One can see that the Φ values for experimental data samples are higher than the values for CEM data [8]. The similar results have been published in [7], where FRITIOF model has been used for comparison. The preliminary uncertainties of Φ are statistical only.

The analysis have been done for various primary nuclei (O,Ne,Si,S) at 4.1- 4.5 A GeV/c on Ag(Br) (Fig.3) and CNO (Fig.4) targets. The Φ values have been

calculated for different multiplicity groups of events. The Φ values for Ag(Br) targets are greater than that for light (CNO) targets for the same primary nuclei, i.e. with increasing mass of target increases the Φ value and the correlations among particles increase. The Φ values are decreasing with increasing average number of relativistic particles for all data. This can be explained by the formation of several independent sources during multiparticle production [7]. The similar results have been published in [7, 9].

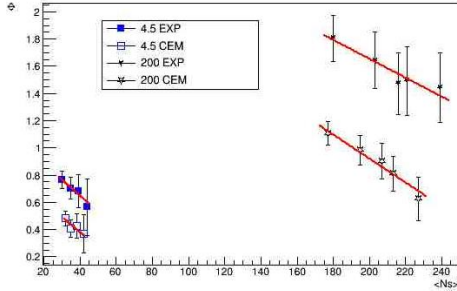


Fig.2: The dependences of Φ values on the average multiplicity (N_s) for O+Ag(Br) at 4.5 and 200 A GeV/c, experimental and CEM data samples.

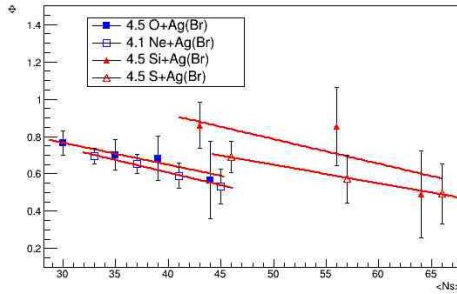


Fig.3: The dependences of Φ values on the average multiplicity (N_s) for A+Ag(Br) at 4.1- 4.5 A GeV/c.

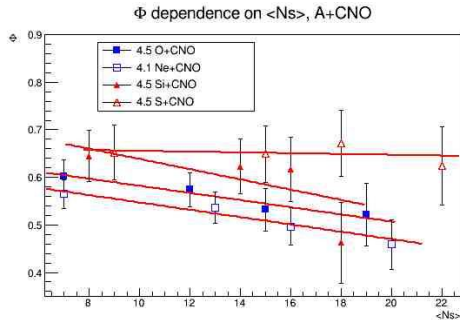


Fig.4: The dependences of Φ values on the average multiplicity (N_s) for A+CNO at 4.1- 4.5 A GeV/c.

The Φ values for various primary nuclei with the heavy emulsion Ag(Br) targets at different momenta are given in the Tab.1, where p is the momentum of primary nucleus A and $\langle N_s \rangle$ is the average number of relativistic particles.

For light primary nuclei ($A=16-32$) the Φ values increase with increasing momenta. For heavy primary nuclei ($A=197, 208$) the Φ values decrease with increasing momenta, this could be caused by the different numbers of produced relativistic particles.

TAB. 1: The Φ values for A+Em interactions

p [A GeV/c]	A	$\langle N_s \rangle$	Φ
4.5	^{16}O	30	0.765 ± 0.066
4.1	^{22}Ne	33	0.696 ± 0.043
4.5	^{28}Si	43	0.859 ± 0.123
4.5	^{32}S	46	0.689 ± 0.084
14.6	^{16}O	65	0.618 ± 0.108
14.6	^{28}Si	93	0.899 ± 0.100
11.6	^{197}Au	189	1.796 ± 0.110
200	^{16}O	180	1.805 ± 0.170
200	^{32}S	259	1.833 ± 0.135
158	^{208}Pb	637	1.148 ± 0.161

CONCLUSIONS

A preliminary study of multiplicity and target dependence of pseudorapidity fluctuations in terms of the quantity Φ has been made for various primary nuclei with Ag(Br) and CNO targets in emulsion detector.

Search for the event-by-event fluctuations of observable Φ , and its dependence on the mass of primary nuclei and their momenta for different groups of events have been performed.

For all interactions and groups of events, the Φ values are found to be greater than zero which indicates the presence of strong correlations in the multiparticle production at momenta from 4.1 to 200 A GeV/c.

The experimental results have been compared with the results obtained from analysis of CEM data sample. The Φ values for experimental data samples are higher than the values for CEM data.

The Φ values for heavy Ag(Br) targets are greater than for light (CNO) ones for the same primary nuclei and momenta, i.e. with increasing target mass the correlations among the final state particles also increase.

ACKNOWLEDGMENT: This research was supported by the Ministry of Education, Science, Research and Sport of the Slovak Republic (VEGA No. 1/0113/18).

REFERENCES

1. L. Van Hove, Z. Phys. C21, 93 (1984).
2. M. Gyulassy et al., Nucl. Phys. B237, 477 (1984).
3. J. Stachel, Nucl. Phys. A525, 23c (1991).
4. M.I. Adamovich et al., Nucl. Phys. A593, 535 (1995).
5. S.Vokál et al., Proc. of RNP, 11th Int. Workshop, June 17- 23, 2012, Stará Lesná, (2012) p.62.
6. M.Gazdzicki, S.Mrowczynski, Z. Phys. C54, 127 (1992).
7. S.Bhattacharyya et al., Phys. Lett. B 726, 194 (2013).
8. S.Vokál et al., Proc. of RNP, 14th Int. Workshop, May 27- June 1, 2019, Stará Lesná, (2019) p.115.
9. M.Val'a et al., Proc. of 24th Conf. of Slov. Phys., Sept. 2-9, 2019, Žilina, (2019) p.77.

STATISTICAL ERROR OF FP EQUATION

V. Mykhailenko, Slava1994111@mail.ru, Institute of Physics, Faculty of Science, P. J. Šafárik University, Park Angelinum 9, 041 54 Košice, P. Bobik, Institute of Experimental Physics, Slovak Academy of Sciences, Kosice, Slovakia

INTRODUCTION

The sun produces and radiates out the charged particles flow which is called the solar wind. Solar wind propagates through the solar system to the moment when the solar wind and interstellar wind pressure going to be are balanced, this region, approximately till 100 AU is called the heliosphere. When the galactic cosmic rays (GCR) reach the heliosphere boundary, then begins the process of so-called solar modulation, which presents a decreasing of GCR intensity inside the heliosphere mostly for particles with energies less than 30 GeV. At the time of solar modulation particles of GCR interact with magnetic irregularities in the solar wind and the process could be approximated as diffusion combined with convection and adiabatic energy losses. As was described by some authors early, the particle starts randomly walking between these irregularities. To describe the GCR propagation inside the heliosphere widely used equation was introduced by Parker (1965). One of the most precise methods to solve this equation is the so-called stochastic integration method which is described in [1]. In this paper were presented GCR spectra at 1 AU evaluated by forward – in - time stochastic integration method, statistical error for this method was described.

MODEL DESCRIPTION

For the forward-in-time model see [1]. The stochastic integration method was used to integrate the stochastic path of charged particles from the border of the heliosphere to the target (Earth) with a position at 1 AU. The set of SDE for Forward integration with momentum p , called the F-p method, is:

$$dr = \left(\frac{2K_{diff}}{r} + V_{sw} \right) dt + \sqrt{2K_{diff}} dW \quad (1)$$

$$dp = -\frac{2V_{sw}p}{3r} dt \quad (2)$$

$$L = -\frac{4V_{sw}}{3r} \quad (3)$$

Here $K_{diff} = K_0 \beta P$ is the diffusion coefficient where K_0 is the diffusion parameter in presented simulation taken to be $K_0 = 5 \times 10^{22} \text{ cm}^2 \text{ s}^{-1} \text{ GV}^{-1}$, β is the particle velocity in speed of light units, and P is particle rigidity in GV. Solar wind speed V_{sw} is taken to be constant and equal to 400 km s^{-1} . In the case of forward-in-time integration, GCR particle starts its path from the heliosphere border, for the presented simulation was taken to be 100 AU. For each moment of time particle lost energy (momentum) by a value calculated in (2).

RESULTS

We evaluated spectra at 1 AU for two different

models of local interstellar spectra (LIS). First one as couple of Gaussian distributions with maxima at different kinetic energies. Second one as Yamada LIS spectrum [2]. For the data processing to obtain the spectra was used so-called binning procedure. Distributions at 1 AU from Gaussian LIS with a maximum at T_0 , $J \propto \exp \left[-300 \left(\ln \frac{T}{T_0} \right)^2 \right]$, were used for calculation of integrals with respect to different numbers of crosses at 1AU. Obtained integral values were normalized by number of crosses (by statistics) and then by value of integral evaluated for highest statistics (approximately for 25 million crosses statistics). The 1 percent statistical error value is related to value of this integral. In this way the integrals as function of statistics for different T_0 values $T_0 = 1, 2, 5, 10 \text{ GeV}$ were calculated.

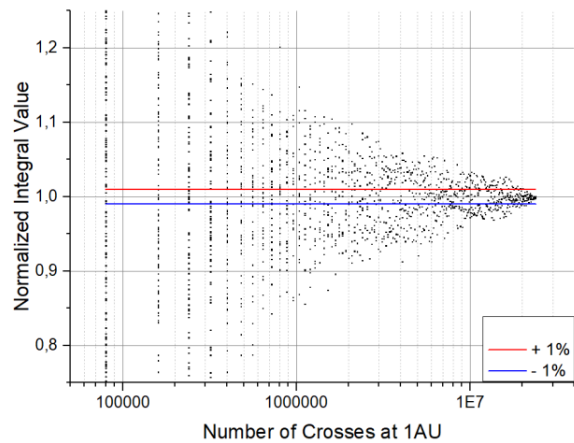


Fig. 1. Integrals evaluated from Gaussian spectra for different $T_0 = 1 \text{ GeV}$

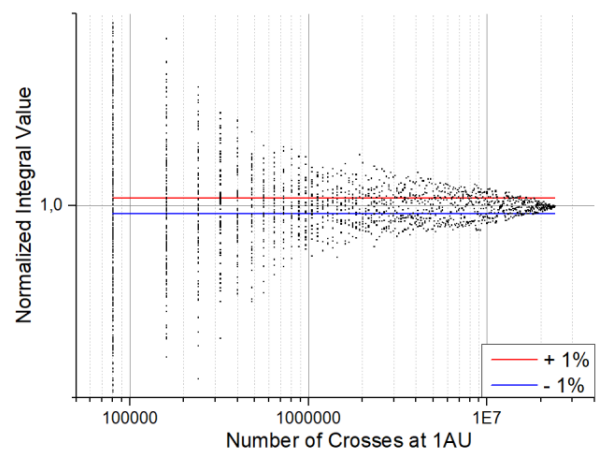


Fig. 2. Integrals evaluated from Gaussian spectra for different $T_0 = 2 \text{ GeV}$

In the second model, the modulated spectrum at 1AU from Yamada LIS was evaluated for six different values of injected trajectories, from 10 billion (black one) to 60

billion (the blue one).

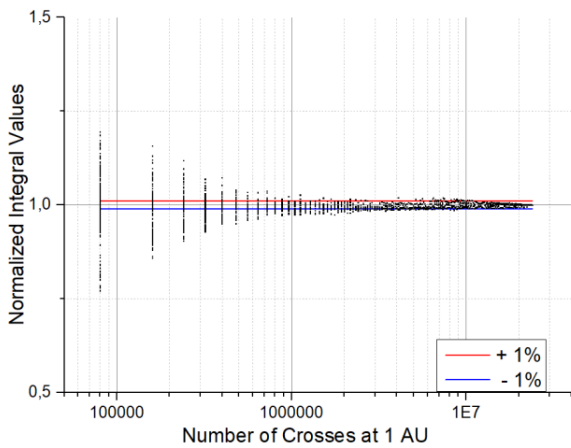


Fig. 3. Integrals evaluated from Gaussian spectra for different $T_0 = 5$ GeV

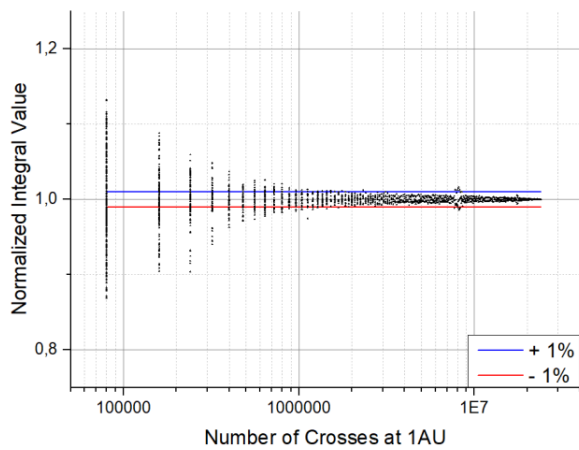


Fig. 4. Integrals evaluated from Gaussian spectra for different $T_0 = 10$ GeV

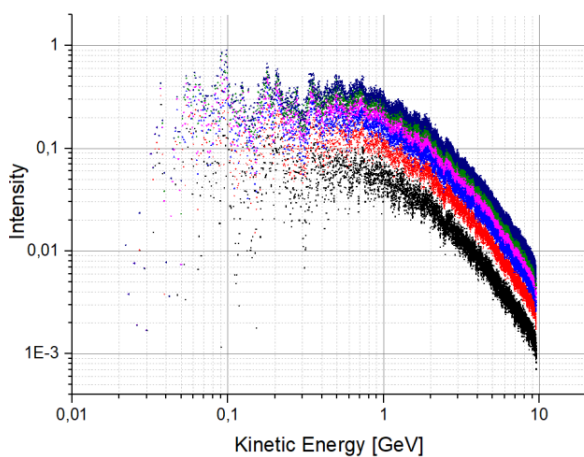


Fig. 5. Intensity value with respect to the different number of injected trajectories, from 10 billion injected trajectories to 60 billion respectively with a step of 10 billion trajectories

Differential intensity of Yamada LIS was taken to be $J \propto p(m^2c^4 + p^2c^2)^{-1.85}$. Integrals of the whole spectrum between 0.001 GeV and 10 GeV for different

statistics (numbers of crosses radius 1AU) are presented in Figure 6. Starting from 10 thousand crosses where we could evaluate many of such integrals (hundreds of integrals) till a couple of millions crosses with few integrals. The normalization procedure is identical to the one used with the Gaussian LIS spectra. Results for whole spectra integrals presented in Figure 6. show a convergence of integral value to a specific value. Statistical error decreases with higher statistics, reaching 1% value around statistics in order of millions of crosses.

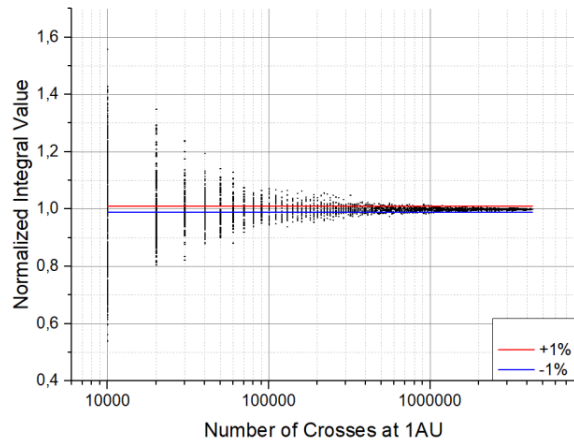


Fig. 6. Normalized integral of Yamada spectrum in range 0.001 – 10 GeV value distribution with respect to number of crosses at 1 AU

CONCLUSIONS

The evaluation of statistical error of cosmic rays modulation in heliosphere at 1AU (input parameters: $V_{sw} = 400 \text{ km s}^{-1}$, $K_0 = 5 \times 10^{22} \text{ cm}^2 \text{ s}^{-1} \text{ GV}^{-1}$) was done in F-p method for Gaussian LIS spectra for selected energies and Yamada LIS spectrum. For Gaussian spectra needed statistics to reach 1% statistical error was approximately 20 million for $T_0 = 1$ GeV, and 2 GeV, and approximately 10 million for $T_0 = 5$ GeV, and 10 GeV. For Yamada spectra in range from 0.0001 to 10 GeV needed statistics to reach 1% statistical error of integral of spectra was approximately couple of millions. In the future the same methods will be applied for another combination of the input parameters and errors will be evaluated as standard deviation dependency on simulation statistics.

ACKNOWLEDGMENT: This research was supported by the Ministry of Education, Science, Research and Sport of the Slovak Republic (VEGA No. 1/0113/18).

REFERENCES

1. Bobik, P., et al., J. Geophys. Res. Space Physics **121**, (2016).
2. Yamada, Y., S. Yanagita, and T. Yoshida, Geophys. Res. Lett. **25**, (1998).

STUDY OF P3HT THIN FILM PHOTOLUMINESCENCE SPECTRA USING H- AND J-AGGREGATE THEORY

S. Kotorová, sona.kotorova@stuba.sk, J. Chlpík, T. Váry, J. Cirák, Faculty of Electrical Engineering and Information Technology, Slovak University of Technology, Ilkovičova 3, Bratislava, Slovakia, V. Nádaždy, Institute of Physics, Slovak Academy of Sciences, Dúbravská cesta 9, Bratislava, Slovakia

INTRODUCTION

Poly(3-hexylthiophene) (P3HT) is a commercially available semiconducting polymer with controlled molecular weight, low polydispersity and regular end-to-end arrangement of the side chain. Based on its properties, it has been the subject of research for several years and number of papers was published [1, 2]. Although P3HT is nowadays considered as an obsolete material, it is still used as a part of solar cells or light-emitting diodes [3, 4]. Better understanding of the photophysics of P3HT is therefore needed desirable for wider knowledge of the details of processes in a certain class of photosensitive polymers. Spano and co-workers [5] developed a model describing the vibrational structure of absorption and emission spectra of conjugated polymers using H- and J-aggregate theory. H-aggregates are called molecules in a coplanar stacked manner with intrachain bonding interactions. J-aggregates are called molecules in a sequential co-linear and parallel manner with interchain Coulombic interactions.

In this paper, we report on study of emission spectra of P3HT layers. The usual interband transitions S_0-S_0 , S_0-S_1 , S_0-S_2 can be clearly identified in the published photoluminescence measurements on P3HT layers [6]. However, in many cases the spectra are characterized by weaker ripples besides these main features. We point out their possible interpretation by means of the H- and J-aggregates theory proposed by Spano.

EXPERIMENTAL DETAILS

Two kinds of samples were prepared on different substrates: ITO coated glass, and p-type heavily doped polished crystalline silicon (c-Si). The substrate cleaning procedures were performed according to [7].

The studied layers were prepared by spin coating deposition (parameters: 30 rps for 45 sec.) from a 1.5% solution of P3HT in dichlorobenzene. The samples were subsequently solvent annealed (dried closed in Petri dish with solvent vapours) and then thermally annealed at 110 °C for 5 min as well. The complete process of samples production, including treatment, took place in an inert Ar atmosphere. Regioregular polymer P3HT without any other purification was purchased from Sigma-Aldrich. The applied procedure with maintaining the appropriate parameters results in the production of 110 nm thick polymer films on both types of the substrates [8].

The photoluminescence (PL) measurements were performed by Horiba Jobin-Yvon SPEX Fluorolog-3 with double gratings monochromators, Hamamatsu R928P photomultiplier tube detector and Xe lamp as the excitation source. The measured samples were held in

specially adapted closed cuvettes with Ar atmosphere ensuring perpendicular excitation light impact on the sample. The detected signal entered the emission monochromator in so-called front face geometry at the angle of 22.5 degrees with respect to the sample normal.

RESULTS AND DISCUSSION

The PL emission spectra of P3HT layer on c-Si (Fig. 1) and on ITO (Fig. 2) exhibit some important features. There are clearly recognizable global maxima at approx. 1.96 eV in the graphs. These peaks are being mostly assigned to the S_0-S_0 (0-0) intramolecular vibronic transition. The secondary maxima in the vicinity of 1.8 eV and 1.5 eV belong to the S_0-S_1 (0-1) or S_0-S_2 (0-2) transitions, respectively [6]. The transitions 0-0 and 0-1 are usually interesting from the point of view of investigating the layers structure. As Spano et al. showed, the ratio of the intensities I_{01}/I_{00} of the transitions 0-0 and 0-1 is related to the molecules disorder [9]. In order to evaluate this ratio, it is important to identify the exact position of the respective maximum in the spectrum, as well as its amplitude. Individual maxima can be extracted e.g. by fitting the curves assuming a series of Gaussian functions, since a random broadening of the spectral lines is expected.

According to the theory, the distances of the main neighbouring transitions tend to be approximately 1 eV. However, the ripples seen in the analyzed spectra are twice as close. This phenomenon can elicit several interpretations. The molecules in the studied layers might be in at least two different crystalline phases. The formation of two phases was observed by Grazing-incidence wide-angle X-ray scattering technique only in the layers on ITO substrates [8]. P3HT on a smooth c-Si substrate is characterized just by one crystalline phase. There is a certain proportion of the amorphous phase material in addition to the molecules in the crystalline phase. Another possibility is that weakly interacting H- and J-aggregated molecules exist side by side in the layer. We chose this option due to the well-known fact of the presence of both kinds of aggregates in P3HT layers prepared by spin-coating. It is generally considered that H-aggregates dominate in such films [10].

Based on the above assumptions, we tried to fit the spectra with two three-member series of Gauss functions. One triplet had a common width σ , the main 0-0 transition frequency ω_0 and a constant distance $\Delta\omega$ between the maxima. Each set represented a series of maxima belonging to one aggregate type (J or H). Despite the relatively large number of 9 free parameters, it was possible to find the exact positions of the individual transitions. These are indicated as J-like and H-like in the Figures 1 and 2 and their values are

summarized in Tables 1 and 2. The designations H and J were chosen because the H-aggregates are usually blue shifted relative to the J-aggregates. As the exact nature of the spectral features is not actually clear, we rather use the suffix *-like* in the labels.

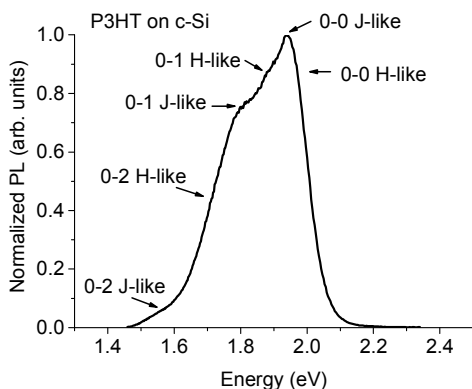


Fig. 1. Photoluminescence emission spectrum of P3HT layer on c-Si substrate with excitation at 525 nm. The spectrum is normalized to its maxima at the 0-0 vibronic transmission peak

Tab. 1. Table of vibronic transmission energies from PL emission spectrum of P3HT layer on c-Si substrate

Vibronic transmission	H-like E (eV)	J-like E (eV)
0-0	2.05	1.96
0-1	1.90	1.76
0-2	1.76	1.56

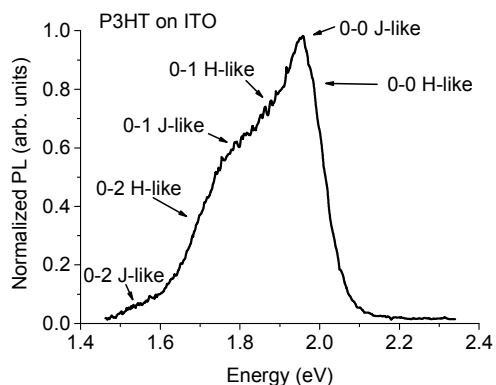


Fig. 2. Photoluminescence emission spectrum of P3HT layer on ITO substrate with excitation at 525 nm. The spectrum is normalized to its maxima at the 0-0 vibronic transmission peak

Tab. 2. Table of vibronic transmission energies from PL emission spectrum of P3HT layer on ITO substrate

Vibronic transmission	H-like E (eV)	J-like E (eV)
0-0	2.07	1.97
0-1	1.91	1.77
0-2	1.75	1.56

Although, it is not an objective of this work to

compare the spectra nor evaluate the parameters of the internal structure of the layers, one small remark should be noted regarding the visible fundamental difference between the plotted data. This applies to the area of 0-1 transitions, in which a significant decrease of the signal from the main 0-0 maximum in the case of the P3HT layer on the ITO substrate can be seen. As mentioned above, the phenomenon is commonly attributed to the greater disorder of the material in the layer. This fact could be attributed to the greater roughness of the substrate (~ 6 nm) compared to c-Si (< 1 nm). It turns out that these differences are related to the nature of the substrate surface indeed. Our intention was to point out that a more complex spectrum analysis, which requires further in-depth investigation, could help to understand the physical phenomena affecting the formation of defect states in the electronic structure. This ultimately leads to the effect on the efficiency of photoelectric elements based on organic polymers.

CONCLUSION

According to the Spano's calculations [11], if only H or J aggregates are in the layer, the mutual distance of the spectral peaks was 1.0 – 1.2 eV. The ripples in the spectra of real P3HT layers seem to be as twice as closer. These spectral features might indicate the presence of both types of weakly interacting aggregates. Their identification and evaluation can be helpful for understanding processes in the polymer layers.

ACKNOWLEDGMENT: The work was supported by grant of Cultural and Educational Grant Agency (KEGA) of the Ministry of Education, Science, Research and Sport of the Slovak Republic No. 025STU-4/2020.

REFERENCES

- V. P. Litvinov, Adv. Heterocyclic. Chem. **90**, 125 (2006).
- V. C. Gonçalves, D. T. Balogh, Sens. Actuator B-Chem. **162**, 307 (2012).
- W. Yan et. al., J. Photochem. and Photobiol. A: Chem. **389**, 112627 (2020).
- M. A. T. da Silva et. al., Opt. Mater. **62**, 119 (2016).
- F. C. Spano et. al., Annu. Rev. Phys. Chem. **65**, 477 (2014).
- P. Ehrenreich et. al., Scientific Reports **6**, 064203 (2003).
- S. Halászová et. al., AIP Conference Proceedings **1996**, 020015 (2018).
- V. Nádaždy et. al., J. Phys. Chem. C **122**, 5881 (2018).
- F. C. Spano J. Chem. Phys. **112**, 234701 (2005).
- A. Köhler et. al.: Electronic Processes in Organic Semiconductors (Wiley-VCH Verlag GmbH & Co. KGaA – 2015).
- F. C. Spano et. al., Acc. Chem. Res. **43**, 429 (2010).

H-FUNCTION CALCULATION FOR SELECTED SPECTRAL BANDS OF OXYGEN

J. Pokorný, xpokor31 at stud.feec.vutbr.cz, Faculty of Electrical Engineering and Communication, Brno University of Technology, Technická 3058/10, 616 00 Brno, Czech republic

INTRODUCTION

The Oxygen, from the reason of its uniqueness and irreplaceability in the meaning for the whole life and now in climate-change, is under intensive scientific research, mainly for its absorption properties. The present work deals with the calculation of absorption properties of oxygen molecule with the help of a program using modern density theory, the basis of which was laid by Enrico Fermi.

BASIC RELATIONS

For the calculations of absorption properties, where belongs H -function as their integral part, it is necessary to know values of vibrational frequencies of molecules. Vibrational frequencies of diatomic molecule of oxygen could be approximately described by the Hook Law:

$$\nu(\text{Hz}) = \frac{1}{2\pi} \sqrt{\frac{k}{\mu}}, \quad (1)$$

or with the usage of common spectroscopic units (cm^{-1}), so the formula (1) looks like:

$$x \nu(\text{cm}^{-1}) = \frac{1}{2\pi c} \sqrt{\frac{k}{\mu}}, \quad (2)$$

where k is a force constant, μ is the reduced mass of oxygen molecule:

$$\mu = \frac{m_1 m_2}{m_1 + m_2}. \quad (3)$$

Vibronic energy of atomic level, when oscillator anharmonicity was included, is given by:

$$G(\nu) = A - B + C + \dots, \quad (4)$$

Where

$$\begin{aligned} A &= \omega_e \left(\nu + \frac{1}{2} \right), \\ B &= \omega_e x_e \left(\nu + \frac{1}{2} \right)^2, \\ C &= \omega_e y_e \left(\nu + \frac{1}{2} \right)^3. \end{aligned} \quad (5)$$

where $G(\nu)$ is the vibronic energy, ν is the vibronic

quantum number, ω_e is the harmonic frequency, $\omega_e x_e$ and $\omega_e y_e$ are the anharmonic constants. B. Rosen [1] wrote a book called Spectroscopic Data Relative to Diatomic Molecules, where he divides the spectrum, for example for selected oxygen molecule O_2 into 11 electronic bands in total with appropriate vibrations. The foundation of the calculations is the ground state, [2] where the oxygen molecule is in the triplet state $X^3\Sigma_g^-$ [3]. When our system absorbs energy it changes its energetic state. The perturbations theory in the Quantum mechanics states for transition probability w of a quantum system from initial state Ψ_i to final state Ψ_f this equation:

$$w = \frac{2\pi}{\hbar} |\langle \Psi_f^* | w(r) | \Psi_i \rangle|^2 \rho_f(E_f) \quad (6)$$

where the energy of the final state:

$$E_f = E_i + \hbar\omega \quad (7)$$

where $\rho_f(E_f)$ is the density of the state and $w(r)$ is the perturbation operator. For the purpose of calculating the H -function of the absorption coefficient for oxygen, it is necessary to know the oscillator strength f . Program Orca allows this important physical quantity to be calculated according to the following relation.

$$f = f_D + f_M, \quad (8)$$

where f_D represents the oscillator strength given by the dipole moment in the relation:

$$f_D = \frac{2m_{ed}}{3\hbar^2 e^2} E_{if} |D_{if}|^2, \quad (9)$$

and magnetic dipole moment f_M :

$$f_M = \frac{2m_{ed}}{3\hbar^2 e^2} E_{if} |M_{if}|^2, \quad (10)$$

The absorption coefficient is given by:

$$\kappa(\nu) = N_L B_{LU} \hbar \nu_{LU} F(\nu), \quad (11)$$

where N_L is the occupancy of the lower level, B_{LU} is the Einstein absorption coefficient, ν_{LU} is the frequency of the line, $F(\nu)$ is the line profile. The H -function itself is given by the relation:

$$H_{LU} = G \cdot J, \quad (12)$$

Where

$$G = \frac{8\pi^3}{3hc} \frac{\omega_I}{\omega_\Lambda (2S+1) Q_{nucl}}$$

$$J = |R_e^{v''v'}|^2 S_{J''} \omega_{LU}, \quad (13)$$

where ω_I is the nuclear spin of atoms, ω_Λ the statistical weight of the orbital angular momentum Λ with respect to the internuclear axis, S is the total electron spin, Q_{nucl} is the kernel part of the partition function, $|R_e^{v''v'}|$ is the vibronic transition moment, $S_{J''}$ are Hoehn-London factors and ω_{LU} is the wavenumber of the transition.

```

*** CONVERGENCE OF RESIDUAL NORM REACHED ***
--- The CIS iterations have converged ---

-----
UHF CIS RESULTS
-----

IR00T= 1:  0.176542 au    4.804 eV   38746.5 cm**-1
5b -> 7b  0.321106 (-0.566662)
5b -> 8b  0.106447 ( 0.326263)
5b -> 14b 0.049941 ( 0.223476)
5b -> 15b 0.014255 ( 0.119396)
6b -> 7b  0.106447 (-0.326263)
6b -> 8b  0.321106 (-0.566662)
6b -> 14b 0.014255 ( 0.119396)
6b -> 15b 0.049941 (-0.223476)

```

Fig. 1. An example of frequency calculation for individual states

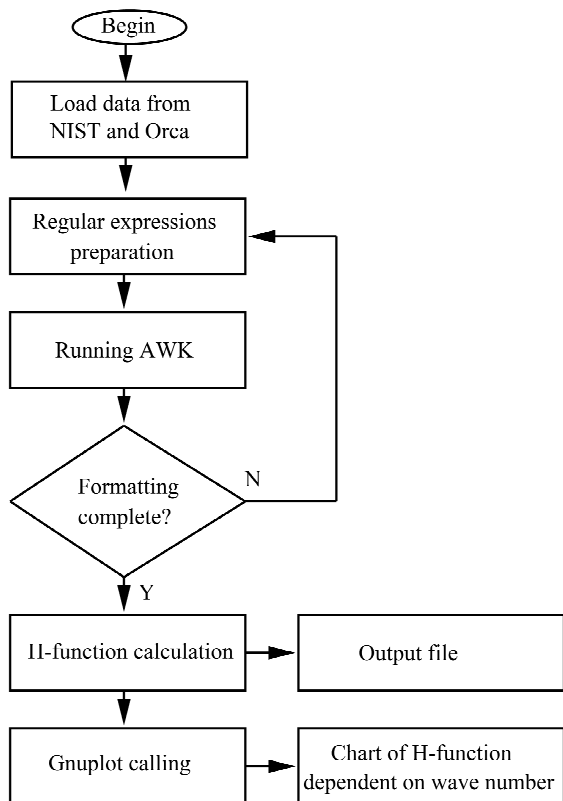


Fig. 2. Block diagram of our program NKrov2

Program Orca [4] has a wide range of computational functions related to the closed and unclosed shells which are represented by unpaired electrons. Program Orca can calculate according theory Complete Active Space Self-Consistent Field (CASSCF), which differs from broadly used methods according to Density Functional Theory (DFT), which is not a black box, so you can choose group of orbitals and electrons creating active space. An example of calculating the frequency of individual states is shown in Fig. 1. Principal solution for processing of input data from the Orca program and NIST [5] database and H -function calculation is provided in our program NKrov2. NKrov2 was designed for this purpose, its block scheme is on fig. 2. The output of our program NKrov2 is set of values of H -function plotted in a graph in dependence on the wavenumber ω , see Fig. 3.

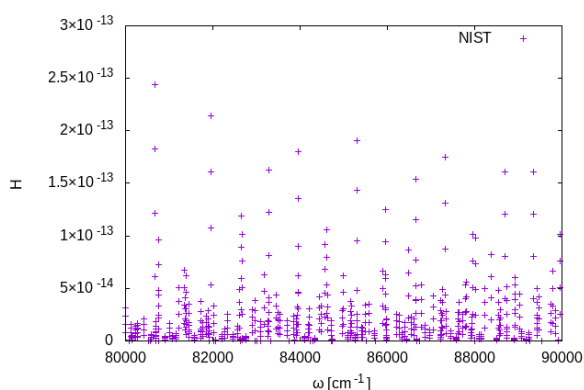


Fig. 3. Concentration independent part of (H -function) of the absorption coefficient

CONCLUSION

The use of these programs allows to tabulate H -function which greatly simplifies calculation of the absorption coefficient for a subsequent physical research.

ACKNOWLEDGEMENT: This work was supported by the Internal Grant Agency of Brno University of Technology, grant No. FEKT-S-20-6352.

REFERENCES

1. B. Rosen: Spectroscopic Data relative to Diatomic Molecules (Pergamon Press, Oxford – 1970).
2. Y. Endo, M. Mizushima, Japanese J. of Applied Physics **6**, 21 (1982).
3. M. Laing, Journal of Chemical Education **6**, 66 (1989).
4. Orca Forum, <https://orcaforum.kofo.mpg.de/app/php/portal>
5. NIST Oxygen, <https://webbook.nist.gov/cgi/cbook.cgi?ID=\C7782447\verb&|Mask=1000>

A SETUP FOR MEASUREMENT OF THE TOTAL REACTION CROSS SECTION

I. Siváček, sivacek@ujf.cas.cz, Institute of Nuclear Physics, Academy of Sciences of Czech republic, Prague, Czech republic, Yu. E. Penionzhkevich, pyuer@jinr.ru, Yu. G. Sobolev, sobolev@jinr.ru, V. V. Samarin, samarin@jinr.ru, M. A. Naumenko, anaumenko@jinr.ru, S. S. Stukalov, stukalov@jinr.ru, Joint Institute for Nuclear Research in Dubna, Moscow, Russia

INTRODUCTION

Radioactive beams offer a unique opportunity to investigate nuclear reactions with exotic, weakly-bound nuclei far from β -stability line. Measurements with beams of light, short-lived neutron-rich isotopes make it possible to obtain information about the inner structure of nuclei (clusters, neutron halo, neutron skin) and its manifestation in reactions [1]. The total reaction cross section, σ_R , is one of the important quantities available for measurement. There are two main methods of measurement of this parameter – attenuation method [2] and transmission method [3]. Our previous measurements, based on modification of the transmission method, showed a local rise of this quantity above predicted values [4]. Obtained results provide a good set of data for testing microscopic models of nuclear reactions [5, 6].

EXPERIMENTAL SETUP

The setup for total reaction cross section measurements consists of an in-beam multi-element telescope for particle identification and beam intensity measurement and a 4π gamma-ray spectrometer for detection of gamma-rays and neutrons accompanying nuclear reactions, located around the target. The setup is subject to continuous development, aimed at the improvement of the setup parameters (registration efficiency, background characteristics, etc.). Detailed description of the previous version of the spectrometer, MULTI, can be found in [7]; current setup, MULTI-2, is described in [8]. Upgrade possibilities of the spectrometer with high-resolution scintillation $\text{CeBr}_3 + \text{NaI(Tl)}$ phoswich detectors was analyzed by Monte Carlo method in [9].

The spectrometer is assembled in the beamline of the ACCULINNA fragment separator in the Flerov Laboratory of Nuclear Reactions, Joint Institute for Nuclear Research in Dubna, Russia [10]. Scheme of the setup is shown in fig. 1. The in-beam part includes polyethylene absorbers for adjusting secondary beam energy, active collimators AC1 and AC2, silicon detector dE_0 , a removable silicon pixel detector for beam position adjustment on the target. Active collimators define the irradiated area of the target and provide measurement of the secondary beam intensity. Silicon detector dE_0 is used for secondary beam projectile identification by $dE:E$ method, where total energy E is provided by time-of-flight measurement between active collimators. Signal over threshold from detectors in the gamma-ray spectrometer is used as a tag of a nuclear reaction event in the target. Registration efficiency for each reaction event is evaluated with the Monte Carlo simulations as a function of the number of triggered detectors in the gamma-ray spectrometer [8, 11]. Results of the simulations are verified with

excellent agreement by measurement with ^{60}Co spectroscopic source [8]. Crucial aspect for correct measurement is shielding of the spectrometer from background events, mainly gamma-rays and neutrons, emerging from nuclear reactions outside the target and X-rays produced in the process of beam interaction with detectors and construction materials. The gamma-ray spectrometer has several background-shielding layers (fig. 1). The first layer on the outer side of the gamma-ray spectrometer is made of 500 μm thick copper foil. Its purpose is to shield detectors from X-rays emerging from surrounding materials. The second layer is composed of 500 μm cadmium plate, for shielding the spectrometer from thermal neutrons. The outermost layer is made of 5 mm thick lead plate for shielding from outer gamma rays. A dome made of 50 mm thick low-background lead bricks is built around the spectrometer. It is designed as a shield from all possible external sources of gamma rays in the low-energy region, where prompt gamma rays are registered.

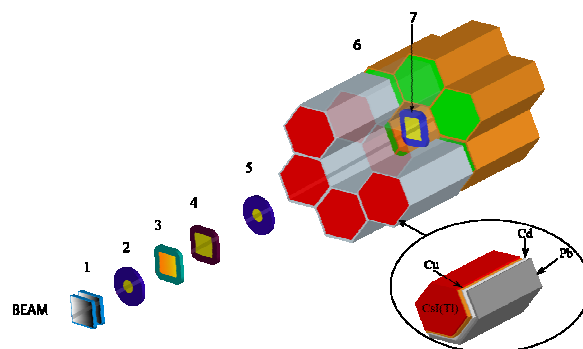


Fig. 1. Scheme of the setup: 1 — CH_2 absorbers, 2 — active collimator AC1, 3 — silicon dE_0 detector, 4 — removable pixel detector $16 \times 16 \mu\text{m}$, 5 — active collimator AC2, 6 — gamma-ray spectrometer consisting of $12 \times \text{CsI(Tl)}$ detectors, 7 — target.

RESULTS OF THE MEASUREMENTS

A series of experimental measurements of the total reaction cross section with exotic nuclei was conducted on this setup [12, 13]. The obtained results are in good agreement with the previous measurements [11]. The principle is in the measurement of secondary beam intensity, I_0 , hitting the target with N target nuclei per unit area. The intensity I_R , corresponding to inelastic nuclear reaction channels, is determined from the number of tagged events T . They are detected by the gamma-ray spectrometer with efficiency $\eta(M_\gamma, E_\gamma)$, which is a function of energy E_γ and multiplicity M_γ of the emitted gamma rays and neutrons

$$I_R = \frac{T}{\eta(M_\gamma, E_\gamma)}. \quad (1)$$

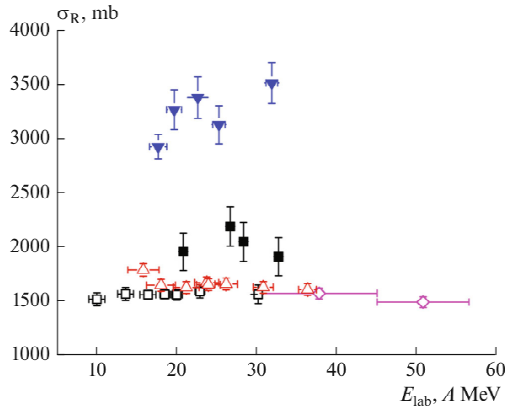


Fig. 2. Total cross sections of the reactions of ${}^9\text{Li}$ nuclei on ${}^{28}\text{Si}$ (empty triangles), ${}^{59}\text{Co}$ (solid squares), and ${}^{181}\text{Ta}$ (solid triangles) targets obtained in our recent work [13], compared to the total cross section of the ${}^7\text{Li} + {}^{28}\text{Si}$ reaction obtained in our previous work [4] (empty squares) and work of R. E. Warner [14] (diamonds). Figure originally published in [13]

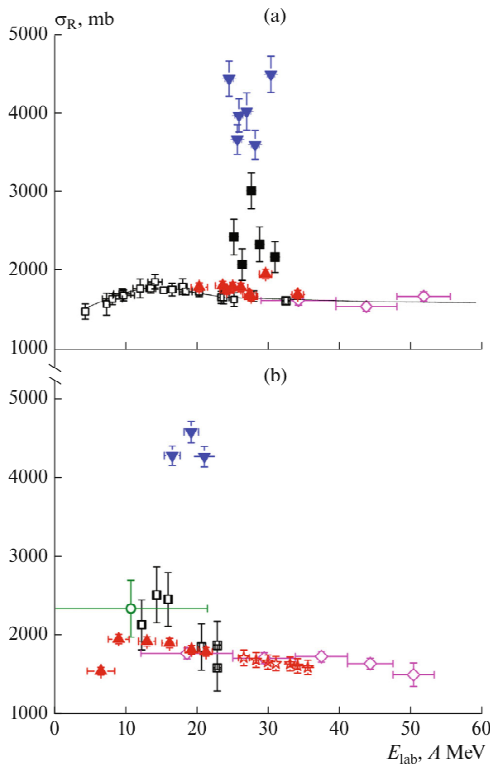


Fig. 3: (a) Total cross sections of reactions ${}^6\text{He} + {}^{28}\text{Si}$ (upright triangles), ${}^6\text{He} + {}^{59}\text{Co}$ (solid squares), and ${}^6\text{He} + {}^{181}\text{Ta}$ (inverted triangles) obtained in our recent work [13], compared to the results of the ${}^6\text{He} + {}^{28}\text{Si}$ reaction obtained in our previous work [4] (empty squares) and [14] (diamonds) (b) Total cross sections of the reactions ${}^8\text{He} + {}^{28}\text{Si}$ (upright triangles) and ${}^8\text{He} + {}^{181}\text{Ta}$ (inverted triangles) from our recent work [13], compared to the results of ${}^8\text{He} + {}^{28}\text{Si}$ reaction obtained in our previous work [15] (empty squares) and works [14] (diamonds), [3] (circle), and [16] (stars). Figure originally published in [13].

The total reaction cross section, σ_R , is determined as

$$\sigma_R = \frac{I_R}{NI_0}. \quad (2)$$

Detailed procedure of σ_R evaluation, taking into account measurement of background events, is described in [11]. Energy dependence of the total reaction cross section for the projectile ${}^7\text{Li}$ with ${}^{28}\text{Si}$, ${}^{59}\text{Co}$, and ${}^{181}\text{Ta}$ targets is shown in fig. 2 and for the projectiles ${}^6,8\text{He}$ with the same targets in fig. 3(a) and 3(b), respectively. Previous results were subject to theoretical analysis with optical model calculations, whose real part was obtained by a double-folding procedure [5]. However, it succeeded to describe only the high-energy regions of measured σ_R energy dependencies. The low-energy region (10 – 20 A MeV), where the rise above theoretical predictions was obtained, was successfully described by the time-dependent Schrödinger approach. Results are published only for reaction ${}^{11}\text{Li} + {}^{28}\text{Si}$ [11].

CONCLUSIONS

A spectrometer for direct measurement of the total reaction cross section with radioactive beams was described. Results for the reactions of ${}^6,8\text{He}$ and ${}^9,11\text{Li}$ projectiles with ${}^{28}\text{Si}$, ${}^{59}\text{Co}$ with ${}^{181}\text{Ta}$ targets were presented. Results show good agreement with our previous measurements and works of other authors.

ACKNOWLEDGMENT: This research work was supported by the Joint grant of JINR and Czech Republic “3+3” (2020), p. 47: “Development of the MULTI-purpose spectrometer” and the Grant of the Plenipotentiary of the Government of the Czech Republic in JINR (2020), p. 24: “Total cross section study in reaction with exotic nuclei by MULTI setup”.

REFERENCES

1. Yu. E. Penionzhkevich, Phys. At. Nucl. **74**, 1615 (2011).
2. R. F. Carlson, Nucl. Instr. Meth. **123**, 509 (1975).
3. A. C. C. Villari et al., Phys. Lett. B **268**, 345 (1991).
4. Yu. G. Sobolev et al., Bull. Russ. Acad. Sci.: Phys. **67**, 1603 (2005).
5. K. V. Lukyanov et al., J. Phys. Conf. Ser. **1023**, 012026 (2018).
6. V. V. Samarin et al., Nuovo Cimento C **42**, 105/1-4 (2019).
7. Yu. G. Sobolev, Inst. Exp. Tech. **55**, 618 (2012).
8. I. Sivacek, Nucl. Instr. Meth. A **976**, 164255 (2020).
9. I. Sivacek et al., p. 444 of Exon-2018: Proceedings of the International Symposium on Exotic Nuclei (World Scientific, ISBN 9811209448).
10. L. V. Grigorenko et al., Phys. Usp. **59**, 321 (2016).
11. Yu. E. Penionzhkevich et al., Phys. Rev. C **99**, 014609 (2019).
12. Yu. E. Penionzhkevich et al., p. 94 of Exon-2018: Proceedings of the International Symposium on Exotic Nuclei (World Scientific, ISBN 9811209448).
13. Yu. G. Sobolev et al., Bull. Russ. Acad. Sci.: Phys. **84**, 948 (2020).
14. R. E. Warner et al., Phys. Rev. C **54**, 1700 (1996).
15. Yu. G. Sobolev et al., Bull. Russ. Acad. Sci.: Phys. **83**, 402 (2019).
16. M. G. Saint-Laurent et al., Z. Phys. A – Atom. Nucl. **332**, 457 (1989).

PRESSURE INDUCED SUPERCONDUCTIVITY IN A CeRhSi₃ SINGLE CRYSTAL – THE HIGH PRESSURE STUDY

D. Staško¹, J. Valenta^{1,2}, M. Kratochvílová¹, J. Prchal¹, P. Proschek¹, M. Klicpera¹

¹Charles University, Faculty of Mathematics and Physics, Department of Condensed Matter Physics, Ke Karlovu 5, 12116 Prague 2, Czech Republic

²National Institute for Materials Science, Thermal Energy Materials Group, International Center for Materials Nanoarchitectonics (MANA), 1-2-1, Sengen, Tsukuba, Ibaraki 305-0047, Japan

INTRODUCTION

Ce-based intermetallic compounds frequently exhibit complex magnetic and transport properties connected to a single electron localized at 4f-level and an interplay among indirect exchange interactions, Kondo screening, spin-orbit coupling, and crystal electrical field (CEF). CeRhSi₃, the subject of present study (with a tetragonal structure of the BaNiSn3-type 1 4 m m, no. 107 without an inversion symmetry) orders antiferromagnetically below 1.6 K. Moreover, upon the application of pressure of about 1 GPa, superconductivity (SC) can be induced at low temperatures [1]. Previous high-pressure experiments on CeRhSi₃ were performed utilizing the hybrid-cylinder piston pressure cell with a maximal reachable pressure of 3 GPa. The measurement at pressures higher than 3 GPa was missing, and is the subject of our present study.

EXPERIMENTAL METHODS

CeRhSi₃ single crystals were grown by the Sn-tri-flux method. With dimensions not bigger than 1 mm, these small crystals are convenient to use in pressure cells, and can be also perfectly oriented thanks to their clearly distinguishable facets. EDX measurements confirmed desirable composition and stoichiometry, Laue diffraction was employed to orient the crystals. Temperature dependencies of electrical resistivity and specific heat at ambient pressure are in agreement with the previous results [1, 2].

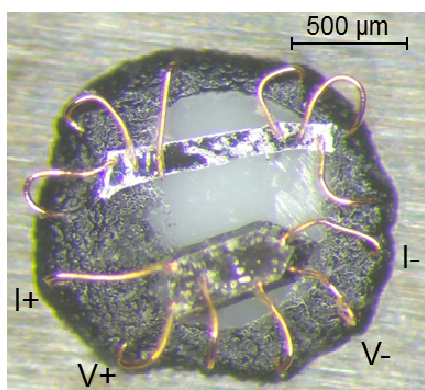


Fig. 1. top view of the experimental montage of CeRhSi₃ (bottom) and lead (top) within the sample space of the Bridgman anvil cell.

Bridgman anvil cell (BAC) and a liquid pressure transmitting medium, Daphne Oil 7373, were used for the high-pressure experiment. With a theoretical limit of

6 GPa, this pressure cell was employed to measure resistivity with the AC four probe method (see Fig. 1.). Pressure was determined with the superconducting transition of lead at low temperatures. The experiment was conducted at temperatures down to 0.3 K and in magnetic fields up to 19 T employing '20 T & 30mK' system, Cryogenic Limited.

RESULTS AND DISCUSSION

Firstly, let us focus on the results from non-magnetic measurements. In Fig. 2., we can see that CeRhSi₃ at pressure 0.3 GPa orders antiferromagnetically at 1.65 K, with a pronounced kink at the Néel temperature T_N , similarly as at ambient pressure. At 1.1 GPa, T_N is shifted to higher temperature (2 K), while the first signs of the forming SC transition can be seen at the lowest temperatures. At 1.8 GPa, a broad SC transition is observed, which becomes very sharp at 2.4 GPa. Between pressures 2.4 and 3.0 GPa,

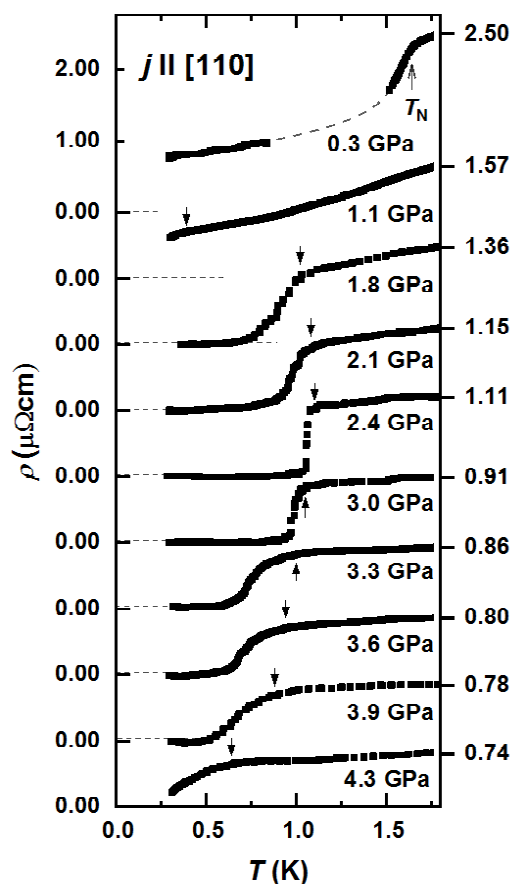


Fig. 2. Electrical resistivity data with pronounced magnetic and superconducting transitions under applied pressure. The arrows indicate T_c , except the arrow for 0.3 GPa marking T_N .

critical temperature reaches a maximum of 1.1 K, forming a plateau (see Fig. 3.). Continuing at 3.0 GPa, further application of pressure continuously suppresses the SC transition to lower temperatures. Moreover, SC transition has a tendency to broaden in the highest pressures. This can be partly attributed to the non-hydrostatic pressure conditions which arise after the pressure medium solidifies at 2.2 GPa. Nevertheless, measurements below 2.2 GPa exhibit broad transitions too, which is connected to the behaviour of the unconventional superconductivity. Based on how severely was the SC transition suppressed at 4.3 GPa and the overall behaviour of the superconducting-paramagnetic (SC-PM) phase border, we expect that the SC dome closes completely between pressures 4.5 and 5.0 GPa.

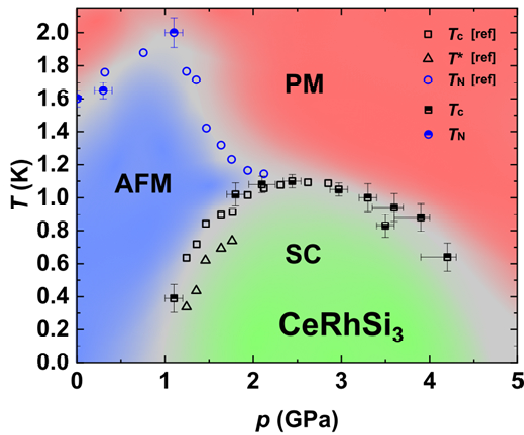


Fig. 3. T - p phase diagram of pressure induced SC in CeRhSi_3 . The data collected employing first (upper-part-filled symbols) and second pressure cell (bottom-part-filled symbols) are summarized in the plot. The data adopted from Ref. [2] were measured with $j \parallel [100]$ and are shown as empty symbols.

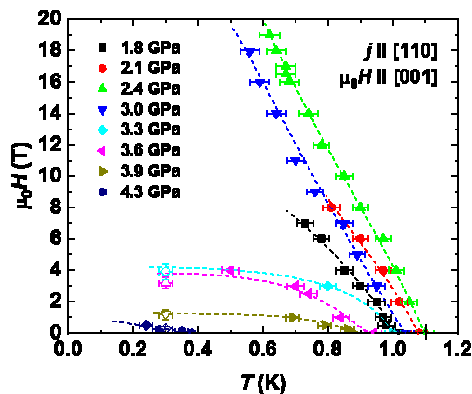


Fig. 4. H - T phase diagram constructed from T (full symbol) and $\mu_0 H$ (open symbols) dependencies of the electrical resistivity under pressure. The lines are guide to the eye.

At every applied pressure, temperature dependencies of electrical resistivity were measured at constant magnetic fields. As expected, the SC transition was pushed to lower temperatures with larger applied magnetic field. Moreover, magnetoresistance measurements were done at lowest achieved temperature

0.3 K. Results from both types of measurements are presented in Fig. 4, forming a H - T phase diagram. Critical field increased rapidly with the emergence of SC and reached huge values at the pressure plateau between 2.4 and 3.0 GPa. Indeed, the SC phase is very robust at these two pressures, with a critical field exceeding 19 T above 0.6 K, which is in agreement with the previous results with magnetic field applied along the c -axis [3, 4]. Interestingly, critical field is much lower (not exceeding 8 T down to 0.1 K) with magnetic field applied along the a -axis, which was attributed to the absence of the paramagnetic pair-breaking effect [1, 2, 5]. Further application of pressure beyond 3 GPa results in rapid suppression of the critical field to very small values, compared to the initially slow decrease in critical temperature.

CONCLUSIONS

This study focused on the behaviour of the pressure induced superconductivity in the pressure region above 3 GPa in a heavy-fermion intermetallic compound CeRhSi_3 . After the SC phase reaches maximal critical temperature of 1.1 K between 2.4 and 3.0 GPa, further application of pressure results in a continuous suppression of the SC phase, accompanied by visible broadening of the SC transition. The SC phase is expected to follow a classic dome behaviour, with the complete closing of the dome expected between 4.5 and 5 GPa. Moreover, measurements in magnetic field show that a huge critical field, which exceeds 19T at 0.6 K between 2.4 and 3.0 GPa is rapidly suppressed above 3 GPa.

For more detailed information, please search for the whole article (with the same name) in Journal of Physics: Condensed Matter, as it will be hopefully published in the near future.

ACKNOWLEDGMENT: We thank Petr Čermák for his assistance with ‘20 T & 30mK’ system operation. This work was supported by the Czech Science Foundation under Grant No. 17-04925J. The sample preparation, characterization and high-pressure experiments were performed in MGML (<http://mgml.eu/>), which was supported within the program of Czech Research Infrastructures (project no. LM2018096).

REFERENCES

1. N. Kimura, K. Ito, K. Saitoh, Y. Umeda, H. Aoki, Phys. Rev. Lett. **95**, 247004 (2005).
2. N. Kimura, Y. Muro, H. Aoki, J. Phys. Soc. Jpn. **76**, 051010 (2007).
3. N. Kimura, K. Ito, H. Aoki, S. Uji, T. Terashima, Phys. Rev. Lett. **98**, 197001 (2007).
4. T. Sugawara, N. Kimura, H. Aoki, F. Lévy, I. Sheikin, T. Terashima, J. Phys. Soc. Jpn. **79**, 063701 (2010).
5. T. Sugawara, H. Iida, H. Aoki, N. Kimura, J. Phys. Soc. Jpn. **81**, 054711 (2012).

PHASE DIAGRAMS OF $\text{Ce}_2\text{Pd}_2\text{In}$ INTERMETALLIC COMPOUND

P. Král, petrkrál@karlov.mff.cuni.cz, J. Prchal, prchal@karlov.mff.cuni.cz, M. Klicpera, Mi.Klicpera@seznam.cz, P. Doležal, Petr.Dolezal@mff.cuni.cz, Charles University, Faculty of Mathematics and Physics, Department of Condensed Matter Physics, Ke Karlovu 5, 121 16, Prague 2, Czech Republic, J. Kaštil, kastil@fzu.cz, Institute of Physics, Czech Academy of Sciences, Na Slovance 1999/2, 182 21, Prague 8, Czech Republic

INTRODUCTION

Thanks to the specific electronic structure the rare earth element-based compounds, especially those containing Yb, Ce or Eu, often exhibit exceptional magnetic properties. In our study we have focused on cerium-based $\text{Ce}_2\text{Pd}_2\text{In}$ compound belonging to the family of R_2T_2X compounds crystallizing in tetragonal Mo_2FeB_2 -type structure [1].

Specific magnetic properties of this group of compounds are related to details of crystal structure. The lattice is formed by R -planes alternated by planes containing other elements. The Ce ions lying in basal plane in $\text{Ce}_2\text{Pd}_2\text{In}$ form Ce dimers arranged in a square motif. The Ce-Ce distance in these dimers $d_{\text{Ce-Ce}} = 3.866(2)$ is also the shortest Ce-Ce distance in this compound. Ce-distances are responsible for the character of exchange interactions and the unique way, how to affect them without changes of chemical composition, is application of mechanical pressure.

TEMPERATURE EVOLUTION OF LATTICE

Low temperature X-ray diffraction was employed to investigate the temperature evolution of lattice parameters revealing strongly anisotropic behavior. While the parameter a decreases with decreasing temperature, parameter c is even increasing. The main parameter responsible for the temperature evolution of the unit cell is a -parameter as the temperature impact on the dimensions is approximately three times stronger in this direction compared to c .

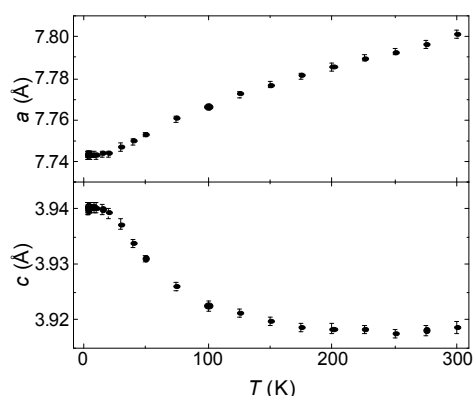


Fig. 1. Temperature evolution of crystal lattice parameters a and c determined from the low temperature X-ray diffraction

EFFECT OF MAGNETIC FIELD

Evolution of temperatures of phase transitions with external magnetic field was investigated for field directions $[001]$ and $[110]$. For field along crystallographic c -axis, the anomalies connected with

transitions are broadened and overlapped already in small magnetic field of ≈ 0.05 T, while for field applied along the basal plane direction $[110]$, the critical temperatures are not affected up to 0.1 T.

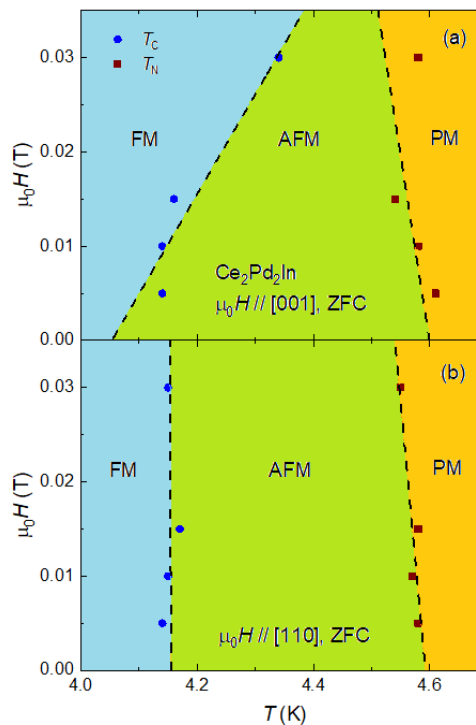


Fig. 2. Magnetic phase diagrams – effect of magnetic field applied along $[001]$ (a) and $[110]$ (b) in zero field cooled regime (ZFC)

PRESSURE EFFECT

Hydrostatic pressure experiments were carried out in two types of pressure cells – double layered (CuBe, NiCrAl) piston pressure cell allowing measurement of electrical resistivity and AC magnetic susceptibility [2] and CuBe hydrostatic pressure cell for magnetization measurement [3]. For application of uniaxial pressure, CuBe uniaxial pressure cell for magnetization measurement was used [4].

Temperatures of phase transitions were found to be sensitive to applied pressure. Hydrostatic pressure leads to systematical suppression of T_C (AFM phase remains down to the lower temperatures), while T_N is almost unaffected by applied pressure. According to the low- T XRD, higher impact on Ce-distances in basal plane, where the AFM interaction prevails (follows from DC magnetic susceptibility measurement in paramagnetic region), can be expected leading to preference of AFM interaction with respect to the FM one. On the contrary to the hydrostatic pressure, the uniaxial one acts on the parameter c showing no significant effect on the temperatures of phase transitions.

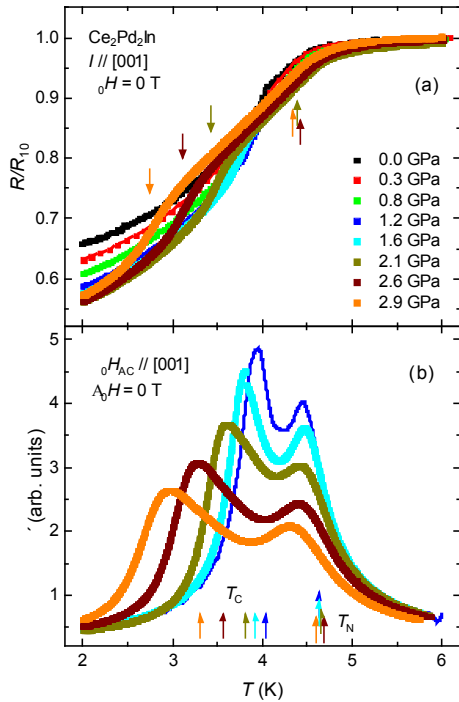


Fig. 3. Hydrostatic pressure effect on anomalies connected with magnetic phase transitions

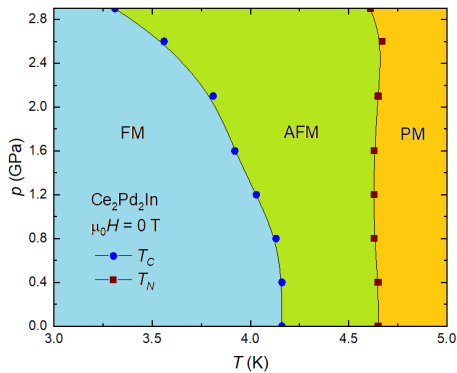


Fig. 4. Effect of hydrostatic pressure on magnetic phases in $\text{Ce}_2\text{Pd}_2\text{In}$

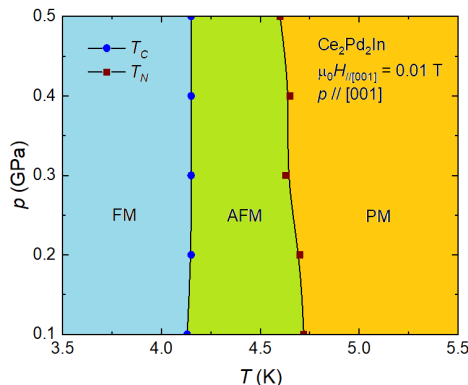


Fig. 5. Effect of uniaxial pressure along [001] on magnetic phases in $\text{Ce}_2\text{Pd}_2\text{In}$

Pressure, both hydrostatic (Fig. 6.) and uniaxial (not shown), leads to suppression of Ce-magnetic moment, probably due to increase of magnetic fluctuations in agreement with observed increase of ρ (2 K) with

increasing the pressure.

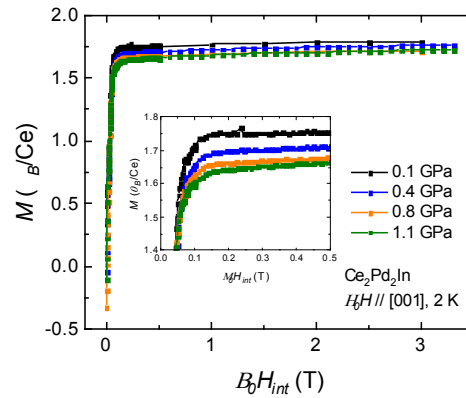


Fig. 6. Suppression of Ce-magnetic moment upon the hydrostatic pressure application

CONCLUSIONS

Temperature evolution of crystal lattice is strongly anisotropic, decreasing of temperature leads to decrease of a -parameter and increase of parameter c . Volume changes are driven mainly by parameter a .

Magnetic transitions of $\text{Ce}_2\text{Pd}_2\text{In}$ are sensitive to external magnetic field and to application of mechanical pressure. Field applied along [001] results in suppression of AFM phase. Hydrostatic pressure is supposed to act more on a -parameter, the atoms in basal plane are getting closer and the AFM interaction is preferred over the FM one. Field along [110] as well as the uniaxial pressure acting in the opposite direction with respect to the hydrostatic one do not affect critical temperatures significantly.

ACKNOWLEDGMENT: Experiments were performed in MGML (www.mgml.eu), which is supported within the program of Czech Research Infrastructures (project no. LM2018096).

REFERENCES

1. M. Klicpera et al., J. Magn. Magn. Mater. **404**, 250 (2016) and refs. therein.
2. N. Fujiwara et al., Rev. Sci. Instrum. **78**, 073905 (2007).
3. J. Kamarád et al., Rev. Sci. Instrum. **75**, 5022 (2004).
4. J. Kamarád et al., High Press Res **28**, 633 (2008).

OPEN DATA OF THE LHC EXPERIMENT ATLAS

J. Chudoba, jiri.chudoba@cern.ch, FZU - Institute of Physics of the Czech Academy of Sciences, Na Slovance 2, 182 21 Praha 8, Czechia

INTRODUCTION

Large Hadron Collider (LHC) [1] is the largest man-made accelerator in the world in terms of the total length (about 27 km) and also the energy of accelerated particles (6.5 GeV for protons in 2018). Four huge detectors record data from particle collisions which are subsequently processed and analysed by thousands of experimentalists. Only members of collaborations which have built and operate those detectors, had access to data and rights to publish scientific results based on these data. Growing demand for FAIR [2] data management principles leads to initiatives to open stored data for general public together with necessary tools and documentation.

ATLAS EXPERIMENT DATA

The ATLAS experiment [3] is one of the four main experiments at LHC. More than 3000 collaborators from 181 institutions from 38 countries has participated in design, construction, operation and data analysis. Data recording frequency and raw event size increase with time and available technology. The experiment was able to select and store 1000 events every second from 40 million collisions per second during the Run 2 data taking period. The typical raw data size is 1 MB. These numbers lead to 57 PB total size of collected raw data.

Two copies of raw data are kept on tapes in geographically distributed data centres to avoid any data loss. The raw data files consume only a fraction of needed space for storage. Several intermediate data formats are produced during reconstruction before the final format suitable for data analysis (currently DAOD – Derived Analysis Data Objects) is reached. These steps decrease the size of event by a factor 10 to 100 depending on the event type. The reconstruction algorithms, which produce information about particle types and tracks from the detector response, are continuously improved and stable new versions are used for reprocessing of all data.

Actual raw data and their derived formats account for only a smaller part of disk space requirements. The comparison of theoretical models to measured properties of collisions is done via events simulated by a Monte Carlo method. Many processes predicted by the Standard Model of elementary particles and by other models are computed to get a simulated detector response and stored in similar formats as the real data. In total, ATLAS managed about 500 PB of data in 2020.

The whole data processing is done in the distributed Tier centres of the Worldwide LHC Computing Grid (WLCG). One of the Tier centres [4] is hosted by the Computing Centre of the Institute of Physics of the CAS with additional resources provided by Nuclear Physics Institute of the CAS and Faculty of Mathematics and Physics of the Charles University. The DAOD files are

distributed to Tier centres in several copies to insure fast response of the whole system.

ATLAS OPEN DATA POLICY

The ATLAS collaboration agreed on policy [5] for open access to ATLAS data by people outside the collaboration. Published Results (Level 1) Policy: Peer-reviewed publications represent the primary scientific output. All such publications are available with Open Access, and so are available to the public. Additional information and data are made public at the time of publication. Outreach and Education (Level 2) Policy: Dedicated subsets of data are used, selected and formatted to provide rich samples and to facilitate the easy use of the data. The data are provided in simplified, portable and self-contained formats. Reconstructed Data (Level 3) Policy: The ATLAS experiment will release calibrated reconstructed data with the level of detail useful for algorithmic, performance and physics studies. The release of these data will be accompanied by provenance metadata, and by a concurrent release of appropriate simulated data samples, software, reproducible example analysis workflows, and documentation. Virtual computing environments that are compatible with the data and software will be made available.

Raw Data (Level 4) Policy: It is not practically possible to make the full raw data-set usable in a meaningful way outside the collaboration. This is due to the complexity of the data, metadata and software, the required knowledge of the detector itself and the methods of reconstruction, the extensive computing resources necessary and the access issues for the enormous volume of data stored in archival media. It should be noted that, for these reasons, general direct access to the raw data is not even available to individuals within the collaboration, and that instead the production of reconstructed data is performed centrally.

ATLAS OPEN DATA FOR OUTREACH AND EDUCATION

ATLAS experiment released first data for education and outreach in xml format in 2012. ROOT [6] data format was used for a release of 1 fb^{-1} in 2016 followed by a release of 10 fb^{-1} data sample from 13 TeV collisions. The data volume of the 13 TeV sample is 28 GB and represents about 270 million of collisions. Corresponding MC simulations are also available. They consist of 120 samples of different processes and occupy 88 GB of disk space, so the all released 13 TeV datasets can be stored on a reasonably modern personal computer.

Several tools for novice users are available for data analyses on the ATLAS Open Data web portal [7]. The easiest start is a JavaScript based histogram analysis,

where students can do event selection via GUI in the web browser. Another possibility is to download an image of a linux virtual machine and run it on a local system (students have usually experience only with Windows 10 or macOS) using VirtualBox. Students with less performant hardware can use publicly available external resources like MyBinder [8] or create virtual machine in the Czech national e-Infrastructure [9]. Although the knowledge of linux commands and bash scripting is an advantage, one can also use prepared Jupyter notebooks [10]. These notebooks can be easily edited and a user get an immediate output to see results from changes. Several examples of the simplified real analyses published by ATLAS can be readily executed. Starting from some minimal knowledge users can gradually built more sophisticated data selection and visualisation.

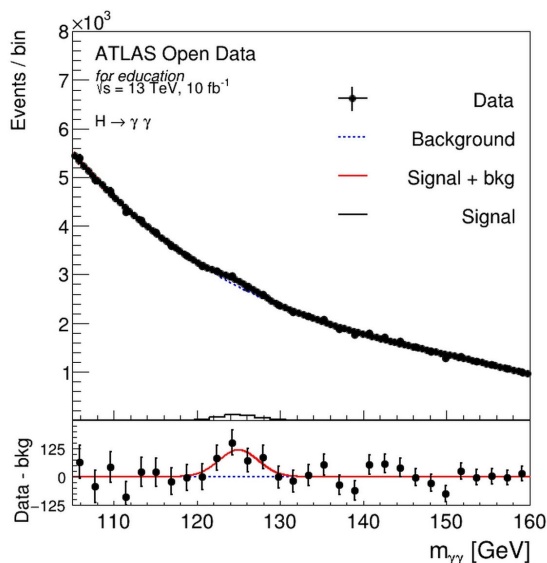


Fig. 1. The output histogram of simplified Higgs to gamma gamma analysis of the ATLAS open data

PROJECT OPEN SCIENCE

The Open Science project [11] is organized by the Centre of Administration and Operations of the Czech Academy of Sciences (CAS) for several years. Secondary school students can apply for a practical training in laboratories of scientist from CAS. They visit institutes at least monthly with a total expected workload 8 hours per month. The work starts in January and culminates in November by presentation of results at a student conference.

A project LHC Data Analysis is a part of Open Science programme since 2017. It attracts many applications, but only maximum three students per year can be involved according the programme rules. Secondary school students had to first learn at least basic terms from particle physics and then get acquainted with suitable tools to be able to understand principles of data processing in high energy physics. They installed software ATLAS@Home on their home computers and participated in a worldwide public effort

to increase simulation capacities for the ATLAS experiment. Via a social network they were able to promote this activity to their fellow students.

Students involved in the Open Science programme gradually tested all tools available on the ATLAS Open Data Portal and helped to give a feedback on usage and suggestions for further improvements.

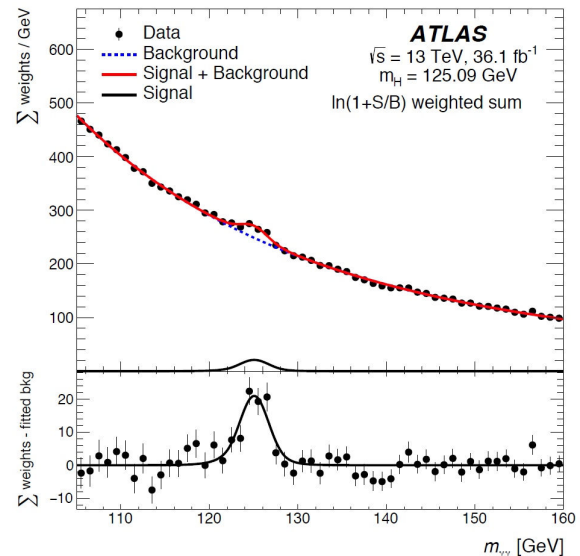


Fig. 2. The published ATLAS result [12] with more than three times more data for a comparison with open data result

CONCLUSIONS

The ATLAS collaboration publicly released several datasets with proton-proton collision events from the LHC together with tools for their analysis. Secondary school students used these tools within the Open Science project.

ACKNOWLEDGMENT: This work was partially supported by the LRI CERN-CZ, project LM2015058.

REFERENCES

1. L. Evans, JINST **3**, S08001 (2008).
2. M. Wilkinson et al., Sci. Data **3**, 160018 (2016).
3. ATLAS Collaboration, JINST **3**, S08003 (2008).
4. D. Adamova et al., Journal of Physics Conf. Ser. **608**, 012035 (2015).
5. ATLAS Collaboration, ATL-CB-PUB-2015-001 (2015).
6. R. Brun, F. Rademakers, Nucl. Instrum. Meth. **A389**, 81 (1997).
7. ATLAS Open Data Portal, <http://opendata.atlas.cern/>
8. Binder, <http://mybinder.org>
9. MetaCentrum Cloud, <https://cloud.metacentrum.cz/>
10. Jupyter Notebook, <https://jupyter.org/>
11. Otevřená věda, <http://www.otevrenaveda.cz/>
12. ATLAS Collaboration, Phys. Rev. **D98**, 052005 (2018).

UHECR ACCELERATION CAPABILITIES OF THE NEARBY SUPERMASSIVE BLACK HOLES

A. Tursunov, arman.tursunov@physics.slu.cz, M. Kološ, Z. Stuchlík, Research Centre for Theoretical Physics and Astrophysics, Institute of Physics, Silesian University in Opava, Bezručovo nám. 13, CZ-74601 Opava, Czech Republic.

INTRODUCTION

The origin and acceleration mechanism of ultra-high-energy cosmic rays (UHECRs) with energy exceeding the GZK-cutoff remain unknown. It is often speculated that supermassive black holes (SMBHs) located at the centers of many galaxies can serve as possible sources of UHECRs. This is also supported by recent detections of high-energy neutrinos from blazar, as neutrinos are the tracers of UHECRs. In this contribution we explore the capabilities of some SMBHs to accelerate UHECR protons of certain energies by the induced electric field generated due to frame-dragging effect of twisting of magnetic field lines near horizon of rotating SMBHs. In particular, we study the ionization of freely-falling neutral particles, such as the hydrogen ionization or neutron beta-decay in the vicinity of SMBHs immersed into external magnetic field and calculate the energies of escaping protons after the ionization. We choose 25 nearby SMBH candidates (within 100 Mpc) with measured and estimated masses, spins and magnetic fields, for which we present a table with mean proton energy and explore their acceleration capabilities.

Energy of charged particles in ultra-high-energy cosmic rays (UHECRs) may exceed 10^{20} eV with constituents dominated by protons at lower energies towards mixed compositions at higher energies [1, 2]. Anisotropy studies in arrival directions of primary cosmic rays clearly indicate the extragalactic origin of UHECRs at energies $> 10^{18}$ eV [3, 4]. All-particle energy spectrum exhibits the existence of two knees at $10^{15.5}$ eV and $10^{17.5}$ eV with significant lowering of flux and ankle starting at around $10^{18.5}$ eV with flattening in the spectrum. Though several studies suggested extragalactic origin of cosmic rays with energy exceeding $10^{15.5}$ eV, the origin of cosmic rays with energies between knee and ankle remains under debate. At high energies (exceeding $\sim 10^{19.5}$ eV for protons), the maximum energy of primary cosmic rays is bounded if the propagation distance from the origin is greater than ~ 100 Mpc [5]. This limit known as the GZK-cutoff [6, 7] arises due to interaction of charged particles with cosmic microwave background photons and may slightly vary depending on the particle's type. Detection of UHECRs at energies greater than GZK-cutoff limit in both northern and southern hemispheres may imply the necessity of search of powerful extragalactic accelerators within the distance < 100 Mpc from the Solar system. There have been many attempts to explain the origin of highest-energy cosmic rays. Several exotic scenarios have been proposed [8, 9]. Among astrophysical scenarios one can mention shock acceleration in relativistic jets [10]. Recently, another acceleration scenario has been suggested [11], which attempted to explain UHECRs by the ionization of the neutral matter in the vicinity of magnetized SMBHs.

In this scenario, the energy of cosmic rays comes in expense of rotational energy of SMBH. In this paper, we apply this model for 25 selected nearby SMBH candidates in order to investigate their UHECR acceleration capabilities.

ULTRA-EFFICIENT ENERGY EXTRACTION FROM ROTATING BLACK HOLE

Multiwavelength and multimessenger observations related to both stellar mass and supermassive black hole candidates show no convincing indication of any deviation of the spacetime around these objects from rotating Kerr black hole spacetime, so that it is widely accepted that any astrophysical black hole can be well described by only two parameters, its mass M and spin a . Supermassive black holes are also the largest energy reservoirs in the Universe with up to 29% of their total energy being the rotational energy, therefore, available for extraction [14]. For example, for SMBH with mass of $M = 10^8 M_\odot$ and average dimensionless spin of $a = 0.5$, the rotational energy available for extraction is of the order of 10^{73} eV. This puts a question: how to extract this tremendous energy in the most efficient way?

Roger Penrose in 1969 pointed out [15] the possibility of test particle moving inside the ergosphere of rotating Kerr black hole to have negative energy with respect to a static observer at infinity, while locally measured energy would remain positive. Using this fact Penrose proposed the first mechanism of the energy extraction from rotating black holes by the fragmentation of a freely falling particle inside the ergosphere into two particles. If one of the fragments attains negative energy, eventually falling into black hole, another one may come out from the ergosphere with energy exceeding the energy of mother particle. Infall of negative energy into black hole is equivalent to the extraction of black hole's rotational energy. Efficiency of Penrose process (defined as the ratio of gained and input energies) was, however, limited to maximum of 21%. In mid 1980's, the magnetic Penrose process (MPP) has been formulated [16, 17, 18] with interacting particles being charged and black hole immersed into external electromagnetic field. It was shown that the efficiency of this process can exceed 100% due to interaction of charged particles with magnetic field surrounding black hole. Recently, it was shown [11, 19, 20] that MPP works in three regimes of efficiencies, namely, low, moderate and ultra. In the latter case, the efficiency can be as large as $10^{13}\%$ when applied to typical SMBHs, allowing the direct application of this mechanism for the explanation of UHECRs.

Here a freely falling neutral particle is supposed to be ionized in vicinity of rotating black hole in the presence of external magnetic field. Twisting of magnetic field lines due to black hole's rotation generates electric field components, which can be associated with an elec-

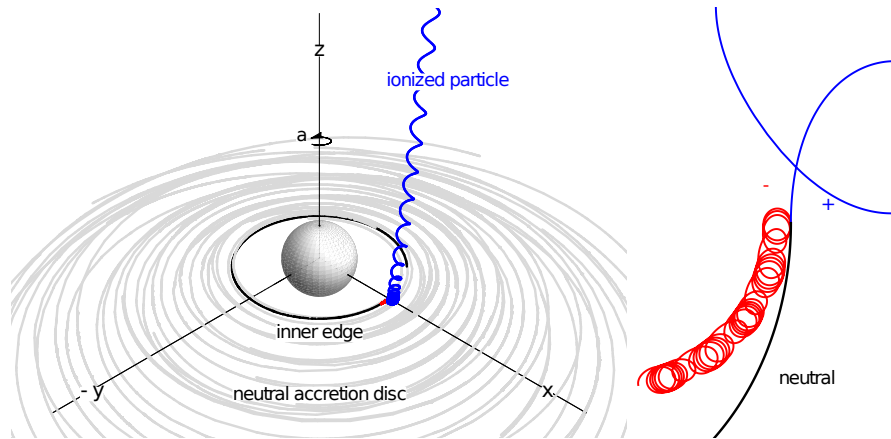


Fig. 1. Numerical modelling of the ionization of initially neutral particle (thick grey) falling from the inner edge of Keplerian accretion disk onto rotating black hole and resulting escape of positively charged particle (blue curve). Negatively charged fragment after ionization (red) collapses into black hole. The escaping particle after ionization is more likely a positively charged particle due to the presence of more likely positive induced charge of black hole produced by twisting of magnetic field lines [11, 12, 13]. Right subfigure is zoomed ionization region.

tric charge of the black hole [13, 21, 22]. Neutral particle is able to reach arbitrarily close to the event horizon without influence of electromagnetic field, hence the ionization process may occur very close to black hole. Therefore, charged fragment after ionization of the neutral particle would have very strong Coloumbic contribution to the energy in addition to gravitational negative energy in ergosphere. On the other hand, charged particles in a plasma (without ionization) are not able to gain Coloumbic contribution.

ELECTROMAGNETIC FIELD PROPERTIES AROUND BLACK HOLE

In the black hole vicinity, where the gravity plays a leading role, one can use natural assumption of stationarity and axial symmetry of external magnetic field that is sharing the background symmetries of the Kerr metric spacetime. This assumption is relevant for magnetic field of any origin, which has a strength satisfying the condition $B \ll 10^{18}\text{G}$ for stellar mass black holes and $B \ll 10^{11}$ for SMBHs [23]. In realistic cases, typical strength of magnetic field for stellar mass black holes vary from few Gauss up to 10^8G , while for SMBH it is of the order of 10^4G [24, 25]. Therefore, independently from the shapes of magnetic field lines, any astrophysical magnetic field can be considered as a weak test field. However, as we show below, the effect of magnetic field on the motion of charged particles is crucially important. For the sake of simplicity we choose the magnetic field to be asymptotically homogeneous with the strength B . In this case, known as the Wald solution [12], the nonvanishing components of the four-vector potential of electromagnetic field take the following form

$$A_t = \frac{B}{2}(g_{t\phi} + 2ag_{tt}) - \frac{Q}{2}g_{tt}, \quad (1)$$

$$A_\phi = \frac{B}{2}(g_{\phi\phi} + 2ag_{t\phi}) - \frac{Q}{2}g_{t\phi}. \quad (2)$$

Assumption of the axial symmetry eliminates remain-

ing two components of the electromagnetic potential $A_r = A_\theta = 0$. Here, Q denotes the electric charge of the black hole that is not necessarily zero in realistic situations. The charge of black hole arises due to frame-dragging effect of twisting of magnetic field lines that leads to the non-zero potential difference between the event horizon and infinity. This causes a selective accretion into BH until the electric potential in a local frame is neutralized, i.e. when $A^t = 0$. The covariant components of A_μ at the final stage of the selective accretion have the following form

$$A_t = \frac{B}{2}g_{t\phi}, \quad A_\phi = \frac{B}{2}g_{\phi\phi}. \quad (3)$$

At this stage the black hole accretes the net charge that is equal to $Q_W = 2aMB$, which is known as the induced Wald charge [12]. Timescale of selective accretion is extremely short for astrophysical black holes, therefore, the most plausible scenario is the one with the induced BH charge. Note, that induced charge (different from Q_W) also arises in any other axially symmetric magnetic field configuration different from uniformity. Therefore, one can conclude that any astrophysical black hole candidate possesses non-zero electric charge that is gravitationally weak, however its effect on the charged particles cannot be neglected [13, 26].

IONIZATION PROCESS IN BLACK HOLE VICINITY

Symmetries of Kerr metric imply allows one to find two conserved quantities, which are the components of the canonical four-momentum $P_\mu = mu_\mu + qA_\mu$:

$$E = -P_t = mu_t + qA_t, \quad (4)$$

$$L = P_\phi = mu_\phi + qA_\phi, \quad (5)$$

where m , q and u^μ are particle's mass, charge and four-velocity. Dynamics of charged particles around Kerr black hole in presence of magnetic field has been widely

studied in past; we mention some of them: [23, 27, 28, 29].

Let us now consider split of a particle (A), into two charged fragments (B) and (C) in the black hole ergosphere at the equatorial plane. The conservation laws before and after split can be written in the form

$$E_A = E_B + E_C, \quad (6)$$

$$L_A = L_B + L_C, \quad (7)$$

$$q_A = q_B + q_C, \quad (8)$$

$$m_A \geq m_B + m_C, \quad (9)$$

$$m_A \dot{r}_A = m_B \dot{r}_B + m_C \dot{r}_C, \quad (10)$$

$$m_A \dot{\theta}_A = m_B \dot{\theta}_B + m_C \dot{\theta}_C, \quad (11)$$

where dots denote derivative with respect to the proper time. If one of the particles after split, e.g. particle (B), attains negative energy, the particle (C) comes out with energy exceeding the energy of incident particle (A) in expense of rotational energy of the black hole.

Skipping routine calculations that can be found in [19], we focus on the conditions, for which the energy extraction efficiency grows ultra high. We fix the plane of the motion of the incident particle A to the equatorial plane $\theta = \pi/2$ and assume that the particle A is neutral, splitting into two charged fragments. Defining the efficiency as the ratio between gain and input energies, $\eta = (E_C - E_A)/E_A = -E_B/E_A$, we solve the equations (6) - (11) with respect to E_C and find the following expression for efficiency of energy extraction in ultra regime

$$\eta_{\text{BH}} = \frac{M}{\sqrt{2}a} \left[1 - \left(1 - \frac{a^2}{M^2} \right)^{\frac{1}{2}} \right]^{\frac{1}{2}} - \frac{1}{2} + \frac{q_3}{m_1} A_t. \quad (12)$$

The first two terms on the right hand side of Eq.(12) are independent from electromagnetic field, being purely geometrical. The largest contribution from these two terms is 0.21 for extremal Kerr black hole. Due to large factor of q/m for protons and ions, the leading contribution to the efficiency (12) is the third term on the right hand side of this equation. Therefore, in realistic situations, one can justifiably rewrite Eq.(12) in the following simple form

$$\eta_{\text{BH}} \approx \frac{q_C}{m_A} A_t^{\text{ion}}, \quad (13)$$

where A_t^{ion} as the function of the distance r , should be calculated at the ionization point of the incident neutral particle A. Energy of escaping particle (C) is then, given by

$$E_C = (\eta_{\text{BH}} + 1) E_A \approx \frac{q_C}{m_A} A_t^{\text{ion}} E_A, \quad (14)$$

which can grow ultra-high as we show below.

ENERGY OF IONIZED PARTICLE ACCELERATED BY BLACK HOLE

In general, magnetic field has complicated structure in vicinity of the horizon, however in a small fraction of a space where split occurs one can consider the field to

be approximately uniform. In this case, using Eqs.(3) one can find the expression for the efficiency in the following form

$$\eta_{\text{ultra}} \approx \frac{q_C B a r_g}{2m_A c^2} \left(1 - \frac{r_g}{2r_{\text{ion}}} \right), \quad (15)$$

where r_{ion} is the ionization point (splitting point) of the neutral particle and $r_g = 2GM/c^2$ is the gravitational radius of a black hole. For the ionization of neutral hydrogen atom with energy $E = m_H c^2 \sim 10^9$ eV, we obtain the following estimate of the energy of escaping proton

$$E_{p^+} \approx 2 \times 10^{20} \text{eV} \frac{q_C}{e} \frac{m_{p^+}}{m_A} \frac{B}{10^4 \text{G}} \frac{M}{10^9 M_\odot} \frac{a}{0.8}. \quad (16)$$

Similar estimate is obtained for the neutron beta decay $n^0 \rightarrow p^+ + e^- + \bar{\nu}_e$. Thus, the model predicts the energy of proton E_p exceeding 10^{20} eV for typical SMBH of mass $M \sim 10^9 M_\odot$ and magnetic field $B \sim 10^4 G$. Here, we take decay point at $r_{\text{ion}} = r_g$, i.e. far enough from the event horizon, so that the proton is able to escape from the inner region of SMBH. A schematic view of the process is illustrated in Figure 1, where we depict results of numerical modelling of the ionization of neutral particle presented in [11]. Trajectory of escaping high-energy particle after ionization of freely falling neutral particle from the accretion disk is indicated by blue colour. It is important to note, that escaping particle after ionization or neutron beta-decay is more likely a proton in the astrophysically favourable cases. This is due to the reason that the Wald charge (or any black hole charge produced by twisting of magnetic field lines) is more likely to be positive in realistic cases [13, 12].

MEAN PROTON ENERGY FOR SELECTED NEARBY SMBH CANDIDATES

According to the Standard Model of particle physics, there exists an upper bound on the propagation distance of UHECR protons for a given energy due to collisions with photons of the cosmic microwave background (CMB). This limit called the GZK-cutoff [6, 7] predicts the maximum distance for protons that are able to reach the Earth to $< 100 \text{Mpc}$ [5]. The maximum energy of protons reaching our Galaxy from longer distances in this process is limited to about 5×10^{19} eV. Detection of UHECR events with energies greater than GZK-cutoff limit leaves open questions on the origin, propagation and composition of cosmic rays at the highest energies. If UHECRs are constituted by heavier nucleons, interaction of high-energy ions with intergalactic radiation leads to excitation of nuclei and their photodisintegration and fragmentation up to protons and neutrons due to internal resonances if the energy of nucleus is about 10^{20} eV. This implies the importance of GZK and photodisintegration phenomena in the propagation of UHECRs.

Being electrically charged, UHECRs inevitably interact with magnetic fields both in the acceleration zone and after leaving it along the propagation. Although suppression of energy due to synchrotron radiation in a Galactic and intergalactic magnetic fields is

TAB. 1. A list of 25 selected nearby SMBH candidates with measured mass M and distance d , estimated spin a and magnetic field strength B and predicted mean energy of proton E_{p+}^{mean} escaping from corresponding source after the process of ionization of neutral particle in the vicinity of SMBH.

SMBH	$\text{Log}(M/M_{\odot})$	Spin a	d (Mpc)	$\text{Log}(B/1\text{G})$	$\text{Log}(E_{p+}^{\text{mean}}/1\text{eV})$
Sgr A*	6.63	0.5	0.008	2	15.64
NGC 1052	8.19	$\lesssim 1$	19	4.8	20.11
NGC 1068 / M77	6.9	$\lesssim 1$	15	4.54	18.56
NGC 1365	6.3	$\lesssim 1$	17.2	4.70	18.12
NGC 2273	6.9	0.97	29	4.58	18.41
NGC 2787	7.6	$\lesssim 1$	8	3.73	18.45
NGC 3079	6.4	$\lesssim 1$	22	4.06	17.58
NGC 3516	7.4	0.64	42	4.88	19.37
NGC 3783	7.5	0.98	41	4.15	18.77
NGC 3998	8.9	0.54	15	3.58	19.52
NGC 4151	7.8	0.84	14	4.6	19.53
NGC 4258 / M106	7.6	0.38	8	4.14	18.65
NGC 4261	8.7	$\lesssim 1$	32	3.51	19.33
NGC 4374 / M84	9	0.98	20	3	19.12
NGC 4388	6.9	0.51	18	5.19	19.11
NGC 4486 / M87	9.7	$\lesssim 1$	17	2.84	19.66
NGC 4579	8	0.82	18	4.11	19.23
NGC 4594	8.8	0.6	11	3.18	19.05
NGC 5033	7.2	0.68	20	4.47	18.77
NGC 5194 / M51	6.0	0.57	8	4.51	17.57
MCG-6-30-15	7.3	0.98	33	4.74	19.16
NGC 5548	7.8	0.58	75	4.48	19.34
NGC 6251	8.8	$\lesssim 1$	102	3.70	19.62
NGC 6500	8.6	$\lesssim 1$	43	3.60	19.32
IC 1459	9.4	$\lesssim 1$	31	3.20	19.72

relatively small, UHECRs can lose sufficient amount of their energies in the source regions where magnetic fields can be considerably large. For ultra-relativistic particle with charge q and mass m the timescale of synchrotron loss is given by [28]

$$\tau_{\text{syn}} \approx \frac{3m^3c^5}{q^4B^2f(r)}, \quad f(r) = 1 - \frac{2GM}{rc^2}. \quad (17)$$

Note, that cubic dependence of the synchrotron timescale (17) on the particle's mass implies that electrons lose their energy $\sim 10^{10}$ times faster than protons. Characteristic timescale of synchrotron energy loss for high-energy electrons propagating in a magnetic field of 10^4G strength is of the order of $\sim 1\text{s}$, against similar timescale for protons, that is $\sim 10^{10}\text{s}$.

Taking into account GZK, photodisintegration and synchrotron energy loss mechanisms, one could arrive at the conclusion that the highest energy cosmic rays have their local sources. In the table 1 we present a list of 25 nearby SMBHs located within the distance of 100Mpc with the predicted mean values of ultra-high-energy proton for each source produced in the ionization processes. We assume pure proton acceleration within above discussed model. We emphasize that it is not an exhaustive list, but intended mainly to bring an idea on capability of SMBH candidates with the state of the art measurements of masses, spins and magnetic fields to produce the highest energy cosmic particles. The masses M and distances d in table 1 are

based on the observations and direct measurements, while spin a and magnetic field B estimates are obtained by well-established methods based on the measurements of luminosities, spectra and polarimetric parameters of the sources. These data are taken from [24, 25, 30, 31, 32, 33]. Last column on the right demonstrates predicted mean energies of protons E_{p+}^{mean} .

CONCLUSIONS

In this paper we studied the energy transfer from nearby rotating SMBHs to UHECRs in the process of ionization of neutral particles skirting close to black holes. Rotation of a black hole in external magnetic field gives a rise to an induced electric field due to frame-dragging effect and subsequent net charging of the black hole. Since this charge is induced by the black hole rotation, its discharge is equivalent to the extraction of rotational energy of the black hole. The best efficiency of energy extraction can be achieved in the processes involving ionization of neutral matter at the event horizon scales, in which the ionized particle in addition to its mass energy obtains also the Coulombic contribution due to interaction with an electric charge of the black hole. Due to certain alignment of the magnetic field lines produced by the co-rotating plasma it is more plausible that the induced black hole charge is positive, which accelerates protons and ions to ultra-high energies along the symmetry axis. Other frag-

ments, the electrons eventually collapse into the black hole decreasing thus, the black hole's angular momentum.

We have selected 25 nearby SMBH candidates located within 100 Mpc distance with estimated masses, spins and magnetic fields in their vicinities. Calculating the mean proton energy resulting from the ionization, we presented results in a table 1. Although the presented list of sources is far from being complete, we found several plausible candidates for UHECR sources at energies greater than GZK-limit. We also applied our model to Sgr A* located at the center of our Galaxy, which is far the best known SMBH candidate. Remarkably, we found that Sgr A* can serve as a PeVatron with proton energy at the level of 5×10^{15} eV. This implies that the Galactic centre can potentially contribute to the sharpness of the knee of the cosmic ray spectrum. One can also note that the model predicts similar orders of magnitudes of energies of accelerated protons for selected SMBH candidates, which have different masses, locations and magnetic field estimates. The mean proton energy averaged over all selected extragalactic sources appears to be around 10^{19} eV. Existence of many sources at such energies can be potentially relevant in the interpretation of the ankle of the cosmic ray spectra, though, expected cosmic ray spectrum from particular objects are yet to be determined. We leave these discussions to further studies.

ACKNOWLEDGMENT: A.T. thanks the organizers of 20th Conference of Czech and Slovak Physicists held in Prague from 7th to 10th September 2020. The authors would like to acknowledge to the Research Centre for Theoretical Physics and Astrophysics and Institute of Physics of Silesian University in Opava for institutional support.

REFERENCES

1. R. U. Abbasi et al., *Astropart. Phys.* **64**, 49 (2015).
2. A. Aab et al., *JCAP* **1704** 038 (2017). [Erratum: *JCAP* **1803** E02 (2018)].
3. Pierre Auger Collaboration, *Astrophysical Journal Letters* **853** L29, (2018).
4. R. U. Abbasi and et al., *Astroparticle Physics* **86**, 21 (2017).
5. F. W. Stecker, *Phys. Rev. Lett.* **21**, 1016 (1968).
6. K. Greisen, *Phys. Rev. Lett.* **16**, 748 (1966).
7. G. T. Zatsepin, V. A. Kuzmin, *JETP Lett.* **4**, 78 (1966). [*Pisma Zh. Eksp. Teor. Fiz.* **4**, 114 (1966)].
8. G. Rubtsov, P. Satumin, S. Sibiryakov, *JCAP* **1705**, 049 (2017).
9. P. Bhattacharjee, G. Sigl, *Phys. Rept.* **327**, 109 (2000).
10. R. D. Blandford, *Physica Scripta Volume T* **85**, 191 (2000).
11. A. Tursunov, Z. Stuchlík, M. Kološ, N. Dadhich, B. Ahmedov, *The Astrophysical Journal* **895**, 14 (2020).
12. R. M. Wald, *Phys. Rev. D* **10**, 1680 (1974).
13. M. Zajaček, A. Tursunov, A. Eckart, S. Britzen, *Monthly Notices of the Royal Astronomical Society* **480**, 4408 (2018).
14. D. Christodoulou, R. Ruffini, *Phys. Rev. D* **4**, 3552 (1971).
15. R. Penrose, *Nuovo Cimento Rivista Serie* **1** (1969).
16. S. M. Wagh, S. V. Dhurandhar, N. Dadhich, *The Astrophysical Journal* **290**, 12 (1985).
17. S. Parthasarathy, S. M. Wagh, S. V. Dhurandhar, N. Dadhich, *The Astrophysical Journal* **307**, 38 (1986).
18. M. Bhat, S. Dhurandhar, N. Dadhich, *Journal of Astrophysics and Astronomy* **6**, 85 (1985).
19. A. Tursunov, N. Dadhich, *Universe* **5**, 125 (2019).
20. N. Dadhich, A. Tursunov, B. Ahmedov, Z. Stuchlík, *Monthly Notices of the Royal Astronomical Society* **478**, L89 (2018).
21. J. Levin, D. J. D'Orazio, S. Garcia-Saenz, *Phys. Rev. D* **98**, 123002 (2018).
22. M. Zajacek, A. Tursunov, *The Observatory* **139**, 231 (2019).
23. A. Tursunov, Z. Stuchlík, M. Kološ, *Phys. Rev. D* **93**, 084012 (2016).
24. R. A. Daly, *The Astrophysical Journal* **886**, 37 (2019).
25. M. Yu Piotrovich, A. G. Mikhailov, S. D. Buliga, T. M. Natsvlshvili, *Monthly Notices of the Royal Astronomical Society* **495**, 614 (2020).
26. A. Tursunov, M. Zajaček, A. Eckart, M. Kološ, S. Britzen, Z. Stuchlík, B. Czerny, V. Karas, *The Astrophysical Journal* **897**, 99 (2020).
27. Z. Stuchlík, M. Kološ, *European Physical Journal C* **76**, 32 (2016).
28. A. Tursunov, M. Kološ, Z. Stuchlík, D. V. Gal'tsov, *The Astrophysical Journal* **861**, 2 (2018).
29. Z. Stuchlík, M. Kološ, J. Kovář, P. Slaný, A. Tursunov, *Universe* **6**, 26 (2020).
30. A.-K. Baczkó et al., *Astronomy and Astrophysics* **593**, A47 (2016).
31. A. Eckart et al., *Astronomy and Astrophysics* **537**, A52 (2012).
32. S. S. Doeleman et al., *Science* **338**, 355 (2012).
33. M. Kino, F. Takahara, K. Hada, K. Akiyama, H. Nagai, B. W. Sohn, *The Astrophysical Journal* **803**, 30 (2015).

PLASMALAB@CTU - NEW FACILITIES IN SUPPORT OF FUSION EDUCATION

J. Brotánková, jana.brotankova@fjfi.cvut.cz, FNSPE, Czech Technical University, Prague, Czech Republic, J. Mlynář, jan.mlynar.fjfi.cvut.cz, FNSPE, Czech Technical University, Prague, Czech Republic, Institute of Plasma Physics of the CAS, Prague, Czech Republic, M. Pfeifer, pfeifer@pals.cas.cz, Institute of Plasma Physics of the CAS, Prague, Czech Republic, Institute of Physics of the CAS, Prague, Czech Republic, V. Svoboda, vojtech.svoboda@fjfi.cvut.cz, FNSPE, Czech Technical University, Prague, Czech Republic

JOINT PHD IN FUSION

The joint doctoral programme "High Temperature Plasma Physics and Thermonuclear Fusion" [1], was proposed by Universitait Gent in Belgium and the Czech Technical University in Prague. The agreements were signed by the rectors of the Universities at the beginning of 2020. The students will be admitted by both the Universities. The joint training programme is supervised by international Supervisory Board that consists of lecturers from CTU, Universitait Gent, and external experts. Students must past within their studies at least six months at the partner University or in an institute or in the Participating Institution determined by the partner University. Every student must pass the state doctoral exam and the defence of the doctoral thesis according to the rules of both the Universities.

PLASMALAB@CTU

PlasmaLab@CTU [2] was established primarily as a laboratory to support the Joint doctoral programme. It's also determined to be used for other levels, including Bc and MSc. It consists of four main parts: Plasma, Magnetic and electric fields, Optics, and the GOLEM tokamak [3]. The first three parts are in a new room, while the tokamak is an established experiment which has been included and undergoes upgrades in the scope of the project. The goal of the laboratory is to teach fusion relevant basic physics and technology to the future fusion researchers.

Remote control

PlasmaLab@CTU aims to be a remotely operated laboratory. The GOLEM tokamak is a fully remote device which performs many international schools and campaigns. The new part of the lab follows this trend as much as the hardware and the idea of the experiment allow. Most of the devices is controlled by LAN or USB. Devices like step motors and some power sources are controlled by arduinos and/or Raspberry Pi. Devices with LAN are connected directly to the inner network. Each experiment is controlled by a Raspberry Pi, that controls and communicate with other components.

Plasma

The workspace Plasma includes four experiments: Linear magnetic trap, Paschen curve, Discharge tubes, and Resonance cavity. The trap (fig. 1) will study transmission of microwaves along and across magnetic



Fig. 1. From left: Paschen curve, resonance cavity, probes stand. Right panel: linear magnetic trap.



Fig. 2. From left: iodine tube, tube with variable pressure and one electrode; from top: set of spectral tubes, resonance cavity with plasma.

field which will reach up to 100 mT in the centre of the chamber. Resonance cavity (fig. 1, 2) gives insight into resonators; plasma density can be established by the change of resonant frequencies with and without plasma. The trap, the Paschen and the cavity are fully remotely operated.

Magnetic and electric fields

This workspace includes three experiments. Magnetic stand (fig. 3 right) is in fact a simulation of a feed back system in tokamak, with different geometry. An electric current in a wire generates magnetic field which is measured with a ring of magnetic coils. With changing of the spatial distribution in the (adjusted) wire, phenomena of plasma current measurements are simulated. Electric probes stand (fig. 1) is a test bed for different designs of electrostatic probes. Microwave interferometry (fig. 3 left) consists of two antennas, an interferometer, and teaches basic physics of microwave transmission.

Optics

Optics part of the PlasmaLab include three ba-



Fig. 3. Left: interferometry, right: magnetic stand.

sic experiments and several independent components. The experiments are: Laser spectroscopy, 3D microscope, and sonoluminescence. Apart of those, it posses two spectrometers in visible part of the spectrum, several detectors like a photomultiplier and photo diodes, a bolometric camera etc.

The 3D microscope (fig. 4) is Leica DVM6 which makes 3D pictures from reconstruction of scanned photos with different focal length. The LAS X software can measure parameters like depth, distances or volumes of the surface of the surveyed sample. $2350\times$ magnification shows details down to $0.4\ \mu\text{m}$. The head can be tilted by 60° . Relatively large space between the lens and the table enables observe objects as large as e.g. tiles from a tokamak. This microscope is meant to train material physics, focused on damages caused by plasma-walls interactions.

Laser spectroscopy shows absorption and stimulated emission in rubidium vapors, using a tunable diode laser on 780 nm.

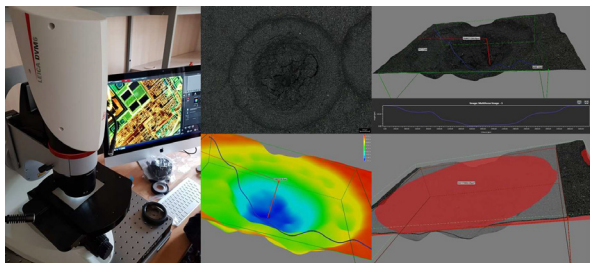


Fig. 4. The microscope with pictures of a 3D processed hole in a carbon target burnt by a laser. The depth is about 1 mm, the volume about $2.5\ \text{mm}^3$.

Common

The vacuum experiments have common vacuum and gas inlet system. Five experiments (Paschen curve, resonance cavity, probes stand, magnetic trap, and discharge tube with variable pressure) are connected to five gas cylinders (He, Ar, Ne, N_2 , air) individually via the common gas inlet system in fig. 5. The board is fully remotely operated. These experiments will be connected to a common vacuum system. The Cube (fig. 5) is an extra vacuum recipient playing a role of a testing bed of various ideas for lab work. It has several ports and a big front door made of acrylic glass.



Fig. 5. Left: the inlet system, right: the Cube.

The GOLEM tokamak

The GOLEM tokamak is the first functional tokamak in the world. The original TM-1-MH from the Kurchatov Institute in Moscow was transported to Prague in 1977 and operated as CASTOR at the Czech Academy of Sciences. In 2007, CASTOR was transported to the FSNPE building, upgraded for fully remote operation, and renamed as GOLEM. Its main deal is to serve as an educational experimental device, but it also has a scientific programme, including Run-away and plasma edge physics studies.

Students in PlasmaLab

First lab works in the new part of PlasmaLab were in the academic year 2019/2020. It was a two semester master lab work, with 6 students. This year, three students are on the same course, and the first Bc student got enrolled.

CONCLUSIONS

A new laboratory for fusion education is being built on the FSNPE CTU in Prague. It consists from the GOLEM tokamak being upgraded, and a brand new part "upstairs" with basic experiments relevant to fusion research, mainly diagnostics, plasma, and vacuum physics. This part is preferentially for PhD students, but serves for all other levels - undergraduates and bachelor. It is being put into operation and first students have enrolled and passed through the lab works. Being a remotely operated laboratory, PlasmaLab has the potential of organizing remote educational campaigns; the GOLEM tokamak is a flagship of these activities.

ACKNOWLEDGMENT: PlasmaLab@CTU received financial support from the project "Laborator horkeho plazmatu a fuzni techniky PlasmaLab@CTU" CZ.02.1.01/0.0/0.0/16 017/0002248.

REFERENCES

1. Joint PhD in fusion [Online] [Cited 15.12.2020] <http://physics.fjfi.cvut.cz/en/academics/joint-phd-in-fusion>.
2. PlasmaLab@CTU [Online] [Cited 15.12.2020] <http://www.plasmalab.cz/>.
3. O. Grover et al., Fusion Eng. Design **112**, 1038 (2016).

ISBN 978-80-89855-13-1
EAN 9788089855131